RADIATIVE FORCING OF THE SOUTHWEST SUMMER MONSOON
(A SATELLITE PERSPECTIVE)

By

Eric A. Smith

Department of Atmospheric Science
Colorado State University
Fort Collins, Colorado

Colorado State University

Department of Atmospheric Science

Paper No. 383

DISSERTATION

RADIATIVE FORCING OF THE SOUTHWEST SUMMER MONSOON

(A SATELLITE PERSPECTIVE)

Submitted by

Eric A. Smith

Department of Atmospheric Science

In partial fulfillment of the requirements

for the Degree of Doctor of Philosophy

Colorado State University

Fort Collins, Colorado

Summer 1984

COLORADO STATE UNIVERSITY

July 3, 19 84

WE HEREBY RECOMMEND THAT THE THESIS PREPARED UNDER OUR SUPERVISION

BY Eric A. Smith

ENTITLED RADIATIVE FORCING OF THE SOUTHWEST SUMMER MONSOON

(A SATELLITE PERSPECTIVE)

BE ACCEPTED AS FULFILLING IN PART REQUIREMENTS FOR THE DEGREE OF

Doctor of Philosophy

Committee on Graduate Work

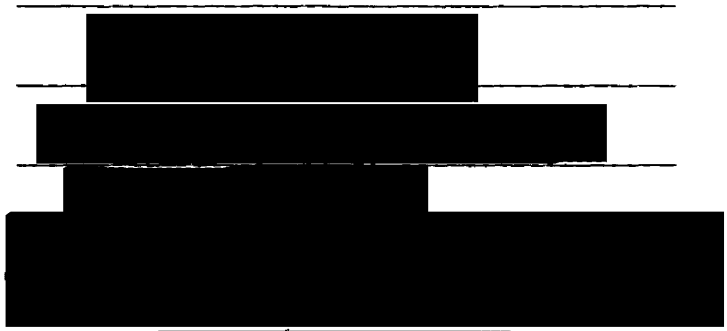

Adviser

Department Head

ABSTRACT OF DISSERTATION

RADIATIVE FORCING OF THE SOUTHWEST SUMMER MONSOON

(A SATELLITE PERSPECTIVE)

This investigation, presented in four parts (Chapters 2-5), examines the nature of radiative forcing within the Southwest Summer Monsoon. A short introduction is provided in Chapter 1.

Chapter 2 explores the problem of converting narrow-field-of-view filtered radiance information, characteristic of operational weather satellite imaging measurements, to estimates of top-of-atmosphere radiation budget parameters. This chapter first provides a discussion of some of the earlier approaches to this problem and their shortcomings. A parameterization approach is then developed which addresses a portion of the physics which dominates the relationships between spectral radiance and broad band flux. The parameterization is tested on two types of operational weather satellite data sets; the first is derived from the TIROS-N polar orbiting satellite, the second is derived from the GOES-1 geosynchronous orbiting satellite. Both of these data sets were prepared in a navigationally-grided and calibrated fashion over a large region encompassing the Southwest Monsoon system in support of the 1979 Summer Monsoon Experiment (SMONEX).

The radiation budget estimates are verified against wide-field-of-view broad band radiation budget parameters measured by the Nimbus-7 Earth Radiation Budget (ERB) instrument. The GOES-1 data are also used in an intercomparison with the diurnal radiation budget cycle over the

Arabian Desert Empty Quarter; the reference cycle is derived from a combination of aircraft (Convair-990) radiometer data and surface radiometer data, in conjunction with theoretical radiative transfer models needed for various transmission calculations.

Chapter 2 concludes with a discussion of some of the scientific consequences that have arisen based on the use of radiation budget estimates derived from NOAA operational weather satellite data.

Chapter 3 considers exchange processes within the 1979 Southwest Monsoon interpreted with the aid of satellite observations. To set the stage for this analysis, a review of previous research based on satellite measurements is provided. This includes a discussion of the various periodicities that have been identified in terms of monsoon fluctuations. Descriptions of the polar orbiting (TIROS-N) and geosynchronous (GOES-1) weather satellite data sets used in the investigation are provided. Two additional data sets derived from the radiation budget and passive microwave experiments on the Nimbus-7 experimental satellite are used to augment the research. Descriptions of these data sets are also provided. A general discussion of the techniques used to adapt spectral radiance measures obtained from weather satellites, in a radiation budget mode, is also given.

First, the large scale radiative forcing of the monsoon is considered. The results are presented in the form of 5-day averaged mean fields of the essential radiation budget parameters. These mean fields are used to facilitate a discussion of the phenomonological aspects of the evolution of the monsoon. Results are then presented in the form of time series of the zonal and meridional averages of the radiation budget, over the complete monsoon domain. The domain averaged

time–latitude and time–longitude sections provide graphic evidence that the principal modulation in monsoon radiative forcing arises from a quasi-long period oscillation related to the systematic propagation of cloud bands out of the equatorial regions and into monsoon latitudes. It is shown that on the large monsoon-domain scale, the quasi-biweekly and shorter period oscillations are in evidence but lack clear organization. It is also shown how 'monsoon breaks' manifest themselves in the meridionally averaged sections of the net radiation parameter. Finally, in terms of large scale forcing, it is shown how in the course of a single month surrounding monsoon onset, the monsoon undergoes a systematic depletion of net radiative convergence into the monsoon, on the order of 5 peta-watts.

Next, the contrasts in the monsoon radiation signals are presented, by way of time series, over various oceanic and continental regimes within the monsoon domain. It is pointed out how the shorter period oscillations appear to be much more robust at the local scale. The diurnal cycles over 12 localized regions within the monsoon domain are presented; these are also used to illustrate the large contrasts over the monsoon region on a 10-day time scale. These contrasts are emphasized by the use of space and time gradients of the diurnal radiation cycle.

Finally, the phenomenon of radiative decoupling is discussed. It is pointed out how cloud fields, which are known to 'decorrelate' the short and longwave radiative fluxes at the earth's surface, have a far more general property in which they also 'decorrelate' the top-of-atmosphere fluxes.

Chapter 4 describes a research program and a methodology designed to investigate the surface energy budget parameters in remote desert and mountain environments. The objectives of this program are twofold: The first is to quantify the surface energetics of two important heat source regions lying at the periphery of the Southwest Indian Monsoon, i.e. the Arabian Empty Quarter and the Qinghai-Xizang Plateau (Tibetan Plateau). The second is to compare and contrast the surface energetics of the Qinghai-Xizang Plateau with another major plateau system, the North American Plateau. The results of this program are intended to augment our understanding of the controls of desert heat sources (both lowland and highland) on the associated Southwest, East-Asian, and Rocky Mountain Monsoon systems.

The characterization of the surface energy budgets is based on a measuring system designed to provide a continuous record of the essential components of surface heat exchange process. The monitoring systems are based on conventional atmospheric and soil sensors configured with microprocessor driven data logging electronics. The system has been designed for both portability and reliability. Sensor components are configured to operate in a virtually automated mode with minimal maintenance. The electronics have been designed to carry out the calibration transformations and most of the statistical processing on-site and to record the output data on conventional cassette tapes for use on simple home and office computer systems.

Descriptions of measuring programs carried out in the deserts of Saudi Arabia and in the Rocky Mountain region are discussed. Characteristics of the surface energy budget in the Arabian Empty Quarter and its impact on the Arabian heat low are described. System

tests carried out in the Rocky Mountain area were designed as feasibility trials in preparation for a new measurement program to be carried out on the Qinghai-Xizang Plateau. Examples of how surface measurements can be incorporated with satellite radiation data for describing bulk atmospheric heat exchange are shown. There are suggestions of how measuring programs similar to those described can be used to quantify the surface energetics of 'spot coordinates' on the globe to support the problem of developing a global land surface climatology from remote platforms such as proposed by the International Satellite Land Surface Climatology Project.

An investigation of the Arabian heat low is given in Chapter 5. This research is supported by observations from various satellites, an experimental aircraft and a surface energy budget monitoring station. The observations confirm that the Arabian heat low is neither a radiation sink nor a total energy sink, disputing previous notions of desert heat lows. Top-of-atmosphere radiation budget analysis illustrates the high contrast properties of the radiative exchange fields over the southern Arabian Peninsula, with respect to its surroundings. However, an examination of a four-month time series of net radiative exchange over the Arabian Empty Quarter, indicates the heat low region is in slight radiative excess.

Combining these results with estimates of the surface energy budget within the Arabian Empty Quarter and the radiative heating rate estimates of Ackerman and Cox (1982) within the heat low region, provides a relatively complete picture of the energy exchange process of the heat low. A synthesis of these results indicates that the heat low is a total energy source region. It is shown that the surface energy

budget is in a relatively steady state in the daily mean, but undergoes dramatic diurnal variations and an occasional perturbation due to a moisture driven negative feedback process during intensification. A conceptual structure of the heat low is offered, based on a three layer stratification of the heating mechanisms. The possible role of the Arabian heat low in controlling thermodynamic conditions and forcing baroclinicity in the western Arabian Sea is discussed. It is concluded that the surplus energy properties of the heat low may serve as an important mechanism in controlling moisture transport into the monsoon rainfall regions.

Chapter 6 is provided in order to summarize the findings of the four parts discussed above.

Eric A. Smith
Department of Atmospheric Science
Colorado State University
Fort Collins, CO 80523
Summer, 1984

ACKNOWLEDGEMENTS

My deepest gratitude must go to Professor Verner Suomi whose vision was foremost in creating the field in which I have labored for eighteen years. The first half of that period was spent under his tutelage and it was during that time that I gained my appreciation for both the advantages and limitations of meteorological satellite platforms. In the course of the research presented, I was often guided by the many practical lessons I gained from his wise counsel.

I also acknowledge my major advisor for this dissertation, Professor Thomas Vonder Haar. The remainder of my Ph.D. Committee was composed of Professors Thomas Brubaker, Thomas McKee and Wayne Schubert, to whom I extend my appreciation.

There are a number of others who have been of great help to me on this project. Drs. Graeme Stephens and Warren Wiscombe and Professor Steve Cox have been particularly helpful. I am deeply indebted to Mr. John Graffy for his dedication in completing the computational aspects of this project, well beyond the time he was a salaried employee. His assistance has been absolutely essential. I also express my gratitude to Steve Ackerman, John Davis, Teizi Henmi, Leighton Klein, Dave Loranger, Chris Pasqua, Richard Peek, Dave Randel, Paul Rozenzweig and Charlie Wilkins. They have provided me with both direct assistance and the informal discussions essential to conducting applied research.

I extend my warmest regards to Dr. Fawaz Alamy and Professor Marwan Sakkal of King Abdul-Aziz University, Mr. Abdul-Karim Heneidy of the

Saudi Arabian General Directorate of Meteorology, and Major-Colonel Ali-Hasan El-Naimee, Commander of the Saudi Arabian Southern Force Army Group, whose assistance and hospitality made possible the collection of the Empty Quarter data in a truly formidable but fascinating environment. In addition, these latter acknowledgements would not be complete without mentioning the contributions of Professor Martin Fogle of the University of Arizona and Professor Jeffrey Eighmy of the Colorado State University Anthropology Department, whose resourcefulness in setting up the Saudi Arabian project, necessary for carrying out desert research, should not go unnoticed.

I extend my appreciation to Dr. Robert Fox of SSEC - University of Wisconsin for providing the GOES-1 tape recordings, Gregg Hunolt of the National Environmental Satellite Data Information Service for providing the AVHRR data, and the Nimbus-7 ERB Science Team for providing the Nimbus-7 ERB data.

I am most grateful to Mrs. Bonnie Grantham, Mrs. Susan Lini and Miss Loretta Stevens for their excellent care in preparing the manuscript, to Ms. Judy Sorbie who provided her artistry in drafting many of the figures, and to Duane Barnhardt for providing photographic assistance.

I cannot conclude this section without expressing my gratitude to my wife, Ms. Karen Greiner, whose encouragement, assistance and advice were instrumental in my efforts to complete this dissertation.

This research has been supported under CID-ARMETED Project Contract CSU-SA-KUA-02 and National Science Foundation Grants ATM 78-20375 and ATM 82-00808. Part of the computations were performed at the National

Center for Atmospheric Research, a division of the National Science Foundation.

TABLE OF CONTENTS

LIST OF TABLE CAPTIONS

LIST OF FIGURE CAPTIONS

1.0 INTRODUCTION

Much of what is now known about the terrestrial radiation budget process is based on satellite observations at the seasonal, annual and multi-annual time scales and at the large space scales out to the zonal average. Previous satellite investigations have mainly focused on the 'global radiation budget' and the required atmospheric and oceanic transports needed to balance the zonal radiation gradients imparted by the net radiative convergence term.

This investigation is an attempt to concentrate within these scales and to investigate a feature of the global radiation budget, i.e., the 'Southwest Summer Monsoon System', which manifests itself as a significant anomaly in terms of mean top-of-atmosphere radiation exchange.

The overall study is designed around the use of weather satellite data to reveal features of the monsoon that cannot readily be described by traditional wide-field-of-view radiation budget instruments. In so doing, there are various fundamental problems that arise. The foremost is the development and testing of a methodology which is consistent with utilizing weather satellite spectral radiance information in a 'radiation budget mode'. Chapter 2 of this investigation specifically addresses this problem.

Based on the methodology and parameterizations developed in Chapter 2, Chapter 3 then goes on to examine the radiative exchange processes within the 1979 Southwest Monsoon. This monsoon was the subject of an

extensive observational program under the auspices of The 1979 Summer Monsoon Experiment (SMONEX), a component part of the global scale First GARP Global Experiment (FGGE) of 1979. Figure 1.1, provided by Johnson and Houze (1984), is used to illustrate the Southwest Summer Monsoon domain and to highlight what are now considered to be the foremost elements of the 'Southwest Summer Monsoon System'.

In an attempt to focus in more detail on various key radiative elements of the monsoon, Chapter 4 proceeds to develop a strategy for monitoring monsoon heat source regions, specifically the Arabian heat low and the Tibetan elevated heat source. The monitoring approach incorporates the use of satellite, aircraft, and surface platforms which are used to describe the external boundary conditions essential in depicting the radiative structure of an atmospheric heat source feature.

Finally, Chapter 5 explores in detail the Arabian heat low, based on the monitoring strategy outlined in Chapter 4. This chapter of the investigation is concerned specifically with the energetic structure and potential role of the Arabian heat low within the larger scale Southwest Monsoon.

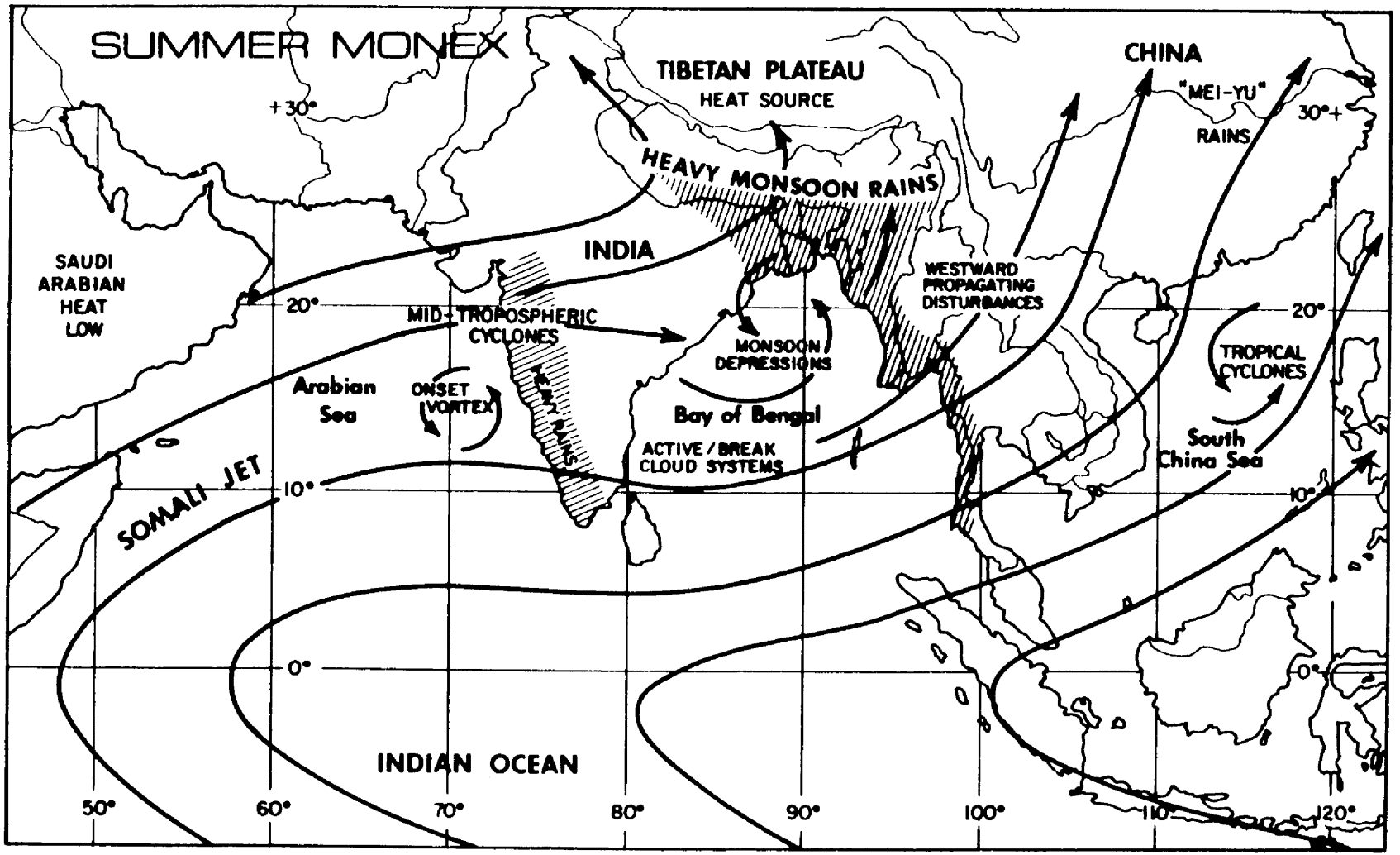

Fig. 1.1. The Southwest Monsoon domain and its associated meteorological components [from Johnson and Houze (1984)].

2.0 THE ESTIMATION OF RADIATION BUDGET PARAMETERS FROM WEATHER SATELLITE SPECTRAL MEASUREMENTS

This investigation focuses on a historical problem in satellite meteorology concerned with the use of spectral radiance measurements, obtained from operational weather satellites, to estimate flux exchange across the upper boundary of the earth's atmosphere. This problem has its roots in the very early period of radiation budget science, during the time when satellite estimates of the global radiation budget could only be obtained from a somewhat patchwork collection of satellite radiation measurements taken over a variety of spectral and angular configurations. The early results of Vonder Haar (1968) and Vonder Haar and Suomi (1969, 1971) gave testimony to the fact that the earth's radiation budget could be monitored quite well with non-idealized sensors. Since the advent of the modern sun-synchronous polar orbiter and geosynchronous orbiter operational weather satellite programs (1970 and 1974 respectively), there has been a continuous interest in using data from these systems for radiation budget research.

2.1 Background

There is an established literature addressing problems in radiation exchange, climate controls and cloud-circulation-radiation feedback which incorporates radiation budget estimates from both polar orbiting and geosynchronous meteorological satellites. These data have been applied to a variety of scientific problems. For example, the investigations of Heddinghaus and Krueger (1981), Ohring and Gruber (1983), Saunders and Hunt (1983), Short and Cahalan (1983), and Virji,

et al. (1982) have all focused on using weather satellite data, in a radiation budget mode, to map either global or regional scale radiation budgets or the correlative variables of cloudiness and rainfall. Short and Wallace (1980) have extended the use of longwave radiation budget estimates, derived from sun-synchronous polar orbiter satellite data, to examine 12 hour difference in cloudiness. Smith (1980b) has investigated the diurnal modulation of the radiation budget by cloud systems, using radiation budget estimates derived from geosynchronous satellite data.

In the attempt to assess and validate a climate model of the 3-dimensional GCM type (in this case the ECMWF model), Geleyn, et al. (1982) have incorporated radiation budget estimates from operational polar orbiters. Along these lines, Ohring and Adler (1978) have employed the same data to assess the accuracy of a zonally averaged energy balance climate model (EBCM), incorporating simple dynamics, in simulating the zonally averaged emitted infrared radiation budget term. Simmonds and Chidzey (1982) have also used these types of data to develop longwave emittance parameterizations for EBCM's.

There have been a number of studies designed to determine the role of clouds on the radiation budget, i.e. the cloud sensitivity type studies motivated by the earlier works of Schneider (1972), Budyko (1974), and Cess (1976). The results of Cess and Ramanathan (1978), Cess, et al. (1982), Hartman and Short (1980), Ohring and Clapp (1980), Ohring, et al. (1981), and Potter, et al. (1981) have attempted to come to grips with the debate over cloud 'reciprocity' and the space and time scales associated with the cancellation effect. These studies are intended to provide the essential 'climate signal' needed to interpret

the purely artificial cloud sensitivity experiments carried out in GCM environments; see e.g. Meleshko and Wetherald (1981), Schneider, et al. (1978), Shukla and Sud (1981), and Wetherald and Manabe (1980).

Finally, in a fairly new branch of radiation budget science, various investigators have utilized radiation budget data obtained from weather satellites to try to quantify the relationships between radiation budget parameters and measures of the general circulation. Jensenius, et al. (1978) have attempted estimating outgoing longwave radiation (OLR) at the top-of-atmosphere based on predictor variables diagnosed from the National Meteorological Center's Limited Fine Mesh Forecast Model. OLR estimates have been used by Liebmann and Hartmann (1982), Lyons (1981), and Weickmann (1983) to study various elements of the general circulation. Lau and Chan (1983a, 1983b) have used OLR estimates to investigate atmospheric teleconnections while Murakami (1980a, 1980b) has studied oscillations in the Winter Monsoon based on OLR estimates.

The advantages of using weather satellite radiation budget (RADBUD) estimates over the traditional wide-field-of-view measurements are threefold: 1) the spatial resolution is much higher; 2) global coverage is near real-time, continuous, and the data is readily available; 3) and in the case of geosynchronous satellite data, diurnal processes can be examined. Thus, there is an ongoing need for parameterizations which can be used to overcome the main disadvantage in using weather satellite measurements for proxy radiation budget estimates; i.e., the fact that the measurements represent narrow-band (NB), narrow-field-of-view

(NFOV) radiances rather than the preferred broad-band (BB), wide-field-of-view (WFOV) fluxes associated with hemispheric irradiances.

The problem of transforming spectral radiance measures [both shortwave (SW) VIS and longwave (LW) IR terms] obtained from weather satellites to broad band flux estimates has, to date, been treated rather crudely. The foremost approach taken by various investigators has been the use of simplified quasi-linear regression equations relating the narrow band parameters (independent variables) to the broad band parameters (dependent variables) [see e.g. Abel and Gruber (1979), Gruber, et al. (1983), Gube (1980, 1982a, 1982b)), Ohring, et al. (1984), Smith and Vonder Haar (1980a), and Wydick (1983)]. This approach as applied to the NOAA scanning radiometer (SR) data (see Gruber and Winston, 1978) has led to various ambiguities particularly evident in the studies of Cess, et al. (1982) and Simmonds and Chidzey (1982). Although the regression approach is indicative of the first order differences between the NB-NFOV and the BB-WFOV quantities, it does not address the essential physics leading to these differences, nor does it account for a variety of non-linear processes inherent to the transformation problem. For brevity, the problem can be divided into geometric considerations (SW anisotropy and LW limb darkening), and spectral considerations (SW and LW narrow to broad band transformations), taking place in either clear or cloudy atmospheres.

In the following investigation there are four basic objectives. The first is to develop a thorough but practical parameterization procedure for transforming weather satellite measurements to radiation flux estimates, an approach which is intended to overcome many of the fallacies associated with the linear or quasi-linear type statistical

regression techniques. Second, the parameterization is tested on polar orbiting [TIROS-N/Advanced Very High Resolution Radiometer (AVHRR)] and geosynchronous [GOES-1/Visible-Infrared Spin Scan Radiometer (VISSR)] satellite data taken over the Southwest Monsoon region. Third, the accuracy of the radiation budget estimates are verified and assessed by intercomparison with a combination of satellite WFOV data (from the Nimbus 7 Earth Radiation Budget Experiment), aircraft radiometer data (from the NASA Convair-990), surface radiometer data (from a Saudi Arabian Desert Empty Quarter Site), and various theoretical calculations needed in the intercomparison analysis. Finally there is an attempt to resolve some of the controversy that has arisen associated with the use of weather satellite type radiation budget data.

2.2 Radiation Budget Data Archives

The historical archives of earth radiation budget data consist of two basic types of products; those derived from broad band (BB), wide-field of view (WFOV) flate plate radiometers specifically designed for global radiation budget monitoring, and those derived from narrow-band (NB), narrow-field of view (NFOV) collimated radiometers designed for pictorial weather system monitoring. The principal BB-WFOV data have been derived from a series of radiation budget experiments flown on the Nimbus-2, Nimbus-3, Nimbus-6, and Nimbus-7 NASA experimental satellites. All of these experiments incorporated broad band radiation detectors (the MRIR instruments on Nimbus-2 and 3 utilized four spectral infrared channels to integrate up to the total terrestrial spectrum). The principal NB-NFOV data have been derived from the scanning radiometers (SR) and advanced very high resolution radiometers (AVHRR) flown on the NOAA operational sun-synchronous polar orbiting satellite series. There

have also been sporadic attempts to retrieve RADBUD parameters from geosynchronous satellite imaging radiometers, particularly those flown on the U.S. GOES vehicles and the European METEOSAT vehicles.

The basic designs and descriptions of the series of instruments flown on the Nimbus satellites can be found in the reports of Nimbus Project (1965), McCulloch (1969), W. L. Smith, et al. (1975, 1977) and Jacobowitz, et al. (1978). The further reports of ERB Science Team (1984) and Soule (1983) are helpful in reviewing the details of the Earth Radiation Budget (ERB) data and the sensors flown on the most recent earth radiation budget experiments, i.e. those of Nimbus-6 and Nimbus-7.

The BB data sets themselves, and the scientific results of these experiments, have been described elsewhere. The results of Vonder Haar (1968) and Vonder Haar and Suomi (1969, 1971), which suggested the earth was somewhat warmer and darker than suggested by earlier 'non-satellite' studies [see London and Sasamori (1971)], were essentially confirmed by the investigations of Raschke and Bandeen (1970), Raschke, et al. (1971), Raschke, et al. (1973), and Vonder Haar, et al. (1972), based on the Nimbus-2 and Nimbus-3 data.

The combined data sets from the earlier Vonder Haar (1968) study were then combined with the Nimbus-2 and Nimbus-3 data by Vonder Haar and Ellis (1974) in order to perform a series of studies. These later investigations considered the monthly, seasonal, and annual zonal averaged radiation budget climatology [Ellis and Vonder Haar (1976)], the required oceanic transport [Oort and Vonder Haar (1976)], the interannual variability of the global heat balance [Ellis, et al.

(1978)], and the effects of cloudiness on the global radiation budget [Ellis (1978)].

The Nimbus-6 experiment promoted a completely new generation of earth radiation budget studies. With the addition of a scanner which can be used to partially decompose the angular components of the radiative flux term [see Stowe (1983)], and a renewed interest in the mathematics of basic radiation budget principals, a series of theoretical papers came out of the university and NASA laboratories. The studies of Campbell and Vonder Haar (1978), Bess, et al. (1980, 1981), Green (1981, 1983), G. L. Smith and Green (1981), and G. L. Smith and Bess (1983), focused on the problem of enhancing the spatial resolution of wide-field-of-view (WFOV) measurements through deconvolution techniques. King and Curran (1980) explored theoretically the possible differences in interpreting the albedo field due to anistropy.

In applied studies, Jacobowitz, et al. (1979) reproduced almost exactly the earlier findings of the 'sixties' satellites with an 18 month Nimbus-6 satellite data set [approximately 31% global albedo and a 254^{o}K terrestrial equilibrium temperature]. Campbell and Vonder Haar (1980a) provided an updated climatological survey using a two year Nimbus-6 data set, and in a following report [Campbell and Vonder Haar (1980b)], went on to investigate the source of year-to-year differences using this data set (July 1975 to June 1977). Next, Campbell (1980) studied the transport problem on an annual scale, in terms of both the required equator to pole exchange and the more subtle east to west exchanges. In addition, the divergence of energy flux was divided into an oceanic component and a continental component; these results depicted

the annual cycle of winter inflow and summer outflow associated with continental radiative energy exchange. Stephens, et al. (1981) synthesized the Nimbus-6 period by directing their attention to the geographical distribution of the annual variability of the net flux after the removal of the semi-annual and annual cycles forced by the periodic variation in solar declination and distance. This investigation attempted to identify the 'global action spots' principally responsible for inter-annual changes in the radiation budget climate. The regions identified were the equatorial western Pacific, the stratocumulus regime off the west coast of South America, the Sahara Desert, and notably, the Southwest-Asian Monsoon.

The most recent measurements of the earth radiation budget now available from the Nimbus-7 ERB experiment have just begun to be scrutinized. Smith and Vonder Haar (1983) have examined the fluctuations in the Southwest Monsoon based on 6-day averaged fields of net radiation through the 1979 monsoon season. Randel (1983) has completed a study of the space-time variations in the global radiation budget (based on a one-year Nimbus-7 data set) with some emphasis on the hemispheric contrasts. This study also looks into the differences in the resultant albedo field based on whether wide-field-of-view or narrow-field-of-view (scanner) data were used. Arking and Vemury (1983) have suggested that the probable cause of these differences is the application of angular correction models to the scanner measurements.

Based on the two most recent earth radiation budget experiments, broadband WFOV data have been available continuously since the Nimbus-6 launch (June, 1975) and Nimbus-7 launch (November, 1978), with the exception of a 4.5 month gap from July, 1978 to mid-November 1978. The

Earth Radiation Budget Experiment (ERBE) planned to start in the mid-1980's is expected to continue the broadband WFOV time series on into the late 1980's; see Hall and Barkstrom (1981).

The availability of continuous records of 'radiation budget estimates' based on operational weather satellites is confined to the Scanning Radiometer (SR) and Advanced High Resolution Radiometer (AVHRR) data sets of Winston, et al. (1979) and Gruber, et al. (1983). These data have been used extensively by a number of investigators as discussed in the preceeding section. Descriptions of the processing of these data are found in Gruber (1978), Gruber and Winston (1978), Gruber, et al. (1983), and Ohring and Gruber (1983). Background information on the SR and the newer AVHRR radiometers can be found in the reports of Fortuna and Hambrick (1979), Lauritson, et al. (1979), and Schwalb (1978).

These so called NOAA data have been available almost continuously since June, 1974 with the exception of a ten month gap from March, 1978 to December, 1978 due to the changeover from the NOAA SR type instruments to the TIROS-N AVHRR type instruments.

2.3 An Ongoing Controversy

The two types of data discussed above have been used for a variety of scientific purposes as indicated in the Section 2.1. In the course of these studies a pattern has been established in which the results and inferences of similar type investigations are often in dispute due to the type of data set used in the analysis. It goes without saying, of course, that scientific conclusions should not be based on the inaccuracies and biases inherent in the input data, nevertheless, the history of atmospheric science has been plagued with this problem,

particularly on the global scale. Satellite radiation budget science is no more immune from data set inconsistency than temperature profile science is immune from disparity between balloon and satellite temperature-moisture retrievals.

However, there is one key aspect to the radiation budget controversy that should be kept in mind. It must be assumed at the outset that the BB-WFOV measurements are far more representative of broad band top-of-atmosphere fluxes than the NB-NFOV measurements, simply due to the selective absorption properties of the atmosphere (the gas, aerosol, and clouds constituents) and the oft-time anisotropic nature of the atmospheric radiation field due to both atmospheric constituents and the lower surface. The WFOV instruments are for the most part designed to make direct measurements of the desired radiation budget parameters. The errors inherent in a measurement are essentially those due to residual calibration problems which are presumably very small. On the other hand a NFOV measurement represents only a tiny slice of the overall geometric-spectral domain that constitutes a shortwave or longwave flux or irradiance measure. Thus there are large gaps (even after instrument calibration) between weather satellite radiance measures and top-of atmosphere flux estimates. It is in trying to fill these gaps that one would expect errors to arise and, in fact, it is the shortcomings in filling these gaps that have led to the various pitfalls radiation budget science has often found itself mired in.

An important example of a discrepancy between data sets is discussed in the study of Cess, et al. (1982) in which they examined the cloud-radiation feedback problem in conjunction with a pair of WFOV data

sets and a NFOV data set. Their results indicated that the now familiar cloud sensitivity factor (δ) given by:

$$\delta = \partial K\downarrow/\partial F_c - \partial L\uparrow/\partial F_c \qquad (2.1)$$

where $K\downarrow$ = Absorbed Shortwave Radiation
$L\uparrow$ = Outgoing Longwave Radiation
F_c = Fractional Cloud Cover

and averaged on a global scale leads to a negative value(cloud albedo dominates) if NB-NFOV data are used, but leads to a positive value (cloud greenhouse effect dominates) if BB-WFOV data are used. This is a ludicrous contradiction and bodes ill for the future of climate modeling if it is not resolved.

A second outstanding example of a data set discrepancy is found in a study by Simmonds and Chidzey (1982) in which they conclude that on a global-seasonal basis the NB-NFOV NOAA radiation budget data leads to a much improved parameterization over BB-WFOV Nimbus data in estimating longwave radiative emittance from surface temperature and cloud cover. This method of parameterization, of course, is part of the bedrock of the energy balance type climate models. There is an obvious explanation for this contradiction which is discussed in Section 2.7.

A more subtle pitfall in radiation budget science is illustrated in a study by Geleyn, et al. (1982). They attempted to resolve inadequacies in the radiation component of an operational version of the European Center's Medium Range Forecast Model. They tested two radiation algorithms by intercomparing the zonal annual averages of planetary albedo and IR emittance with the 1976 NOAA RADBUD data composited in the same fashion. There is wisdom in this approach up to some point, however, as pointed out in Ohring and Gruber(1983) there are

still significant inconsistencies remaining in the zonal annual averages between the NOAA NB-NFOV data and the NIMBUS BB-WFOV data. Furthermore, zonal-annual averages serve to obscure the even larger inconsistencies on the more localized space and time scales. Until these inconsistencies are resolved it is questionable as to how much tuning should be done to the radiation algorithms in weather forecasting or GCM models based on weather satellite RADBUD parameters.

A final example is based on this author's investigation (Smith, 1980b) of the contrast in the diurnal radiative structure between a suppressed tropical atmosphere, an atmosphere containing stratus cloud, an atmosphere containing moderate broken convection, and a heavily convectively enhanced atmosphere (see Fig. 2.1). This investigation was carried out over the 1974 GATE B-Scale Array in the tropical eastern Atlantic. Bulk tropospheric radiation budget estimates were derived by applying some fairly simple geometric and spectral transformation schemes to SMS-1 geosynchronous satellite radiance measurements and combining these estimates with ship board radiometer flux measurements; see part c of Fig. 2.1 for a schematic illustration of the method (surface flux parameterizations were not employed for any of these results).

The results for the four types of cloud regimes are illustrated in parts a and b of Fig. 2.1. Whereas there are some obvious and dramatic differences in the magnitudes and diurnal asymmetrics of the various radiative terms indicative of the real atmosphere (note specifically the net atmospheric radiation terms which have been stipled), there are also some questionable results. A close examination of the solar radiation convergence under convectively enhanced conditions, for example,

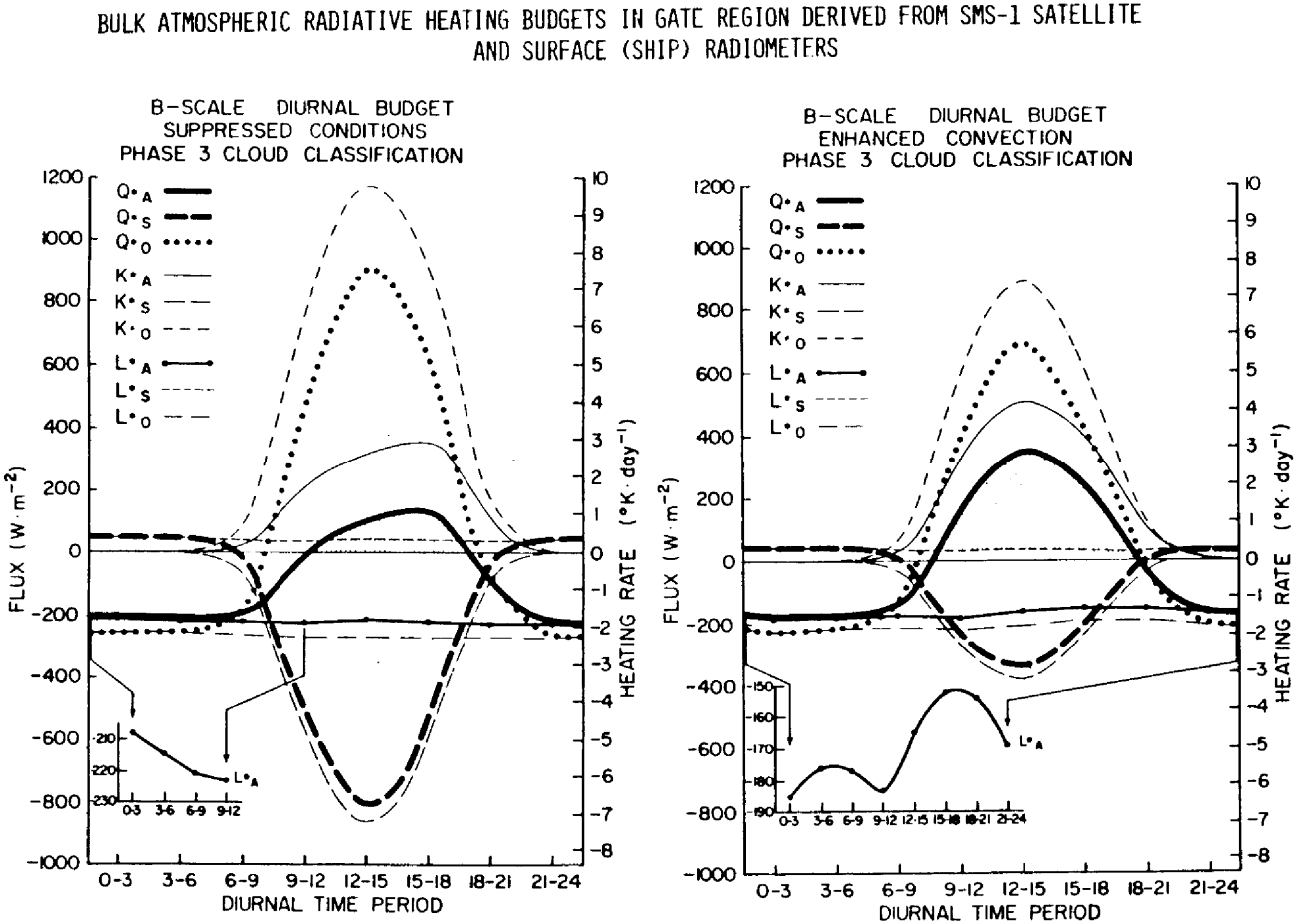

Fig. 2.1a. The diurnal radiative structure of the tropical troposphere under suppressed and convectively enhanced cloud conditions. The top-of-atmosphere terms are based on a RADBUD parameterization applied to SMS-1 geosynchronous satellite measurements. The surface terms are based on GATE B-scale shipboard radiometers. The insets in the lower left corners represent ordinate magnifications of the net longwave radiation term to illustrate its diurnal or semi-diurnal characteristics.

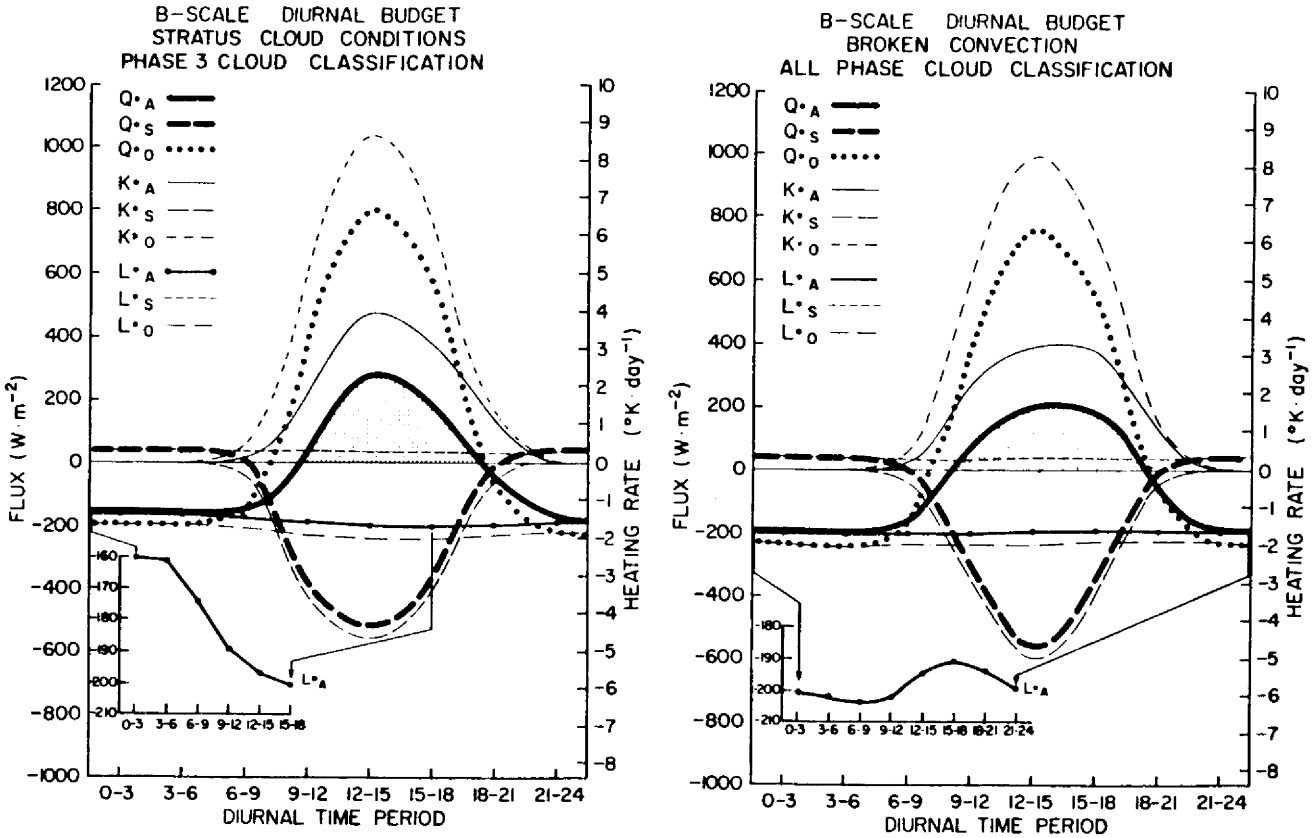

Fig. 2.1b. The same as Fig. 2.1a for stratus cloud and broken convective cloud conditions.

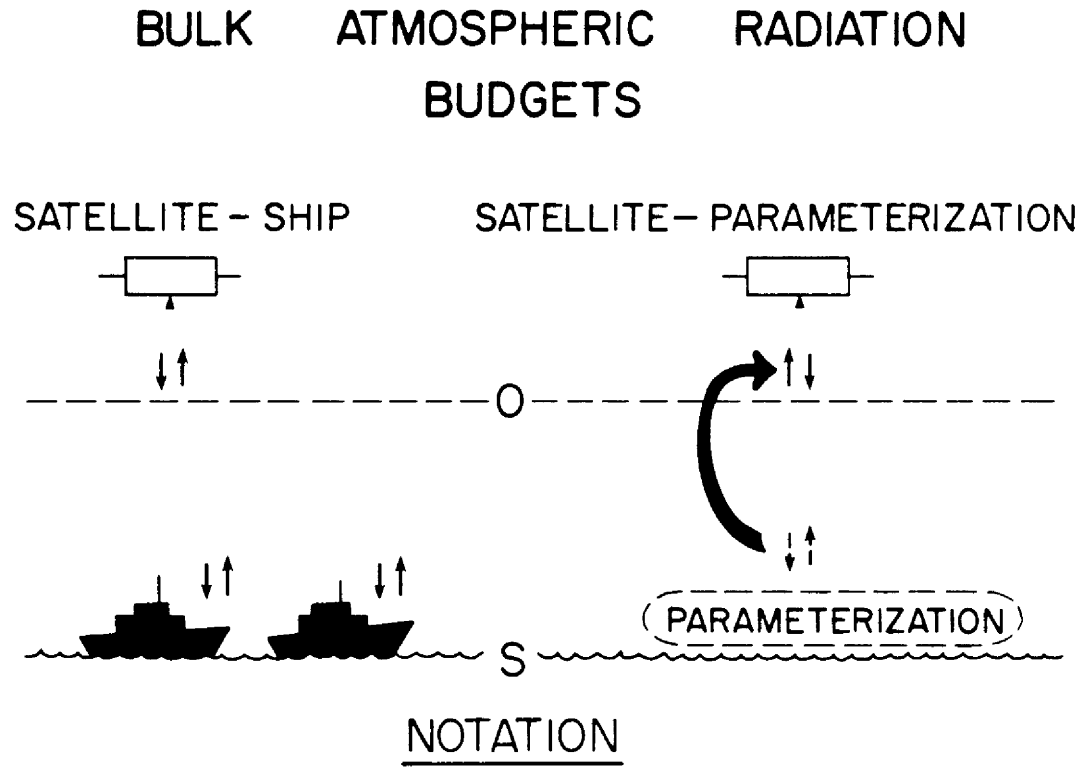

Fig. 2.1c. Schematic of GATE tropospheric bulk radiative heat budget methodology and RADBUD notational key.

indicates total solar absorption of over 40%. Although there is an ongoing debate as to the magnitude and cause of anomalous in-cloud shortwave absorption [observations exceed theory by up to 15%; see Welch, et al. (1980)] a magnitude of greater than 40% is somewhat beyond the acceptable maximum observed levels of 35%.

What all the above examples have in common is quite straightforward. The radiation budget parameters derived from the weather satellites are known to be only ballpark estimates. In the case of the NOAA data, the planetary albedo is derived by assuming no spectral difference between the radiometer band pass and the total solar spectrum, as well as assuming isotropy in calculating directional reflectances. Broad band longwave flux is estimated by assuming a quasi-linear relationship between the equivalent black body window temperature (T_{NB}) and the equivalent black body terrestrial temperature (T_{BB}), i.e.:

$$T_{BB} = w_o + w_1 \cdot T_{NB} + w_2 \cdot T_{NB}^2 \qquad (2.2)$$

where the w_i's are empirical coefficients and w_2 is very small. In the Smith (1980b) analysis shortwave anisotropy was considered however the spectral transformations were fairly elementary [see also Gube (1982a), and Saunders, et al. (1983)].

Thus there are known shortcomings in the radiation budget data derived from weather satellite information. Much of the physics of the atmosphere so strictly adhered to in theoretical radiative transfer applications have been virtually ignored. It is essential, therefore, to place qualifiers on many of the weather satellite RADBUD studies as the input data have been indirect estimates with uncertain error bars.

2.4 A Parameterization Approach for Transforming Narrow Band Radiance Measurements to Broad Band Flux Estimates

Transforming radiance measures to flux estimates can be considered a two-fold problem. The first deals with geometric relationships; the second with spectral relationships. In addition, both of these topics separate into either shortwave or longwave considerations. The longwave process is primarily one of emission and thus requires a different modeling approach than the shortwave process, which is partly a problem in absorption and partly a problem in reflection and scattering. Furthermore, the parameterizations are complicated by the fundamentally different radiative processes that occur in clear and cloudy atmospheres. Therefore, to place this general problem of spectral radiance to broad band flux transformation within a conceptual framework, it is described in terms of a three order parameterization problem involving two radiative processes, two radiative spectrums, and two media:

Radiative Spectrum	Radiative Process	
	Geometric	Spectral
	radiative medium	radiative medium
Shortwave	a) clear	a) clear
	b) cloudy	b) cloudy
Longwave	a) clear	a) clear
	b) cloudy	b) cloudy

Figure 2.2 illustrates the proposed transformation procedure in a schematic fashion. In this figure the χ and ξ functions indicate shortwave and longwave geometric transformations respectively. The η_{sw} and η_{lw} functions indicate the shortwave and longwave spectral transformations.

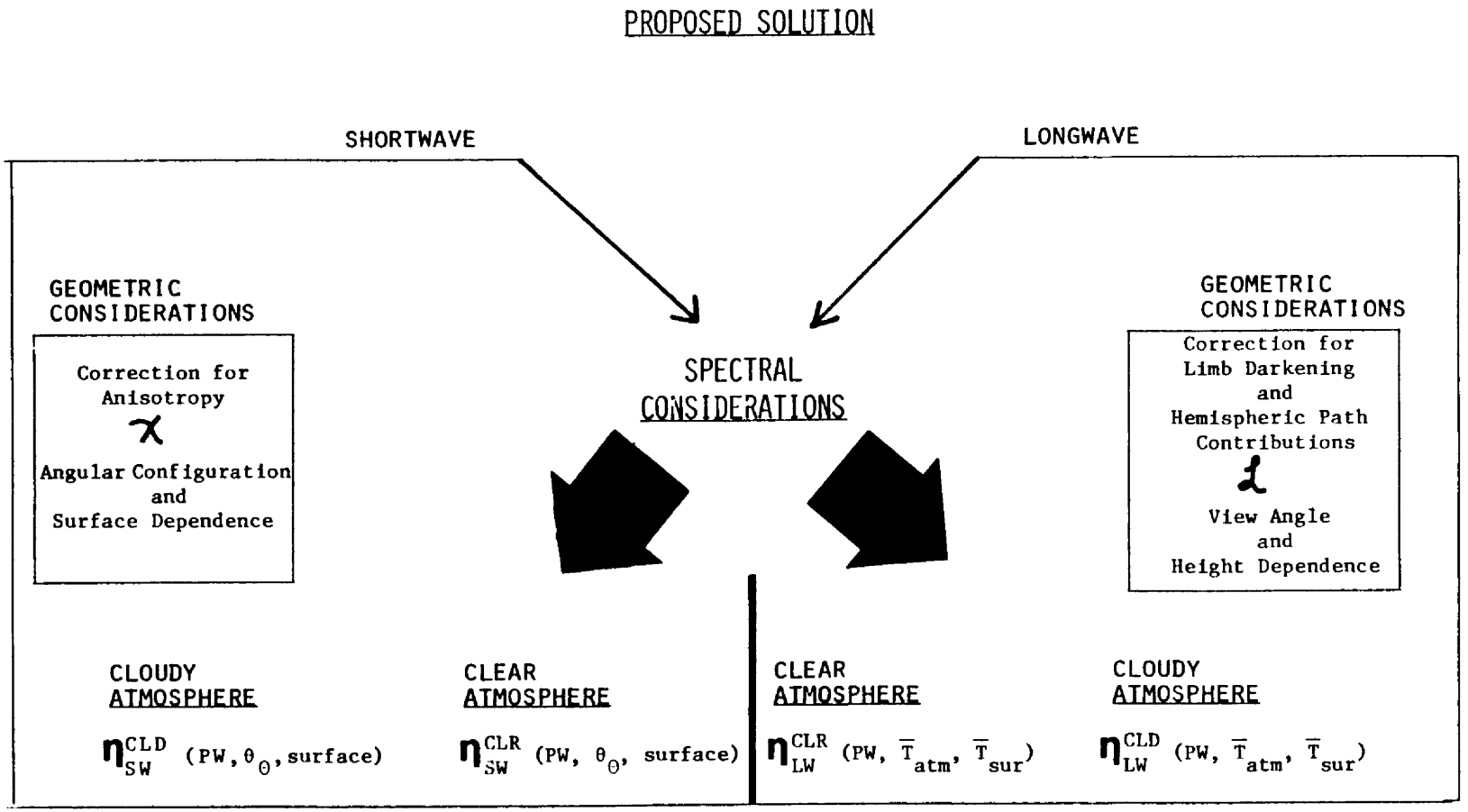

Fig. 2.2. Conceptual diagram of the geometric-spectral parameterization scheme.

2.4.1 Geometric Considerations

In the classic treatment of the shortwave geometrical transformation problem, bi-directional reflectance normalization models are used to correct natural occurring anisotropy implicit in the raw radiance measurements. In the infrared spectrum, limb darkening models are used to correct any path length induced biases in the raw radiance measurements. For this parameterization experiment models have been constructed for both the shortwave spectrum and the longwave spectrum based on current data sets and synthetic radiative transfer calculations.

2.4.2 Shortwave Spectrum and Bi-Directional Reflectance Normalization

Historically, bi-directional reflectance normalization models, devised for satellite radiation budget applications, have been designed in two ways. The first approach has been to describe a particular terrestrial surface (e.g. water, desert, or cloud) as an anisotropic reflector with invariant properties. This 'surface dependent' approach requires the generation of 'statistically stable' radiance fields describing the reflection process over the relevant set of earth surfaces occurring in the analysis domain. The requirement of 'statistical stability' suggests that this method of solution is affected by 'statistical noise'. That is relevant if the radiance fields are generated from actual measurements (satellite or aircraft) over a set of solar and observer zenith angles, and the associated relative azimuth angles.

On the other hand, the radiance fields may be described synthetically by the application of intensity-form radiative transfer models, which can be used to produce smooth fields. However, in this

case, the 'statistical stability' requirement is implicity embodied in the model assumptions, which must be stipulated very realistically if the resultant bi-directional reflectance normalization models are to have any validity.

In general, it is not possible to define realistic reflective surface boundary conditions for natural occurring earth surfaces such as forest canopies or mixed snow-ice fields. That is, most naturally occurring earth surfaces have such highly complex topographic structure and inhomogeneous compositions that theoretical treatment is ruled out apriori. There are exceptions, such as the reflection properties of a still water surface (Fresnel reflection), however, very little of the earth's surface can be characterized by ideal reflectors, such as still water ponds or perfectly flat and uniform sand deserts. Thus, 'empirical' or measurement based models are frequently used and thus the concern with 'statistical stability'.

It is very important in the generation of empirically derived bi-directional reflectance normalization models, that the data sample sizes associated with the mean fields are sufficient to characterize the 'average' reflection properties of the surfaces. There are a variety of factors that perturb the average radiative appearance of a surface. These include composition changes (e.g. vegetative cycles), topographic changes (such as induced by variable wind fields), and general inhomogeneities (e.g. the highly variable nature of cloud top surfaces). Therefore, surface invariant models are intrinsically related to time and space scales, insofar as their validity in representing average reflection characteristics.

The second approach for generating bi-directional reflection models is best referred to as a 'climatological dependent' method. Here, the radiance fields over discrete regions of the globe are characterized for given periods of time by angular models describing the average spatial and temporal reflectance conditions. This method attempts to average the effects of the underlying surfaces and the overlying atmosphere, for all meteorological conditions (clear and/or cloudy), during the specified time period. This methodology has been proposed for application with the upcoming Earth Radiation Budget Experiment (ERBE) based on composited radiance data from the Nimbus-7 ERB scanning instrument. The main advantage of this approach is that it circumvents the problem of having to discriminate what type of surface is being viewed (e.g. a warm land surface versus a low warm stratus cloud deck). The main disadvantages of this approach are 1) that the time/space scales of model utilization must conform to the time/space scales over which the models were generated originally; and 2) cloud situations are not discriminated from clear conditions. In addition there is a tacit assumption that angular biases cannot be overcome in the day-to-day treatment of radiance measurements.

It is important to note at this point that bi-directional reflectance normalization models are dependent upon the amount of atmosphere overlying the surface in question. There are two extreme cases; the top-of-atmosphere case and the directly-above-surface case. Although bi-directional normalization reflectance models can be defined at any level in-between these two extremes, they are of limited interest. In general, top-of-atmosphere models are useful in transforming remotely sensed radiance measurements to flux quantities;

thus correcting for naturally occurring anisotropy. Directly-above-surface models are useful when specifying the lower surface boundary condition for multi-stream radiative transfer models.

An interesting theoretical problem concerns the retrieval of a surface bi-directional reflectance normalization model from a model specified at some arbitrary level above the surface (including above the top of atmosphere). This is an inversion problem in which the effect of the atmosphere must be removed so as to arrive at the actual boundary condition. This problem can usually be solved iteratively, using an isotropic surface condition as an initial guess.

For this investigation, since the concern is with high time and space resolution computations (e.g. diurnal variations at a 1/2 degree grid scale), the requirement is for 'surface dependent' models. These have been constructed from the composited data of Minnis and Harrison (1984), and Davis and Cox (1981, 1982). Bi-directional reflectance normalization models are applied for four individual earth surfaces and for clouds. The four earth surface types and their associated geographic domains are as follows:

1. Water (Arabian Sea, Bay of Bengal, Indian Ocean)
2. Desert (Arabian Peninsula, Southern Asia East Africa)
3. Semi-Arid Continent (East African Highlands, Southern Asia, Indian Sub-continent)
4. Partially Snow Covered Mountain Range (Himalayas)

The decision to select only 4 surface models and a single cloud model was dictated by the availability of data sets over the Southwest Summer Monsoon region characterizing the angular variability of the 4 types of surfaces. The Minnis and Harrison (1984) composites of GOES Satellite VIS channel data have been used to specify angular models for

water and cloud. Davis in his Ph.D. dissertation [Davis and Cox (1981)], composited CV-990 bugeye data, for the Arabian desert, the Himalayas, and parts of the Indian Sub-continent. The Indian model is referred to as the semi-arid case for purposes of this investigation. These data were taken prior to the monsoon and thus prior to the burst of vegetation that evolves in July.

The models are given as a function of solar zenith angle (θ_o), satellite zenith angle (θ_s), and sun-satellite relative azimuth angle (Φ_r). A bi-directional reflectance normalization coefficient is expressed as:

$$\chi_i = f(\theta_o, \theta_s, \Phi_r) \tag{2.3}$$

where i indicates the surface type category.

The χ's represent ratios of integrated directional reflectance factors [$(R_i(\theta_o)$] to bi-directional reflectance values [$\rho_i(\theta_o, \theta_s, \Phi_r)$] multiplied by the isotropic scale factor (π), i.e.:

$$\chi_i(\theta_o, \theta_s, \Phi_r) = R_i\ (\theta_o)/[\rho_i(\theta_o, \theta_s, \Phi_r)\cdot\pi] \tag{2.4}$$

Thus any particular spectral radiance [$N_{\Delta\lambda}\ (\theta_o,\ \theta_s,\ \Phi_r)$] can be transformed to a spectral flux estimate [$F_{\Delta\lambda}(\theta_o)$] by utilizing the appropriate bi-directional reflectance normalization coefficient in conjunction with the isotropic scale factor, i.e.:

$$F(\theta_o) = \pi\cdot N_{\Delta\lambda}(\theta_o, \theta_s, \Phi_r)\cdot\ \chi_i(\theta_o, \theta_s, \Phi_r) \tag{2.5}$$

Now it is easily seen that χ is a measure of how much to increase or reduce a particular isotropic flux estimate ($\pi\cdot N$) based on the bias due to angular orientation. That is, if the radiance is larger than the isotropic magnitude (e.g. in a forward scatter peak), the χ factor

would be less than 1.0 so as to decrease the isotropic estimate. If the radiance is smaller than the isotropic magnitude (e.g. in a side lobe), the factor would be greater than 1.0 so as to increase the isotropic estimate. It should be noted that a graph of $1/\chi$ would then represent the invariant angular radiative appearance of a model surface. In Fig. 2.3 contoured diagrams of $1/\chi$ fields have been provided for various of the model surfaces, at discrete solar zenith angles. The key feature to note in these diagrams is that the ocean model embodies the largest angular dependence due to the large forward scattering effect of a water surface, which under smooth conditions yields nearly specular reflection. Note that the two land models and the cloud model show far less angular dependence. Models for the five surfaces have been constructed with a solar and satellite zenith angle resolution of 10^{o} (10 abscissas each) and a relative azimuth angle resolution of 15^{o} (13 abscissas). Azimuthal symmetry is assumed.

Note that in the transformation of a spectral radiance measurement $[N_{\Delta\lambda}(\theta_o,\theta_s,\Phi_r)]$ to a spectral radiative flux estimate $[F_{\Delta\lambda}(\theta_o)]$, the geometric functions (χ's) have been separated from the spectral functions (η's). The χ functions must conform to a spectral bandpass which approximates that of the satellite radiometer; the η functions are used to transform to flux quantities. Since the χ and η functions are separable, the order of transformation is immaterial. That is, the process is generally commutative, i.e.:

$$F(\theta_o) = (\pi \cdot N \cdot \chi) \cdot \eta = (\pi \cdot N \cdot \eta) \cdot \chi \qquad (2.6)$$

CORRECTION FOR ANISOTROPY

Ocean

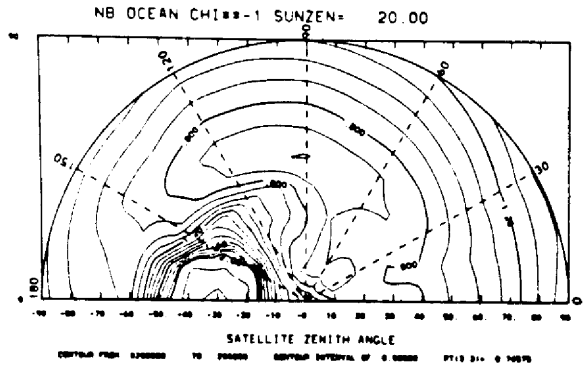

Desert

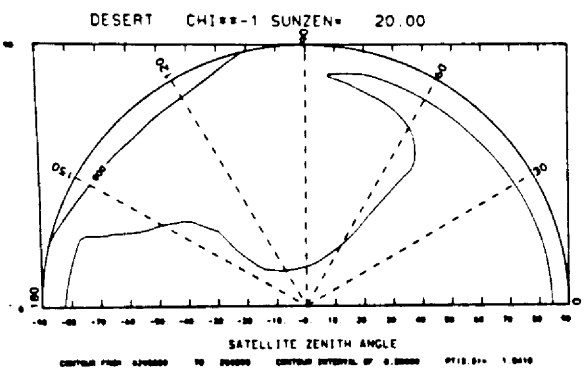

Himalayas

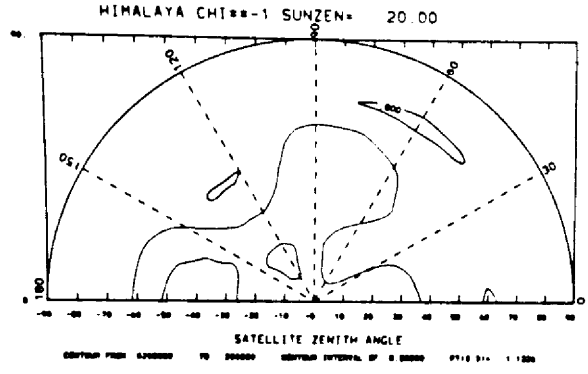

Cloud

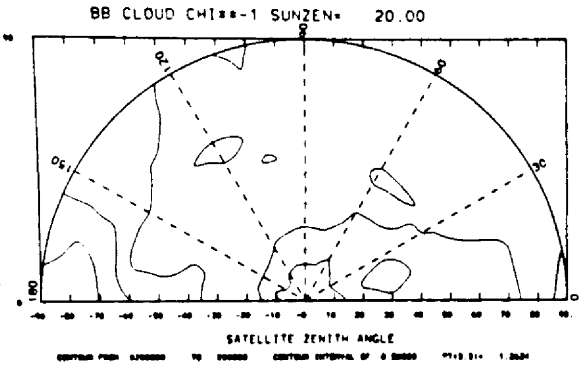

Fig. 2.3. Examples of bi-directional reflectance normalization models for ocean, desert, Himalayan range, and cloud.

2.4.3 Longwave Spectrum and Limb/Path Darkening

The analagous geometric transformation in the longwave spectrum is a limb darkening correction. It is actually a dual problem. The standard limb darkening correction involves adjusting an infrared radiance, measured along a non-zero nadir path, to a radiance value which is estimated to arise along a zero-nadir or normal (overhead) path. In addition to this standard correction, a correction for all angular contributions within the hemispheric flux coordinate system must be taken into account. This is equivalent to applying a spectral flux diffusivity factor.

The limb darkening correction has been parameterized, based on theoretical calculations, from an intensity-form spectral infrared radiative transfer model (Cox, et al., 1976). The parameterization applies to the atmospheric window (i.e. 10.0-12.5 μm). The model is parameterized in terms of satellite zenith angle (θ_s) and the non-limb corrected equivalent black body window temperature (T_{ebb}) derived from the window radiance itself. The formulation for the path effect is given by:

$$P(\theta_s, T_{ebb}) = f_o \cdot [\cos(f_1 \cdot \theta_s^{h_o})] \cdot \gamma \qquad (2.7)$$

where

$$\gamma = g_o + g_1 \cdot \theta_s + g_2 \cdot \theta_s^{h_1} + g_3 \cdot T_{ebb} + g_4 \cdot T_{ebb}^{h_2} + g_5 \cdot \theta_s^{h_3} \cdot T_{ebb}^{h_4}$$

and the f_i's, g_i's, and h_i's are best-fit coefficients given below.

Thus, in order to adjust a radiance [$N(\theta_s)$] taken along a non-nominal view angle ($\theta_s \neq 0$) to a normalized radiance [N(0)] where θ_s=0, the following is used:

$$N(0) = P(\theta_s, T_{ebb}) \cdot N(\theta_s) \tag{2.8}$$

Note that:

$$N(\theta_s) = \int_{10.0}^{12.0} B(T_{ebb}, \lambda) d\lambda \tag{2.9}$$

Now in order to include the contributions along all paths (the diffusivity correction), the following integration is required:

$$\varepsilon = \int_{0}^{2\pi} \int_{0}^{\pi/2} [1/P(\theta, T_{ebb}] \cos(\theta) \cdot \sin(\theta) \cdot d\theta \cdot d\varphi \tag{2.10}$$

Defining the limb darkening coefficient:

$$\zeta(\theta_s, T_{ebb}) = \varepsilon \cdot P(\theta_s, T_{ebb}) \tag{2.11}$$

an infrared window flux estimate (F_{win}) is then defined by:

$$F_{win} = \zeta(\theta_s, T_{ebb}) \cdot N(\theta_s) \tag{2.12}$$

Note that the temperature parameter serves to account for the height of the emitting surface in the atmospheric column under scrutiny.

A graphical representation of the parameterization is given in Fig. 2.4. Note as θ_s ranges from 0^o to 60^o, at the warmer emission temperatures ($T_{ebb} > 265^oK$), the limb darkening coefficient [$\zeta(\theta_s, T_{ebb})$] increases from a value less then 1.0 to a value greater than 1.0. That means that at the smaller observation zenith angles (i.e. nearly overhead measurements), for the higher temperatures (lower altitudes), in terms of flux estimates, the measurements can be considered to be 'limb brightened'.

The following provides the numerical values of the best-fit coefficients in the non-linear $P(\theta_s, T_{ebb})$ formulation:

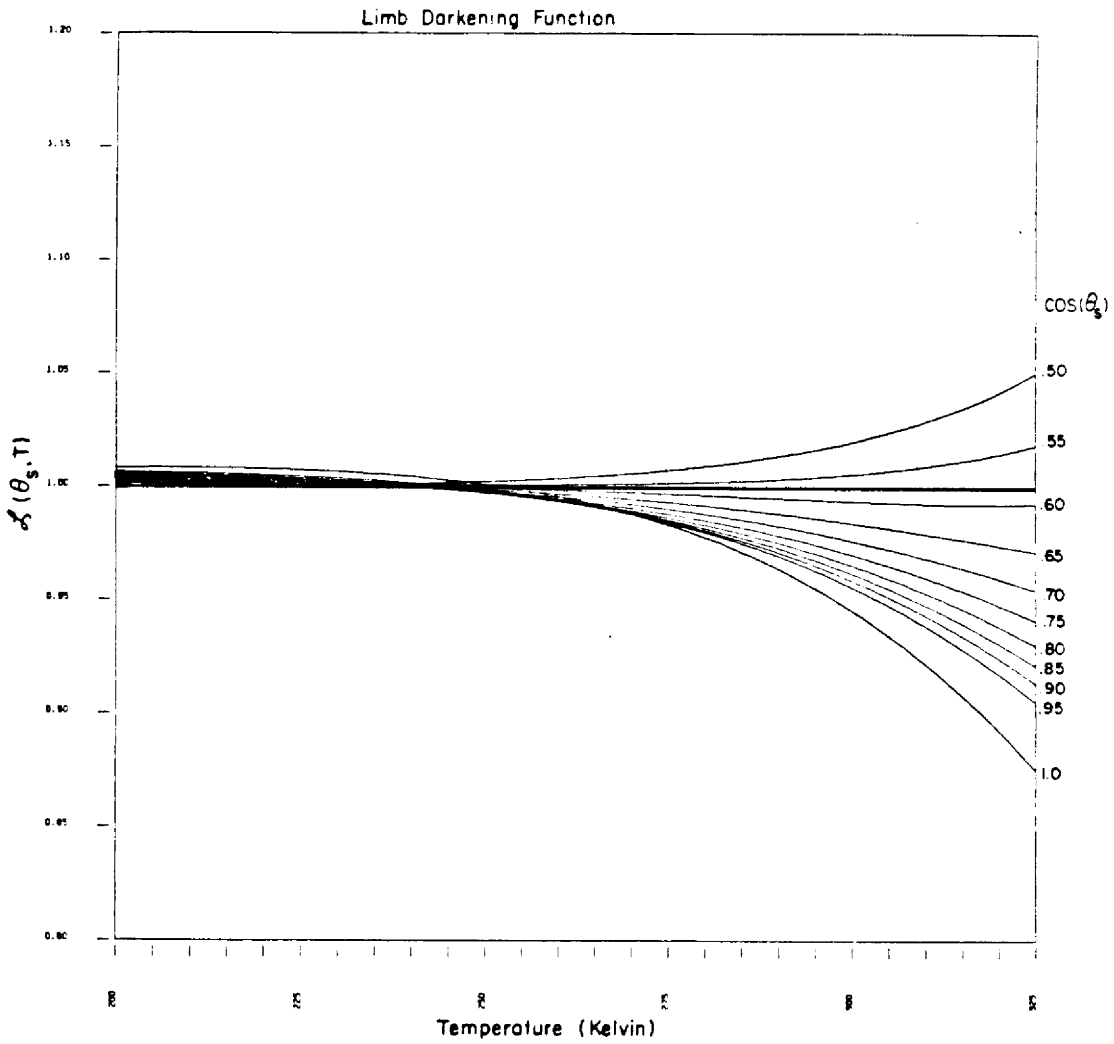

Fig. 2.4. Limb darkening parameterization given in terms of measured window temperature (T_{ebb}) and the satellite zenith angle (θ_s).

$f_o = 1.0000$	$g_o = -4.2969$	$h_o = 0.2999$
$f_1 = 0.1068$	$g_1 = +0.4739$	$h_1 = 5.7762$
	$g_2 = +0.4926$	$h_2 = 9.9844$
	$g_3 = +7.3765$	$h_3 = 4.3619$
	$g_4 = -6.9614$	$h_4 = 8.7175$
	$g_5 = -8.2874$	

2.4.4 Spectral Considerations

As pointed out in the introduction, the conversion of narrow band (spectral) fluxes measured by satellites, to broad band flux estimates has often been given scant treatment even though the relevance of the problem was first recognized over 20 years ago [see Wark, et al. (1962)]. In general, linear or quasi-linear regression relationships have been used in which the equations are formulated in terms of either the measured spectral albedo or window temperature. These relationships, which are mostly empirical and ignore the relevant physics which couple narrow band processes to broad band processes, are generally susceptible to wide scatter.

The approach taken here attempts to address the underlying factors which lead to differences between the narrow band and the broad band spectrums for both the shortwave and longwave regions. That is, the relationships are based on a set of parameters whose natural variability leads to differences in the ratios of the NB flux to the BB flux. In so doing the problem has been parameterized. As noted earlier, the spectral transformation functions are used in a multiplicative fashion. This is why a functional value represents a ratio of a broad band value to a narrow band value. By constructing the functions in this manner, much of the effect of theoretical biases that go into the two terms of the ratio is cancelled.

It is important in the generation of the parameterizations that the designated independent variables are readily accessible and can be conveniently introduced to the computational environment. Thus, to some extent, there are sacrifices that must be made with respect to the desired physics. Clearly a parameterization is of no relevance if the independent variables are unobtainable either externally or internally to the computational model.

The forms of the parameterizations, in-so-far as the independent variables, are given below:

Shortwave	Longwave
1. CZ - Cosine of solar zenith angle.	1. TM - Pressure weighted temperature of the atmosphere above the cloud free earth surface, or in the case of cloud cover, above the cloud top.
2. PW - Total precipitable water above either the cloud free surface or the cloud top.	2. PW - Total precipitable water above either the cloud free surface or the cloud top.
3. ST - Type of surface (water, desert, semi-arid continent, mountain).	3. WT - Equivalent black body window temperature of either the surface or cloud top.

For the shortwave case, parameter 1 (CZ) is based on the geometrical configuration between the sun position, and the earth coordinate of the measurement in question; parameter 2 (PW) is obtained from a coincident radiosonde profile, integrated from the top of the atmosphere down to either the earth or cloud surface depending on the situation; parameter 3 (ST) is determined apriori. A brief

summarization of the essential physics pertaining to each of these parameters is given below:

	Parameter	Purpose of Variable
1.	CZ	The directional reflectance process is spectrally dependent.
2.	PW	The broad band process is sensitive to water vapor absorption in the near-infrared strong lines.
3.	ST	Different earth surfaces have large discrepencies in their respective ratio's of visible albedo to near-infrared albedo.

For the longwave case, parameter 1 (TM) treats the non-linear Planckian emission effect of the atmospheric column over the surface in question. The column effect is reduced to a single temperature which involves a pressure weighted averaging procedure to account for density decrease with altitude. Parameter 2 (PW) is important in the longwave spectrum because of the critically important selective absorption characteristics of water vapor in the longwave spectrum. The effects of the variation of the other two principal active gases in the infrared (ozone and carbon dioxide) are assumed to have a negligible effect on the BB-NB ratio's with respect to water vapor. Finally, the non-linear Planckian effect of the surface temperature is accounted for by the EBBT of the measurement itself. The measured EBBT does not represent the true surface EBBT because of atmospheric attenuation; however, that difference has negligible effects on the parameterization accuracy. The following summarizes the reasons behind the selection of the parameters:

	Parameter	Purpose of Variable
1.	TM	Accounts for the non-linear spectral Planck effect of the atmospheric contribution to the total thermal emission.
2.	PW	Accounts for the effect of selective H_2O absorption.
3.	WT	Accounts for the non-linear spectral Planck effect of the surface contribution to the total thermal emission.

To develop consistent relationships over a realistic range of the variables, synthetic radiative transfer calculations are used in conjunction with actual climatological profiles for both the shortwave. and longwave domains and for clear and cloudy atmospheres. The basic methodology is given below:

1. Use the RTE models, in conjunction with many climatological profiles, to calculate the ratio's of broad-band reflectance to narrow-band reflectance and broad-band EBBT to narrow-band EBBT.

2. Compile these ratios at the discrete indices within the coordinate space defined by the independent variables of the parameterizations. By using climatological profiles, only those regions of the coordinate space representative of the real earth-atmosphere system actually include calculations.

3. Statistically average the ratios at each discrete index of the three dimensional space for which calculations were made.

4. Fit analytic expressions to the statistical composites over each 3-space of the SW-clear, SW-cloud, LW-clear, and LW-cloud domains. The analytic expressions provide smooth, continuous relationships which are also computationally efficient.

2.4.5 Radiative Transfer Models

The shortwave model is a parameterized 2-stream adding model in which layer properties are specified based on a formulation discussed by Coakley (1975); see Liou (1980) for a discussion of the principles of invariance needed in the adding recursion. It includes the

parameterization technique of Stephens (1978) and Stephens, et al. (1984) for clouds in which optical depth is given in terms of cloud liquid water content (LWC) or ice water content (IWC); and the optical path parameterization techniques of Lacis and Hansen (1974) and Sasamori, et al. (1972) for atmospheric gases (H_2O, CO_2, O_3, and O_2). The vertical structure of ozone mixing ratio is the climatological tropical profile given by McClatchey, et al. (1972). A uniform CO_2 concentration of 330 ppm is used. The solar constant used in these calculations is 1370.0 $W \cdot m^{-2}$. Molecular scattering is treated following the work of Elterman (1964), and Deirmendjian and Sekera (1954). The solar spectrum is divided into five regions: 1) ultra violet; 2) blue/violet; 3) green/yellow; 4) red/orange; 5) near-infrared. Scattering and absorption by the atmospheric gases are parameterized as well as the reflection and absorption processes in clouds.

A major control of the shortwave NB to BB relationships is the critically important spectrally resolved surface reflectance. For this investigation the spectral surface albedo for water is taken from Paltridge and Platt (1976); the spectral surface albedos of the three (3) land surfaces are based on the CV-990 near-surface SMONEX radiation flights discussed in an Atlas by Smith, et al. (1980). Table 2.1 provides a summary of the shortwave model physics. This model was verified against an exact model of Wiscombe (1982); the clear atmosphere upward and downward flux intercomparisons were within 2%. Fig. 2.5 provides a schematic illustration of the model structure for both SW and LW spectrums.

The longwave model is a non-scattering 17-band transmissivity model in which cloud processes have been parameterized. Gaseous transmission

TABLE 2.1

Summary of Shortwave RTE Model Physics

5-Band Parameterized Adding Method

A) Designed for remote sensing purposes

B) Two stream-flux formulation

C) Spectral albedo of the surface specified as boundary condition. Solar constant is 1370 $W \cdot m^{-2}$

D) Rayleigh reflectance of a clear layer based on the Deirmendjian and Sekera (1954) formulations for clear sky radiation

E) Gaseous absorption due to H_2O, O_3, CO_2, and O_2 based on various parameterizations techniques

F) Cloud layer properties based on LWC parameterization techniques

G) Provides for multi-layer and discontinuous cloud structure

Band Structure

Band	Region	Band Pass (μm)
1	Ultra-Violet	0.20 - 0.40
2	Violet/Blue	0.40 - 0.50
3	Green/Yellow	0.50 - 0.60
4	Orange/Red	0.60 - 0.78
5	Near Infrared	0.78 - 4.00

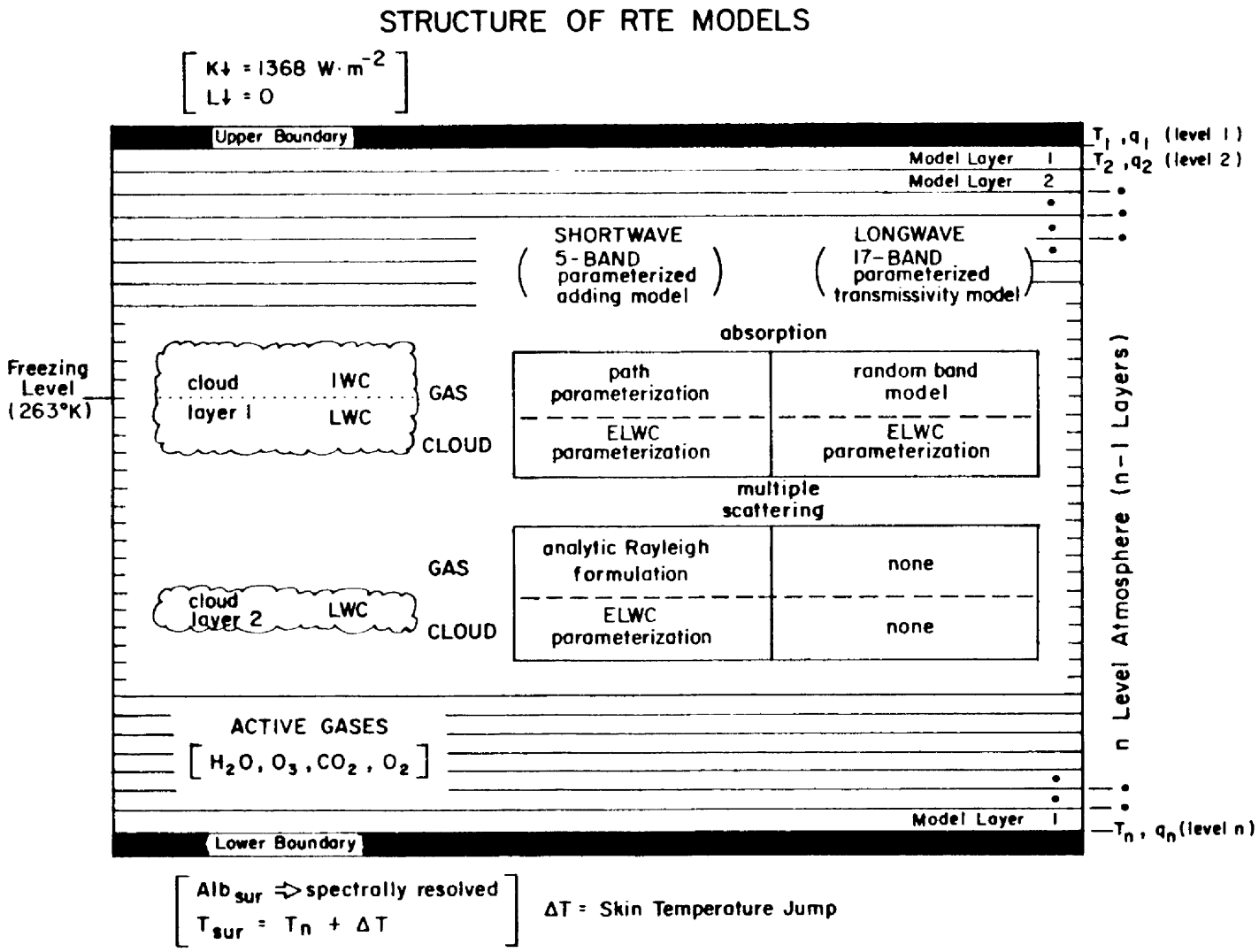

Fig. 2.5. Schematic illustration of the SW and LW radiative transfer model structure.

in the water vapor bands incorporates the Goody (1952) random band model approach. Band parameters are calculated from the LOWTRAN-5 transmission data provided by the Air Force Geophysics Laboratory [see Kneizys, et al. (1980)]. The regression and weighting procedures developed by Rodgers and Walshaw (1966) are used to fit the band model with the LOWTRAN-5 data.

Gaseous absorption in the continuum is based on some improvements to the method of Cox (1973) who utilized the Bignell (1970) laboratory data; see also Stephens (1976). The 9.6μm ozone region involves a four parameter pressure correction technique suggested by Goody (1964), extended by Stephens (1977), and applied to a two path Malkmus (1967) random band model discussed by Rodgers (1968); see also Walshaw (1957). The CO_2 overlap uses the Goody random band model parameters suggested by Rodgers and Walshaw (1966). The O_3 and CO_2 mixing ratios are equivalent to those used in the shortwave calculations.

Transmission in clouds is based on the parameterization work of Stephens (1978). For clouds, the infrared spectrum is divided into three bands. The H_2O vibration-rotation region (5000-1200 cm^{-1}), the continuum region (1200-800 cm^{-1}), and the H_2O pure rotation region (800-40 cm^{-1}). Cloud processes are parameterized in terms of cloud liquid water content (LWC) or ice water content (IWC). The mass absorption coefficients for water clouds are based on theoretical calculations given by Stephens (1978). The mass absorption coefficients for ice clouds are based on the measurements of Griffith, et al. (1980) and Paltridge and Platt (1981). Table 2.2 summerizes the longwave model physics. The model has been verified against the exact models of Ellingson and Gille (1978) and Wiscombe (1982). The largest differences

TABLE 2.2

Summary of Longwave RTE Model Physics

17 - Band Transmission Method

A) Designed for remote sensing purposes

B) Non-scattering-flux formulation

C) Lower boundary condition allows for discontinuous temperature jump providing for realistic skin temperatures

D) Gaseous absorption in the H_2O, O_3, and CO_2 bands based on random band models utilizing the LOWTRAN-5 Transmission Data to calculate band parameters

E) Continuum absorption resolved to 5 bands-Incorporates e-type pressure scaling

F) Cloud layer properties based on LWC parameterization techniques

G) Provides for multi-layer and discontinuous cloud structure

Band Structure

Band	Region	Band Pass (μm)
1	Near IR tail	2.00 - 3.57
2	3.7 μm weak window	3.57 - 4.00
3	Tail of the H_2O V-R band	4.00 - 4.46
4	Low wing of the H_2O V-R band (pt. 1)	4.46 - 5.05
5	Low wing of the H_2O V-R band (pt. 2)	5.05 - 5.81
6	6.3 μm H_2O strong region	5.81 - 7.35
7	High wing of H_2O V-R band	7.35 - 8.33
8	Lower end of IR continuum	8.33 - 9.26
9	9.6 μm O_3 - IR continuum	9.26 - 10.20
10	Clean portion of IR continuum	10.20 - 11.36
11	Dirty portion of IR continuum	11.36 - 12.50
12	High End of IR continuum - low wing of H_2O rotation band	12.50 - 13.51
13	15.0 μm CO_2 - H_2O overlap	13.51 - 17.24
14	Center of H_2O rotation band	17.24 - 26.32
15	High wing of H_2O rotation band	26.32 - 35.71
16	Far wing of H_2O rotation band	35.71 - 62.50
17	Far infrared region	62.50 - 00

for clear atmospheres are on the order of 3% which take place in the moist boundary layer and are due to differences in how the exact models treat the IR continuum (the exact models use the Roberts, et al. (1976) fit of D. E. Burch laboratory data). Refer to Fig. 2.5 for a schematic illustration of the model.

The atmospheric profiles used for the raw RTE computations have been extracted from various data sets. They include the global climatological profiles of Oort and Rasmusson (1971) and Jenne, et al. (1974); the tropical profiles based on easterly wave composites of Reed, et al. (1977); and finally profiles characteristic of precipitating atmospheres given by Smith and Vonder Haar (1980c).

In compiling the statistical composites of the theoretical calculations, for the cloudy parameterizations, cloud layers have been inserted over a range of equivalent liquid water contents (ELWC's) from 0.001 to 1.0 $g \cdot m^{-3}$. The cloud water is considered to be in the liquid stage at temperatures greater than $263^{o}K$; in the ice stage at temperatures less than $263^{o}K$. Cloud layer heights are generated in a random fashion in order to simulate the variable distribution of cloud tops in a real atmosphere.

2.4.6 Smoothed Functional Form Spectral Transformation Models.

To configure smooth transformation models, analytic fits to the statistical composites have been carried out. The following equations express the parameterizations in mathematical form:

A. Shortwave - Clear

$$\eta_{sw}^{clear}(CZ,PW,ST)=A0_{ST}+A1_{ST}\cdot PW+A2_{ST}\cdot PW^2+A3_{ST}\cdot PW^3 \\ +B1_{ST}\cdot CZ+B2_{ST}\cdot CZ^2+B3_{ST}\cdot CZ^3 \tag{2.13}$$

where the A and B coefficients are derived from the fitting procedure.

B. Shortwave - Cloudy

$$\eta_{sw}^{cloudy}(CZ,PW,ST)=CO_{ST}+C1_{ST}/(CZ+PW+0.25) \\ +[1.0-\delta(ST-2)]\cdot[C2_{ST}/(PW+1.5) \\ +C3_{ST}/(PW^2+12.0) \\ +C4_{ST}/(CZ\cdot PW+1.5)] \\ +[\delta(ST-2)\cdot CZ]\cdot[C2_{ST}/(PW+1.5) \\ +C3_{ST}/(CZ+PW^2+0.25) \\ +C4_{ST}/(CZ^2+PW+0.25)] \tag{2.14}$$

where the C coefficients are derived from the fitting procedure and the δ indicates the Dirac Delta Function.

For η_{sw}^{clear} and η_{sw}^{cloudy}

CZ = Cosine of solar zenith angle
PW = Precipitable water in cm
ST = Integer designating surface type
= 1 for water
= 2 for desert
= 3 for semi-arid
= 4 for partially snow covered mountain

C. Longwave - Clear

$$\eta_{lw}^{clear}(TM,PW,WT)=[a_o+a_1\cdot S1+a_2\cdot S1^2]\cdot [b_o+erfc[b_1\cdot(T+b_2)]]\cdot [erfc[c_1\cdot S2\cdot(c_2-PW)]]+ [d_o+d_1\cdot PW+[d_2+(d_3\cdot(d_4-PW))^2]^{1/2}] \quad (2.15)$$

where $S1 = 0.01 \cdot (WT - 235)$

$S2 = (0.01 \cdot WT)^{e_o}$

$T = 0.01 \cdot (TM - 245)$

and the a, b, c, d, and e coefficients are derived from the fitting procedure.

D. Longwave - Cloudy

$$\eta_{lw}^{cloudy}(TM,PW,WT)=[a_o'+a_1'\cdot S1+a_2'\cdot S1^2]\cdot [b_o'+erfc[b_1'\cdot(T+b_2')]]\cdot [erfc[c_1'\cdot S2\cdot(c_2'-PW)]]+ [d_o'+d_2'\cdot PW+[d_2'+(d_3'\cdot(d_4'-PW))^2]^{1/2}] \quad (2.16)$$

where $S1 = 0.01 \cdot (WT - 220)$

$S2 = (0.01 \cdot WT)^{e_o'}$

$T = 0.01 \cdot (TM - 245)$

and the a', b', c', d' and e' coefficients are derived from the fitting procedure.

For η_{lw}^{clear} and η_{lw}^{cloudy}

TM = Pressure weighted atmospheric temperature in degrees Kelvin
PW = Precipitable water in cm
WT = Equivalent black body window temperature in degrees Kelvin

and the complementary error function erfc(x) is:

$$\text{erfc}(x) = \frac{2}{\pi}\int_{x}^{\infty} e^{-u^2}\,du \tag{2.17}$$

In the above equations the coefficients take on the values given in Table 2.3.

Examples of the graphical protrayals of the NB to BB relationships both in terms of the raw statistical composites and smooth analytic fits are given in Figs. 2.6-2.12. Figs. 2.6 - 2.9 illustrate the shortwave results for the 4 underlying earth surfaces; water, desert, semi-arid and Himalayas. In Fig. 2.6 the abscissas represent the ratio of broad band reflectance to narrow band reflectance; the ordinates represent CZ; the individual curves are for different values of PW. Note first, that the functions for both clear and cloudy cases are generally less then 1.0; second, that the functions are highly non-linear; third, there are large differences in the spread of the curves between the clear and cloudy cases (between 2.6a and 2.6b). Also note how the discontinuities in the raw statistical composites (unsmoothed averages) have been ironed out in the analytic forms (smoothed functional representations).

Figure 2.7 indicates that for the desert case the functions exceed 1.0 much of the time due to the high near-infrared reflection

TABLE 2.3

Coefficients of the NB to BB Parameterization Equations

Shortwave Functions

	ST=1	ST=2	ST=3	ST=4
A0	0.8846917500	1.1946275000	0.9908988300	0.9879102800
A1	-0.0140759800	-0.1140587500	-0.0419186730	-0.0327143720
A2	0.0027312687	0.0234593030	0.0084882261	0.0066962086
A3	-0.0002015762	-0.0018112258	-0.0006451327	-0.0005098605
B1	0.0336673520	0.1154305500	-0.4362438200	-1.1432189000
B2	0.0600810770	-0.0743596000	0.6110155800	1.7054933000
B3	-0.1260727300	0.0165458250	-0.3069098800	-0.8298913100
C0	0.767133	0.818573	0.741757	0.672138
C1	0.100697	0.135686	0.094553	0.101547
C2	0.137165	0.305509	0.198753	0.141646
C3	-0.772711	-0.225389	-0.784542	-0.701479
C4	0.079313	0.131624	0.026757	0.054421

Longwave Functions

a_o=-0.000538808	a_o=+0.001025160
a_1=-0.008234283	a_1=-0.013733112
a_2=-0.000531718	a_2=+0.007201844
b_o= 3.541660400	b_o= 5.709408200
b_1=23.997709000	b_1= 3.385208700
b_2=-0.068157973	b_2= 0.008272800
c_1= 1.098624083	c_1= 0.449626922
c_2=+0.014738302	c_2=-0.132324870
d_o= 0.956111320	d_o= 0.907586070
d_1=-0.016906746	d_1=-0.010642382
d_2= 0.000800550	d_2= 0.007036977
d_3= 0.015377198	d_3= 0.016124483
d_4= 0.860151360	d_4= 0.759200880
e_o= 1.460673500	e_o= 1.240391300

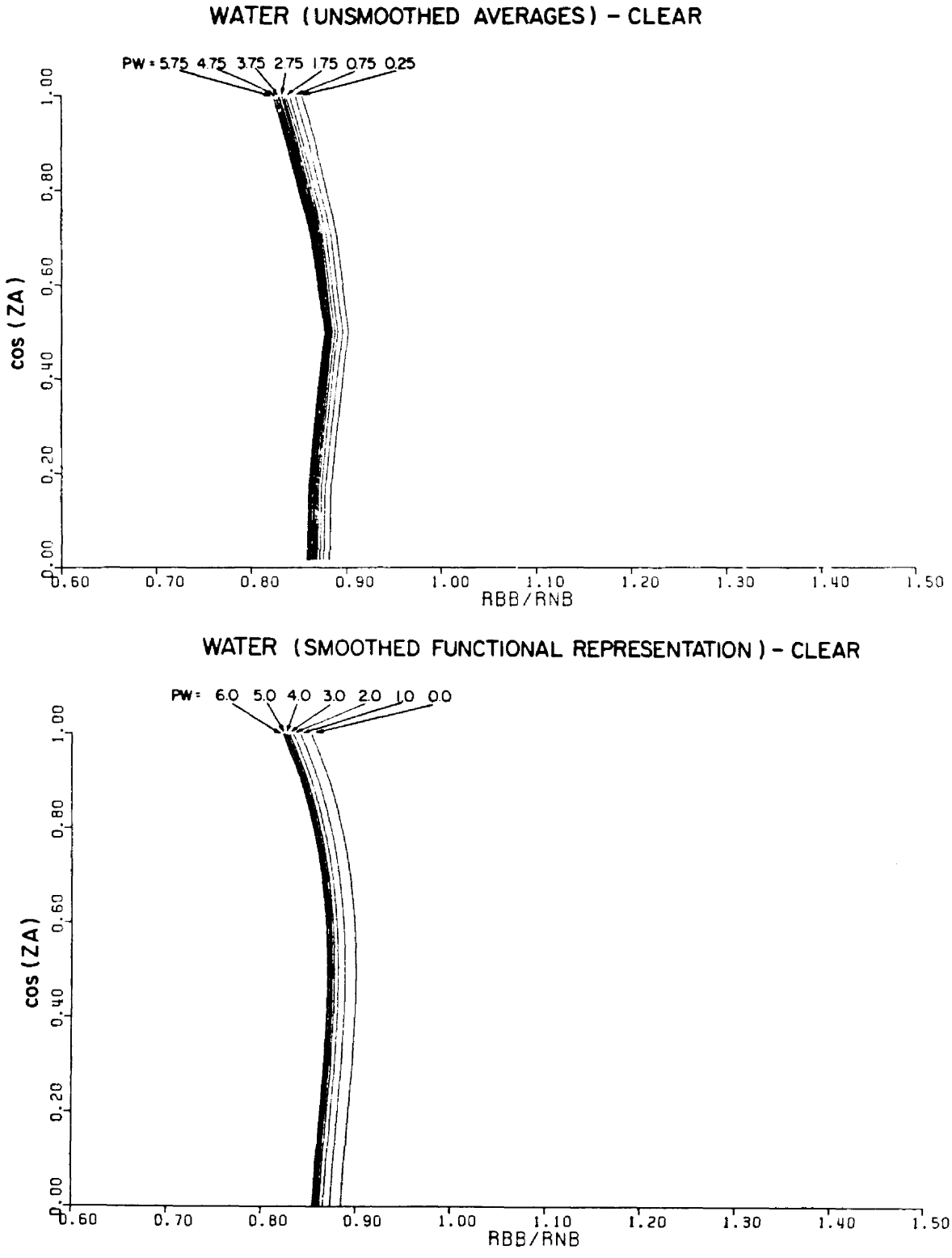

Fig. 2.6a. Shortwave NB to BB relationship for cloud free water surface. Top part shows the statistical averages of the raw model calculations. Bottom part shows the smoothed functional form.

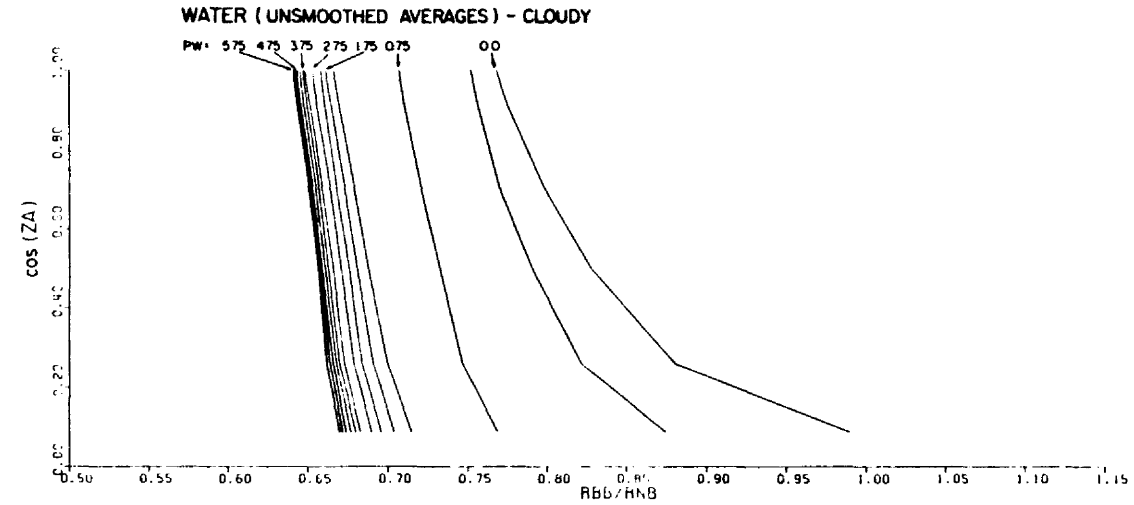

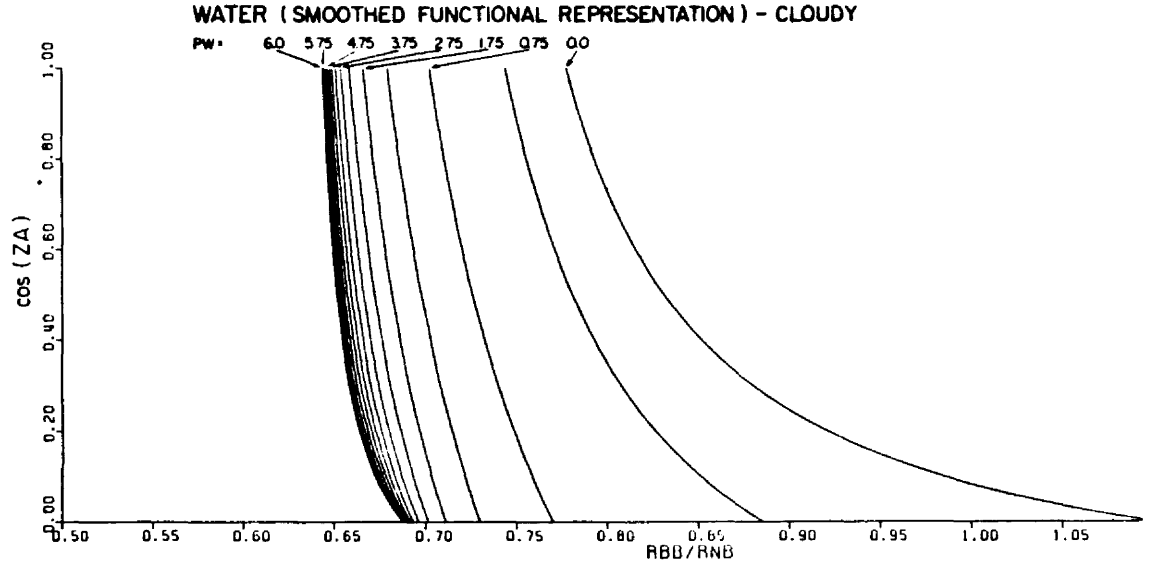

Fig. 2.6b. Same as Fig. 2.6a except for cloud covered water surface.

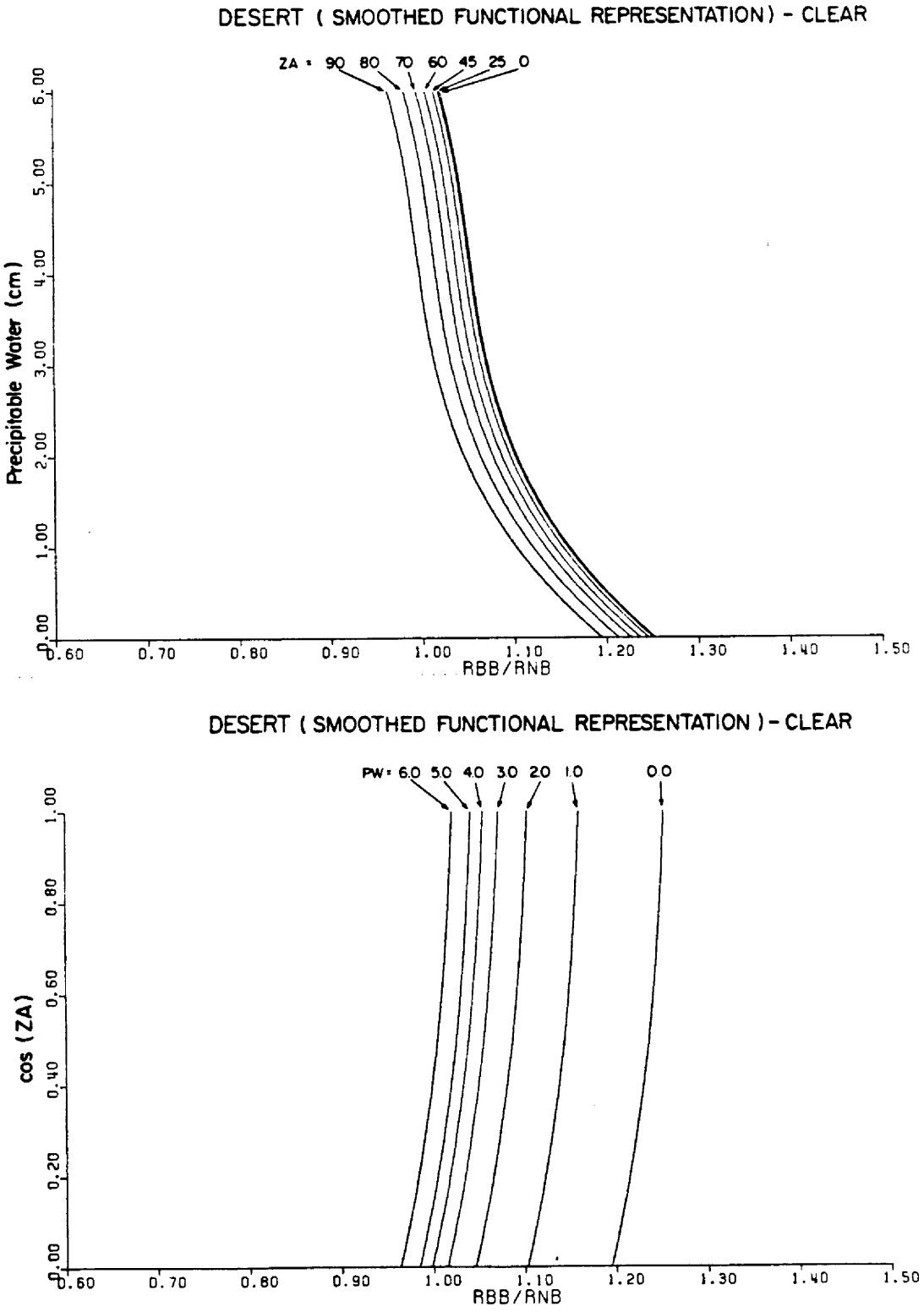

Fig. 2.7a. Shortwave NB to BB relationship for cloud free desert surface. Top part utilizes PW as the ordinate with individual curves respresenting different ZA's. Bottom part reverses the roles of PW and ZA.

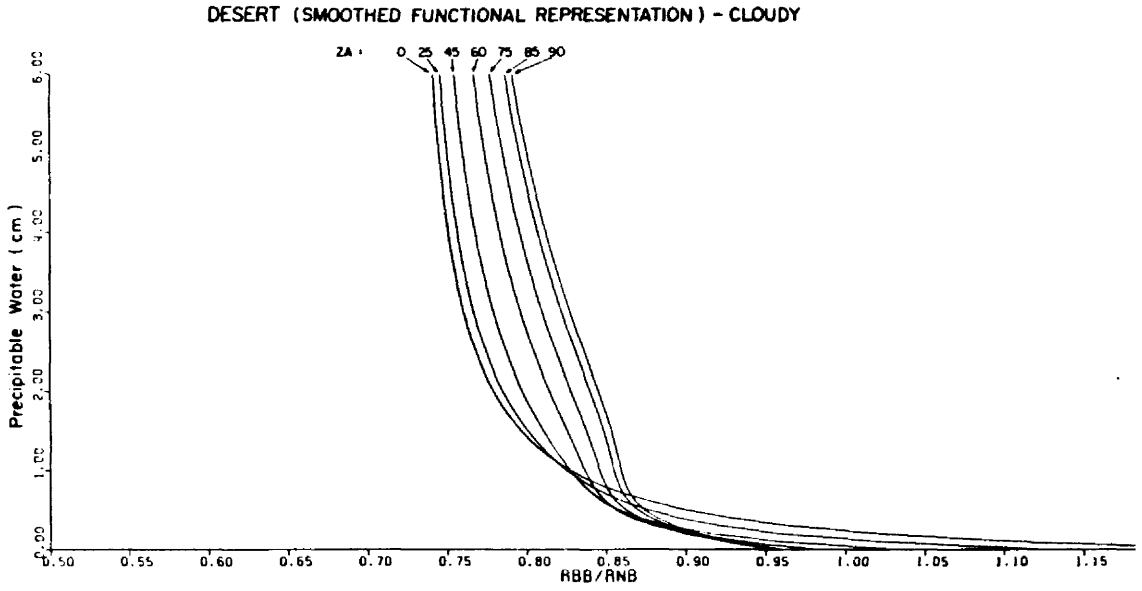

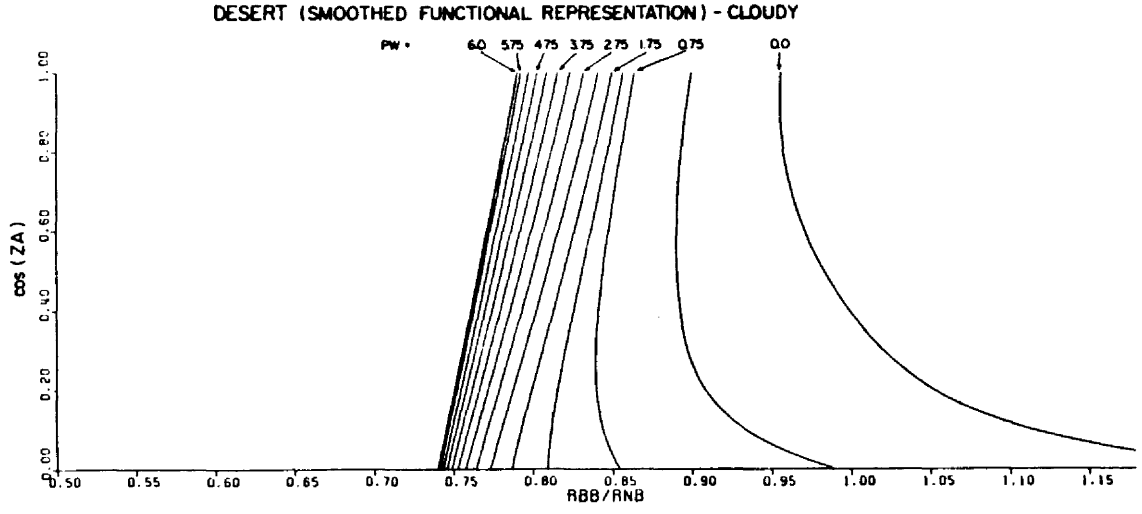

Fig. 2.7b. Same as Fig. 2.6a except for cloud covered desert surface.

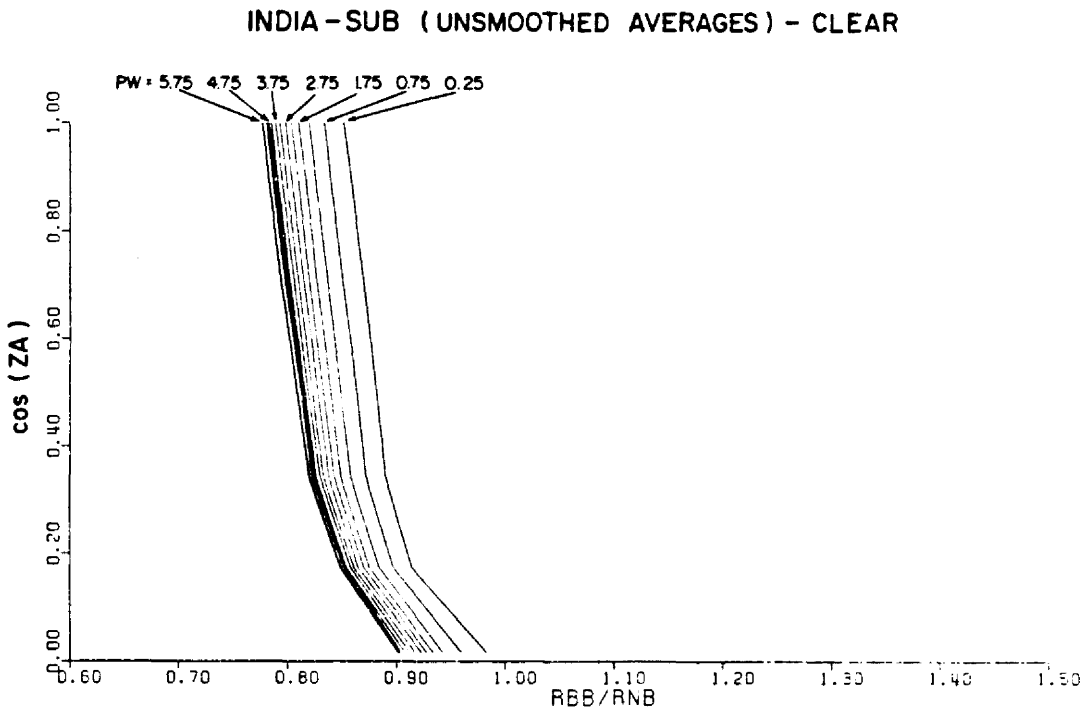

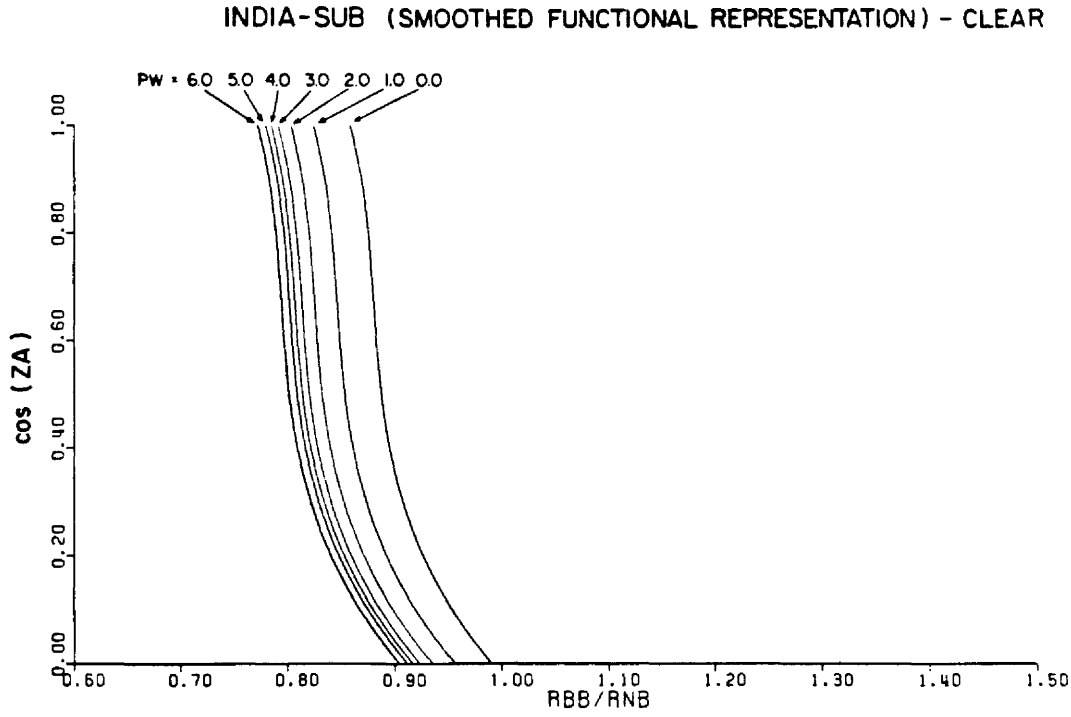

Fig. 2.8a. Same as Fig. 2.6a for cloud free semi-arid surface.

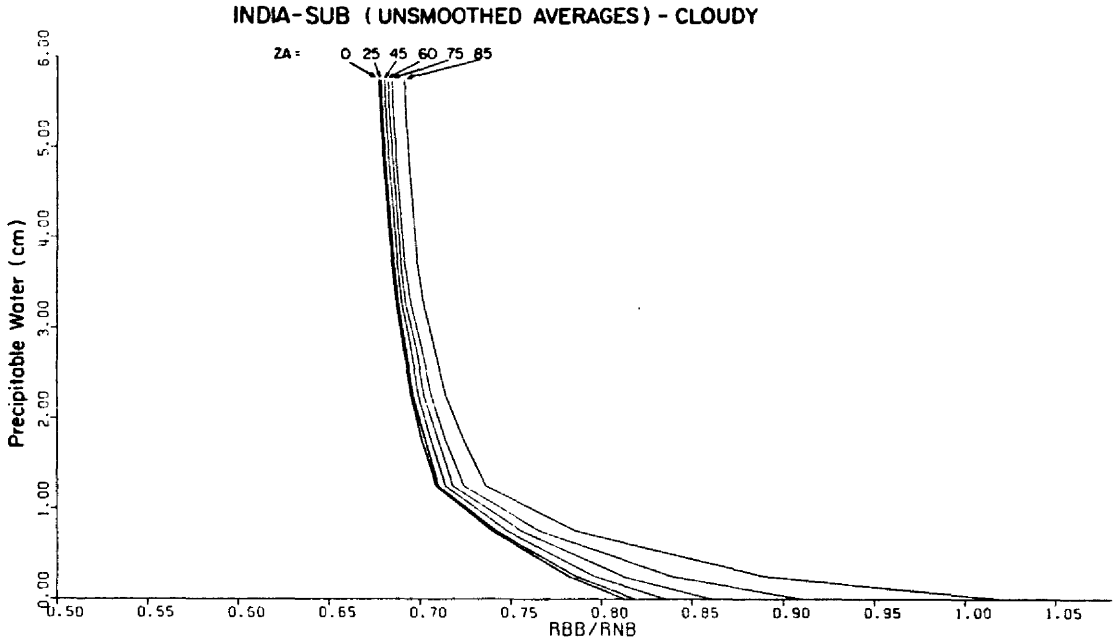

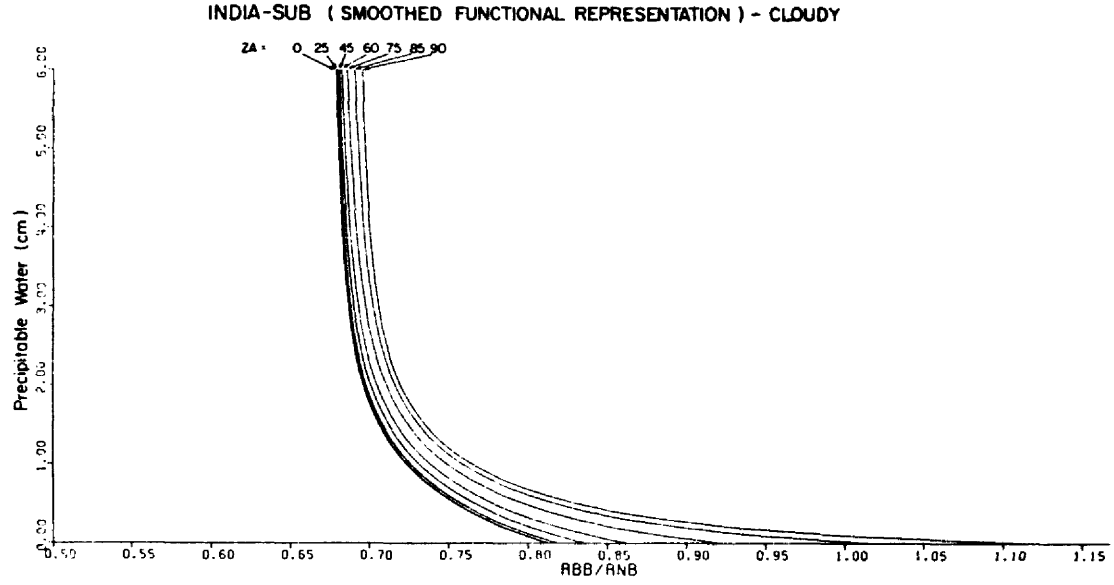

Fig. 2.8b. Same as Fig. 2.6b for cloud covered semi-arid surface. Note that in these two graphs the ordinate is PW.

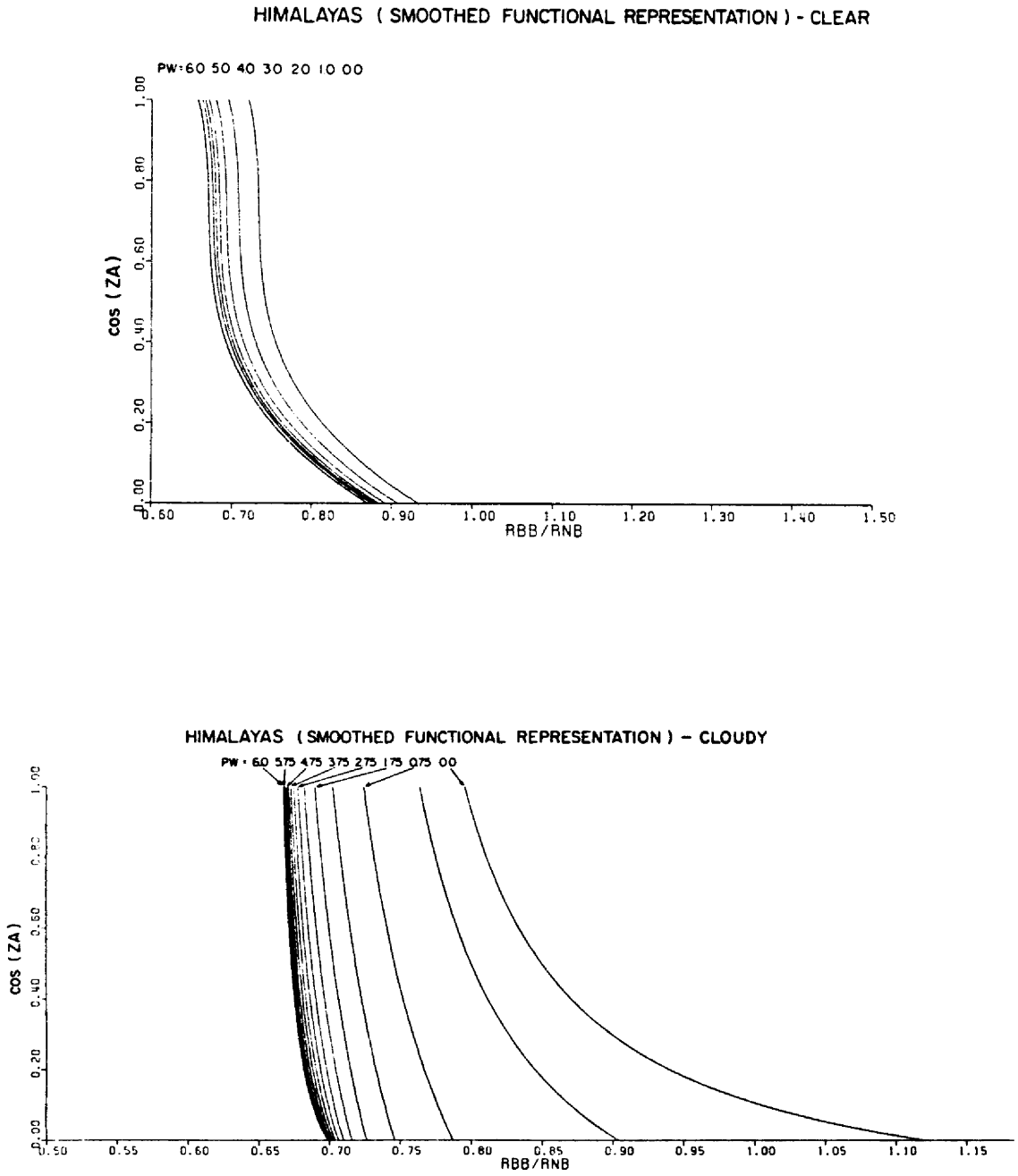

Fig. 2.9. Shortwave NB to BB relationship for Himalayas. The top part is for a cloud-free surface; the bottom part is for a cloud-covered surface.

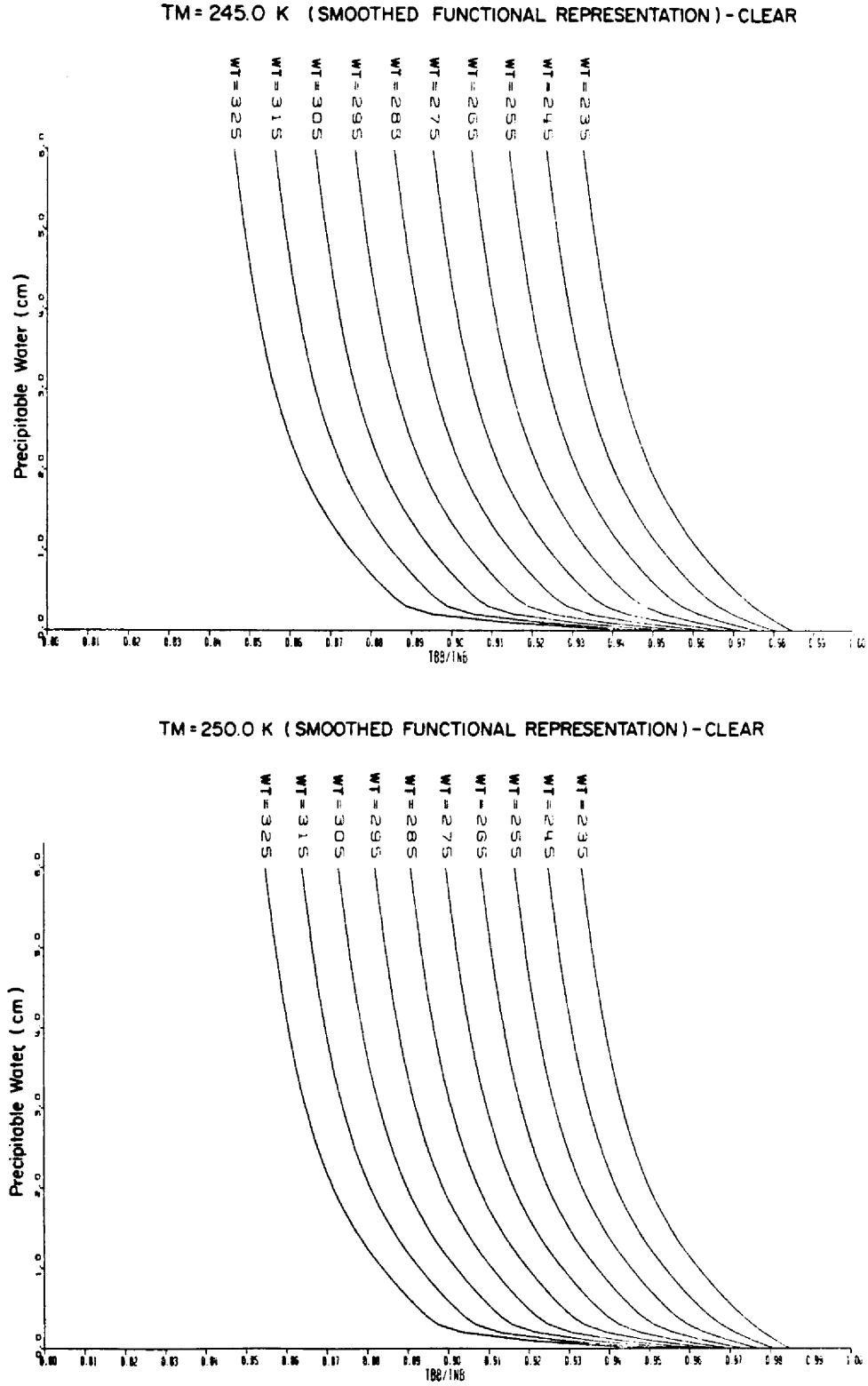

Fig. 2.10a. Longwave NB to BB relationship for clear case. These are smooth analytic representations for TM = 245°K and 250°K.

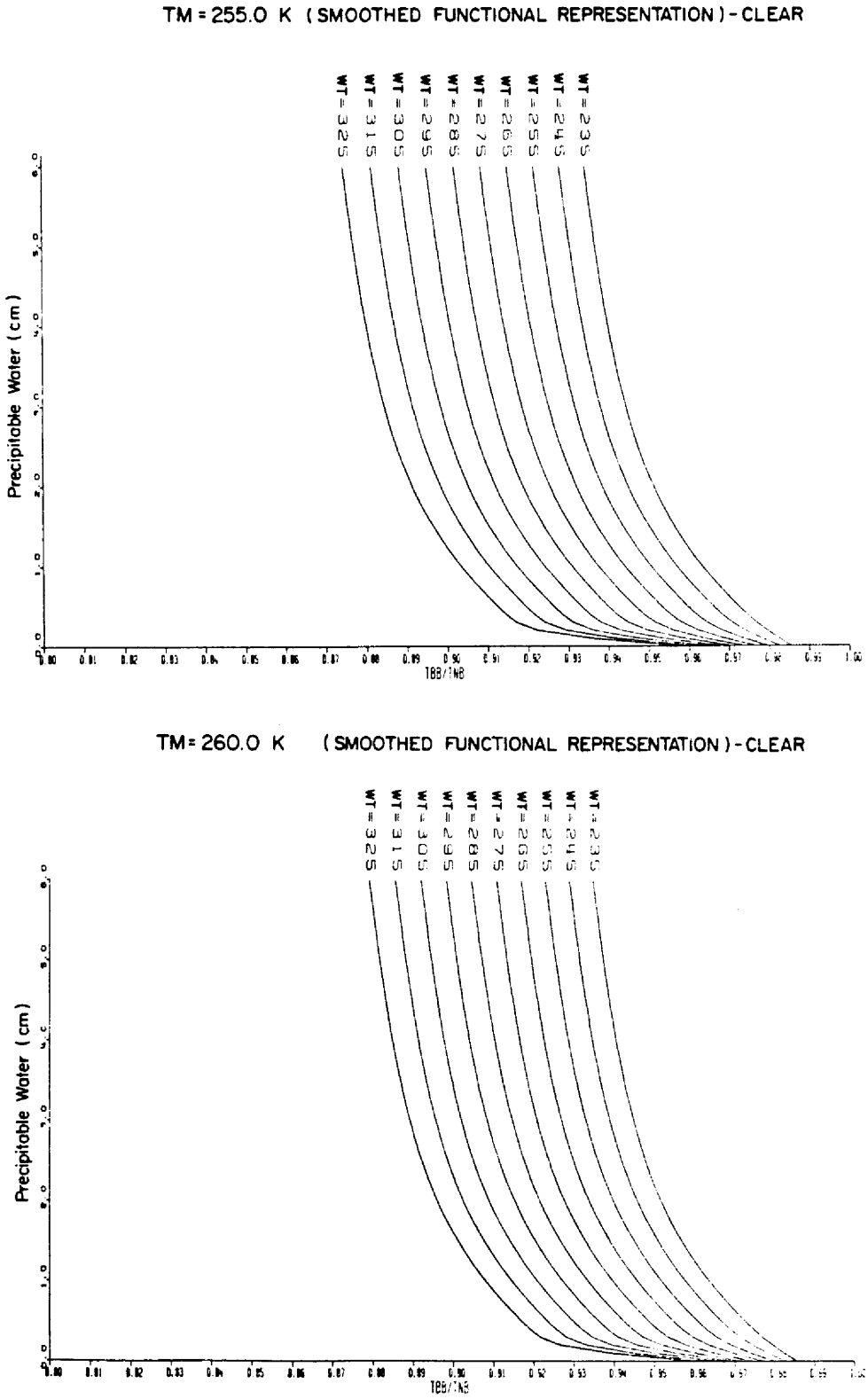

Fig. 2.10b. Continuation of Fig. 2.10a for TM = 255°K and 260°K.

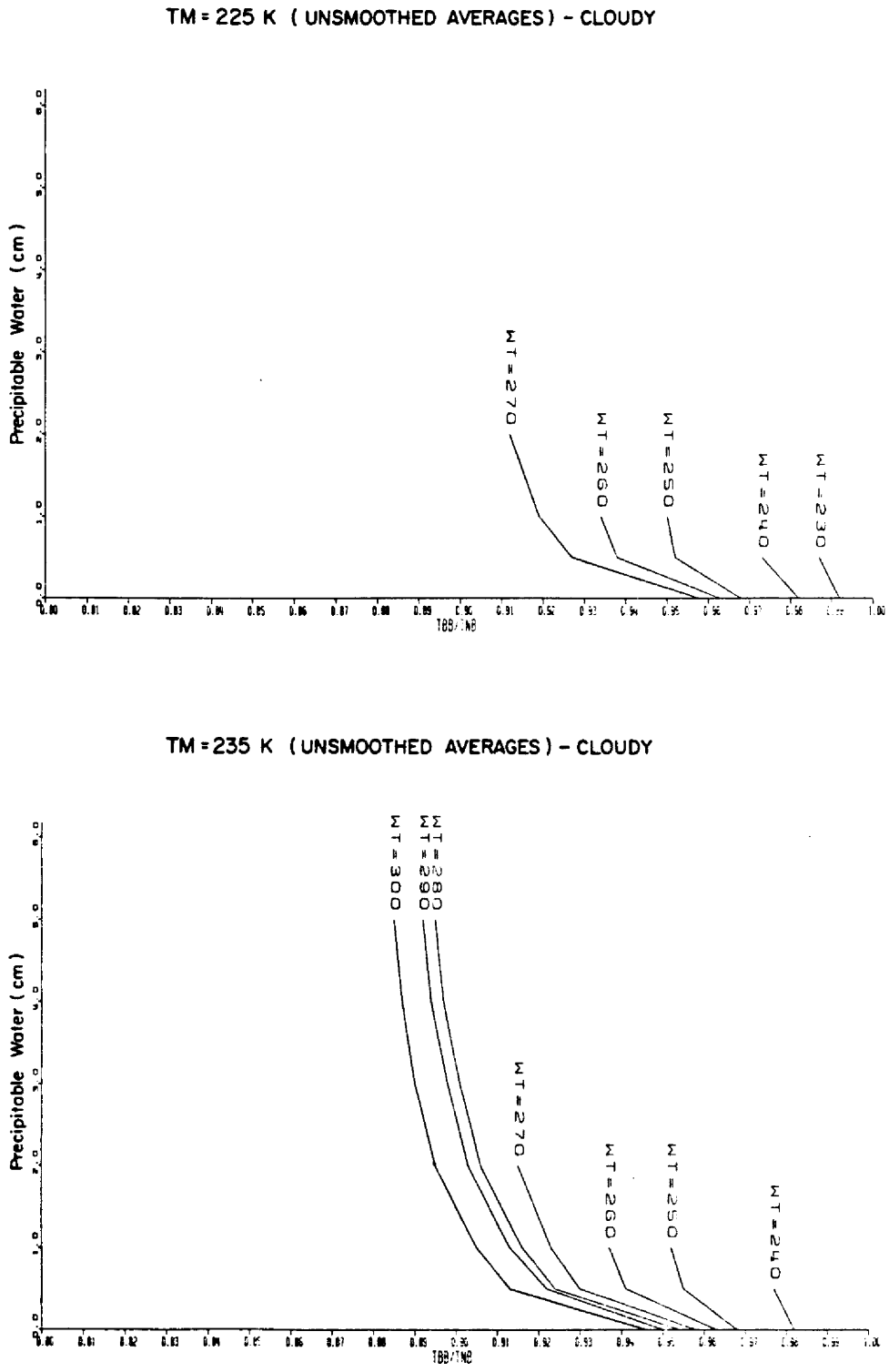

Fig. 2.11. Longwave NB to BB relationship for cloudy case. These are raw statistical composites for TM = 225°K and 235°K.

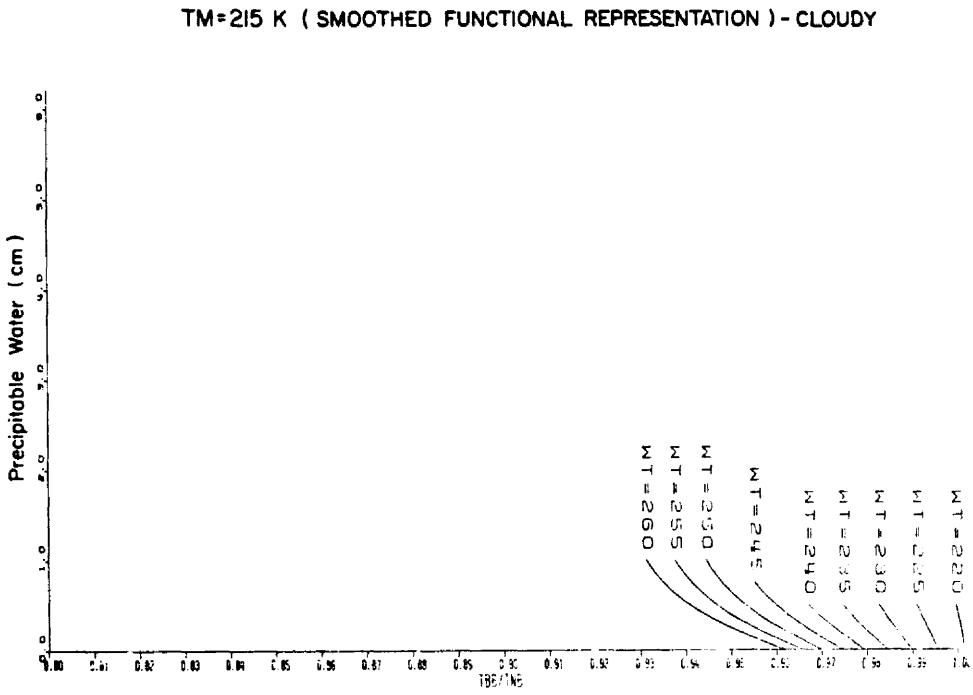

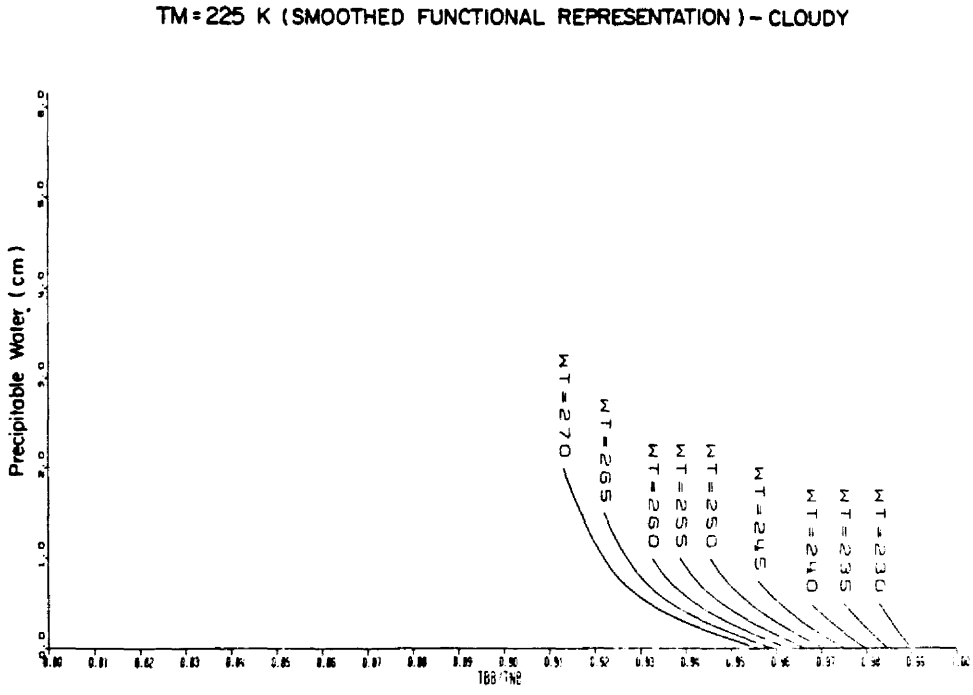

Fig. 2.12a. Longwave NB to BB relationship for cloudy cases. These are smooth functional representations for TM = 215°K and 225°K.

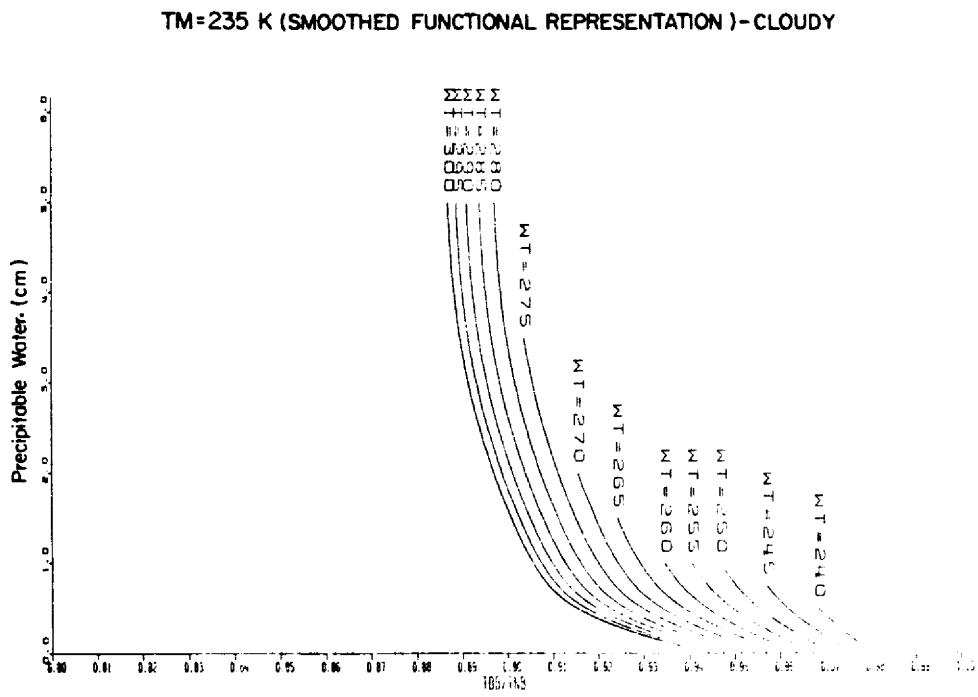

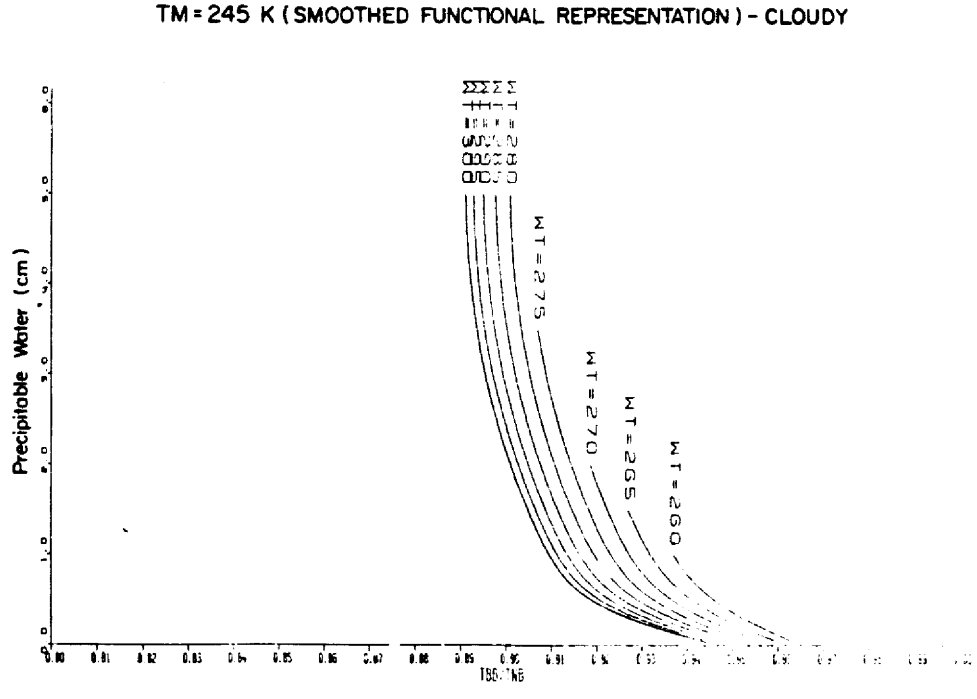

Fig. 2.12b. Continuation of Fig. 2.12a for TM = 235°K and 245°K.

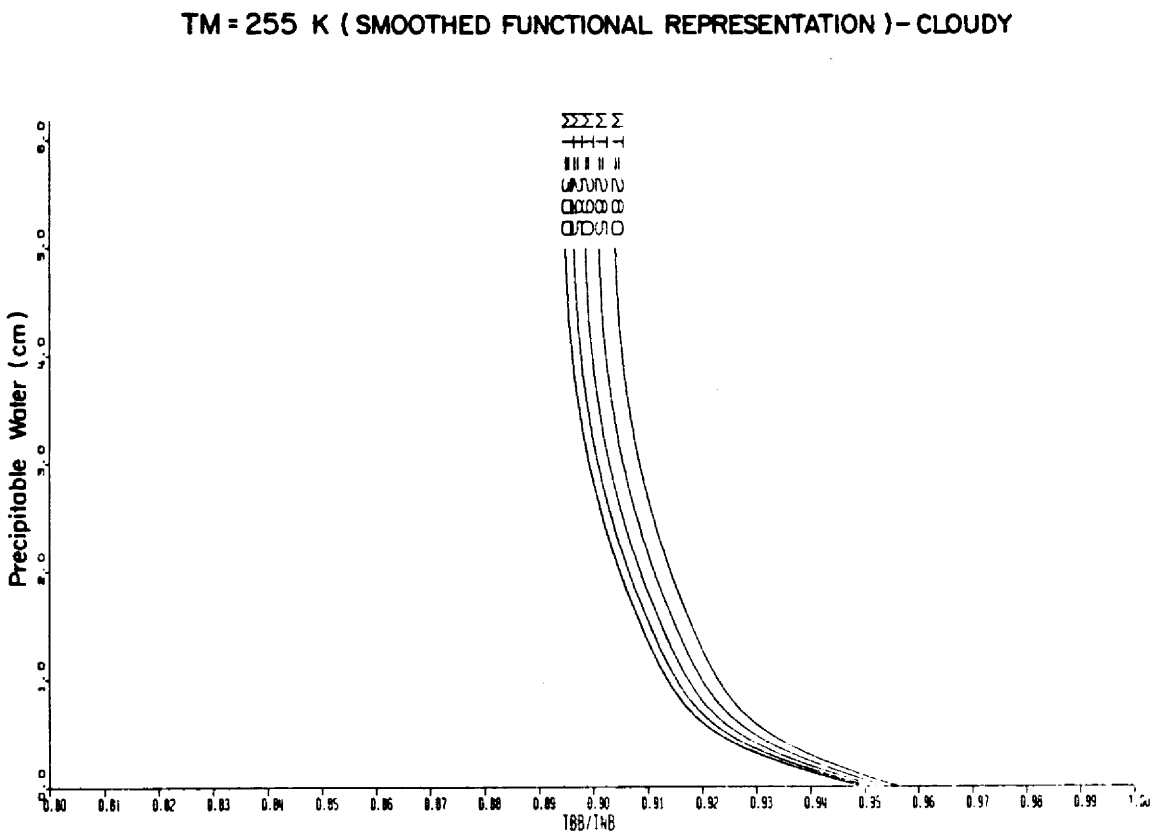

Fig. 2.12c. Continuation of Fig.2.12a for TM = 255°K.

characteristics of many desert surfaces. In this figure the analytic representations are given for both clear and cloudy cases in which the ordinate is switched between PW and CZ thus illustrating the dual non-linear nature of the relationships. A rather interesting effect for the cloud case (i.e. a desert surface underlying cloud) is the cross over seen for small precipitable water amounts. Figures 2.8 and 2.9 illustrate the results for the semi-arid (Indian Sub-Continent) and Himalayan range cases.

Figures 2.10 - 2.12 provide examples for the longwave NB to BB functions. In these figures the abscissa represents the ratio (TBB/TNB) of broad band EBBT to narrow band EBBT; the ordinate represents precipitable water above the earth or cloud surface; and the individual curves represent different values of the proxy surface temperature parameter (WT). Figure 2.10 illustrates the smooth analytic representation for the clear case; part a of the figure includes atmospheric temperatures (TM) of 245°K and 250°K; part b for TM's of 255°K and 260°K. This figure demonstrates the two salient characteristics of the longwave relationships. First the functions are always less then 1.0; and second, the functions are highly non-linear as a function of the overhead water path. Note that the family of curves of WT is compressed when moving from the coldest atmosphere (TM = 245°K) to the warmest atmosphere (TM = 260°K). This is the coupled result of the two Planck effects (i.e., the surface term represented by WT and the atmospheric term represented by TM). The compression is treated as a linear process in the analytic functions.

In Fig. 2.11 results for the cloud case are given in the form of raw statistical composites for TM = 225°K and 235°K. Note that the

curves for a given WT are truncated at varying PW limits to illustrate the natural range of variability of PW, TM and WT implicit in the RTE calculations. Finally in Fig. 2.12 the NB to BB functions are given in smooth analytic form for TM between 215°K and 255°K in steps of 10°C. Note that similar to the clear case, there is a large change in the TBB/TNB ratio as the surface temperature (WT) is varied.

2.4.7 Direct Verification of the Spectral Transformation Functions

Directly verifying NB to BB relationships over the detailed domain inherent in a parameterization study is not possible with conventional aircraft and satellite spectrometer data. However to illustrate some limited longwave intercomparisons Fig. 2.13 is provided. The theoretical calculations are based on a seven (7) band flux emissivity model which served as an earlier and less refined version of the present seventeen (17) band transmissivity model. Figure 2.13a represents an intercomparison for a clear atmosphere: Fig. 2.13b for a cloudy atmosphere. For both the clear and cloudy cases observational results have been compiled from a satellite Infrared Interferometer Spectrometer (IRIS) and a coupled pair of aircraft mounted downward facing radiometers (an Eppley Flux Pyrgeometer and a Barnes PRT-5 directional window radiometer). The IRIS instrument was flown on the Nimbus 3 Experimental Satellite (see Hanel, 1969); the data used here were obtained during July, 1969. The aircraft radiometers were flown on the NASA Convair-990 during May/June 1979 over the Summer MONEX region (see Smith, et al., 1980). Both the satellite and aircraft data show reasonably good comparison with the theoretical calculations. Note that some of the problems with using observational data in the development of

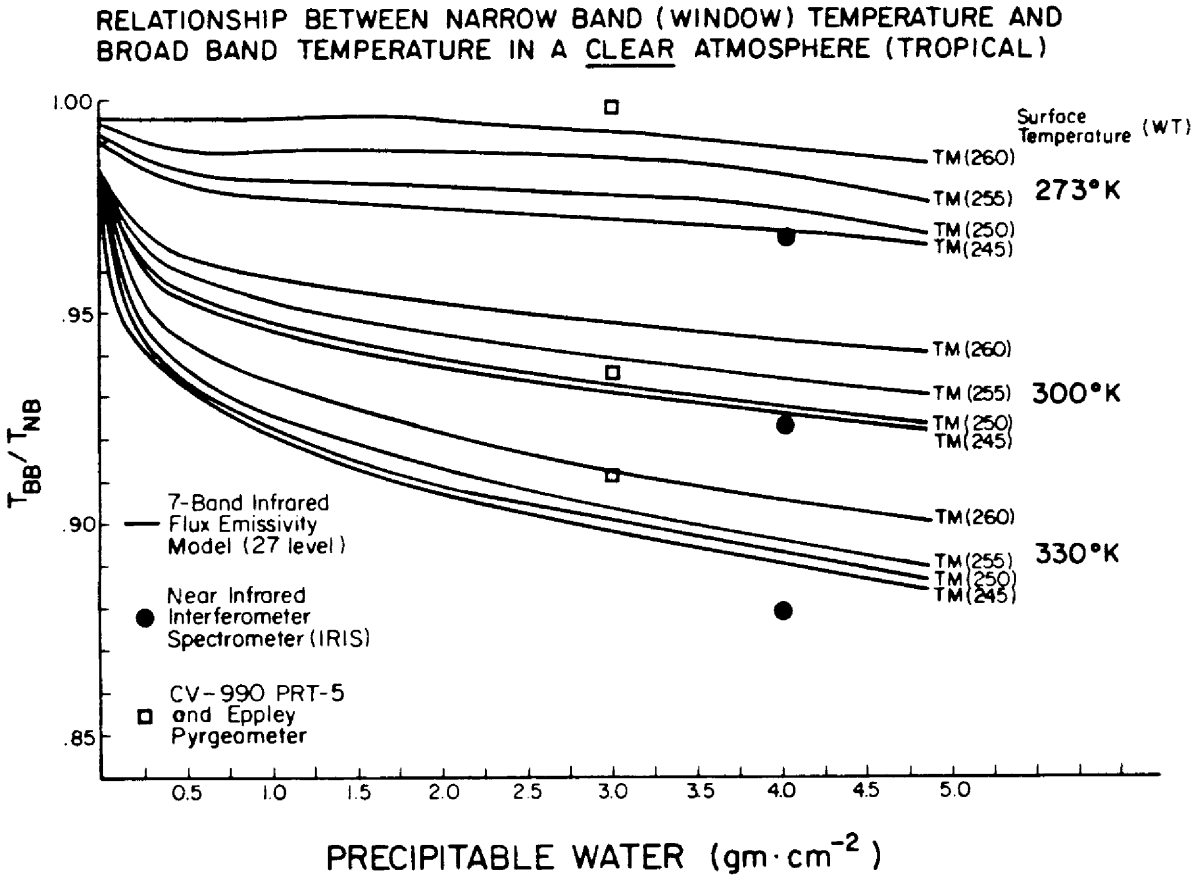

ERRORS DUE TO BLACK BODY ASSUMPTION (W·m^{-2})

	HOT SURFACE	OCEAN SURFACE	COLD SURFACE
DRY Atmosphere	180	80	15
MOIST Atmosphere	250	115	30

Fig. 2.13a. Comparison of theoretically synthesized infrared NB to BB relationships in a clear atmosphere to observationally based relationships derived from satellite and aircraft measurements taken over tropical atmospheres.

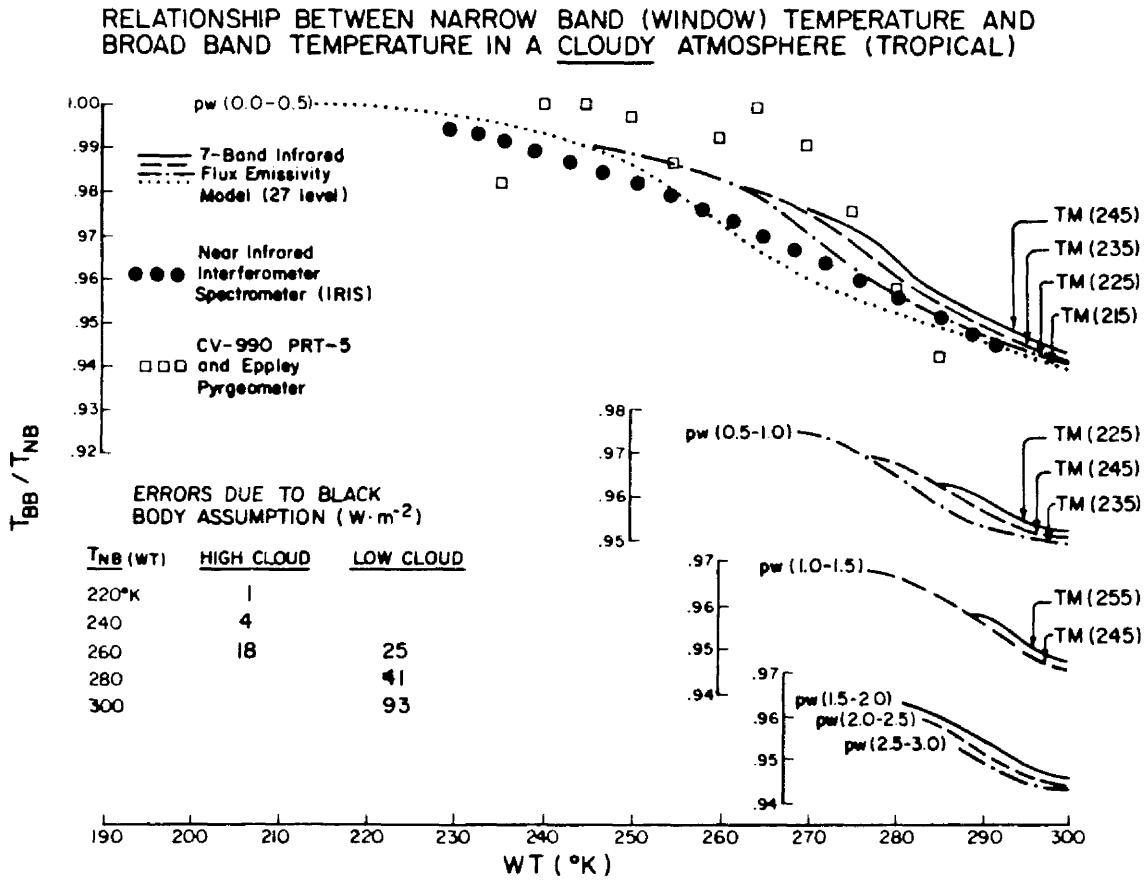

Fig. 2.13b. Same as Fig. 2.13a for a cloudy atmosphere.

a parameterization are apparent in these diagrams; i.e., sparse data sampling and discontinuities caused by statistical noise.

2.5 Application of the Parameterization to Weather Satellite Data Sets

In the application of the geometric and spectral transform models to weather satellite data, the calculations are carried out in conjunction with histograms of the satellite radiance data over a 0.5 by 0.5 degree sub-grid scale. In this fashion transform calculations are only made at the discrete radiance levels on a histogram abscissa associated with a given sub-grid, not for every pixel within a sub-grid. A pre-defined surface type map (see Fig. 2.14) based on a geographic Atlas of Edlin and Huxley (1973) indicates whether a given sub-grid's surface will be characterized as water, desert, semi-arid, or mountainous. A diurnally modulated EBB temperature threshold is used to discriminate between clear and cloudy conditions. The temperature waves used in the thresholding process, which were derived from composited GOES-1 observations, are sinusoidal and symmetric about local noon. The minimum-maximum temperatures values associated with the waves (one for each surface type) are given in Table 2.4.

As indicated in a schematic illustration of the parameterization application procedure, shown in Fig. 2.15, a spectrum of cloud top heights is allowed for at the 0.5 degree sub-grid scale. A set of transformation coefficients are calculated for each member of the cloud ensemble (vertical stratification) and for the clear region. The PW and TM terms are calculated from temperature-moisture profiles based on the 5° resolution/one week average Level III-b FGGE profile data over the Southwest Monsoon region; see Bengtsson, et al. (1982). The sea surface temperature and sea surface vapor pressures are based on the Surface

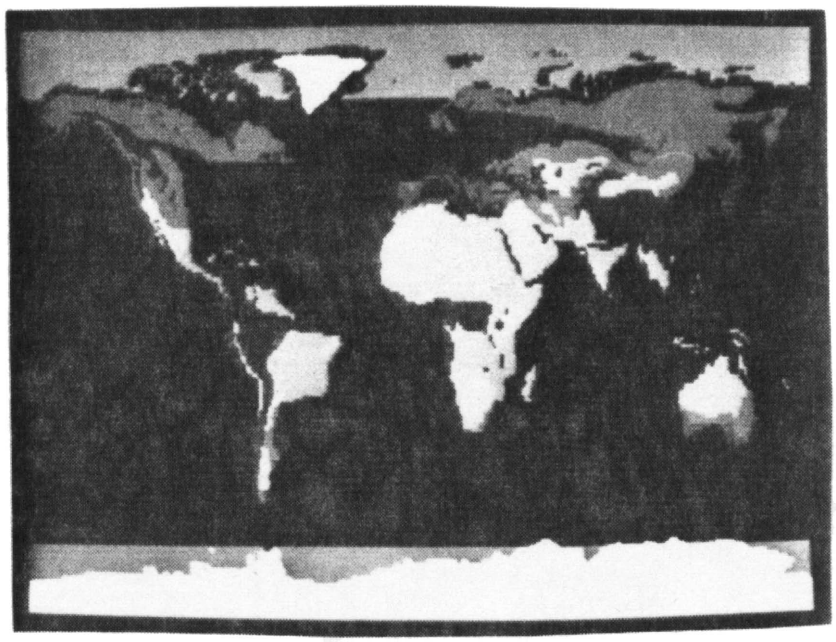

Color Key

1. water	- blue	7. coniferous forest	- dark green
2. snow	- white	8. pasture	- red
3. ice	- grey	9. scrub	- deep orange
4. tundra	- black	10. semi-desert	- light orange
5. high mountain	- purple	11. savannah	- beige
6. deciduous forest	- light green	12. desert	- yellow

Fig. 2.14a. Portrayal of the global surface type map based on the atlas of Edlin and Huxley (1973).

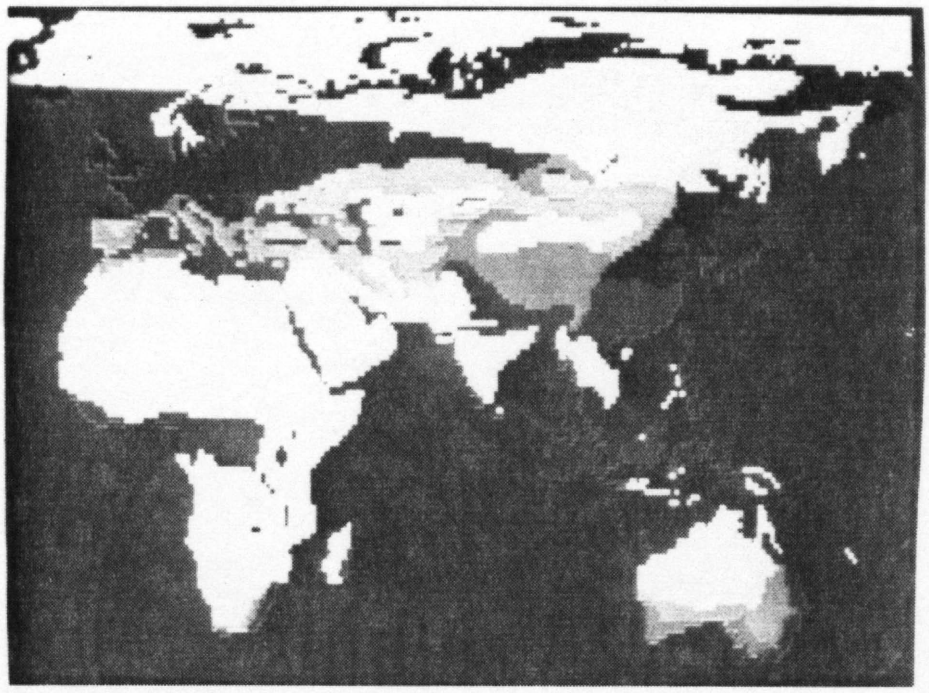

Color Key

1. water	- blue	7. coniferous forest	- dark green
2. snow	- white	8. pasture	- red
3. ice	- grey	9. scrub	- deep orange
4. tundra	- black	10. semi-desert	- light orange
5. high mountain	- purple	11. savannah	- beige
6. deciduous forest	- light green	12. desert	- yellow

Fig. 2.14b. Enlargement of the monsoon region.

TABLE 2.4

Minimum and Maximum EBB Temperatures (degrees Centigrate) of the Sinusoidal Temperature Waves Used to Discriminate Between Clear and Cloudy Conditions for Each of the Four Surface Type Categories.

	Water	Desert	Semi-Arid	Himalayas
Minimum	29.5	22	23	-5
Maximum	29.5	43	40	+12

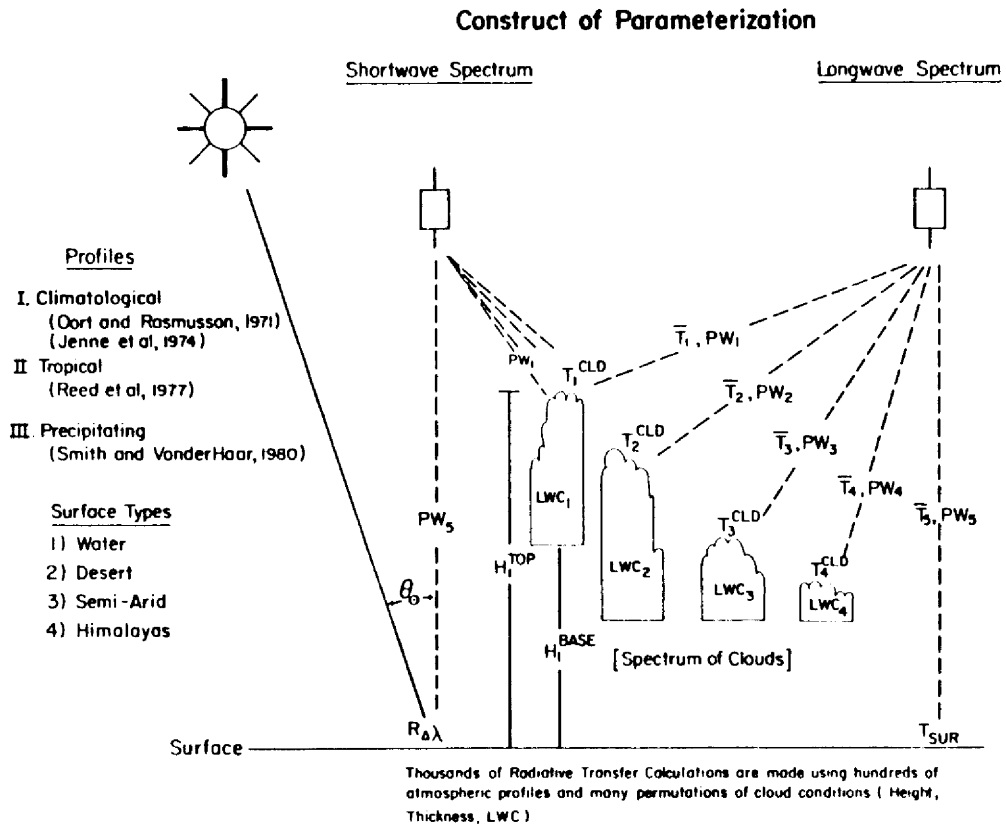

Fig. 2.15. Schematic illustration of the application of the parameterization procedure over a 0.5 by 0.5 degree sub-grid domain containing an ensemble of cloud top heights.

Atlas of Ramage, et al. (1972) which incorporates observations taken during the 1963-1964 International Indian Ocean Expedition. Note that in the case of clouds, the PW and TM terms are calculated by integrating from the top of the atmosphere down to cloud top, not to the earth surface.

2.6 Intercomparison of Weather Satellite Radiation Budget Estimates with Broad Band Flux Quantities

In order to assess the reliability and accuracy of the parameterization scheme, an intercomparison experiment utilizing weather satellite RADBUD estimates has been carried out. The parameterization scheme is tested on two operational satellite data sets collected for the 1979 SMONEX and includes both polar orbiting satellite measurements and geosynchronous orbiting satellite measurements. The first data set has been derived from the TIROS-N AVHRR Global Area Coverage (GAC) data archive prepared by the NOAA Environmental Data and Information Service (EDIS-now part of NESDIS). The calibration of these data has been described by Kidwell (1979); the reformatting and mapping of the raw orbital swath data have been described by Smith and Graffy (1982). The data series processed for the SMONEX research project consists of day and night 4-channel digital monsoon sectors (EQ - 35^{o}N; 30^{o}E - 100^{o}E) for the period from May 1 to August 30, 1979 (with the exception of a 13 day data gap from August 6 - 18 (see Smith and Vonder Haar, 1983). In this study only the channel 1 (VIS) and channel 4 (window IR) data were used.

The second data set has been derived from the GOES-1 VISSR video cassette recordings made at the European Space Agency's (ESA) Villa Franca ground station outside of Madrid during 1979. The VIS and IR data were collected based on a cooperative agreement between ESA and

NOAA under the auspices of the First GARP Global Experiment (FGGE) Project Office and in conjunction with the Summer Monsoon Experiment. A ground system designed for recording the GOES-1 digital imagery on Sony video cassette recorders was developed at the University of Wisconsin's Space Science and Engineering Center (the Offline Data Ingest System - ODIS) and was provided to NOAA for use during FGGE. The Villa Franca ODIS equipment was later loaned to CSU by NOAA in order to facilitate the creation of computer compatible tapes from the video cassettes. In-depth discussions of the GOES-1 VISSR data are given by Smith and Vonder Haar (1980b,1983); an explanation of the navigation and calibration procedures needed in the gridding-mapping phases are found in Smith (1980a), Smith and Phillips (1972), and Smith and Vonder Haar (1980a). The data series processed for the SMONEX research project consists of 3-hourly VIS and IR digital monsoon sectors ($30^{o}S$ - $40^{o}N$; $30^{o}E$ - $100^{o}E$) for 10 day periods during the middle of each month from January to September 1979. In addition all days during the months of May, June, and July are processed at the 3-hourly sequence. There are intermittent periods during the May-August period when the GOES-1 IR detector was not operative (see Smith and Vonder Haar, 1983).

The broad band flux intercomparison data have been obtained from three sources. The first and foremost data for validation purposes have been derived from the Earth Radiation Budget (ERB) instrument flown on the Nimbus-7 experimental satellite [see Jacobowitz, et al. (1978)]. The data used in this study consist of measurements from the wide-field-of-view (WFOV) radiometers. Additional validation data have been obtained from 1) flux radiometers mounted on the NASA CV-990 experimental jet aircraft which participated in the early phases of

SMONEX (see Smith, et al., 1980); and 2) surface flux radiometers based on a surface energy budget experiment which I conducted in the Saudi Arabian Empty Quarter during June 1981; see Smith, et al. (1982a) and Chapter 4. Finally various theoretical calculations based on the aforementioned RTE models are used to generate top-of-atmosphere fluxes in conjunction with the aircraft and surface data (see Ackerman, et al., 1983). Table 2.5 summarizes the inputs to the intercomparison procedure.

2.6.1 Nimbus-7 Intercomparison

In order to implement the Nimbus-7 ERB-WFOV intercomparison it is essential that the weather satellite RADBUD retrievals be placed in a time-space domain similar to that of the WFOV observations. This cannot be done exactly for a variety of reasons (differing sampling times, differences in the FOV response functions, differing missing data problems, differing navigational procedures); however, the impact of these differences lead to fairly small random errors if the intercomparison space and time scales are sufficiently large, and a reasonably large region of the earth is examined. These constraints are met by intercomparing at the nominal ERB-WFOV scales, i.e., monthly averages and 14^{o} spot sizes, and viewing all targets over the SMONEX region. In addition, to eliminate as much eventual bias between the reference data and weather satellite estimates as possible, an independent data set of WFOV targets is ratioed with corresponding TIROS-N and GOES-1 targets in order to produce de-biasing coefficients. This approach negates any requirement to incorporate a shortwave directional reflectance adjustment to bring the albedos into time correspondence The TIROS-N has 3:00 and 15:00 equator transit times; the

TABLE 2.5

Components of the Experiments to Validate the Spectral Radiance to Broad Band Flux Transformations.

METHOD: INTERCOMPARISON

BETWEEN: REFERENCE MEASURES
AND
TIROS-N AND GOES-1 RETRIEVALS

REFERENCE MEASURES

1) NIMBUS 7 ERB/WFOV

2) AIRCRAFT FLUX RADIOMETERS

3) SURFACE FLUX RADIOMETERS

4) THEORETICAL MODEL CALCULATIONS

Nimbus-7 has midnight and noon equator transit times. The de-biasing factors implicitly include all directional reflectance effects (for the polar orbiting data only) as well as adjusting for any data set biases embedded in the parameterizations.

The area selected for the WFOV intercomparison is shown in Fig. 2.16, a large region surrounding the principal meteorological elements of the Southwest Monsoon system. Note that the grid dimensions(footprint size) change slightly as one moves away from the equator. This is due to the quasi-equal area processing of the Nimbus-7 RADBUD information. The GOES-1 data extend over this complete domain; the TIROS-N data do not extend north of 35^{o}N or south of the equator.

In order to equivalence the space and time scales in the intercomparison the 0.5 by 0.5 degree weather satellite RADBUD estimates are averaged up to the monthly time scale and the 14 degree space scale (i.e. a quasi-circular footprint 7^{o} in radius). Since the FOV response function for the ERB-WFOV radiometer is not flat, a weighting procedure has been implemented in the spatial averaging to simulate the Nimbus-7 ERB-WFOV instrument FOV response function. This procedure is illustrated schematically in Fig. 2.17.

Intercomparisons between TIROS-N retrievals and Nimbus-7 retrievals have been carried out for the months of May and June, 1979. This period corresponds to the pre-monsoon and monsoon onset phases in which there are dramatic changes taking place in the cloudiness and precipitation fields as monsoon activity develops. The albedo intercomparison's for May and June are illustrated in Fig. 2.18. Each character in a scattergram represents a retrieval spot - the different character types indicate the characteristic surface background according to the keys in

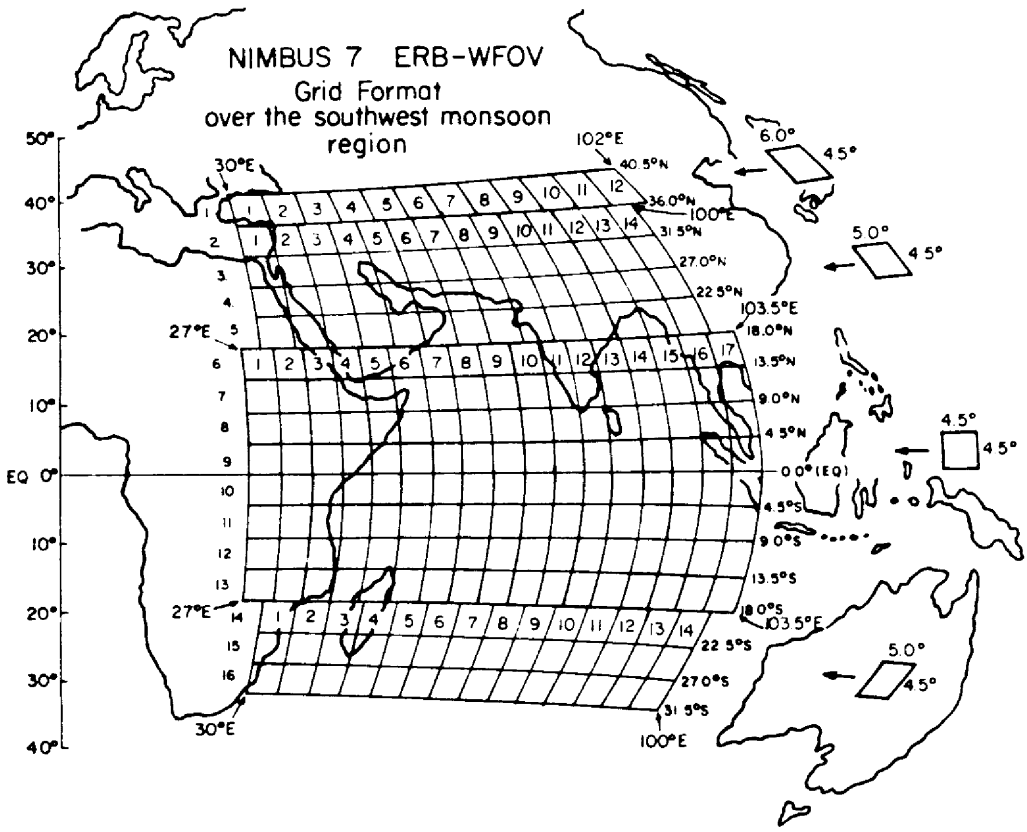

Fig. 2.16. Nimbus-7 ERB-WFOV grid format over the Southwest Monsoon region.

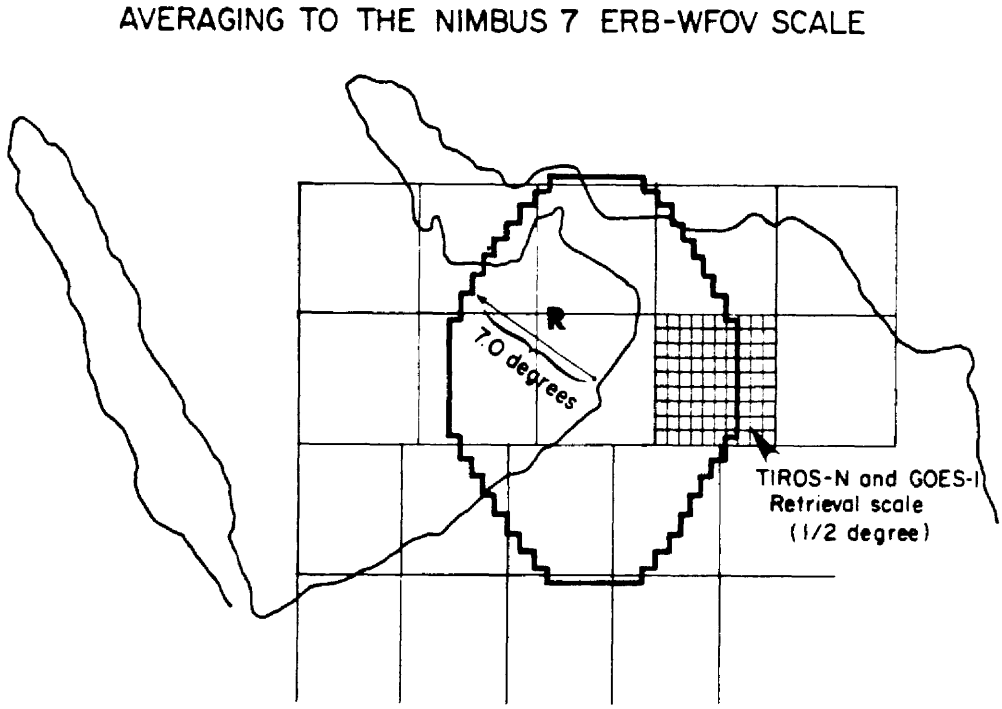

Fig. 2.17. Schematic illustration of the weighting scheme used in the spatial averaging of the weather satellite RADBUD estimates to bring them into geographic spatial correspondence with the Nimbus-7 ERB-WFOV targets.

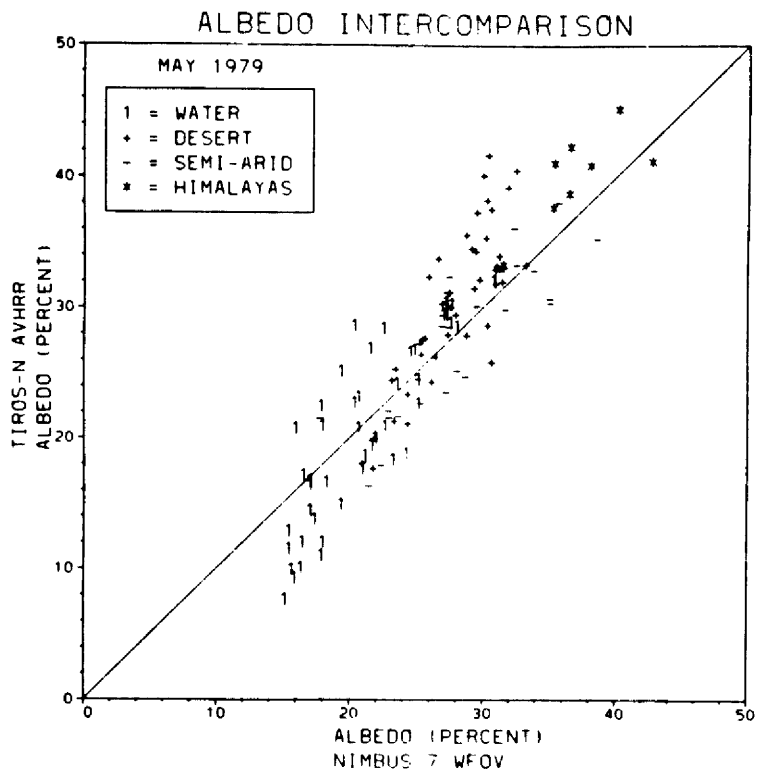

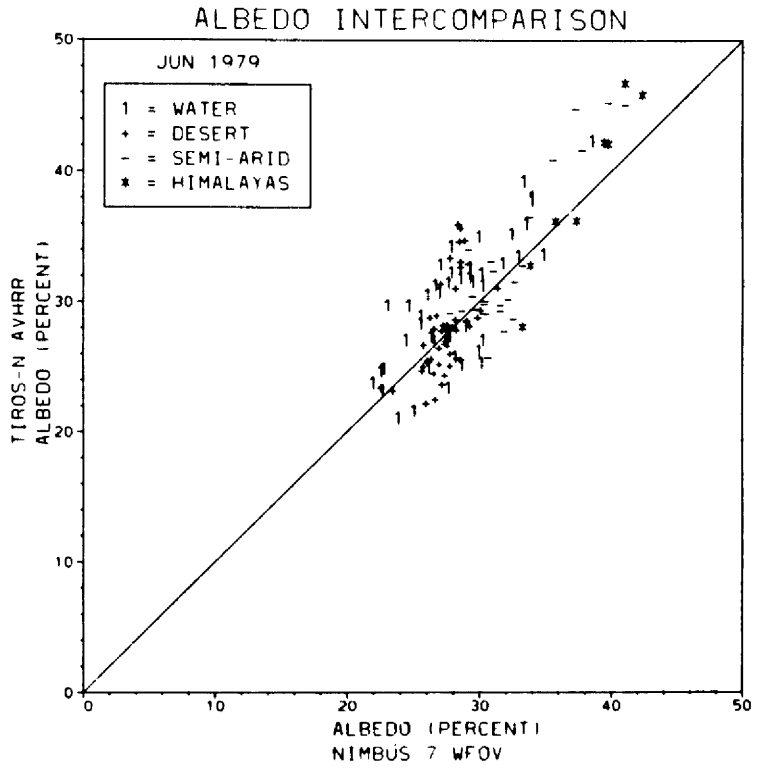

Fig. 2.18. Intercomparison between Nimbus-7 ERB-WFOV albedo measurements and TIROS-N AVHRR (channel 1) albedo estimates during May and June, 1979 over the Southwest Monsoon region.

the upper left hand portions of the scattergrams. The principal statistical parameters are given in Table 2.6. It is apparent that the correlations are high and all significant at the 99% confidence level. The remaining biases are very low; the mean random uncertainty is on the order of 4%. Notice that in the May scattergram there is a wider range of albedos due to the lesser amount of cloud (more surface exposure) associated with pre-monsoon meteorological conditions.

An immediate conclusion that can be drawn in regards to the utilization of albedo retrievals extracted from weather satellite radiances is that they are more than adequate for energetic studies but border-line for long term global climate monitoring. This is not an altogether surprising result; and in light of the fact that it still remains to be seen whether the sampling problems associated with highly accurate WFOV radiometers can be overcome for inter-annual monitoring of the global radiation budget, it is no reason for despair. Clearly the errors are well within a range that make the albedos useful for energy budget studies of medium to large scale weather systems or patterned grid layouts.

The infrared emittance intercomparisons for the same months are given in Figs. 2.19-2.21 corresponding to the daytime period, nighttime period, and the combined day and night periods. There is a considerable improvement in these correlations and difference parameters (biases and RMS differences) as can be seen in Table 2.7. The RMS differences are on the order of 10 $W.m^{-2}$ which represents an error of approximately 5% with respect to the mean. The one anomolously low correlation seen in Table 2.7 for nighttime desert during May is simply due to the fact that during the night, for a relatively cloudless period, the effective range

TABLE 2.6

Nimbus-7:TIROS-N Albedo Intercomparison Statistics (the bias and RWS differences are given in terms of: fractional albedo/percentage wrt mean)

I. May, 1979

	Mean Bias	RMS Difference	Correlation*
Ocean	-0.50/2.4	3.91/19.1	.85
Desert	+2.48/8.2	4.56/15.1	.83
Semi-Arid	-0.48/1.7	2.99/10.7	.85
Himalayas	+2.99/7.5	3.75/9.4	.76
All Categories	+0.76/2.8	4.00/14.9	.90

II. June, 1979

	Mean Bias	RMS Difference	Correlation
Ocean	+1.59/5.3	3.42/11.5	.77
Desert	+0.57/2.0	2.98/10.7	.59
Semi-Arid	+0.70/2.1	3.24/9.9	.88
Himalayas	+0.91/2.4	3.30/8.5	.97
All Categories	+1.00/3.3	3.22/10.6	.83

*All correlations significant at the 99% confidence level.

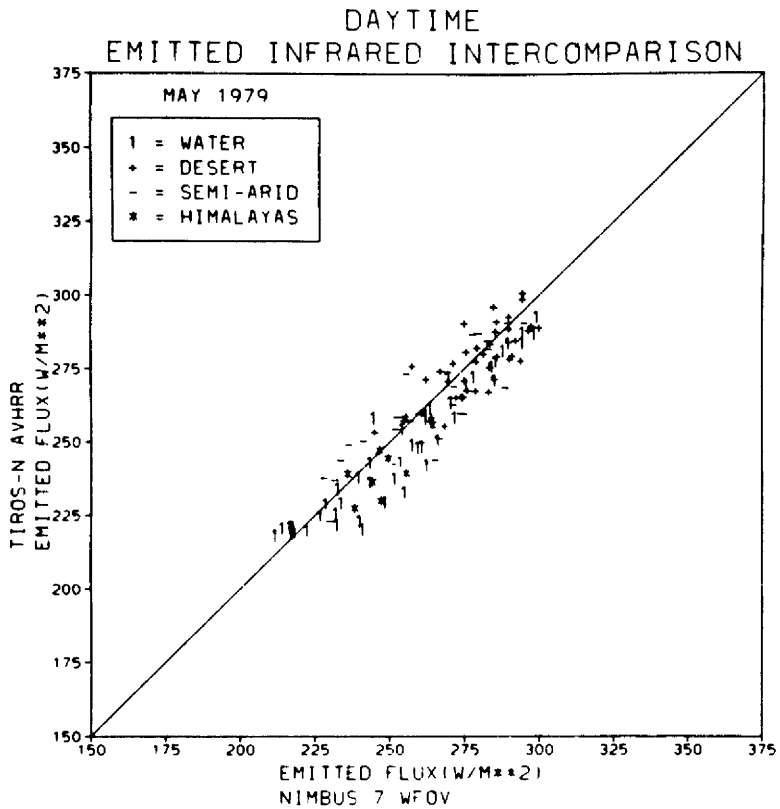

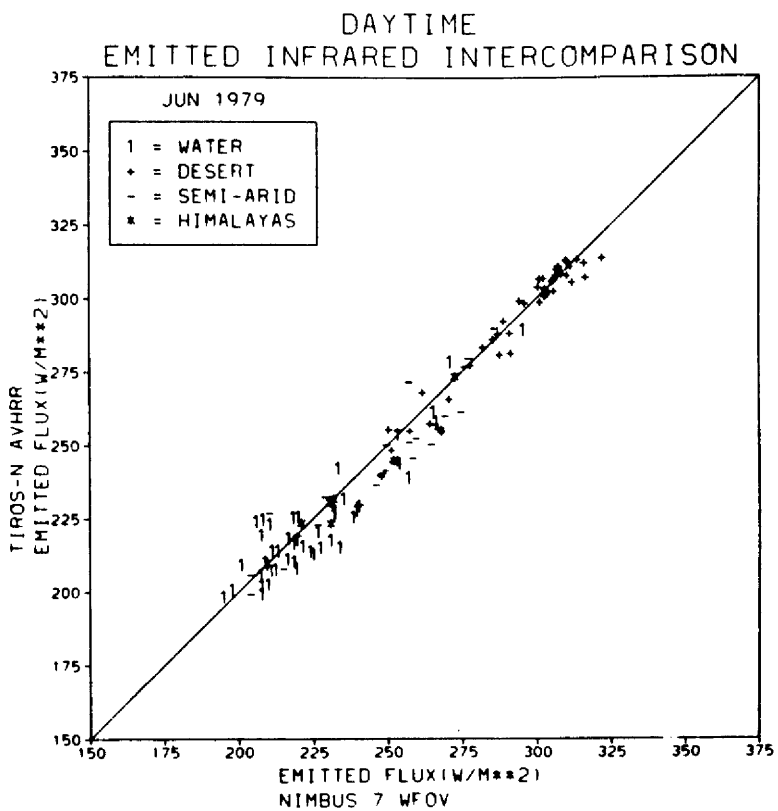

Fig. 2.19. Intercomparison between Nimbus-7 ERB-WFOV Daytime emitted IR measurements and TIROS-N AVHRR (channel 4) daytime emitted IR estimates during May and June, 1979 over the Southwest Monsoon region.

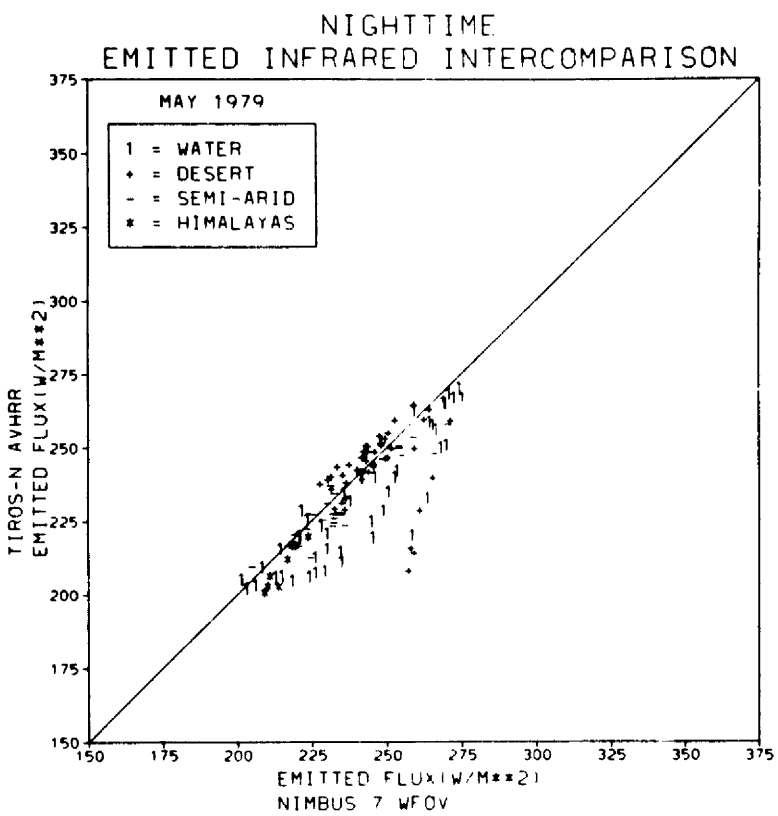

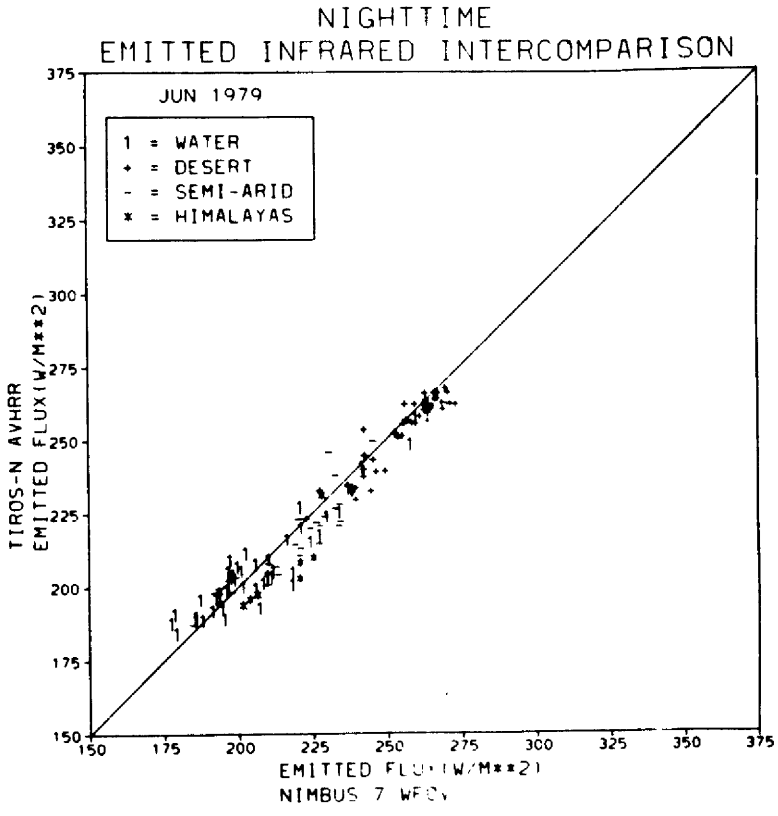

Fig. 2.20. Same as Fig. 2.19 for nighttime IR.

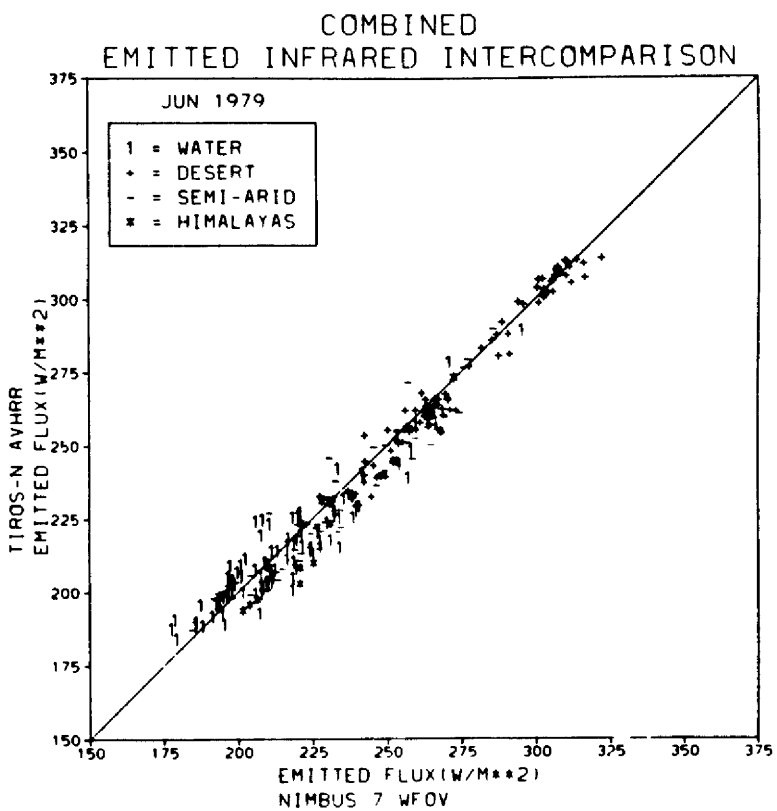

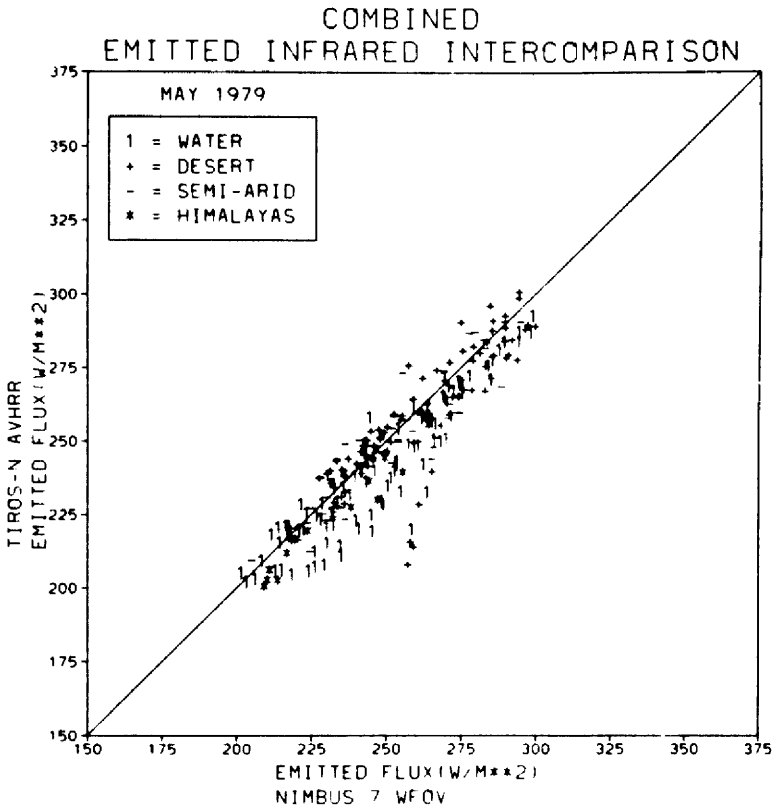

Fig. 2.21. Same as Fig. 2.19 for combined day-night time IR.

TABLE 2.7

Nimbus-7:TIROS-N Infrared Emittance Intercomparison Statistics (the bias and RMS differences are given in terms of: LW flux/percentage wrt mean)

I. May, 1979

		Mean Bias	RMS Difference	Correlation*
Day	Ocean	-6.0/2.4	9.8/4.0	.95
	Desert	-1.9/0.7	8.5/3.1	.78
	Semi-Arid	-0.9/0.3	10.2/3.9	.85
	Himalayas	-7.6/3.2	10.2/4.3	.69
	All Categories	-3.6/1.4	9.5/3.7	.92
Night	Ocean	-9.5/4.1	13.7/5.9	.89
	Desert	-3.0/1.2	14.5/6.0	.22
	Semi-Arid	-3.9/1.7	6.8/2.9	.93
	Himalayas	-5.6/2.7	6.3/3.0	.94
	All Categories	-5.8/2.5	12.5/5.3	.81
Combined	Ocean	-8.2/3.5	12.3/5.2	.93
	Desert	-2.5/1.0	13.0/5.1	.81
	Semi-Arid	-2.5/1.0	8.4/3.5	.93
	Himalayas	-6.5/3.0	8.1/3.7	.96
	All Categories	-4.7/1.9	11.1/4.5	.91

*All correlations significant at 99% confidence level

TABLE 2.7 (Continued)

Nimbus-7:TIROS-N Infrared Emittance Intercomparison Statistics (the bias and RMS differences are given in terms of: LW flux/percentage wrt mean)

II. June, 1979

		Mean Bias	RMS Difference	Correlation*
Day	Ocean	-2.7/1.2	9.0/4.0	.91
	Desert	-0.8/0.3	9.7/1.6	.98
	Semi-Arid	-3.7/1.5	8.5/3.5	.94
	Himalayas	-4.2/1.7	6.7/2.8	.96
	All Categories	-2.4/0.9	7.5/3.0	.98
Night	Ocean	-0.7/0.3	7.2/3.5	.93
	Desert	-2.7/1.1	5.3/2.1	.93
	Semi-Arid	-2.8/1.3	7.1/3.3	.91
	Himalayas	-7.8/3.8	10.9/5.3	.79
	All Categories	-2.3/1.0	6.9/3.1	.97
Combined	Ocean	-1.3/0.6	8.0/3.8	.94
	Desert	-2.1/0.8	5.1/1.9	.98
	Semi-Arid	-3.2/1.4	7.6/3.3	.96
	Himalayas	-6.8/3.1	9.7/4.5	.95
	All Categories	-2.3/1.0	7.2/3.0	.98

*All correlations significant at 99% confidence level

of desert skin temperature is so small that a correlation test is relatively meaningless. The nighttime results for May indicate 7 targets out of good correspondence (there are a total of 124 targets). These discrepancies are not yet understood, however on the whole, the IR estimates are in excellent agreement. These results suggest, therefore, that the accuracy of the daytime net radiation component is mostly driven by uncertainties in the solar estimates, not in the infrared estimates.

2.6.2 Aircraft-Surface Radiometer Intercomparison

In an attempt to assess the validity of RADBUD retrievals for monitoring diurnal processes, diurnal signals constructed from the GOES-1 RADBUD estimates are intercompared to daily radiation budget cycles, representive of the Arabian Desert Empty Quarter. The reference cycles are generated from aircraft and surface observations in conjunction with theoretical calculations. A schematic illustration of the multiple-platform approach used in these intercomparisons is given in Fig. 2.22. It must be kept in mind that in these intercomparisons the aircraft data were taken during June of 1979, whereas the surface data were taken in June, 1981. Therefore, there is a tacit assumption that the desert surface does not change significantly from year to year nor are the atmospheric conditions significantly variable from one year to the next for the same month. For the virtually cloudless and extremely dry interior of the Arabian Empty Quarter during the early summer, this is a well founded assumption. The figures presented in the following discussion incorporate calculations first reported in preliminary form by Ackerman, et al. (1983).

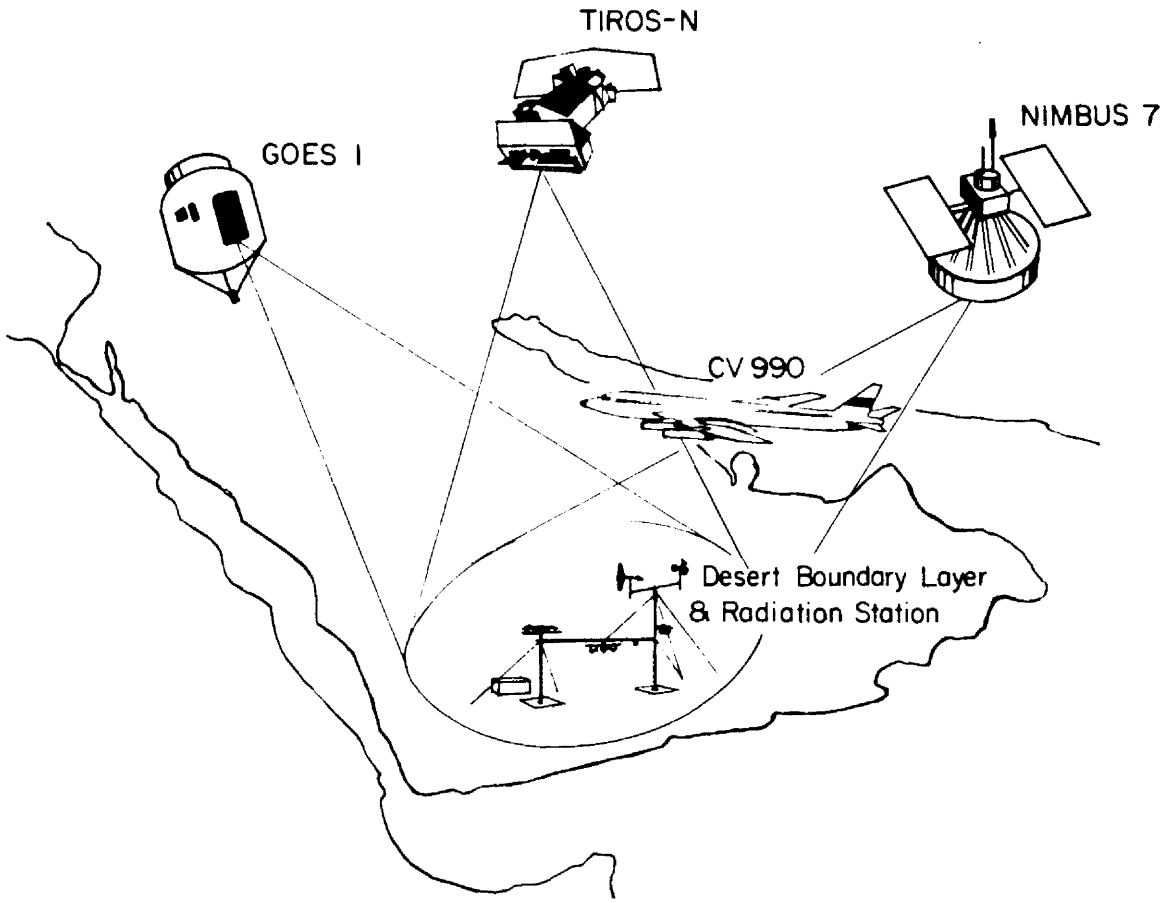

Fig. 2.22. Schematic illustration of a multiple platform design for intercomparison experiments incorporating operational weather satellites, experimental satellites, aircraft, and surface stations.

The first example of intercomparison results is given in Fig. 2.23 in which it is shown how well the LW satellite parameterization can be used to monitor the desert surface temperature. In this analysis the actual surface temperature is based on a surface energy budget monitoring station, which employs downward looking radiometers and soil temperature probes; see Chapter 4. The monitoring site is within about 100 km of the center of the Arabian Empty Quarter near the small Bedouin village of Sharouwrah (17^{o} 45'N; 47^{o}15'E). Satellite window temperature estimates are plotted along with clear sky top-of-atmosphere equivalent-black-body temperatures. The later are obtained from the LW theoretical model using an average June profile based on CV-990 drop sonde data (see International MONEX Management Centre (Summer), 1981). The comparison is excellent and explains why there is a similar degree of comparison in the broad band infrared budget estimates as shown in Fig. 2.24. In this figure the diurnal satellite (GOES-1) retrievals are in good correspondence to the values based on the surface data and model calculations (the daytime satellite estimates are slightly higher). Whether the small differences are related to the LW satellite parameterization, the theoretical model, the mean June profile, or the actual surface pyrgeometer measurements is an impossible question to resolve. Note also, the correspondence between the downward infrared irradiance measured at the Sharouwrah site with the model calculations, which as noted previously, incorporates an atmospheric profile representative of the average June, 1979 Empty Quarter conditions.

In Fig. 2.25, diurnal plots of the shortwave diurnal RADBUD components are given. In this figure the top-of-atmosphere albedo term,

SURFACE TEMPERATURE DIURNAL COMPARISON OVER
SAUDI ARABIA (JUNE, 1979)

GOES-1 VERSUS A COMBINATION OF SURFACE OBSERVATIONS AND THEORETICAL CALCULATIONS

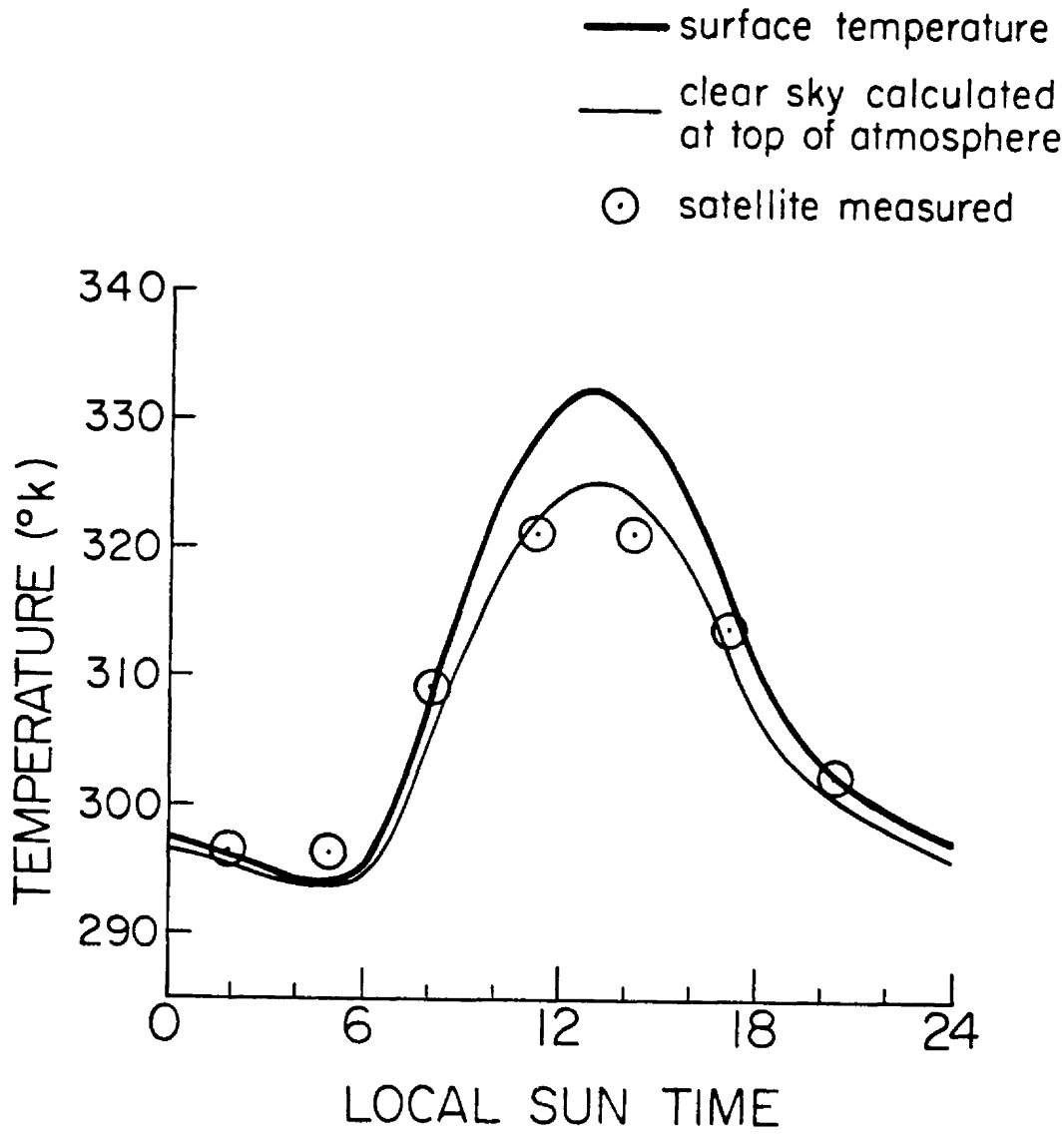

Fig. 2.23. Comparison of GOES-1 diurnal limb-corrected EBBT window temperatures with top-of-atmosphere EBBT model calculations incorporating actual surface temperature measurements to specify the lower boundary conditions.

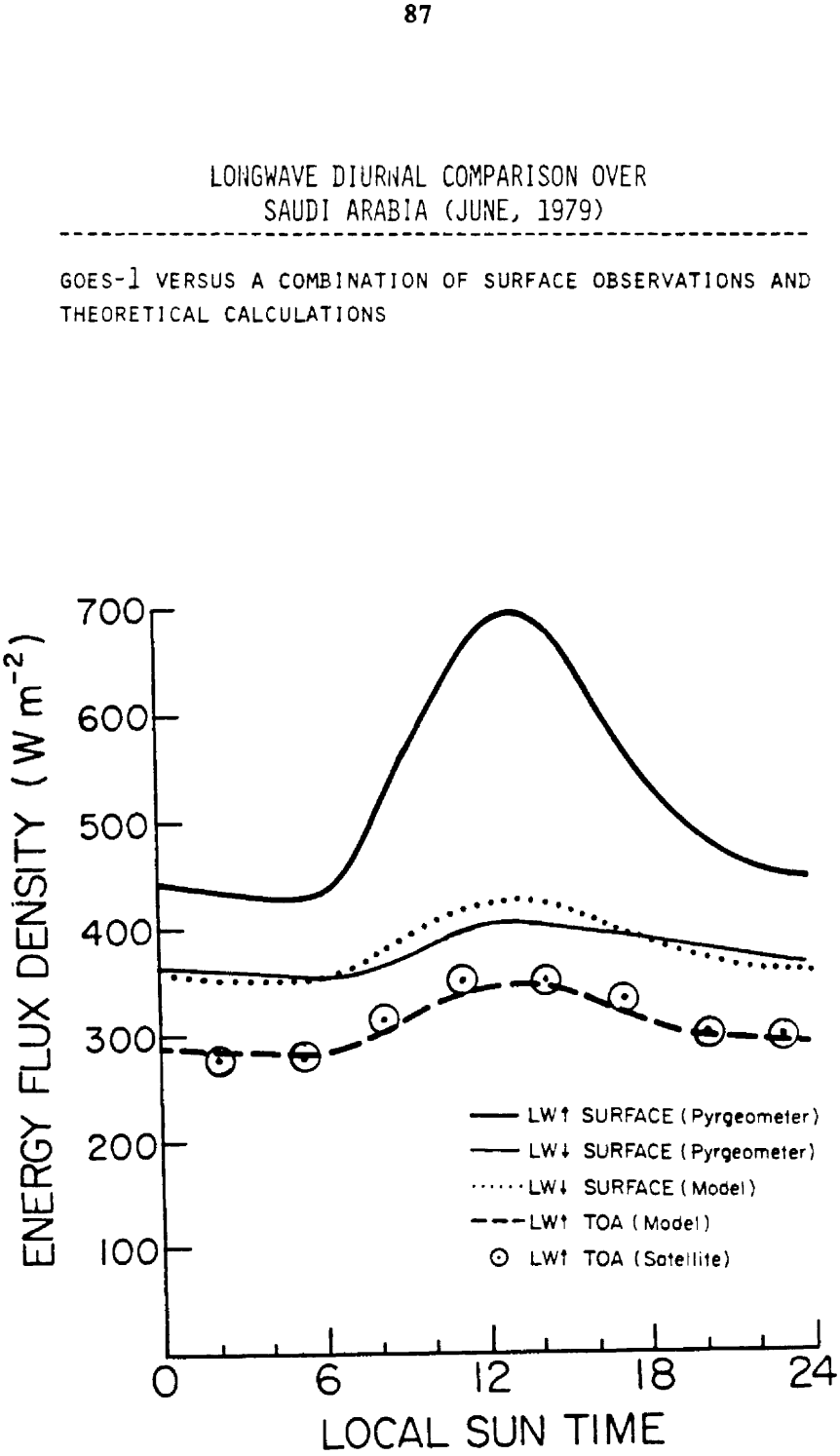

Fig. 2.24. Comparison of GOES-1 diurnal IR emittance estimates with top-of-atmosphere IR flux model calculations incorporating the surface data to specify the lower boundary conditions. The graph also includes the upward and downward surface IR irradiance measurements as well as the model calculated downward surface irradiance.

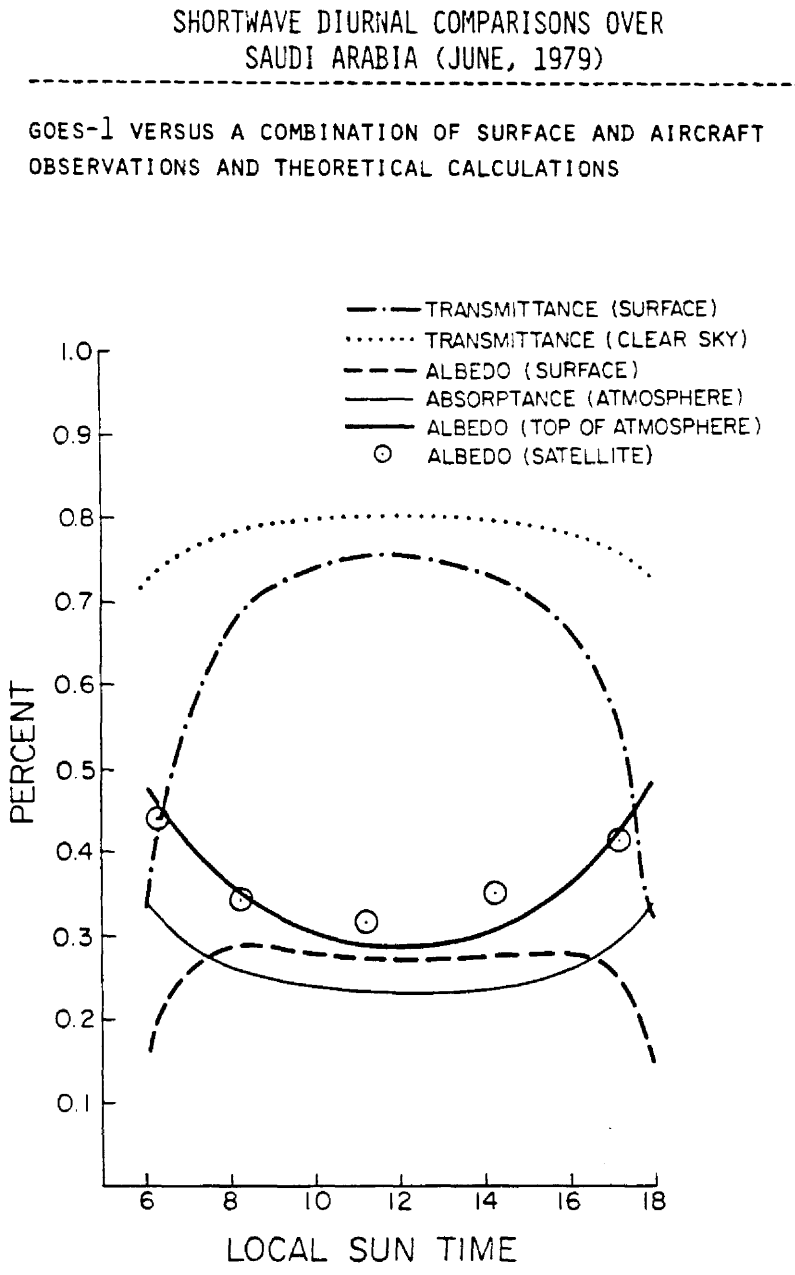

Fig. 2.25. Comparison of GOES-1 diurnal albedo estimates with top-of-atmosphere albedo model calculations incorporating the surface pyranometer data to specify the lower reflectance boundary conditions. The graph also includes the measured surface albedo term, a theoretical clear sky transmittance term, an atmospheric transmittance corrected for aerosol extinction, and an effective atmospheric absorptance term.

given by the thick line, is generated by using the pyranometer measurements of surface albedo obtained at the Sharouwrah site, in conjunction with SW model calculations. In the model calculations, an important aeresol effect is included based on a bulk desert aeresol transmittance formulation developed from the CV-990 aircraft observations (see Ackerman and Cox, 1982). Notice that the GOES-1 retrievals are in excellent correspondence at all but one of the diurnal retrieval times. These later results provide a solid foundation for extending the investigation of desert heat low structures using satellite observations; see Smith, et al. (1982b), Blake, et al. (1983), and Chapter 5.

2.6.3 Magnitude of the Geometric and Spectral Corrections

Finally, as a means to emphasize the importance of applying parameterizations in converting spectral radiances to broad band fluxes, Figs. 2.26 and 2.27 are provided. In these illustrations, the characteristic errors associated with ignoring the application of geometric and spectral corrections are shown. The data set used in this analysis was derived from the first operational geosynchronous weather satellite (SMS-1) which was launched in time for the GARP Atlantic Tropical Experiment (GATE); see Smith, et al., 1979. The parameterization techniques used in calculating the RADBUD estimates were the rather simple formulations used in the Smith (1980b) study. Therefore, the magnitudes of the errors are not exact although the nature of the errors are essentially correct. In this test the fully parameterized RADBUD estimates were intercompared with estimates in which first - the geometric corrections were removed; and second - both the geometric and spectral corrections were removed. The

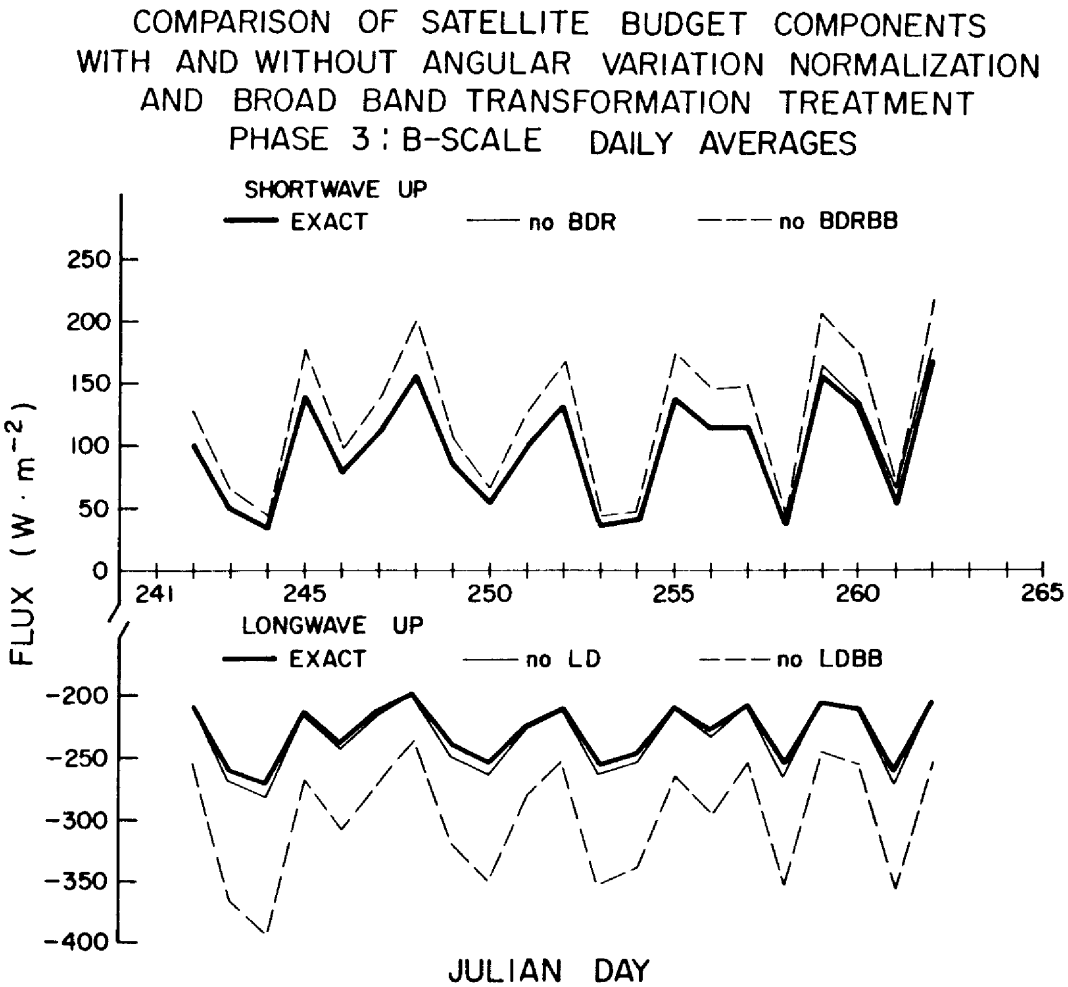

Fig. 2.26. Comparison of SMS-1 daily averaged RADBUD estimates to estimates without geometric corrections (NO BDR; NO LD) and without both geometric and spectral corrections (NO BDRBB, NO LDBB). The RADBUD parameters represent GATE-Phase 3, B-scale averages of 0.5 by 0.5 degree retrievals.

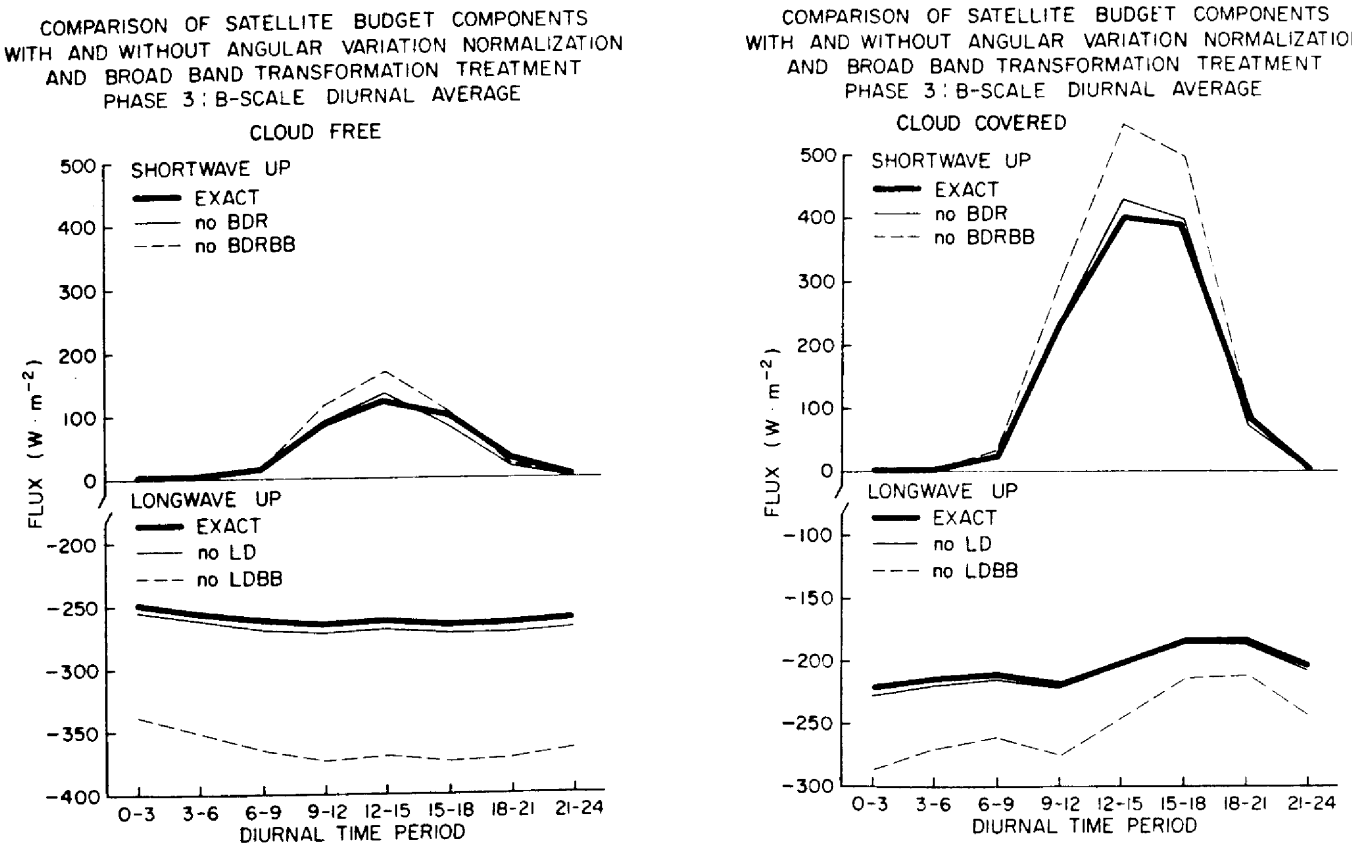

Fig. 2.27. Similar to Fig. 2.26 except in this case the RADBUD time series represent diurnal averages as opposed to daily averages. The left portion of the figure represents supressed (cloud free) conditions; the right portion represents enhanced (cloud covered) conditions.

intercomparisons were carried out for both daily averages and then for diurnal averages. The time period of the study took place during Phase 3 of the GATE (August 30 - September 19). The 0.5 by 0.5 degree estimates over the B-scale GATE array were calculated every hour.

In Fig. 2.26 the daily average intercomparisons are shown for both shortwave and longwave top-of-atmosphere fluxes. It can be noted that the spectral corrections lead to fairly large flux changes, particularly during enhanced cloud events which periodically pass through the GATE B-scale array approximately every four days leading to higher albedos and thus increased SW flux. What is more interesting, however, is that for daily averages the geometric correction (application of bi-directional reflectance normalization) is virtually insignificant. This suggests that the bi-directional reflectance normalization operator has an identity property with the daily averaging operator, although a precise mathematical explanation would be elusive based on the somewhat empirical nature of the bi-directional reflectance normalization functions. The longwave results, on the other hand, indicate that the limb darkening correction is important mostly for cloud free conditions (longer atmospheric transmission paths), but far less important than the spectral correction. Note that the spectral correction is not only large but highly dependent on cloudiness.

Finally in Fig. 2.27 a similar comparison is carried out for suppressed (cloud free) and enhanced (cloud covered) conditions. Note in both the cloud free and cloud covered cases the shortwave geometric correction leads to flux increases earlier in the day and flux decreases later in the day. This clearly illustrates why the daily averaging procedure cancels the effect of bi-directional reflectance

normalization. On the other hand the longwave geometric correction leads to a fairly uniform reduction in flux for both clear and cloud conditions. It is important to note that the magnitude of reduction is a function of the relative position of satellite and target site. It is also easily noted that the cloud free correction is somewhat large because atmospheric transmission paths are longer when no cloud is present and the path itself includes the more dense, moister boundary layer. The spectral corrections are seen to be not only large, but highly dependent on cloudiness. The SW and LW effects are inverted in the presence of cloud. In the SW, the spectral correction over water is smaller for no cloud than for cloud; in the longwave the opposite is true.

The above relationships are important to consider when designing a data processing strategy. As indicated, when daily averaging is involved, it is not essential to incorporate bi-directional reflectance normalization functions. However, if a diurnal signal is under investigation, the geometric corrections become very relevant. It may be possible, therefore, to generate the magnitudes and shapes of corrections for various averaging schemes for differing atmospheric and surface conditions. This avenue of research has not yet been explored but seems plausible.

2.7 Implications for Cloud-Radiation-Climate Studies Using RADBUD Estimates from Weather Satellites

It is apparent from the geometric and spectral transformation functions that conversion of spectral radiance to broad band flux is not necessarily a simple statistical problem, particularly for the smaller space and time scales. Although one cannot dispute the model results of Briegleb and Ramanathan (1982) -- which indicate that in clear

atmospheres on a monthly-zonal-average basis, there is virtual equivalence between narrow band (VIS) albedo (0.5-0.7 μm) and broad band albedo (0.2-4.0 μm) -- this is not to say that one can outright ignore geometric and spectral relationships. Their results do suggest that the globe, as a whole, has a fascinating property in which land and ocean surfaces compensate their respective differences in NB-BB relationships (at least when cloud is not present) leading to monthly zonal-average equivalance. However, it must be understood that the implied statistical relationship implicit in their results is only applicable at those particular scales and for an idealized cloud free atmosphere.

The parameterizations presented in this investigation are not to be interpreted as a totally thorough treatment of converting weather satellite radiances to RADBUD flux estimates. They are intended to demonstrate the sensitivity of radiative fluxes to surface and atmospheric variables and to illustrate the highly non-linear aspects of the conversion problem which is not readily apparent in regressing NB-NFOV observations with BB-WFOV observations. It is a virtual certainty that the discrepancies noted by Cess, et al. (1982) between the cloud-radiation sensitivity factors derived from the NOAA data of Winston, et al. (1979) and the WFOV data of Ellis and Vonder Haar (1976) and Campbell and Vonder Haar (1980a) are due to an inadequate treatment of the NOAA-SR radiances, particularly in cloudy situations. Cess, et al. (1982), after all, commented on this problem in their conclusions. What is of remaining interest is: What are the most significant deficiencies in the NOAA-NESS data set and can they be corrected? There is a tendency to accept the longwave emittances as being more correct then the albedos based on the fact that a regression type spectral conversion

has been applied, however, the results of Ellingson and Ferraro (1983) suggest that even the IR fluxes are overestimated for cloudy conditions.

My own belief is that the natural variability of atmospheric water vapor and cloudiness, and the highly variable land surface properties have such a massive influence on radiative exchange, in both shortwave and longwave spectrums, that any transformation scheme which does not incorporate these parameters directly is forever limited to gross approximation. It is along these lines that I suggest the findings of Simmonds and Chidzey (1982) must be set aside. In their study on energy balance model parameterizations they maintain that the NOAA-NESS data, as opposed to the Nimbus WFOV data, lead to an improved parameterization in estimating LW emittance as a function of surface temperature over a global domain incorporating a seasonal cycle. Now it is perfectly obvious apriori that surface temperature and window flux correlate better than surface temperature and broad band longwave flux. This is the effect of the fundamental selective absorption nature of the atmosphere discussed in any introductory text on atmospheric physics. The NOAA agency flys window sensors on operational weather satellites for the very purpose of optimally monitoring surface and cloud top temperatures. Since the NOAA IR RADBUD measurements are essentially transformed by a nearly linear function, one would then expect the correlation finding of Simmonds and Chidzey (1982). Nevertheless, their results should not be interpreted in the sense that the NOAA-NESS data leads to an 'improved' parameterization for use in energy balance climate models (EBCM's). What is required in the EBCM's is a parameterization of the actual total broad band infrared loss to space,

because that is the real energy term which is needed to simulate actual climate variability.

Clearly there are a host of additional criticisms that could be leveled at other studies; however, this is not the intention of the investigation. Instead the suggestion is offered to members of the radiation budget community to seek out more improved physical algorithms for processing weather satellite data into the desired radiation budget quantities. The value of these data need not be emphasized. The level of interest over a host of topics now available in the modern literature speaks for itself. Although global radiation budget monitoring is tending toward an operational reality with the upcoming ERBE program, there are definite advantages in using weather satellite data for specific applications. The high resolution features of both polar and geosynchronous orbitors, as well as the diurnal monitoring capabilty of the geosynchronous satellites, are critically important. In essence, weather satellites, whether they are of the polar orbiting or geosynchronous orbiting variety, can operate in the mode of narrow-field-of-view (NFOV) scanners. Given the short lifetimes of the Nimbus-6 and Nimbus-7 ERB NFOV scanners (2 months and 18 months respectively), and the growing concern with the reliability of the future ERBE scanners, it would seem only reasonable that weather satellites be given a fair chance as 'stand ins' for the precision scanners when they are either out of operation or fail completely. In fact, the ERBE Science Team is prepared to utilize geosynchronous 'weather pictures' to help fill the diurnal sampling gaps inherent in the ERBE satellite global monitoring design (the first two radiometers

will be flown on NOAA operational polar orbiting sun-synchronous satellites).

A final note on this topic is that our science may not always have an operational radiation budget programme. Although I would be the last to recommend the elimination of quality radiation budget satellites and sensor systems, history has taught us that there are no guarantees. Thus it is incumbent on our science to continually upgrade the weather satellite applications beyond their normal role in the weather forecasting mode. As to the stability of a programme of weather satellites in the future, we will most likely see a continuation. What is not certain at this time is the future availability and cost of the digital data if NOAA were to hand over the management of the operational programs to private agencies; Science News (1983a, 1983b).

2.8 Summary

It has been shown from the parameterization study that weather satellite filtered radiance measurements are readily adaptable for radiation budget analyses, but only within certain limits of accuracy. It is very important to understand at the outset that the time and space scales chosen for an analysis scheme dictate the resulting biases and RMS uncertainties. It is also apparent that the problem of transforming narrow band satellite radiances to broad band flux estimates is best treated as a problem in atmospheric physics not observational statistics. By choosing the former course there is not only considerable room for improvement, but also the solutions will exhibit more solid foundations for diagnosing the causes and effects of the uncertainties.

It has been shown that the NB-NFOV to BB-WFOV relationships are highly non-linear and strongly forced by natural variations in atmospheric and surface properties. The impacts of these non-linearities on the more localized space and time scales will be examined in a future study incorporating the ERB narrow-field-of-view (NFOV) scanner data. It has also been shown that the selected radiation budget averaging strategy may preclude the requirement of applying portions of a parmeterization. The foremost example pointed out in this investigation was the cancellation of bi-directional reflectance normalization effects when taking daily averages of shortwave fluxes over ocean-cloud domains.

There are obvious cases in the existing literature in which weather satellite RADBUD estimates have been used in such a fashion to obscure scientific understanding, not to clarify. One must always guard against this possibility when using indirect measures of a physical process. In-so-far as the ultimate objectives of developing the above parameterization scheme, the primary concern is with the generation of high resolution daily and diurnal time series of the radiation exchange terms over the SMONEX region, in the form of latitude and longitude cross-sections, derived from TIROS-N and GOES-1 radiance data. These analyses are being used to understand the role of radiative forcing associated with the Southwest Monsoon system and to characterize the dramatic and discontinuous gradients associated with the radiation terms going from pre-monsoon to monsoon-onset phases, and during the monsoon-surge and monsoon-break oscillations that characterize a complete Southwest Monsoon season.

3.0 A MULTI-PLATFORM SATELLITE INTERPOLATION OF RADIATIVE FORCING OVER THE 1979 SOUTHWEST SUMMER MONSOON

The Southwest Monsoon system encompasses a region of over 10% of the earth's surface and persists for nearly half of the annual cycle (May-September). Its creation, evolution, and maintenance are fundamental to an explanation of the vagaries in the radiation climate of the globe. The development of cloud systems associated with the Southwest Monsoon, as well as the transformation of the surface climate of large portions of Southern Asia, lead to paramount signals in the seasonal transformation of the global radiation budget. Interannual differences in the intensity of the monsoon, its date of onset, and in its natural fluctuations during the course of the monsoon season are, in turn, responsible for predominant global anomalies in the radiation signals at the top-of-atmosphere. Various of these aspects of the monsoon in terms of the global radiation budget have been noted by Stephens, et al. (1981).

Nevertheless, to date, we do not have a firm understanding of the evolution of the monsoon radiation fields, nor the degree of radiative forcing to the monsoon atmosphere in terms of mean seasonal progress, in terms of the natural fluctuations, and in terms of the year-to-year changes of the monsoon itself. This investigation is aimed at shedding light on the first three of of these four topics. The system under investigation is the 1979 Southwest Summer Monsoon which was the subject of intensive study during the course of the 1979 Summer Monsoon

Experiment (SMONEX). This experiment along with the Winter Monsoon Experiment (WMONEX) were the two major regional experiments embedded within the framework of the global scale 1979 First GARP Global Experiment (FGGE).

The Southwest Monsoon (SW Monsoon) is comprised of a diverse set of elements and a fairly rigidly orchestrated sequence of atmospheric and geophysical events. In a very general sense, it is one of the most predictable seasonal weather events on the globe. On the other hand, very minor perturbations in the initiation of the monsoon, in its intensity, and in the sequence of its surges and breaks can lead to devastation for hundreds of millions of Asians. A 20% short fall in diurnal mean monsoon rainfall over the Indian Sub-continent can lead to catastrophic food shortages (along with the twin scourges of malnutrition and starvation), drains on the national treasury due to grain imports at inflated prices, massive relocations of the population to more dependable water reservoirs, and a variety of social and political ills that naturally arise from a severely depressed agricultural economy.

The book of Ramage (1971) and the compilation of papers edited by Lighthill and Pearce (1981) are essential to an appreciation of the complexity of the SW Monsoon, its influence on and response to the general circulation, and of its multi-faceted structure. These sources along with a selection of published scientific papers have documented critical features of the cause of monsoon development, its structure and essential components, its progression and oscillations, and its climatology. However, throughout the course of this body of literature, there is no underlying theme as to the role radiation exchange plays

within the context of a monsoon season or from one season to the next. For a system whose very essence is a radiative mechanism (i.e. the large scale differential heating between ocean and continent) which drives the moist monsoon circulation into the South Asian land mast, it is somewhat perplexing that radiative exchange processes have not received more attention.

Of course, much of this deficiency is due to the historical lack of data which are compatible with the task of estimating radiative exchange and radiative heating and cooling. Not until the era of the weather satellite could this problem even be attempted with any degree of reliability. It was not until the 1979 FGGE period that a global array of operational and experimental satellites was in place which enabled continuous and thorough monitoring of a complete monsoon cycle. This investigation is thus based on utilizing the FGGE satellite network to attempt an examination of radiation processes and radiative exchange of one SW Monsoon season.

The nature and evolution of radiative forcing within the SW Monsoon system is a critical aspect of monsoon development, onset, and maintenance and yet this aspect of monsoon physics has remained somewhat allusive to the numerical modeling community. The reasons for this are straightforward. Radiative processes at the larger scales are principally dictated by the distribution of aerosol, water vapor, and clouds (both horizontally and vertically) and by the nature of the surface boundary conditions (both the spectral reflectance properties and the thermal emission properties); see Stephens and Webster (1979). The prognosis of water vapor and cloud distribution (growth, dissipation, and transport) remains as one of the more difficult

problems in numerical simulation; see Charney and Shukla (1981). The specification of the surface boundary conditions represents a problem in both geomorphology and ground thermodynamics; there are many remaining gaps in our knowledge of surface properties on a global scale.

As a result, radiative exchange and radiative forcing at the monsoon scale are almost by definition an observational problem. And, as is true of all observational approaches, it is often difficult to link the phenomonology with the deterministic physics. This is why we have a better understanding of hydrodynamical monsoon processes than we do of radiative processes. The required boundary conditions of the radiation calculations simply cannot be prognosed at a level of accuracy sufficient for a realistic simulation. Observational analysis has been, and will remain for some time to come, the foremost means to examine radiative processes within monsoon systems.

In the course of this investigation satellite measurements from three different satellite systems are utilized to examine various aspects of the monsoon. In Section 3.1 a description of previous satellite based monsoon research is provided. Sections 3.2 and 3.3 describe the data sets and a brief explanation of how the raw radiance data from the weather satellites are converted to radiative flux estimates. The idiosyncrasies in formulating the radiation budget parameters from the different types of operational platforms (polar and geosynchronous orbiters) are discussed in Section 3.4.

In the remaining sections the analyses of the 1979 SW Monsoon are provided. Section 3.5 presents five day averaged mean fields over the course of the monsoon; the zonal and meridional averages for a monsoon sector (EQ-35^{o}N; 30^{o}-100^{o}E); and a discussion on the phenomonon of

radiation blocking evident in the net radiation term over the monsoon domain. Section 3.6 focuses on contrasts in the radiation budget for different regions within the monsoon domain. Section 3.7 explores briefly the periodicities in radiative exchange and their pertinence to previous studies of oscillations of the SW monsoon system. Then in Section 3.8 the nature of the diurnal radiation budget is presented. In Section 3.9 various correlative results are presented which are used to expand on the notion of radiative decoupling. Finally, Section 3.10 is provided to discuss the conclusions and the need for further research.

3.1 Background

The investigation of radiative processes within the SW Monsoon system has remained a fairly sketchy topic. The following two sub-sections briefly review a series of studies which have addressed radiation budget and cloud processes in the SW Monsoon region based on satellite observations. The remaining three sub-sections review previous findings on oscillations of the SW Monsoon.

3.1.1 Radiation Budget Studies

One of the first radiation budget (RADBUD) studies was that of Rao (1966), who demonstrated that emitted infrared data retrieved from the TIROS-IV polar orbiting satellite could be used to study the northward advance of 1962 SW Monsoon cloudiness. Unfortunately, the data used in this investigation were discontinuous and did not extend beyond June 10 so that it is difficult to extract a coherent view of monsoon evolution from the emitted flux isopleths.

Dittberner and Vonder Haar (1973), utilizing the first generation satellite radiation budget data of Vonder Haar and Suomi (1971), portrayed a three year monsoon sequence (1963-1965), in which the albedo

and emitted infrared fields were used as proxy estimates of precipitation. This study explored the hypothesis that the extensive cloudiness associated with the strong 1964 monsoon reduced surface heating to the extent that the 1965 monsoon was actually weakened. In a similar vein and again examining a three year sequence, Winston and Krueger (1977) illustrated the year-to-year vagaries of the 1974-1976 monsoon seasons, utilizing the more modern Scanning Radiometer (SR) imaging data from the NOAA polar orbiting operational satellites in a radiation budget mode. They pointed out that the more active 1975 monsoon manifested itself in the albedo and emitted IR fields resulting from the increased cloudiness. This was the first investigation that portrayed the monthly advance of radiation fields through the course of the monsoon season (March through August). They also pointed out that there were global differences in radiation budget patterns between the 1975 monsoon and the 1976 'weak' monsoon, suggesting that annual variations in the monsoon system are linked to much larger scale features of the general circulation.

Stephens, et al. (1981), based on the first generation satellite radiation budget estimates of Vonder Haar and Suomi (1971), the Nimbus-3 estimates compiled by Ellis and Vonder Haar (1976), and the more recent Nimbus-6 measurements compiled by Campbell and Vonder Haar (1980), pointed out a very important aspect of large scale radiation exchange processes in the monsoon region. That is, the Asian monsoon, along with three other global centers [the western Pacific Ocean, the stratocumulus region west of South America, and the Saharan Desert] represent highly variable net radiative exchange areas in an interannual time frame. The implication here is that from a climatic point of view, the interannual

fluctuations of the monsoon can produce perturbations in the radiation budget which are realized on a global scale and are every bit as important for climate processes as the regular annual and semiannual periodicities forced by the seasonal change in the solar declination and solar distance vector.

Recently Virji, et al. (1982) compiled an hourly atlas of radiation budget parameters derived from the GOES-1 satellite for a region enclosing the major features of the Southwest Monsoon system (EQ-26°N; 46°-84°E) for the 1979 monsoon onset period (June 10-20). These estimates are based on statistical algorithms developed by W. L. Smith, et al. (1981). Although the atlas does not provide a synthesis of the results, it is evident from the contour maps that the Arabian Sea undergoes very dramatic changes of net radiation exchange during the course of the onset period.

3.1.2 Cloud Studies

Various investigators have utilized satellite imagery to study cloud patterns and oscillations in the cloud fields associated with the Southwest Summer Monsoon. Sadler (1969) provided a relatively complete tropical atlas of mean monthly cloudiness and year-to-year differences for the years 1965 and 1966, based on the operational satellite nephanalyses prepared by the National Satellite Center (at that time NESC). These results were an extension of the cloud charts he originally prepared for the International Indian Ocean Expedition (IIOE) based on TIROS V-VIII data; see Ramage, et al. (1972). A brief glance at the cloud charts of May, June and July provides a preview of what Stephens, et al. (1981) pointed out 12 years later using the multi-year radiation budget data, i.e. the year-to-year differences in the cloud

fields (which provide the major control on net radiative exchange), are a maximum in the monsoon region. Mean July differences between Eq-10°N latitude and 55°-75°E longitude for years 1965 and 1966 were +2 octas. The differences are even more extreme for June means southeast of Somalia (>3 octas). Another IIOE study of Bunker and Chaffee (1969), based on time lapse cameras mounted on research aircraft, documented some detailed information on cloud layering, cloud orientation and cloud type for the 1963-1964 period, although the compilation is far from complete based on the limited area sampling nature of experimental aircraft.

Saha (1971a) incorporated first and second generation operational polar orbiter satellite imagery (ESSA, ITOS) to study how increased sea surface temperatures in the Indian Ocean and Arabian Sea lead to increased cloudiness. In another study, Saha (1971b) demonstrated, using ESSA satellite photos, that the eastern Indian Ocean (west of 60°E) is generally more cloudy than the western portion.

Sikka and Gadgil (1980), using scanning radiometer (SR) imagery data from the 1970's NOAA operational polar orbiting satellites, investigated the appearance and oscillations of the large scale monsoon cloud bands [the equatorial and monsoon Minimum Cloud Zones (MCZs)] and their relationship to continental and equatorial Intertropical Convergence Zones (ITCZs). Their findings indicated that the two MCZs operated in sequence (a type of 'flip-flop' mode) in which the equatorial MCZ (0-10°N) makes an appearance and moves north to replace a dissipated monsoon MCZ (>15°N).

3.1.3 Long Period Oscillations of the Monsoon

Zangvil (1975), utilizing ESSA-3 and -5 visible brightness data, studied the time spectrum of tropical cloud amount. This was one of the first satellite based investigations to identify the short period (4 to 9 day) and long period (40 day) easterly wave motions manifested in the Indian Ocean cloud fields along with a 15-day westward moving wave at monsoon latitudes in summer. Yasunari (1979, 1980) later referred to the 40-day wave mode, which he identified in NOAA-2 visible mosaic images, as a northward moving wave associated with the 'major' active and break cycles in the large scale South Asian monsoon domain. In a follow-up study, Yasunari (1981) identified the 40-day oscillation in the geopotential height and wind data over and around the Indian sub-continent. There is, most likely, a relationship between this wave mode and the MCZ 'flip-flop' reported by Sikka and Gadgil (1980), which was identified as having approximately a 30-day periodicity. The 40-day mode was not evident in the cloudiness fields during the drought monsoon of 1972; see Yasunari (1980).

This organization of Asian monsoon cloudiness was earlier revealed by T. Murakami (1976) who used Sadler's (1969) cloudiness data to demonstrate that monsoon cloudiness changes were positively correlated with cloudiness changes over the Malaysian Indonesian region but negatively correlated with cloudiness changes in Africa, the equatorial Indian Ocean and the western Pacific. He also found that zones of correlation basically advanced northward ($\approx 1^{\circ}$ latitude per day) as Sikka and Gadgil's (1980) study would imply.

The tie-in of the 40-day northward moving wave with the eastward wave found by Zangvil (1975) was explained by Yasunari (1979) as the

consequence of initially eastward moving cloud disturbances developing over the Indian Ocean with a periodicity corresponding to the 40-50 day east-west global tropical pressure oscillation investigated by Madden and Julian (1971, 1972b) and more recently by Anderson and Rosen (1983) and Mertz and Mysak (1984). This result has been emphasized by Krishnamurti and Subrahmanyam (1982), based on examining the SMONEX wind field data and confirming the existence of a 30-50 day mode in the northward passage of ridge trough lines moving at approximately 0.75 degrees latitude per day.

The cause of the large scale tropical pressure oscillations goes well beyond the scope of this investigation, but it is important to note that it is these large scale perturbations in the mass field that give rise to eastward traveling tropical disturbances (circulation cells), which in turn can act to weaken the upper level easterly and low level westerly monsoon currents. The appearance and passage of these circulation cells thus lead to breaks and re-intensifications of the monsoon. This point has been emphasized by Julian and Madden (1981). Cadet and Olory-Togbé (1977), using both constant level balloon trajectories and satellite images, identified an eastward moving disturbance in the 1975 monsoon that actually caused low level flow reversal, followed by a monsoon break. The pressure oscillations are also intrinsically connected to the now popular concept of teleconnections to which the Southwest Monsoon is often associated.

3.1.4 Quasi-Biweekly Oscillations

The 'active-break' cycle of the Indian monsoon itself [Koteswaram (1950), Ramaswamy (1962), Ramamurthy (1969), Raghavan (1973)], i.e. that process which results from a northward advance of the monsoon trough

into the Himalayas and bringing decreased rainfall to northwest and central India (but increased rainfall to northeast and southern India), is now assumed to have a quasi-biweekly periodicity. For many years Indian meteorologists had documented the tendency of monsoon rains to fluctuate in intensity at periods of greater than 10 days. These observational reports had led T. Murakami (1972, 1973, 1974) to conduct a series of theoretical experiments designed to test the effect of a fluctuating diabatic heat source associated with Indian monsoon latitudes (20^{o}N, and prescribed at 15 or 16 days) on exciting equatorial stratospheric Kelvin and/or possibly Wallace-Kousky waves (yes and no, respectively), and/or exciting steady and transient trophospheric waves from the diabatic heat source. At the same time Krishnamurti, et al. (1973) had noted a two week periodicity in the intensity of the Tibetan high, based on a spectrum analysis of the stream function. The Tibetan high is, of course, a major feature of the Southwest-East Asian monsoon. Yasunari (1976) and M. Murakami (1976, 1977) have also conducted spectrum analyses using conventional data sets indicating the dominance of the two week periodicity in monsoon processes.

Zangvil (1975) in his satellite cloud study, had noted >10-day periodicities in northern summer equatorial latitudes, although there was no clear tie-in with the monsoon. As Wallace and Chang (1972) had pointed out prior to the Zangvil (1975) investigation, spectrum analysis of cloudiness data tends to proliferate a continuous spectrum of periodicities between 4 and 20 days and often disguises clear-cut dynamical processes responsible for the cloud fields themselves.

The first definitive study to identify and describe quantitatively the quasi-biweekly nature of monson fluctuations throughout the monsoon

system was provided by Krishnamurti and Bhalme (1976). This investigation went well beyond simple harmonic analysis of individual pressure, wind, precipitation or cloudiness parameters. Instead, they posed a conceptual model of the Southwest Monsoon system as a combination of a diverse set of dynamic and thermodynamic modules and then, using a variety of data sources, examined the oscillations in all the component monsoon parts. This investigation led to the suggestion that the monsoon fluctuates in all regimes (i.e. monsoon trough, Mascarene high, low level westerly jet, Tibetan high, upper level easterly jet, cloudiness, rainfall, dry and moist static stability) with an approximately two week periodicity. They also noted a <6 day periodicity which will be discussed shortly. They very carefully pointed out that the link between the quasi-biweekly oscillation and monsoon breaks is not clear-cut in light of the fact that past monsoons have occurred which exhibit quasi-biweekly fluctuations but which do not produce actual breaks. Nevertheless they offered an explanation for why a monsoon might naturally fluctuate. Their argument was that since monsoon activity leads to extensive cloudiness, large cloud systems would serve to decrease solar radiation insolation to the surface, resulting in the stabilizing of the lower troposphere and presumably a 'break' in the monsoon.

Webster, et al. (1977), using the numerical model of Webster and Lau (1977), tested this hypothesis in a 'dry' coupled ocean-atmosphere model and found reasonable agreement. Later Webster and Chou (1980) and Webster (1983) pointed out that in order to fully account for the somewhat discontinuous nature of the active-break cycle, a complete simulation of the complete hydrological cycle is required.

Equating the quasi-biweekly oscillation of monsoon intensity to the 'active-break' cycle is now a fairly common conclusion [see Chang (1977) and Krishnamurti and Ardanuy (1980)] although it remains to be seen whether these are, in fact, equivalent processes. There has not yet been a complete and concise physical explanation as to the cause of the two week cycle. Other mechanisms have been posed beyond that of Krishnamurti and Bhalme (1976). M. Murakami (1976) has suggested that the periodicity is related to occurrences of major monsoon depressions in the Bay of Bengal [see Krishnamurti, et al. (1975, 1976) and Sanders (1979)] that eventually will move along the monsoon trough [see Sikka (1977)]. These cyclones are differentiated from the higher frequency monsoon lows ($\approx$ 4-6 day) that also move into and along the monsoon trough [see M. Murakami (1978)] and which are possibly westward moving shortwaves originating in the West Pacific; see Krishnamurti, et al. (1977).

Yasunari (1979) has suggested that the oscillation may arise from generally eastward traveling tropical waves which tend to propogate to the north, at Bay of Bengal longitudes, ultimately leading to an interaction and excitation of the tropical easterly wave driven by the Tibetan Heat Source (Tibetan high). These wave-wave interactions are then presumably responsible for the in-situ Bay of Bengal depressions, a process which has been disputed by Krishnamurti, et al. (1977). A somewhat confusing point of the Yasunari (1979) study is that he identifies the active-break cycle with the 40 day oscillation, not the two week oscillation. Since Yasunari utilized daily satellite mosaics rather than precipitation data, he most likely was identifying the equatorial monsoon MCZ sequence reported by Sikka and Gadgil (1980).

Zangvil's (1975) earlier satellite study had identified an eastward moving tropical wave, confined to the equatorial Indian Ocean, however with a periodicity of only 9 days (wave number 5).

Krishnamurti and Ardanuy (1980), while skirting the issue of the relationship between monsoon breaks and the quasi-biweekly rainfall episodes, have suggested that there is predictive skill in determining the arrival of a pressure rise (and thus a break monsoon condition) after the identification of a westward propogating disturbance over central India. They point out that the westward moving disturbances are irregular, however, occuring at intervals between 10 and 20 days. The results of T. Murakami (1980) have not served to clarify the frequency of the oscillation. He finds a 20-30 day periodicity in the emitted longwave radiation budget data of Winston, et al. (1979). Because at monsoon latitudes the cloud disturbances are propogating westward, he equates the oscillation to the active break monsoon cycle.

An important remaining mechanism, which has been explored briefly by Webster (1978), is the lateral effects from the Southern Hemisphere. This study aimed at the problem of whether wave energy propogating equatorward from Southern Hemisphere mid-latitude disturbances could, in fact, penetrate through the equator, in conflict with the theoretical barriers of critical latitude absorption posed by Charney (1969) and Bennet and Young (1971). Webster (1978) pointed out deficiencies in the basic state conditions adopted in the later two studies and argued that the equator is far more porous to energy transport than previously considered. Since it is not uncommon for the mid-latitude trough-ridge sequence to fluctuate every 10 to 20 days, particularly in a winter hemisphere, it is altogether possible that the monsoon is influenced

from the south. However, the general issue of lateral cross-equatorial effects on any part of the globe remains as a serious unresolved problem in dynamics and it is far too soon to draw any firm conclusions on how Southern Hemisphere processes might perturb the SW Monsoon.

3.1.5 Short Period Oscillations

A third dominant frequency that has been identified in terms of monsoon fluctuations is the 3-5 day oscillation. Ananthakrishnan and Keshavamurty (1970) have noted a one week periodicity in pressure and wind field data in central and northern India during the monsoon. Keshavamurty (1973) pointed out a peak at 5-6 days in the power spectrum of the meridional component of the wind over the Indian sub-continent. Bhalme and Parasnis (1975) have noted a similar periodicity in daily indices of north-south pressure gradient data. The later study noted that the short period oscillation in pressure data had been reported as early as the late 1800's by Eliot (1895).

Krishnamurti and Bhalme (1976) also identified this mode in their analysis of the complete monsoon sequence; they concluded that the short period fluctuations are purely local instabilities. M. Murakami (1976, 1977) in his spectrum analysis studies, identified this mode as synoptic scale passages of monsoon lows originating from the Bay of Bengal and moving along the monsoon trough. The factors which discriminate the monsoon low oscillations from the major monsoon depression oscillations ($\approx$ 15 day) are the strength of the cyclone, significant fluctuations in rainfall, and actual movement of the monsoon trough itself.

The unresolved question with the 3-5 day mode is its possible relationship to the global scale westward moving tropical waves which were first carefully documented by Yanai, et al. (1968) and Wallace and

Chang (1969), using conventional upper air data from tropical stations. Madden and Julian (1972b) provided additional evidence of this mode using a much longer data set of pressure at tropical stations, as did Misra (1972), using International Geophysical Year data (1957-1958). Zangvil (1975) had noted this mode in the satellite brightness (cloudiness) data although the 5-day westward propogating wave was found in latitudes 5^{o}-15^{o} (wave number 10), whereas an eastward propogating 4-day wave was noted in the equatorial Indian Ocean (wave number 9). M. Murakami (1971) has also note short period oscillations in tropical Pacific rainfall data; in his study both westward propogation (3.5-5.5 day) and eastward propogation (2.8-3.5 day) modes were noted.

An important remaining question concerning the short period oscillations is the origin of the monsoon lows and depressions which are seen to form in the Bay of Bengal, move along the monsoon trough and ultimately give rise to perturbations in the rainfall over central and northern India. If, as some have suggested, these cyclones form in-situ, then the link to the large scale is somewhat obscure. However, Krishnamurti, et al. (1977) have reported that a number of Bay of Bengal disturbances result from a downstream amplification mechanism in which westward traveling shortwaves from the West Pacific positively interfere with large scale type Rossby wave standing oscillations leading to cyclogenesis at Bay of Bengal longitudes. This mechanism does not address the link to the tropical wave most easily identified in the upper troposphere and stratosphere, nor do Krishnamurti, et al. (1977) confirm that this mechanism fully explains monsoon oscillations. Instead, they point out that a number of monsoon lows and depressions seem to be short wave passage along a quasi-biweekly large scale

standing wave somewhat similar to the process of mid-latitude cyclogenisis. The link and interrelationships to the tropics have therefore remained an open question.

3.2 The Satellite Data Sets

The satellite measurements incorporated into this investigation have been derived from three sources: 1) the TIROS-N Advanced Very High Resolution Radiometer (AVHRR); 2) the GOES-1 Visible and Infrared Spin Scan Radiometer (VISSR); and 3) the NIMBUS-7 Earth Radiation Budget Narrow-Field-of-View radiometer (ERB/NFOV). All of the satellite data used in this study were based on raw digital recordings. At no time during the data reduction procedures were photo digitizations or analog transformations used. All of the data were reduced to standardized geographic map formats to facilitate intercomparison and to allow for graphical display using conventional geographic annotation.

3.2.1 The TIROS-N Data Set

The TIROS-N polar orbiting satellite was launched in time for the FGGE (October 13, 1978) and supported the FGGE observational program on the basis of its 4-channel AVHRR imaging radiometer and its 27-channel TOVS (TIROS Operational Vertical Sounder) three stage temperature retrieval instrument (the HIRS, SSU and MSU subsystems). This was the first of the third generation TIROS-N type vehicles now utilized by the National Environmental Satellite and Data Information Service (NESDIS) for its operational polar orbiter program; see Barnes and Smallwood (1982). This satellite was injected into a sun-synchronous orbit with an inclination of 95.91 degrees and a nodal period of approximately 102 minutes per orbit (14.2 orbits per day). Its average altitude is 854 km. The morning and afternoon equator crossing times are approximately

3:00 (descending) and 15:00 (ascending) in the mean solar time framework (often this is approximately the same as local time, but not necessarily). The reports of Hussey (1979) and Schwalb (1979) can be referred to for additional details.

The TIROS-N AVHRR is a 4-channel cross track scanning instrument (unlike the 5-channel AVHRRs on the later NOAA series satellites). The spectral band passes (half power points) are given in Table 3.1. For this study Channel 1 and Channel 4 Global Area Coverage (GAC) data were utilized. The GAC data, which are available from NESDIS, are a reduced resolution format with respect to the high resolution Local Area Coverage (LAC) raw data from which they are retrieved. GAC resolution is approximately 8 km at Nadir. A 4-month day and night data set was obtained for the period May 1 to August 30, 1979. Various missing data were encountered in the processing stage, including a 13-day data gap from August 6 to August 18. Table 3.2 provides a tabulation of the missing data.

The earth location coordinates available on the GAC data tapes were used in a mapping procedure in which the raw orbital swath imagery were placed in uniform map frames from the equator to 35^{o}N; from 30^{o}E to 100^{o}E. Figure 3.1 provides an illustration of the TIROS-N sector and includes a surface type index. The resolution of these maps were standardized to 15 points per degree latitude and longitude, or a pixel size of 4 x4 n.m. A schematic illustration of the mapping procedure is given in Fig. 3.2. Figures 3.3a-3.3d provide illustrations of the Channel 1 and Channel 4 maps on May 23, 1979. The mapping procedures are discussed in more detail by Smith and Graffy (1982).

TABLE 3.1

Band Passes of the 4-Channel TIROS-N AVHRR Instrument

Channel	Name	Band Pass
1	VIS	0.55 - 0.90 μm
2	Near IR	0.71 - 1.02 μm
3	Weak Window	3.58 - 3.97 μm
4	IR	10.50 - 11.50 μm

TABLE 3.2

TIROS-N AVHRR Missing Data Between May 1 and August 30, 1979

No.	Date	Comments
1	May 28	All Sectors
2	June 7	All Sectors
3	June 13	All Sectors
4	June 24	All Sectors
5	July 5	All Sectors
6	August 1	All Sectors
7	August 5	Nighttime Sectors
8	August 6-18	All Sectors
9	August 19	Nighttime Sectors
10	August 21-22	Daytime Sectors

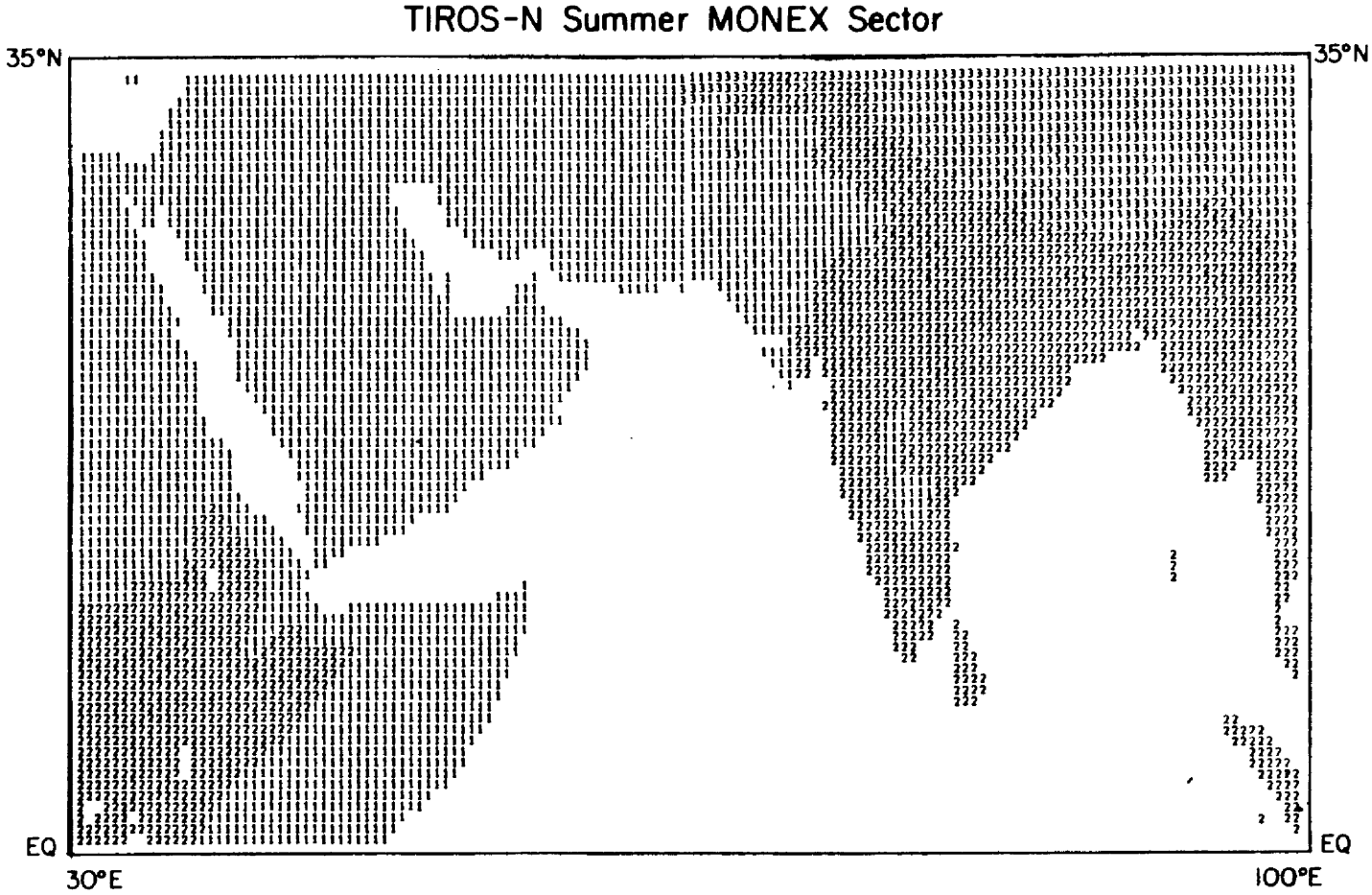

Fig. 3.1. Depiction of the TIROS-N analysis region (Eq-35°N; 30°E-100°E). The numbers indicate the background type (blank-water; 1-desert; 2-semi-arid; 3-Tibetan Plateau).

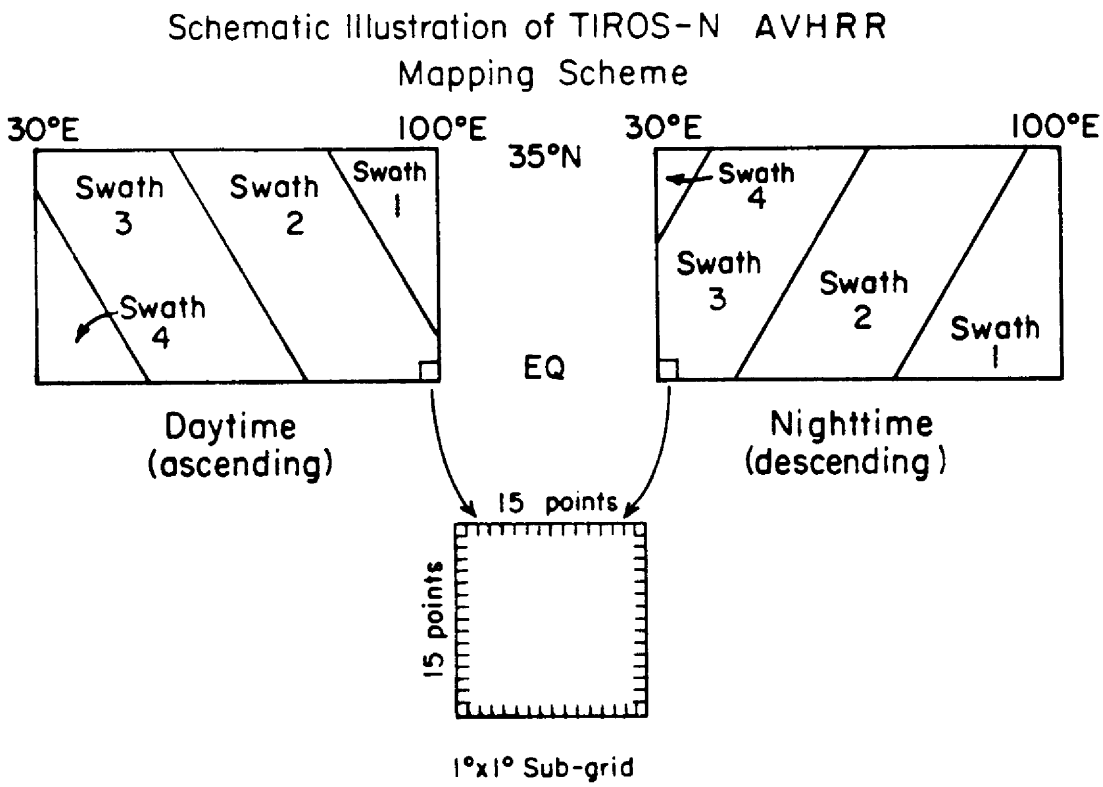

Fig. 3.2. Schematic illustration of the multi-orbital swath TIROS-N mapping scheme.

Fig. 3.3a. TIROS-N AVHRR Channel 1 Arabian sector (daytime) on May 23, 1979.

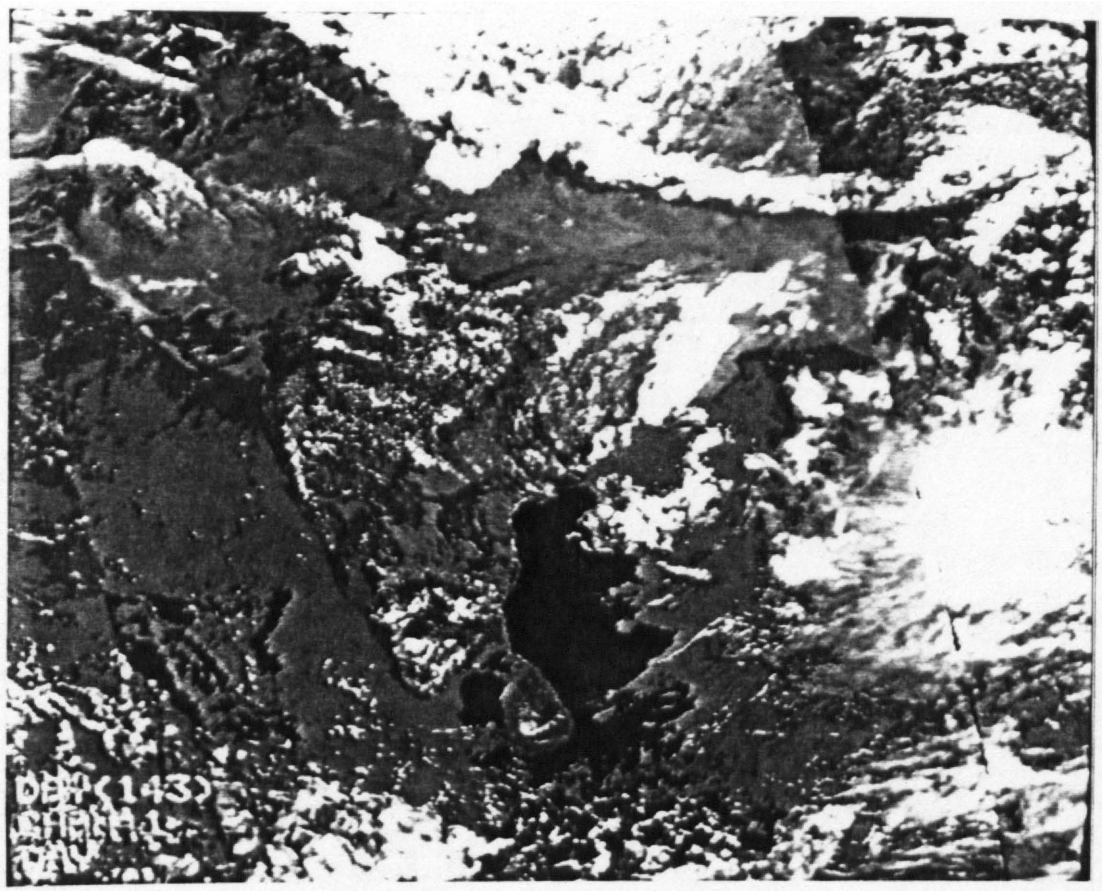

Fig. 3.3b. Same as Fig. 3.3a for Indian sector.

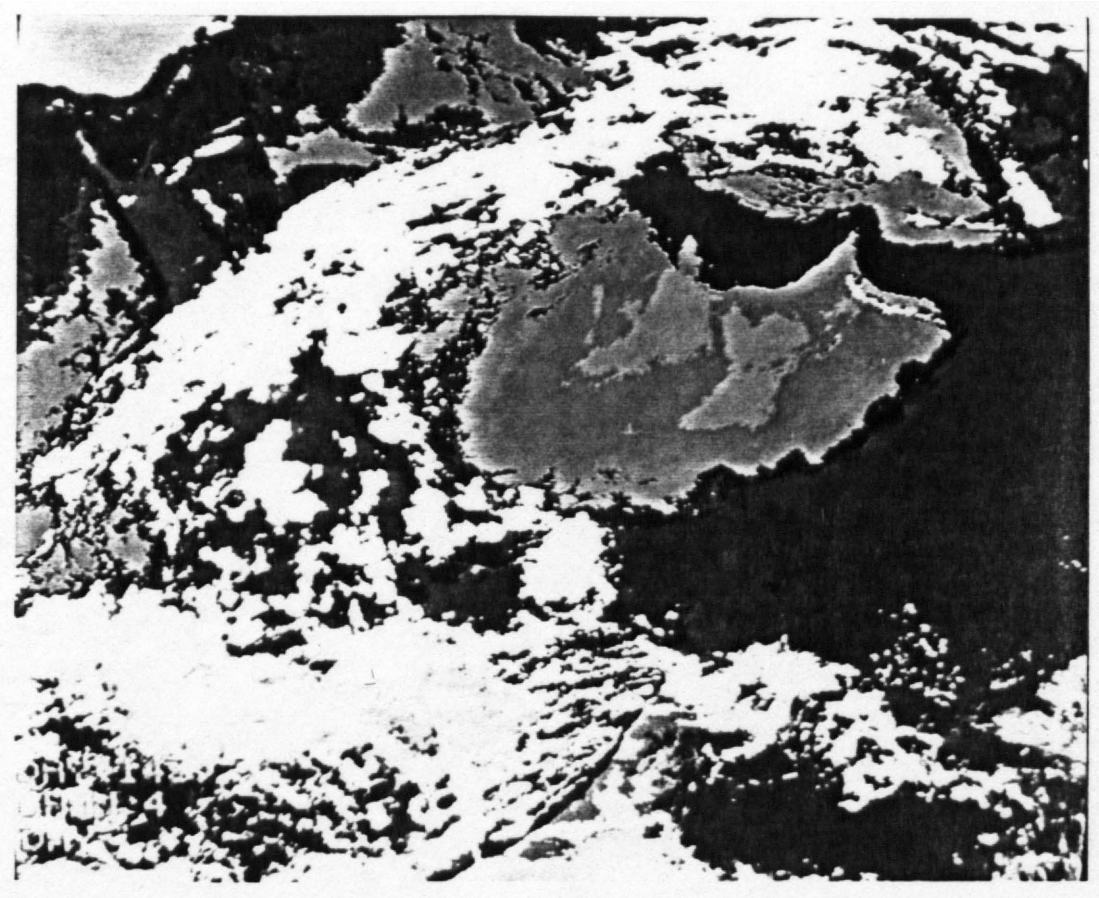

Fig. 3.3c. TIROS-N AVHRR Channel 4 Indian sector (daytime) on May 23, 1979.

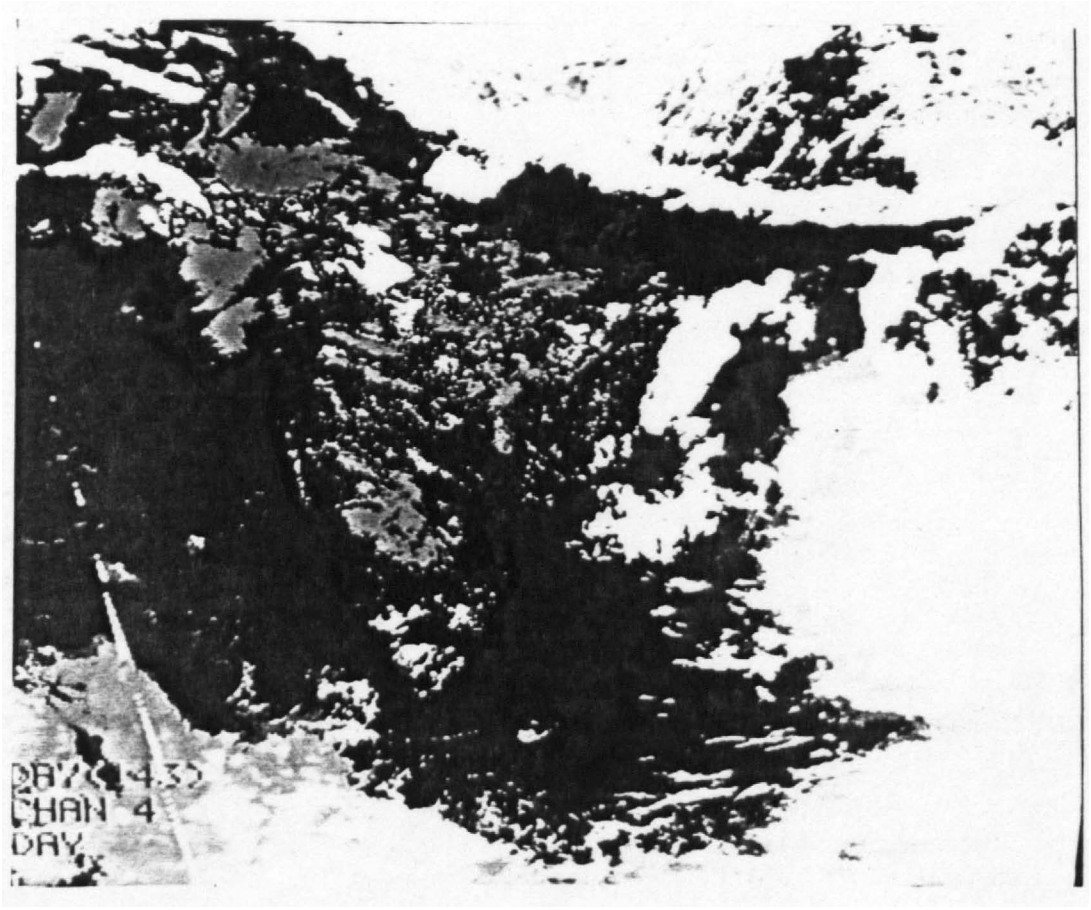

Fig. 3.3d. Same as Fig. 3.3c for Indian sector.

A scheme for converting the raw digital counts to the physical units needed for transforming to filtered radiance is discussed in the reports of Lauritson, et al. (1979) and Kidwell (1979). As illustrations of the mapped top-of-atmosphere radiation budget products that are eventually derived from the raw count data, Figs. 3.4 and 3.5 are provided. In Fig. 3.4 the albedo (A) and absorbed solar flux (K*) fields are shown for the monsoon sector. Note that the absorbed solar flux field exhibits the changing solar zenith across each of the four individual orbit swaths that went into this map (thus the scan lines and gradients of contrast within each orbital swath). The absorbed flux field, which is defined in terms of the downward (K↓) and upward (K↑) fluxes, or with respect to albedo (A), i.e.:

$$\begin{aligned} K^* &= K\downarrow - K\uparrow \\ &= K\downarrow\ (1-A) \end{aligned} \tag{3.1}$$

is calculated at the 4 n.m. space scale with respect to the sun-synchronous time frame. The albedo field (A), on the other hand, appears uniform since for this calculation the filtered radiances ($N_{\Delta\lambda}^{VIS}$) have been normalized by the solar zenith angle (θ_o) and solar distance factor ($\bar{D}/D$), thus yielding a normalized reflectance:

$$A \quad N_{\Delta\lambda}^{VIS} / [\cos \theta_o \cdot (\bar{D}/D)^2] \tag{3.2}$$

where $\bar{D}$ is 1 A.U. and D is the actual earth-sun distance.

Figure 3.5 illustrates the flux equivalent temperature fields (the equivalent broad band temperatures based on the infrared broad band flux estimates) for both the daytime and nighttime periods. Although there are slight temperature gradients over the continental regions within

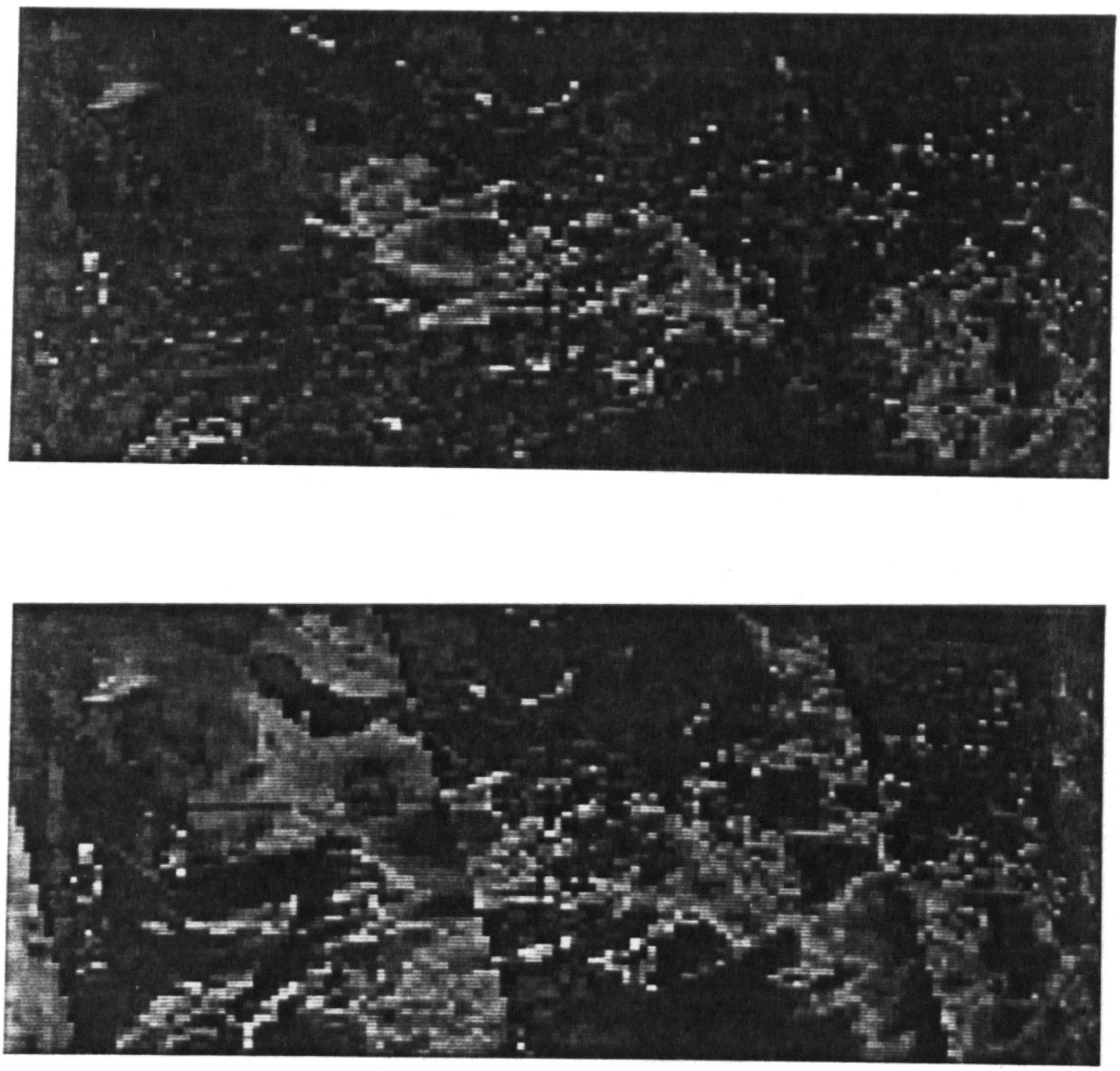

Fig. 3.4. Albedo (top) and shortwave absorbed flux (bottom) fields derived from TIROS-N AVHRR imagery on June 18, 1979.

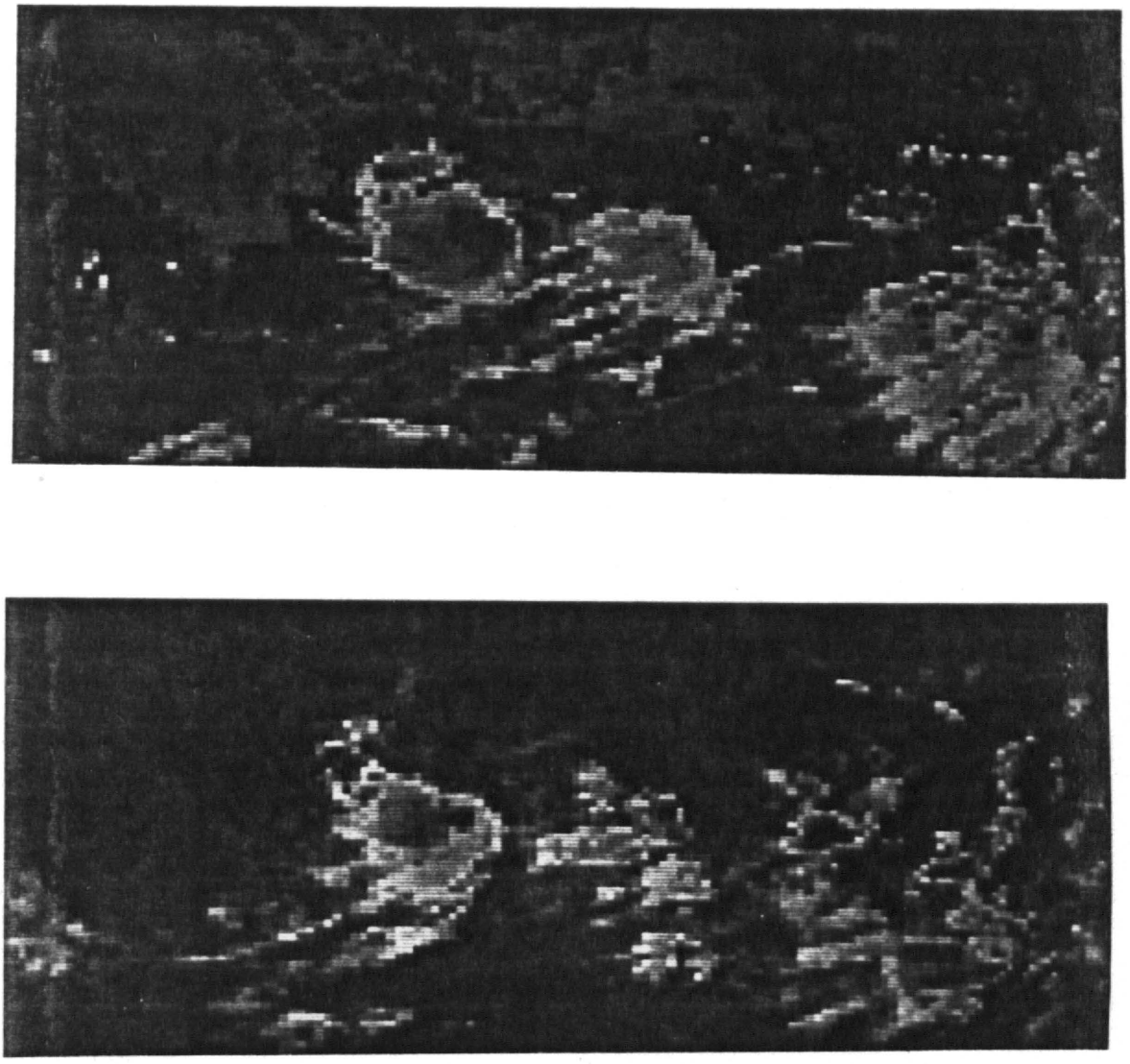

Fig. 3.5. Daytime (top) and nighttime (bottom) flux equivalent temperature fields derived from TIROS-N AVHRR imagery on June 18, 1979.

each orbital swath, due to the diurnal cycle, these are not readily apparent because the local time range across an orbital swath is only a few hours. This effect would be more evident during the daytime than at night if the images were presented in a high contrast format. Thus these images do not exhibit the patchwork appearance resulting from individual orbital swaths which constitute the complete map. Note that at night the temperatures over the oceanic and continental regimes tend to blend together with only the cloud systems standing out in high contrast. This is the simplest illustration of how the globe tends to thermal equilibrium at a given vertical coodinate when the solar source term goes to zero.

3.2.2 The GOES-1 Data Set

The GOES-1 geosynchronous orbiting satellite was launched on October 10, 1975 under the auspices of the National Environmental Satellite Service (NESS). At that time it was used as the GOES-East vehicle to support National Weather Service operations and other National Oceanic and Atmospheric Administration (NOAA) operational services. This was the third of the operational Synchronous Meteorological Satellite (SMS) series following SMS-1 and SMS-2. More detailed information on the GOES spacecraft can be found in the reports of Corbell, et al. (1971), Ensor (1978), and Hughes (1976).

Because GOES-1 was retired from main line operations prior to the FGGE, it effectively became a spare vehicle. As the FGGE approached, it became obvious to the World Meteorological Organization that the Soviet Union would not meet their commitment to place a geosynchronous satellite in orbit over the Indian Ocean to complete the five satellite geostationary configuration planned as part of the worldwide FGGE

satellite network. As a result, NOAA agreed to move GOES-1 over the Indian Ocean for one year in support of the FGGE (December 1, 1978 to November 30, 1979).

Since the satellite sub-point was beyond longitudes (55^{o}-60^{o}E) at which the NESS could receive and retransmit the Direct Readout Ground Station (DRGS) signals, the European Space Agency offered to utilize one of their ground facilities in Villa Franca, Spain (outside of Madrid) to receive and record digital VISSR imagery on NOAA processor and recording equipment provided to NOAA by the University of Wisconsin's Space Science and Engineering Center (SSEC). The recording system utilized in Villa Franca was called an Offline Data Ingest System (ODIS). This system was eventually shipped to Colorado State University to be used under MONEX grants to create computer compatible imagery from the raw ODIS video cassette tapes recorded in Spain in real time (these tapes were kindly provided to the author by Professor Verner Suomi, whose center acted in the role of data depository for the GOES-1 raw recordings).

A nine month VIS-IR data set was extracted and processed from the ODIS recordings in support of the CSU SMONEX research projects (January to September, 1979). For this investigation a one month data set (every 3 hours) has been incorporated. The details of the data extraction and processing have been documented in Smith and Vonder Haar (1980b, 1983). The GOES-1 SMONEX sector covers the region from 30^{o}S to 40^{o}N; 30^{o}E to 100^{o}E. Thus it is twice the size of the TIROS-N sector. Figure 3.6 illustrates the geographic region used in the GOES-1 processing; the numbered regions correspond to a regional classification scheme which

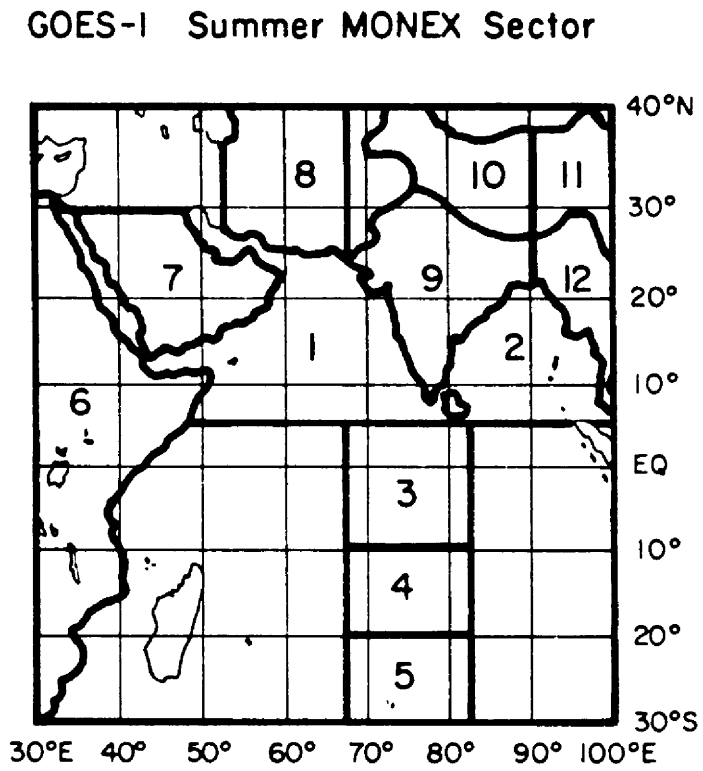

1- Arabian Sea
2- Bay of Bengal
3- Indian Ocean (5°N-10°S)
4- Indian Ocean (10°S-20°S)
5- Indian Ocean (20°S-30°S)
6- East Africa
7-Arabian Peninsula
8-Northern Deserts
9-Indian Sub-continent
10-Western Tibetan Plateau
11-Eastern Tibetan Plateau
12-South East Asia

Fig. 3.6. Depiction of the GOES-1 analysis region (30°S-40°N; 30°E-100°E). The numbered regions are named below the map. These regions correspond to the geographic divisions used in the diurnal analysis.

will be referred to in subsequent sections on diurnal processes and rainfall.

The GOES-1 data set is not a perfect and pristine data set. This has been the result of a variety of problems that cropped up during the course of a somewhat ad-hoc scenario involving data reception, recording, and retrieval. Engineering and software complications inevitably arise whenever data streams and data transfers go beyond the very simplest procedures. In the case of the GOES-1 data, the procedures were more like a scientist's nightmare. The nature of these problems is far too complicated a study to present here; suffice it to say that, in general, four types of problems have been in evidence.

The first is missing data due to poor or missing ODIS recordings. The second is the lack of IR data which occurred sporadically throughout the course of SMONEX because of slowly deteriorating components on the satellite essential for the bias normalization of the infrared detector channel. During SMONEX, GOES-1 was in its feeble years and as a result, data quality suffered. The third problem arose based on the data collection requirements of FGGE itself. On many days during the course of SMONEX, the GOES-1 scan region was cut short in order to generate high frequency tropical scan imagery used in the generation of satellite cloud winds. As a result, the 7:30, 8:00 and 8:30 GMT images were not always generated in the normal fashion. In essence, the top portion of the 7:30-8:30 GMT images were cut off down to approximately 25^{o}N. These images are referred to as short scans. The final problem was that an occasional scan line appeared noisy during computer processing. Any one of a host of reasons could have been responsible; no effort was made to tabulate the source of these errors.

Thus, the resulting data set has gaps, missing IR sectors, short scans, and occasional missing scans. Nevertheless, enough data has been retrieved to enable the computation of diurnal analyses for 10-day periods. Three 10-day June periods, corresponding to pre-onset, onset, and post-onset conditions will be discussed in Section 3.8. Table 3.3 provides a thorough tabulation of the data recovered for the June period.

The normal retrieval times used for this investigation are 2:00, 5:00, 8:00, 11:00, 14:00, 17:00, 20:00, and 23:00 GMT. VIS sectors are not obtained after the 14:00 GMT image. Occasionally a retrieval time one-half hour prior to or later than the normal time was used to circumvent missing data problems. For the central portion of the SMONEX sector, this procedure provides five VIS retrievals; for the left and right portions only four VIS retrievals are possible, due to the appearance of the impending or receeding limb. Figure 3.7 provides VIS and IR photos on June 19, 1979 illustrating a full retrieval sequence. Although two bad scans are evident in the bottom of the 11:00 GMT VIS image, in general, the retrieved imagery is of excellent quality. Note the limb cutoffs in the 2:00 and 14:00 GMT VIS images.

The transformation of the raw image framework into a mapped coordinate system is based on linearly transforming quadrangles of raw pixels into uniform $1^{o} \times 1^{o}$ sub-grids. To enable this transformation, an analytic earth location procedure is required which allows for continuous relationships between the satellite frame of reference (line-element) and the terrestrial frame of reference (latitude-longitude). Mathematical descriptions of these navigational procedures for a geosynchronous problem have been outlined in Smith and Phillips

TABLE 3.3

GOES-1 VISSR Data Tabulation for June, 1979
(x-full sector; s-short scan; m-missing sector)

Day	2 V	I	P Time	5 V	I	P Time	8 V	I	P Time	11 V	I	P Time	14 V	I	P Time	17 I	P Time	20 I	P Time	23 I	P Time
152	M	X/4	2,0001	M	M	-	M	M	-	X/2	X/5	11,0858	X/3	X/6	14,0001	X/7	17,0001	X/8	20,0001	X/9	23,0001
153	X/1	X/5	2,0000	X/2	X/6	5,0001	M	M	-	X/3	X/7	11,0835	X/4	X/8	14,0000	X/9	17,0001	M	-	X/10	23,0001
154	X/2	X/7	2,0001	X/3	X/8	5,0001	S/13	S/14	7,5533	X/12	X/10	11,0814	X/6	X/11	14,0001	M	-	M	-	M	-
155	X/4	M	2,0000	X/1	M	5,0001	M	M	-	X/2	M	11,0834	X/3	M	14,0001	M	-	M	-	M	-
156	X/1	X/5	2,0001	M	M	-	S/11	S/12	7,5529	X/3	X/7	11,0901	X/4	X/8	14,0001	X/9	17,0001	X/10	20,0001	M	-
157	X/1	M	2,0000	M	M	-	M	M	-	M	M	-	M	M	-	X/2	17,0001	X/3	20,0001	M	-
158	X/1	X/3	2,0000	M	M	-	S/5	M	7,5531	M	M	-	M	M	-	M	-	M	-	X/4	23,0000
159	X/2	X/5	2,0001	X/6	X/7	5,0000	S/3	S/4	7,5537	X/8	M	11,1027	X/9	M	14,0001	M	-	M	-	M	-
160	M	M	-	X/1	M	5,0001	S/3	M	7,5536	M	M	-	M	M	-	M	-	M	-	M	-
161	M	M	-	X/1	M	5,0002	S/4	M	7,5538	X/2	M	11,0951	X/3	M	14,0001	M	-	M	-	M	-
162	X/1	M	2,0000	M	M	-	S/11	S/12	7,5538	X/3	X/6	11,0751	X/4	X/7	14,0001	X/8	17,0001	X/9	20,0001	X/10	23,0000
163	X/1	X/3	2,3000	X/2	X/4	5,0001	M	M	-	X/5	X/7	11,0846	X/6	X/8	13,3001	X/9	17,0001	X/10	20,0000	M	-

TABLE 3.3 (Continued)

Day	V	I	2 P Time	V	I	5 P Time	V	I	8 P Time	V	I	11 P Time	V	I	14 P Time	I	17 P Time	I	20 P Time	I	23 P Time
164	X/1	X/5	2,0000	X/2	X/6	5,0001	S/13	S/14	7,5533	X/4	X/8	11,0001	X/11	M	14,0001	X/9	17,0001	X/10	20,0000	X/12	23,0002
165	X/1	X/6	2,0001	X/2	X/7	5,0001	S/12	S/13	7,5538	X/4	X/9	11,0001	X/5	X/10	14,0002	M	17,0001	X/11	20,0000	M	-
166	X/1	X/3	2,0001	X/2	X/4	5,0001	S/5	S/6	7,5533	X/7	X/9	11,0901	X/8	X/10	14,0001	X/11	17,0001	X/12	20,0000	X/13	23,0000
167	X/1	X/6	2,0000	S/13	S/14	5,0001	S/15	M	7,5532	X/4	X/8	11,1131	X/5	X/9	14,0001	X/10	17,0002	X/11	20,0001	X/12	23,0001
168	X/1	X/6	3,0001	X/2	X/7	5,0001	S/13	S/14	7,5534	X/4	M	11,0701	X/5	X/9	14,0001	X/10	17,0001	X/11	20,0001	X/12	23,0001
169	X/10	X/4	2,0001	X/13	X/5	5,0001	S/11	S/12	7,5537	X/2	X/6	11,3321	X/3	X/7	14,0001	X/8	17,0001	X/9	20,0000	-	-
170	X/1	X/6	2,0001	X/2	X/7	5,0001	S/13	S/14	7,5539	X/4	X/9	11,0831	X/5	X/10	14,0001	X/11	17,0001	X/12	20,0000	M	-
171	X/1	X/4	2,0000	X/2	X/5	5,0001	M	M	-	M	M	-	X/3	X/6	14,0001	M	-	M	-	M	-
172	X/1	X/4	2,0001	X/2	X/5	5,0001	M	M	-	M	M	-	X/3	X/6	14,0001	X/7	17,0001	X/8	20,0000	X/9	23,0001
173	X/1	X/6	2,0001	X/2	M	5,0001	S/11	S/12	7,5537	X/4	X/8	11,0951	X/5	X/9	14,0001	X/10	17,0001	M	-	M	-
174	X/1	X/6	2,0000	X/7	M	5,0000	S/3	M	7,5541	X/4	M	11,1031	X/5	M	14,0001	M	-	M	-	M	-
175	X/1	M	2,0001	X/2	M	5,0001	M	M	-	X/3	M	11,0931	X/4	M	14,0001	M	-	M	-	M	-
176	X/1	M	2,0000	X/2	M	5,0001	S/6	M	7,5531	X/4	M	11,0101	X/5	M	14,0001	M	-	M	-	M	-
177	X/1	M	2,0002	M	M	-	M	M	-	M	M	-	X/2		14,0001	M	-	X/3	20,3930	X/4	23,0000
178	X/1	X/6	2,0000	X/2	X/7	5,0001	X/3	X/8	7,5534	X/4	X/9	11,0000	M	M	-	X/10	17,0001	M	-	X/11	23,0000
179	X/1	X/6	2,0000	X/2	X/7	5,0001	X/3	M	8,5533	X/4	X/8	11,0041	X/5	X/9	14,0001	X/10	17,0001	X/11	20,0000	X/12	23,0000
180	M	M	-	M	M	-	M	M	-	M	X/2	11,0129	X/1	X/3	14,0001	X/4	17,0001	M	-	X/5	23,0000
181	X/1	X/4	2,0001	X/2	X/5	5,0001	M	M	-	M	M	-	X/3	X/6	14,0001	X/7	17,0001	X/8	20,0000	M	-

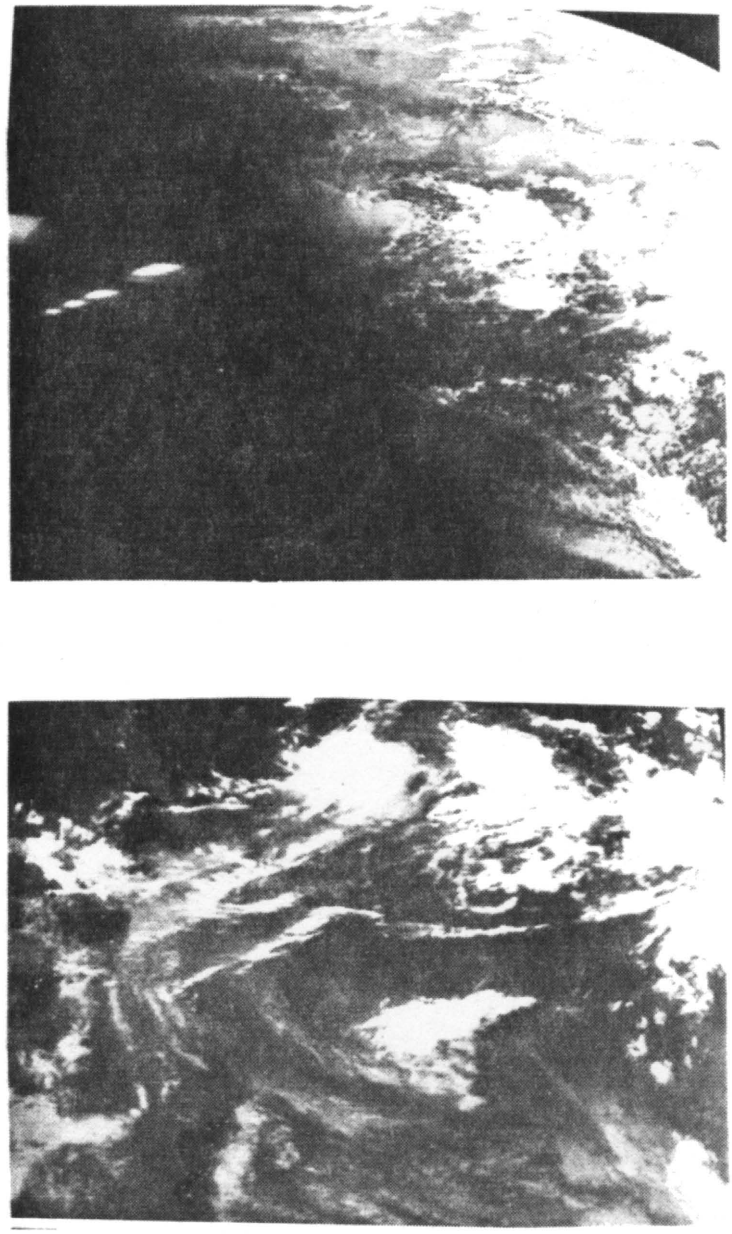

Fig. 3.7a. The 2:00 GMT VIS (top) and IR (bottom) GOES-1 sectors for June 19, 1979.

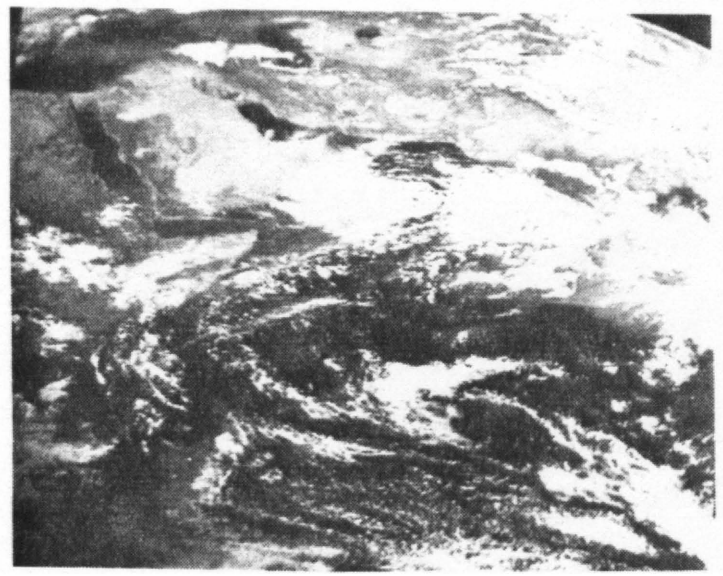

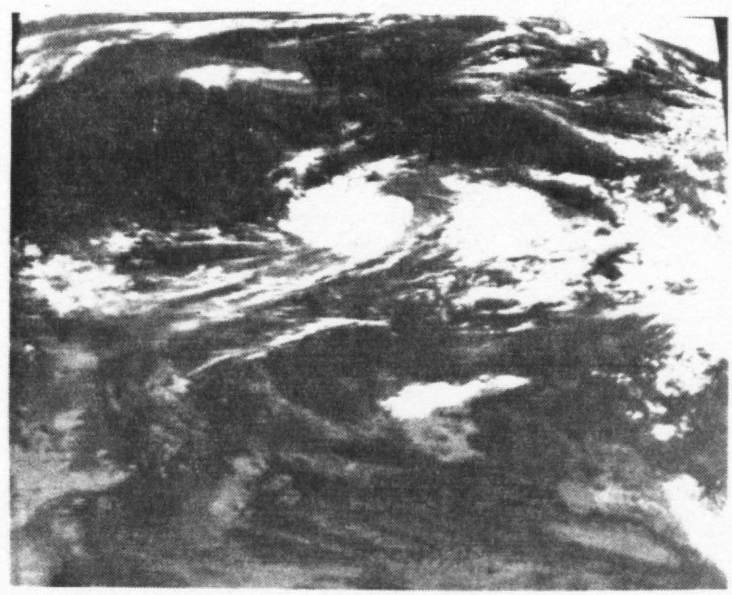

Fig. 3.7b. Same as Fig. 3.7a for 5:00 GMT.

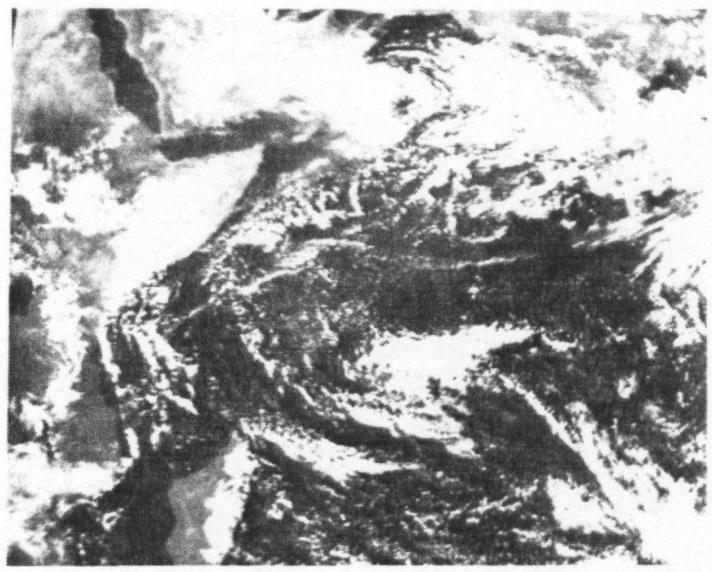

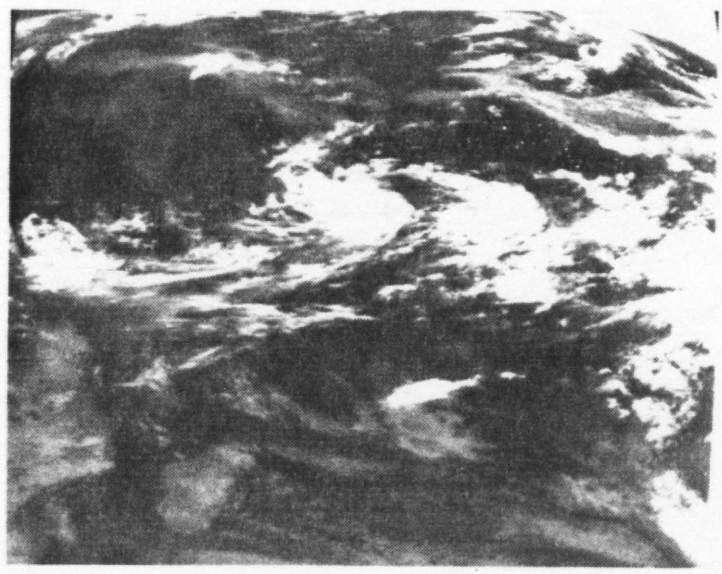

Fig. 3.7c. Same as Fig. 3.7a for 8:00 GMT.

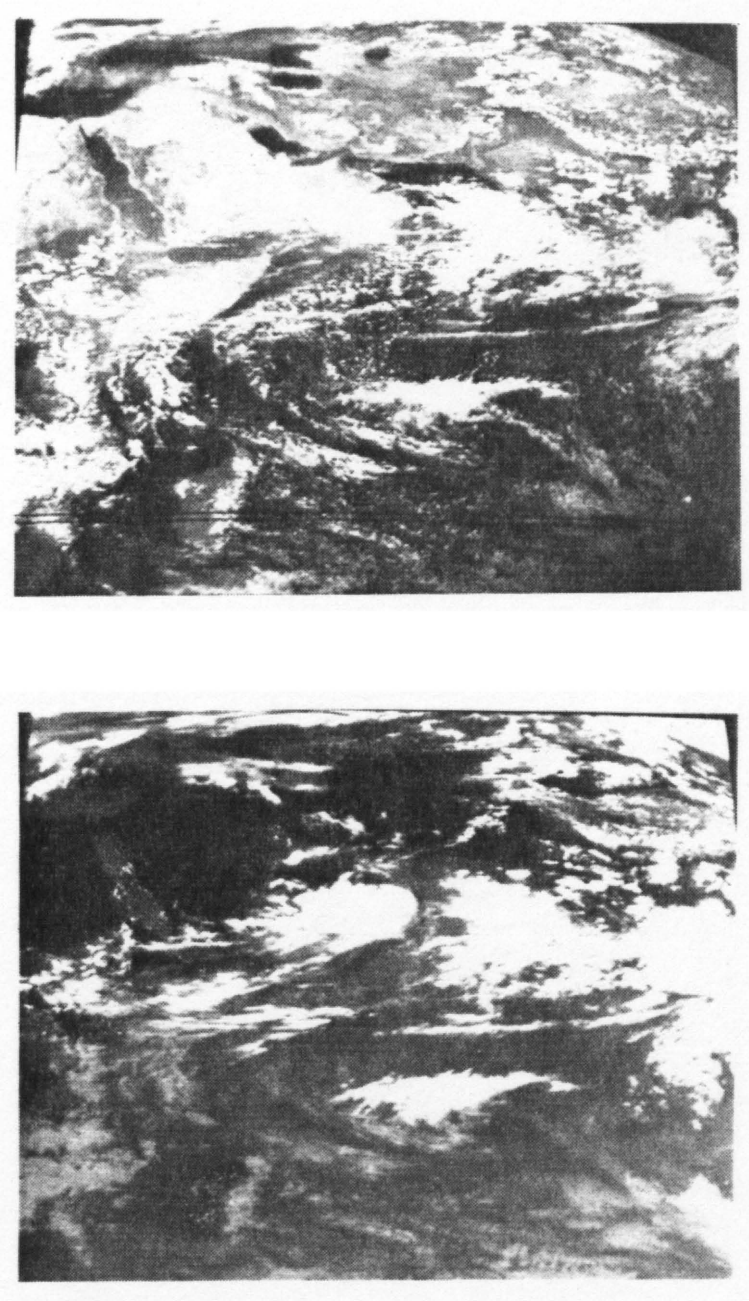

Fig. 3.7d. Same as Fig. 3.7a for 11:00 GMT.

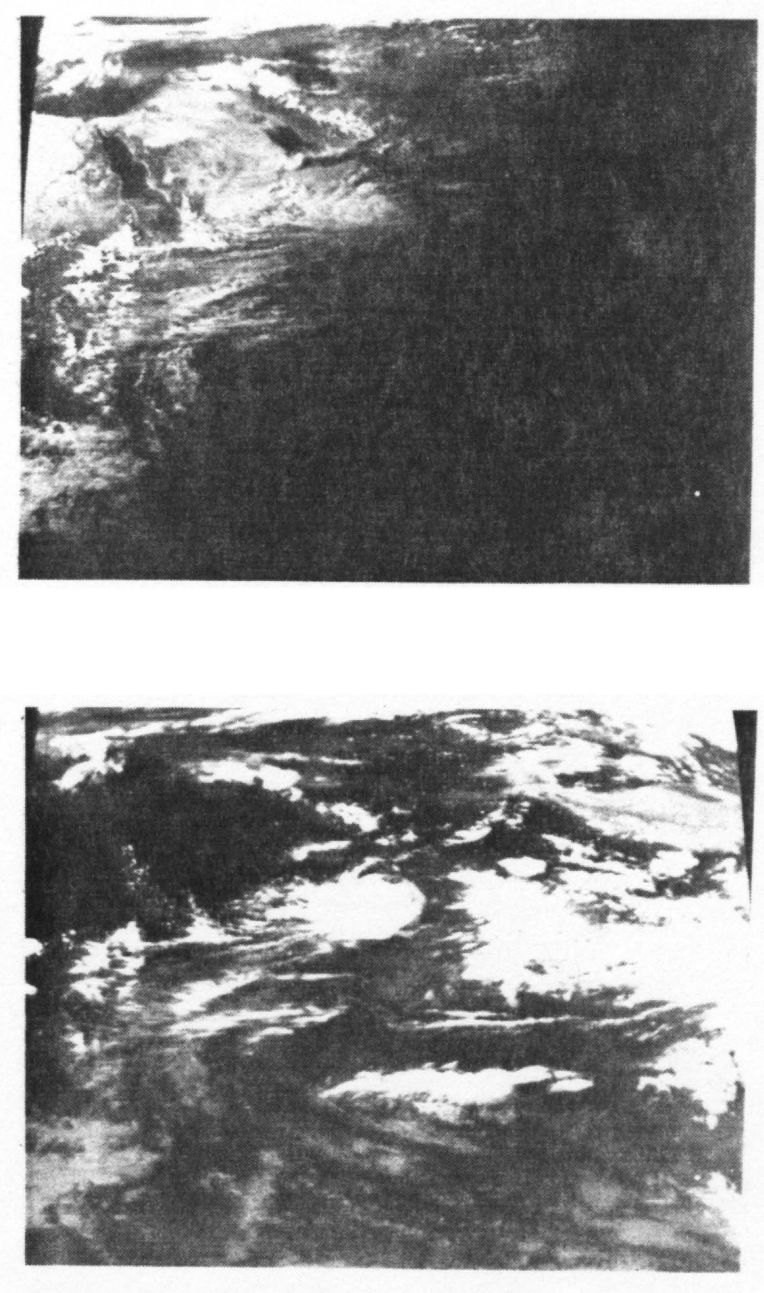

Fig. 3.7e. Same as Fig. 3.7a for 14:00 GMT.

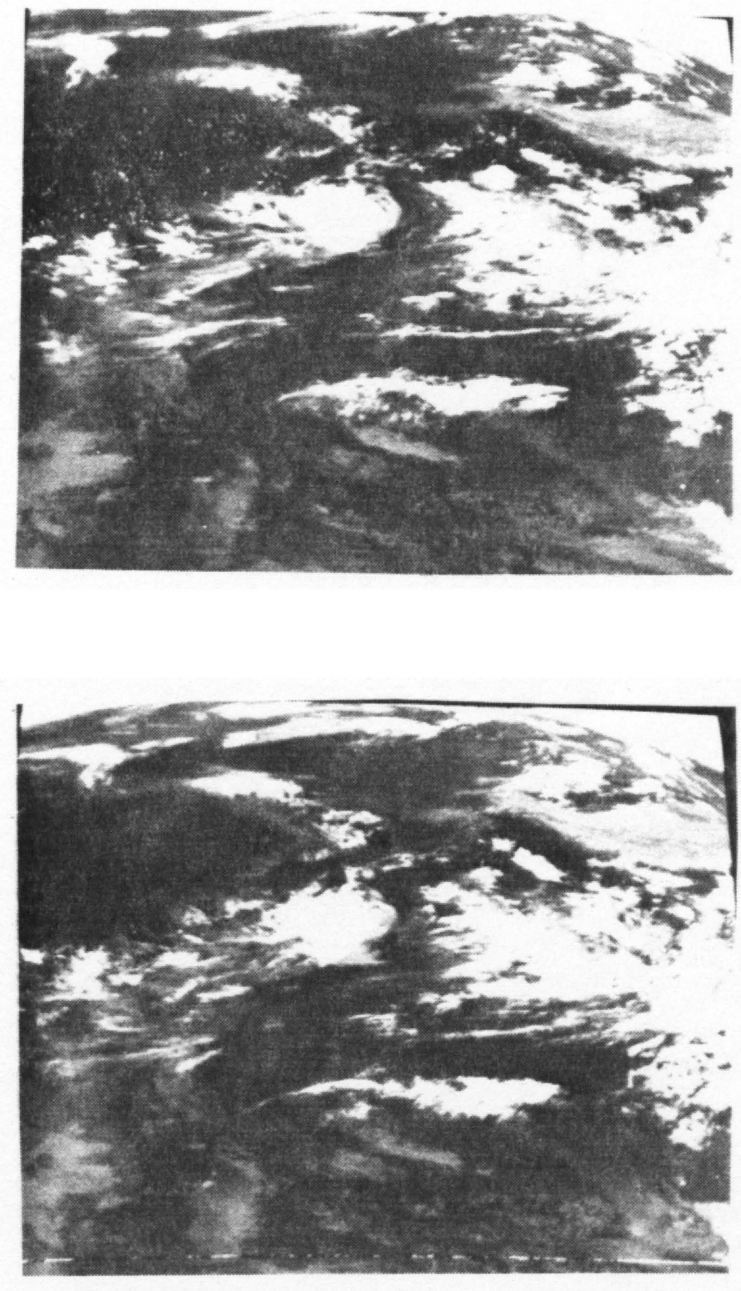

Fig. 3.7f. The 17:00 and 20:00 GMT GOES-1 IR sectors for June 19, 1979.

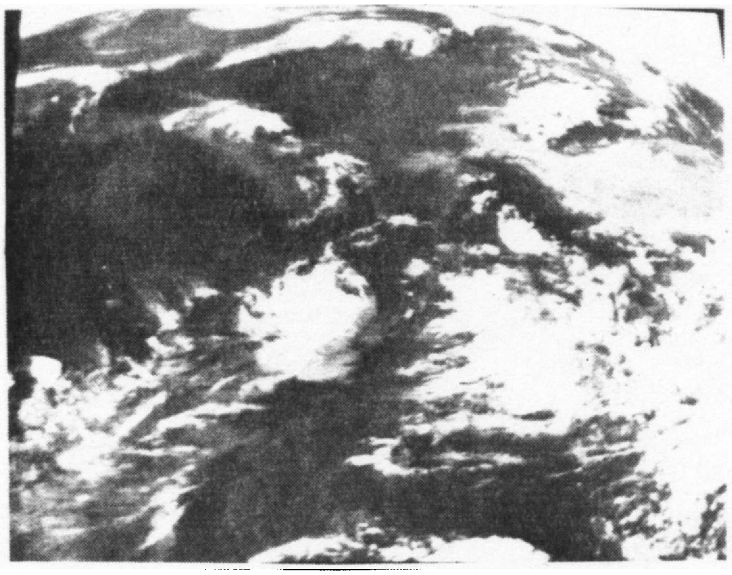

Fig. 3.7g. Same as Fig. 3.7f for 23:00 GMT.

(1972), Smith, et al. (1979), Smith (1980) and Hambrick and Phillips (1980).

The schematic shown in Fig. 3.8 illustrates the GOES-1 mapping procedure. Part of the requirement in earth location is the measurement, in the satellite coordinate system, of a set of known coordinates (generally well recognizable landmarks), needed in estimating the spin axis orientation. Figure 3.9 illustrates a GOES-1 image along with annotation of five landmarks and their earth coordinates which were used in the course of the GOES-1 navigational calculations.

As an illustration of the mapping process, Figs. 3.10a-b are provided. In Fig. 3.10a the raw VIS imagery, truncated near the map boundaries, is shown for May 1, 1979 (7:30 GMT); Fig. 3.10b presents the data in the map framework. Note how a small arc is removed on the left hand side as a result of the truncation procedure used in generating raw images from the ODIS. The pixels within that arc are beyond the truncation point. In Figs. 3.11a-b an intercomparison between the GOES-1 VIS and TIROS-N VIS (Channel 1) Arabian sectors is carried out. The 7:30 GMT image is equivalent to approximately a 10:30 LT image at Arabian Peninsula longitudes. Thus there is a 4.5 hour difference between the two images. There are a few more convective elements apparent in the TIROS-N image since it corresponds to a time three hours after local noon.

The transformation of the GOES-1 VIS-IR raw counts to calibrated filtered radiances is not a straightforward procedure. In the case of the IR conversion, the standard NESS count to EBBT transformation table was used with the understanding that throughout the course of the SMONEX

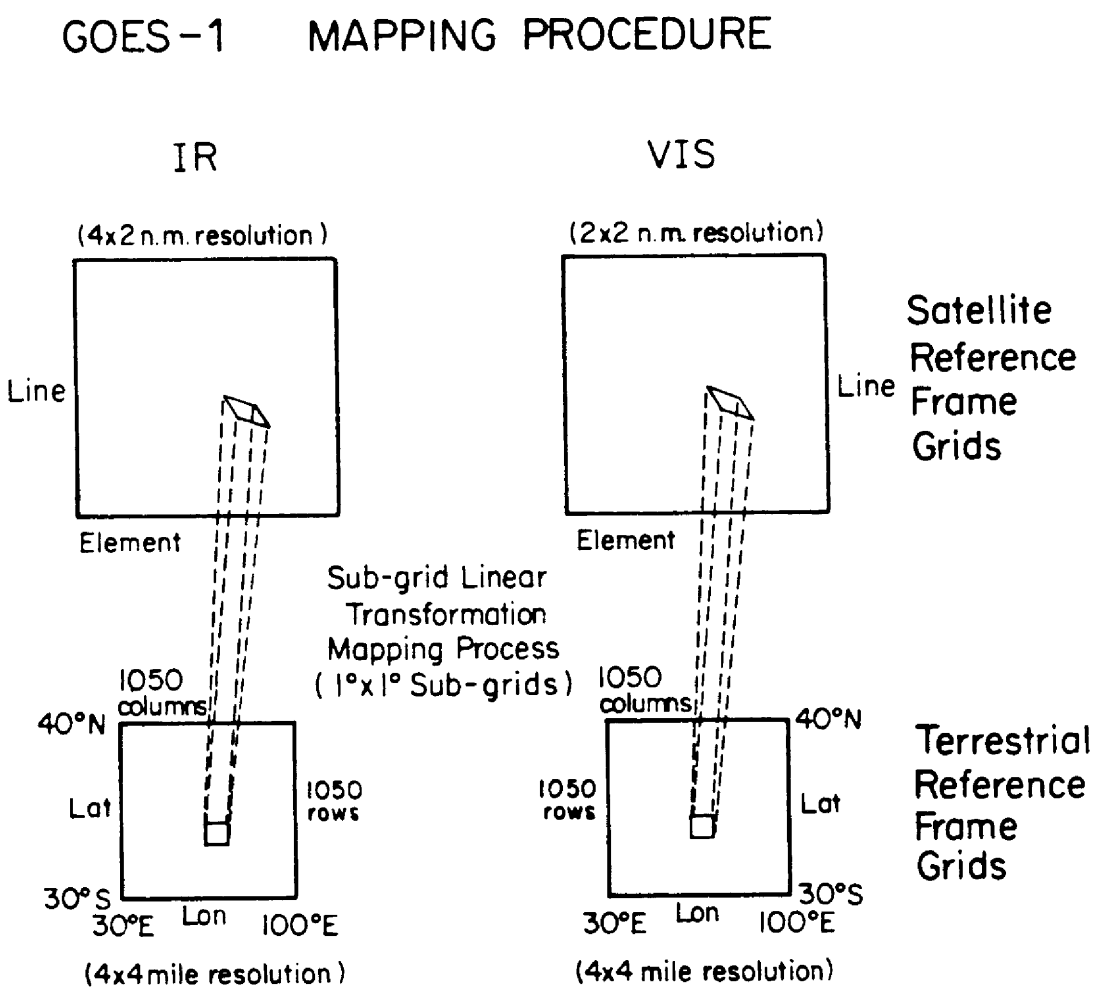

Fig. 3.8. Schematic illustration of the mapping scheme used for the GOES-1 processing.

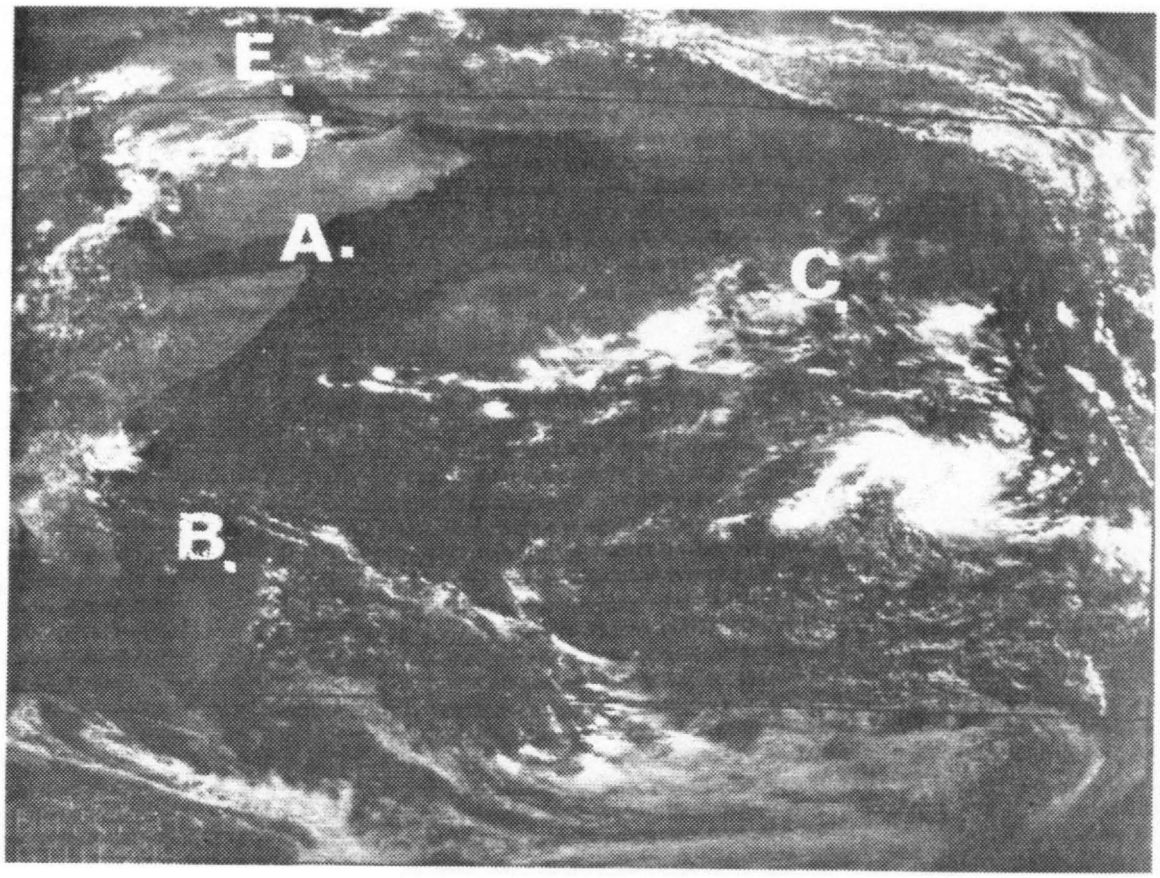

Fig. 3.9. Portrayal of the landmarks and coordinates used for the GOES-1 navigation analysis [image is May 4, 1979 (day 124), 8:00 GMT]

A. Socotra/Ra's Shu'ab - 12°32'30"N, 53°19'00"E
B. Madagascar/Nosy Lava - 14°34'00"S, 47°36'30"E
C. Sri Lanka Strait/Rameswaram - 9°19'00"N, 79°18'30"E
D. Bahrain/Ra's Al Barr - 25°48'00"N, 50°35'00"E
E. Kuwait/Jazirat Faylakah - 29°24'00"N, 48°23'30"E.

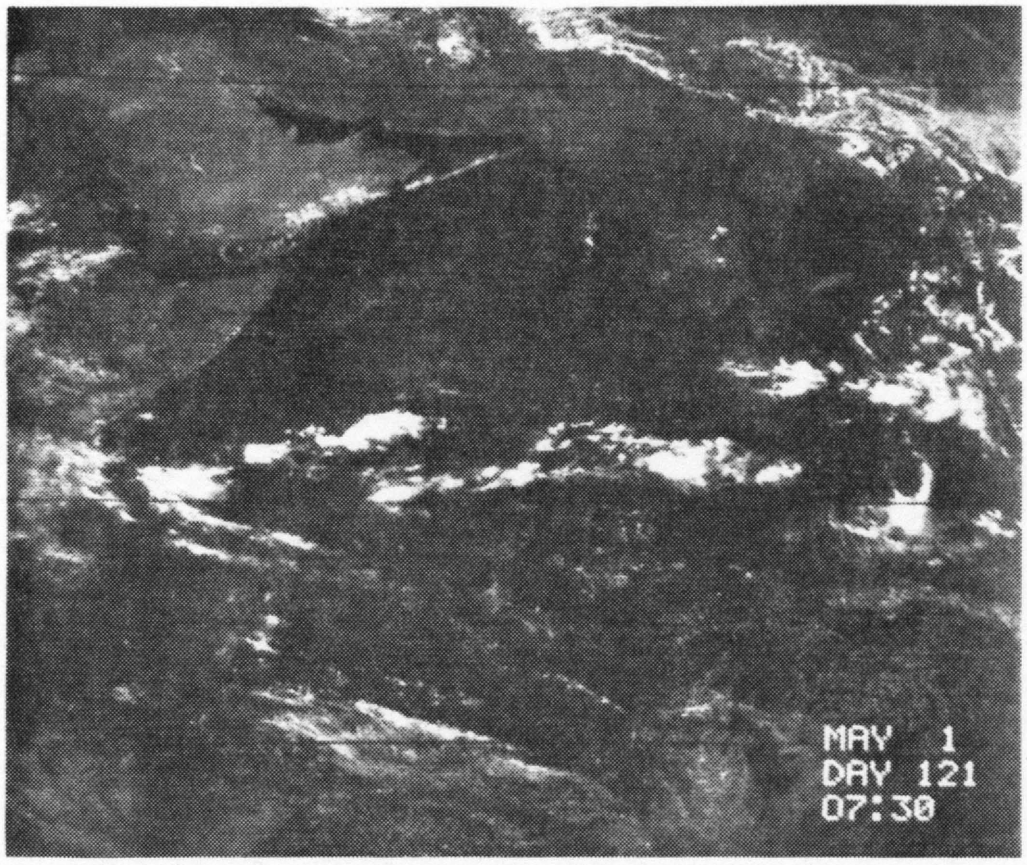

Fig. 3.10a. Unmapped GOES-1 VIS image on May 1, 1979.

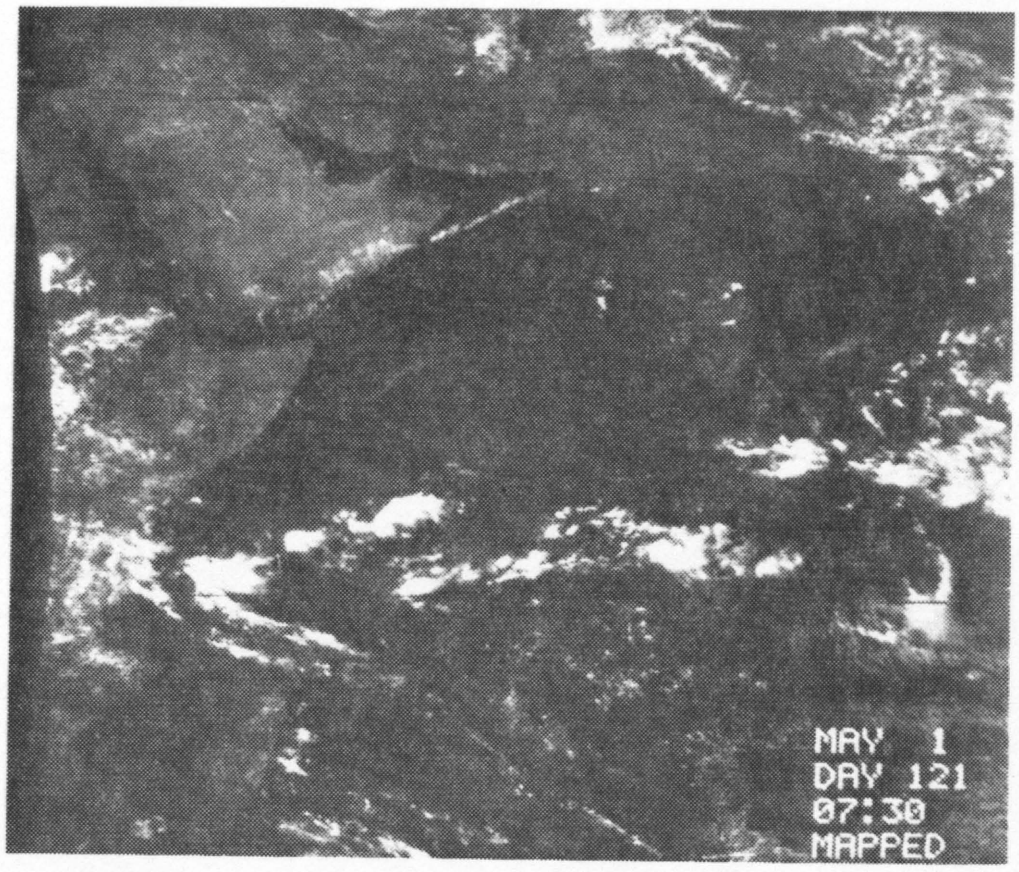

Fig. 3.10b. Same as Fig. 3.10a for the mapped version.

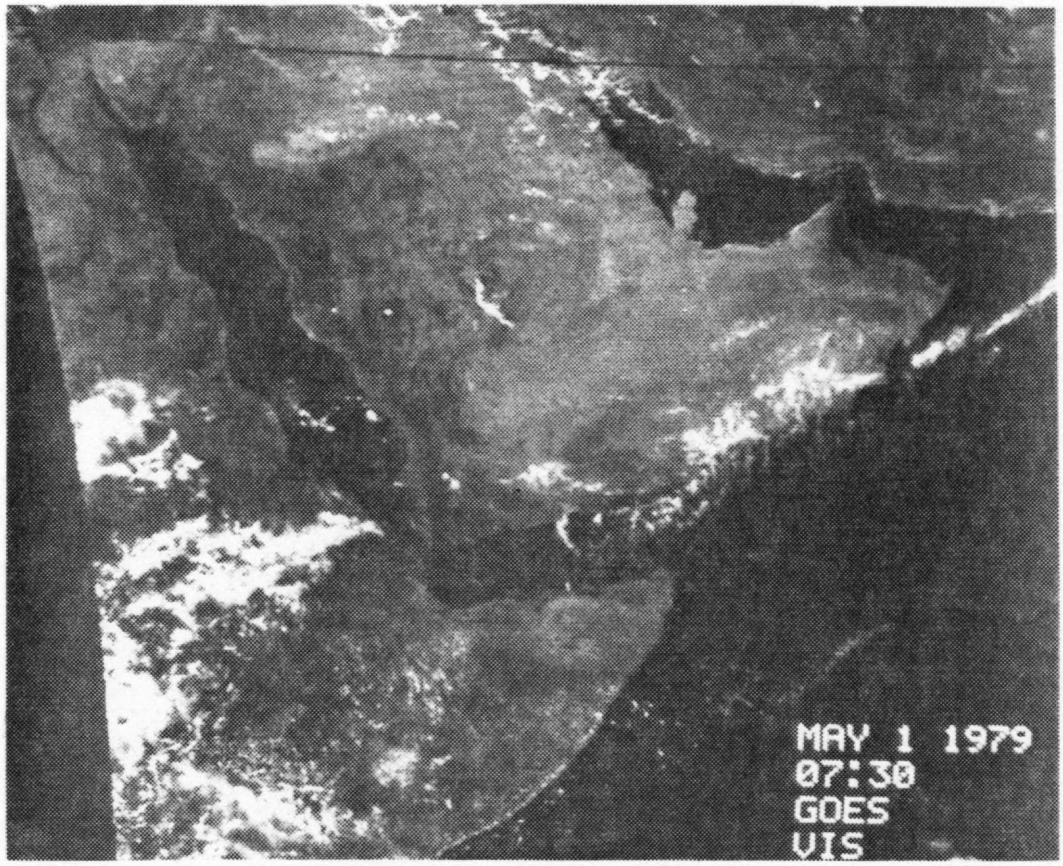

Fig. 3.11a. GOES-1 VISSR mapped Arabian sector (VIS channel) on May 1, 1979 (≈10:30 LT).

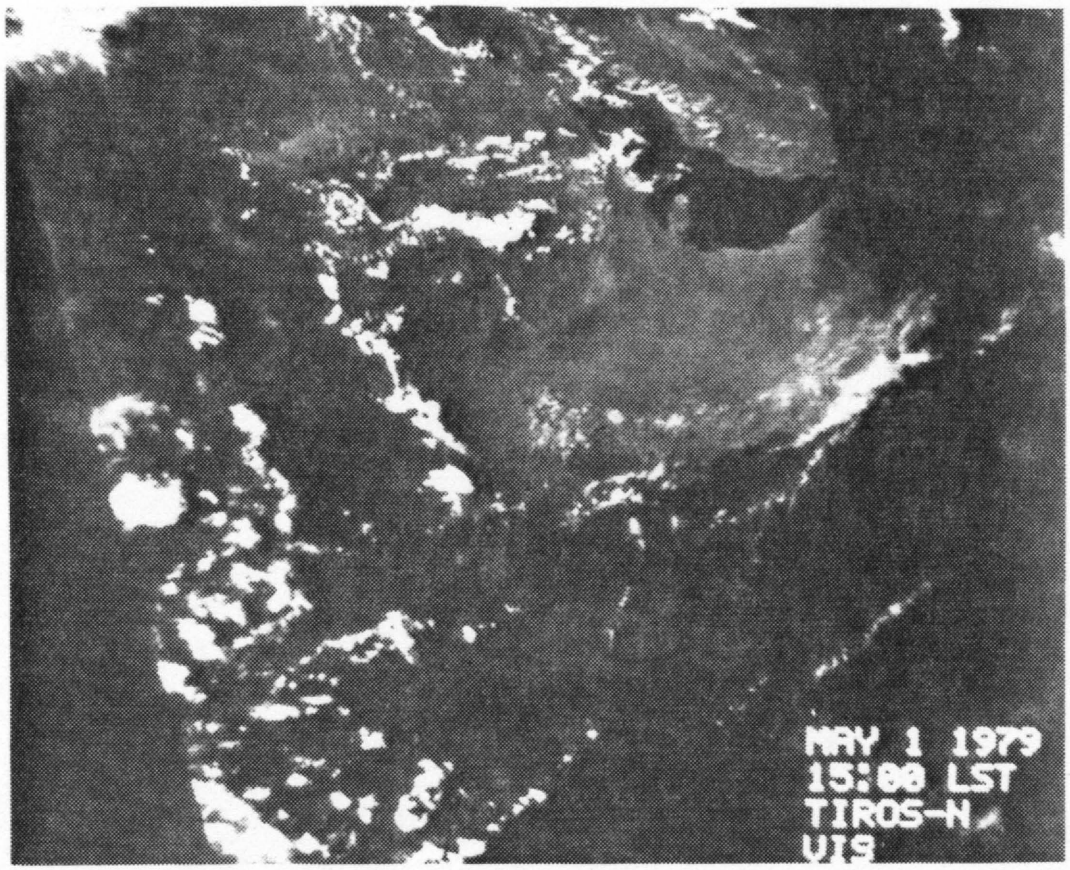

Fig. 3.11b. TIROS-N AVHRR mapped Arabian sector (VIS channel) on May 1, 1979 (≈15:00 LT).

period, the Villa Franca Groundstation personnel provided no checks or adjustments to the Synchronous Data Buffer (SDB) tables normally used to periodically update the GOES IR channel calibration. Therefore, to keep the GOES-1 IR data consistent with the TIROS-N IR data (Channel 4), a linear regression between co-located VISSR and AVHRR data was carried out for four days in June. This regression provided a correction equation for the GOES-1 IR data as follows:

$$T_{GC} = 26.57 + 0.92 \cdot T_{GR} \tag{3.3}$$

where T_{GR} and T_{GC} are the raw and corrected GOES-1 EBBTs. An intercomparison between uncorrected GOES-1 IR data and TIROS-N AVHRR data is shown in Fig. 3.12, along with the regression line associated with the correction.

The VIS channel is uncalibrated for the GOES satellites. Thus an indirect calibration scheme is required. This has been accomplished by combining aircraft measurements with theoretical calculations used to conform to the GOES-1 VIS channel band pass. The design and mathematics of the VIS channel calibration scheme have been reported by Smith and Vonder Haar (1980a).

3.2.3 The Nimbus-7 ERB/NFOV Data Set

One aspect of Radiation Budget (RADBUD) analysis based on weather satellite data, that has caused historical concern, is the estimation of the net radiation term (Q*). It has been shown in Chapter 2 that there are definite uncertainties in the reflected and emitted flux terms that arise in the estimation of broad band fluxes based on spectral radiance measurements. Thus it stands to reason that these errors are reproduced in the net term. Therefore, to put this investigation on more solid footing, measurements from the Nimbus-7 Earth Radiation Budget (ERB)

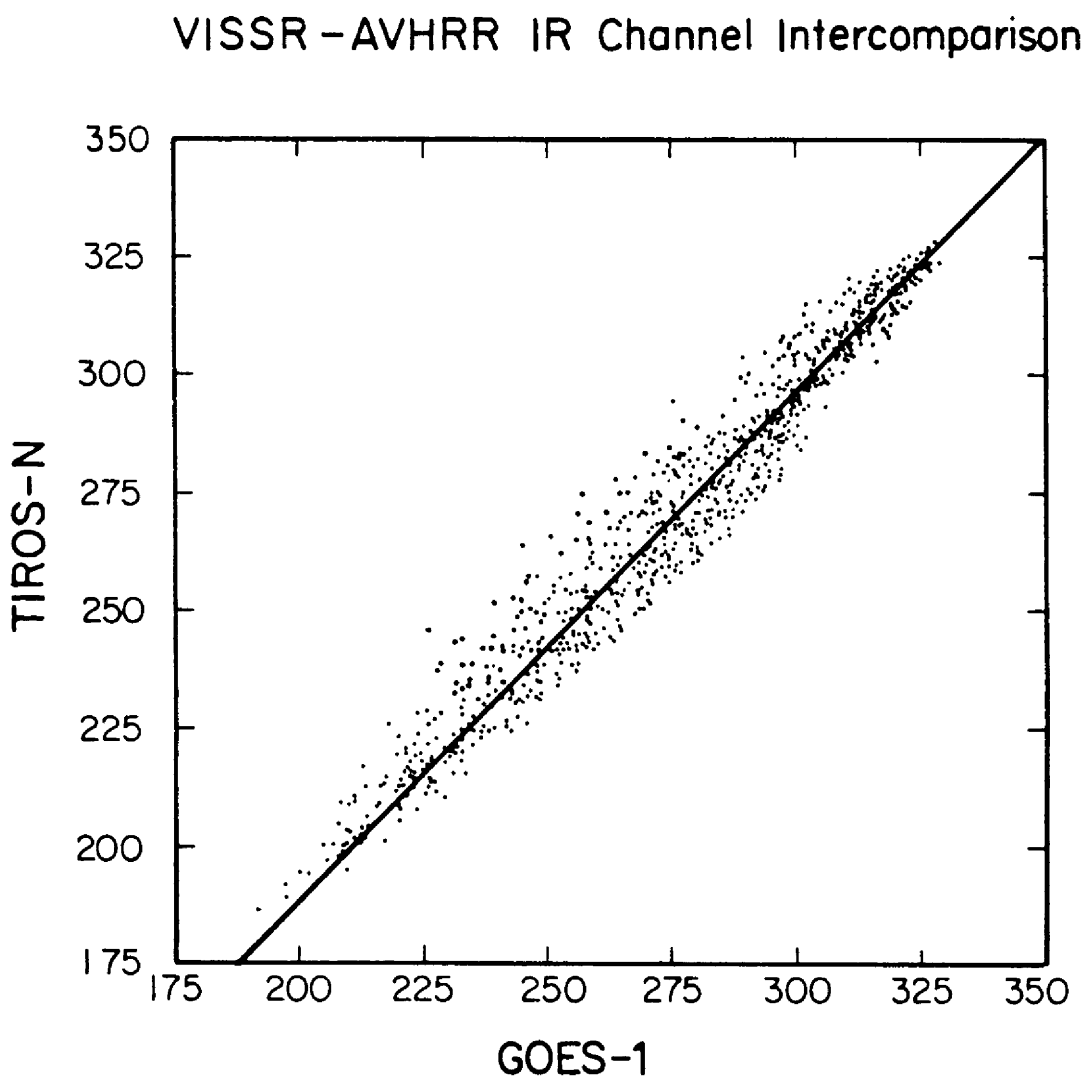

Fig. 3.12. Intercomparison between GOES-1 VISSR and TIROS-N AVHRR EBB temperatures for 4 days in June. An individual point represents the means for a $1^{\circ}x1^{\circ}$ box; the comparison regions extends from Eq-35°N; 55°-65°E. The GOES-1 sectors are at 11:00 GMT which corresponds closely to the 15:00 LT TIROS-N pass at the 60°E longitude.

instrument have been incorporated whenever an accurate measure of the daily integral of net radiation is required. Furthermore, these measurements have been used to assist in the validation and correction of the TIROS-N and GOES-1 RADBUD estimates. It was demonstrated in Chapter 2 how ERB wide-field-of-view (WFOV) data could be used in the validation and correction of AVHRR RADBUD estimates. In this investigation, narrow-field-of-view measurements have been incorporated in much the same fashion.

The ERB instrument was flown on the Nimbus-7 experimental satellite; it started providing radiation budget data on November 16, 1978. The Nimbus-7 satellite is a sun-synchronous polar orbiting experimental platform flying at an altitude of approximately 1100 km. The equator crossings are at noon and midnight, local time. The Nimbus-7 ERB design is very smilar to its counterpart on Nimbus-6 with the exception that one of the ERB-6 ultra-violet solar channels was replaced by a sun viewing cavity radiometer; see Smith, et al. (1983). Descriptions of ERB-6 and ERB-7 can be found in W. L. Smith, et al. (1975) and Jacobwitz, et al. (1978). The success of both these radiation budget missions has led to the advent of the soon to be operational Earth Radiation Budget Experiment (ERBE), which will begin in 1985.

Part of the ERB design, in addition to the WFOV channels, is the scanning portion of the instrument which provides the NFOV data. The ERB scanner is comprised of four solar channels (0.2-4.8μm) and four infrared channels (4.5-5.0μm). The NFOV radiometer is capable of retrieving quality broad band estimates of radiation exchange at the top-of-atmosphere at a medium resolution scale (approximately 0.5 x 0.5

degree). Part of the motivation of the ERB science team for including a scanner was that the NFOV data can be used to develop broad band bi-directional reflectance normalization models which have applications in radiation budget science; see Stowe (1983). In addition, the NFOV data, because of their higher spatial resolution, more closely conform to the resolution characteristics of the weather satellites' imagers.

However, because of the nature of the scanner deployment mode, the satellite orbit configuration, and the spacecraft power allocation schedule, it is not possible to obtain continuous scanner coverage on a daily basis. To obtain complete coverage of the monsoon sector requires from four to six days of NFOV compositing. Thus it is not always convenient or correct to use the high quality RADBUD data if detailed resolution of the radiation fields is required. Since part of the purpose of this investigation is to depict the high time and space resolution features of the monsoon, the weather satellite estimates have been used where they are most suitable. However, there are instances where the ERB-NFOV measurements are the appropriate choice. Additional information on the NFOV radiometer can be found in the reports of Soule (1983) and Stowe and Fromm (1983).

As a simple illustration of the Southwest Monsoon from the ERB-NFOV perspective, Fig. 3.13 is provided. This is a 3-month composite of infrared flux during the middle of the monsoon season (June-August). Note that in terms of the globe as a whole, the Southwest-East Asian Monsoon is the dominant feature in terms of interrupting the zonal symmetry. This is due, of course, to the dominance of the monsoon cloud fields responsible ultimately for monsoon rainfall throughout Southern Asia. Note that in the December and March averages of the same

Fig. 3.13. Three month (June-July-August, 1979) global mean of the infrared emitted flux field derived from the Nimbus-7 ERB-NFOV measurements.

parameter, seen in Figs.3.14a-b, the major tropical cloud features are the Indian Ocean-Western Pacific ITCZ cloudiness, associated with the winter monsoon, and the active convection zones over southern hemisphere, South America, and Africa (Southern Hemisphere Summer). The Southwest Monsoon region, on the other hand, is dominated by very high infrared emittance.

3.3 Estimation of Radiative Fluxes

The utilization of weather satellite spectral radiance measurements for the purpose of estimating radiative fluxes at the top-of-atmosphere has been discussed extensively in Chapter 2. The reader is referred to that study for details. The following provides a brief descriptive account of the methodology, the validation, and the potential shortcomings of this approach to RADBUD analysis.

There are three basic steps in estimating radiative fluxes from raw VIS-IR satellite imagery:

1) Calibration

2) Geometric Normalization

3) Spectral Transformation

3.3.1 Calibration

The calibration step invokes a transformation to the raw count information [C_{VIS} and C_{IR}] to yield spectral visible and infrared window radiance measures ($N^{VIS}_{\Delta\lambda}$, $N^{WIN}_{\Delta\lambda}$). In general, the weather satellite radiometer detector and electronics subsystems generate an output (voltage) which is linearly proportional to the irradiant energy. However, the quantization of the voltage signals may incorpoate non-linear or discontinuous and discretized processes. Thus the eventual raw satellite counts are not necessarily proportional to radiance. For

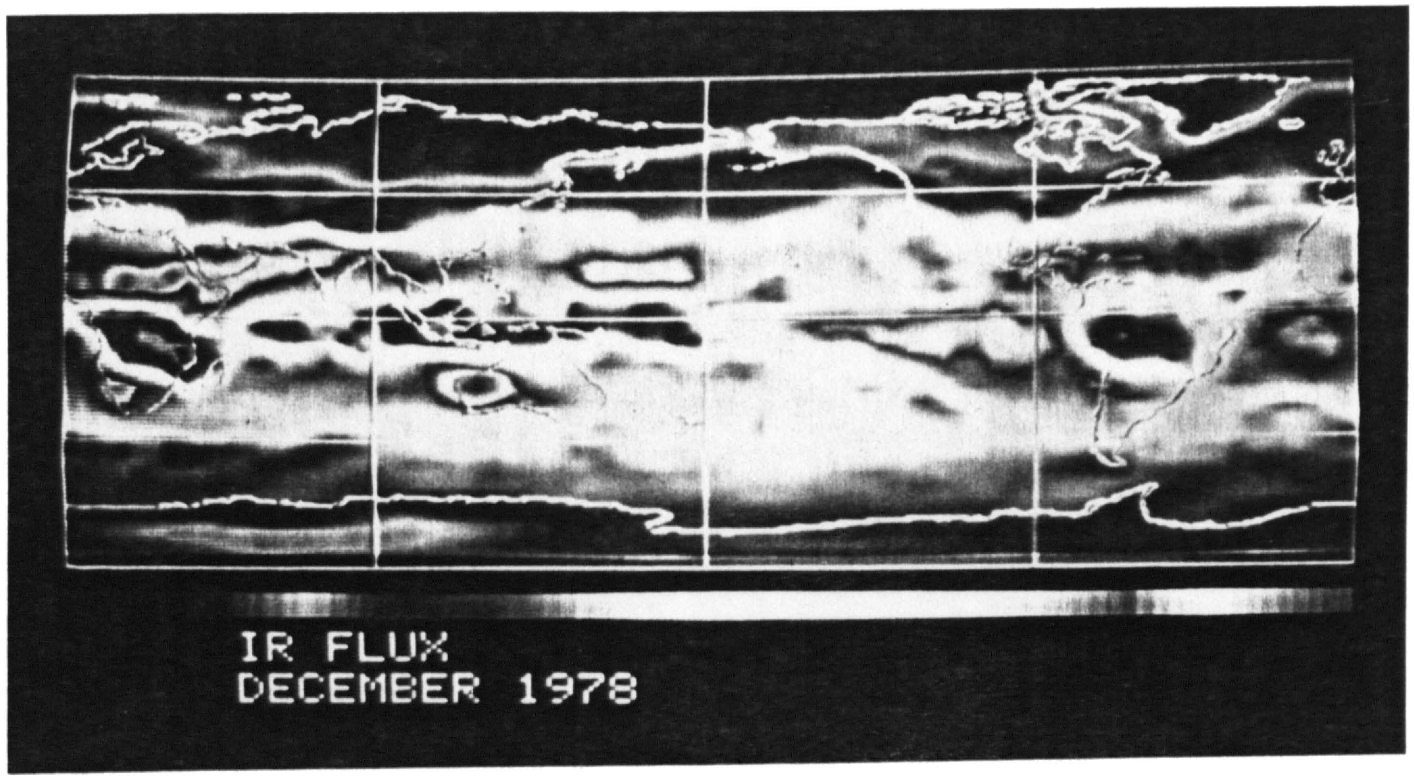

Fig. 3.14a. Same as Fig. 3.13 for December, 1979.

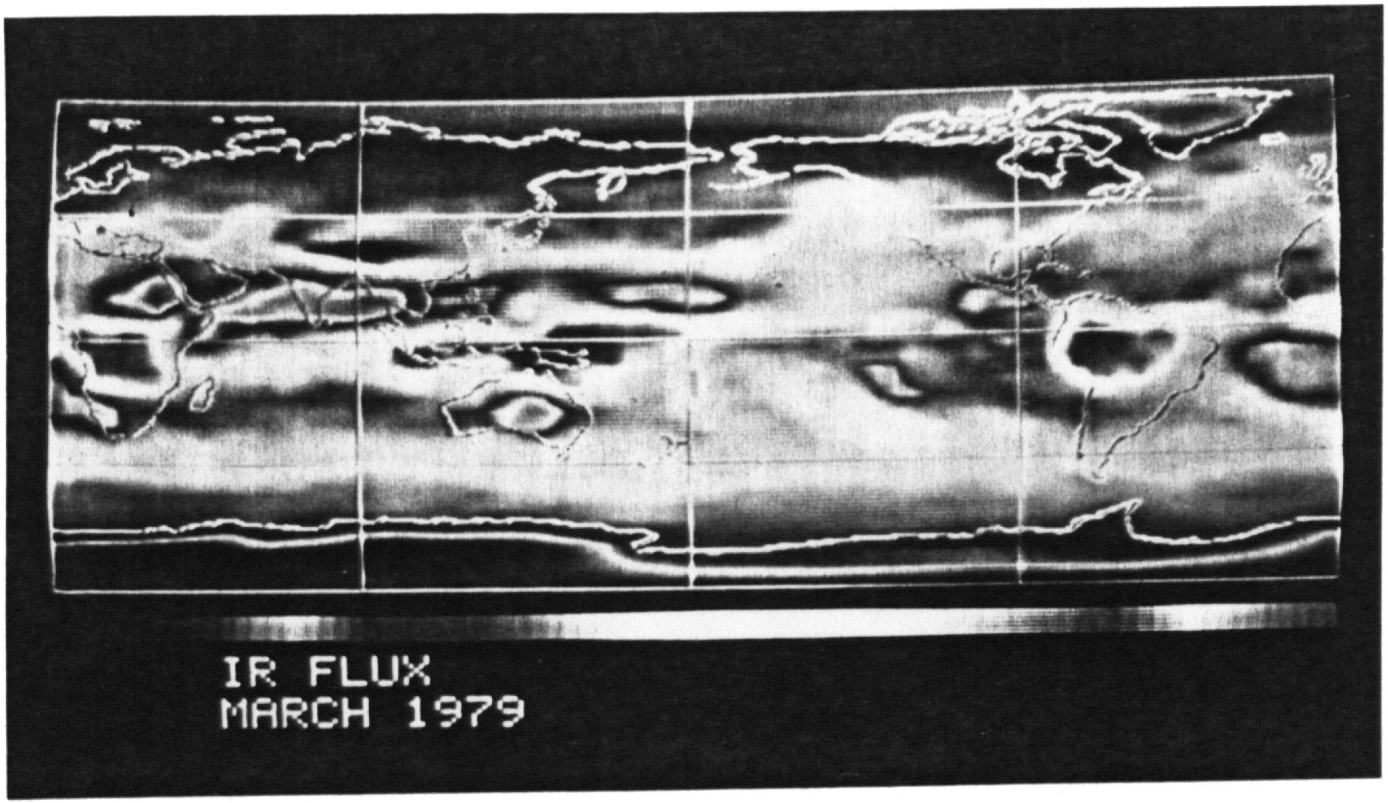

Fig. 3.14b. Same as Fig. 3.13 for March, 1979.

example, the GOES-1 VISSR quantization scheme for the VIS channel results in counts whose squares are linearly proportional to received energy. The IR channel quantization results in scale which is linearly proportional to EBB temperature (not radiance) and which has a breakpoint in the scale at which point the sensitivity factor is doubled. Therefore it is essential in transforming to spectral or filtered radiance to first convert to a linearized count scale, i.e.:

$$\begin{aligned} C'_{VIS} &= T_V(C_{VIS}) \\ C'_{IR} &= T_I(C_{IR}) \end{aligned} \tag{3.4}$$

where T_V and T_I are the non-linear and discretized transformation functions and the primed quantities (C'_{VIS}, C'_{IR}) correspond to the linearized digital count scales. Now, in general:

$$N^{VIS}_{\Delta\lambda} = a_0 + a_1 \cdot C'_{VIS} \tag{3.5}$$

where a_1 is a sensitivity factor in $W \cdot m^{-2} \cdot sr^{-1} \cdot count^{-1}$ and a_0 is an offset ($W \cdot m^{-2} \cdot sr^{-1}$). Furthermore:

$$N^{WIN}_{\Delta\lambda} = \int_{\lambda_1}^{\lambda_2} B\,(b_0 + b_1 \cdot C'_{IR})\,d\lambda \tag{3.6}$$

where b_1 is the sensitivity factor in $^oK \cdot count^{-1}$, b_0 is the offset in ^oK, B is the Planck function, and λ_1 and λ_2 are the half-power points of the spectral window channel. It is, of course, the generation of the a_1 and b_1 sensitivity factors that represents the essential difficulty in calibrating a satellite detector. The reader is referred to Smith and Vonder Haar (1980a) and Lauritson, et al. (1979) for detailed discussions of these procedures for GOES-1 and TIROS-N, respectively.

3.3.2 Geometric Normalization

The geometric normalization step accounts for the fact that a satellite measurement represents an integral of radiant energy over a very small solid angle. Thus to refer to raw satellite observations as radiances is somewhat misleading since no detector aperature conforms exactly to a single steradian. This nuance aside, geometric normalization accounts for the directional dependence of radiation in a hemisphere.

In the solar spectrum the required correction is referred to as bi-directional reflectance normalization in which normalization functions (χ) are applied. These functions are dependent upon the three principal angles in satellite geometry, i.e. solar zenith (θ_o), satellite zenith (θ_s) and relative azimuth (ϕ_r). The χ functions are generally dependent also on the underlying surface, i.e. forest, desert, water, cloud, etc. The χ functions can be generated empirically from aircraft or satellite observations, or theoretically from radiative transfer physics. It remains to be seen whether intensity form radiative transfer models are useful for this purpose based on the simplifcations inherent to the modeling process.

A futher requirement of a χ function is that it must conform spectrally to the filtered radiances to which it will be applied. Bidirectional reflectance normalization simply denotes that, for a given angular configuration (θ_o, θ_s, ϕ_r), the angular intensity or bi-directional reflectance $\rho(\theta_o, \theta_s, \phi_r)$ is not necessarily in unit ratio with the hemispheric integral of intensity [directional reflectance $R(\theta_o)$] over π, i.e.:

$$R(\theta_o)\ \pi^{-1}/\rho(\theta_o,\theta_s,\phi_r) \neq 1 \tag{3.7}$$

Thus a χ function, in general, represents a tabulation of these ratios at discrete angles. Note that 1's are allowed to occur in χ functions.

A spectral shortwave flux $[F^{SW}_{\Delta\lambda}(\theta_o)]$ can then be obtained by:

$$F^{SW}_{\Delta\lambda}(\theta_o) = \pi \cdot N^{VIS}_{\Delta\lambda} \cdot \chi_i(\theta_o,\theta_s,\phi_r) \tag{3.8}$$

where the subscript i represents the underlying surface category.

For the purposes of this investigation bi-directional reflectance normalization functions have been generated for five surface types applicable to water, desert, semi-arid continent, snow covered mountains, and clouds. These models are empirical in nature, and are based on the satellite and aircraft measurement composites for these surface types reported by Minnis and Harrison (1982) and Davis and Cox (1981, 1982).

Geometric correction in the infrared spectrum is a two-stage process. The filtered radiances are first adjusted to a zero nadir path which is the classic limb darkening correction. A second step then accounts for all paths in a hemispheric integral of radiation streams. For this investigation, these steps were parameterized based on the application of an intensity form non-scattering infrared radiative transfer model utilized in a tropical atmosphere. The parameterization scheme, designed to generate a spectral longwave flux $[F^{LW}_{\Delta\lambda}]$, described in Chapter 2, is formulated as follows:

$$F^{LW}_{\Delta\lambda} = \xi(\theta_s, T(\theta_s)) \cdot N^{WIN}_{\Delta\lambda} \tag{3.9}$$

where ξ is a function which combines the limb darkening and hemispheric correction processes as a function of satellite zenith angle and the

measured black body window temperature (which is used as a proxy estimate of height).

3.3.3 Spectral Transformations

The third step in estimating radiative fluxes is the conversion to the broad band spectrum. This is the step which has received insufficient attention in past studies, but which is a major error source if not considered. The approach used here is based on the parameterization developed in Chapter 2 in which transformation functions (η_{SW}, η_{LW}) are developed theoretically for both shortwave and longwave spectrums. The independent variables assigned to the transformation functions in both of the spectrums are based on readily accessible atmospheric parameters, the raw satellite window temperatures themselves, and surface categories assigned apriori.

The application of the η functions is with respect to filtered fluxes. The procedures are as follows for the shortwave (SW) and longwave (LW) spectrums:

$$\begin{aligned} F_{BB}^{SW}(\theta_o) &= \eta_{SW}(CZ, PW, ST) \cdot F_{\Delta\lambda}^{SW}(\theta_o) \\ F_{BB}^{LW} &= \eta_{LW}(TM, PW, WT) \cdot F_{\Delta\lambda}^{LW} \end{aligned} \tag{3.10}$$

where $F_{BB}^{SW}(\theta_o)$ and F_{BB}^{LW} are the estimated broad band shortwave and longwave fluxes, $F_{\Delta\lambda}^{SW}(\theta_o)$ and $F_{\Delta\lambda}^{LW}$ are the filtered shortwave and longwave fluxes, and η_{SW} and η_{LW} are the narrow to broad band transformation functions, dependent upon the following variables:

CZ ≡ Cosine of solar zenith angle

ST ≡ Underlying surface category

PW ≡ Total precipitable water above cloud free or cloud surface in question

TM = Pressure weighted temperature of the atmosphere above the cloud free or cloud surface in question

WT = Measured EBB window temperature of the cloud free or cloud surface in question

3.3.4 Radiation Budget Parameters

The radiation budget calculations are then straightforward. Eight terms are relevant to the RADBUD process at the top-of-atmosphere (TOA):

$K\downarrow$ = Solar irradiance at TOA

$K\uparrow$ = Upward solar flux at TOA

K^* = Net solar flux (absorbed solar radiation) at TOA

A = Albedo of earth-atmosphere system (3.11)

$L\uparrow$ = Emitted infrared flux at TOA

L^* = Net infrared flux at TOA

$EBBT\uparrow$ = Flux equivalent temperature at TOA

Q^* = Total net exchange at TOA

The relationships are as follows:

$$
\begin{aligned}
K\downarrow &= SC\cdot\cos(\theta_o)\cdot(\bar{D}/D)^2 \\
K\uparrow &= F_{BB}^{SW}(\theta_o) \\
K^* &= K\downarrow - K\uparrow \\
A &= K\uparrow/K\downarrow \\
L\uparrow &= F_{BB}^{LW} \\
L^* &= -L\uparrow \\
EBBT\uparrow &= (L\uparrow/\sigma)^{0.25} \\
Q^* &= K^* + L^*
\end{aligned}
\qquad (3.12)
$$

where SC is the solar constant (1370 $W\cdot m^{-2}$) and σ is the Stefan-Boltzman constant.

3.3.5 Validation

The most dangerous tack to pursue in satellite data related analysis is to presume an algorithm applied to a raw radiance data set is correct simply on the basis of all the carefully laid plans and well thought out physics and mathematics that go into the retrieval scheme. Based on the axiom that satellite estimates of any physicl process are not quantitative until validated by an external data source or irrefutable physical principals, some effort has gone into the validation and bias correction of the RADBUD estimates.

It was shown in Chapter 2 (1984) how ERB-WFOV monthly mean data were used to assess the biases in the uncorrected A and $L\uparrow$ estimates derived from the AVHRR data. The biases evident in the first pass estimates were then removed via a regression procedure thus yielding the second pass estimates. Second pass estimates from an independent data set, intercompared to the associated WFOV measurements, demonstrated that AVHRR RADBUD error magnitudes are as given in Table 3.4. A similar analysis to that given in Chapter 2 for the AVHRR retrievals, has been repeated for the GOES-1 RADBUD estimates. Table 3.5 provides the bias and random uncertainties.

Additional discussion of the validation problem will be provided in Section 3.6 concerning contrasts in the Southwest Monsoon radiation budget. In this subsequent section, ERB/NFOV time series are used to portray radiation budget variations in the different monsoon regions. In order to pursue further the nature of the uncertainties in the weather satellite RADBUD estimates, statistical measures and Fourier analysis are used to illustrate the strong and weak points of the AVHRR data.

TABLE 3.4

Estimated Biases and Uncertainties in the TIROS-N AVHRR RADBUD Estimates

	A(%)	$L\uparrow$(W m^{-2})
Bias	-2.3	-4.7
Uncertainty	7.2	11.1

TABLE 3.5

Estimated Biases and Uncertainties in the GOES-1 VISSR RADBUD Estimates

	A(%)	$L\uparrow$(W m^{-2})
Bias	-2.0	-0.5
Uncertainty	3.4	10.4

3.3.6 Shortcomings

There are a variety of shortcomings associated with basing RADBUD estimate on weather satellite measurements. At each step of the transformation process, calibration, geometric correction, and spectral transformation, there are a host of error sources, of both the absolute and random kind. It is presumed that the validation procedure removes most of the absolute error or bias. The remaining random error or uncertainty remains. Part of this error can be removed by time and space averaging; although at this time I have developed no quantitative rules that can be used to assess the magnitude of uncertainty based on the space-time averaging scales. A recent study of Brooks and Minnis (1984b) has begun to address this problem synthetically. Thus the foremost shortcoming in the following calculations is that uncertainty is almost strictly a function of the averaging scales which will change in the course of the following analyses.

3.4 Idiosyncrasies of the Radiation Budget Calculations

The adaptation of weather satellites to radiation budget science poses different problems for the differing satellite systems beyond the solid angle and narrow band problems. The formulation of the RADBUD parameters for a polar orbiter system are somewhat different than that for a geosynchronous system. The principal difference is that sun-synchronous polar orbiters (the normal mode for the NOAA operational polar orbiters) only provide coverage twice a day for a given region. In addition, because of the finite orbit width, composite polar orbiting imagery involves discontinuous renditions of the weather patterns at the orbit seams. On the other hand, the geosynchronous systems provide continuous coverage (usually every half hour) of the complete satellite

facing projection of the globe (earth disk). Thus a single image is a composite of local times extending over 8 hours for the useful portion of the image.

An excellent example of one advantage of using geosynchronous imagery is illustrated in Fig. 3.15. This photo corresponds to a GOES-1 VIS sector taken at 7:40 GMT on June 3, 1979. An aircraft flight track of the NASA Convair-990 mission on that day is overlaid on the image. Bright cloud tops have been enhanced. The solar point is in the western Arabian Sea near $22^{o}N$; $62^{o}E$. There is a very interesting diagonal channel running from the northeast to the southwest due to variations in sea state and/or air mass differences. This feature disappeared later in the day because of changes in solar configuration. The AVHRR did not pick it up.

3.4.1 The Insolation Term

The first issue that must be resolved in using polar orbiter data for RADBUD retrieval is how to formulate the insolation term. If an orbit composite map is generated and K↓ is calculated in exact correspondence to the solar-time configuration at each map coordinate, the result is a striated insolation pattern. Figure 3.16 provides an example of a K↓ field for the June 18 AVHRR map (top) and the resultant Q* field. Due to the nature of the orbit, the equator crossing times remain the same, however, the equator crossing coordinates drift uniformly on each progressive day. Thus if a set of K↓ fields are averaged for a succession of days, as in the 5 day average shown in Fig. 3.17, a somewhat mottled pattern results. Since it is difficult to interpret the K* term based on a source term given in this fashion, another approach is desirable. If the source term were left in the form

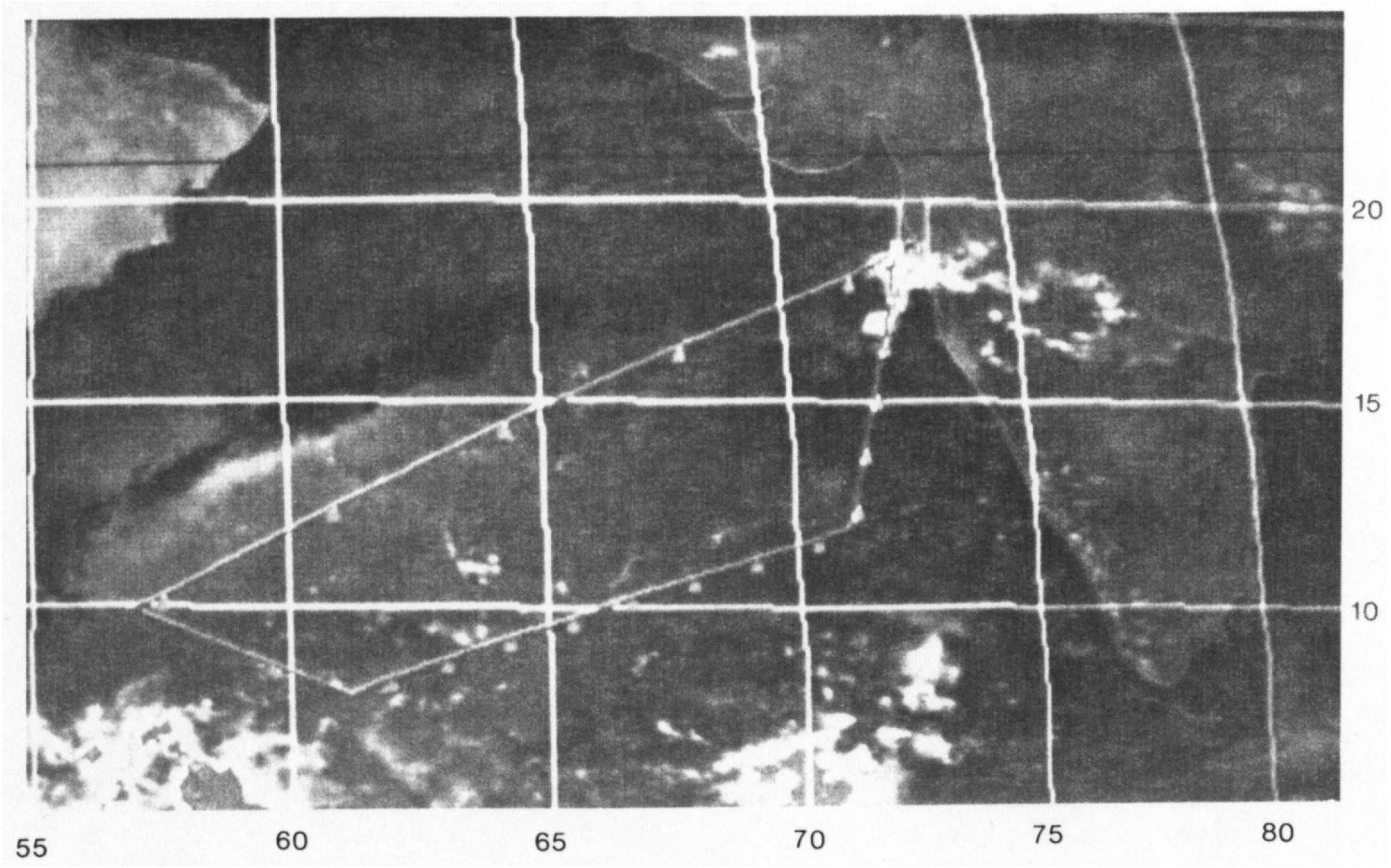

Fig. 3.15. GOES-1 VIS geosynchronous satellite sector over the Arabian Sea; date is June 3, 1979; image time is 7:40 GMT. The aircraft mission track overlaid on the satellite image represents the third Arabian Sea mission flown out of Bombay by the NASA Convair-990 during SMONEX.

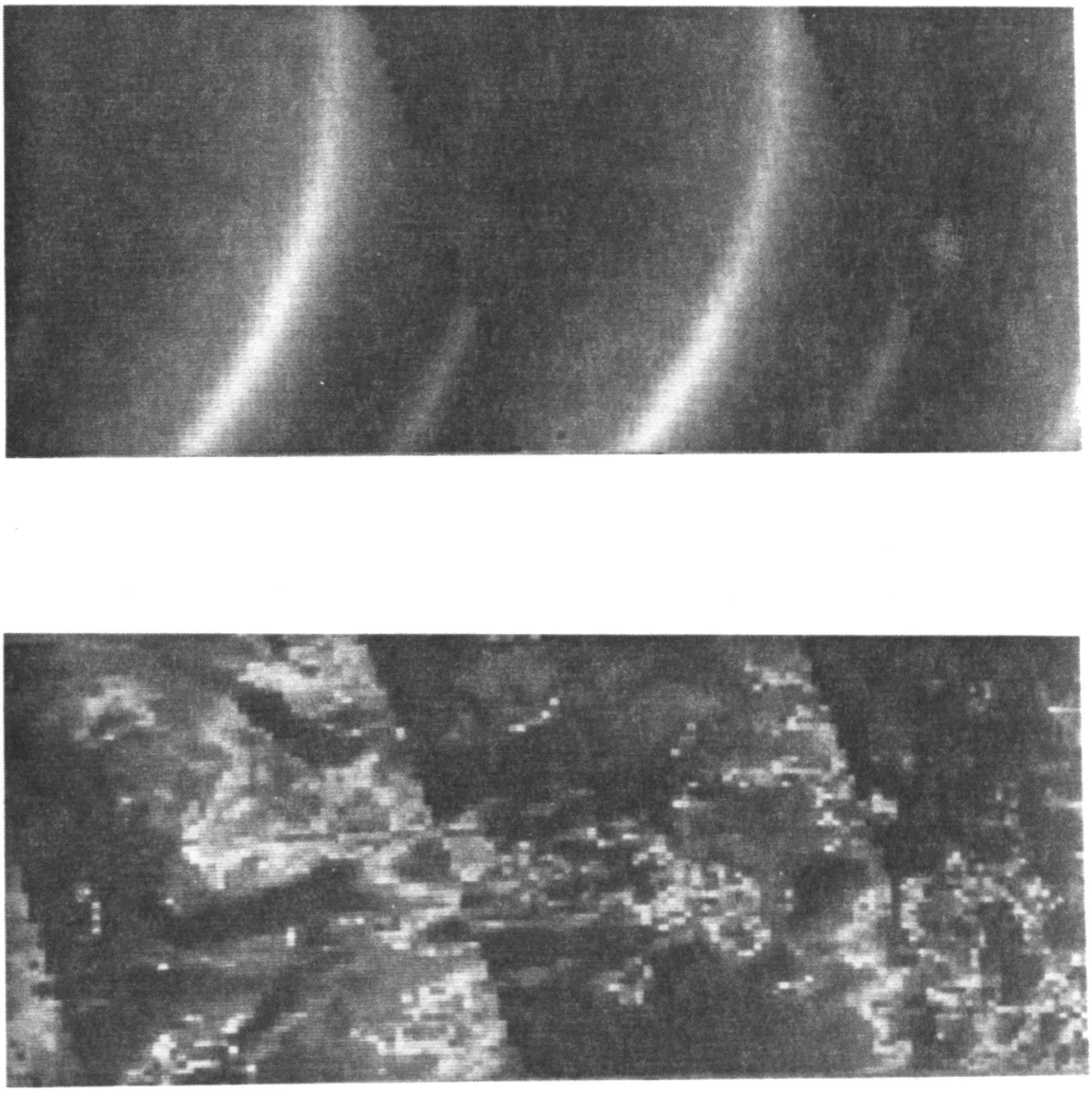

Fig. 3.16. The top photo is the instantaneous downward flux (K↓) at TOA corresponding to the AVHRR composite image on June 18, 1979. The bottom photo is the derived instantaneious noon-time total net flux field (Q*) based on the K↓ source term.

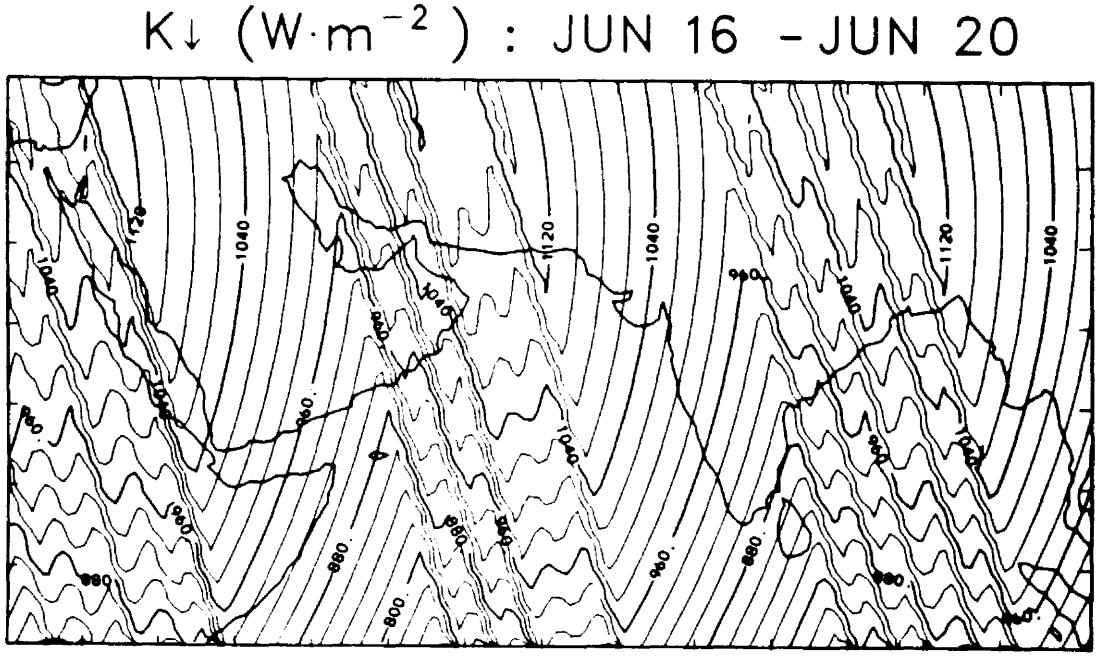

Fig. 3.17. Five day averaged TOA solar irradiance field based on the instantaneous K↓ calculations for the June 16-20 daytime composite AVHRR maps. The contour interval is 80 W m^{-2}.

of Fig. 3.17, for example, a time series of the meridional averages would appear as in Fig. 3.18. Here the x-axis (horizontal) is longitude (30^{o}-100^{o}E), the y-axis (into the paper) is time (May 1 - August 30), and the z-axis (vertical) is the magnitude of the meridionally averaged K↓ term. Formulating a source term in this fashion would result in a dominant periodicity in Q* unrelated to radiative forcing, but instead related only to orbital characteristics.

There are a variety of approaches that can be used to circumvent this ambiguity. The approach selected for this application is to retrieve the actual albedo field based on the originally calculated K↓ field and the measured K↑ field, adjust the albedo field to noon conditions, and then re-calculate K↑ assuming local noon geometry for K↓ (only zonal variation is allowed).

The correction procedure to A is easily done with the AVHRR data during the validation. In the process of removing the biases in A, L↑(day), and L↑(night), the albedo is implicity normalized to the local solar time of the Nimbus-7 satellite (which is local noon). Part of the bias removal is thus an adjustment for the directional reflectance dependence on zenith angle.

When the source term (K↓) is re-calculated, a meridional averaged time series such as shown in Fig. 3.18, would now appear as in Fig. 3.19. The same comparison in zonal averaged time series is illustrated in Fig. 3.20. This process now compensates for the meridional variations in K↓ and thus eliminates the discontinuities in the K* field first shown in Fig. 3.4.

Since L↑ does not include an external source term (L↓ = 0 everywhere) there is no analogous problem in the infrared spectrum.

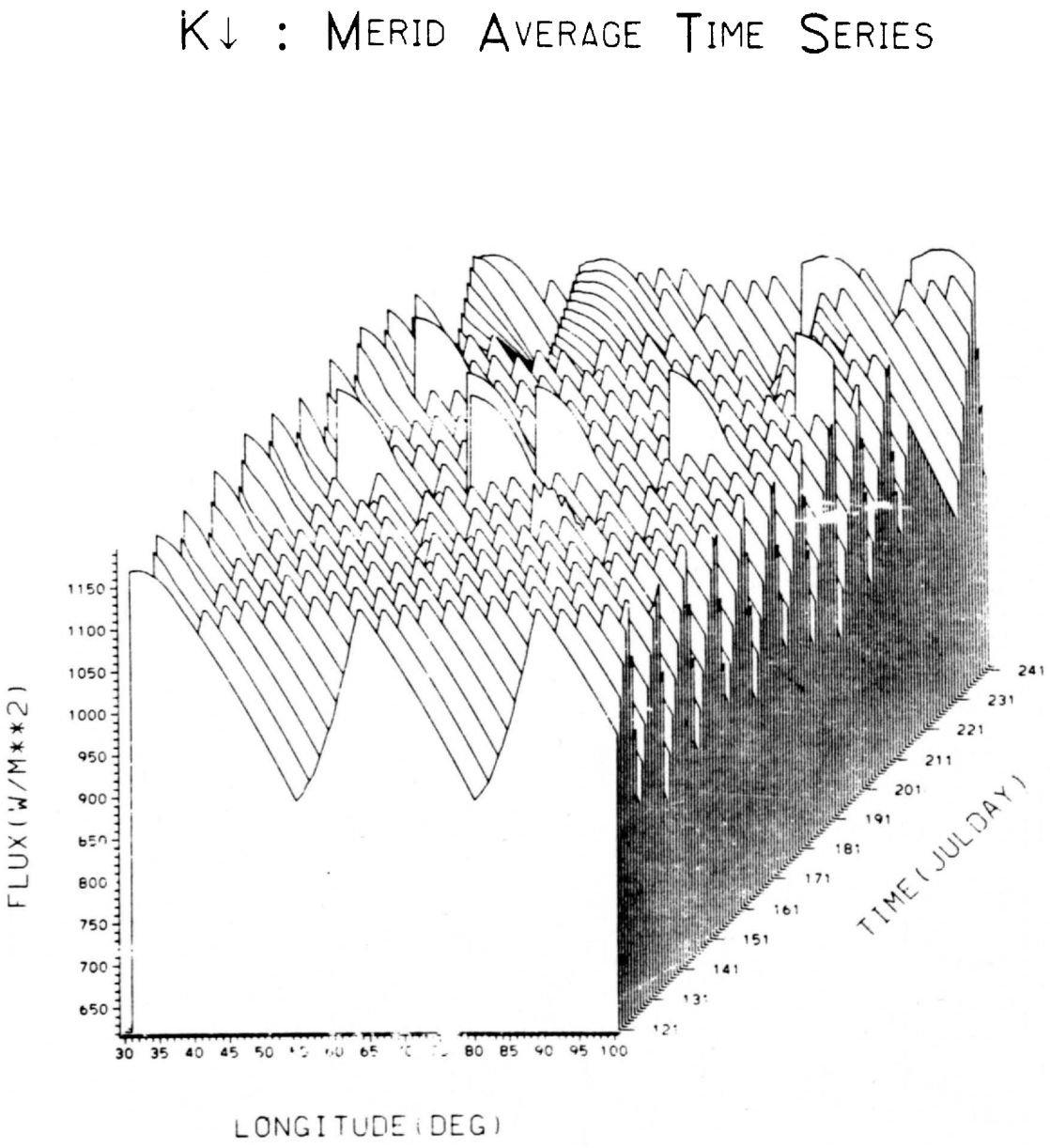

Fig. 3.18. The meridionally averaged K↓ time series based on the 5-day average TOA solar irradiance map shown in Fig. 3.17.

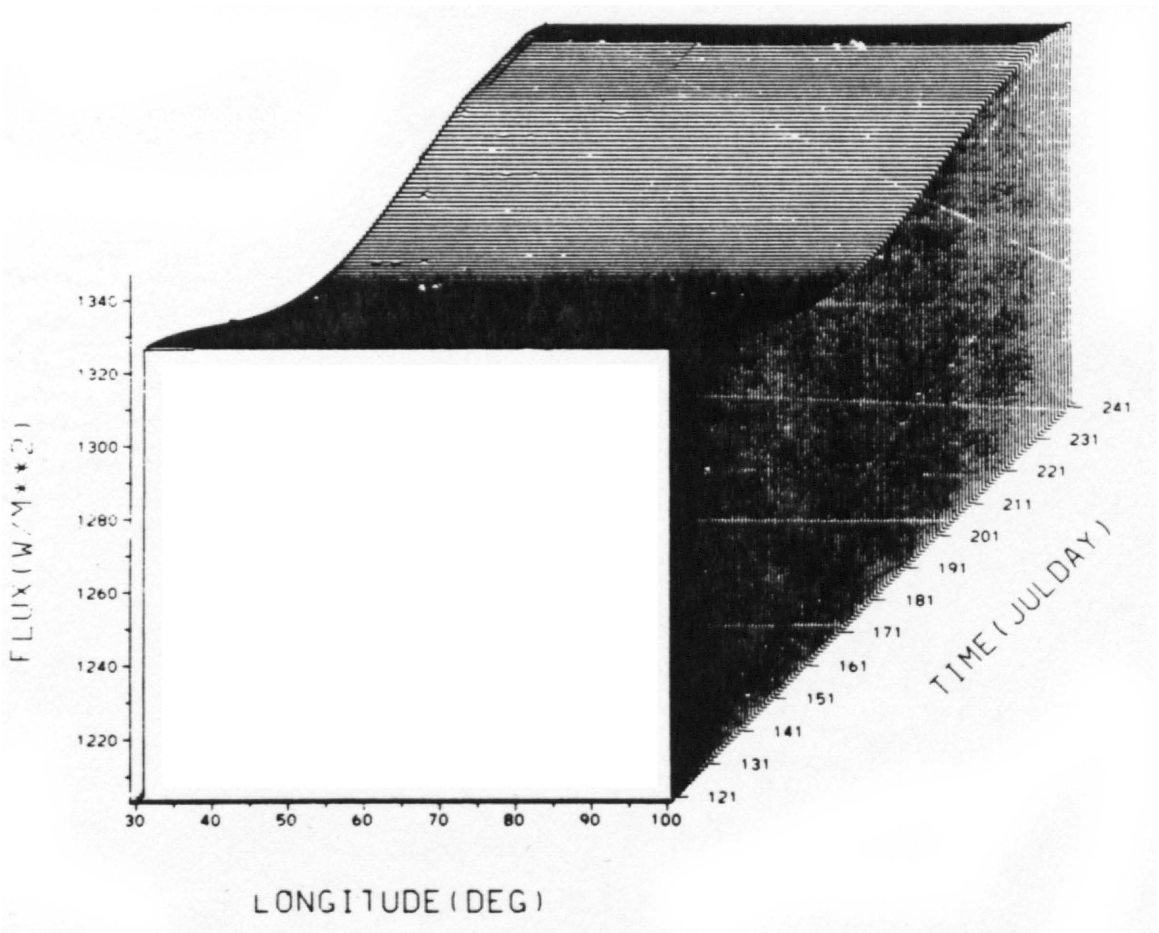

Fig. 3.19. The meridionally averaged K↓ time series based on removing solar time dependence in the irradiance calculation.

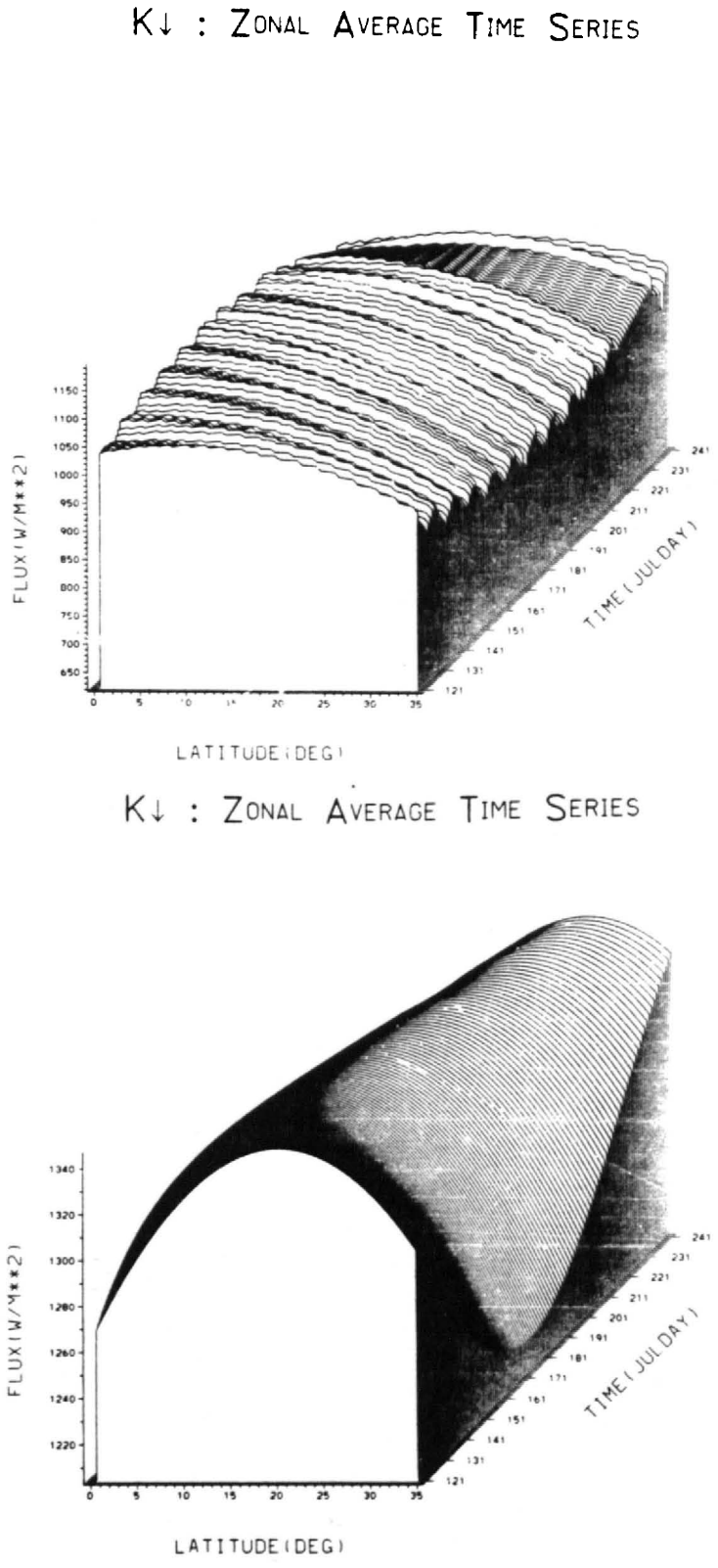

Fig. 3.20. The zonal averaged K↓ time series associated with solar time dependence (top) and no solar time dependence (bottom).

However, during bias correction, the mean diurnal temperature change arising from the three hour gap between TIROS-N and Nimbus-7 overpass times is implicitly removed. Thus the AVHRR emitted infrared flux fields are assumed to conform, in a mean temperature sense, to local noon and midnight conditions even though the cloud scenes are representative of 15:00 and 3:00 LT conditions. Figure 3.21 provides illustrations of the daytime and nighttime emitted IR fields on June 18, 1979 as derived from the AVHRR channel 4 measurements.

3.4.2 Diurnal Variation and Directional Reflectance

A classic problem in using twice a day polar orbiting data is the formulation of a daily average for the total net radiation term ($\bar{Q}*$). ($\bar{Q}*$) is an integral property, i.e.:

$$\bar{Q}* = \int_0^{24} \{K\downarrow(t)[1-A(t)]-L\uparrow(t)\}dt \;/\; 24 \qquad (3.13)$$

Note that $L\uparrow(t)$ is a continuous non-zero function of time whereas $A(t)$ is not defined prior to sun-up and after sundown and is thus discontinuous at $\theta_o = 90$; $K\downarrow(t)$ serves as a weighting function.

There are variations in $L\uparrow(t)$ due principally to the diurnal cycle of continental surface heating, and the diurnal evolution of moisture and cloud fields. The diurnal amplitude of sea surface temperature is small in tropical (moist) environments.

There are also daily variations in $A(t)$, partly related to the moisture and cloud fields, but also due to the phenomonon of directional reflectance variation as a function of incident solar angle. This is a process in which as the incident elevation angle decreases, more radiation is lost from a surface throughout the forward scatter lobe. Thus, generally, most natural earth surfaces and cloud surfaces tend to

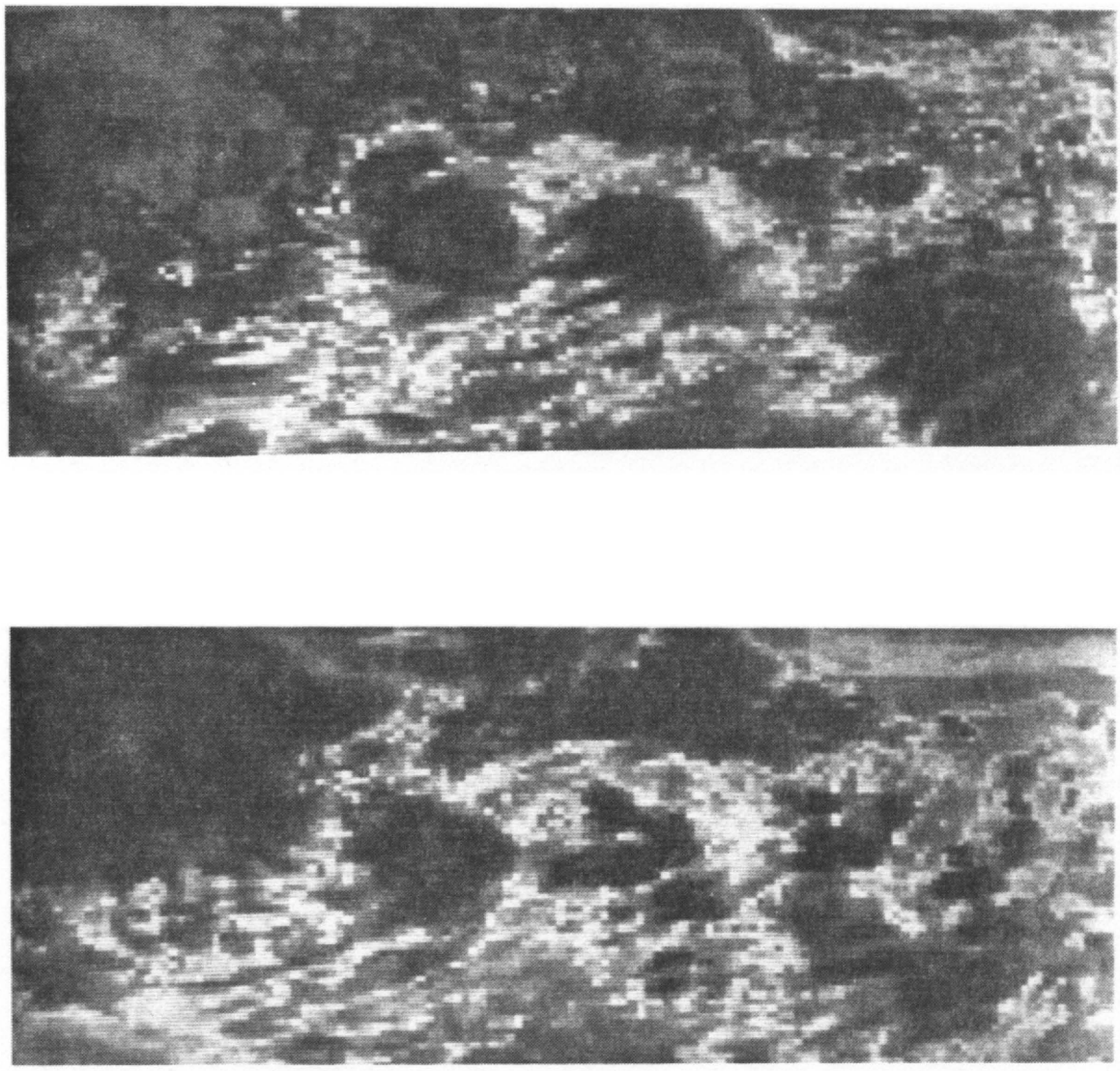

Fig. 3.21. The emitted infrared flux fields for June 18, 1979. The top photo corresponds to daytime; the bottom photo corresponds to nighttime.

increase in albedo as the elevation angle decreases. This process can be reversed, however, by tropographic conditions and by the manifestations of finite geometry of non-flat surfaces (e.g. clouds or mountains). Examples of the dependence of albedo on the incident angle are provided in Figs. 3.22-3.25 for water, snow, ice, and cloud. The directional reflectance curves for water (Fig. 3.22) have been derived from a variety of satellite data, aircraft radiometer measurements, surface radiometer measurements, and a theoretical Fresnel function for a flat water surface. The Smith curve is based on my own analysis of SMS-1 VIS data over the 1974 GARP Atlantic Tropical Experiment (GATE) region. Note that the Fresnal curve and the Payne (1972) surface curve are smaller in magnitude and display a higher variation after $\theta_o > 70^o$. The remaining satellite and aircraft derived curves indicate remarkably good consistency. The atmosphere, of course, is responsible for the differences between the surface derived functions and the remotely sensed functions.

The data that have been plotted for snow (Fig. 3.23) and ice (Fig. 3.24) show very little consistency. The directional reflectance functions for cloud (Fig. 3.25) show poor consistency both in terms of the magnitude of $R(\theta_o)$ and in the θ_o dependence itself. The results labeled Smith are uncertainty bars based on the analysis of the GATE SMS-1 measurements.

It can be seen, in light of the above discussion, that a daily integral estimate of $\overline{Q}*$ retrieved from sun-synchronous polar orbiting satellite data, would require a correction for the diurnal cycles in $L\uparrow(t)$ and $A(t)$ solely due to variation in the source term $K\downarrow(t)$, and due

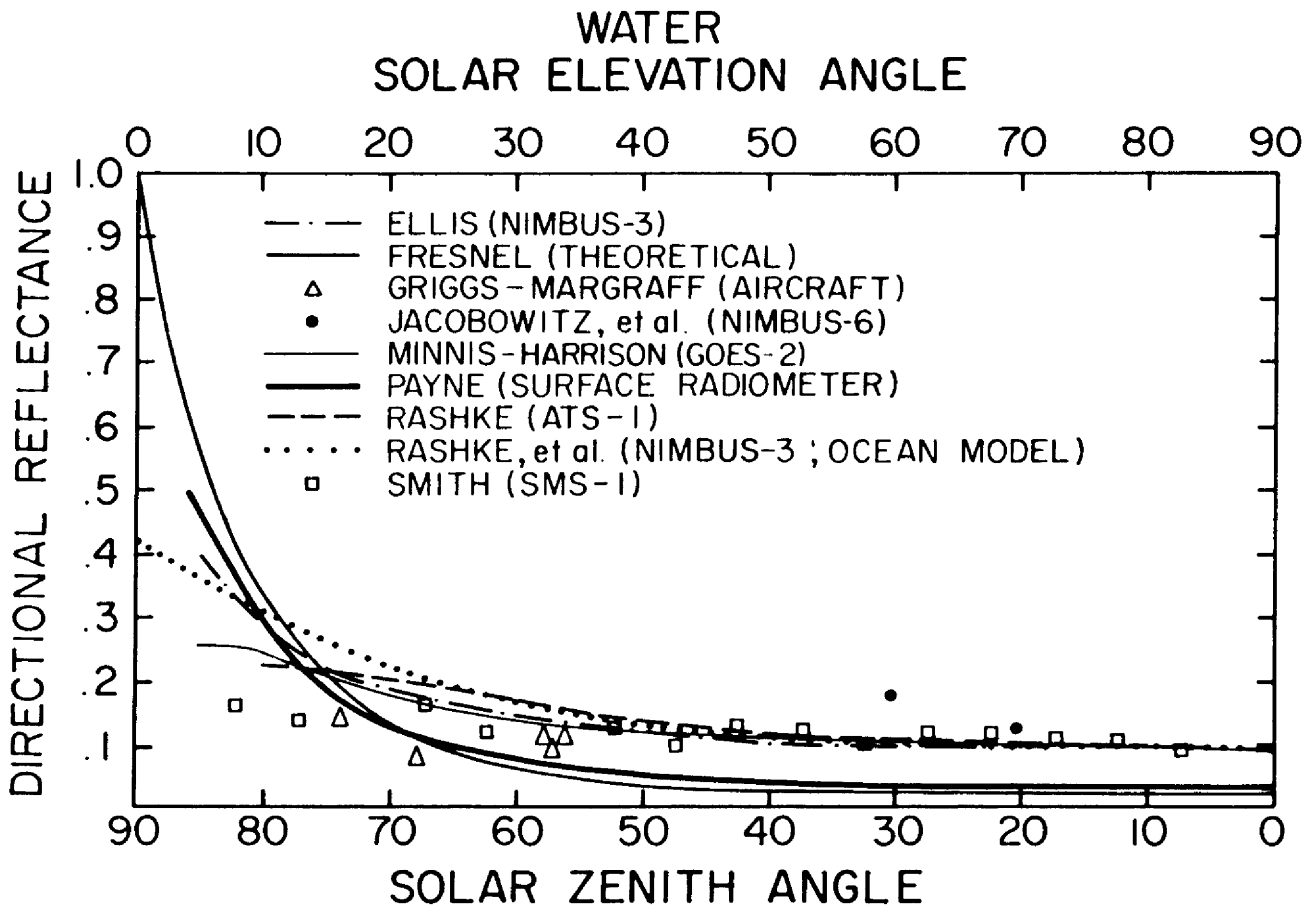

Fig. 3.22. Directional reflectance functions for a water surface based on satellite, aircraft and surface observations and a theoretical plane surface Fresnel calculation. The sources are Ellis (1978), Griggs and Margraff (1967), Jacobowitz, et al. (1976), Minnis and Harrison (1984), Payne (1972), Raschke (1969), and Raschke, et al. (1973).

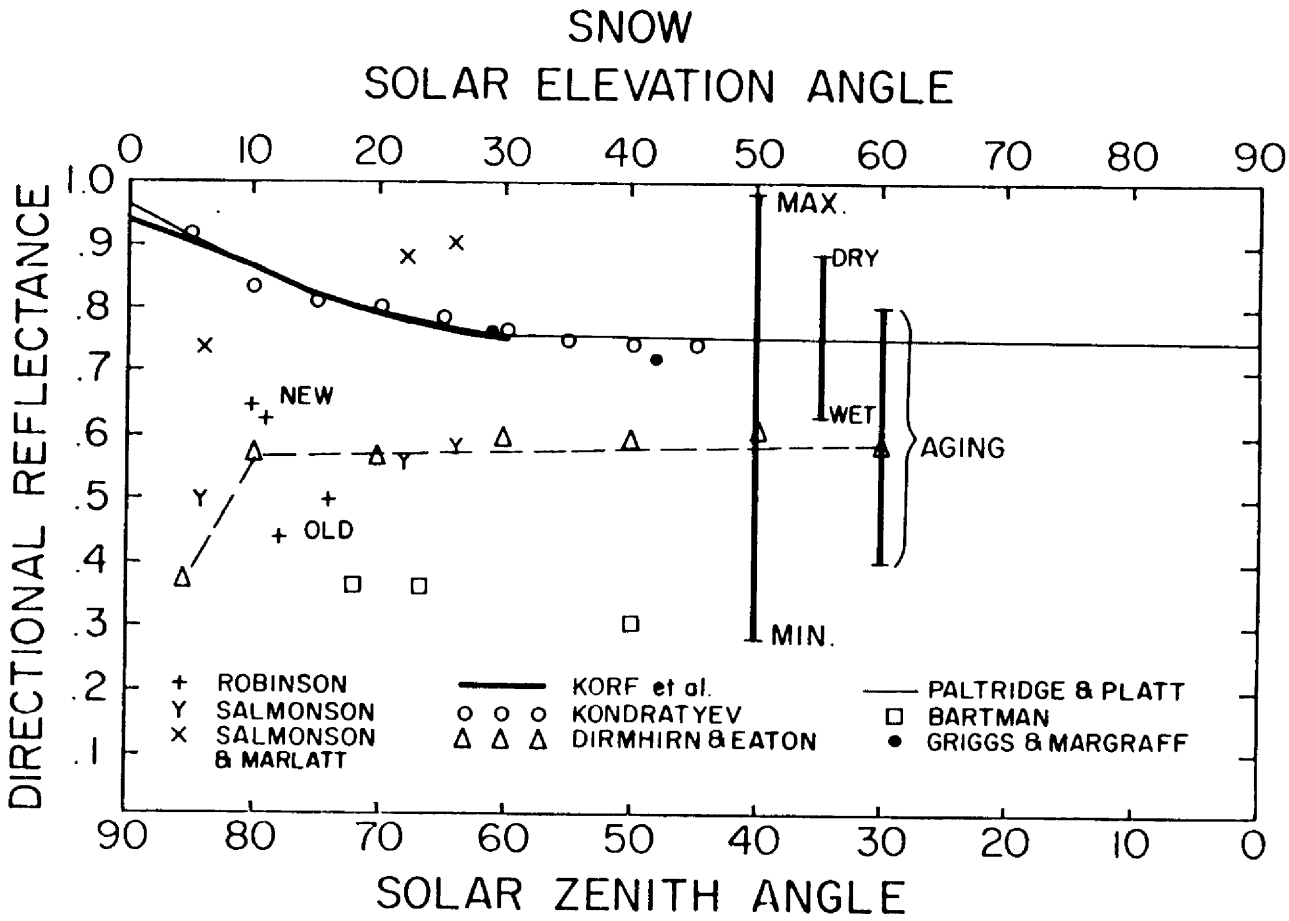

Fig. 3.23. Directional reflectance data for snow based on satellite, aircraft and surface observations. The sources are Bartman (1967), Dirmhirn and Eaton (1975), Griggs and Margraff (1967), Kondratyev (1969), Korff, et al. (1974), Paltridge and Platt (1976), Robinson (1958), Salmonson (1968), and Salmonson and Marlatt (1968).

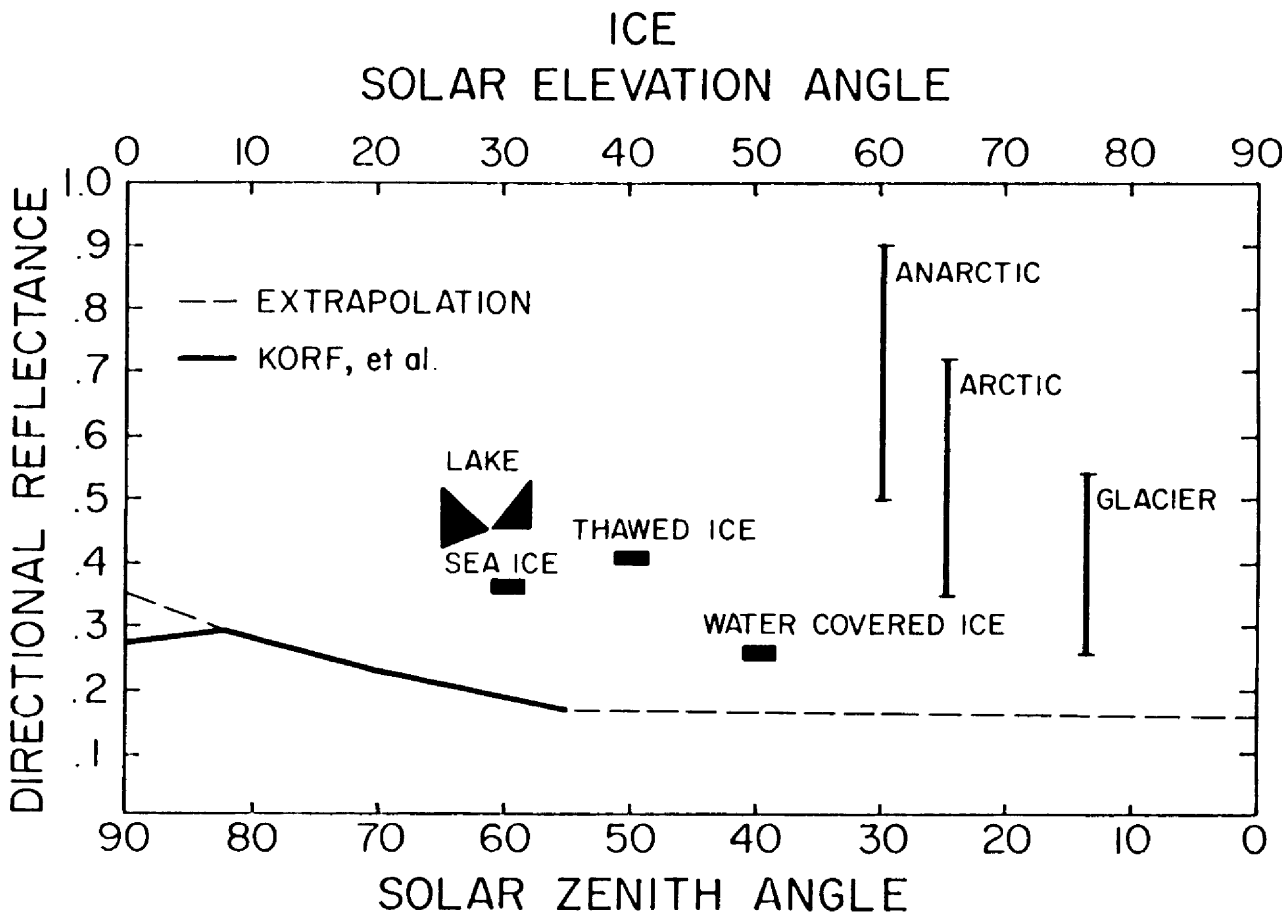

Fig. 3.24. Directional reflectance data for ice based on surface observations of Korff, et al. (1974) and the reference book of Kondratyev (1969).

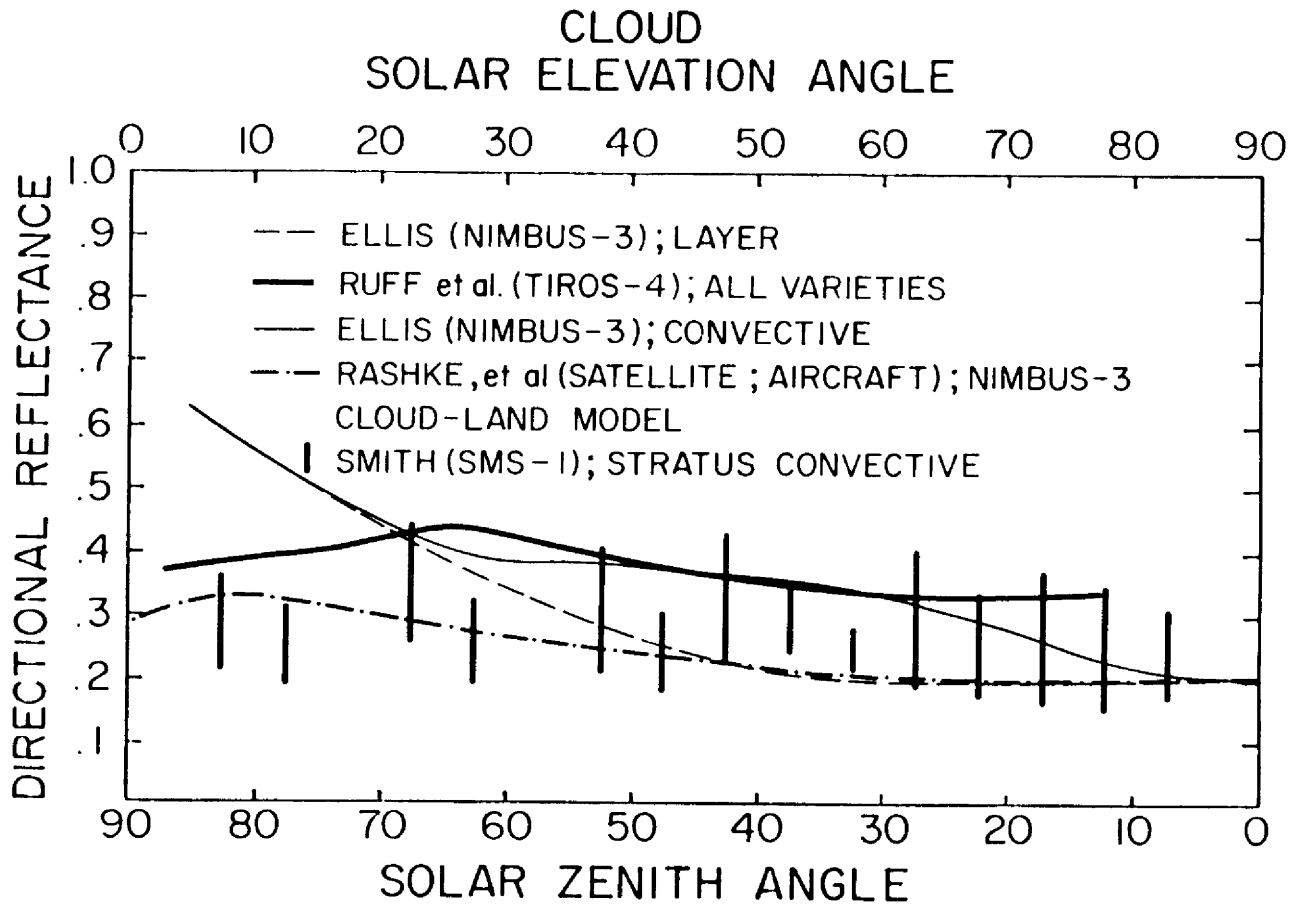

Fig. 3.25. Directional reflectance functions for cloud based on satellite data [the Raschke, et al. function incorporates aircraft and satellite data]. The sources are Ellis (1978), Raschke, et al. (1973), and Ruff, et al. (1968).

to the variations in the cloud and moisture fields. The approximations and uncertainties that go into this subject are beyond the scope of this investigation. These problems are continually addressed in the ongoing ERBE program; see e.g., Brooks and Minnis (1984a). However, the directional reflectance curves shown in Figs. 3.22-3.25 illustrate that, with the exception of a cloud free water surface, diurnal corrections can often lead to nothing more than gross approximation.

The approach used in the following analyses is to utilize instantaneous retrievals for AVHRR, relative to the two fly-by times, and to incorporate the GOES-1 data for estimating the diurnal cycles. The RADBUD formulation used for the geosynchronous satellite, by the nature of its continuous monitoring capability, explicitly avoids the pitfalls of having to estimate the variations in A(t) and L↑(t).

Nevertheless, this investigation uses estimates of $\overline{Q*}$ based on the ERB/NFOV measurements, which do require a treatment of the time variation of A(t) and L↑(t) because Nimbus-7 is also a sun-synchronous satellite. The procedure used in ERB processing is relatively simple. $\overline{L\uparrow}$ is estimated by averaging L↑(day) and L↑(night). Variation in A(t) is based on the use of a few very smooth and conventionally accepted directional reflectance functions. The tradeoff in using the ERB/NFOV data is that the accuracy associated with the A and L↑ measurements exceeds the accuracy of the AVHRR and VISSR estimates. On the other hand, the resolution available from both the AVHRR and VISSR estimates exceeds that of ERB/NFOV and the actual diurnal features retrieved from the GOES-1 are far more realistic than those diurnal assumptions incorporated into ERB/NFOV $\overline{Q*}$ estimates.

3.5 Large Scale Forcing During Monsoon Season

The following sub-sections present the radiative evolution of the monsoon from May through the end of August. The AVHRR retrievals used in this analysis are computed daily at a 0.5°x0.5° space scale. First, the five-day average mean fields (pentad averages) of K*, L↑(day), Q*, and L↑(night) are presented. The K*, L↑(day), and Q* fields all correspond to an instantaneous 12:00 noon solar insolation condition but with respect to 15:00 LT cloud conditions. Thus the solar irradiance is at its peak daily value. The L↑(night) field is with respect to cloud conditions at 3:00 LT but bias adjusted in the validation to local midnight mean values. Occasionally a six-day average is generated to avoid throwing away data. The highs and lows, which are annotated along with the contours, indicate the extremes. They will tend to represent values of highest uncertainty because they are, as pointed out, the outlying values.

It is noted that the Arabian Peninsula orbit pass is consistently missing during nighttime throughout the month of May. The reason for these missing orbits has never been determined.

The second sub-section concerns the progress of the monsoon in terms of the time-latitude and time-longitude sections. These are the time series of zonal and meridional averages. Zonal averages cover the 70° meridional domain (30°-100°E); meridional averages cover the 35° zonal domain (Eq-35°N).

Finally, the phenomenon of radiative blocking is presented. Here we see that during the critical period surrounding monsoon onset, the complete monsoon domain tends to progressively and monotonically shutter the net radiative source term.

The 5-day RADBUD mean fields, or pentad averages, are presented in Figs. 3.26-3.46. The first averaging period (May 1-6) is presented in two parts; Fig. 3.26a gives the K* and Q* fields, whereas Fig. 3.26b gives the L↑(day) and L↑(night) fields. The second period (May 7-11) is given in the next figure pair, and so on. A two-dimensional binomial filter [(1,2,1)x(1,2,1)] has been applied to provide a smooth appearance to the contours. This view of the monsoon is highly dependent on the morphological characteristics of the cloud systems in the sense that these systems give rise to the dominant pentad-to-pentad changes.

The advantage of pentad maps over the classical monthly mean maps is best illustrated in Figs. 3.47a-b. Here we see the mean monthly $\overline{Q^*}$ fields for May and June, 1979, based on the ERB/NFOV data presented in the standardized $5^{\circ}x5^{\circ}$ ERB format. To help interpret the figures, three of the grid points have been annotated with the actual net radiative flux values associated with the grid positions (Arabian Peninsula, northwestern and southeastern Arabian Sea). What is evident in the monsoon region between May and June is diminished radiative convergence over the Arabian Sea, the Indian sub-continent, and the Bay of Bengal. However, these maps in no way present the complex phenomonology of monsoon evolution evident in Figs. 3.26-3.46.

To illustrate the course of the monsoon with the ERB/NFOV measurements, using a very similar temporal averaging scale to the AVHRR, Figs. 3.48a-j are provided. These figures, which are the 6-day

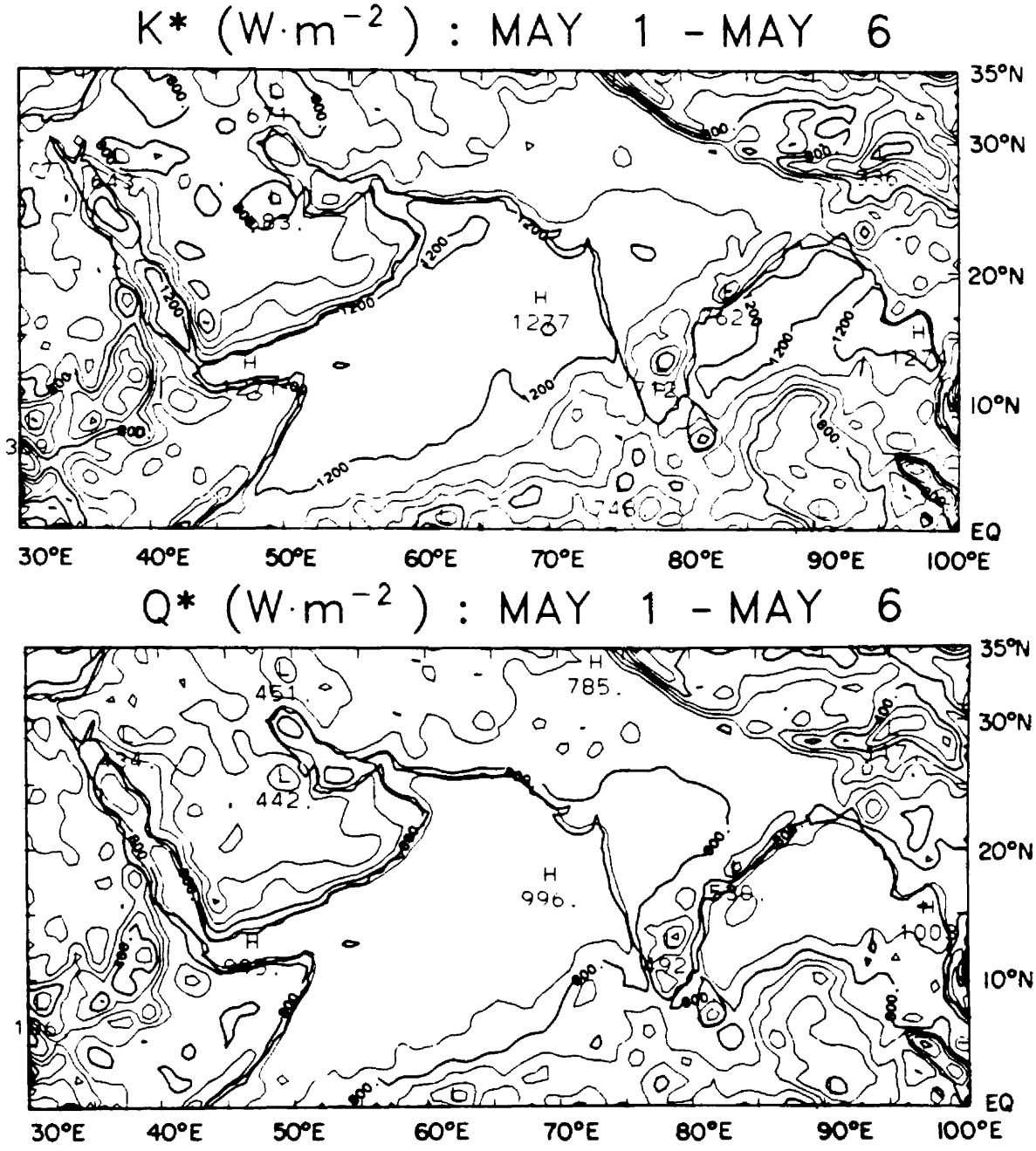

Fig. 3.26a. The May 1-6 (pentad 1) mean fields of shortwave absorbed radiation (K*) and total net radiation (Q*) over the TIROS-N SMONEX domain (Eq-30°N; 30°-100°E). The isopleths are in W m^{-2} based on a 100 W m^{-2} contour interval.

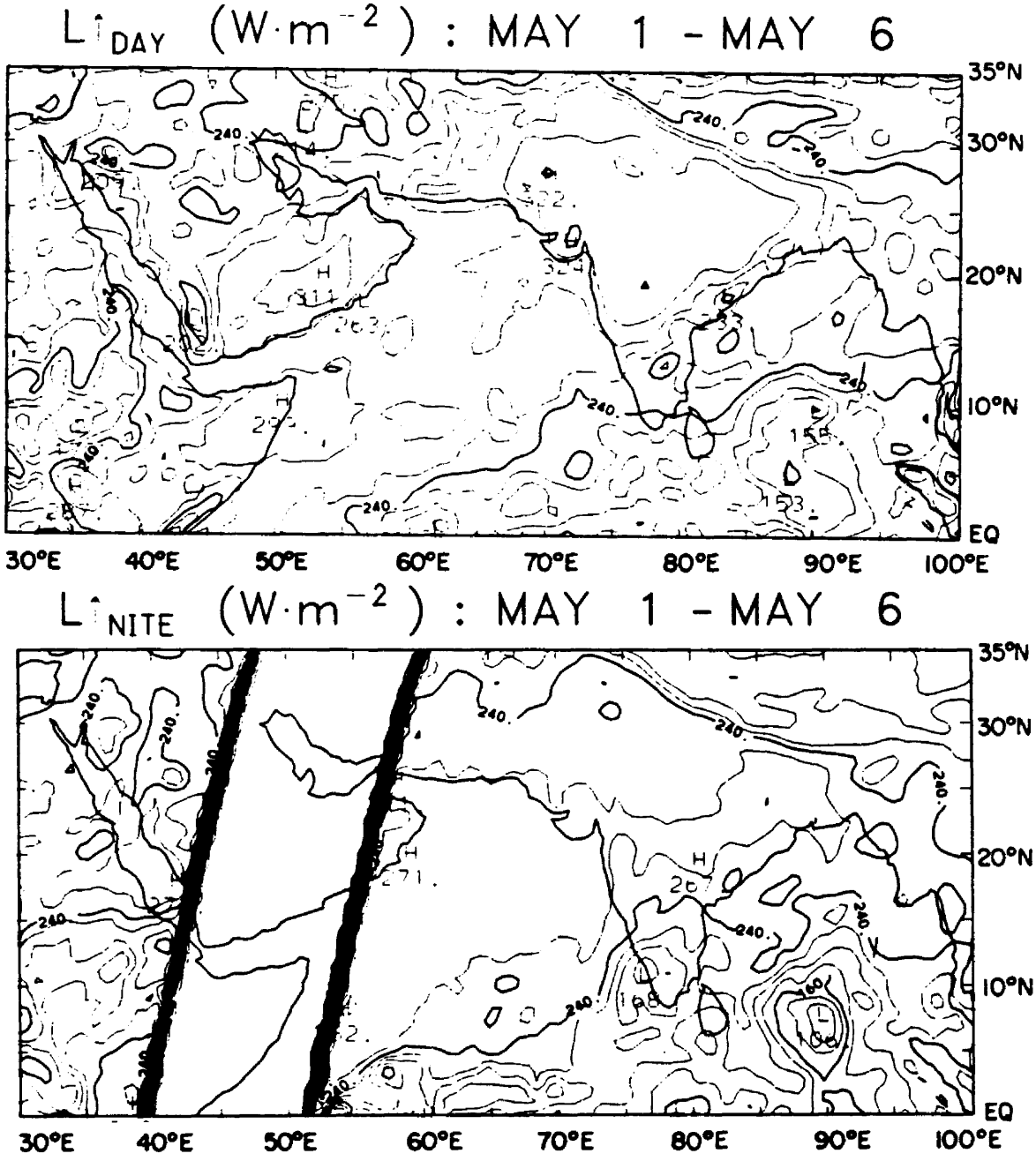

Fig. 3.26b. The May 1-6 (pentad 1) mean fields of daytime emitted longwave radiation [L↑(day)] and nighttime emitted longwave radiation (L↑ (night)] over the TIROS-N SMONEX domain (Eq-30°N; 30°-100°E). The isopleths are in W m^{-2} based on a 20 W m^{-2} contour interval.

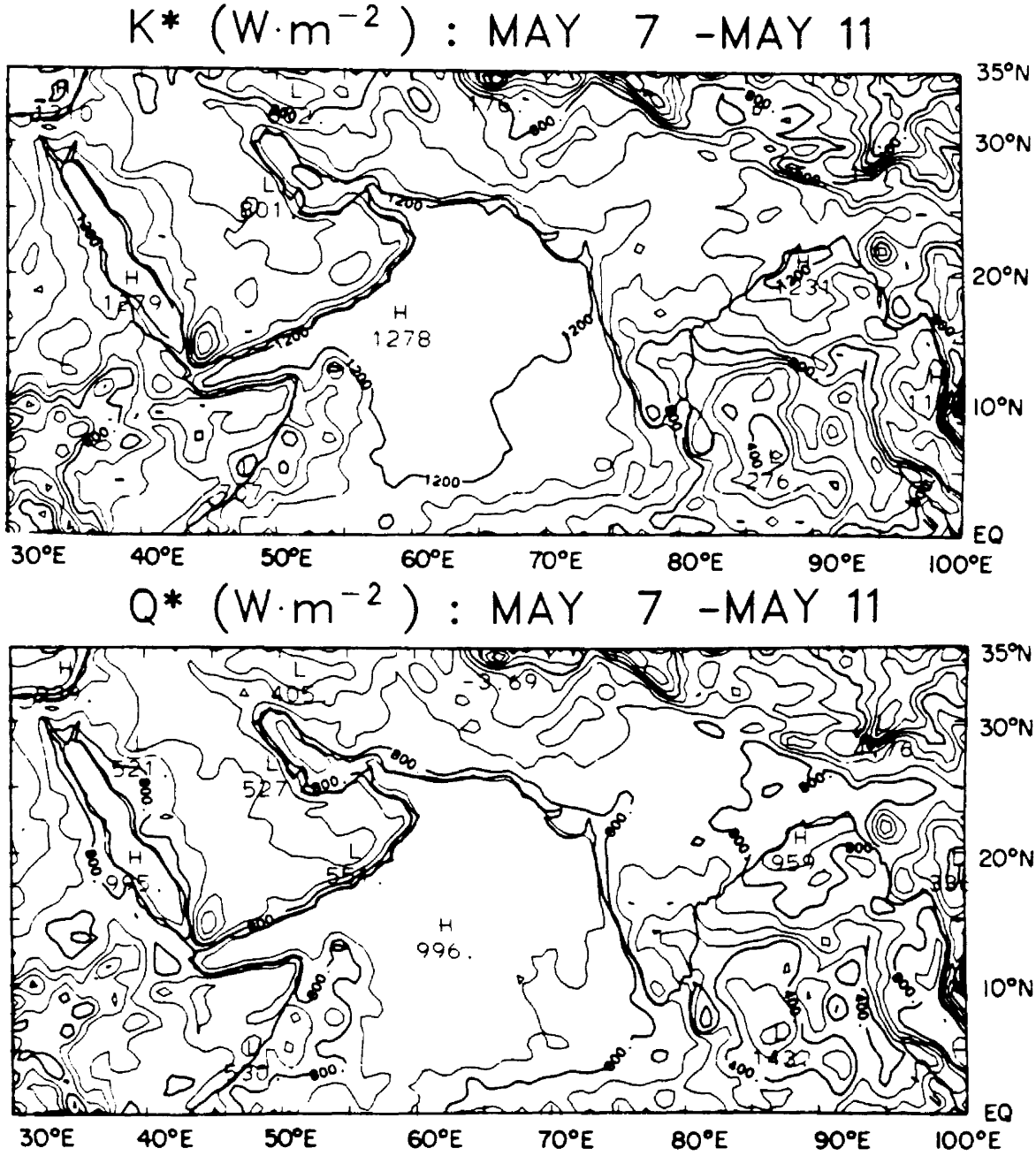

Fig. 3.27a. Same as Fig. 3.26a for May 7-11 (pentad 2).

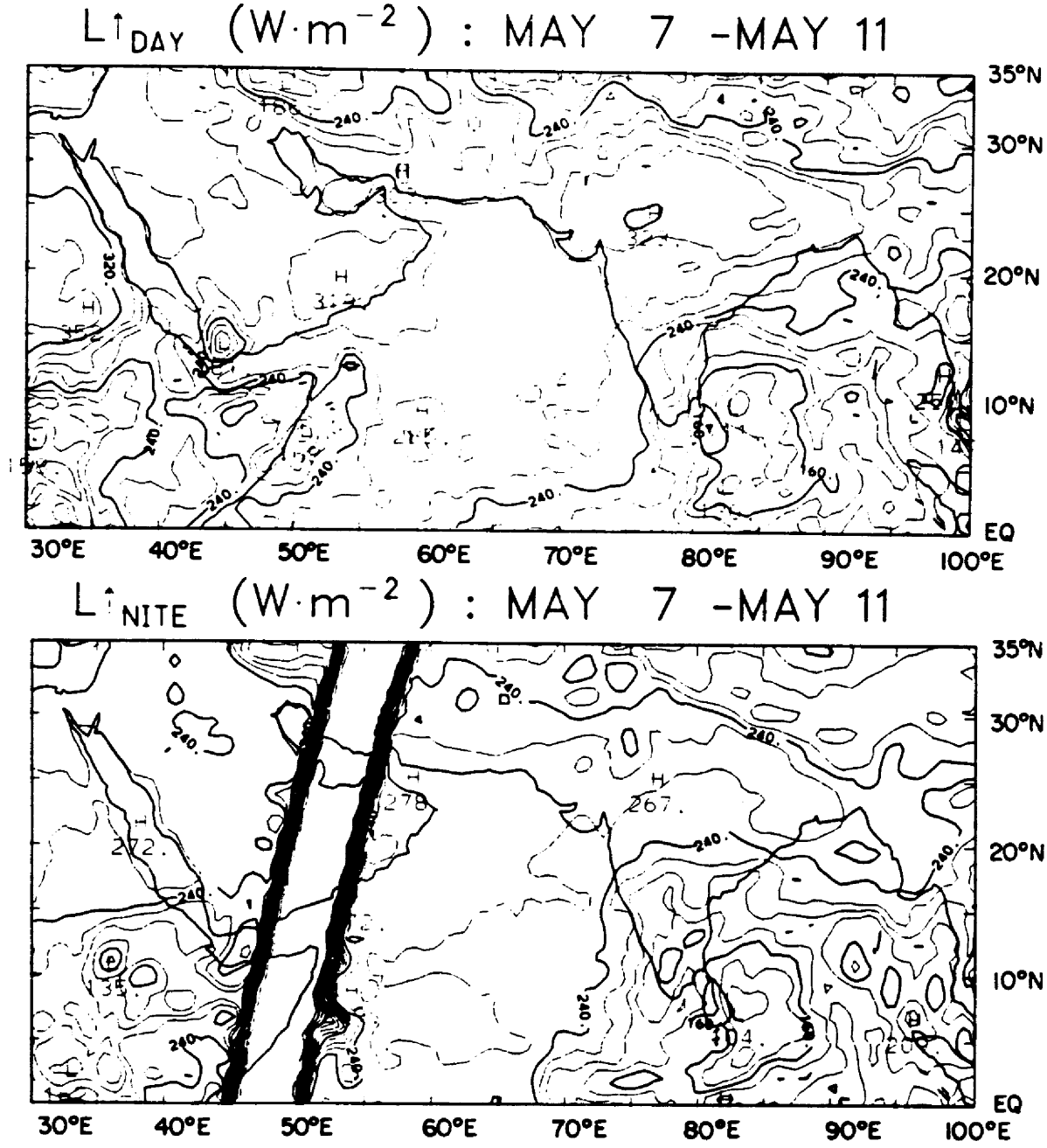

Fig. 3.27b. Same as Fig. 3.26b for May 7-11 (pentad 2).

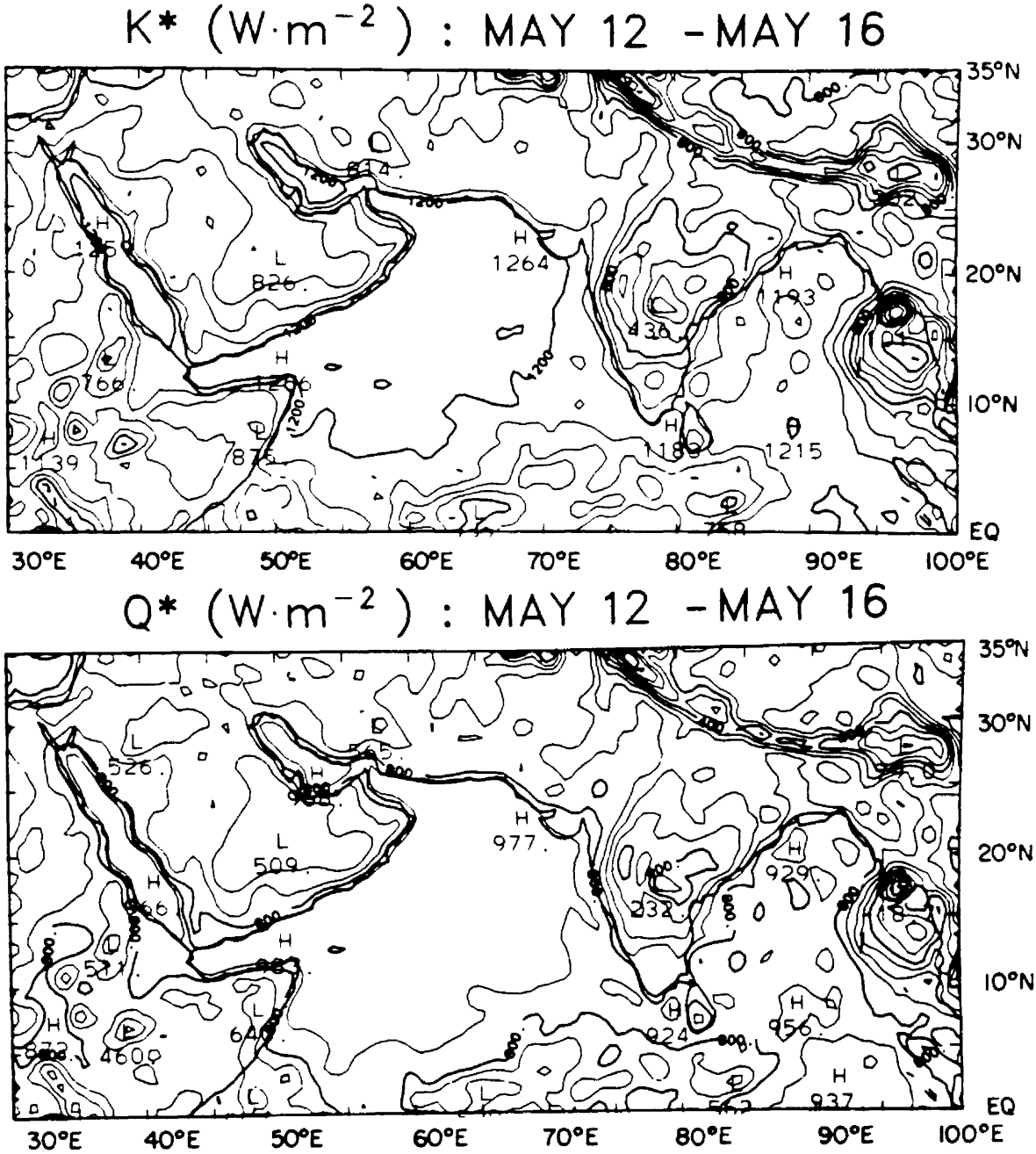

Fig. 3.28a. Same as Fig. 3.26a for May 12-16 (pentad 3).

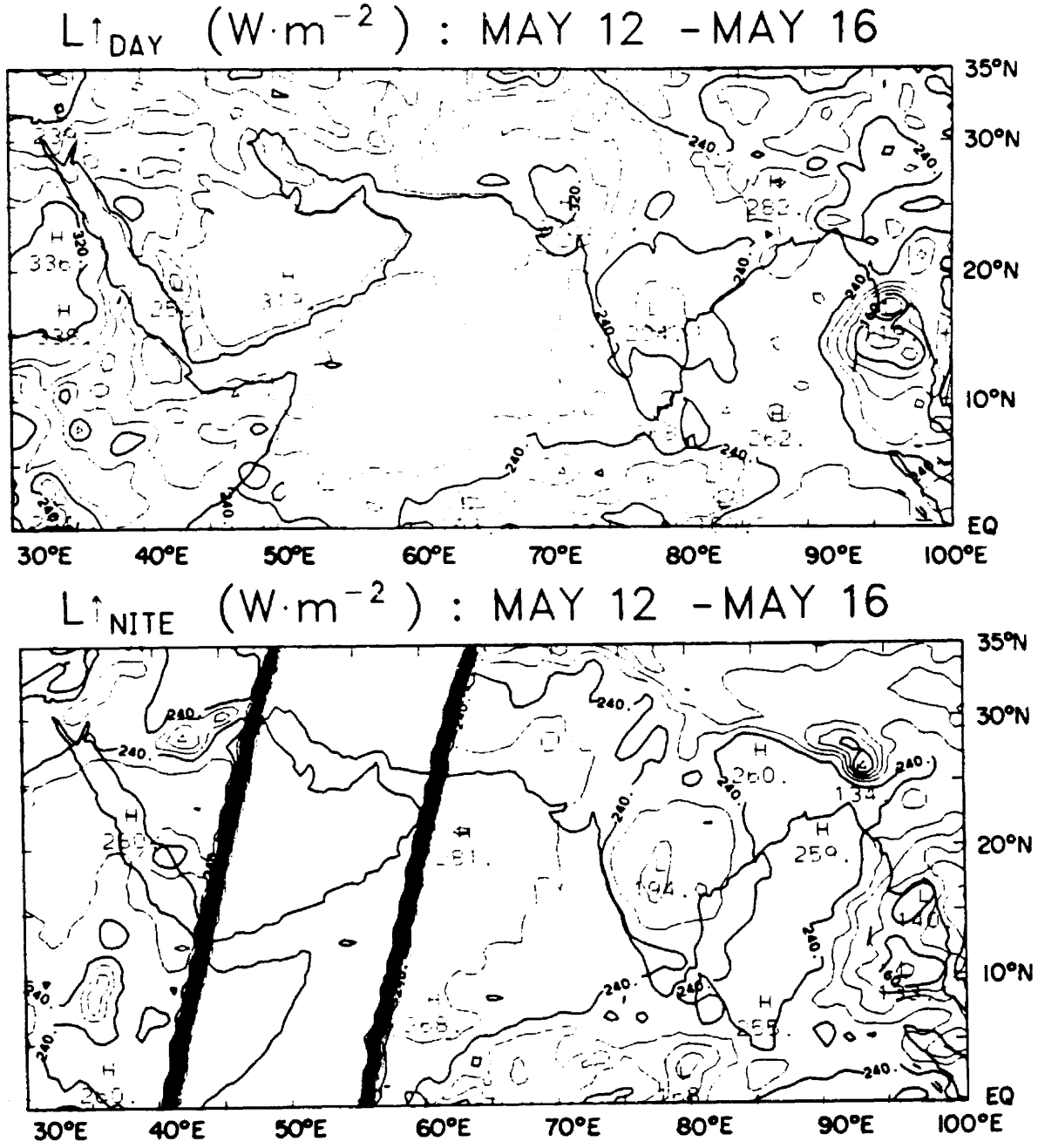

Fig. 3.28b. Same as Fig. 3.26b for May 12-16 (pentad 3).

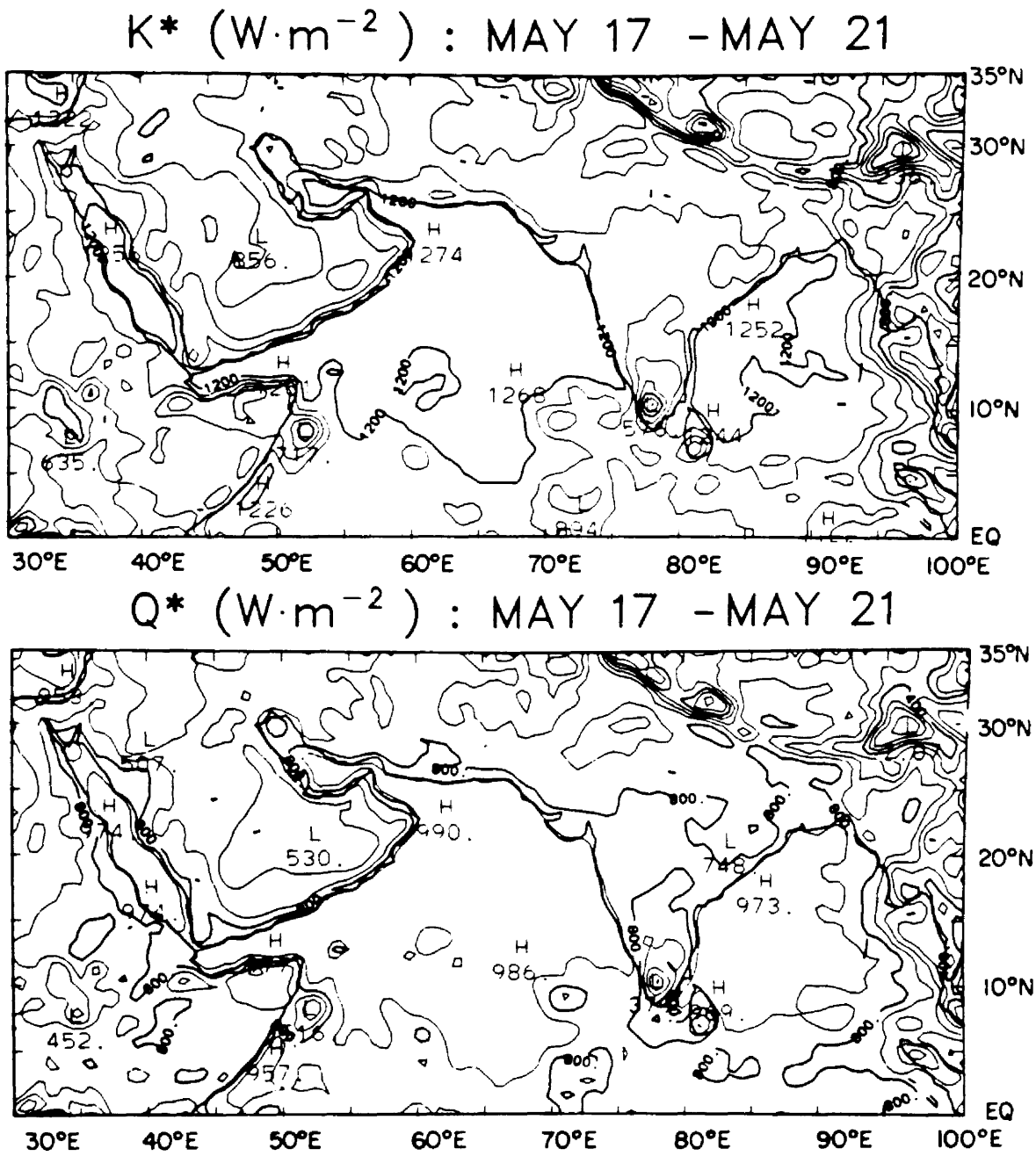

Fig. 3.29a. Same as Fig. 3.26a for May 17-21 (pentad 4).

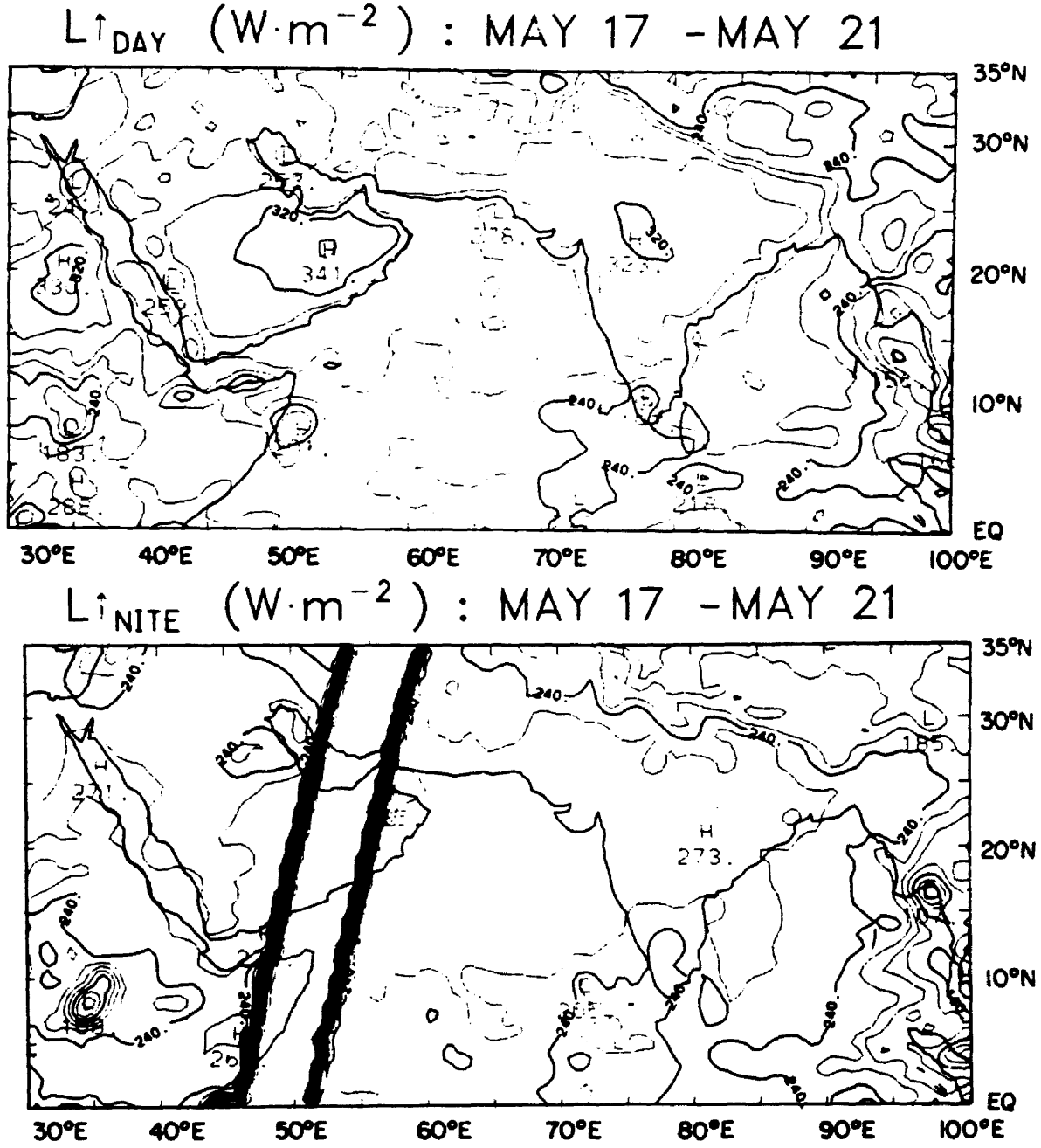

Fig. 3.29b. Same as Fig. 3.26b for May 17-21 (pentad 4).

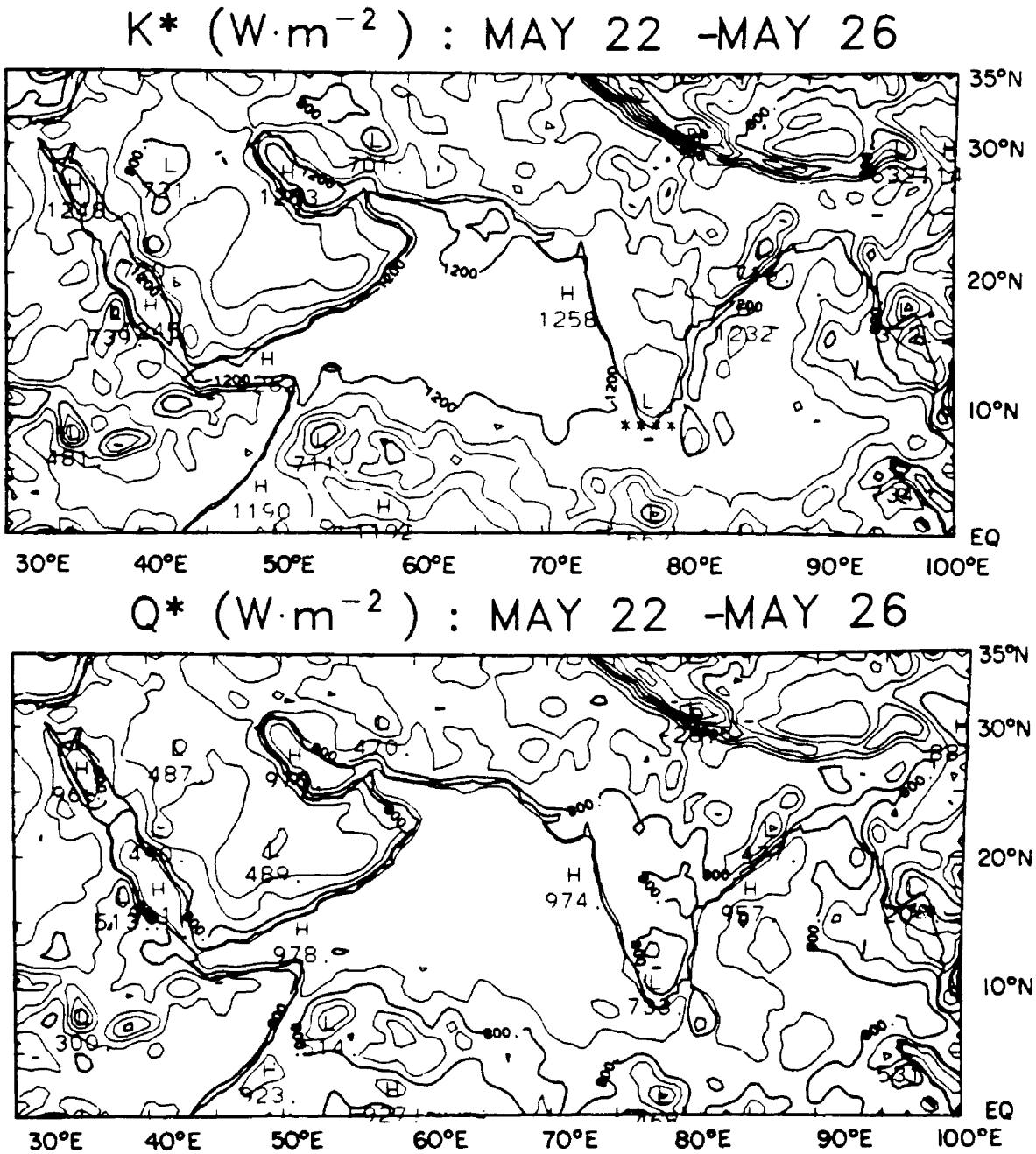

Fig. 3.30a. Same as Fig. 3.26a for May 22-26 (pentad 5).

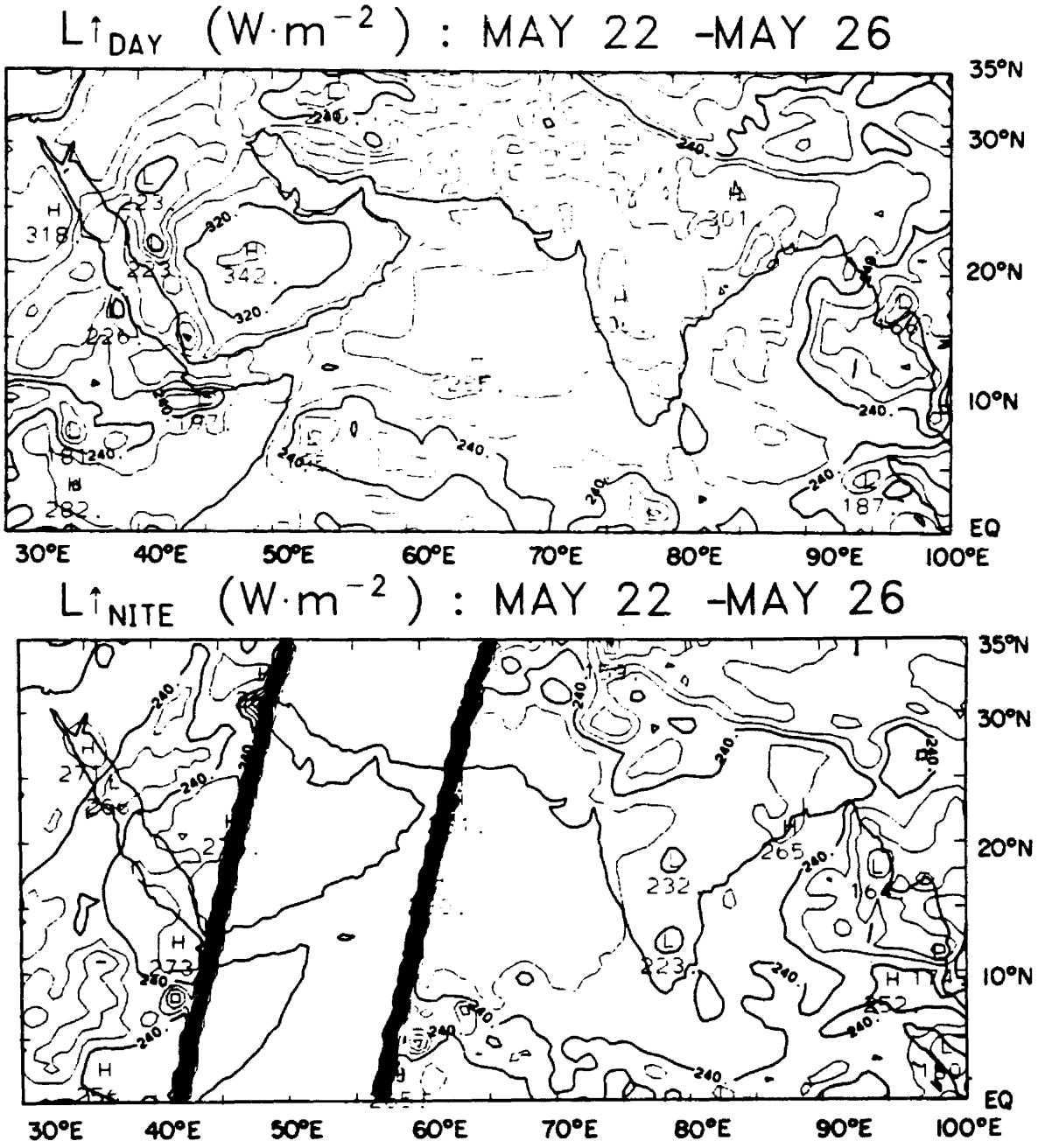

Fig. 3.30b. Same as Fig. 3.26b for May 22-26 (pentad 5).

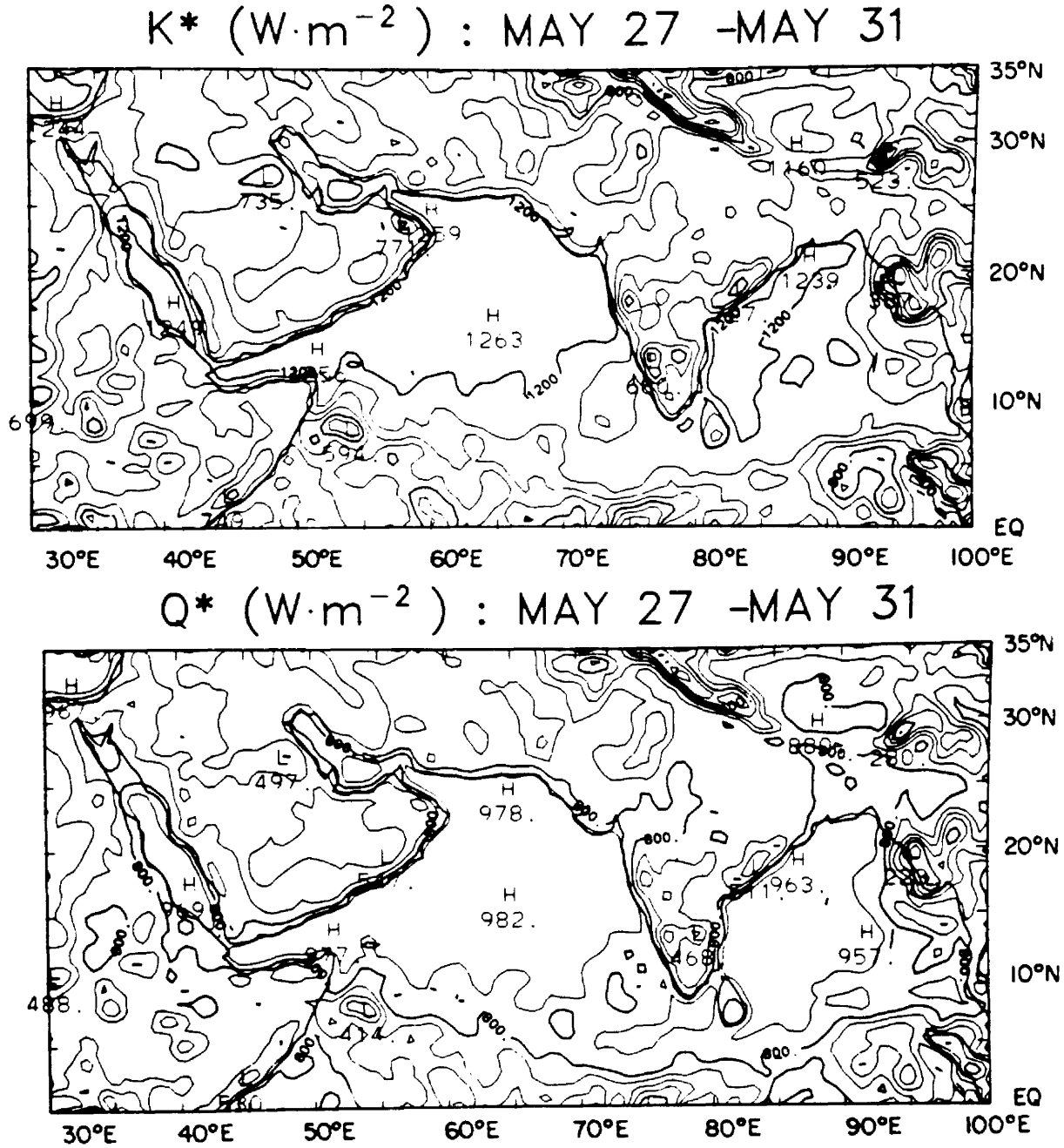

Fig. 3.31a. Same as Fig. 3.26a for May 27-31 (pentad 6).

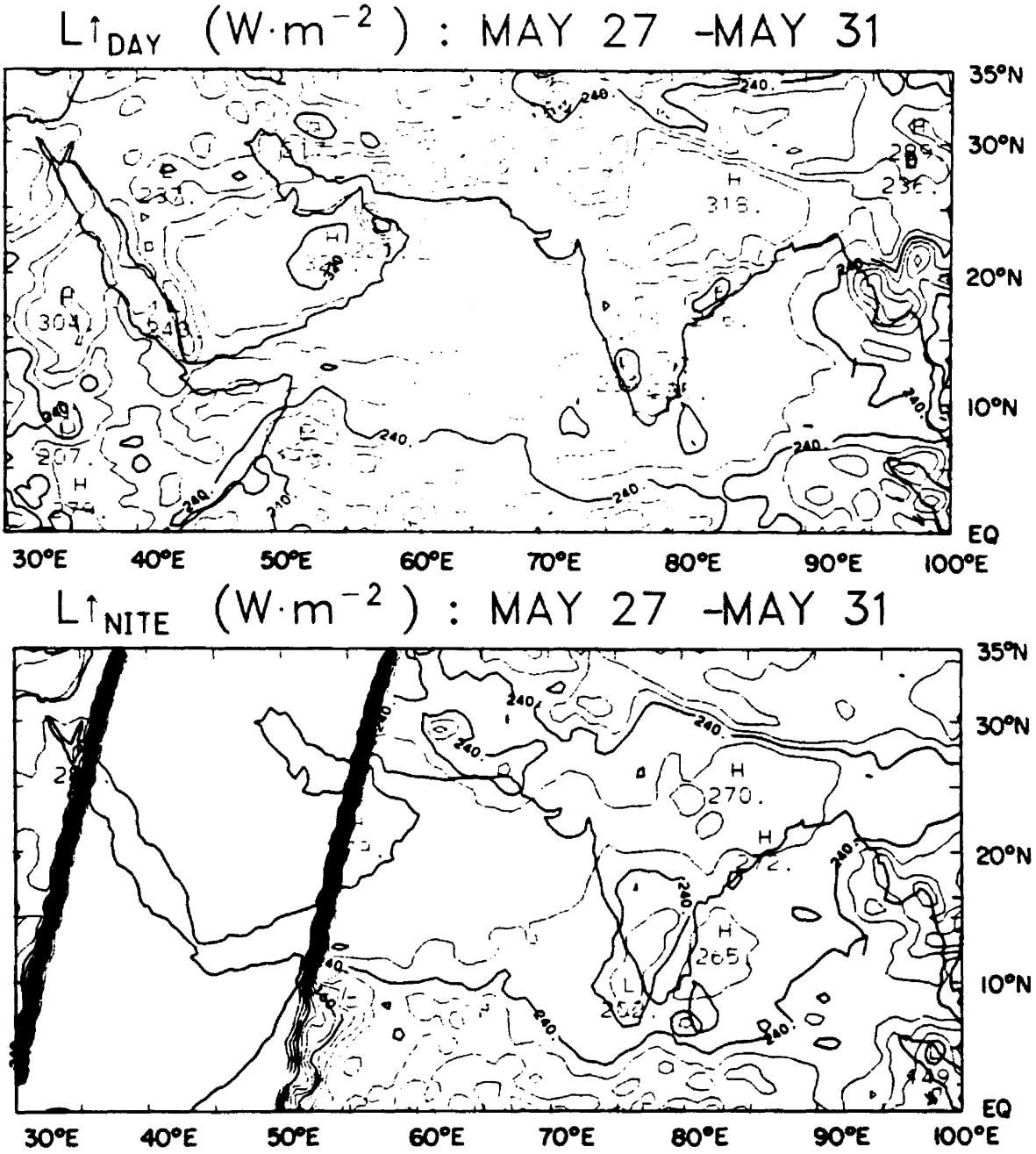

Fig. 3.31b. Same as Fig. 3.26b for May 27-31 (pentad 6).

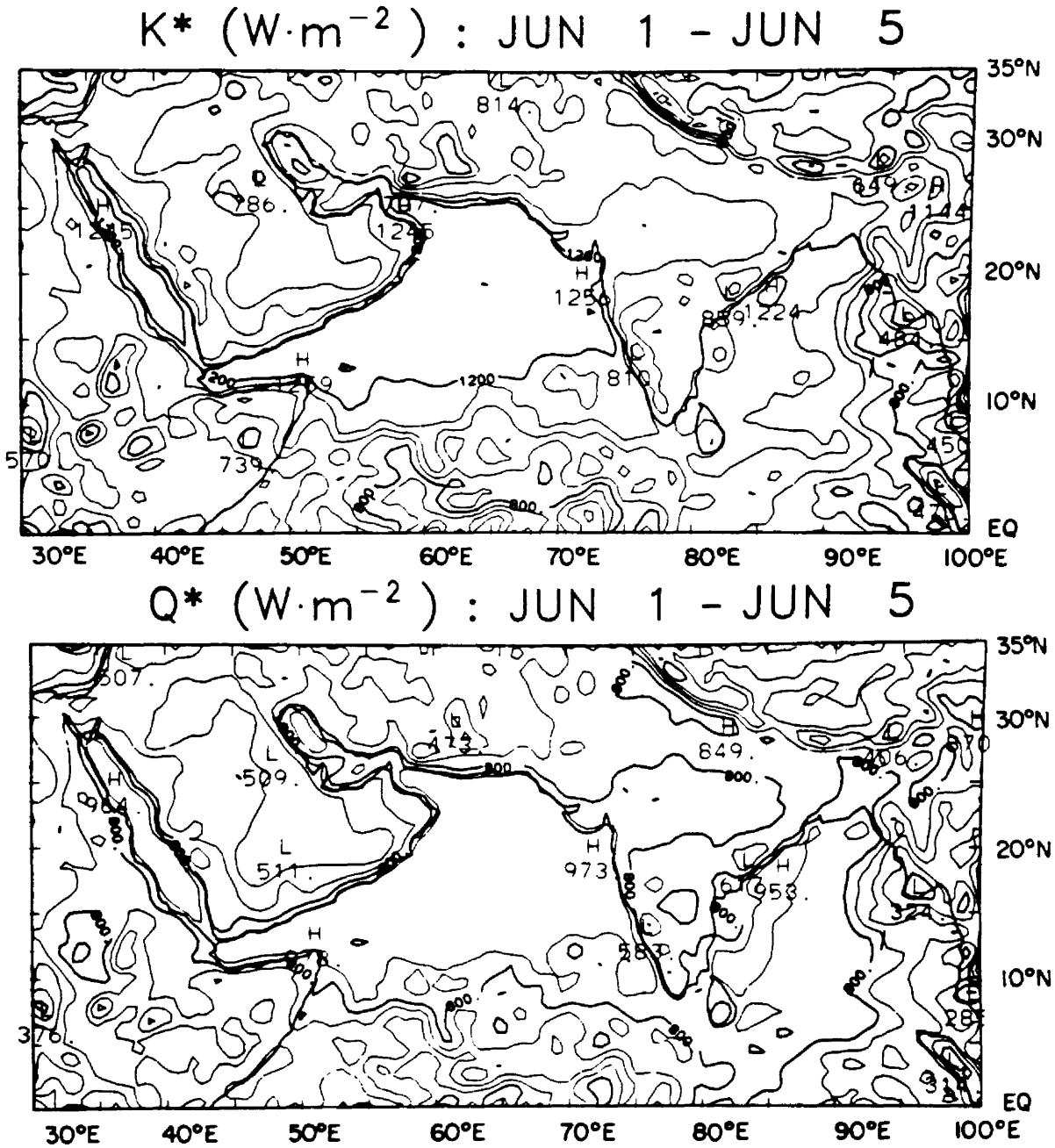

Fig. 3.32a. Same as Fig. 3.26a for June 1-5 (pentad 7).

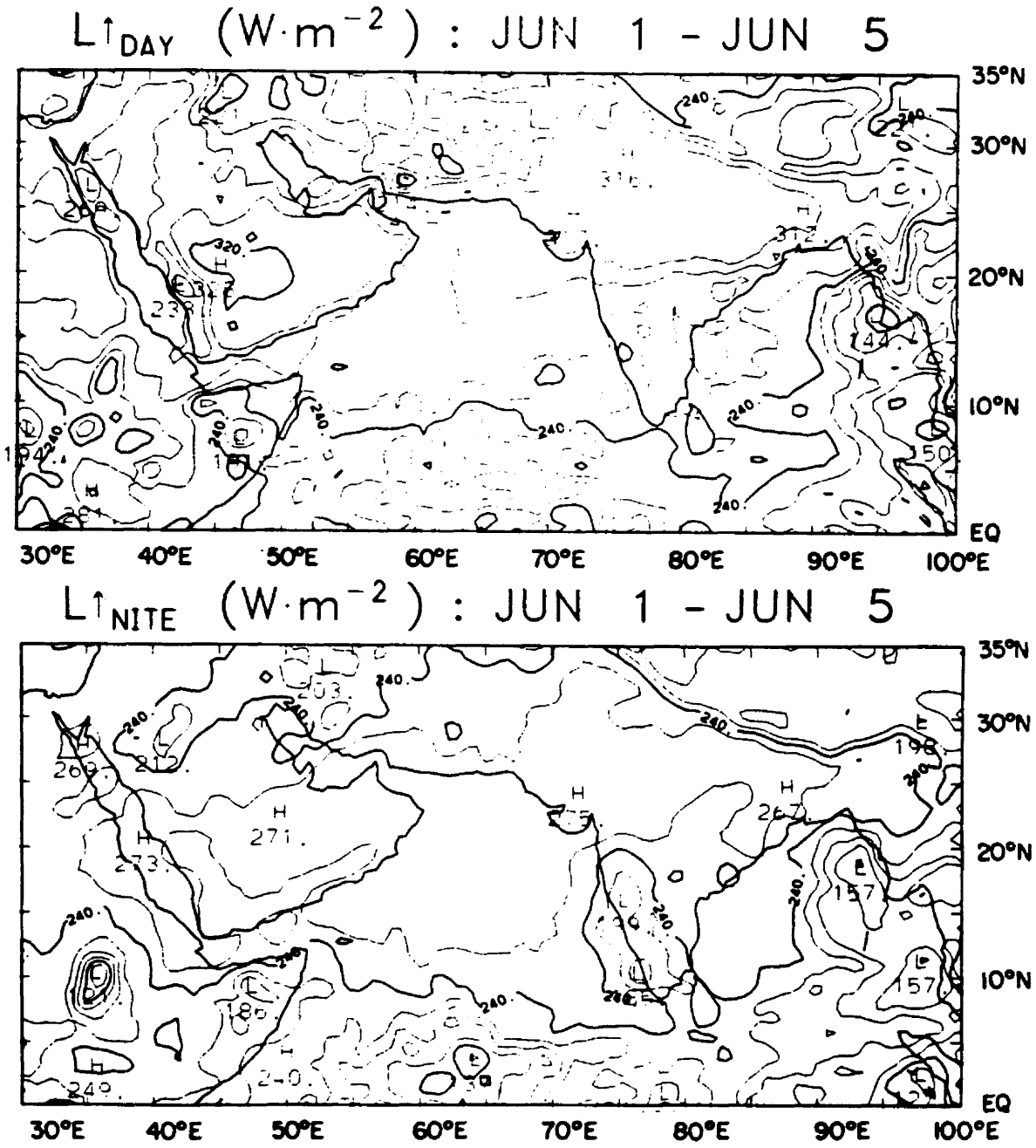

Fig. 3.32b. Same as Fig. 3.26b for June 1-5 (pentad 7).

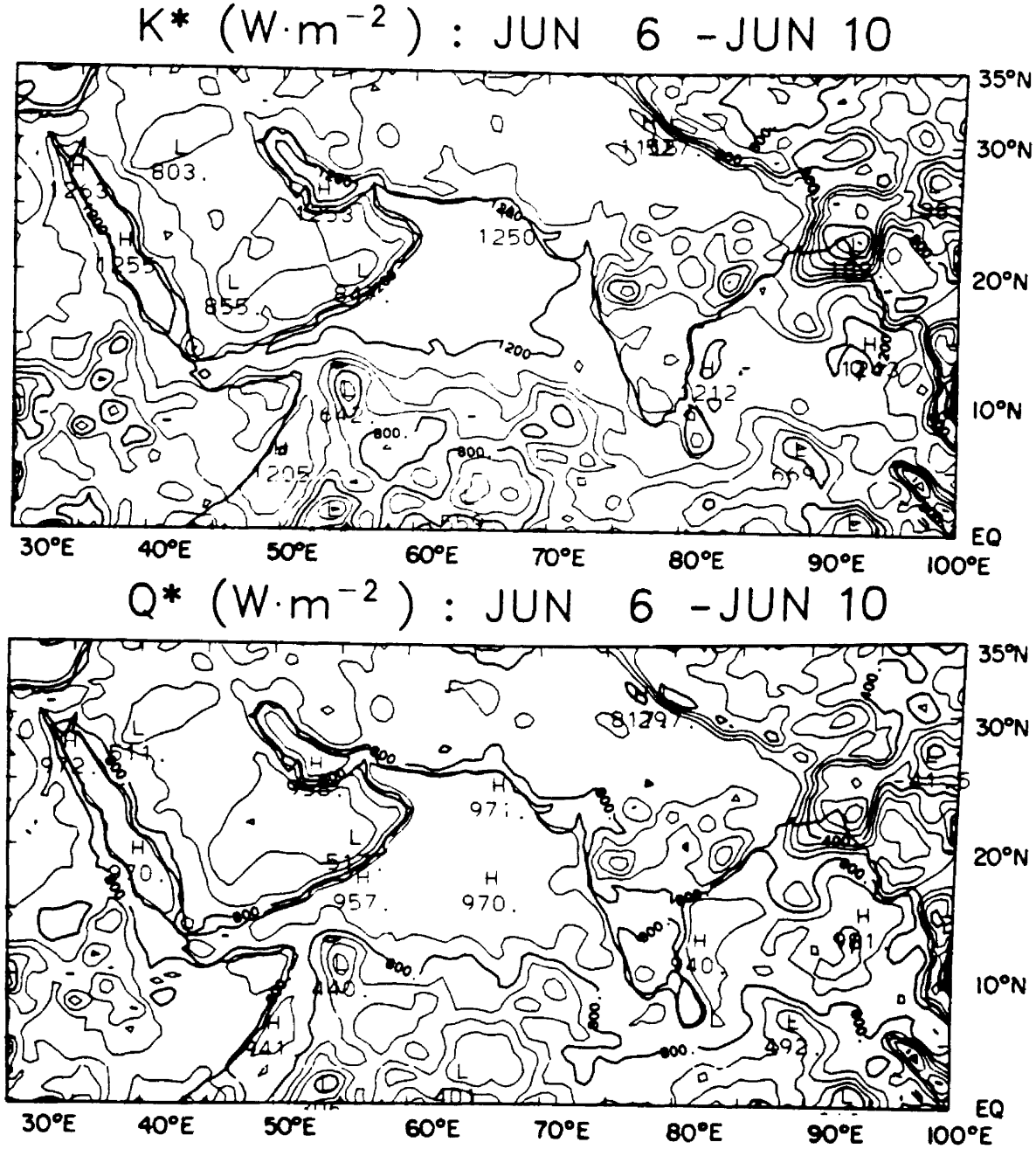

Fig. 3.33a. Same as Fig. 3.26a for June 6-10 (pentad 8).

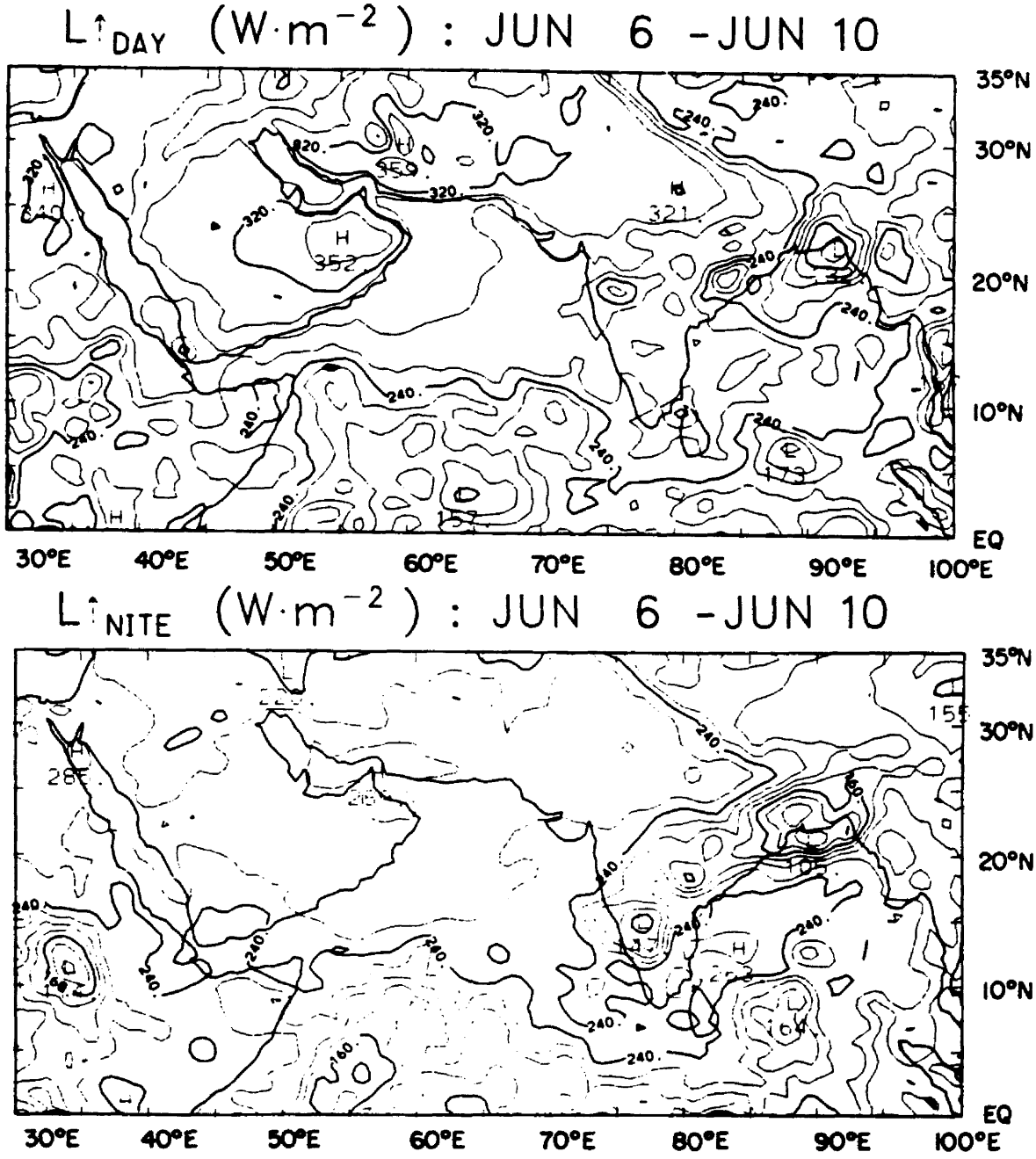

Fig. 3.33b. Same as Fig. 3.26b for June 6-10 (pentad 8).

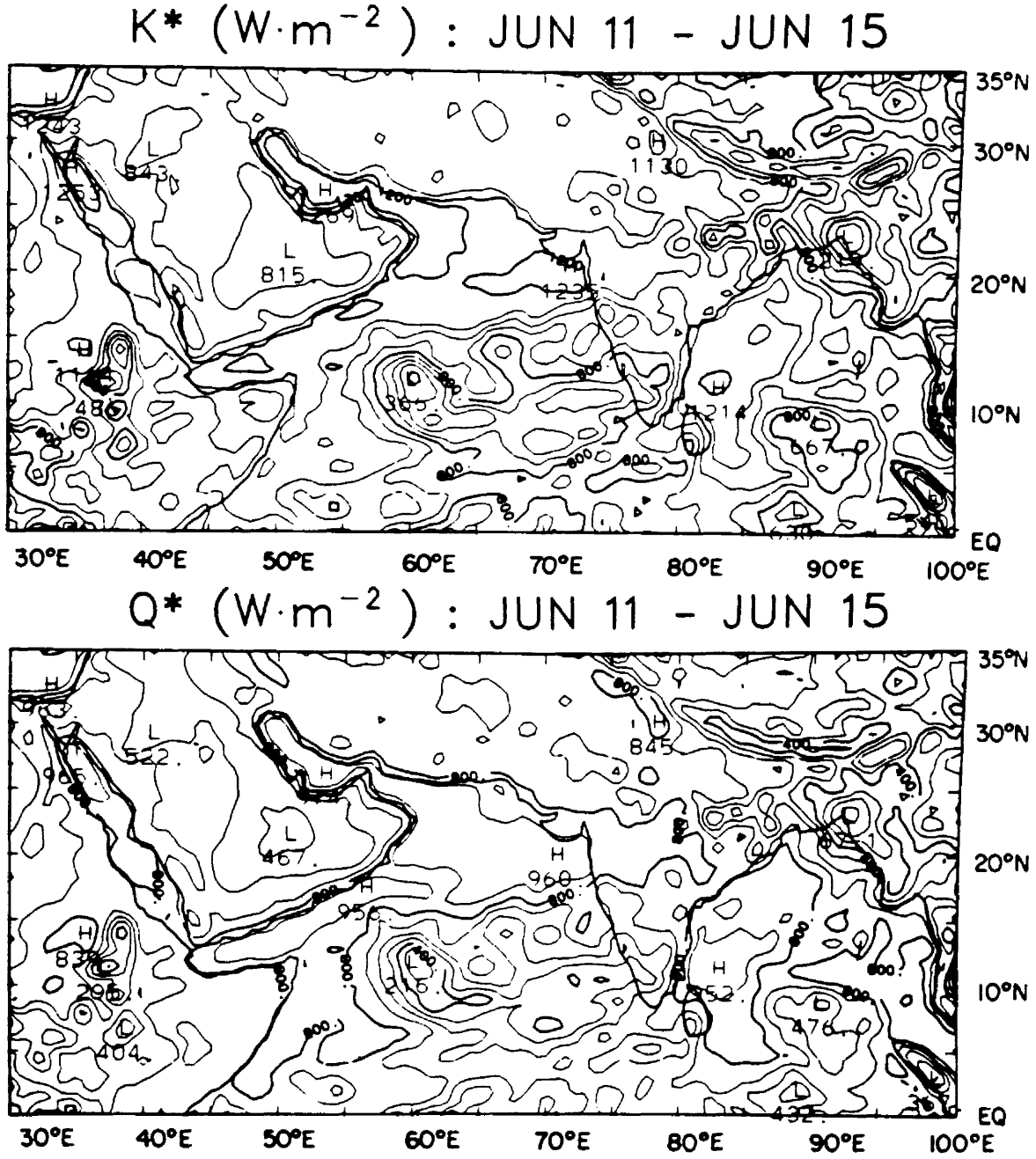

Fig. 3.34a. Same as Fig. 3.26a for June 11-15 (pentad 9).

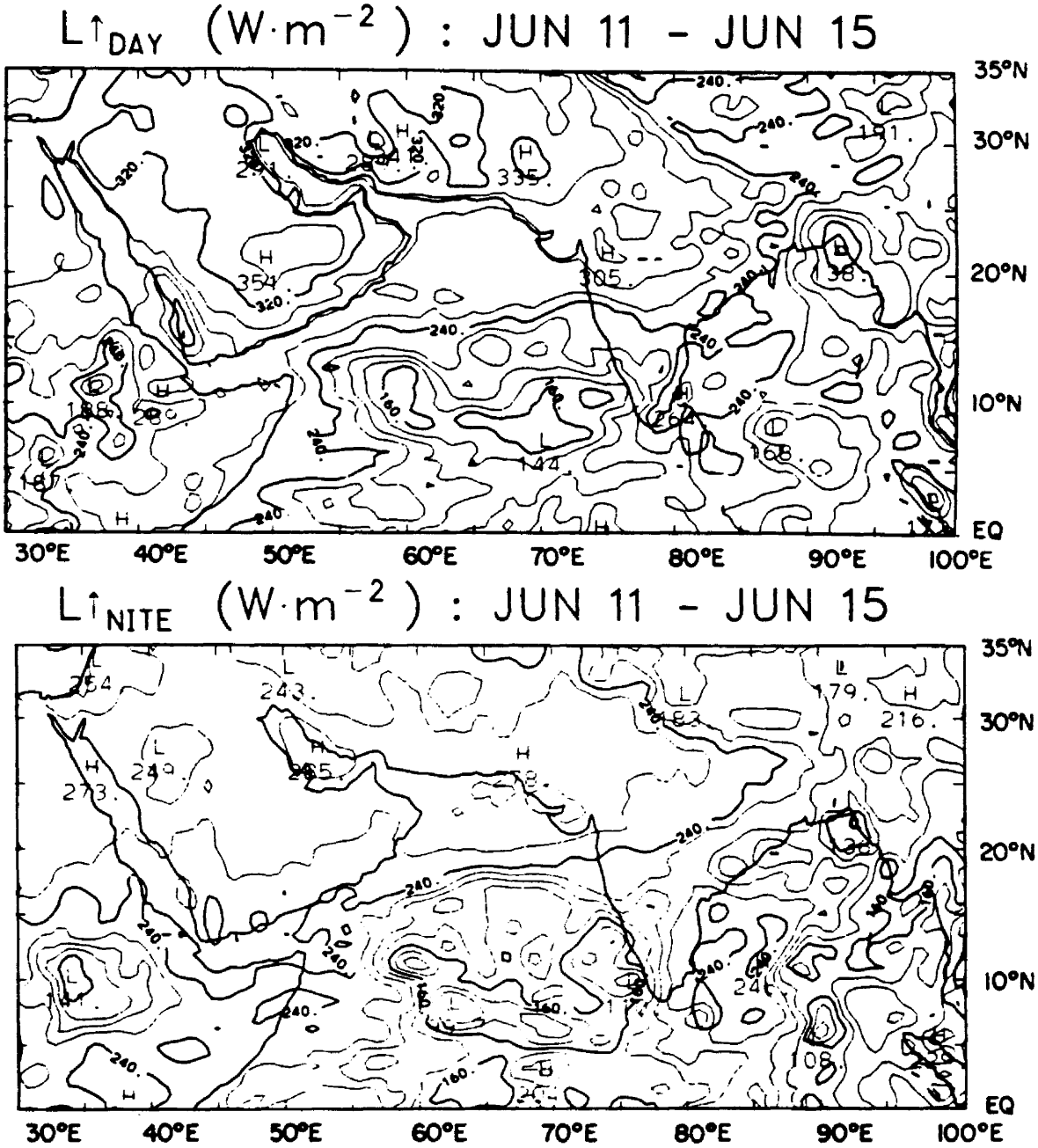

Fig. 3.34b. Same as Fig. 3.26b for June 11-15 (pentad 9).

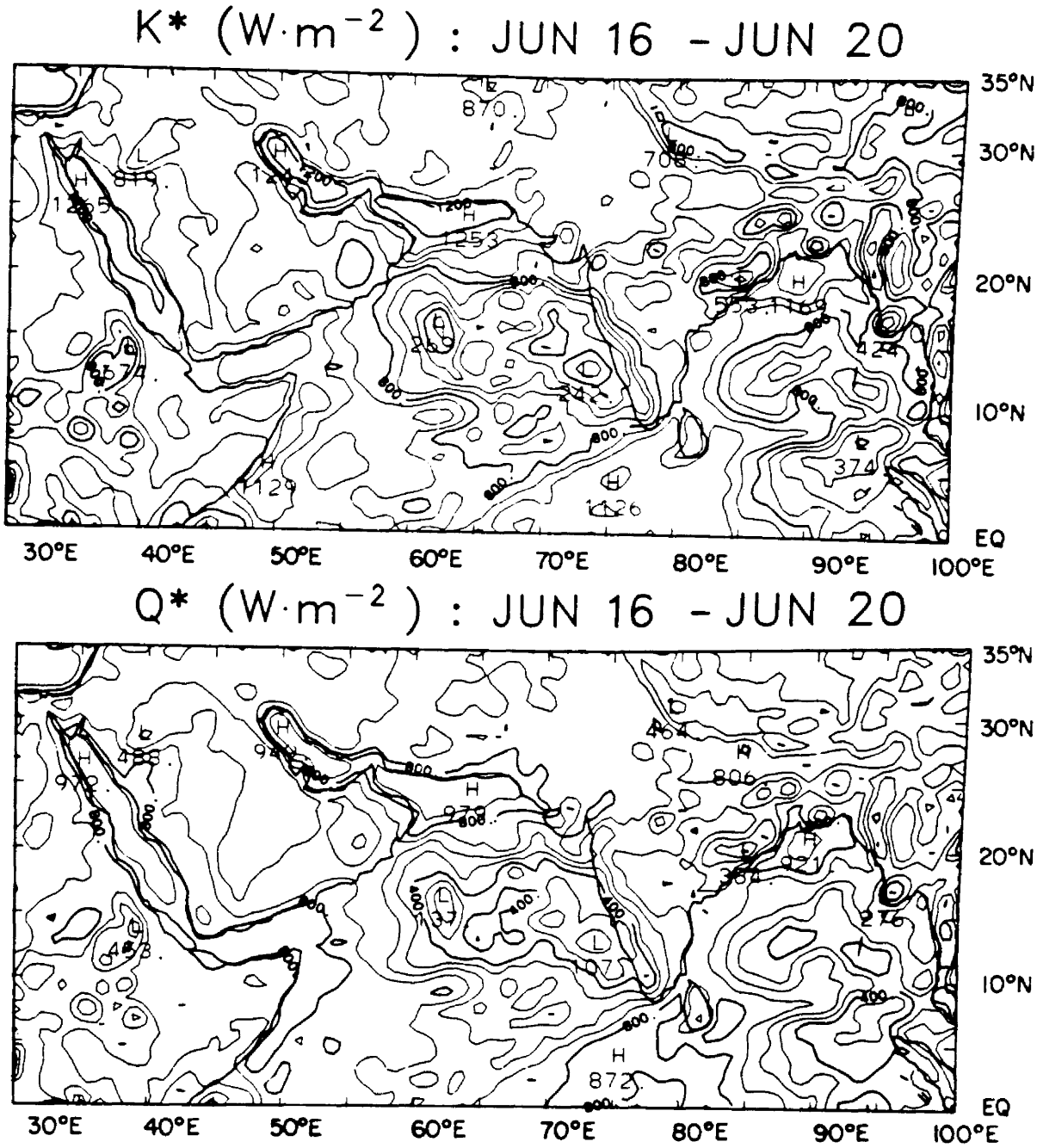

Fig. 3.35a. Same as Fig. 3.26a for June 16-20 (pentad 10).

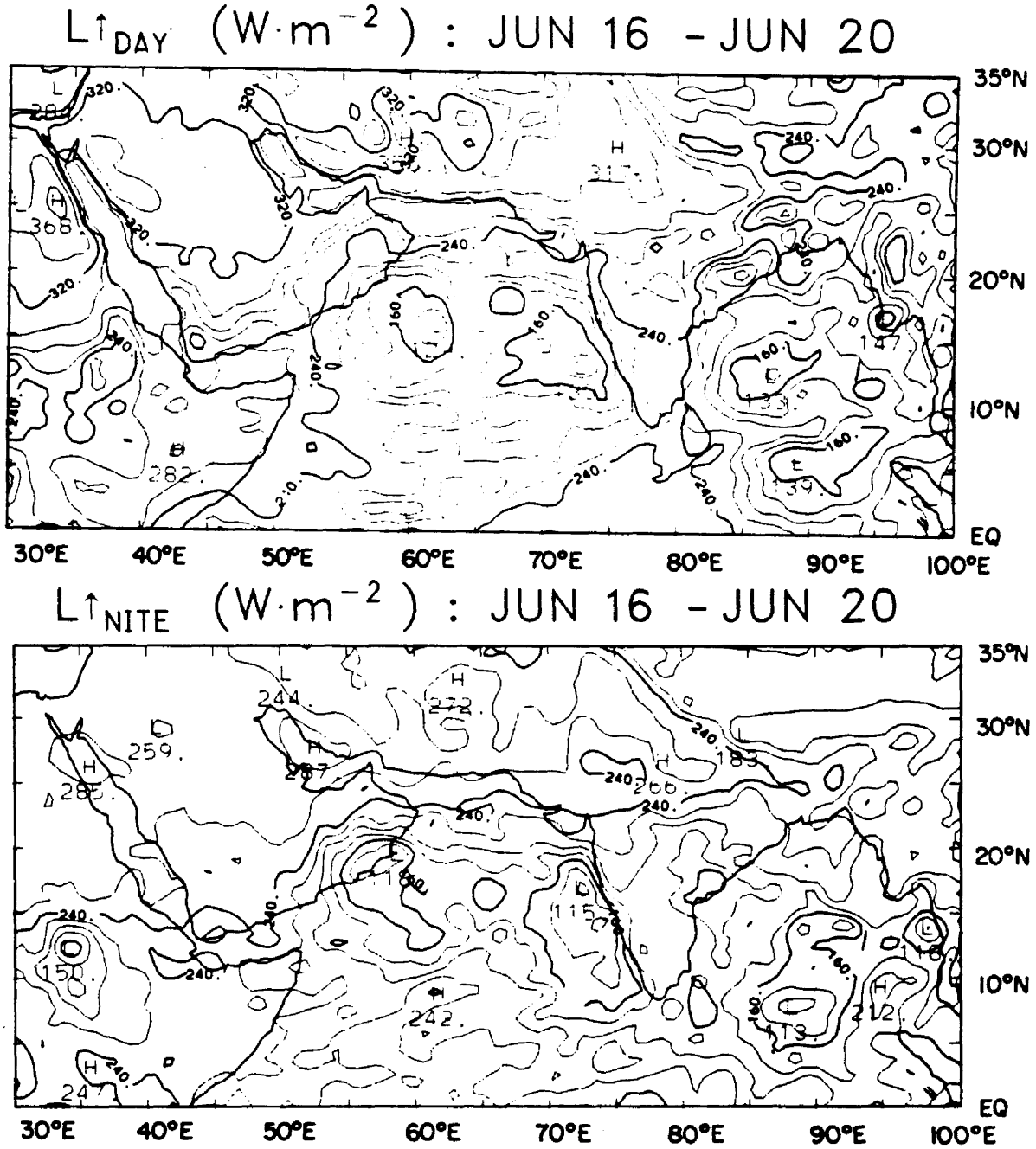

Fig. 3.35b. Same as Fig. 3.26b for June 16-20 (pentad 10).

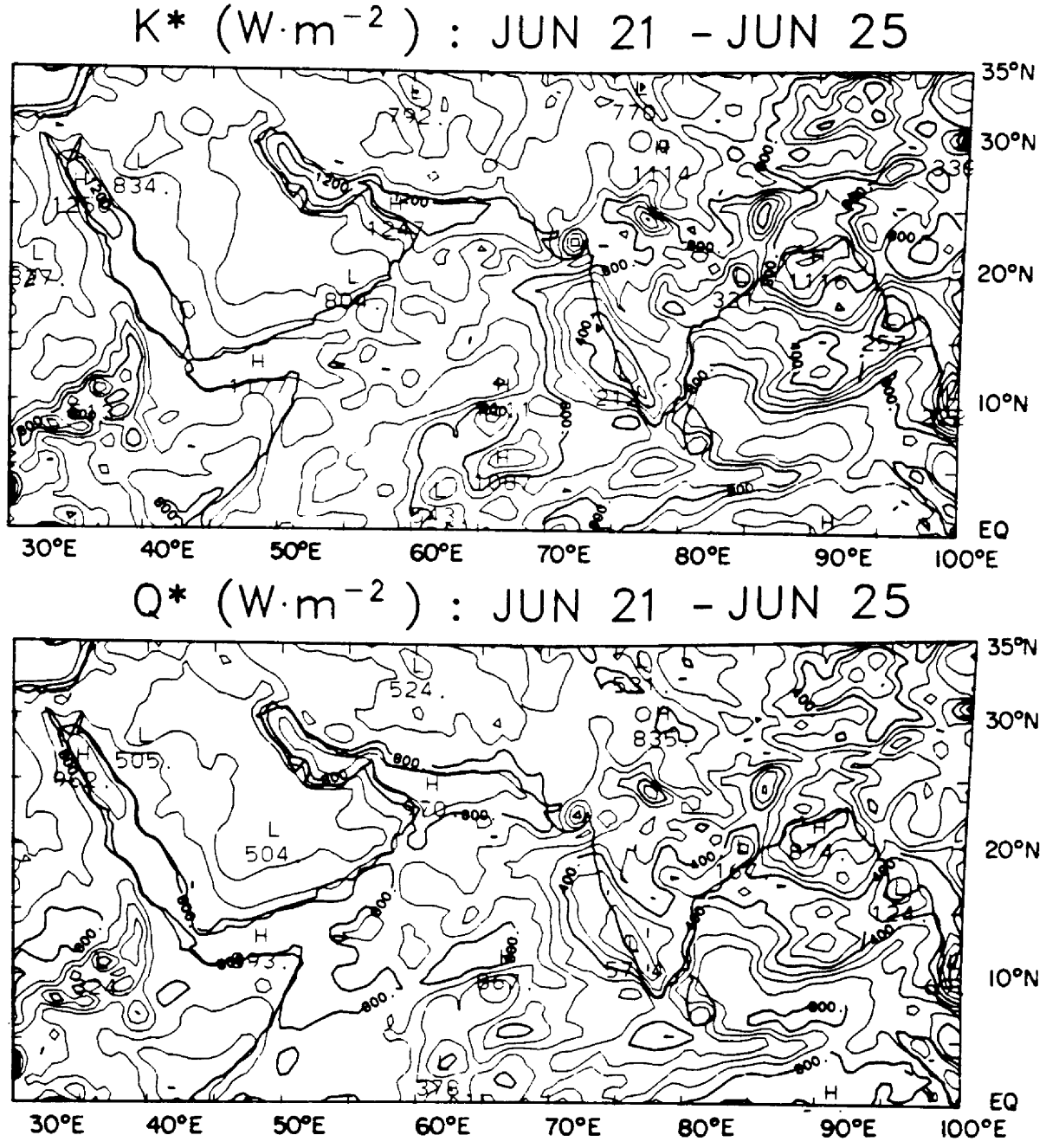

Fig. 3.36a. Same as Fig. 3.26a for June 21-25 (pentad 11).

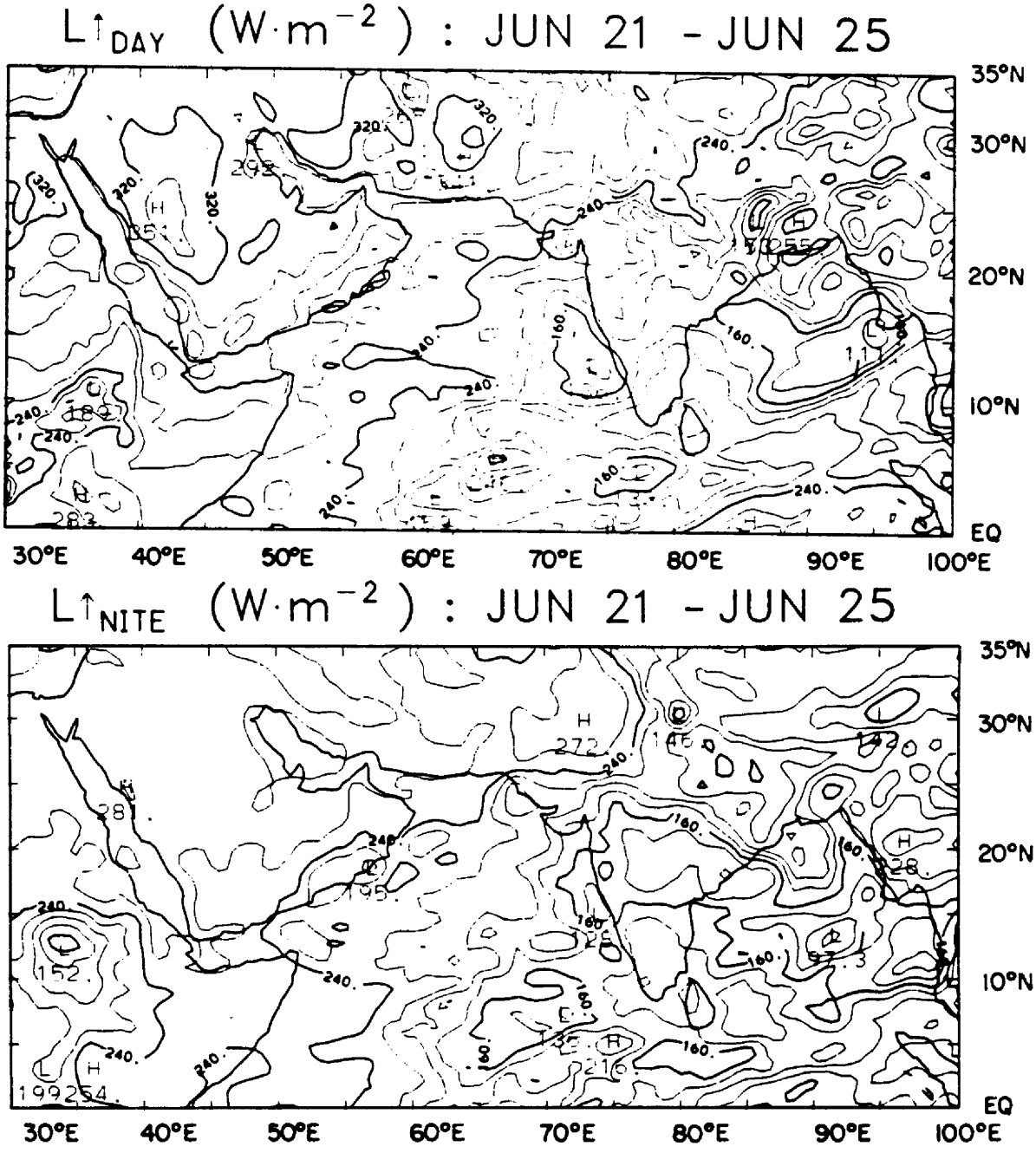

Fig. 3.36b. Same as Fig. 3.26b for June 21-25 (pentad 11).

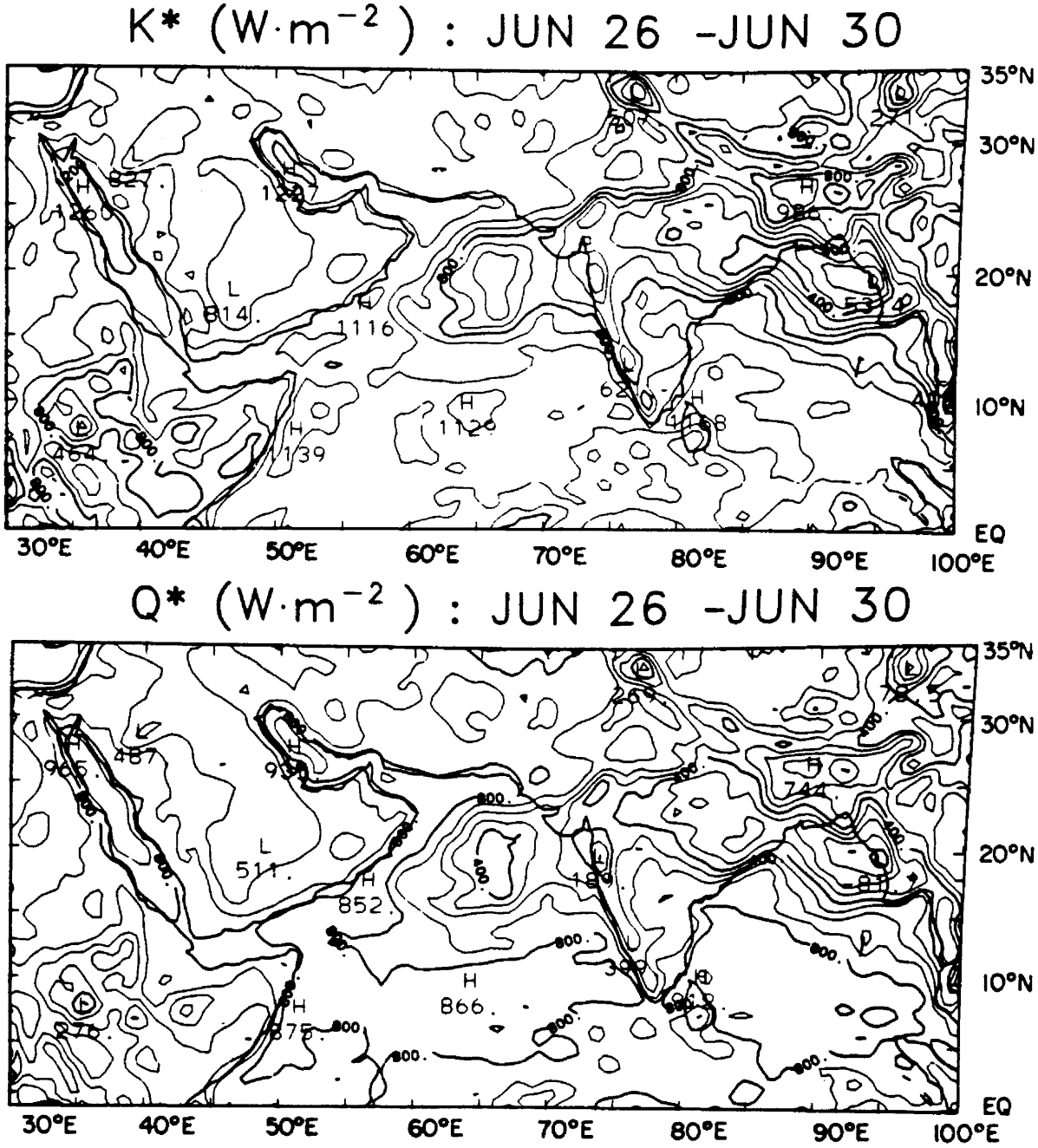

Fig. 3.37a. Same as Fig. 3.26a for June 26-30 (pentad 12).

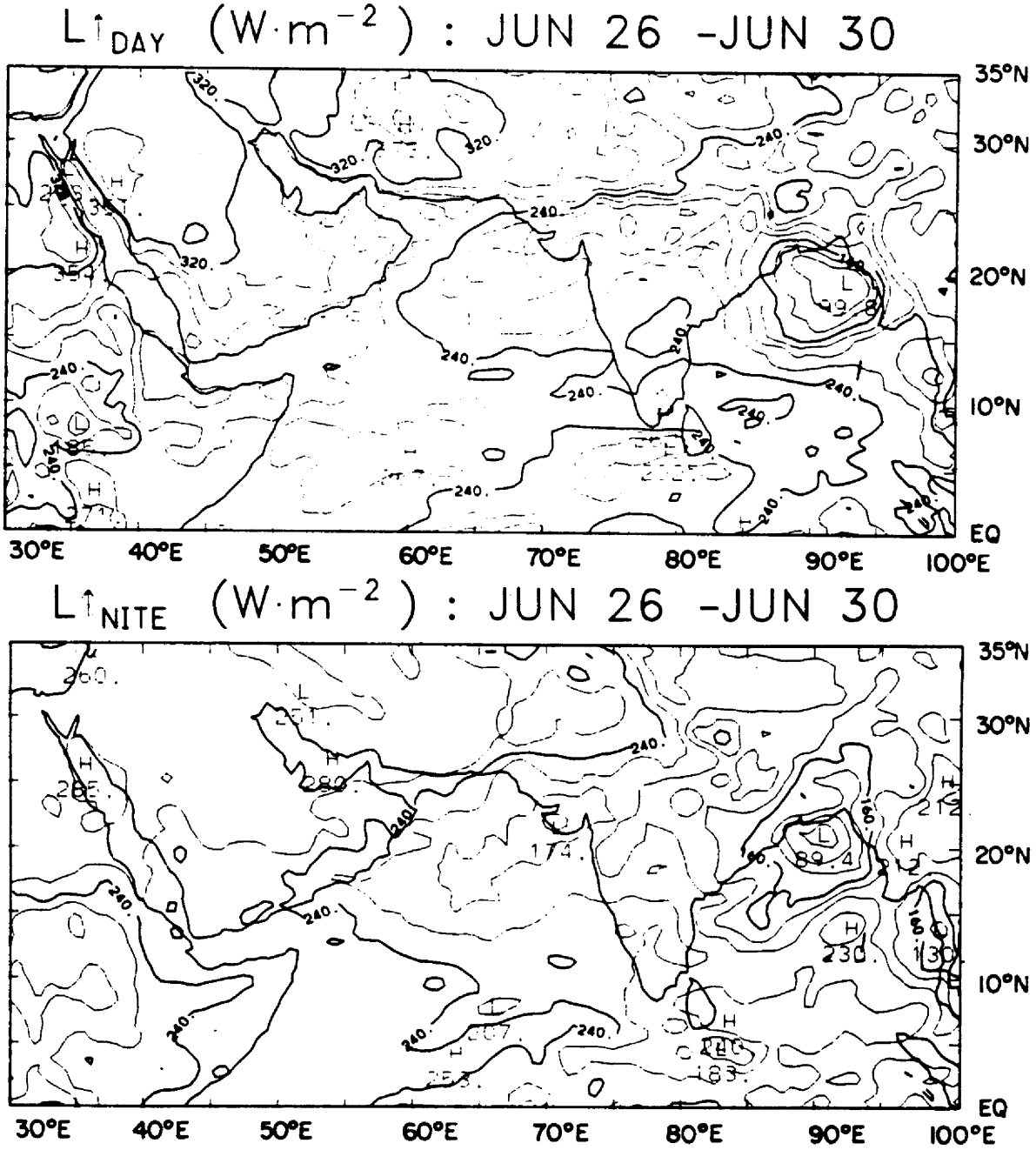

Fig. 3.37b. Same as Fig. 3.26b for June 26-30 (pentad 12).

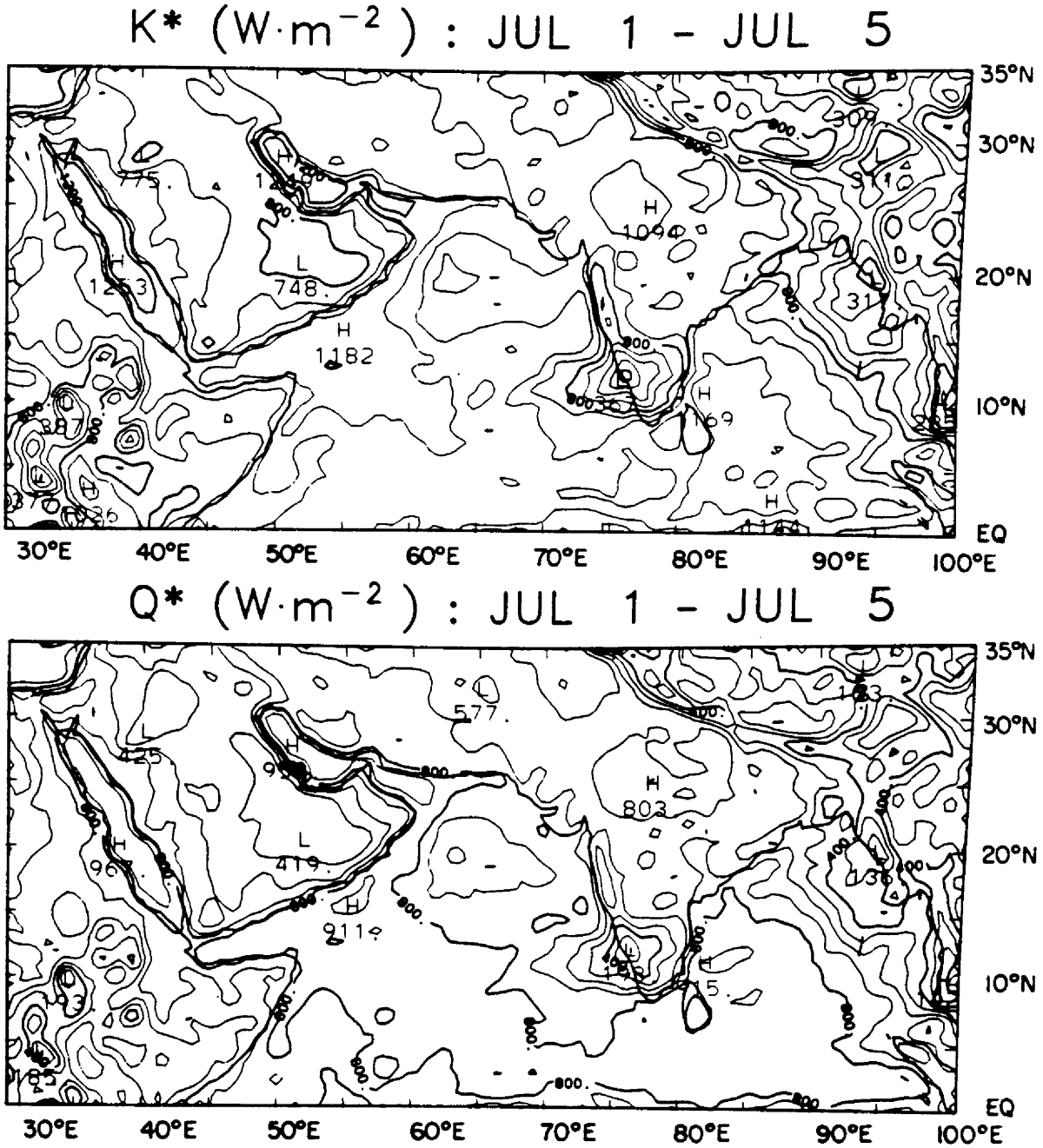

Fig. 3.38a. Same as Fig. 3.26a for July 1-5 (pentad 13).

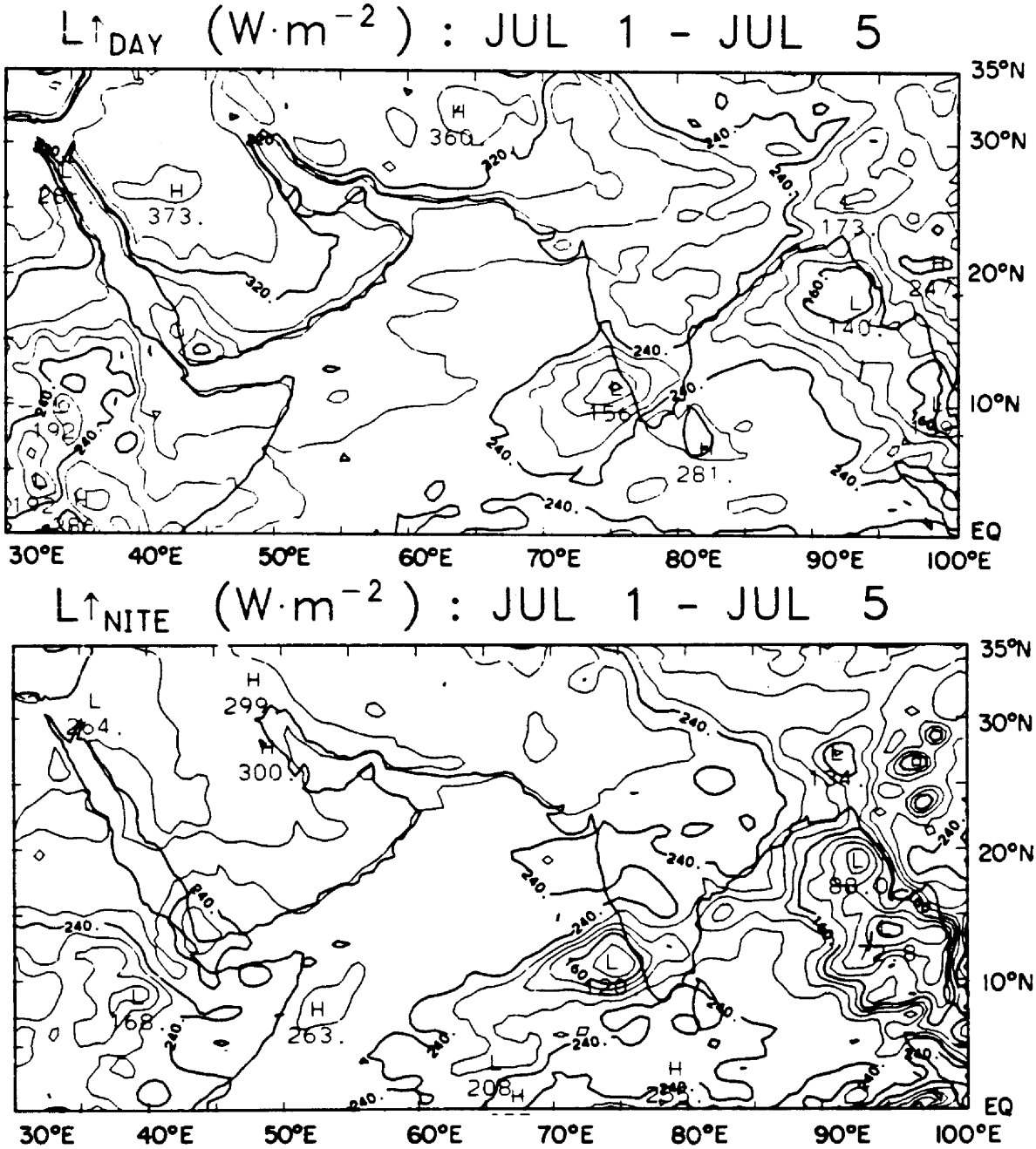

Fig. 3.38b. Same as Fig. 3.26b for July 1-5 (pentad 13).

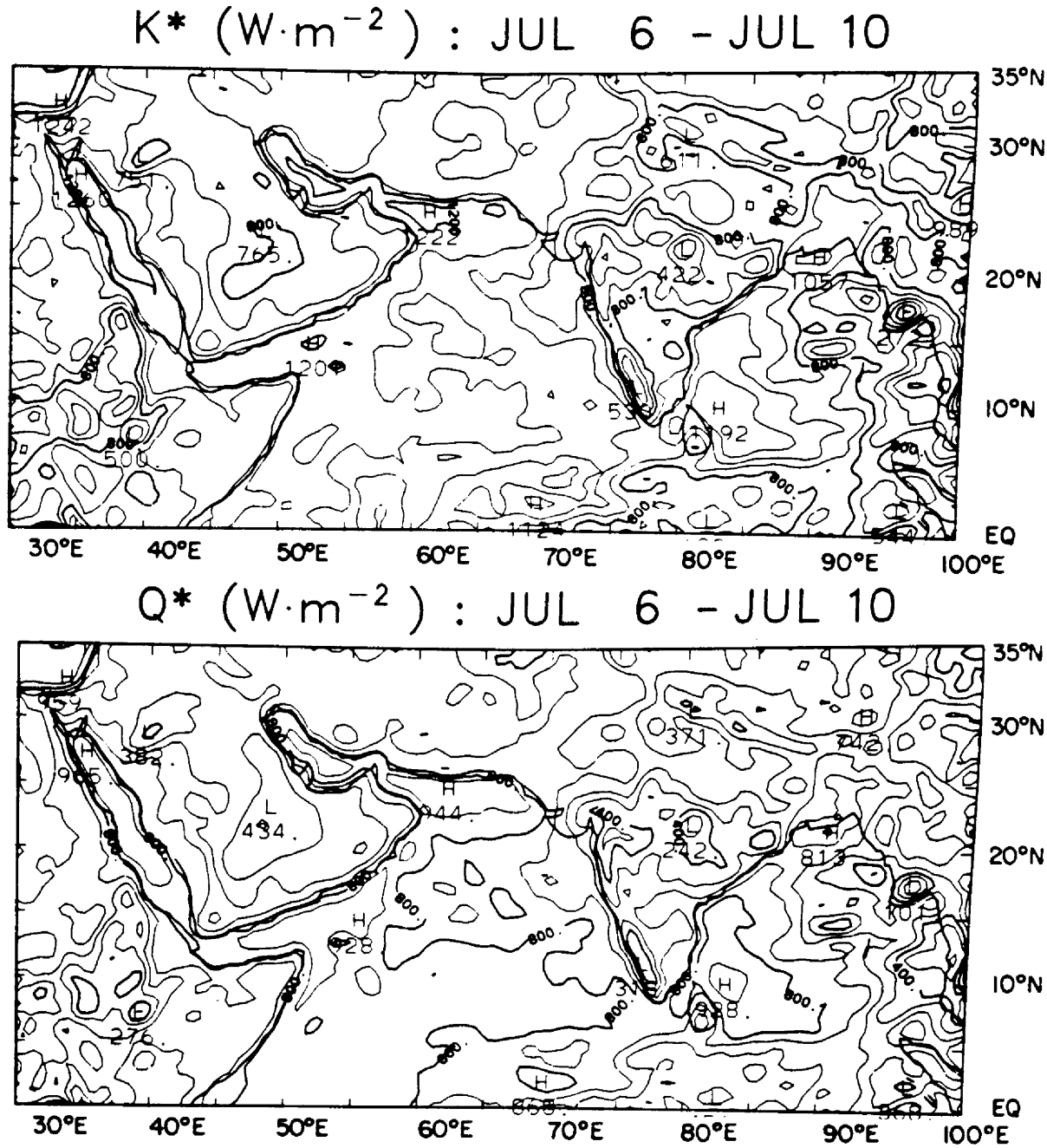

Fig. 3.39a. Same as Fig. 3.26a for July 6-10 (pentad 14).

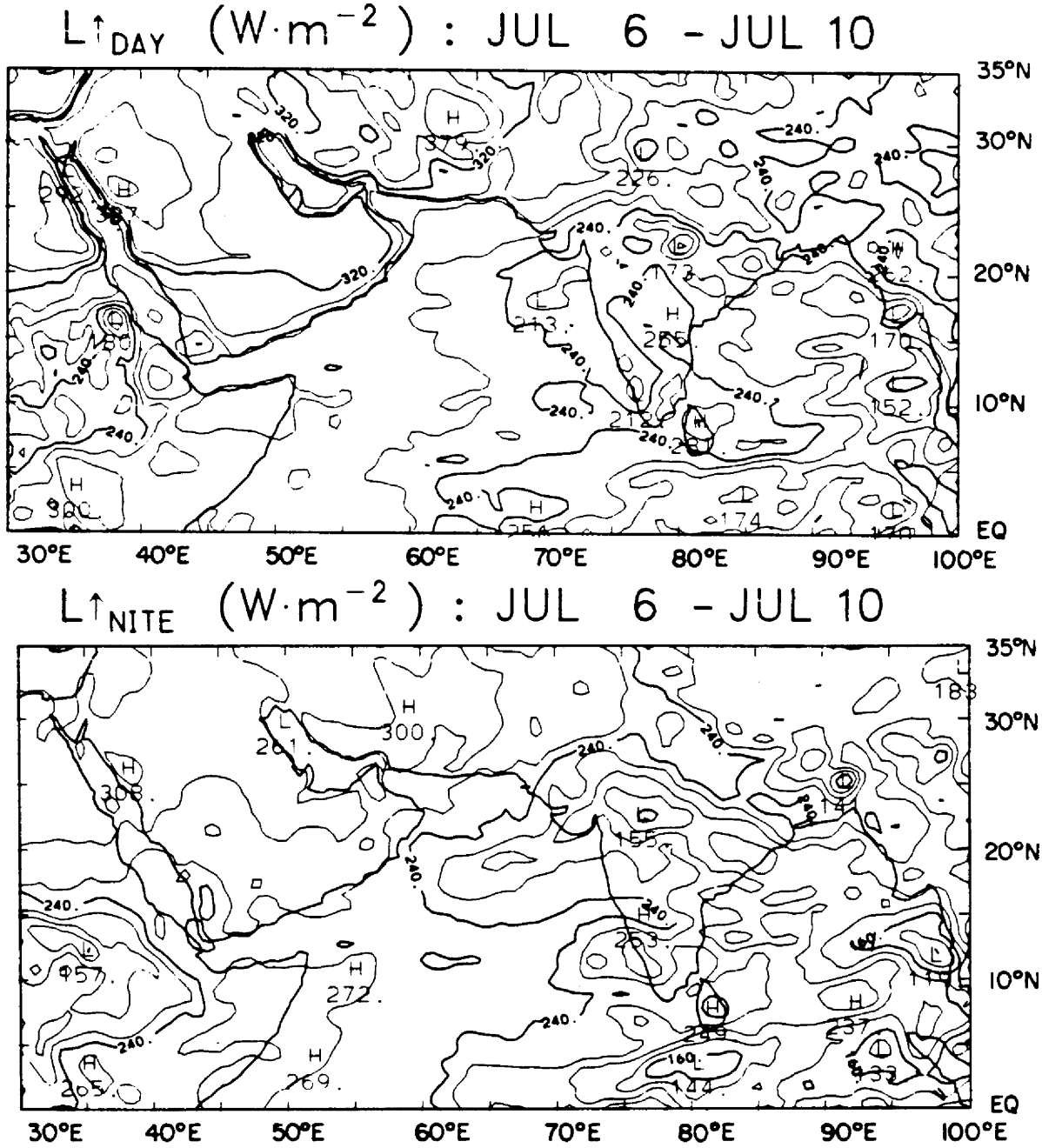

Fig. 3.39b. Same as Fig. 3.26b for July 6-10 (pentad 14).

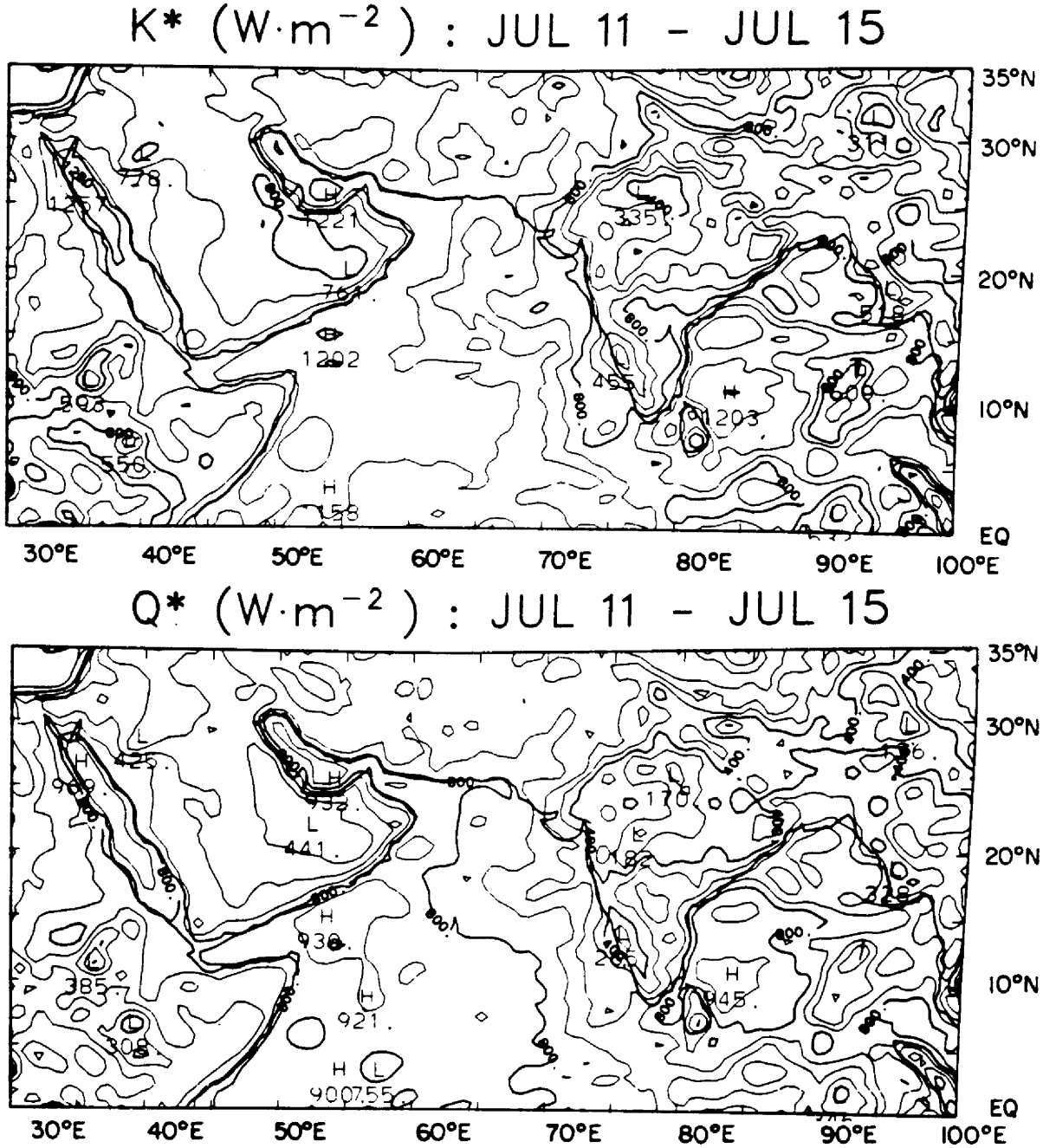

Fig. 3.40a. Same as Fig. 3.26a for July 11-15 (pentad 15).

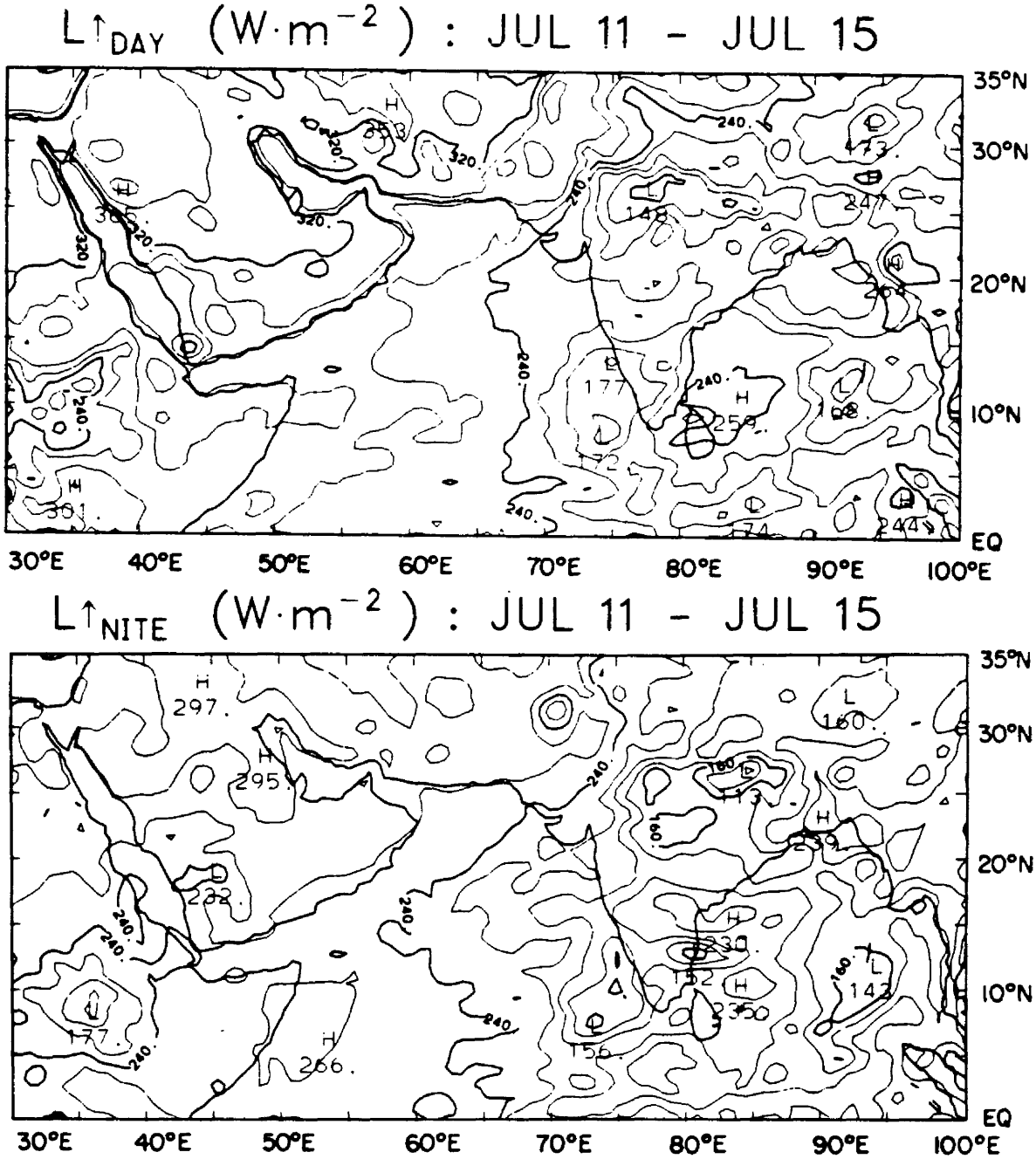

Fig. 3.40b. Same as Fig. 3.26b for July 11-15 (pentad 15).

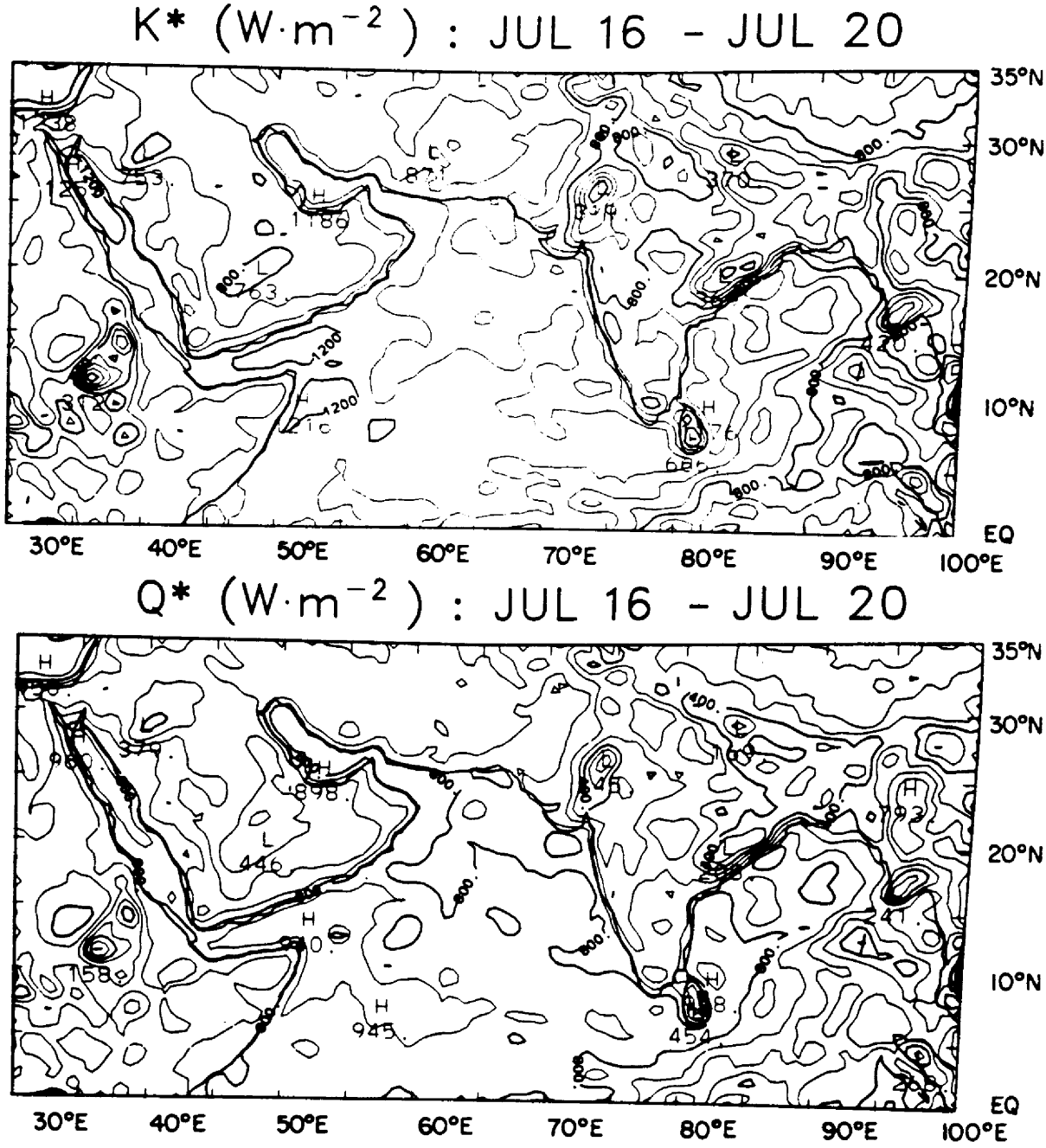

Fig. 3.41a. Same as Fig. 3.26a for July 16-20 (pentad 16).

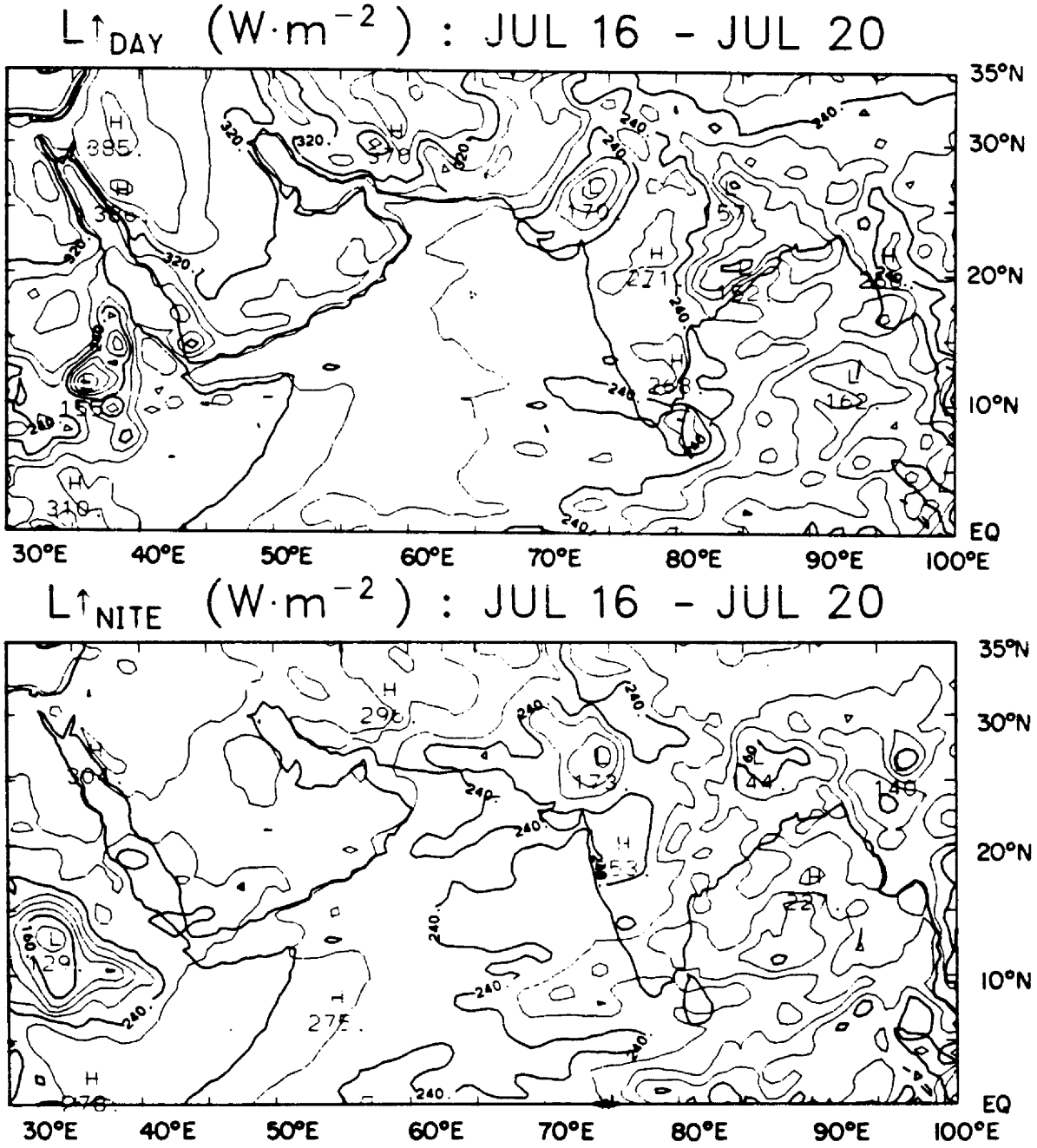

Fig. 3.41b. Same as Fig. 3.26b for July 16-20 (pentad 16).

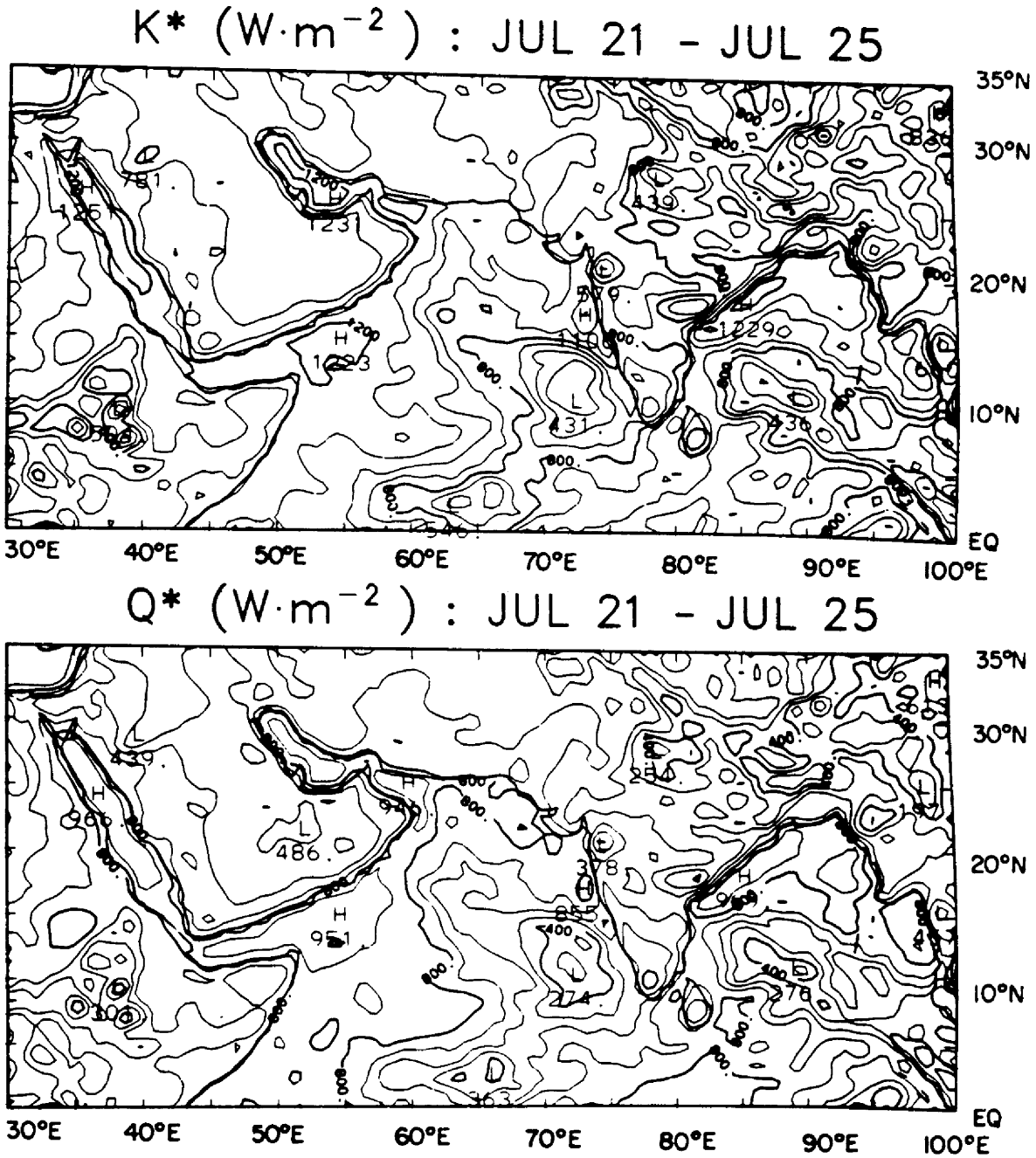

Fig. 3.42a. Same as Fig. 3.26a for July 21-25 (pentad 17).

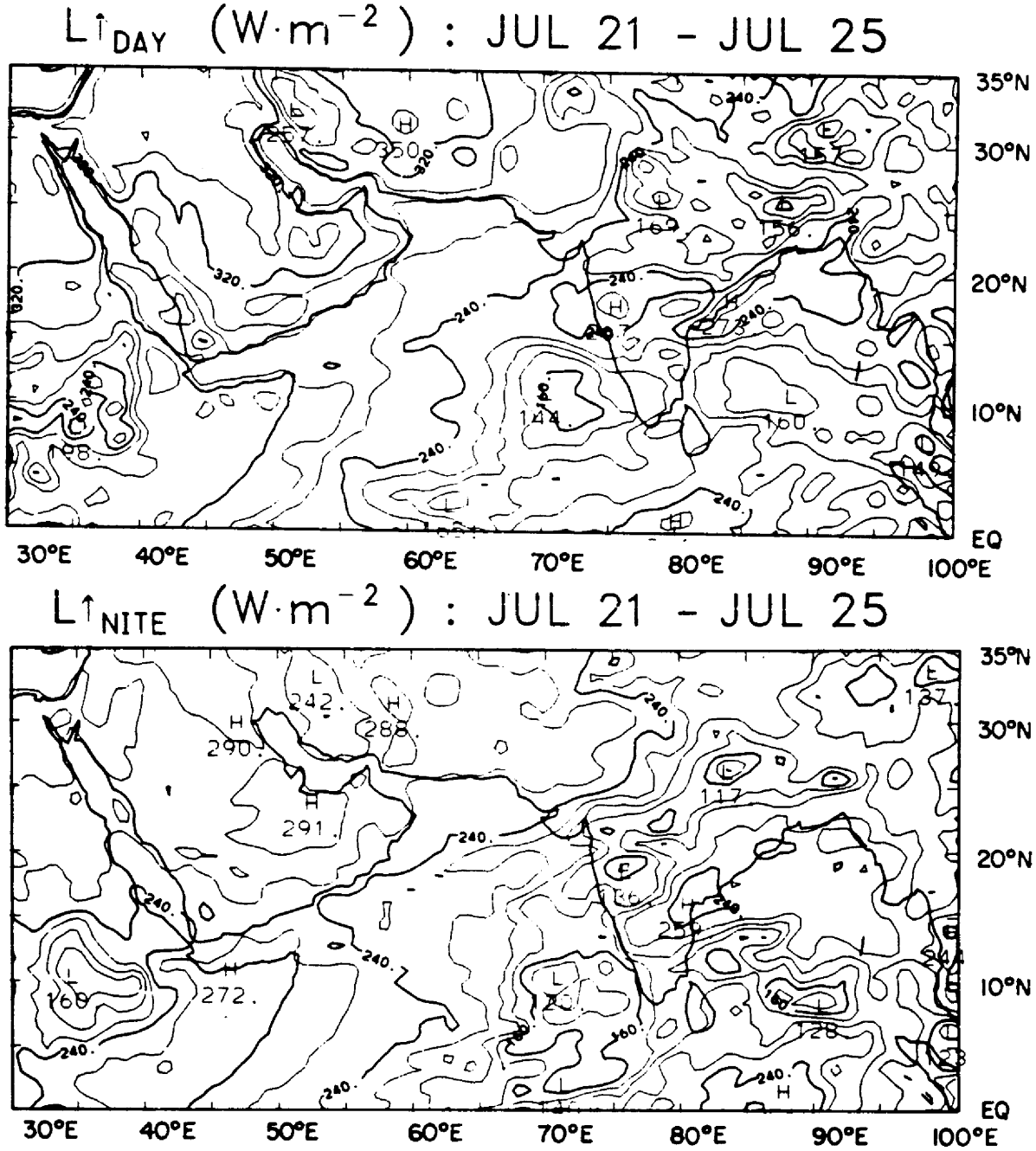

Fig. 3.42b. Same as Fig. 3.26b for July 21-25 (pentad 17).

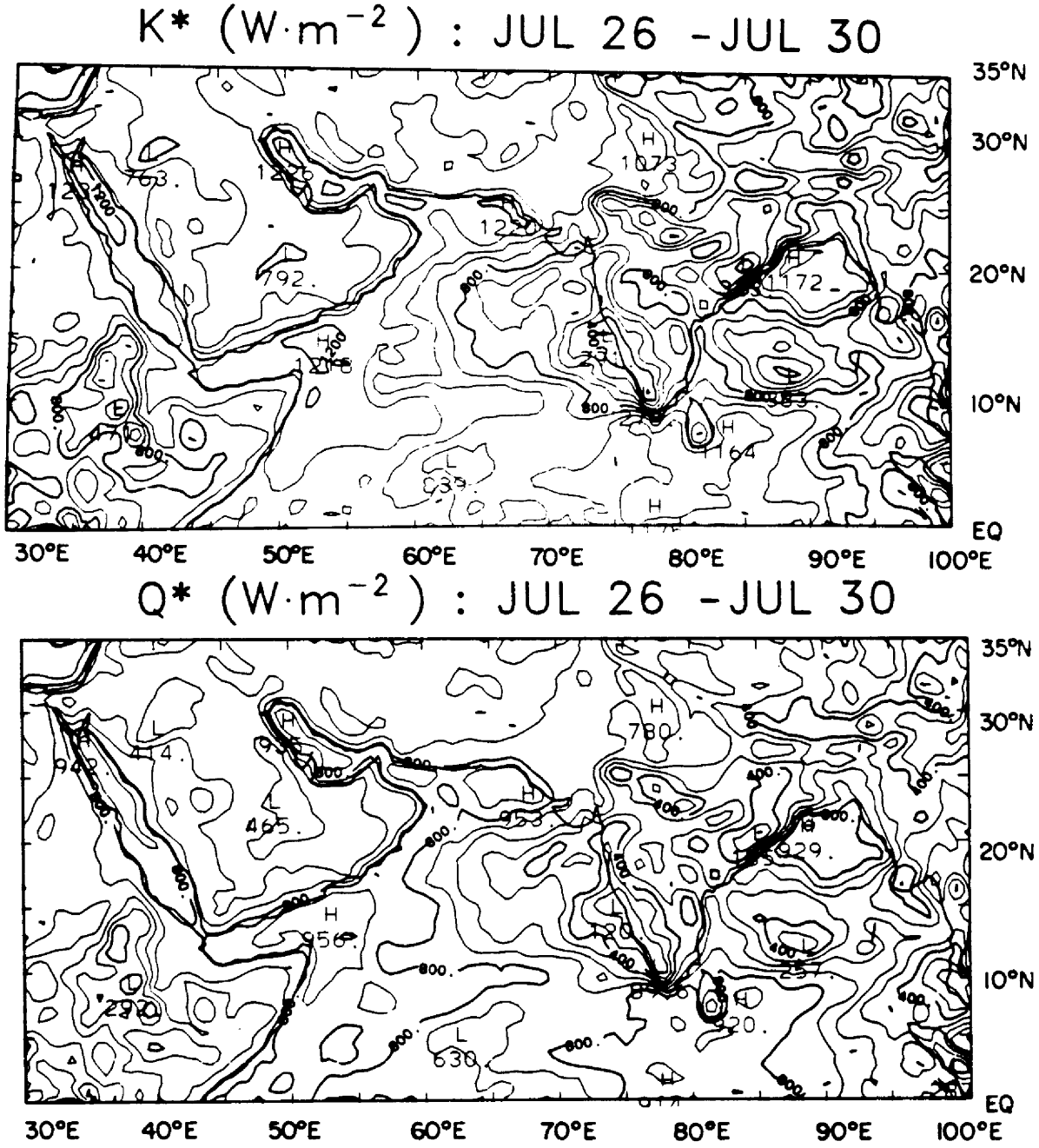

Fig. 3.43a. Same as Fig. 3.26a for July 26-30 (pentad 18).

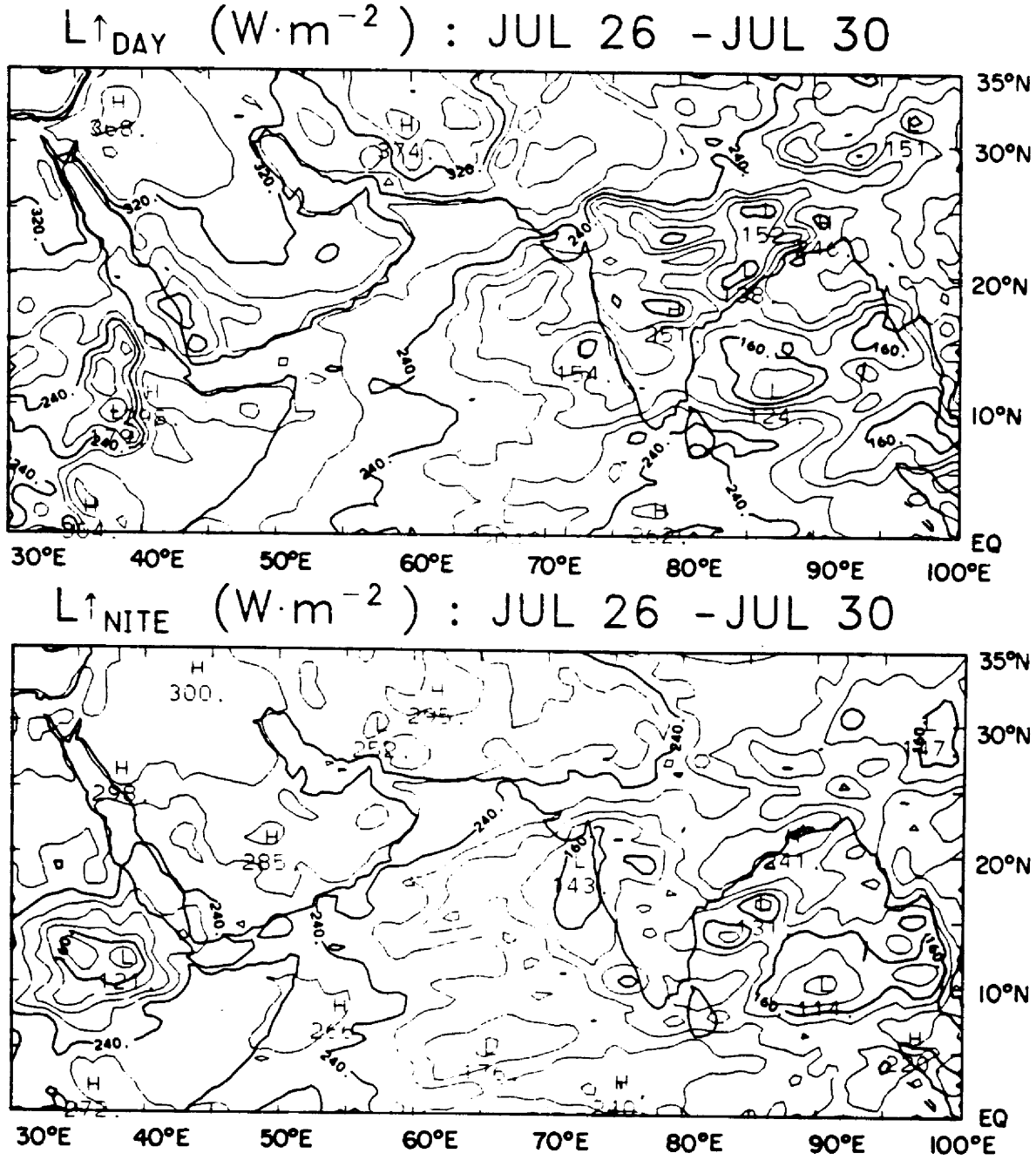

Fig. 3.43b. Same as Fig. 3.26b for July 26-30 (pentad 18).

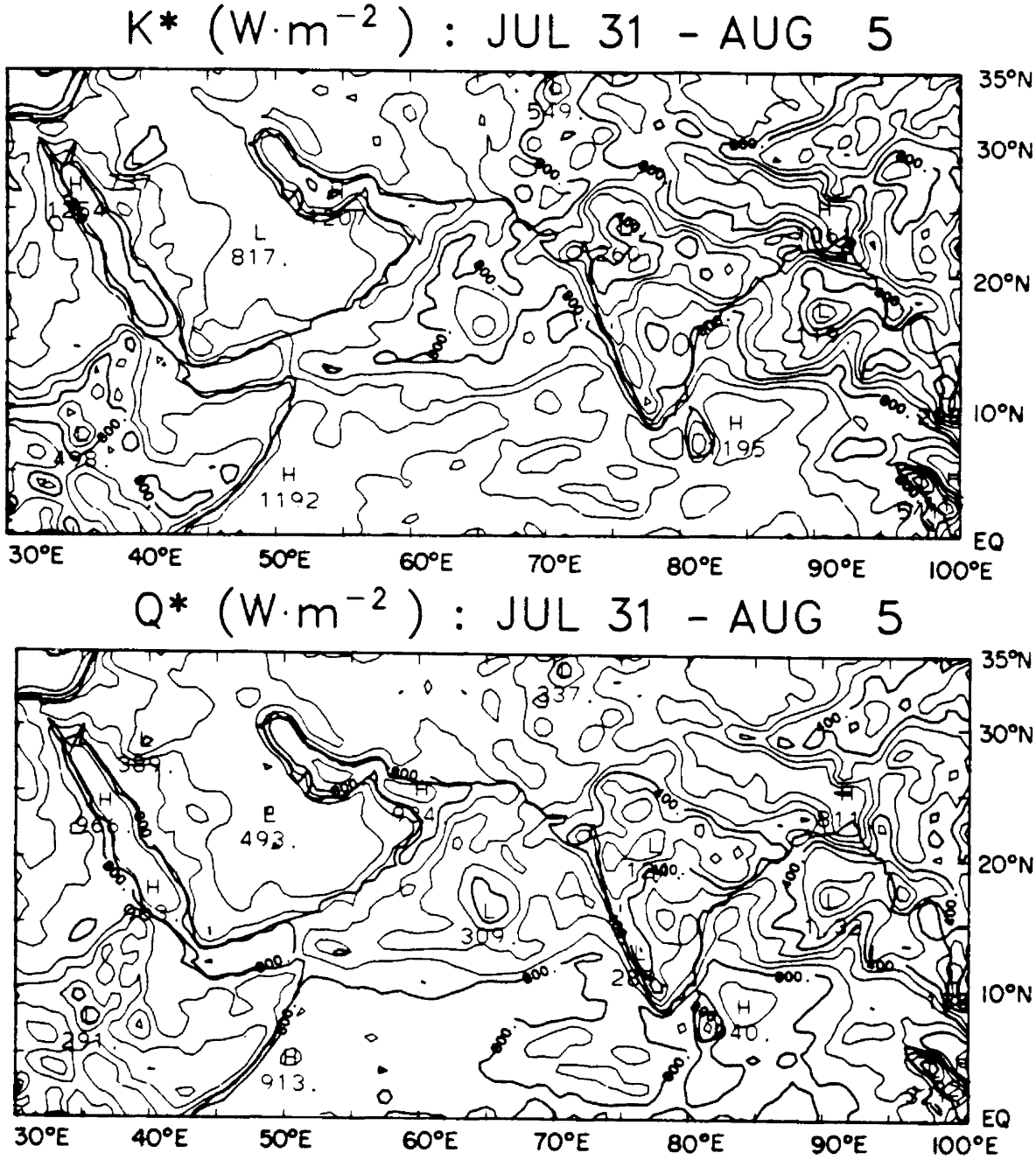

Fig. 3.44a. Same as Fig. 3.26a for July 31-August 5 (pentad 19).

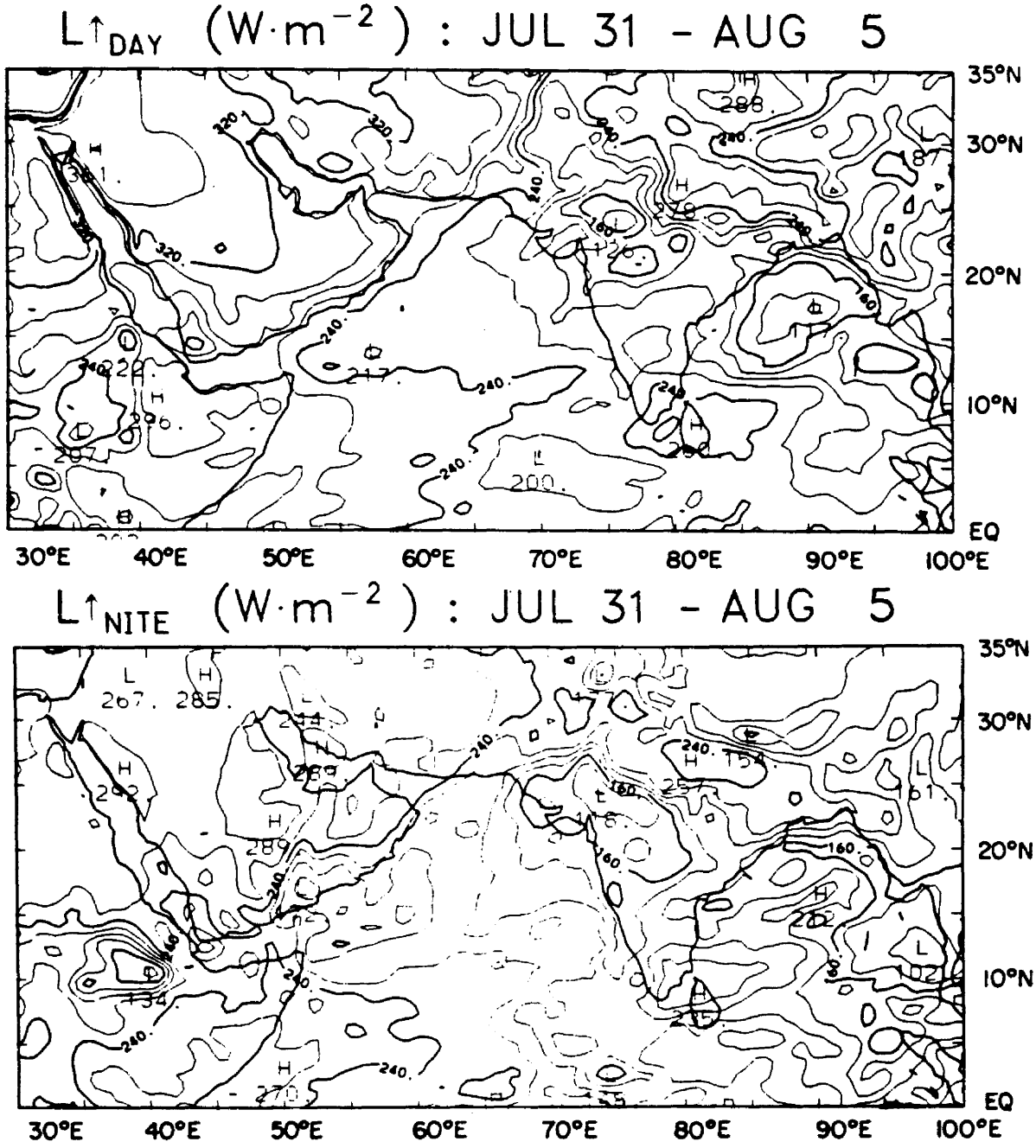

Fig. 3.44.b Same as Fig. 3.26b for July 31-August (pentad 19).

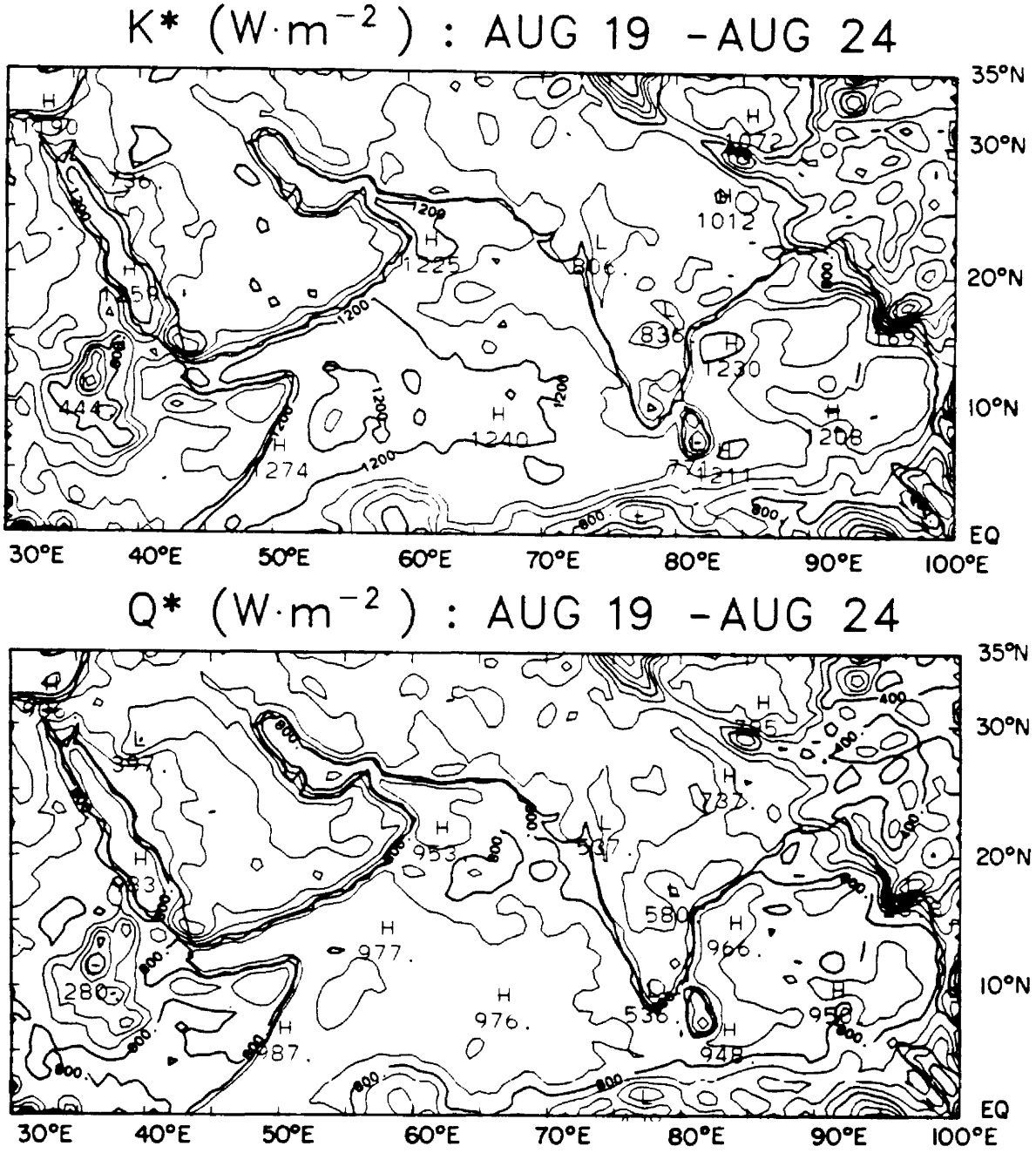

Fig. 3.45a. Same as Fig. 3.26a for August 19-24 (pentad 23).

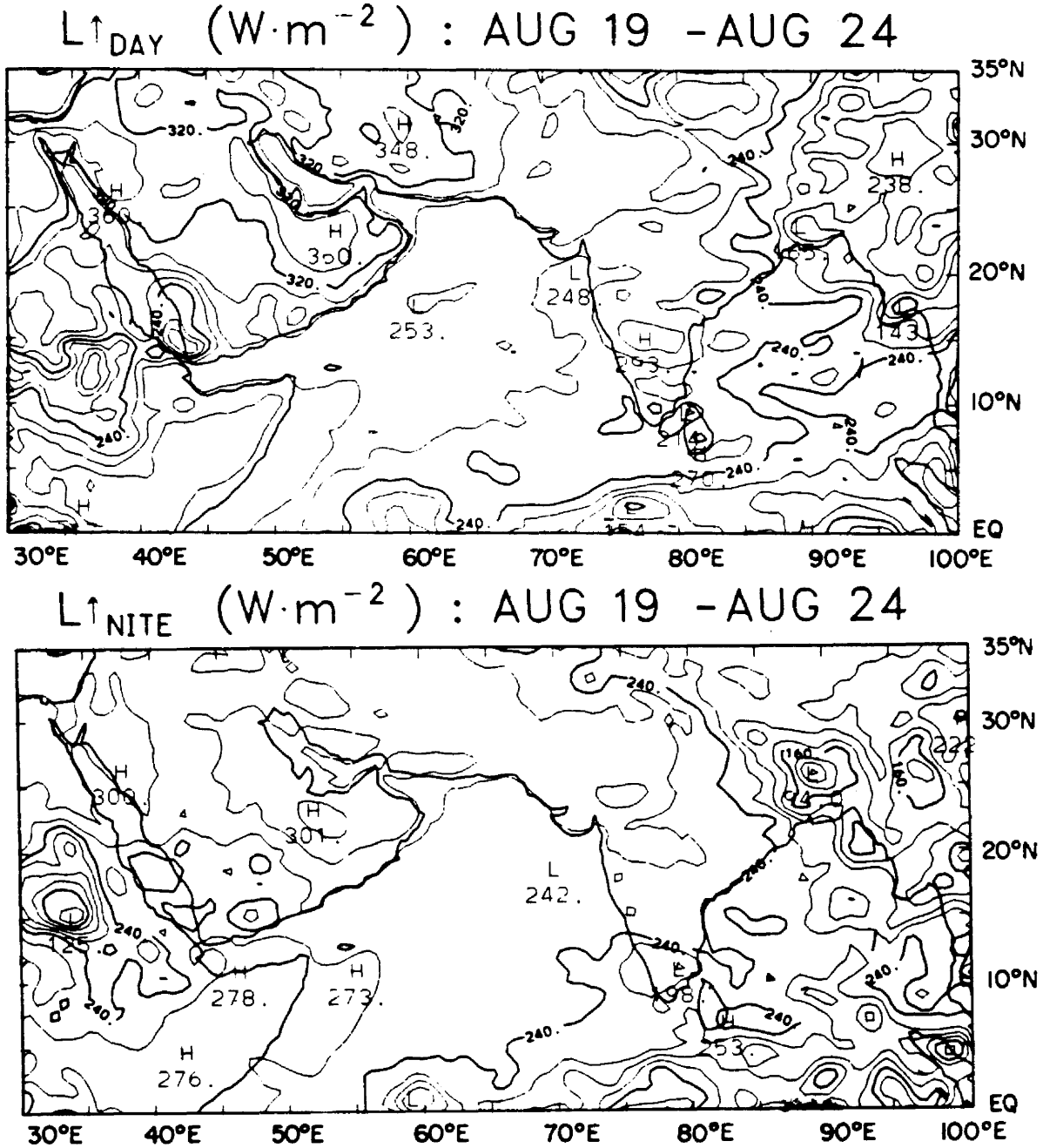

Fig. 3.45b. Same as Fig. 3.26b for August 19-24 (pentad 23).

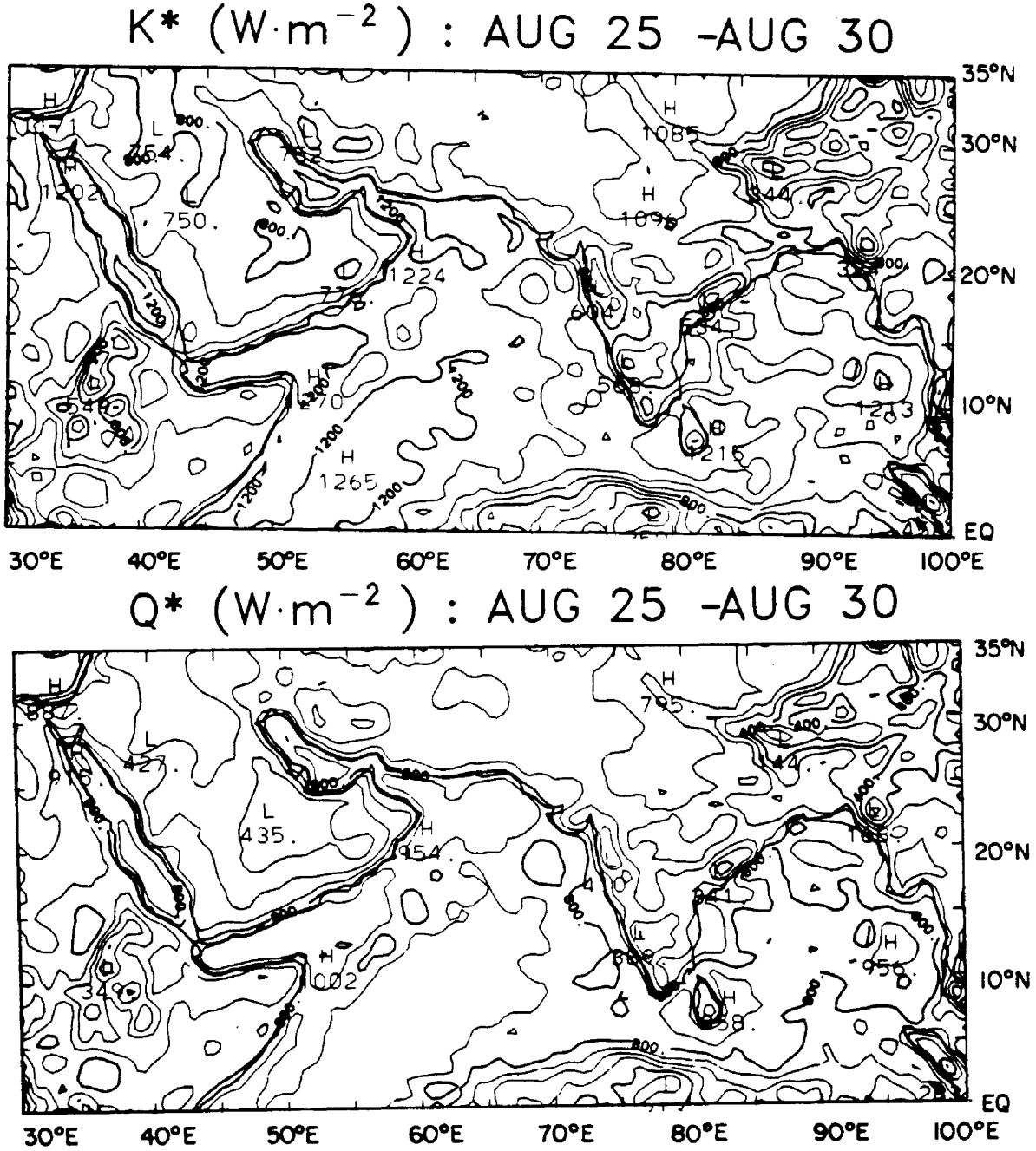

Fig. 3.46a. Same as Fig. 3.26a for August 25-30 (pentad 24).

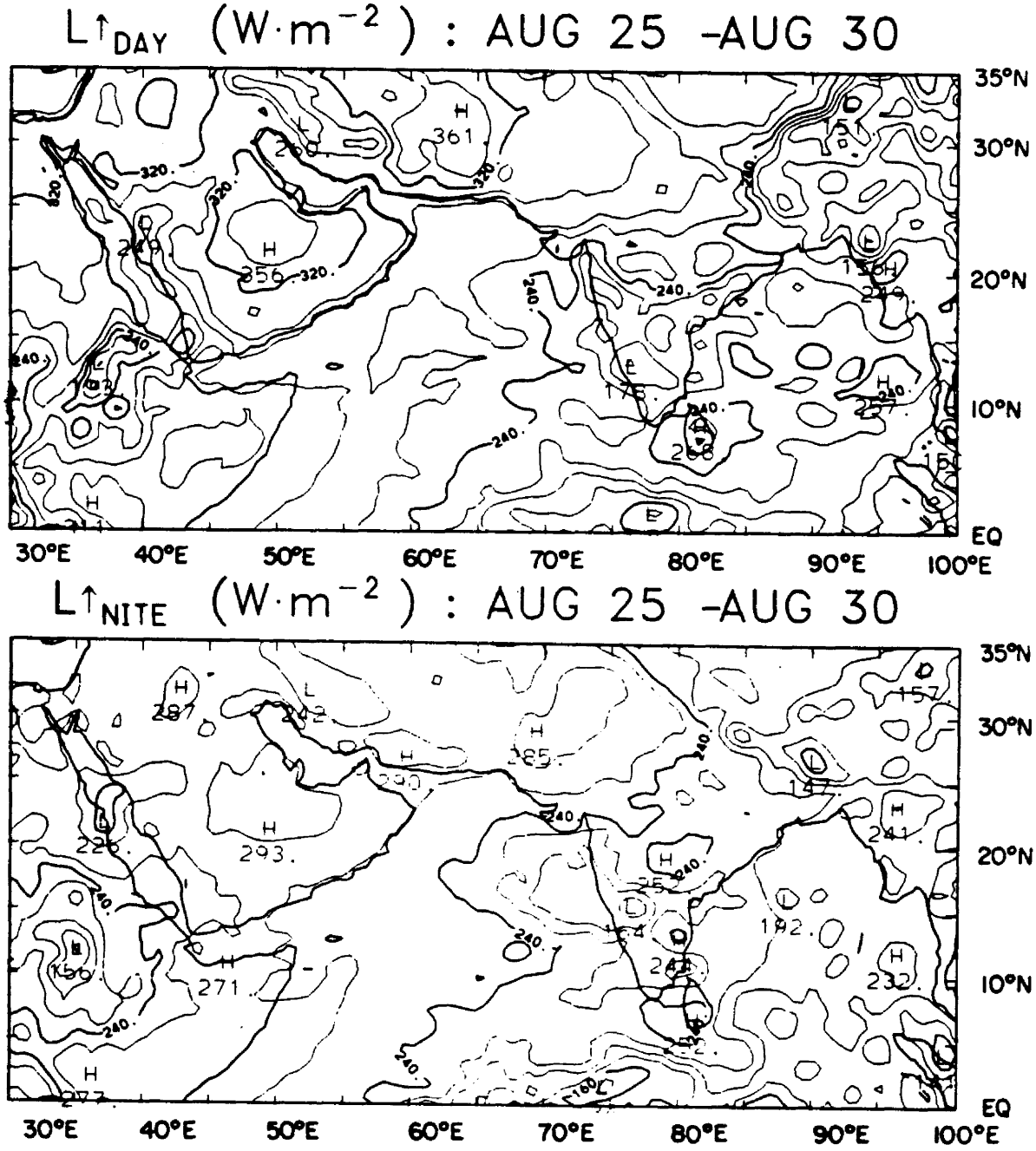

Fig. 3.46b. Same as Fig. 3.26b for August 25-30 (pentad 24).

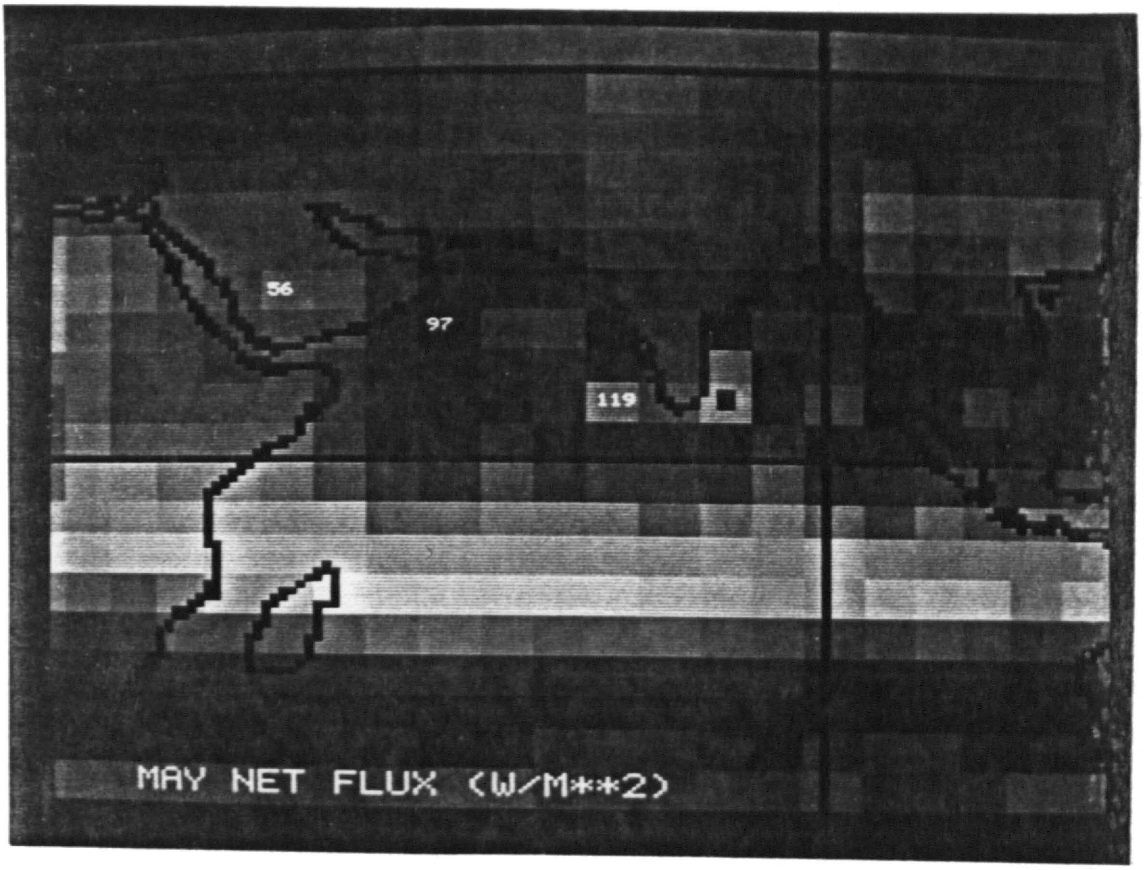

Fig. 3.47a. Mean monthly average of daily integrated net flux (Q*) for May, 1979 based on ERB/NFOV data.

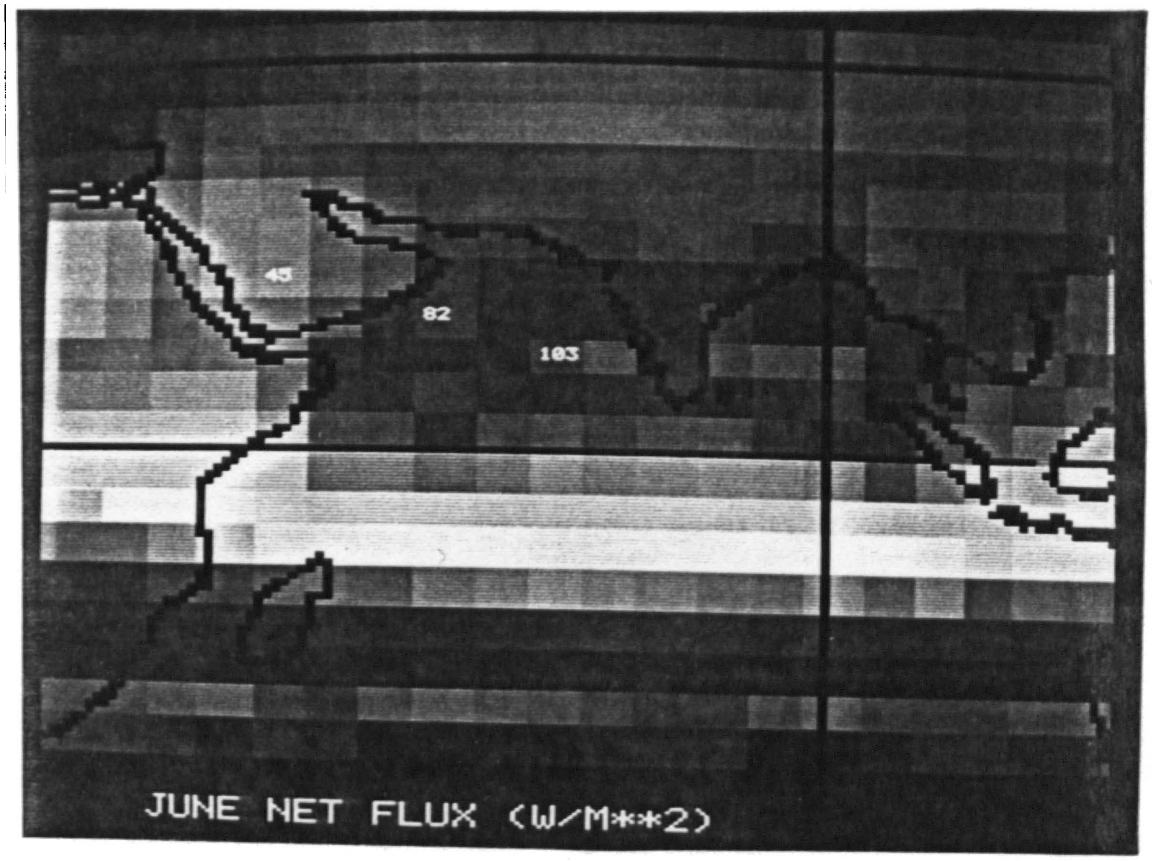

Fig. 3.47b. Same as Fig. 3.47a for June, 1979.

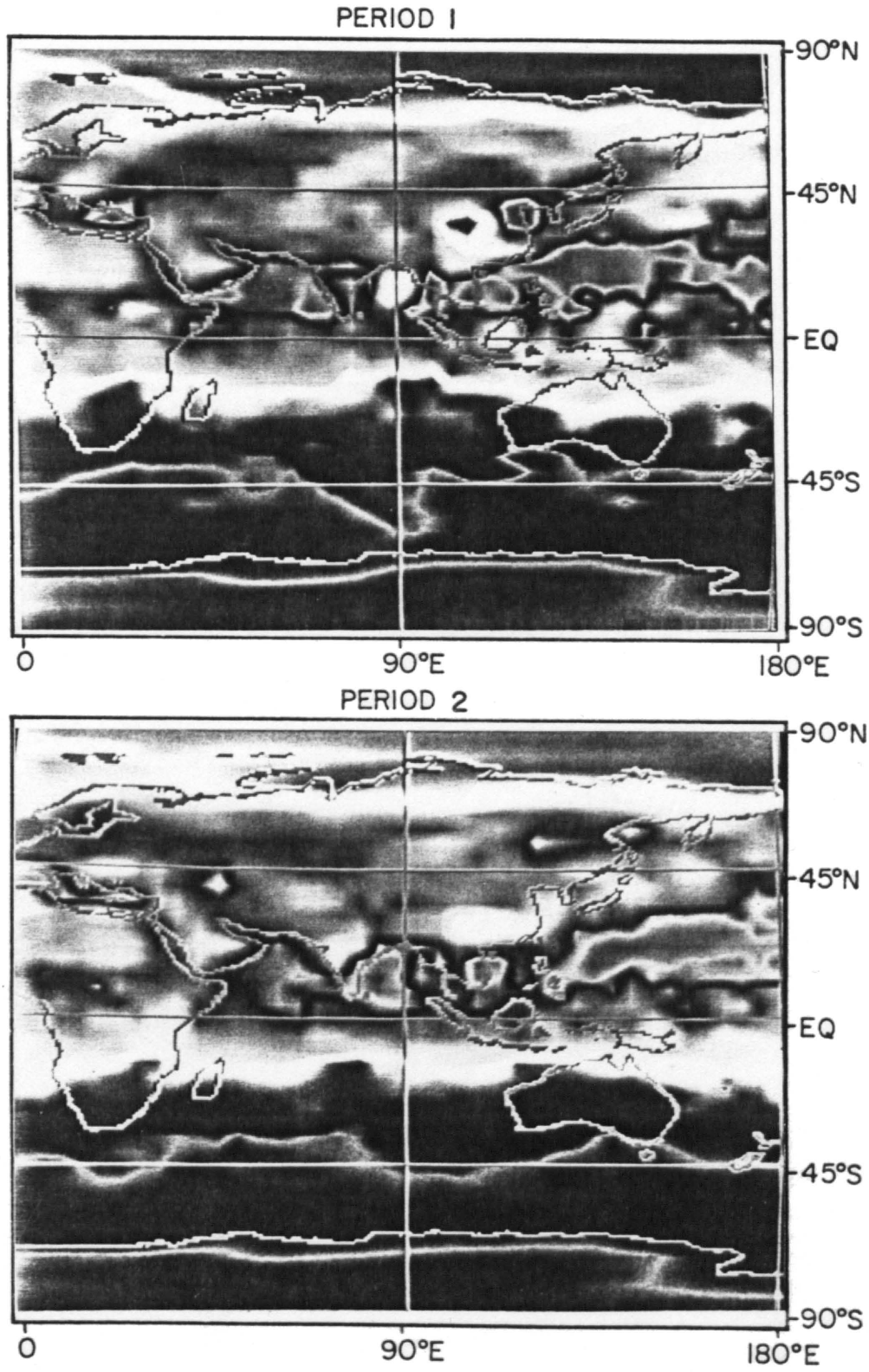

Fig. 3.48a. Mean six-day average of daily integrated net flux (Q*) from the ERB/NFOV measurements for May 7-12 (top-period 1) and May 13-18 (bottom-period 2) over the entire Eastern

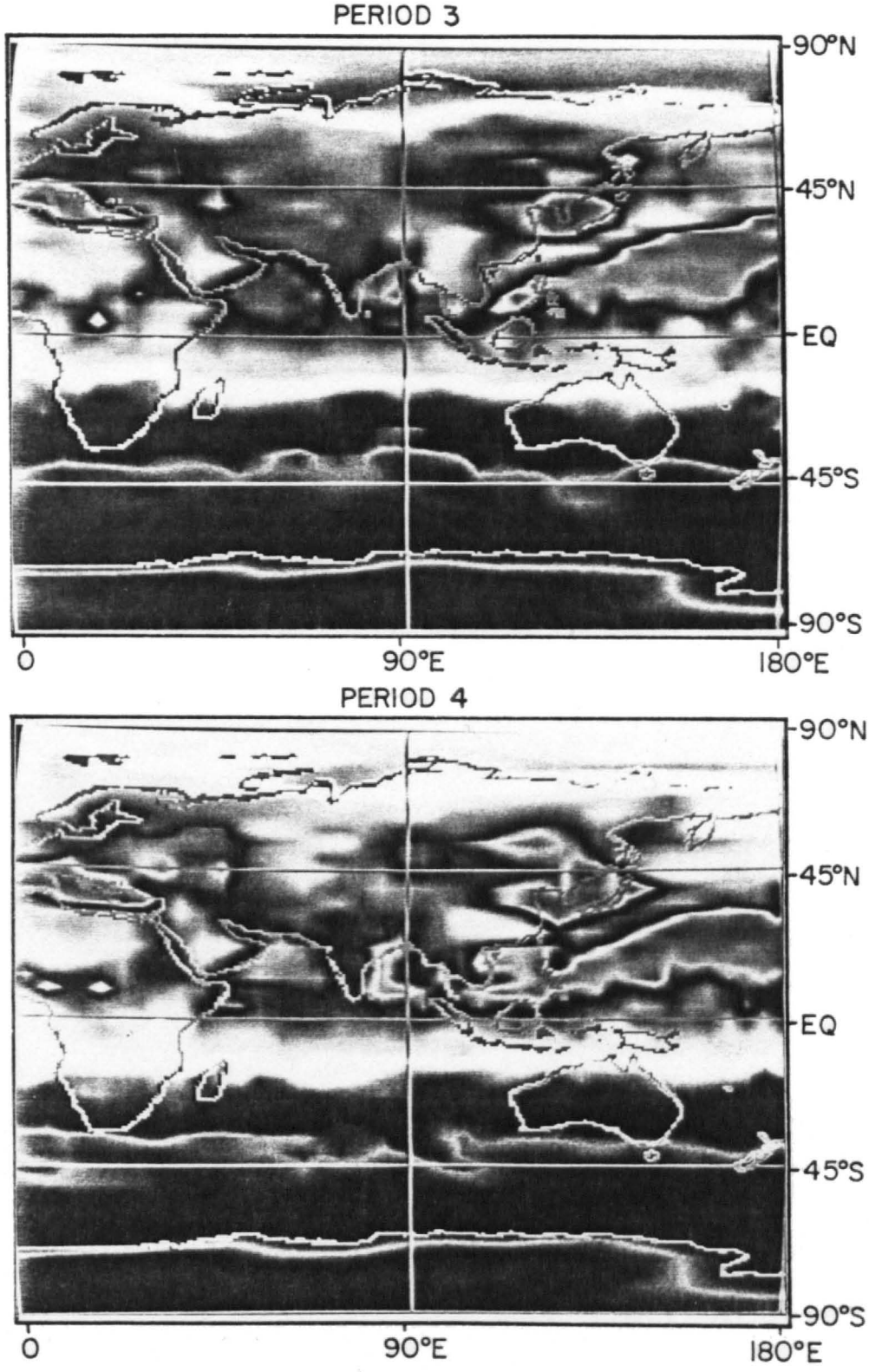

Fig. 3.48b. Same as Fig. 3.48a for May 19-24 (period 3) and May 24-30 (period 4).

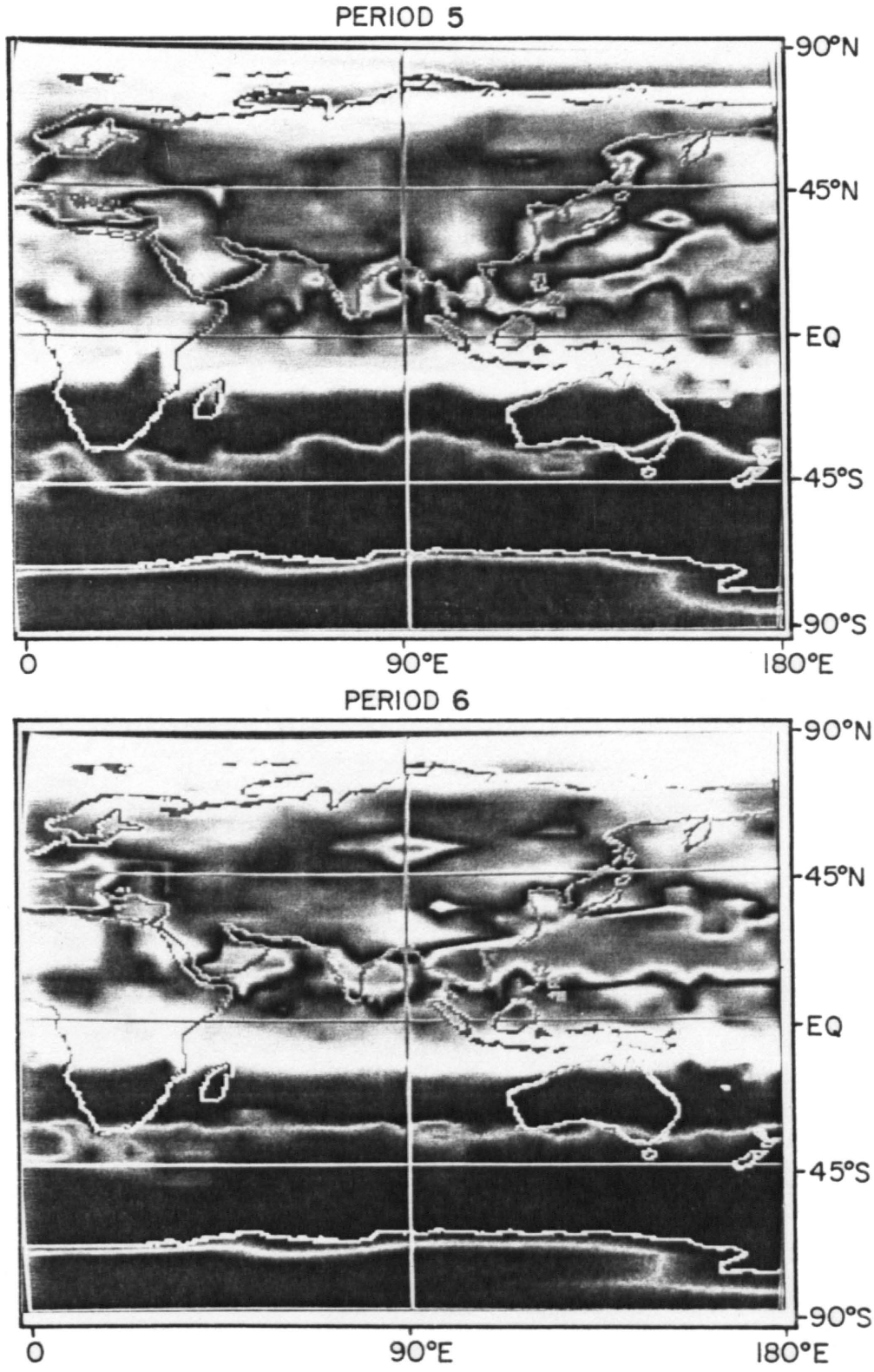

Fig. 3.48c. Same as Fig. 3.48a for May 31-June 5 (period 5) and June 5-10 (period 6).

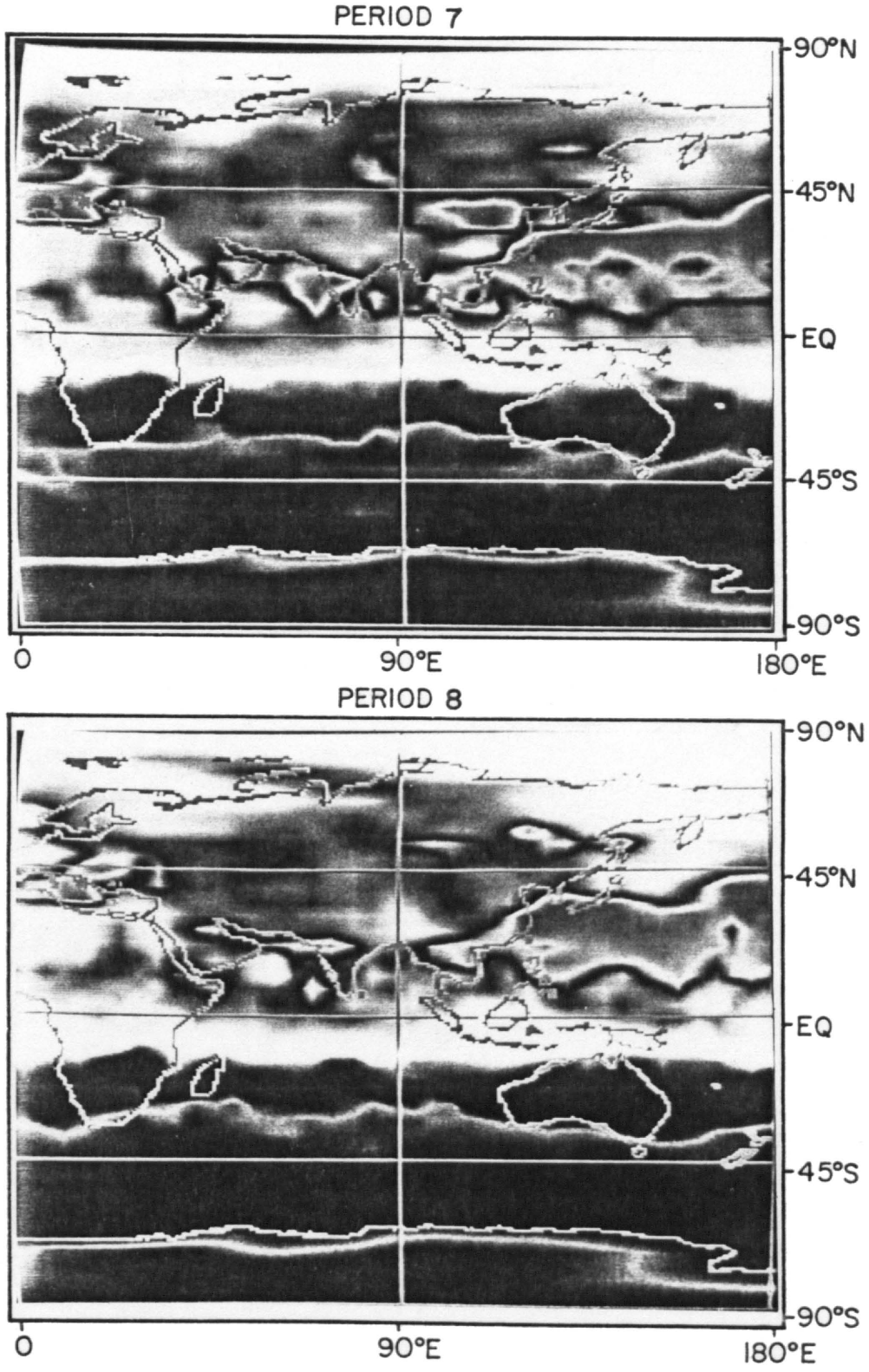

Fig. 3.48d. Same as Fig. 3.48a for June 12-17 (period 7) and June 18-23 (period 8).

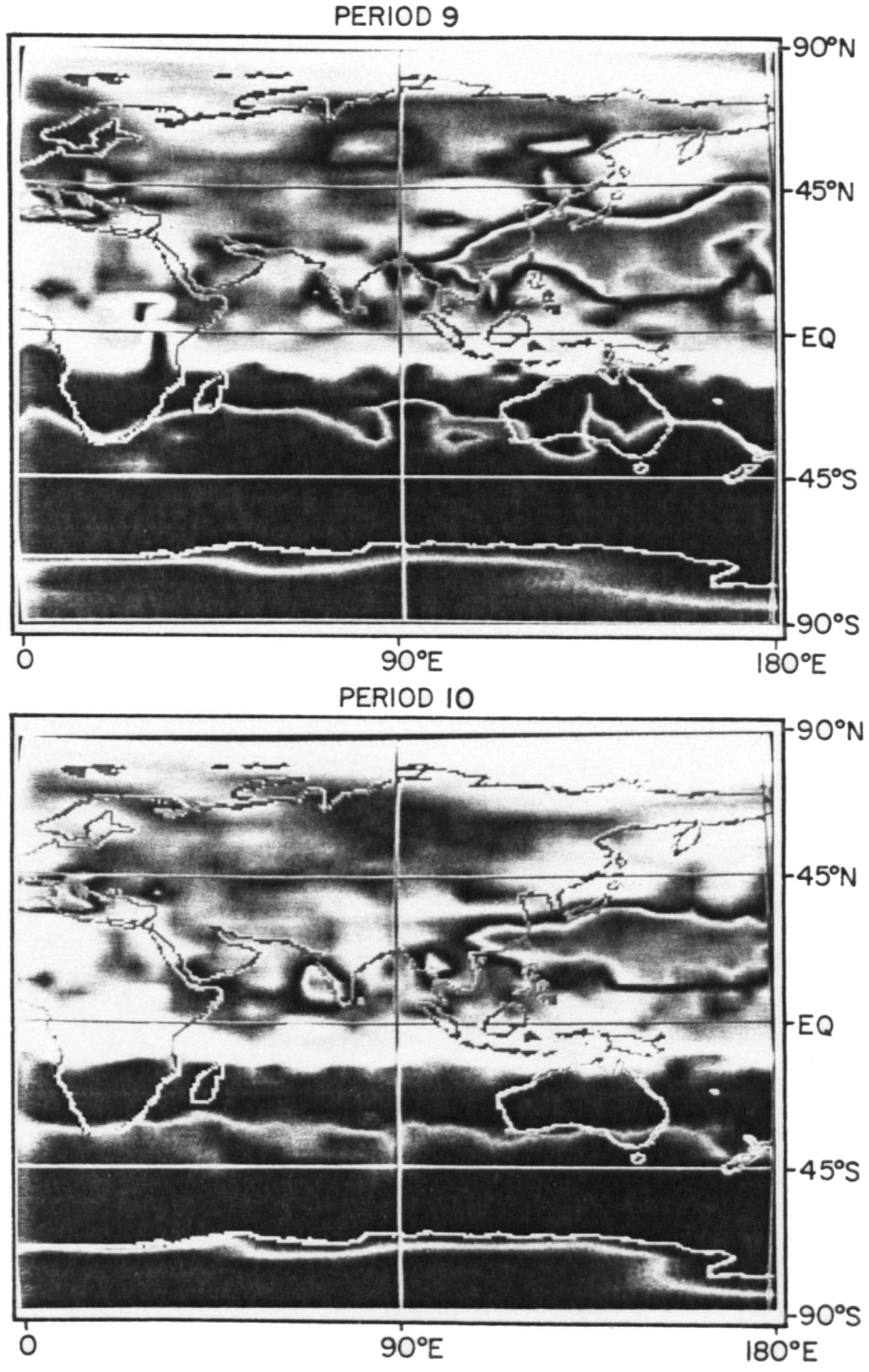

Fig. 3.48e. Same as Fig. 3.48a for June 24-29 (period 9) and June 30-July 5 (period 10).

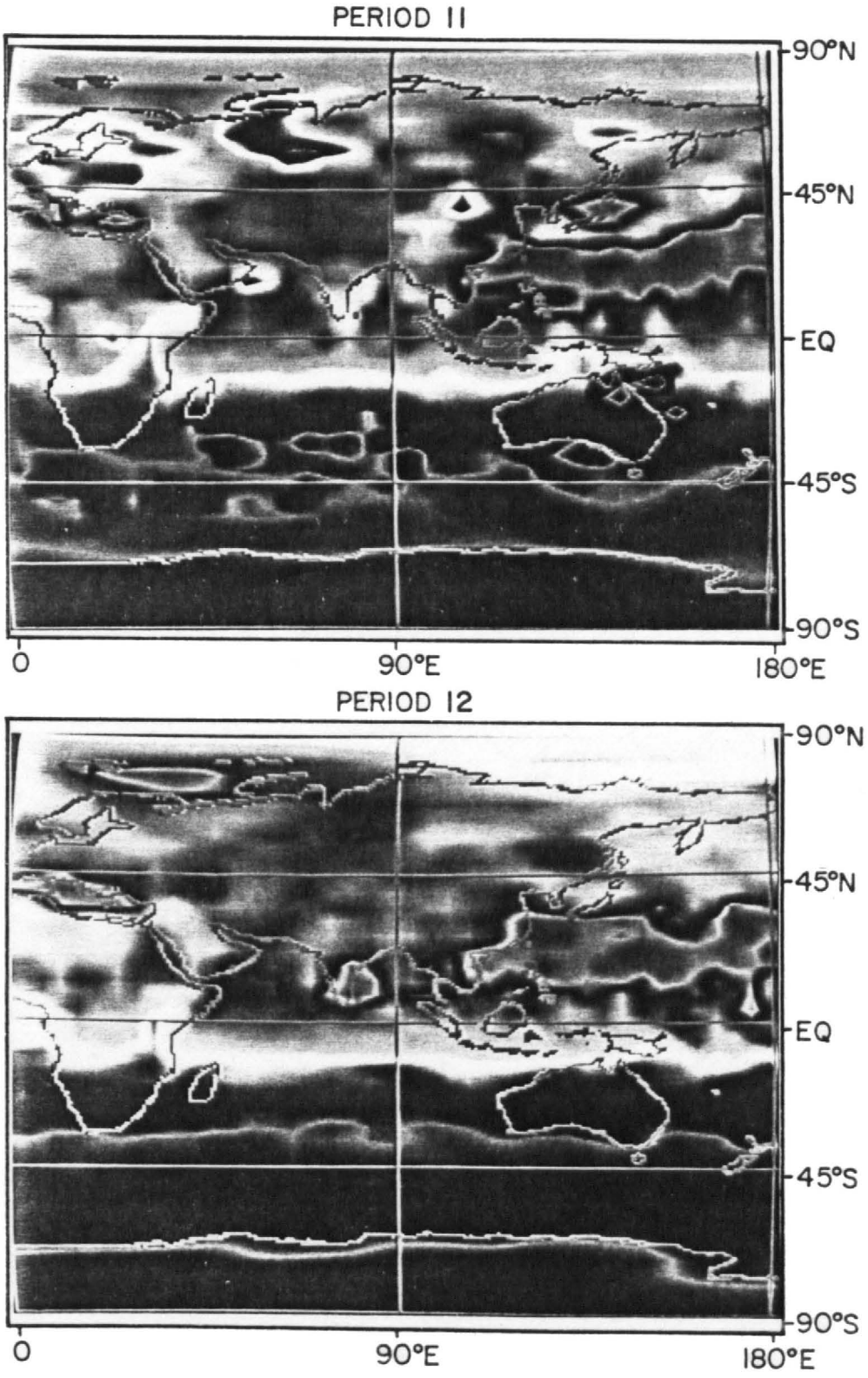

Fig. 3.48f. Same as Fig. 3.48a for July 6-11 (period 11) and July 12-17 (period 12).

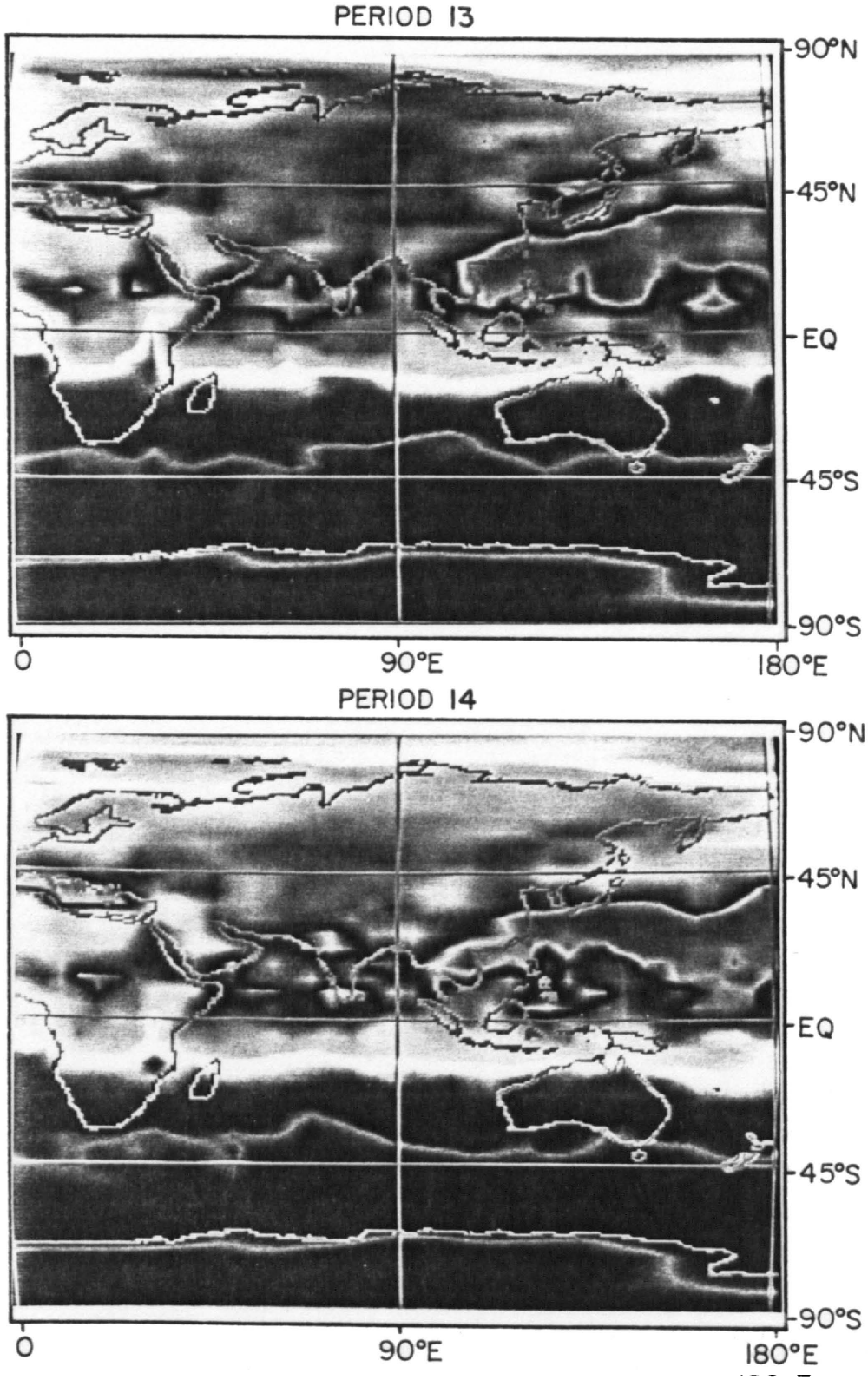

Fig. 3.48g. Same as Fig. 3.48a for July 18-23 (period 13) and July 24-29 (period 14).

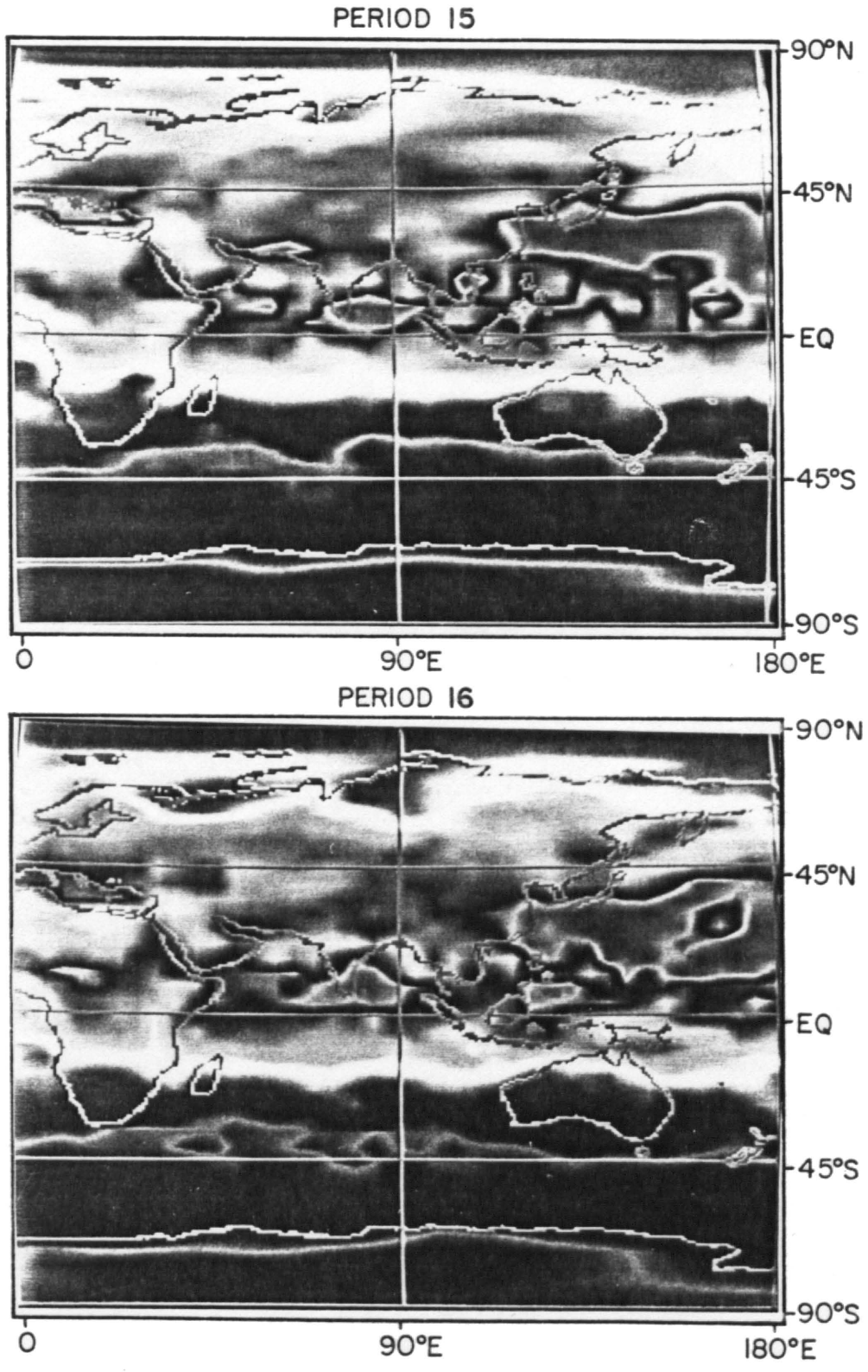

Fig. 3.48h. Same as Fig. 3.48a for July 30-August 4 (period 15) and August 5-10 (period 16).

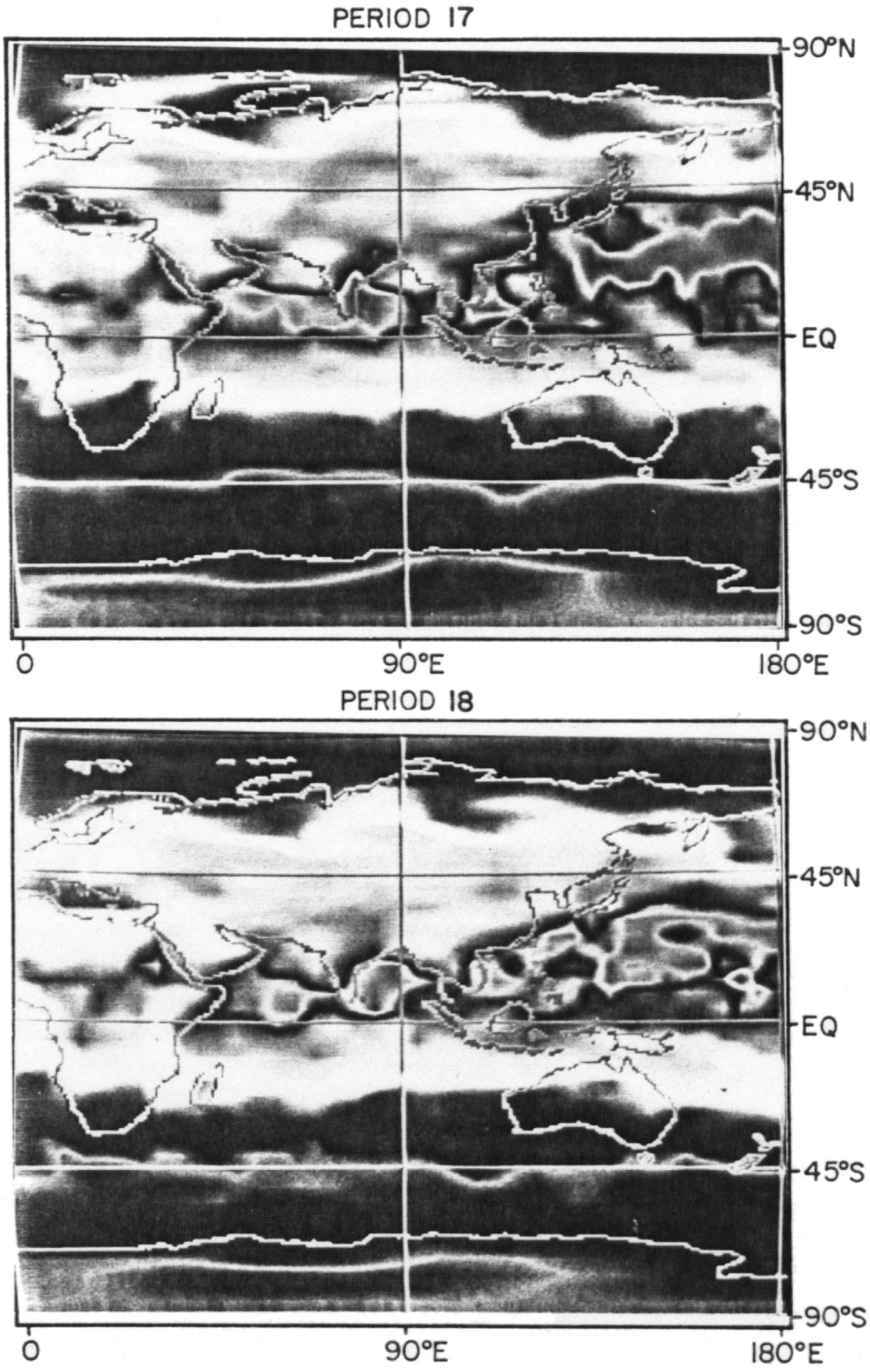

Fig. 3.48i. Same as Fig. 3.48a for August 11-16 (period 17) and August 17-22 (period 18).

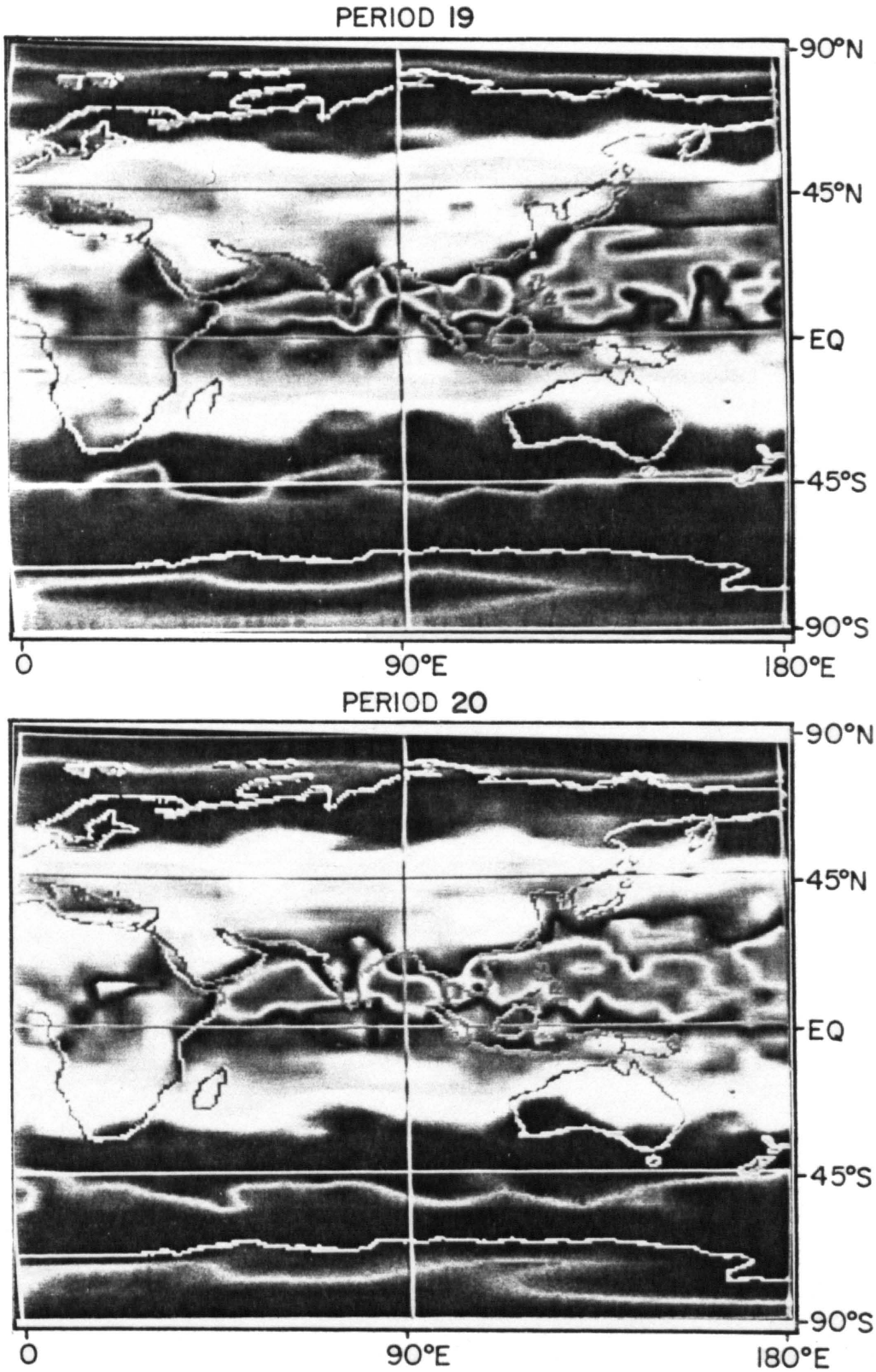

Fig. 3.48j. Same as Fig. 3.48a for August 23-28 (period 19) and August 29-September 3 (period 20).

averaged fields of $\overline{Q^*}$ over a much larger region, are helpful in assessing the monsoon influence on the broader space scales. The spatial grid scale of these maps is approximately $5^{o}x5^{o}$. The relationship between color and the flux scale is given in Table 3.6. Figures 3.48a-j are provided as a means to intercompare the patterns in instantaneous Q*, derived from TIROS-N, to the present best estimates of daily averaged net radiation ($\overline{Q^*}$) available from the NASA radiation budget program. These maps, however, are not nearly as detailed as the AVHRR maps. It is noted that a potential application of this sequence of ERB/NFOV $\overline{Q^*}$ maps is in the detection of meridional interruptions in the Northern Hemisphere sub-tropical radiation pattern extending from the Arabian Sea into the central Pacific. Note the cellular pattern of the large positive net regions (red). Once monsoon onset begins (third week of June) and up to the end of July, the +80 to +140 $W \cdot m^{-2}$ contour is largely suppressed west of South East Asia. Then during August, the cellular pattern is re-established over the Arabian Sea, India, Bay of Bengal, and South East Asian sector.

3.5.1 Five-Day Averaged Mean Fields

During May, well prior to monsoon onset (June 10-20), the monsoon domain undergoes a variety of major developments; refer to Figs. 3.26-3.46. The first easily recognizable feature during this month is the orientation of the radiation exchange isopleths in the central domain. During the first two pentads, the tilt is from northeast to southwest, due to a major cloud system in the south of the Bay of Bengal, and the equatorial MCZ decaying away to the west. By pentad 4, the orientation lines are tending to align zonally, interrupted by continental heating, and by pentad 5 (May 22-26), there is even slight reversal (southeast to

TABLE 3.6

Color Enhancement Table for Figure 48

Color Range	Net Flux Range (W m^{-2})
Dark Red to Light Red	+140 to + 80
Dark Brown to Light Yellow	+ 80 to - 10
White to Grey	- 10 to - 20
Light Green to Dark Green	- 20 to -140
Light Blue to Dark Blue	-140 to -200

northwest orientation). The Arabian Sea has remained virtually cloud free throughout May with the exception of a disturbance moving off of Somalia that has penetrated the southwest corner during pentad 2. By the end of May (pentad 6), however, a well established northward propogating equatorial MCZ has formed which is beginning to penetrate the southern reaches of the Arabian Sea, particularly in the southeast corner.

During this period, the South East Asian (SEA) Monsoon has become established, moving up through Thailand and Burma steadily (note pentad 3) and becoming well established in central Burma by the end of May. At Bay of Bengal longitudes, the early May Indian Ocean cloudiness responsible for the orientation of the isopleths, has dissipated by pentad 3. At this point the eastern region of the Bay of Bengal becomes obscured and remains so throughout May as the SEA Monsoon advances up the west coast of Burma. The fairly quiescent zone, between 30^{o}-35^{o}N, is only interrupted during the second week by westerly disturbances. The Sub-continent of India undergoes a vigorous surge of cloudiness during the third pentad due to the northwestward propogation of a tropical storm over the southern portion of India and arising from the early May disturbance in the southern Bay of Bengal.

During June, the pentad maps are excellent graphics for monitoring monsoon progress. From pentad 7 (June 1-5) to pentad 9 (June 11-15) we see the very dramatic establishment of the monsoon MCZ. Immediately prior to the metamorphosis of this feature, the SEA Monsoon is operating to create the early stages of a latent heat source over Bangladesh, Eastern India, and Northwest Burma, centered at approximately 23^{o}N, 97^{o}W, and tied to the flank of the southern extent of the Himalayas

(Bhutan). This latitude is only 3^{o} to the north of the coordinate T. Murakami (1974) used for the oscillating latent heat source in his earlier theoretical study concerning diabatic forcing of steady and transient waves.

During pentads 9 and 10 we see the impact of the onset vortex in producing a disturbance zone all the way from the southwest Indian coast, across the Arabian Sea to the northwest, and penetrating the southeast coast of Oman; see Krishnamurti, et al. (1981) for a study of the SMONEX onset vortex. After pentad 8 (June 6-10), the solar insolation source to the Arabian Sea is dramatically reduced. By pentad 11 the monsoon is well established over India; there is also the appearance of a new equatorial MCZ.

The Bay of Begal, which was almost totally devoid of clouds by the end of May, is quickly obscured. First in the east by the rapid advance of the SEA Monsoon to its northernmost limit, and then by the northward surge of the equatorial MCZ into the central bay regions, and finally the appearance of a major monsoon depression toward the end of June (pentad 12).

By the end of June, a major zone of relative minimum in the net radiation term extends from coastal Burma, across the northern Bay of Bengal through north central India and then arcing back south into the eastern and central Arabian Sea. The pentad 12 maps (Figs. 3.37a-b) portray the dominance of the monsoon trough; see Keshavamurty and Awade (1970) and Ananthakrishnan (1977) for a discussion of the monsoon trough and monsoon rains. The mean gradient in instantaneous net radiative exchange across the trough axis at noon, from edge to center, is $\approx 400\ W \cdot m^{-2}$.

Major anomalies in the radiation fields continue to appear in July (pentads 13-18) and August (pentads 19, 23, 24) after the monsoon has become established. A major cloud feature develops over the southwest Indian coast during the first pentad in July (pentad 13), as the Bay of Bengal tends to clear from the south. By the pentad 15 (July 11-15), the 800 $W \cdot M^{-2}$ contour in Q* has moved into the central Arabian Sea as mostly high cloud is present. It is interesting to note at this point that the orientation of the Q* isopleths are virtually north-south, which is indicative of the positioning of the water vapor and high cloud fields over Arabian Sea longitudes; see Godbole and Kelkar (1971) and Kelkar and Godbole (1970) for discussions concerning the control of water vapor and cloud on radiative cooling in the monsoon atmosphere.

The uniformity in the monsoon trough, evident through pentad 15, is rapidly transformed in pentad 16 into two relative minima; one in northwest India, the other over the central east coast. The northwest feature arises from a relatively stationary mid-tropospheric cyclone [see Krishnamurti and Hawkins (1970), Mak (1975, 1983), Carr (1977) and Brode and Mak (1983)]. Pentad 16 is associated with the first 'break' monsoon of the season [reported by Sikka and Grossman (1980)], which persisted from July 16 to July 21.

In pentad 17 a new monsoon MCZ makes its appearance but not until the July 31-August 5 period (pentad 19), is the dominant relative minimum band (evident at the end of June), reestablished. The missing period from August 6-18 (pentads 20-22) is unfortunate because the monsoon undergoes another major 'break' on August 13 that persists throughout August 27. Fortunately, enough 'break monsoon' coverage is included past August 18 so as not to lose the impact in the meridional

averages (see following sub-section). The final two pentads in August (pentads 23-24) reveal the reestablishment of an equatorial MCZ and a recovery of the radiation patterns over the Arabian Sea to conditions somewhat similar to pre-monsoon conditions.

3.5.2 The Time-Latitude and Time-Longitude Sections

Possibly the most instructive manner in which to study radiative forcing of the SW Monsoon is through the use of the classical time-latitude and time-longitude sections. For the application here, this involves the creation of zonal and meridional averages over the latitudinal extent (35 degrees) and longitudinal width (70 degrees) of the TIROS-N monsoon domain. Daily zonal and meridional averages are created each day at the 0.5 degree RADBUD retrieval scale.

Pictorial views of the resultant matrices, created for zonal average albedo and daytime flux equivalent temperature parameters, are provided in Figs. 3.49a-b. The analagous matrices for the meridional case are given in Figs. 3.50a-b. These figures portray quite readily that there are well organized, propagating features in the shortwave and longwave radiation budget fields. But how are these fields manifested in terms of net radiative convergence into the monsoon? Figures 3.51 and 3.52 are used to illustrate for the zonal case.

In Fig. 3.51 we see the pattern of solar forcing to the radiation budget that accompanies the averaging strategy. Note that it is symmetric around day 176 (June 25), which corresponds exactly to the monsoon onset surge in the Indian Sub-continent albedo signal (see Sub-section 7.2).

The pattern of radiative forcing, or net radiative convergence, is given in Fig. 3.52. This is a smoothed rendition produced by applying a

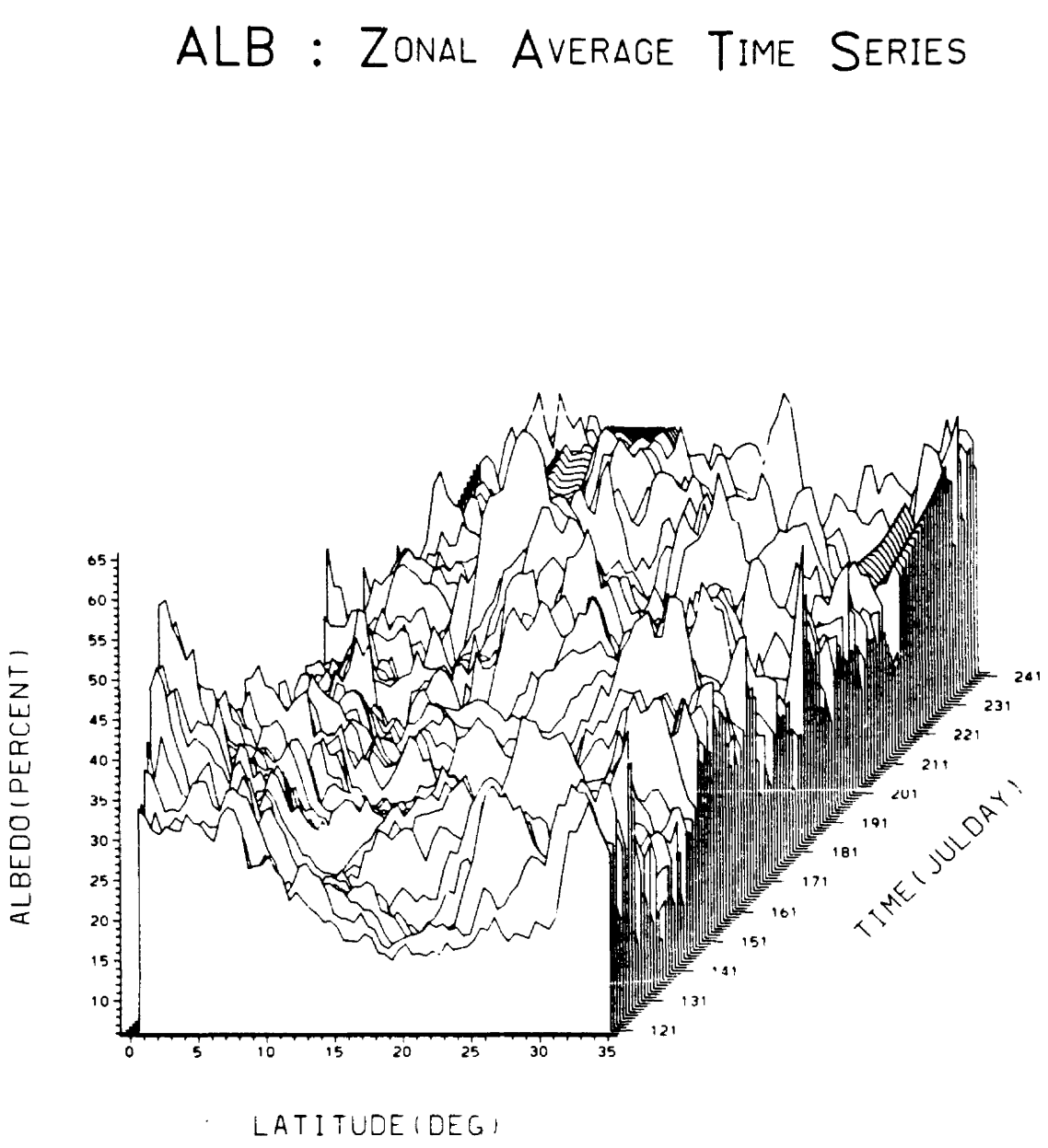

Fig. 3.49a. Zonal average time series of albedo (0.5 degree resolution) over the TIROS-N SMONEX domain.

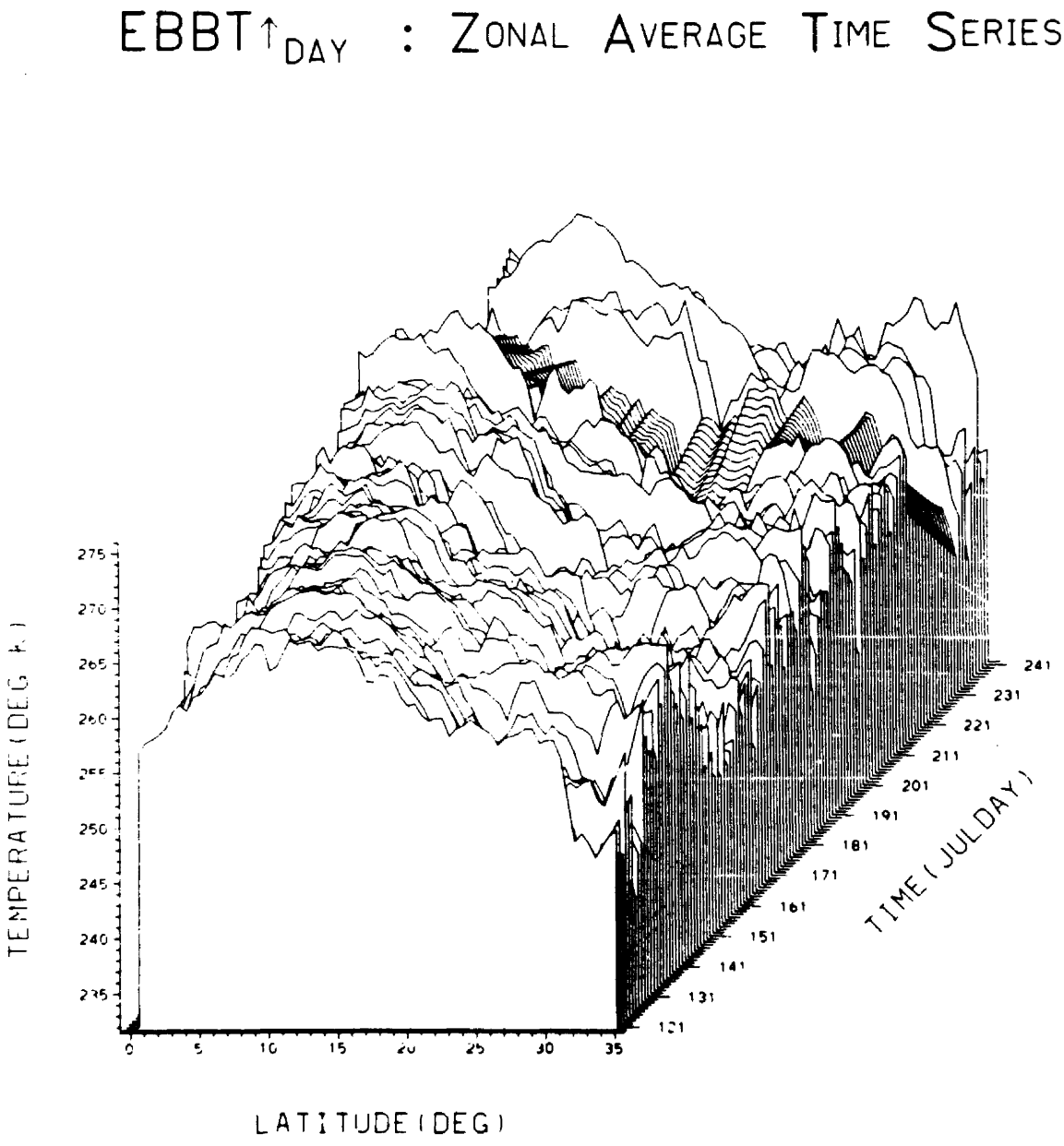

Fig. 3.49b. Same as Fig. 3.49a for daytime flux equivalent temperature [EBBT↑(day)].

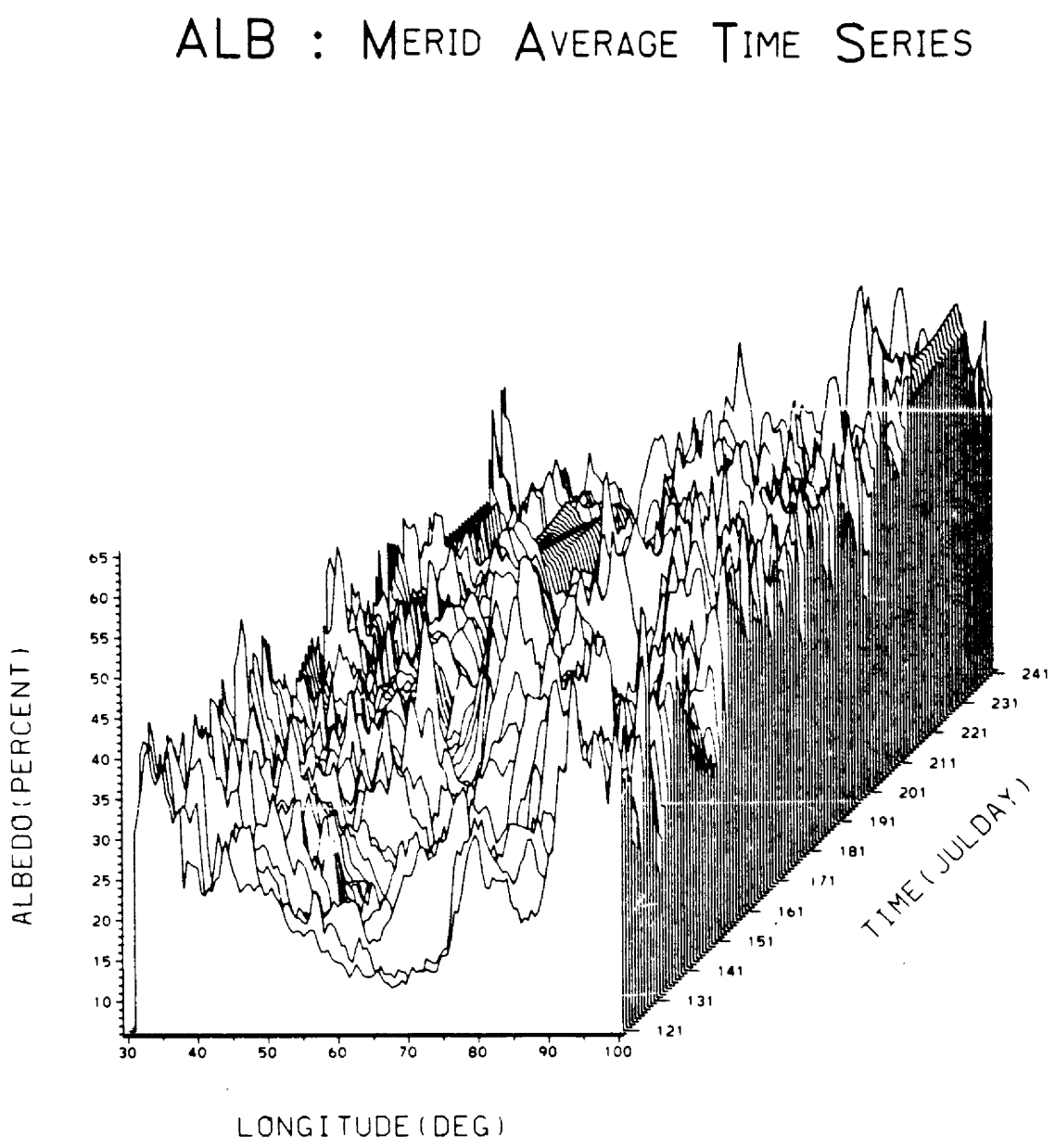

Fig. 3.50a. Meridional average time series of albedo (0.5 degree resolution) over the TIROS-N SMONEX domain.

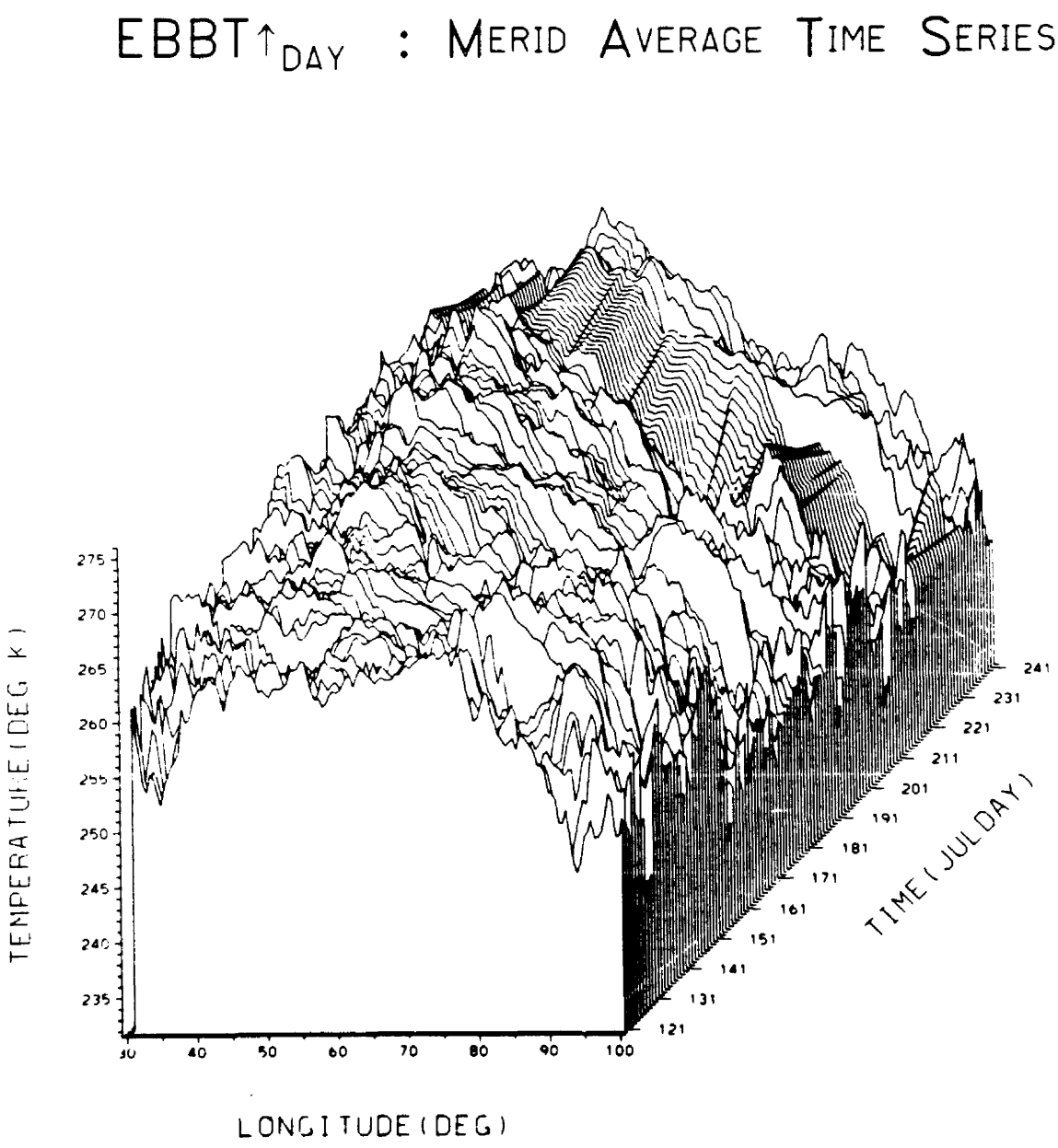

Fig. 3.50b. Same as Fig. 3.50a for daytime flux equivalent temperature [EBBT↑(day)].

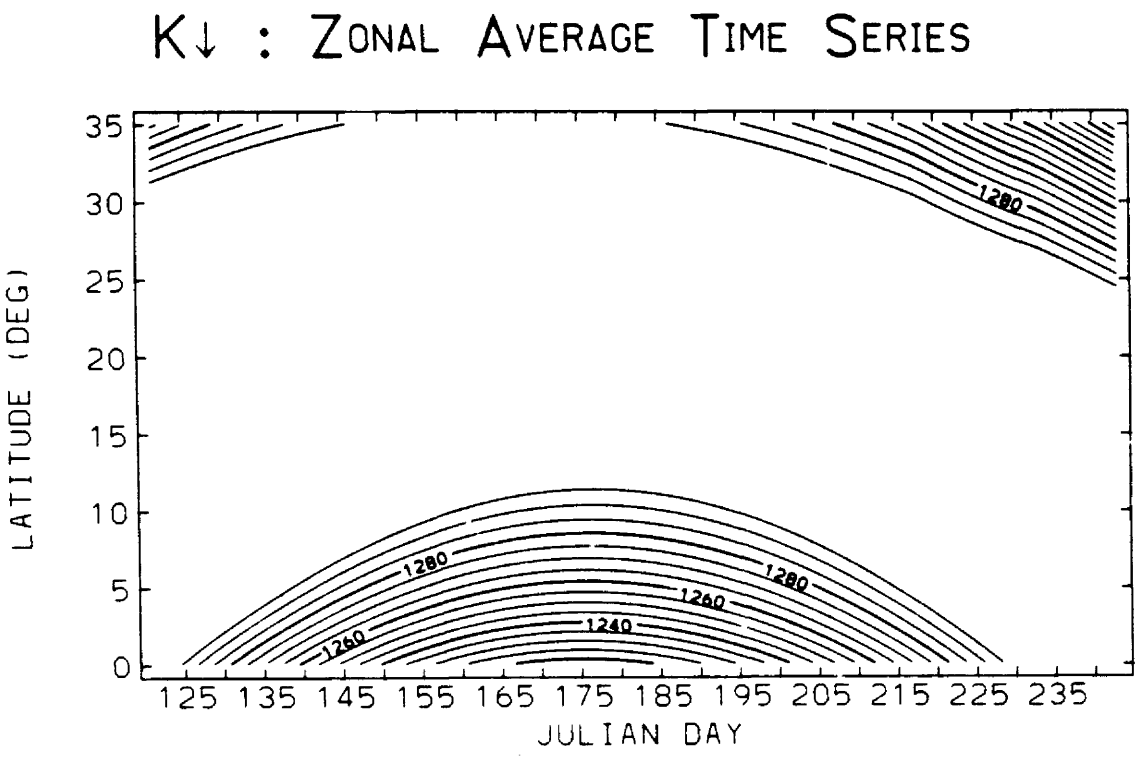

Fig. 3.51. Pattern of solar zonal forcing to the SW Monsoon radiation budget.

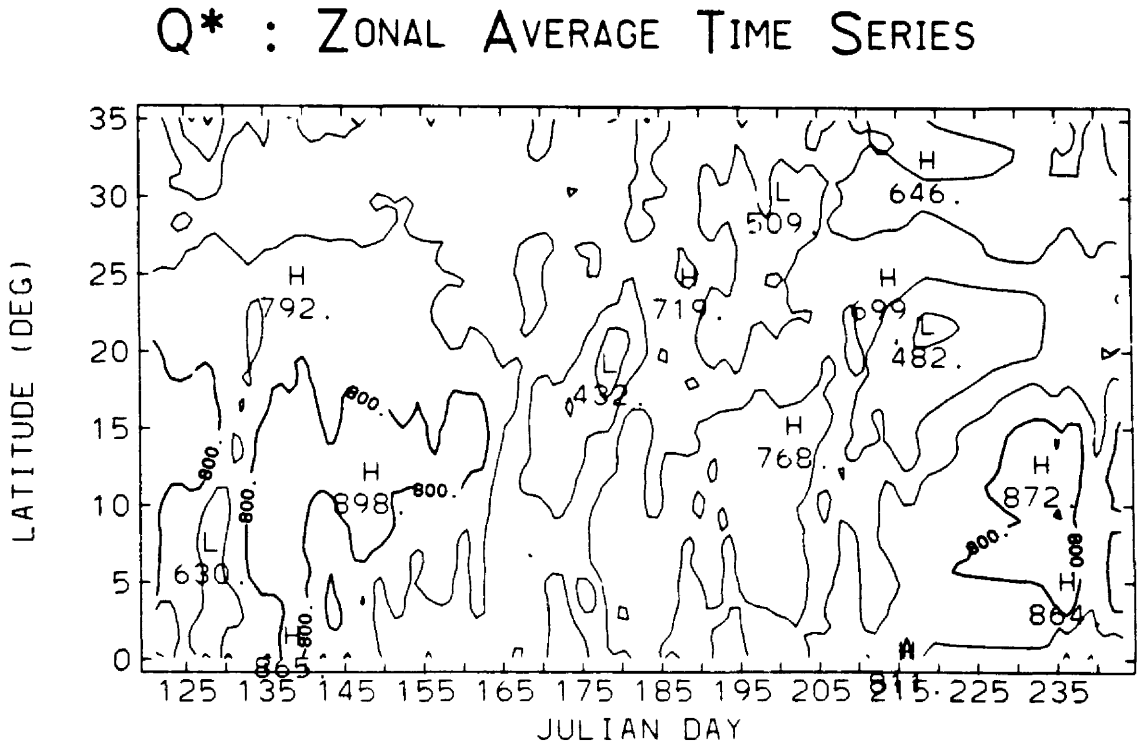

Fig. 3.52. Time-latitude section of noontime net radiative convergence (Q*) into the monsoon domain. The contour interval is 100 W m^{-2}.

two-dimensional smoothing operator to the zonal averaged time series matrix of Q*. There are four important features to note in this diagram:

1) The pre-monsoon and post-monsoon periods in which Q*>800 over a substantial tropical zone.
2) The obvious northward propagation of bands of radiative convergence into the monsoon marked by series of lows and highs throughout the course of the monsoon. The period of this oscillation is 40-50 days.
3) The two-regime structure of propagation after monsoon onset, which marks very clearly the progress of the equatorial and monsoon MCZs investigated by Sikka and Gadgil (1980).
4) The finger-like structures which re-occur over a range of periods from the short period time scale (4-5 days) out to 20 days.

The time-latitude sections diagrams of the remaining key terms in the zonal averaged radiation budget are provided in Figs. 3.53a-b for completeness. These are for the absorbed shortwave (K*), albedo (A), daytime infrared [L↑(day)], and nighttime infrared [L↑(night)] parameters. Note the high correlation between Q* and the two shortwave parameters (K* and albedo). The infrared diagrams illustrate the same basic process, although they depict the higher frequency structure somewhat differently than the Q* diagram.

If we view the monsoon in the analagous meridional perspective, we gain a much better appreciation of the mixture of the short period and quasi-weekly oscillations. As an illustration, Fig. 3.54 presents the time-longitude section of Q*. An evident feature in this diagram is the

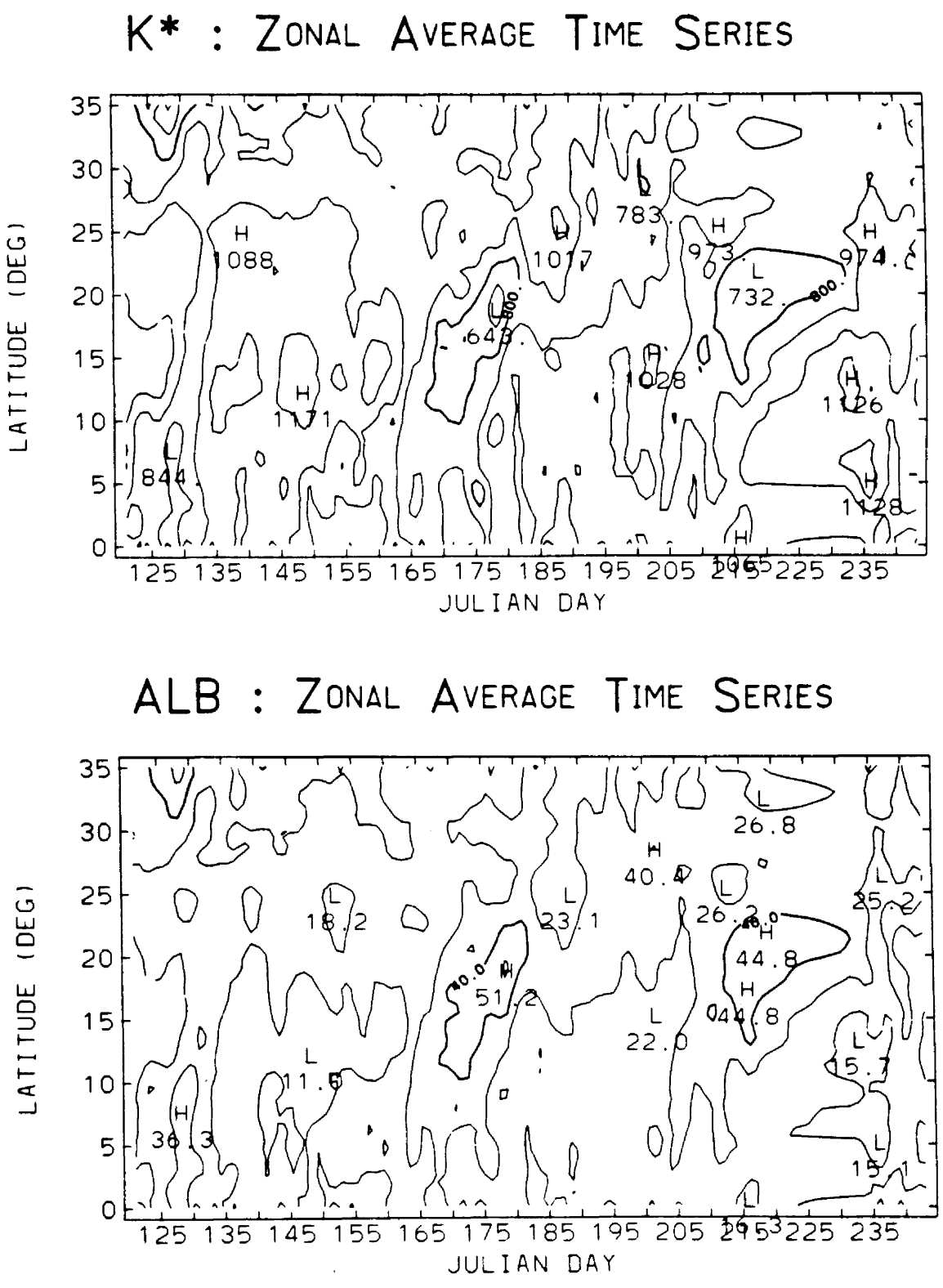

Fig. 3.53a. Same as Fig. 3.52 for K* (top) and Albedo (bottom). Contour intervals are 100 W m^{-2} and 10% respectively.

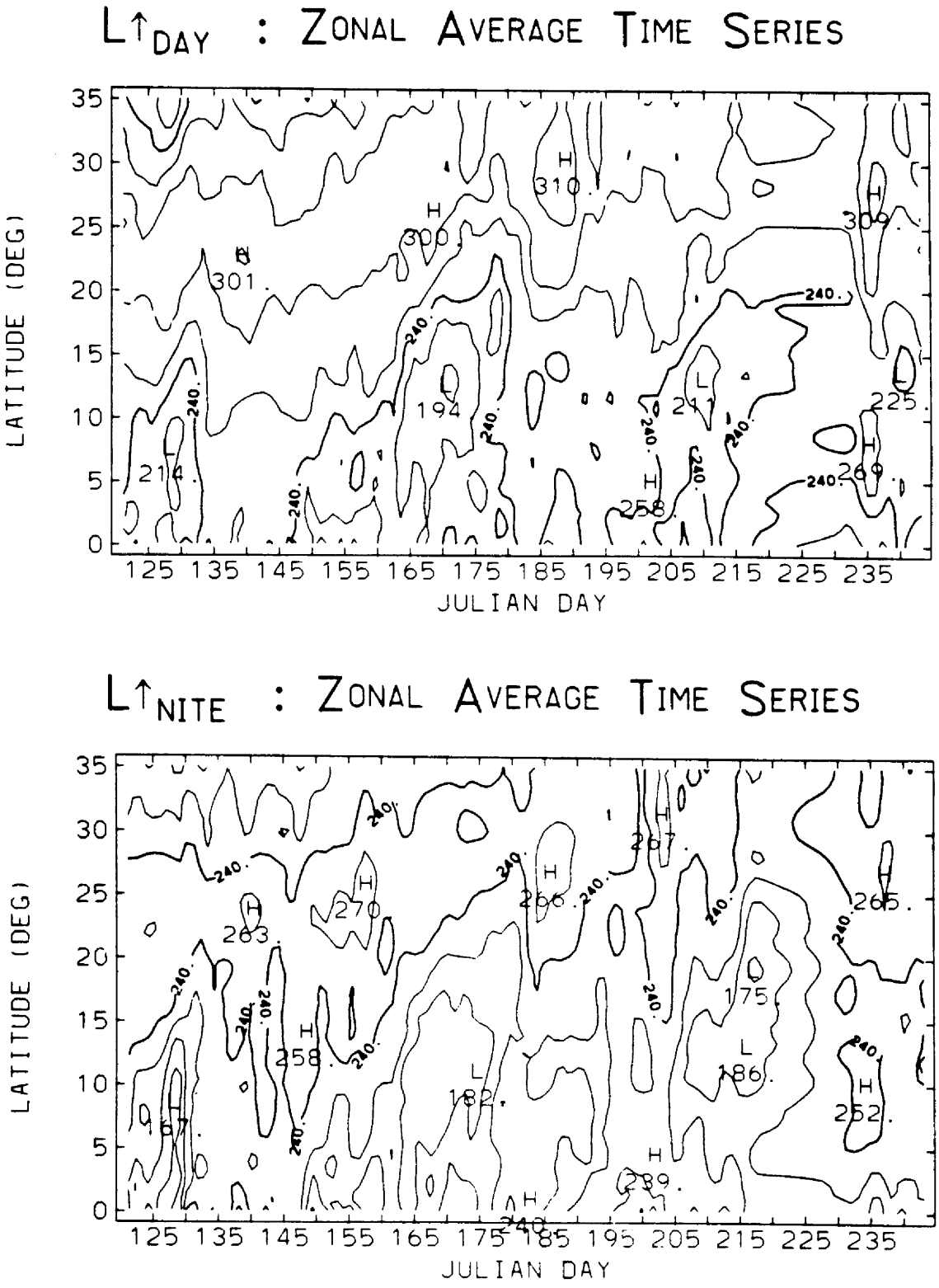

Fig. 3.53b. Same as Fig. 3.53a for L↑(day) and L↑(night). Contour interval is 20 W m^{-2} for both diagrams.

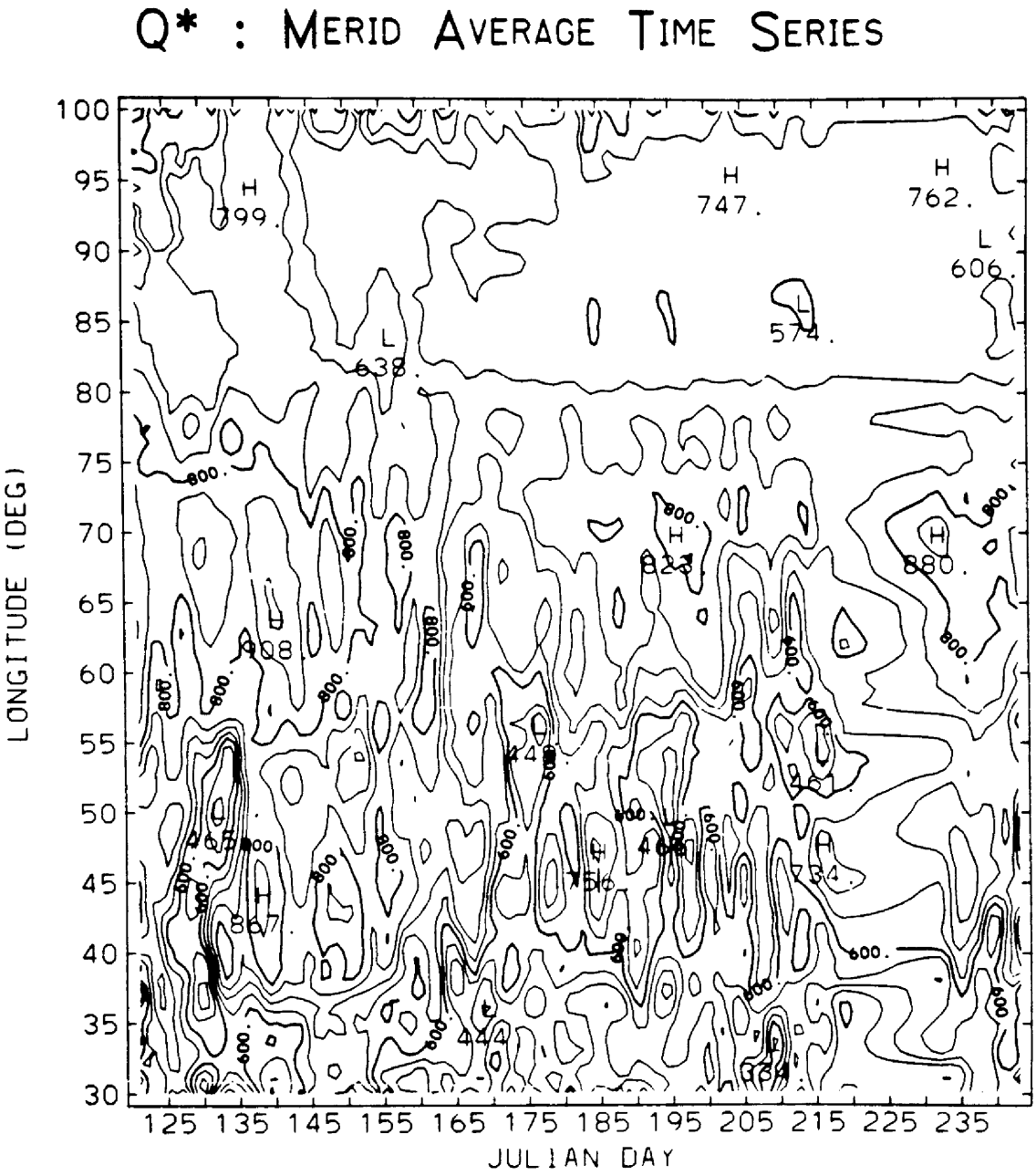

Fig. 3.54. Time-longitude section of noontime net radiative convergence (Q^*) into the monsoon domain. The contour interval is 100 W m^{-2}.

relative lack of meridional uniformity, which represents a curse for simplified models incorporating realistic radiative forcing.

A very important feature of this diagram can be seen between longitudes 67^{o} and 73^{o}E (the meridional strip which includes Pakistan and western India). Note that the 800 W$\cdot$m^{-2} contour reappears twice, first during days 194-200, and then again beginning near day 225. These contours depict the effect of the two major monsoon 'breaks' that ultimately led to the 1979 Indian Monsoon being recorded as a 'weak monsoon'.

As with the zonal case, Figs. 3.55a-b are provided to complete the portrayal of the meridionally averaged monsoon. An interesting feature is pointed out in the albedo diagram. Once the monsoon onset begins, the cloudiness over the Bay of Bengal serves to merge the meridionally averaged albedo of the tropical latitudes with the meridionally averaged albedo of the Tibetan Plateau. This flattens the albedo term between 80^{o}E to 100^{o}E.

As a composite summary of the zonally averaged radiation budget over the monsoon domain, Tables 3.7 and 3.8 are provided. These provide a complete set of statistical parameters describing the 5^{o} zonal averaged time series of albedo and emitted infrared radiation.

3.5.3 Radiation Blocking

A remarkable feature of the Southwest Monsoon is its impact on sytematically shutting off radiative convergence into the monsoon domain, beginning a few weeks prior to monsoon onset and continuing throughout most of June. This process is illustrated by the use of frequency distributions of the net radiative source term (Q*). Figures 3.56-3.59 illustrate the phenomenon. Plotted, in each of these figures,

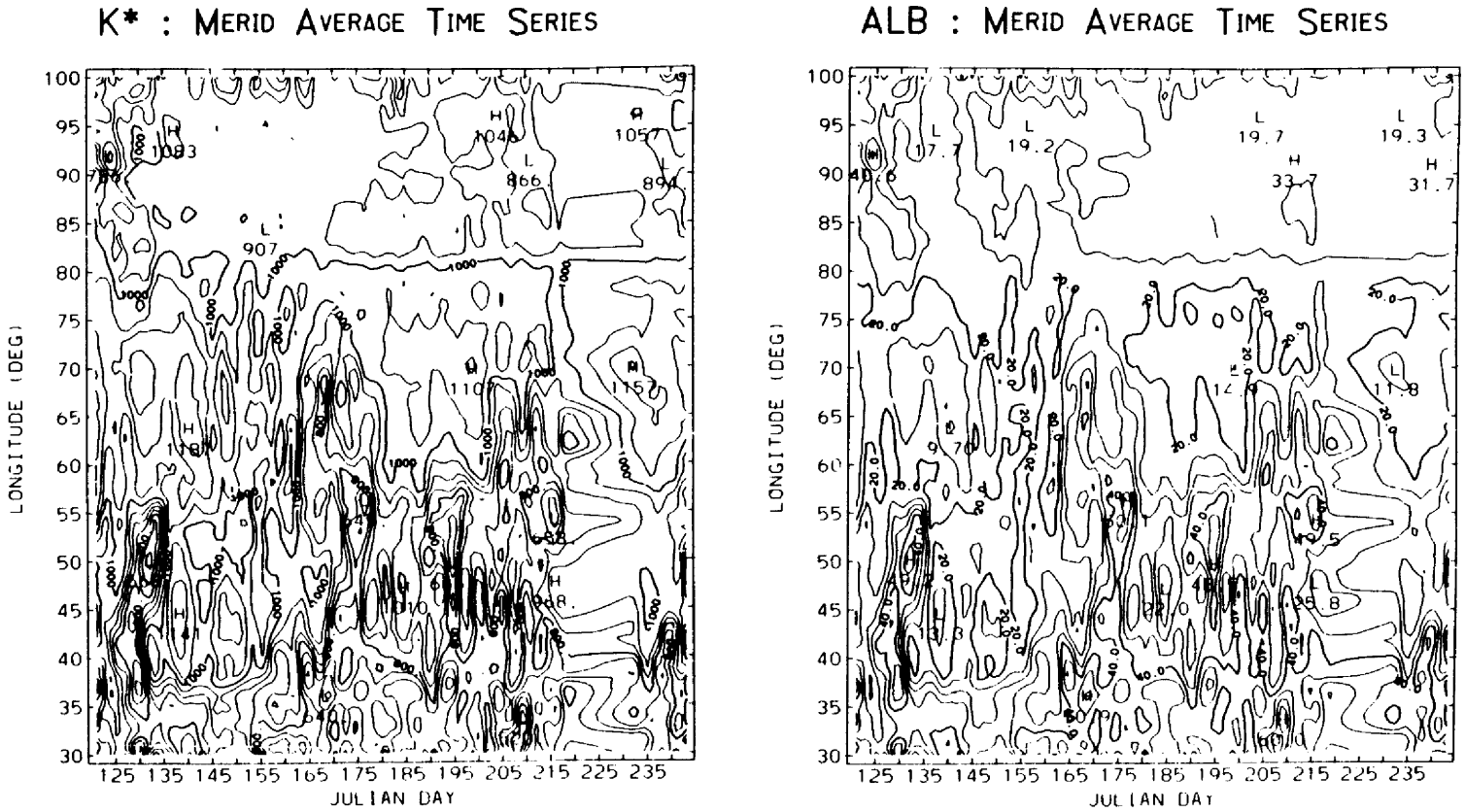

Fig. 3.55a. Same as Fig. 3.54 for K* (top) and Albedo (bottom). Contour intervals are 100 W m^{-2} and 10% respectively.

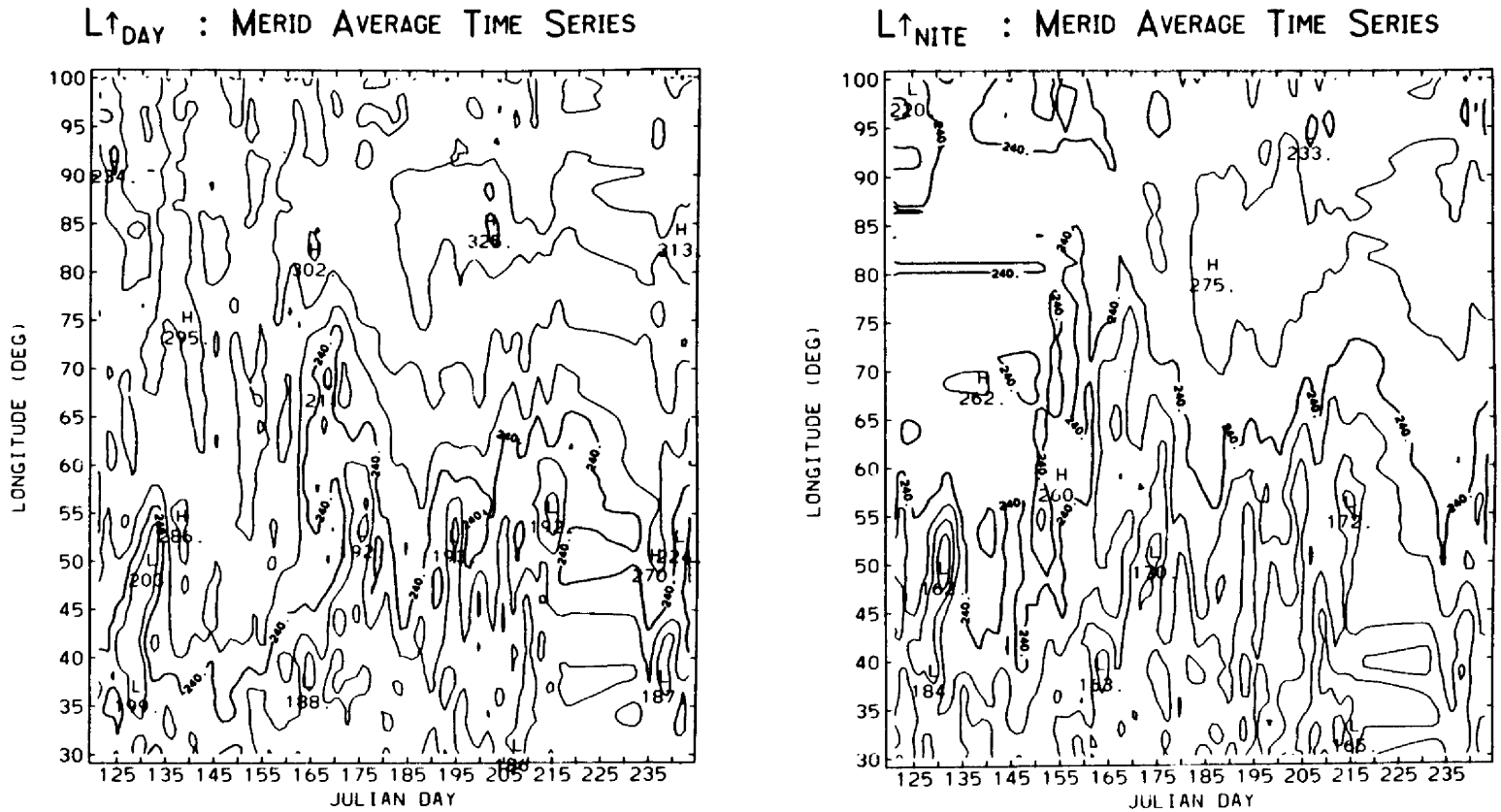

Fig. 3.55b. Same as Fig. 3.55a for L↑(day) and L↑(night). Contour interval is 20 W m^{-2} for both diagrams.

TABLE 3.7

Summary Statistics of 5° Strips of Zonal Mean Albedo (%) Over Monsoon Domain Longitudes (30°-100°E)

	Zone						
	0-5	5-10	10-15	15-20	20-25	25-30	30-35
Minimum	23	22	16	16	13	15	12
Maximum	46	38	44	54	45	39	35
Range	23	16	28	38	32	24	23
Quartile Deviation	3.9	3.3	6.1	9.4	10.6	7.5	5.7
Arithmetic Mean	30.9	30.0	29.9	28.9	25.0	24.4	25.6
Harmonic Mean	30.5	29.8	29.2	27.4	22.9	23.2	24.6
Median	30.9	29.8	30.1	27.2	22.9	22.8	25.9
Mode	31.1	29.4	31.5	22.3	18.4	20.2	18.2
Mean Deviation	2.7	2.2	3.5	5.5	6.2	4.6	3.7
Coeff. of Variation	11.9	9.7	15.4	23.3	30.0	23.0	18.3
Standard Deviation	3.7	2.9	4.6	6.7	7.5	5.6	4.7
Skew	1.11	0.11	0.01	0.83	0.63	0.67	-0.41
Kurtosis	6.07	3.28	3.83	3.62	2.72	2.95	2.90

TABLE 3.8

Summary Statistics of 5^{o} Strips of Zonal Mean Emitted Infrared Flux ($W\ m^{-2}$) Over Monsoon Domain Longitudes (30^{o}-$100^{o}E$)

	Zone						
	0-5	5-10	10-15	15-20	20-25	25-30	30-35
Minimum	235	257	210	194	192	202	210
Maximum	317	317	311	293	268	266	271
Range	82	60	101	99	76	64	60
Quartile Deviation	16.4	13.1	18.2	18.9	20.6	12.7	18.1
Arithmetic Mean	277	282	273	255	243	240	235
Harmonic Mean	276	282	272	254	242	239	235
Median	277	280	273	258	247	241	235
Mode	277	284	274	248	244	242	238
Mean Deviation	10.6	8.7	10.2	11.8	12.8	10.3	9.8
Coeff. of Variation	5.0	3.9	4.9	6.1	6.8	5.6	5.1
Standard Deviation	13.9	11.1	13.4	15.5	16.5	13.3	12.0
Skew	-0.36	0.61	-0.52	-1.03	-0.91	-0.47	0.27
Kurtosis	3.89	3.34	5.88	4.77	3.40	3.06	2.67

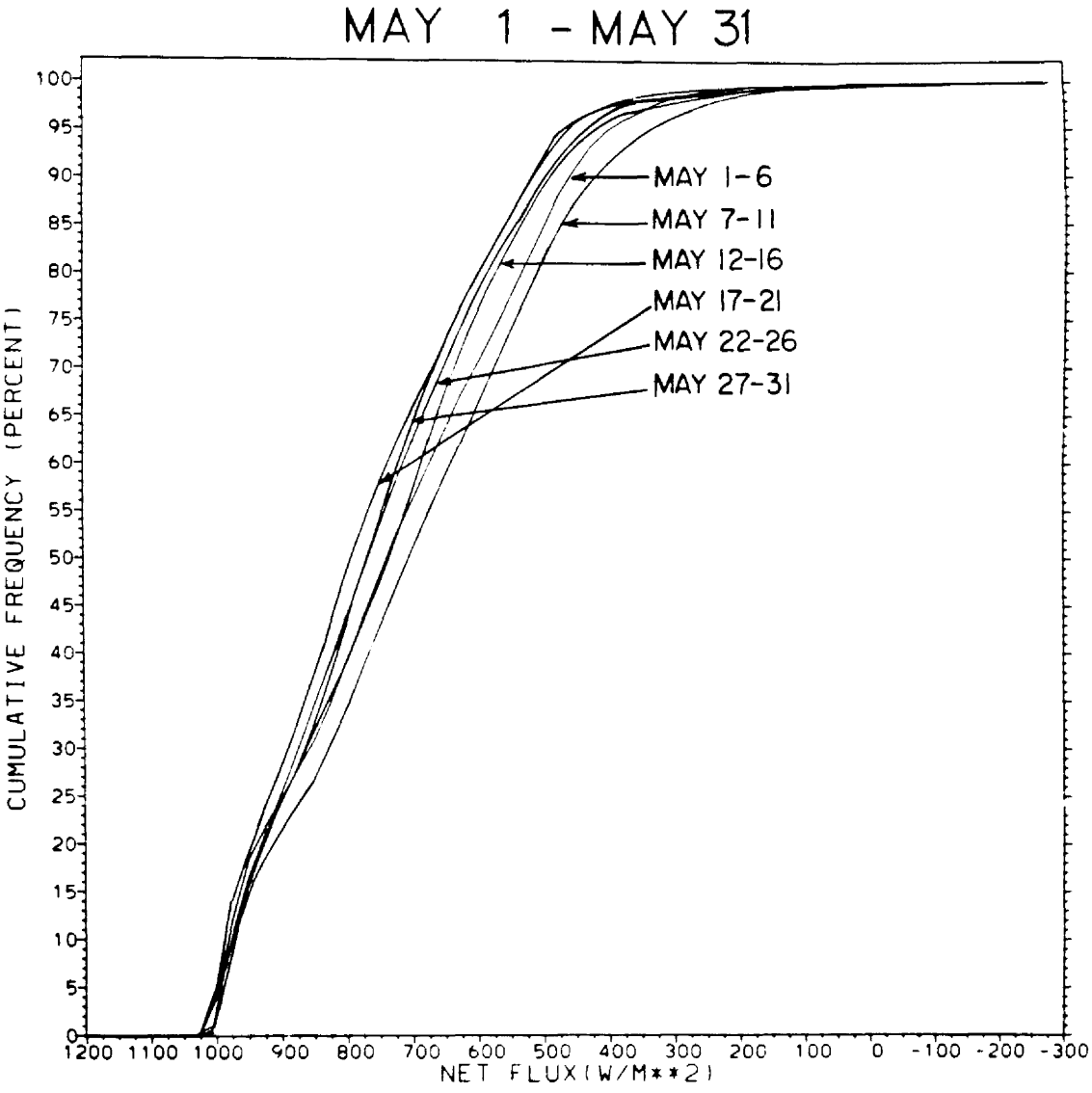

Fig. 3.56. Normalized cumulative frequency distribution functions for the SW Monsoon domain (Eq-30°N; 30°-100°E) of the net radiative exchange term (Q*) for the pentad periods during May, 1979 (the first period represents a 6-day average).

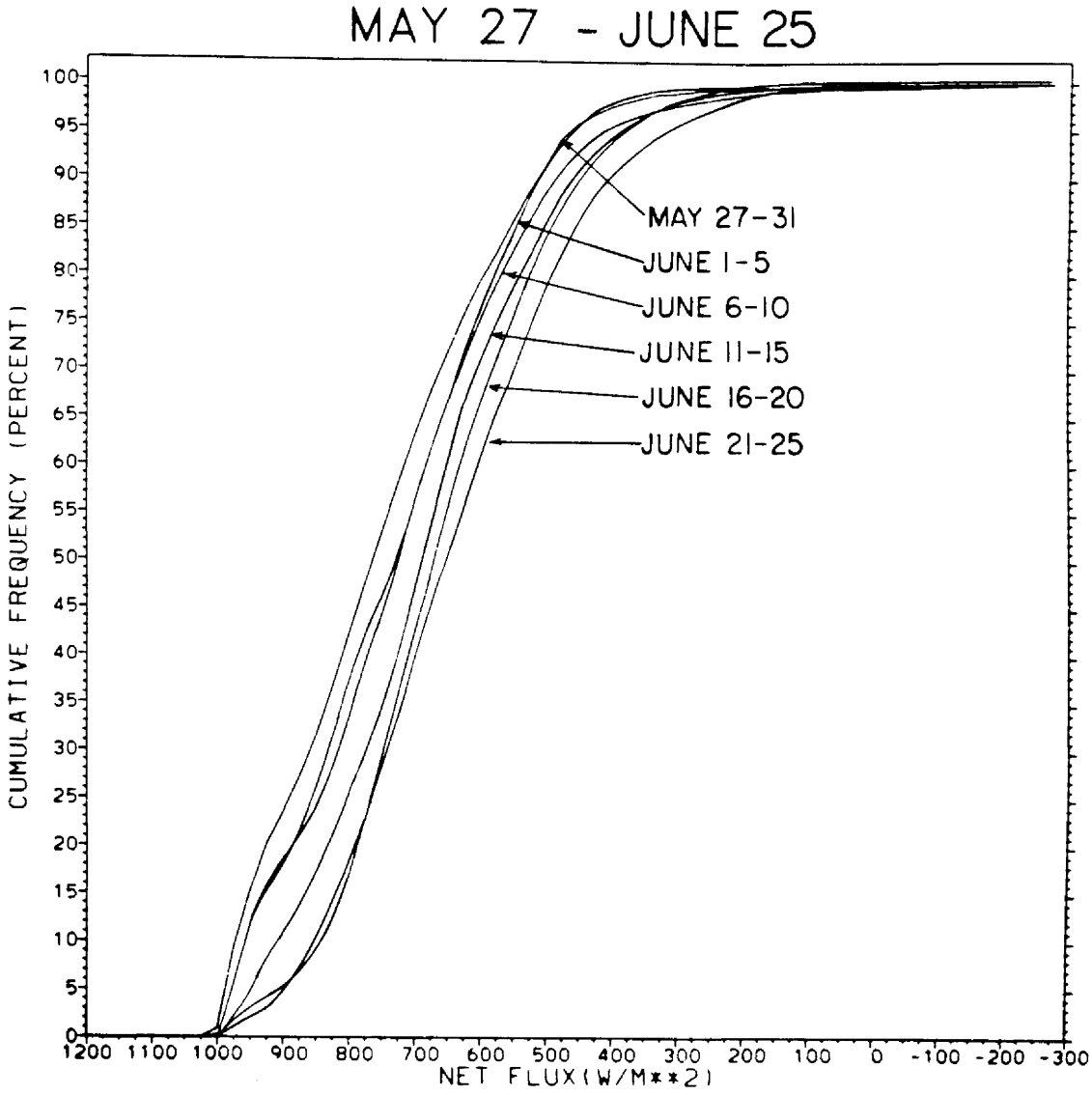

Fig. 3.57. Same as Fig. 3.56 for the six periods between May 27-31 and June 21-25.

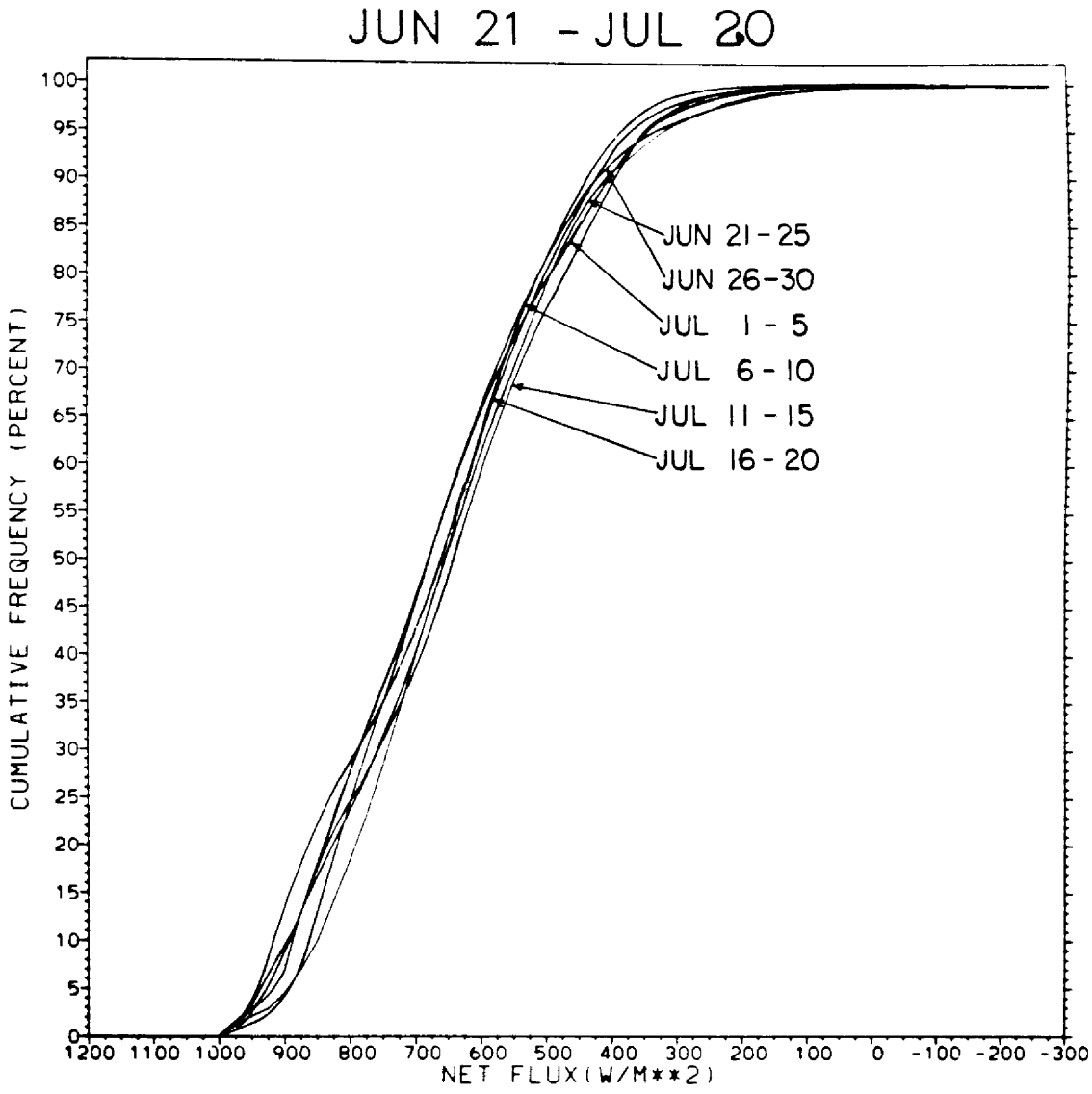

Fig. 3.58. Same as Fig. 3.56 for the six periods between June 15-21 and July 16-20.

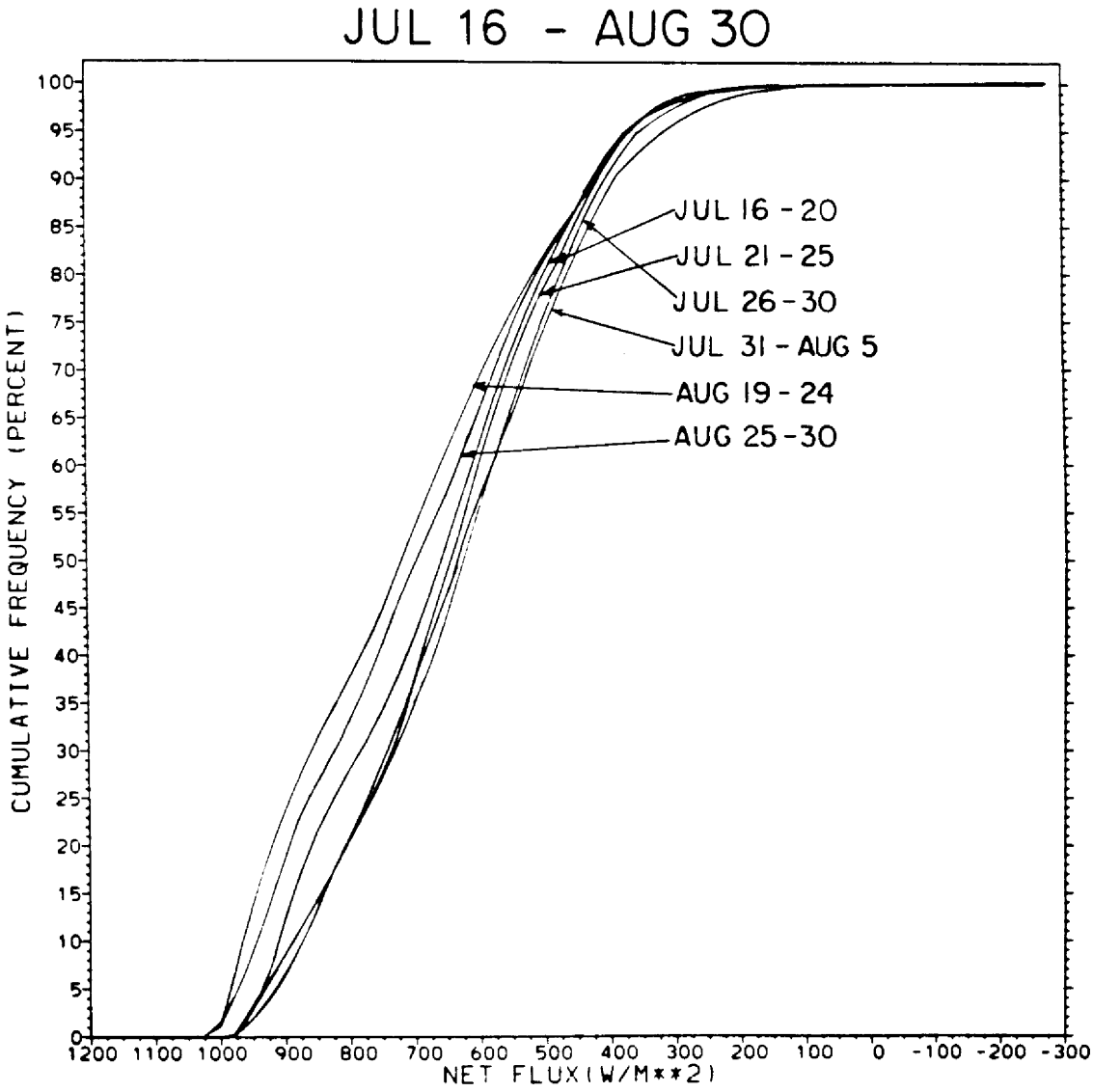

Fig. 3.59. Same as Fig. 3.56 for the six periods from July 16-20 and August 25-30 (there is a 13 day missing data gap from August 6-18).

are the cumulative frequency distribution functions of instantaneous Q* over the complete monsoon domain, at the 0.5x0.5 space scale and for the 5 (or 6) day averaged periods. The abscissa extends from high values at the origin to lower values moving to the right. The ordinate corresponds to cumulative frequency, normalized to a percent scale to account for differences in sample size. Figure 3.56 contains six of these functions for the six periods in May. During this month, these functions tend to flip-flop with a general tendency to move to the left, indicative of radiative gain as Spring progresses.

In Fig. 3.57 six more cumulative frequency plots are given, starting with the last 5-day period in May and extending through the fifth period in June (June 21-25). It is now noted that the Q* functions move monotonically to the right. In essence, the monsoon domain is progressively 'blocking' the radiative source term at the upper boundary. Examining Fig. 3.58, which contains the six cumulative frequency functions beginning with the June 21-25 period, we see that the Q* functions tend toward steady state. The final figure (Fig. 3.59) presents the remainder of July and the final two periods in August. Note as monsoon cloudiness begins to dissipate toward the end of August, the cumulative frequency functions move back to the left.

Why the monsoon systems modifies itself so regularly in June in order to 'block' radiation, is not readily apparent. The energy packet seen in Fig. 3.57, defined by the integral between the furthest left and furthest right cumulative frequency distribution functions, describes a substantial and regulated loss of radiative energy to the monsoon for a period of at least a month ($\approx$ 5 peta-watts). As to whether this is a regular annual feature, further study would be required.

3.6 Contrasts in the Radiation Budget

Another approach in examining the monsoon is to look for contrasts between the different regions within the monsoon system. This is done by generating the time series of the radiative parameters over localized areas. For this analysis, the ERB/NFOV measurements have been used so as to obtain the best measure of a time history of the mean daily net radiation term ($\overline{Q^*}$). The time series are constructed by assigning a single grid region ($\approx 5^{\circ} \times 5^{\circ}$) from the Nimbus-7 ERB Mapped Data Matrix Tape Format as representative of a given region [see Jacobowitz, et al. (1978) for a discussion of the ERB Matrix format]. The grid data are then extracted at these coordinates for whatever days are available. Linear interpolation is used to fill the missing day gaps (usually every fourth day).

Five regions have been selected for this purpose. They are identified along with their associated center coordinates in Table 3.9. For each of these regions, the time series extends from the second week in May until the end of August.

3.6.1 Oceanic Regimes

The times series of A, L↑(day), L↑(night), and $\overline{Q^*}$ for the Arabian Sea and the Bay of Bengal, are shown in Figs. 3.60 and 3.61, respectively. In the first of these figures, the Arabian Sea undergoes a dramatic change around day 168 (June 17). At this point the monsoon vortex begins to spin up, leading to extensive cloudiness over the Arabian Sea. This is most easily identified in the albedo signal. Note the sudden dip in the IR emitted flux signals. After this time the daily net radiation term over the Arabian Sea is reduced from an average value of approximately 100 $W \cdot m^{-2}$ down to 60 $W \cdot m^{-2}$.

TABLE 3.9

Names and Location Coordinates of Five Regions within the Monsoon Domain Used to Study Radiation Budget Contrasts

Region	Center Coordinate of $5^{\circ} \times 5^{\circ}$ Grid
Arabian Sea	$15^{\circ}45'N; 65^{\circ}15'E$
Bay of Bengal	$15^{\circ}45'N; 87^{\circ}45'E$
Indian Sub-Continent	$20^{\circ}15'N; 77^{\circ}30'E$
Tibetan Plateau	$29^{\circ}15'N; 87^{\circ}30'E$
Arabian Empty Quarter	$20^{\circ}15'N; 47^{\circ}30'E$

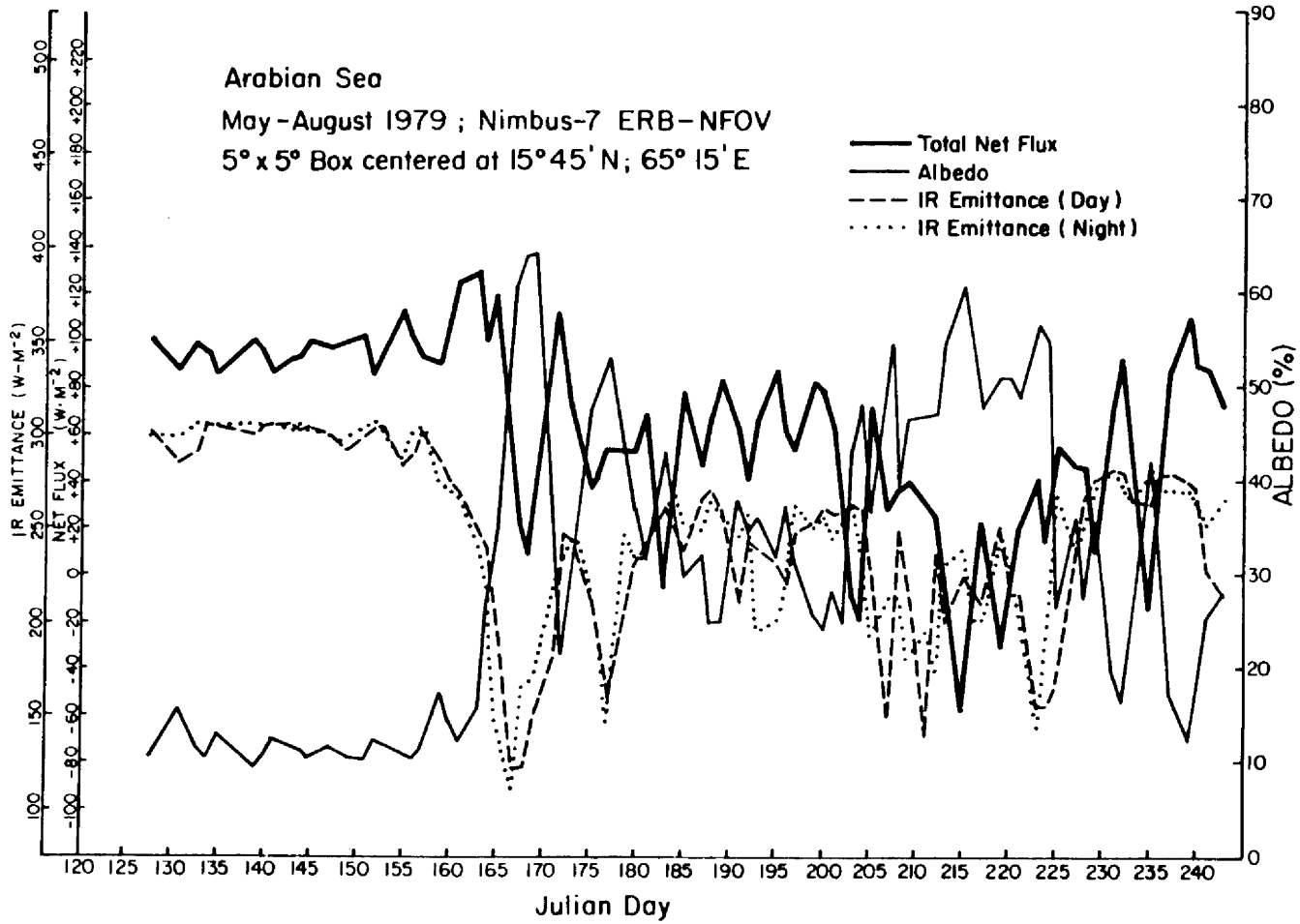

Fig. 3.60. Time series from May to August, 1979 of radiation budget parameters over the Arabian Sea based on ERB/NFOV measurements.

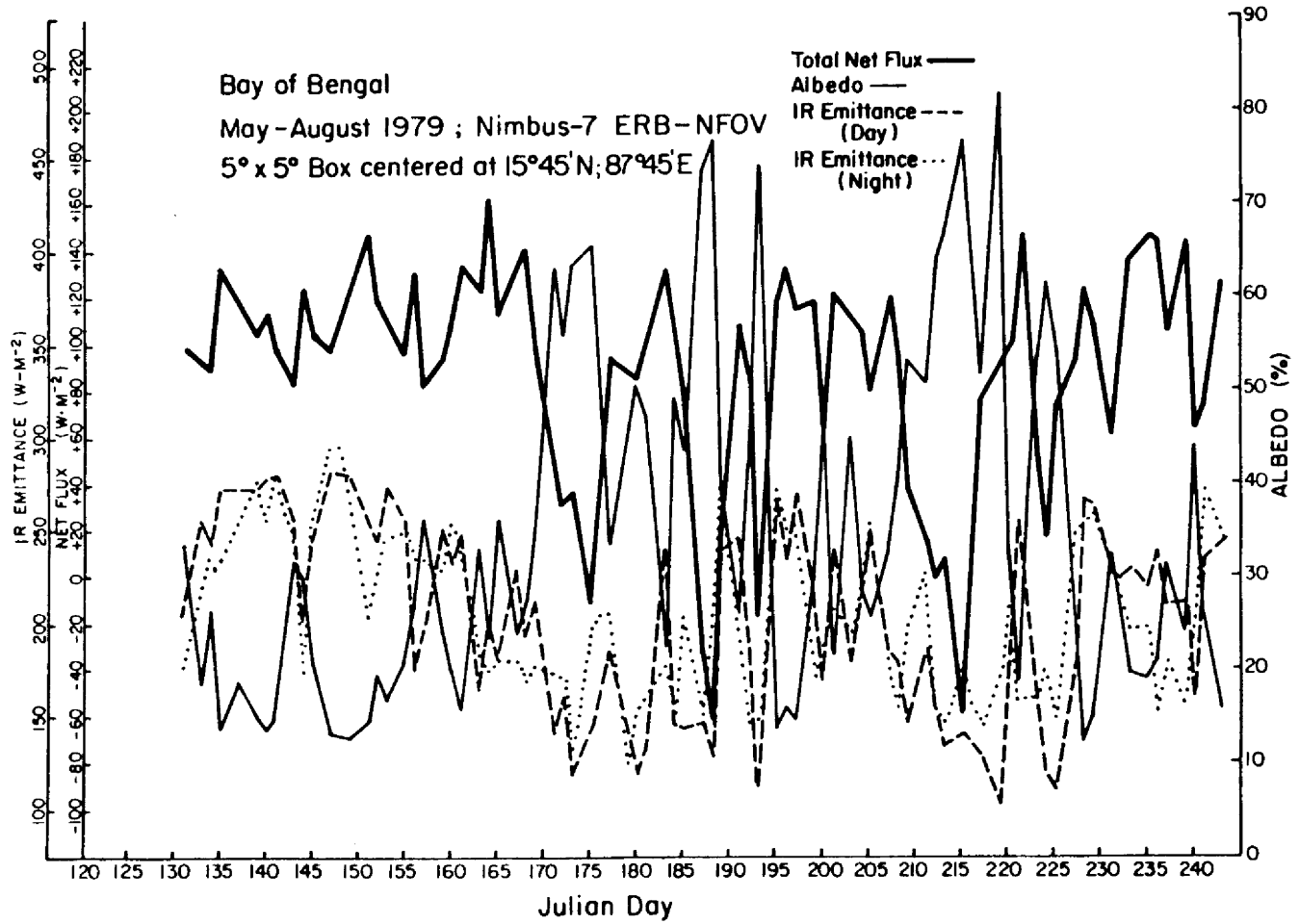

Fig. 3.61. Same as Fig. 3.60 for the Bay of Bengal.

After this sudden shift in the radition budget, the Arabian Sea cloud system undergoes one extreme oscillation [the albedo almost returns to its pre-monsoon value on day 172 (June 21)] and then oscillates fairly regularly until day 203 (July 22), at which point the albedo undergoes a sudden rise. This event takes place immediatedly after the first monsoon break (day 215). The $\overline{Q^*}$ term falls off to its lowest value in the course of the monsoon season to -55 $W \cdot m^{-2}$ on August 3 (day 215). The last two weeks of August terminate with two more high amplitude oscillations. This period corresponds to the second break monsoon period. By the end of August the $\overline{Q^*}$ term has returned to the pre-onset levels.

These time series demonstrate quite clearly the impact of oscillations within the monsoon system on the TOA radiation signals. The 4-5 day periodicity is immediately obvious. The evidence of the long period cycle is most likely identified by the peaks in albedo at day 168 and and day 215 (47 days). These times correspond to the initiations of the two major low features seen in the Q* time-latitude diagram (Fig. 3.52). This intensification in the Arabian Sea was earlier noted in the analysis of the 5-day mean fields. Any evidence of the quasi-biweekly oscillation over the Arabian Sea is difficult to identify from visual analysis.

The radiation signals over the Bay of Bengal (Fig. 3.61) are remarkably similar in some aspects, although there are differences. We see the sudden shift from pre-monsoon to monsoon onset conditions (day 175), but taking place about one week after the albedo spiked upward over the Arabian Sea. Prior to that point, in contrast to the Arabian Sea, the Bay of Bengal undergoes three major oscillations. These very

definately appear to be between 10-15 days apart. They are most easily noted in the albedo and net radiation signals.

The principal difference between the Bay of Bengal and the Arabian Sea is that the amplitudes of the oscillations in the former are greater. On the other hand, the timing of the minimum value in $\overline{Q^*}$ is in exact correspondence to the Arabian Sea (day 215 - August 3). An examination of the variational events themselves indicates a mixture of 4-6 day gaps along with 8-15 day gaps between the major events. The long period oscillation or MCZ 'flip-flop', seen in the Arabian Sea signals, is also apparent in the Bay of Bengal with one significant difference; there is a major rise-dip-rise event between days 188-193. Thus the spacing between major events, for example in the dips, is 13 days (between day 175 and day 188) and 27 days (between day 188 and day 215).

3.6.2 Continental Regimes

The time series graphs shown in Figs. 3.62-3.64 present the radiation budget signals for the three continental regimes. The onset of monsoon cloudiness over India (Fig. 3.62) is sudden and dramatic but the monsoon surge does not arrive until day 177 (June 26). Well prior to the monsoon onset, however, central southern India has undergone major cyclogenisis which is easily identified by the large peak on day 133 (May 13). This tropical cyclone can be identified in Fig. 3.29 in the 5-day mean fields.

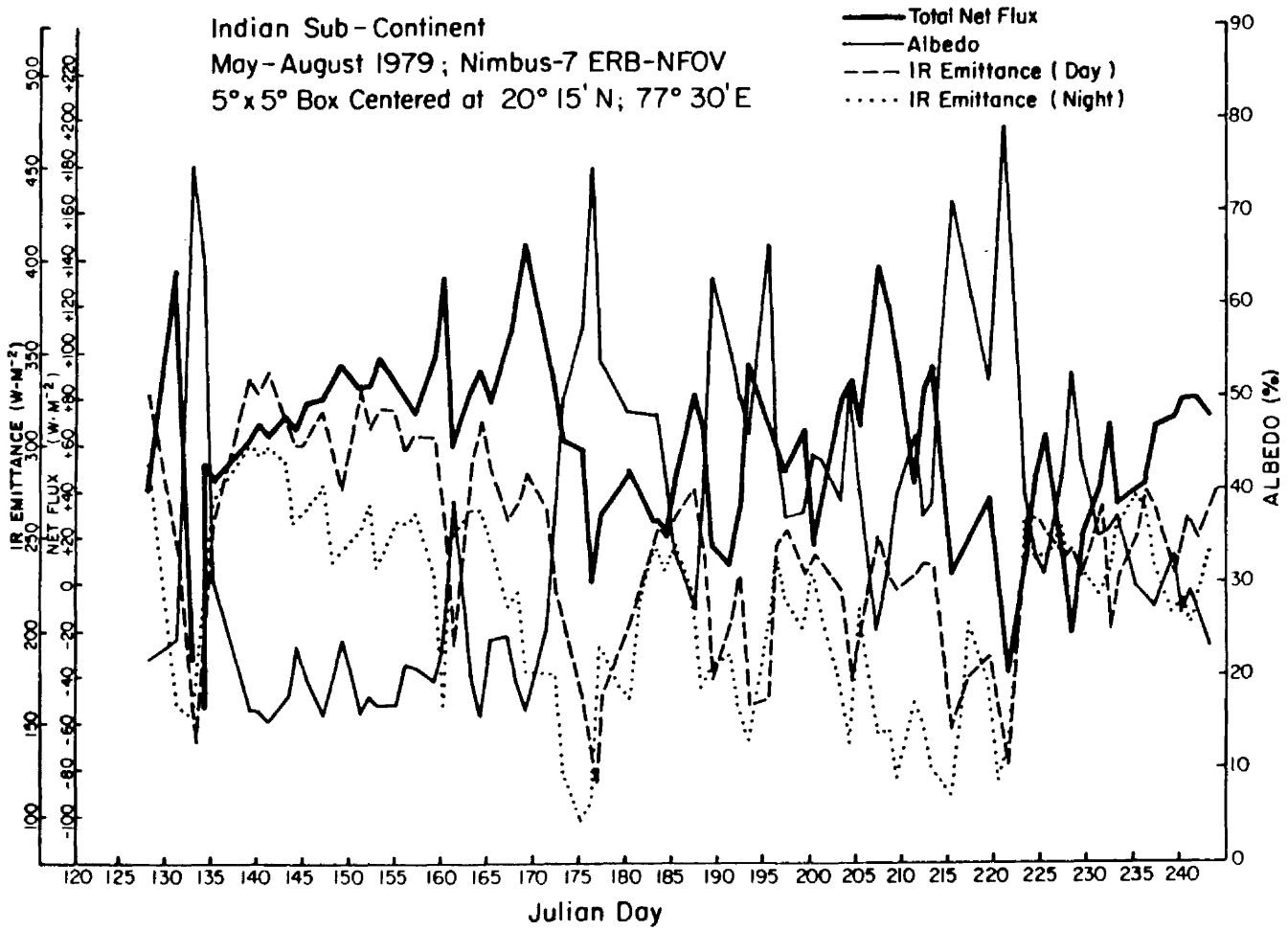

Fig. 3.62. Same as Fig. 3.60 for the Indian Sub-continent.

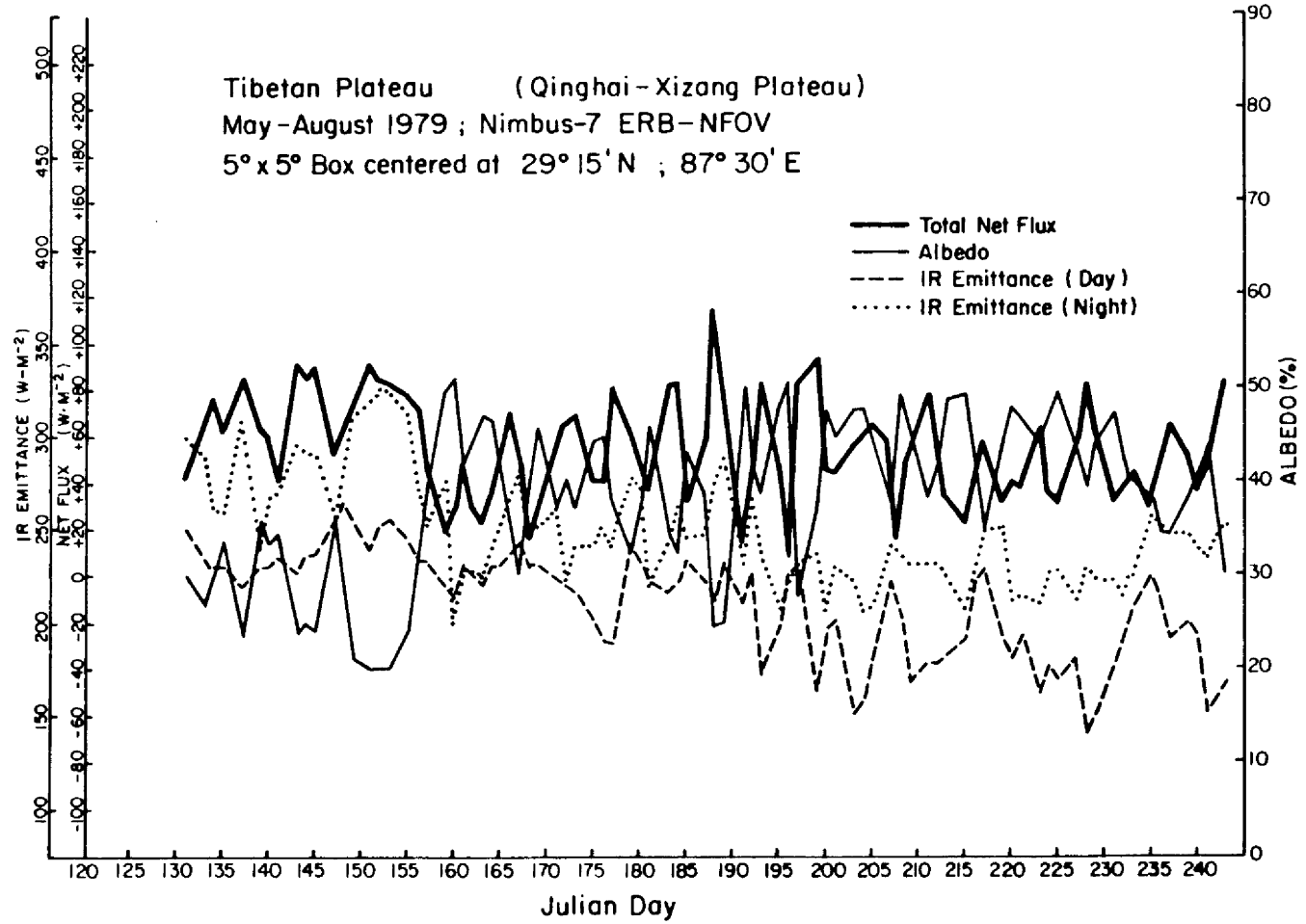

Fig. 3.63. Same as Fig. 3.60 for the Tibetan Plateau.

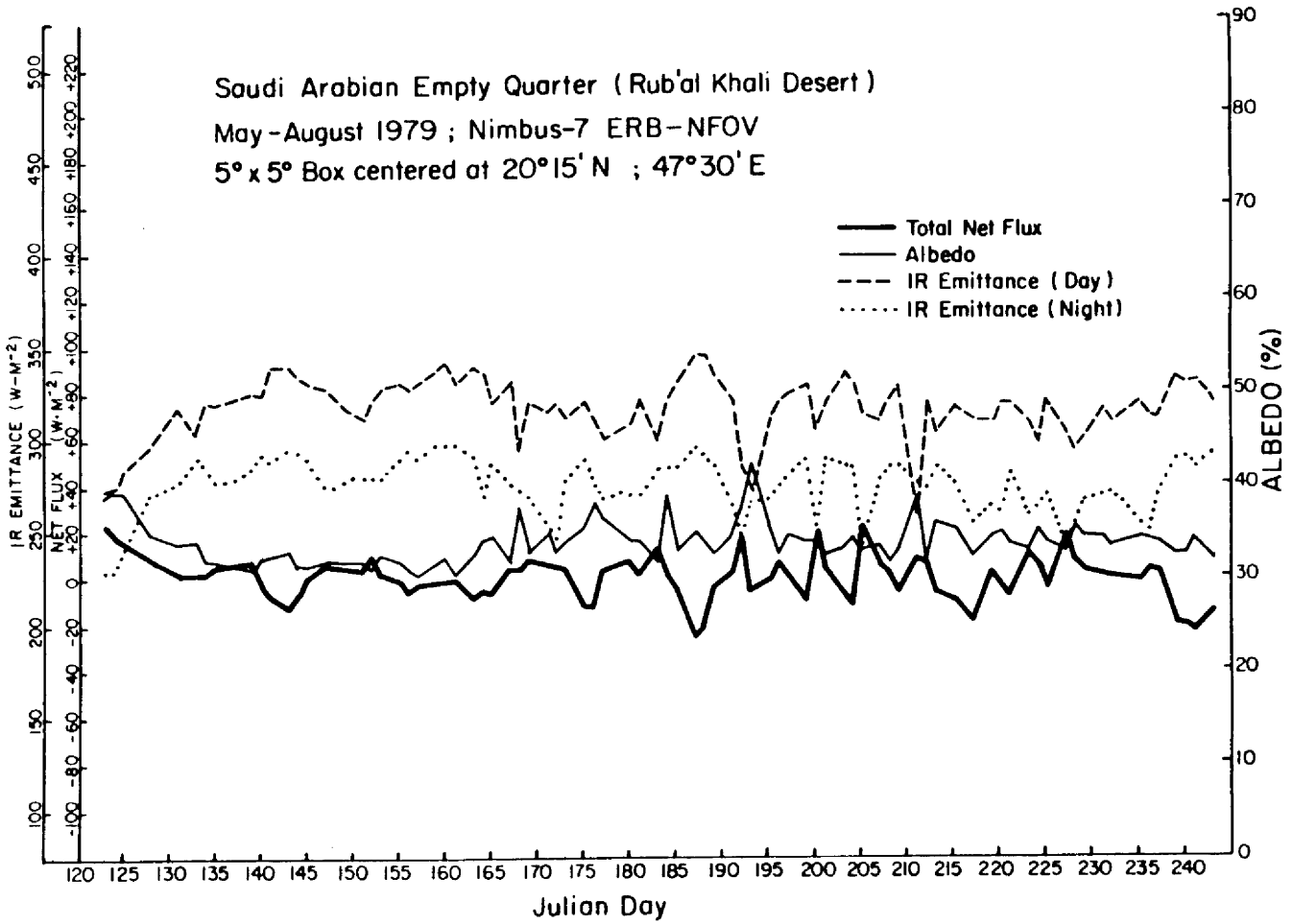

Fig. 3.64. Same as Fig. 3.60 for the Arabian Empty Quarter.

The fluctuations in the Indian Sub-continent radiation signals, similar to the Bay of Bengal, appear as a mixture of the short period and quasi-biweekly periodicities. In addition, if the double peak centered at day 190 is ignored, the three other major peaks (days 133, 177, 221) form a triplicate with an equivalent spacing of 44 days. These events demonstrate why power in the long period spectrum would arise. Two important points to note with this sequence, however, is that the double peak centered at day 190 interrupts the sequence, and there is another major peak close to the day 221 peak (day 215). Thus, on an event-to-event basis, it is difficult to assess the long period monsoon oscillation using the localized radiation time series.

A very important distinction between the Indian region and the oceanic region is the rather large magnitude of mean difference in the day and night emitted infrared terms. This is, of course, a fairly pure manifestation of the diurnal surface heating effect. However, it can be easily noted that the magnitudes of the day-night differences are so strongly modulated by the degree of cloudiness, that at various portions of large relative minima, the diurnal differences tend to zero.

The remaining two figures (Figs. 3.63 and 3.64) illustrate the time series over the central Tibetan Plateau region (the elevated plateau heat source), and the Arabian Empty Quarter (the quintessential example of a pure desert). The key feature to note in the radiation signals is the occurrence of short period periodicities over both plateau and desert regimes, the difference being that the plateau oscillations are in evidence throughout the course of the 4-month period, whereas the oscillations over Arabia do not really begin until after the monsoon is established. Since Empty Quarter cloud coverage is almost non-existent

throughout this period, this oscillation must be mostly due to fluctuations in the aerosol and water vapor mixing ratios.

3.6.3 Further Remarks on Validation

It is instructive, at this point, to estimate the degree to which the time series signals, shown in Figs. 3.60-3.64, can be reproduced in the AVHRR data. This is somewhat of a required precursor test before carrying out spectral analysis with the AVHRR data as will be done in the next section. This intercomparison is accomplished in two ways; first by an intercomparison of the statistical measures; second, by an intercomparison of the periodograms of the Fourier spectrums. It is stressed that in these intercomparisons, an instantaneous noontime referenced Q* value has been used for the AVHRR, whereas a daily averaged $\overline{Q^*}$ estimate has been used for the ERB/NFOV. Thus for the net radiative parameter, only the correlation and spectral tests are meaningful.

The time series that have been used in the intercomparisons are based on a 79-day period from May 19 to August 5. Wherever a missing day occurs in either of the two series, that position is zeroed in both series, to be replaced by a linearly interpolated estimate. In this way the missing date impact is equivalenced.

The results of the statistical intercomparisons are shown in Table 3.10 for all five regimes discussed in the previous two subsections. The four RADBUD parameters plotted in the time series correspond to the parameters used in the intercomparison. Four statistical measures are used in the intercomparison: 1) The mean values of the time series ($\overline{TN}$, $\overline{N7}$); 2) the difference (bias) of these two values ($\overline{N7}$-$\overline{TN}$); 3) the

TABLE 3.10

Statistical Intercomparison Between the 79-Day Time Series of Nimbus-7 and TIROS-N RADBUD Parameters for Two Oceanic and Three Continental Regions

Arabian Sea	TN	N7	Bias	RMSDIF	COR
ALB	26.7	31.5	+4.8	7.7	.946
L↑ Day	242.7	243.5	+0.8	15.4	.972
L↑ Night	225.3	240.9	+15.6	21.5	.977
Q*	722.3	65.2	--	--	.694
Bay of Bengal					
ALB	31.8	35.6	+3.8	7.6	.944
L↑ Day	209.9	204.3	-5.6	17.2	.946
L↑ Night	203.2	205.0	+1.8	18.8	.888
Q*	692.4	84.1	--	--	.813
India					
ALB	37.6	36.2	-1.4	8.2	.886
L↑ Day	245.4	247.9	+2.5	22.6	.912
L↑ Night	209.7	206.9	-2.8	17.8	.951
Q*	578.6	62.7	--	--	.595
Tibetan Plateau					
ALB	40.6	38.0	-2.6	9.7	.719
L↑ Day	234.8	250.7	+15.9	21.2	.890
L↑ Night	201.4	215.6	+14.2	20.0	.842
Q*	542.4	55.8	--	--	.422
Saudi Arabia					
ALB	35.2	33.8	-1.4	3.4	.175
L↑ Day	322.1	321.0	-1.1	14.5	.499
L↑ Night	268.4	278.3	+9.9	15.0	.460
Q*	534.6	1.5	--	--	-.057

RMS difference in these two values; and 4) the correlation between the two time series. All of these measures are provided for all four RADBUD parameters, with the exception of the bias and RMS differences between the ERB/NFOV $\overline{Q^*}$ estimates and the AVHRR instantaneous Q* estimates. These later intercomparisons are ill-defined based on the different definitions of $\overline{Q^*}$ and Q*. Nevertheless, they are expected to have a correlative relationship to some degree.

The intercomparisons show that for the two oceanic regions, albedo is consistently underestimated with the ERB/NFOV by approximately 4%. With the exception of the nighttime emitted IR bias of +15.6 $W \cdot m^{-2}$ over the Arabian Sea, the emitted IR comparisons are excellent. RMS differences are approximately 18 $W \cdot m^{-2}$. The correlations are also excellent includng the net radiation terms (+0.7 for the Arabian Sea and +0.8 for the Bay of Bengal).

The results over the three continental regions are varied. The intercomparisons for the Indian Sub-continent are excellent, although the Q* correlation is somewhat less than for the Bay of Bengl (+0.6). The results over the Tibetan Plateau show bias differences in the day and night IR terms of $\approx$+15 $W \cdot m^{-2}$; albedo bias is - 2.5%. The correlation in Q* is +0.4.

The results over the Empty Quarter show small albedo differences, a small bias in L↑ (day), a + 10 $W \cdot m^{-2}$ bias in L↑ (night), $\approx$ 15 $W \cdot m^{-2}$ RMS differences in the two day-night L↑ terms, and virtually zero correlation in Q*. Why the lack of correlation? This is, in large part, due to the relatively low amplitude characteristics of the desert time series (as shown in Fig. 3.64). Thus, small errors in either the

AVHRR instantaneous Q* or in the ERB/NFOV $\overline{Q^*}$ result in large reduction of the covariance.

The examination of the periodograms of the Fourier transforms exhibit a range in degree of comparison. Table 3.11 provides a summary of the evaluations in terms of a good, fair, and poor rating index. As an example of a 'good' comparison, Fig. 3.65 is provided. The left portion shows the phase-amplitude diagrams for the Nimbus-7 time series for the L↑(day) parameter over the Bay of Bengal; the right portion provides similar diagrams for the TIROS-N time series. The amplitudes at the Fourier frequencies associated with these decompositions are in excellent correspondence out to the ordinal frequency 31 (2.75 cycles per week), i.e. until the very high frequencies. The phase angle graphs are in almost perfect comparison, with the exception that the spectral peak at ordinal frequency 6 (13 day period), which is resolved slightly different in amplitude, shows a much greater phase angle at slightly different period in the Nimbus-7 plot. The single peak in phase angle at ordinal frequency 24 in the Nimbus-7 graph appears as a double peak in the TIROS-N graph, however, the significance of this difference is negated by the lack of power at that particular frequency (3.3 day periodicity).

The implication, based on the above comparisons, is that the total set of radiation budget parameters derived from the weather satellite, for a variety of regions, are reasonably good estimates. There are a few exceptions, however, such as Q* fluctuations over deserts.

3.7 Oscillations in Radiative Forcing

Sections 3.5 and 3.6 demonstrated that the various periodicities inherent to the monsoon system are reproduced in the net radiative

TABLE 3.11

Quality Index of the Nimbus-7 versus TIROS-N Periodogram Intercomparisons

	ALB	L↑(day)	L↑(night)	Q*
Arabian Sea	Good	Good	Good	Fair
Bay of Bengal	Good	Good	Fair	Good
India	Good/ Fair	Good/ Fair	Good	Poor
Tibetan Plateau	Fair	Good	Good	Poor
Saudi Arabia	Poor	Fair	Fair	Poor

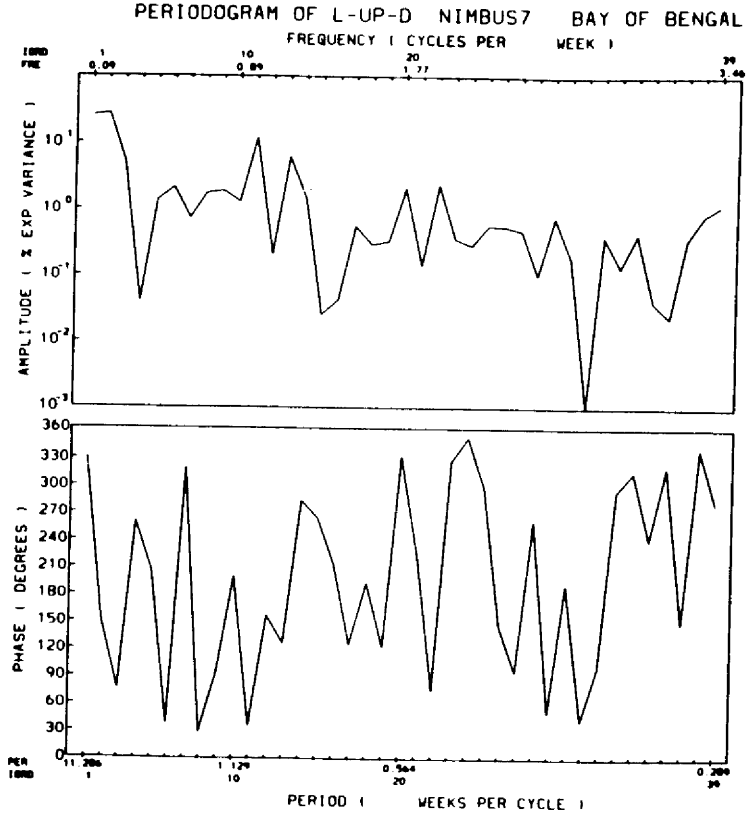

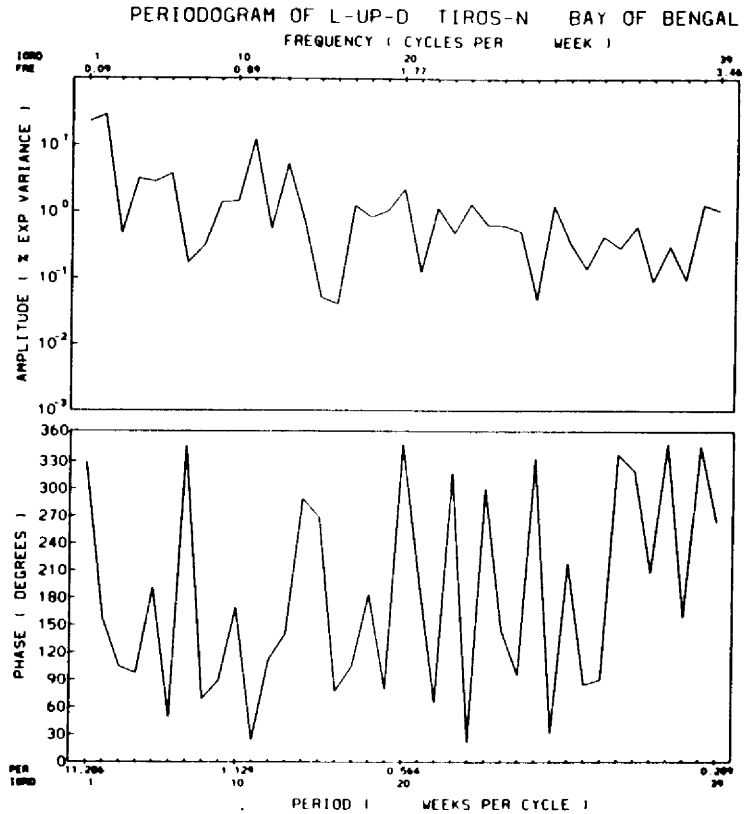

Fig. 3.65. Intercomparison between the periodograms of L↑ (day) for the 7-day time series from Nimbus-7 and TIROS-N over the Bay of Bengal.

convergence term, both in a regional sense and in a zonal or meridional averaged sense. It was noted in sub-section 3.5.2, in the time-latitude section of zonal averaged Q*, that the dominant radiation mode is the long period oscillation corresponding to northward propogating banded cloud systems which Sikka and Gadgil (1980) have conveniently referred to as the equatorial and monsoon MCZ's. Also noteworthy was the evidence of the short period and quasi-biweekly periodicities, although it was clear that in the zonal averaged sense, there is far less organization to the quasi-biweekly oscillation than the long period oscillation.

In Section 3.6, concerning monsoon contrasts, analysis of localized time series demonstrated that the short and quasi-biweekly periodicities were evident, whereas the long period oscillation was somewhat obscure due to the lack of averaging.

In this section the periodicities are extracted quantitatively from both the regional time series of $\overline{Q^*}$ and from the zonally averaged time series of instantaneous Q*. The procedure is very straightforward. It does not involve sophisticated spectrum analysis. The objective here is not to seek evidence of new periodicities in the radiation and cloud fields; the principal oscillations have been identified in previous investigations as discussed in sub-sections 3.1.3-3.1.5. Instead, the following analysis is intended only to identify the robustness of the three recognized modes in the net radiation signals (long period, quasi-biweekly, and short period). To do so, only periodograms of the Fourier transform have been used.

In this scheme, two parameters are assigned for dominant peaks (frequencies) associated with a given mode, for either a given region or

a given 5^{o} zonal average. The first is the ordinal position of a given peak in terms of explained variance; the second is the actual resolved period (in days). The long period oscillations are assumed to reside in a periodicity range of 25-50 days, the quasi-biweekly oscillations between 9-20 days, and the short period oscillations between 3-8 days. The frequency intervals conforming to the above ranges are scanned for a relative maximum peak. The order of that peak, in terms of explained variance and the actual resolved period, are then assigned.

There is no attempt to smooth the periodogram. If a double peak situation occurs at three continuous frequencies in the Fourier domain, a single mode is assumed and the central frequency of the triplicate is used to assign a period in days. There is a tacit assumption that the periodogram will be noisy and contain spurious peaks. This is a well known feature of periodograms. For this reason, a peak within one of the three dominant modes must reside in the first five peaks in terms of explained variance, before it qualifies as a candidate for the tabulation.

3.7.1 Regional Periodicities

The results for the five regional areas are presented first. The 79-day time series of $\overline{Q^{*}}$ presented in Figs. 3.60-3.64 were subjected to the analysis procedure. The results are presented in Table 3.12 for all five regions. It is apparent from this summarization that major spectral peaks arise for all three principal modes. Only one peak (the short period peak for India) falls below the top three peaks in order of explained variance; in this case it is the fourth peak. The periodograms are shown in Figs. 3.66a-c.

TABLE 3.12

Periodicities in the Net Radiation Term at the Regional Scale

	Long Period	Quasi-Biweekly	Short Period
Arabian Sea			
Order	1	2	3
Period	40	11	6
Bay of Bengal			
Order	1	2	3
Period	40	13	6
Indian Sub-Continent			
Order	1	2	4
Period	26	10	5
Tibetan Plateau			
Order	3	2	1
Period	26	11	6
Arabian Empty Quarter			
Order	3	1	2
Period	26	11	6

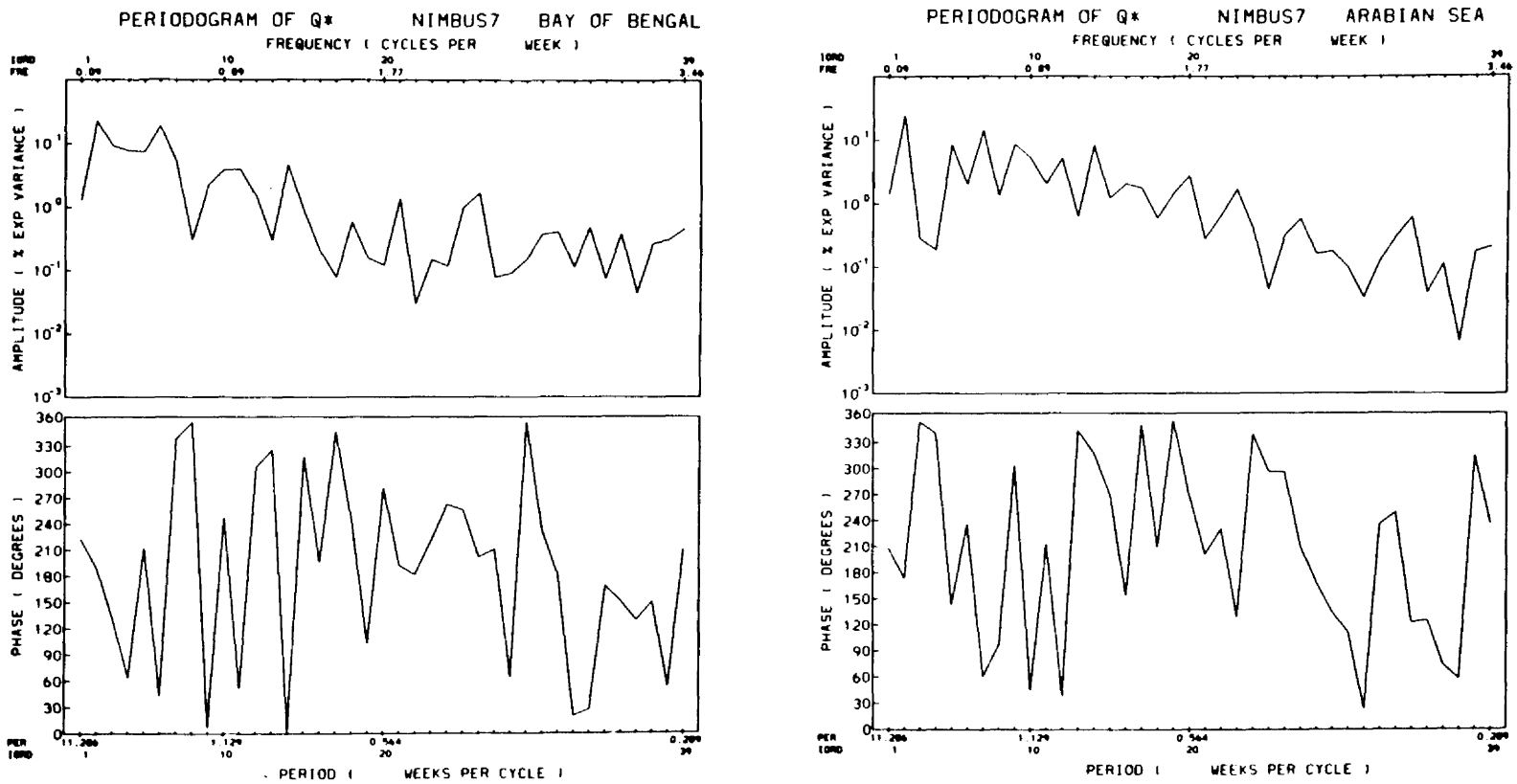

Fig. 3.66a. Periodograms of 79-day (May 19-August 5) time series of Q* derived from Nimbus-7 for grid square over the Arabian Sea (left) and the Bay of Bengal (right).

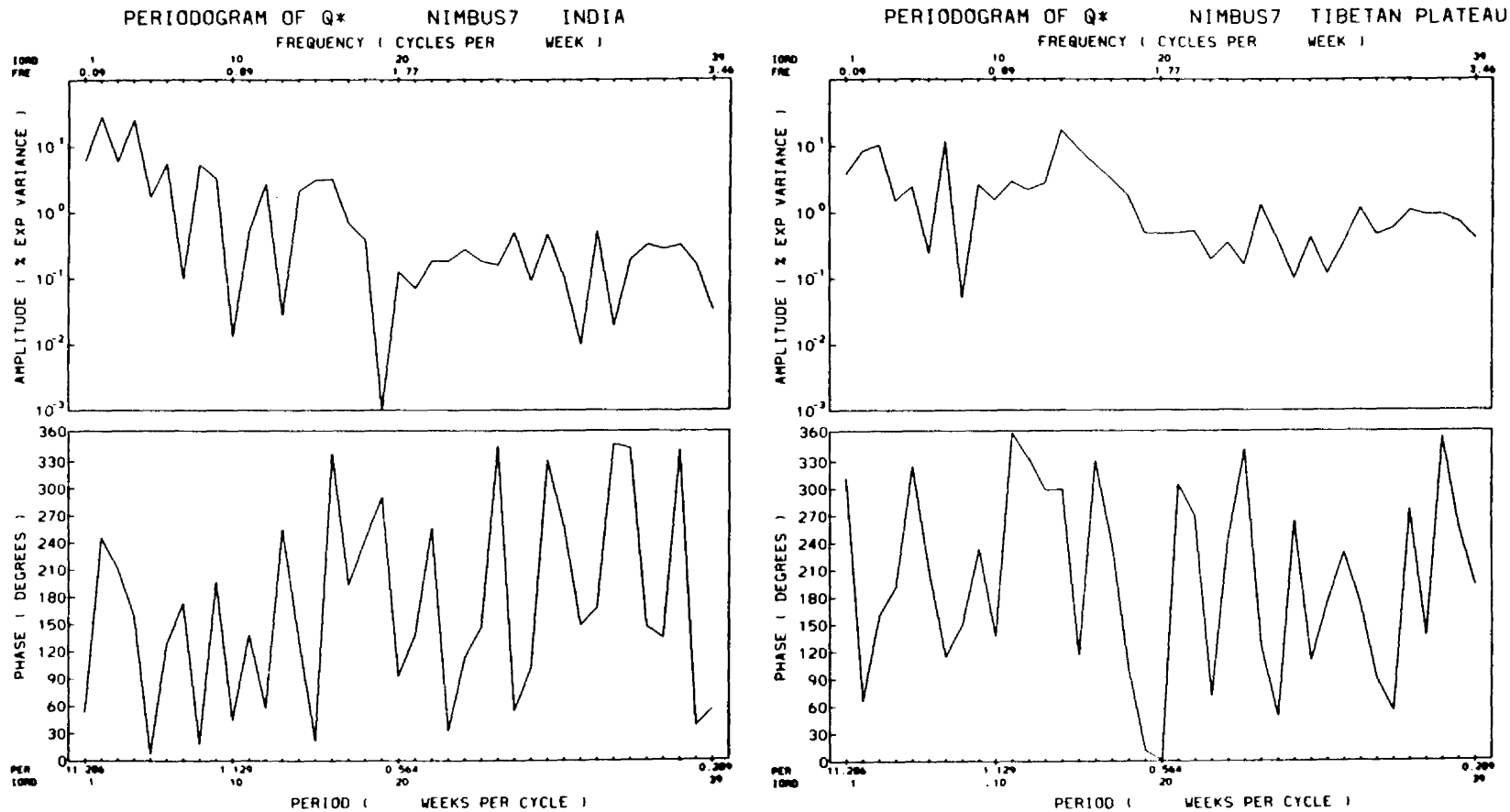

Fig. 3.66b. Same as Fig. 3.66a for the Indian Sub-continent and the Tibetan Plateau.

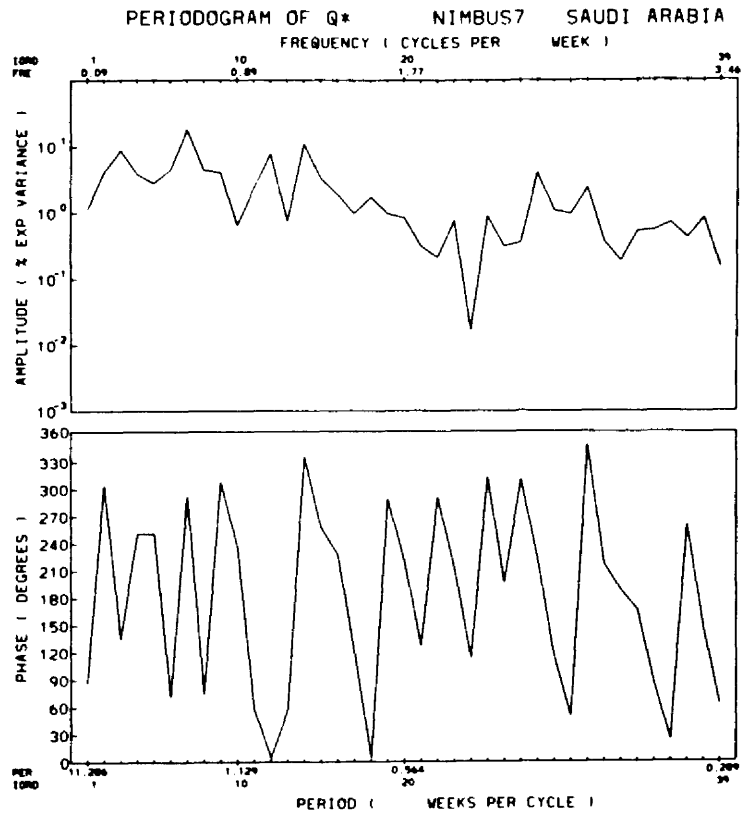

Fig. 3.66c. Same as Fig. 3.66a for the Arabian Empty Quarter.

A brief inspection of Table 3.12 indicates that regional quasi-biweekly oscillations are on the order of 11 days in the net radiation field. The short period oscillations appear to be approximately 6 days. Both 26 day and 40 day periodicities occur in the long period regime but this periodicity cannot be clearly resolved with such a short time series. These results demonstrate that on a localized scale, radiative forcing is damped according to the intensity of the monsoon.

3.7.2 Periodicities in the Zonal Averages

Similar tabulations of the 5^{o} averaged zonal time series of Q*, derived from TIROS-N, are provided in Table 3.13. There are two basic conclusions to be drawn from this table. In a zonally averaged perspective, the long period and short period modes are readily apparent. This is obvious from an examination of the time latitude section of Q* given in Fig. 3.52. The quasi-biweekly oscillation, however, is poorly resolved as indicated by the proliferation of peaks in the 9-20 day period range. This result is not altogether surprising in that the quasi-biweekly oscillation is very likely a manifestation of monsoon depressions that originate in the Bay of Bengal and travel along the monsoon trough giving rise to fluctuations in the rainfall in Central India. Thus the effects of this specific mechanism would not be expected to reveal themselves clearly in the larger scale zonally averaged radiation budget.

3.8 Diurnal Processes

As pointed out in Section 3.4, the geosynchronous satellite is an excellent platform for monitoring the diurnal radiation budget cycle. In fact, if there had been fewer missing data problems during SMONEX associated with the GOES-1 imagery, it would not have been necessary to

TABLE 3.13

Periodicities in the Net Radiation Term for 5° Zonal Averages

	Long Period	Quasi-Biweekly				Short Period	
Eq - 5°N							
Order	3	1	2	3	4	-------	
Period	30	9.4	15	8.1	11		
5° - 10°N							
Order	1		2	3	4		5
Period	60		17	9.4	12		4.9
10° - 15°N							
Order	1		2	3	4		5
Period	40		17	12	9.4		4.7
15° - 20°N							
Order	1		2	3	5		4
Period	40		20	11	7.6		4.4
20° - 25°N							
Order	1			2	3	4	5
Period	40			20	12	6.9	5.6
25° - 30°N							
Order	1			2	3	4	5
Period	40			20	12	5.1	5.8
30° - 35°N							
Order	1			2	3	4	5
Period	40			8.7	12	6.4	3.4

resort to the AVHRR data at all. The results of the diurnal analyses, presented in the following two sub-sections, cover three critical 10-day periods during the course of the SW Monsoon. These are: 1) the pre-monsoon onset period (June 1-10); 2) the monsoon onset period (June 11-20); and 3) the post-monsoon onset period (June 21-30). The dates and times of the GOES-1 imagery retrieved during June for this purpose have been tabulated in Table 3.3. The monsoon domain has been divided into 12 regions in conjunction with these analyses. The regional sectors were depicted in Fig. 3.6.

3.8.1 Evolution of Diurnal Forcing

The depictions of the diurnal cycles are presented in Figs. 3.67-3.78. Each figure is in three parts, corresponding to the three aforementioned periods. The K↓, A, L↑ and Q* are the parameters selected for plotting, as the key in the left hand part of each diagram indicates.

The graphs for the Arabian Sea and the Bay of Bengal exhibit basically similar properties (Figures 3.67,3.68). There is a large increase in albedo between period 1 and 2 (9% at local noon), followed by very little change in magnitude during period 3. There is a very definite distortion of the symetric properties of the daily albedo function in period 3. Concerning the diurnal longwave emission cycles, only the period 1 Arabian Sea signal exhibits any significant amplitude. Otherwise, little meaningful diurnal structure in the L↑ signals is in evidence. Longwave emission is reduced by $\approx 50\ W \cdot m^{-2}$ over the Arabian Sea between period 1 and period 2; the reduction is not as extensive over the Bay of Bengal ($\approx 35\ W \cdot m^{-2}$). The amplitude of instantaneous noontime radiative convergence (Q*) into these two oceanic zones is

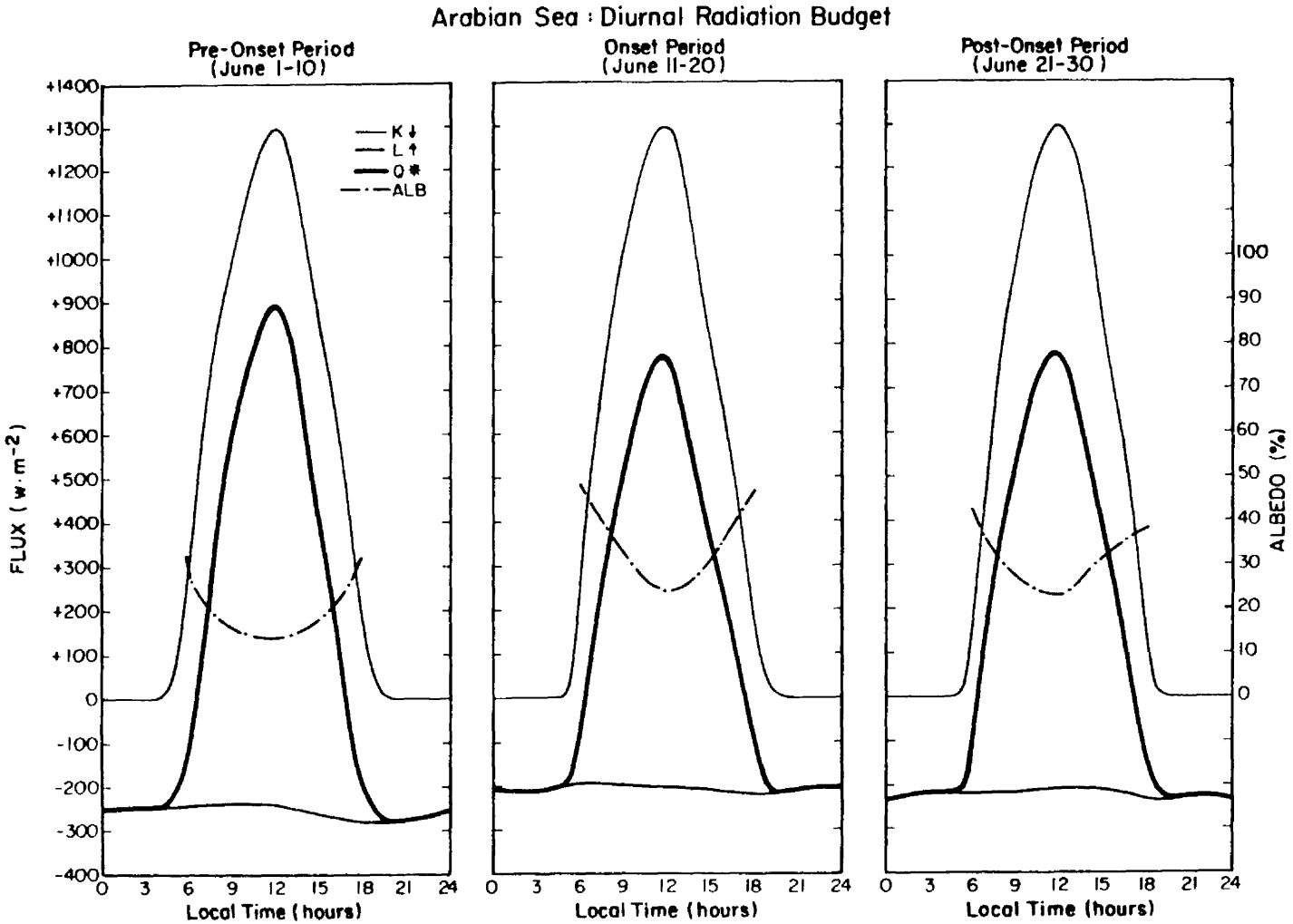

Fig. 3.67. Diurnal radiation budget over Arabian Sea based on GOES-1 measurements for three 10-day periods in June.

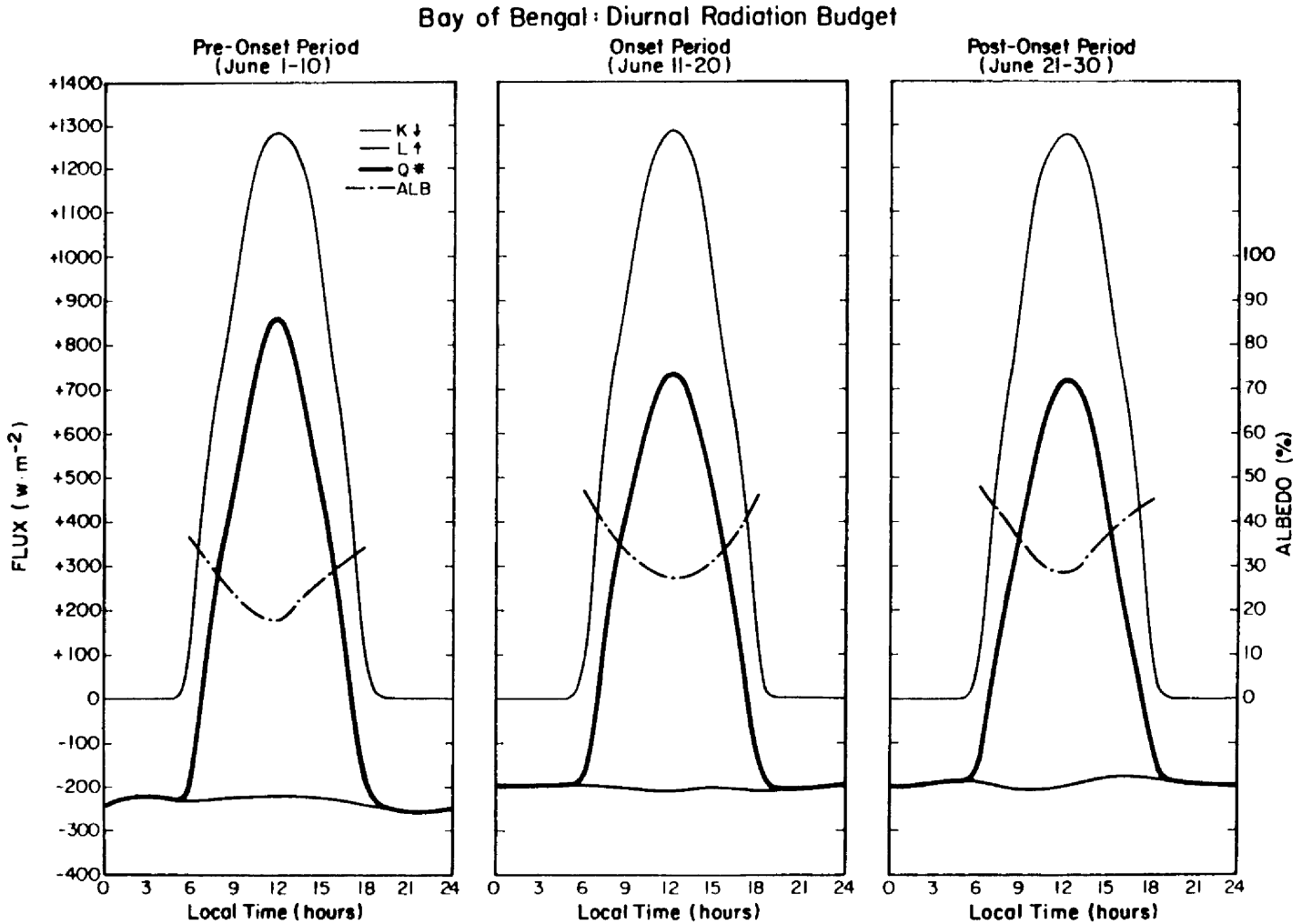

Fig. 3.68. Same as Fig. 3.67 for Bay of Bengal.

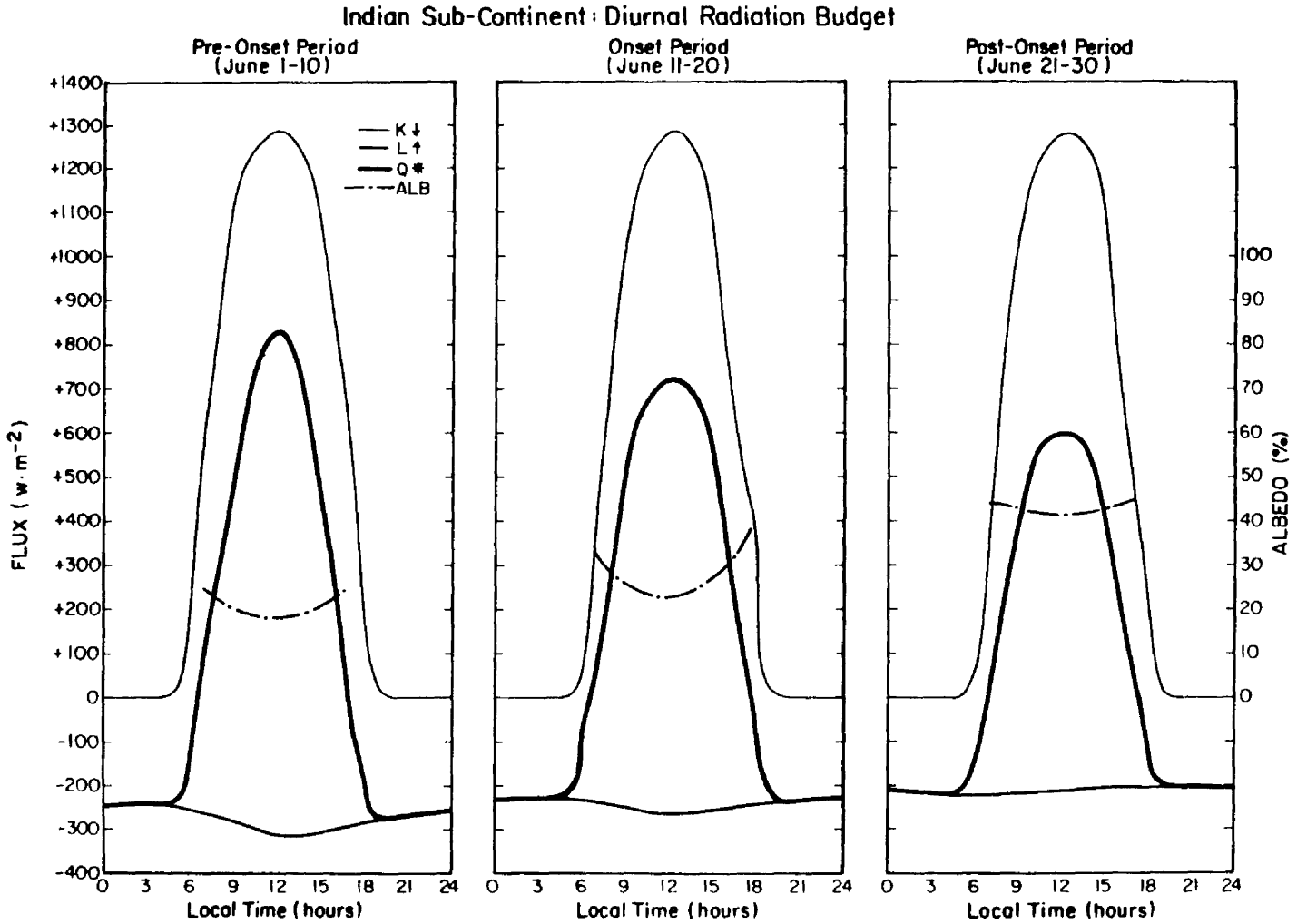

Fig. 3.69. Same as Fig. 3.67 for Indian Sub-continent.

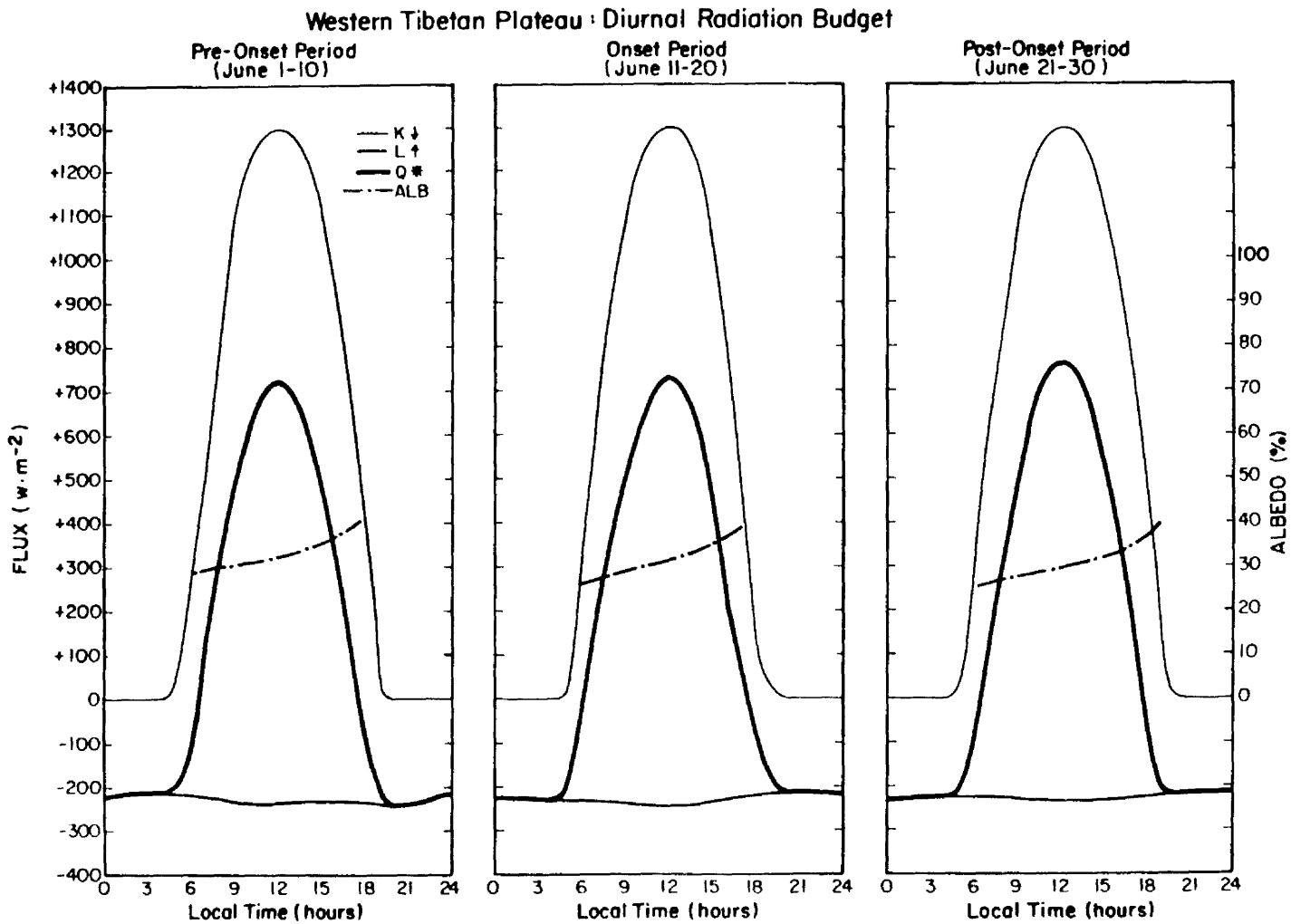

Fig. 3.70. Same as Fig. 3.67 for Western Tibetan Plateau.

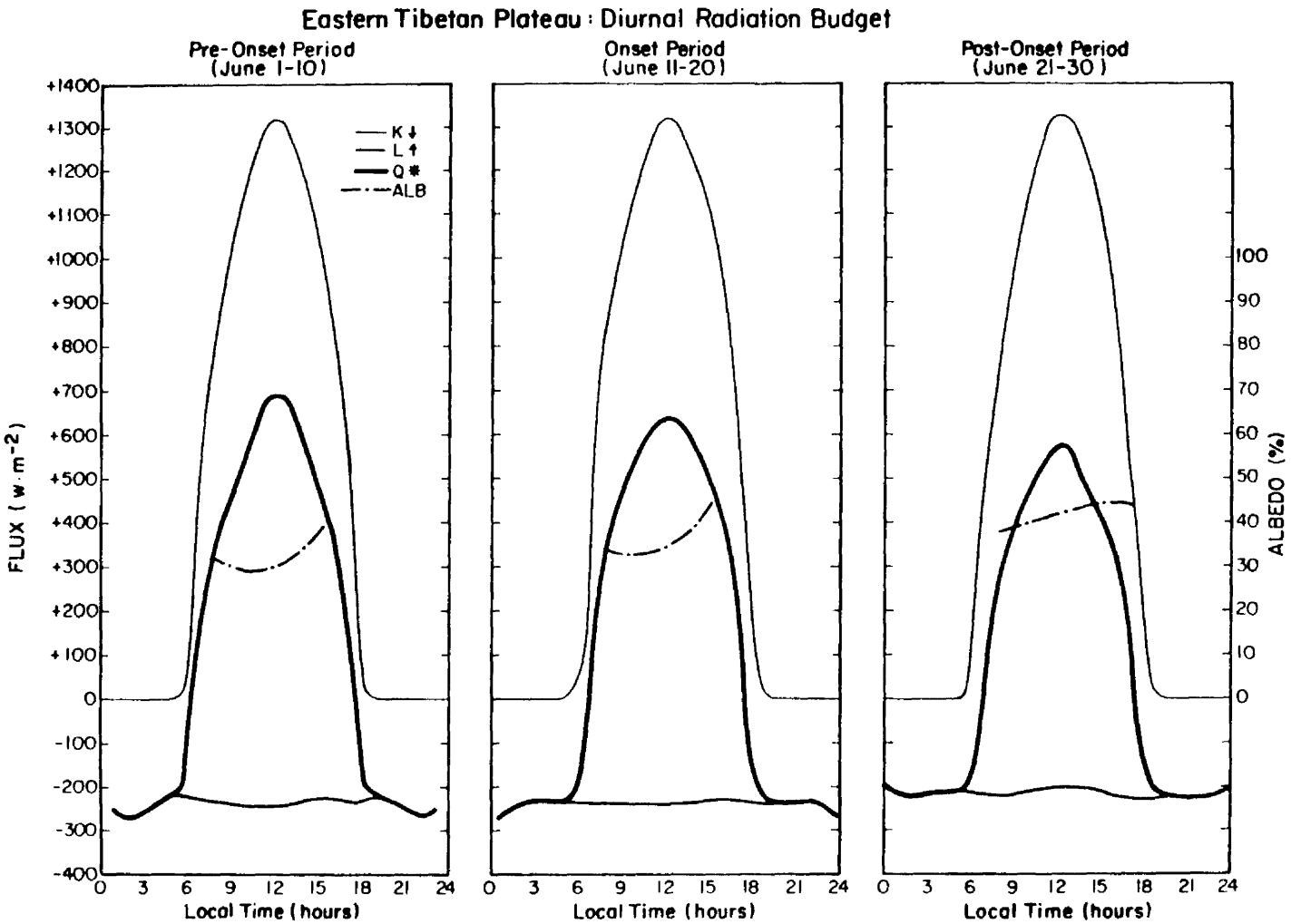

Fig. 3.71. Same as Fig. 3.67 for Eastern Tibetan Plateau.

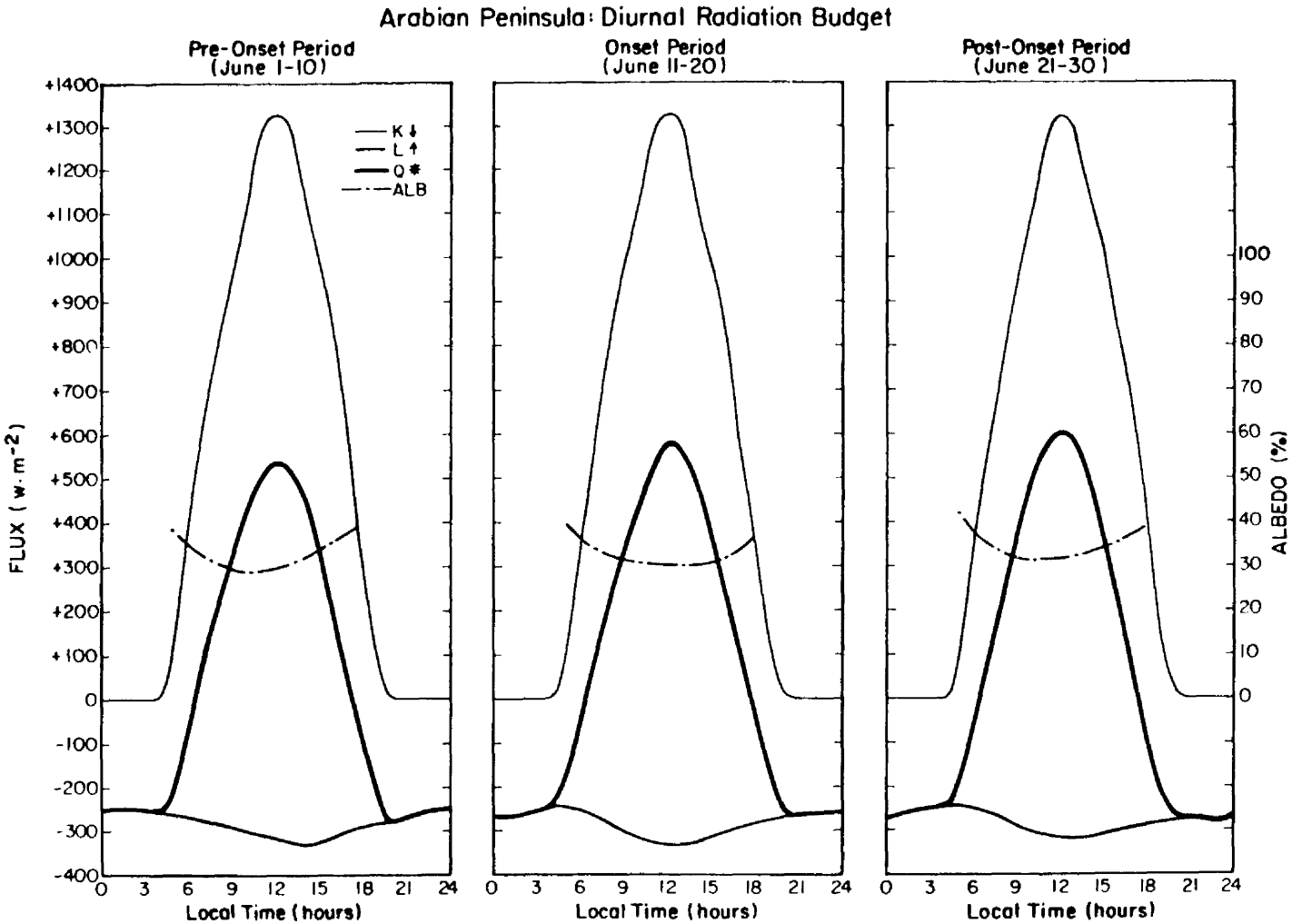

Fig. 3.72. Same as Fig. 3.67 for Arabian Peninsula.

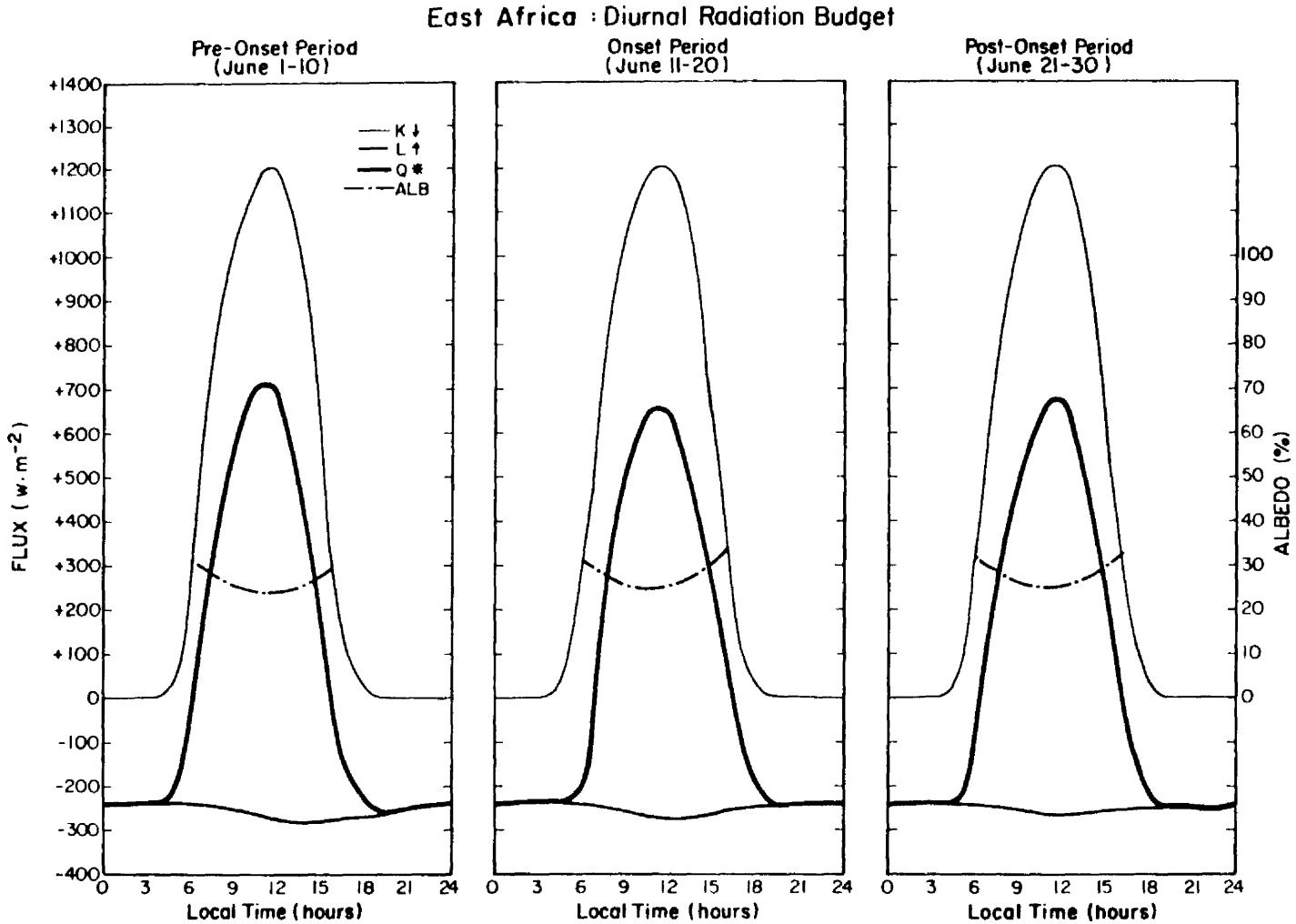

Fig. 3.73. Same as Fig. 3.67 for East Africa.

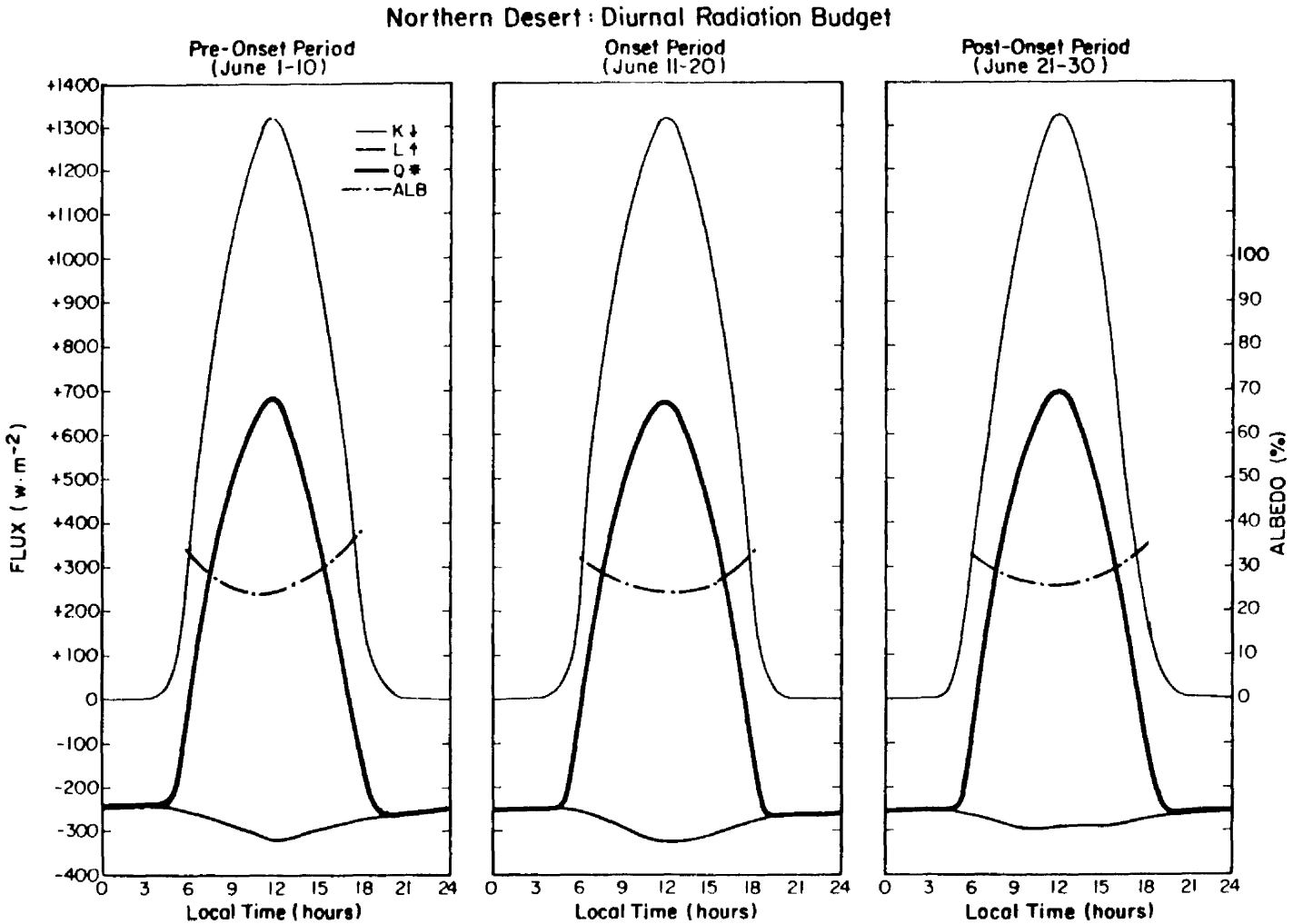

Fig. 3.74. Same as Fig. 3.67 for Northern Deserts.

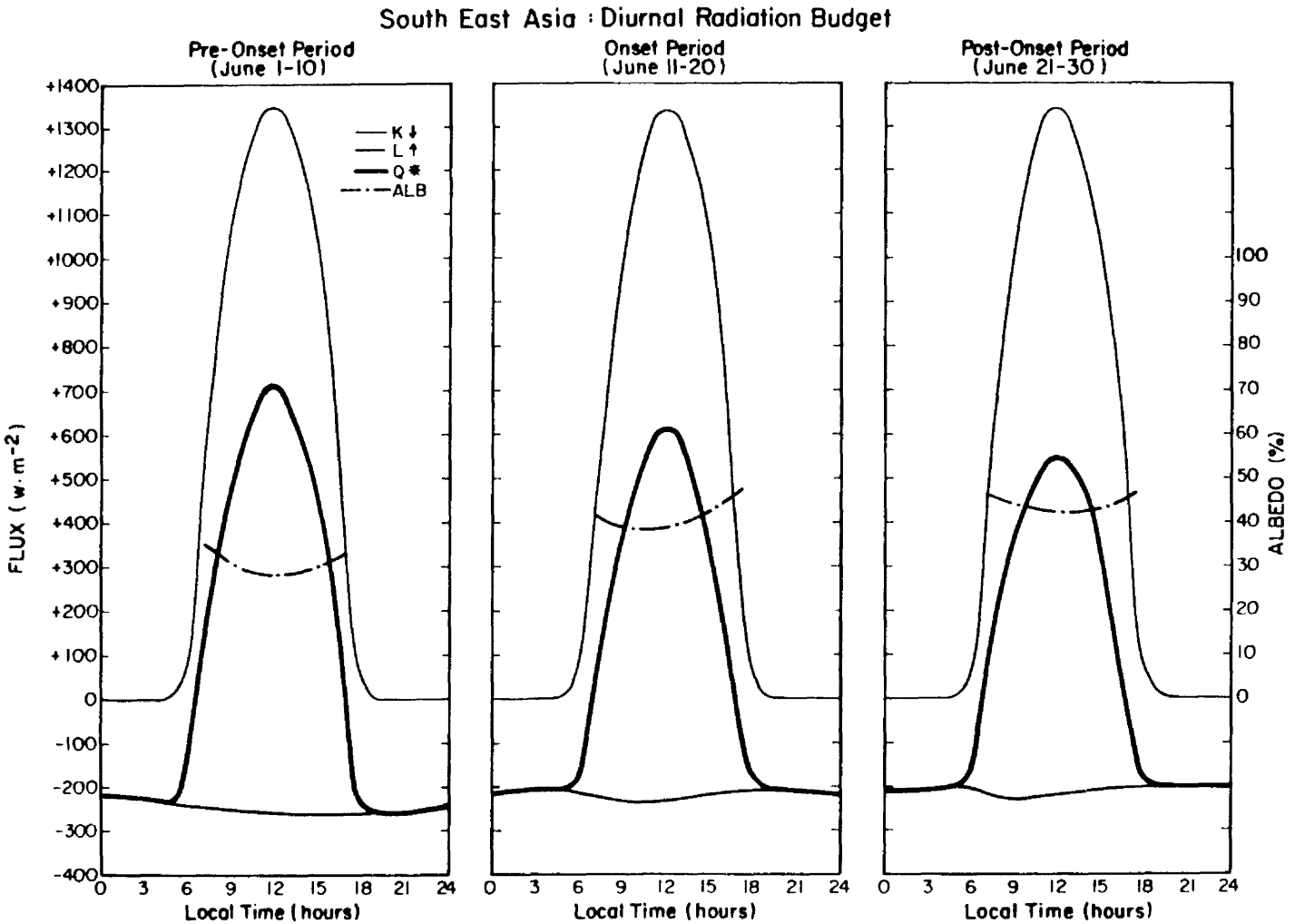

Fig. 3.75. Same as Fig. 3.67 for South East Asia.

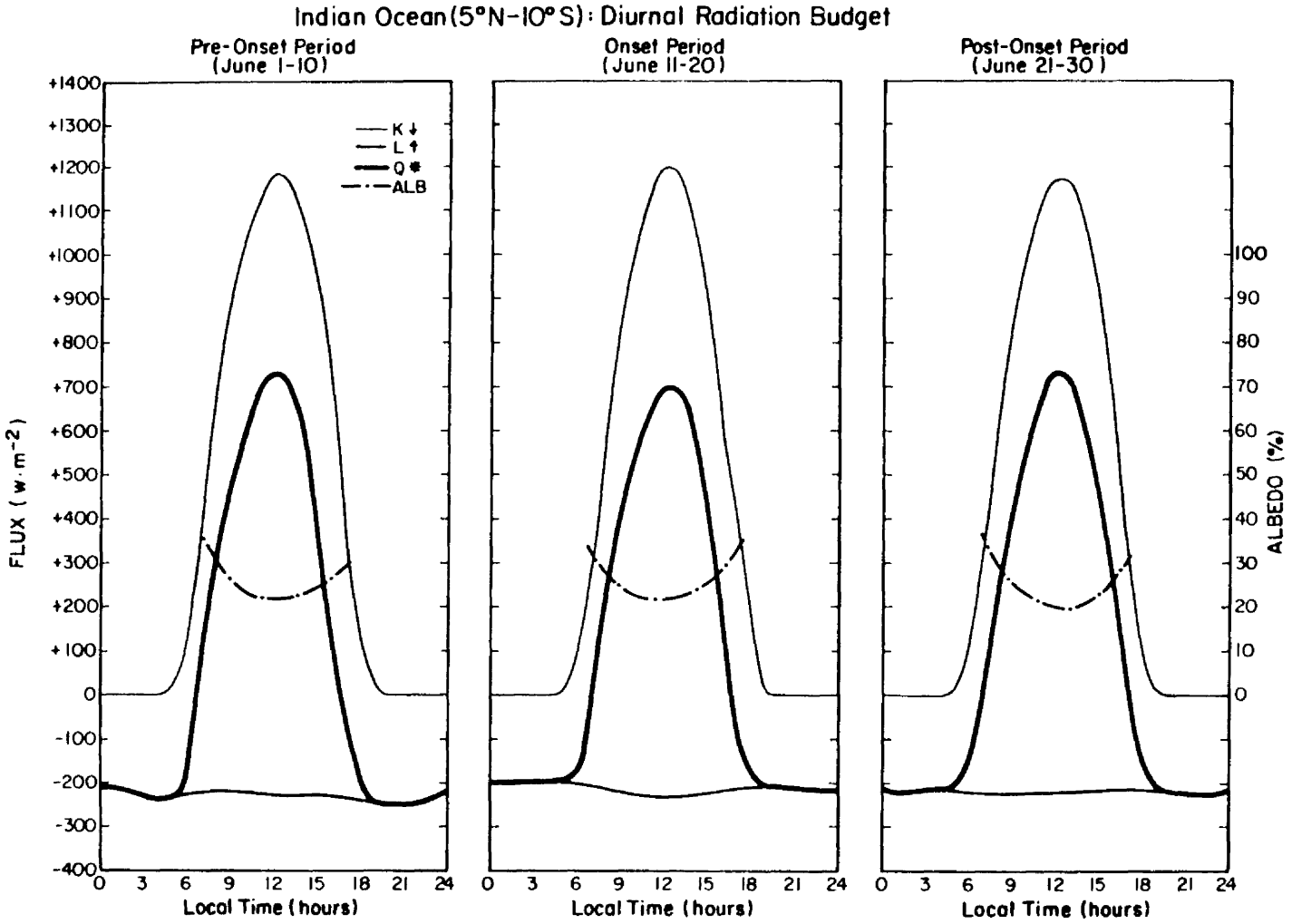

Fig. 3.76. Same as Fig. 3.67 for Indian Ocean (5^{o}N-10^{o}S).

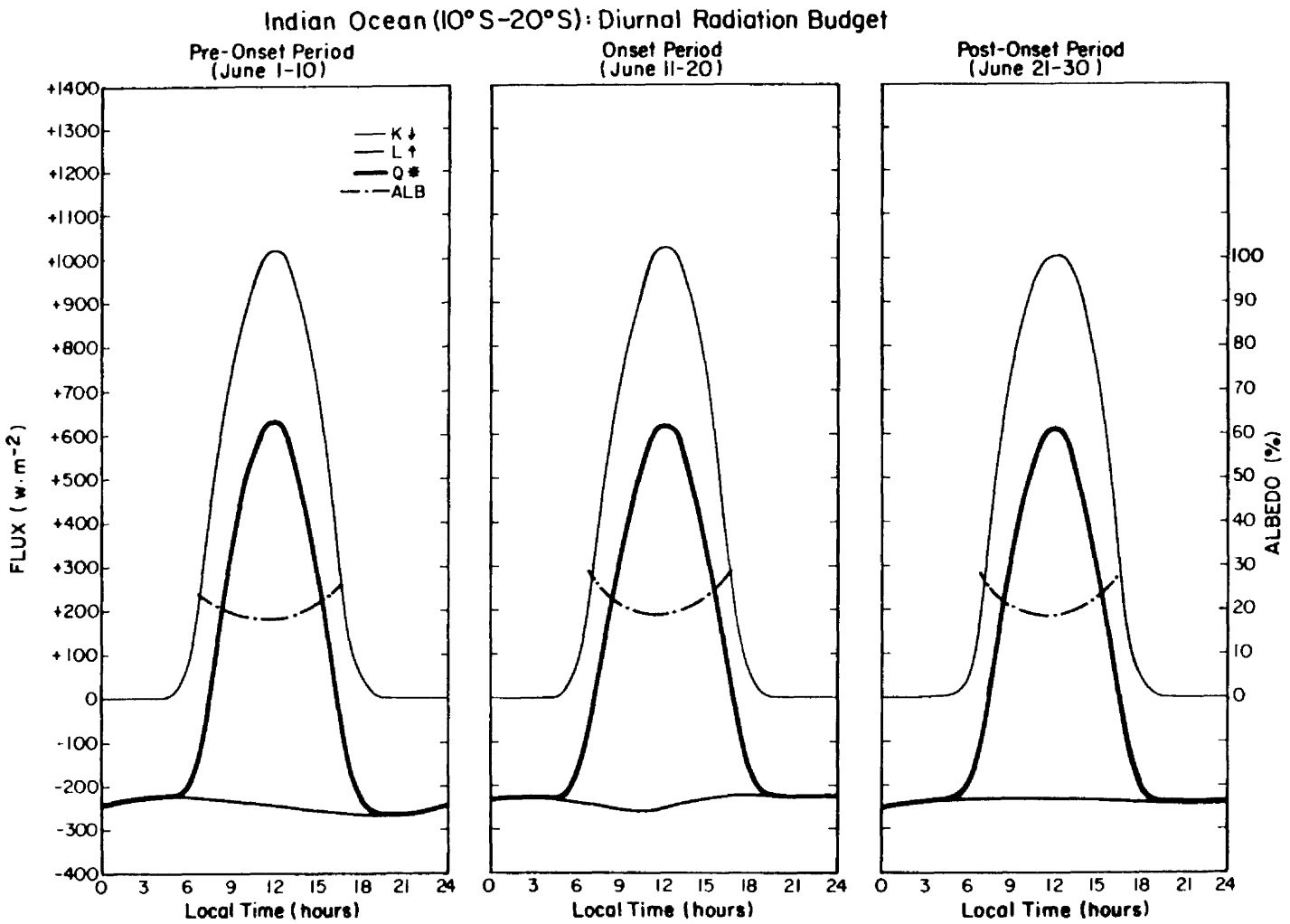

Fig. 3.77. Same as Fig. 3.67 for Indian Ocean (10^{o}S-20^{o}S).

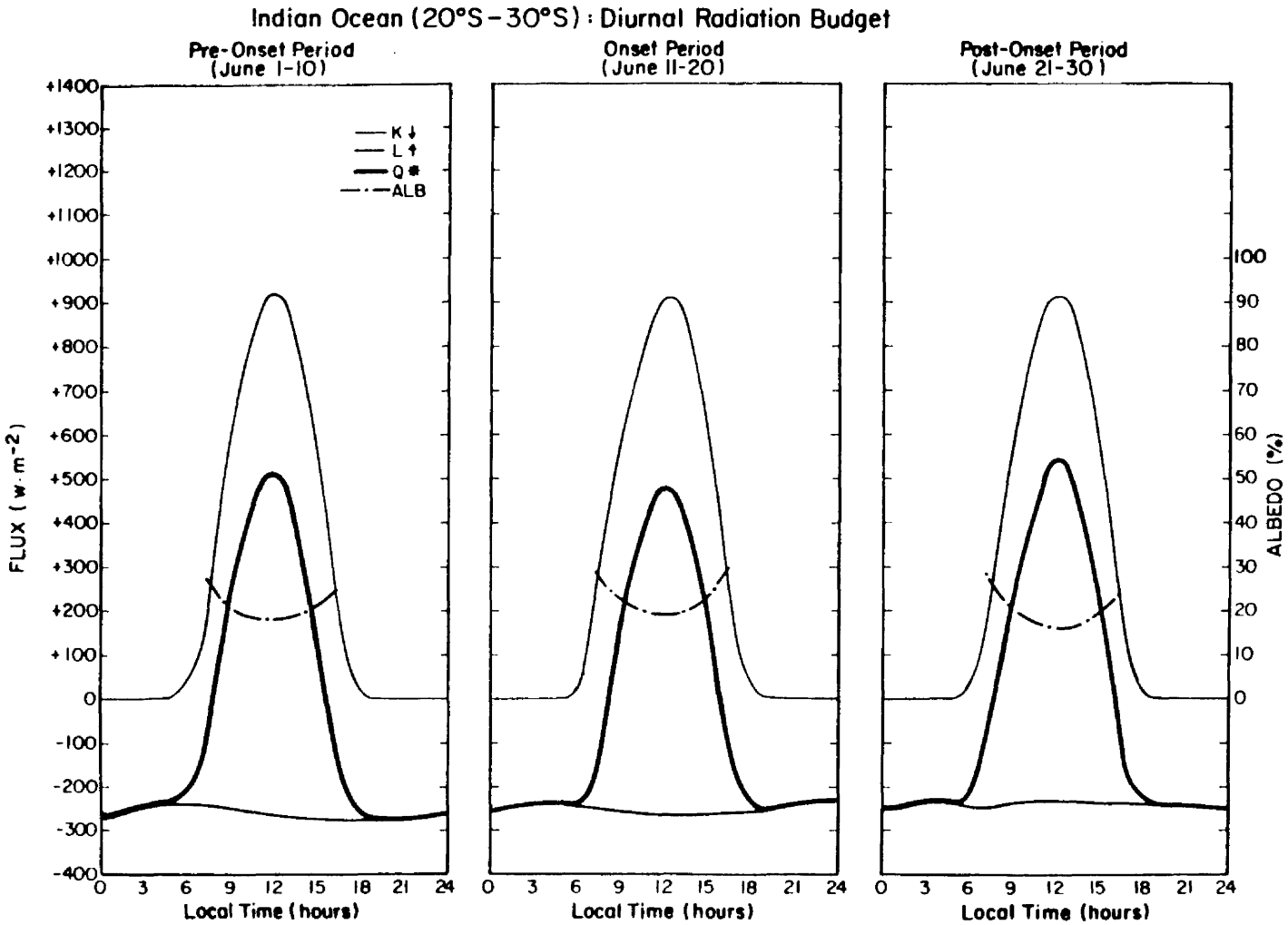

Fig. 3.78. Same as Fig. 3.67 for Indian Ocean (20^{o}S-30^{o}S).

reduced by over 100 $W \cdot m^{-2}$ between periods 1 and 2. Very little change occurs after that during period 3.

The cycles for the Indian Sub-continent (Fig. 3.69) are far more interesting. Note the rapidly changing albedo function as the three periods progress, as well as the reduction in $L\uparrow$ from between 40 to 100 $W \cdot m^{-2}$. The albedo function is almost flat during period 3.

Figures 3.70 and 3.71 provide the contrasts in the radiation budget over the western and eastern Tibetan Plateau regions. It is noted that the albedo functions from both regimes exhibit marked deviation from daily symmetry. The principal difference in these two regimes, is that the drier western plateau Q^* cycle is higher in amplitude in period 1 by ≈ 25 $W \cdot m^{-2}$, increasing to an amplitude difference of 175 $W \cdot m^{-2}$ by period 3. These differences illustrate very clearly the contrasting monsoon impact of the eastern and western plateau regions. Once the monsoon is established over the eastern plateau, the cloudiness effects tend to dominate the ever increasing surface temperatures resulting in a mean reduction of longwave emission by ≈ 25 $W \cdot m^{-2}$.

The diurnal radiation budget over the complete Arabian Peninsula (Fig. 3.72) shows little change between periods 1 and 3; the high amplitude diurnal oscillation in $L\uparrow$ is characteristic of sub-tropical deserts. The diurnal cycles for East Africa, the Northern Deserts, and South East Asia are shown in Figs. 3.73-3.75. The high amplitude daytime surface heating is very obvious in the East African and Northern Desert (Iraq, western Afghanistan and Pakistan) regions. The monsoon has little effect on the diurnal radiation budget cycles of the first two regions, however, in the case of S.E. Asia, the monsoon onset influence is very strong. The amplitude of Q^* is decreased 170 $W \cdot m^{-2}$

between periods 1 and 3; the steady decrease in $|L\uparrow|$, between periods 1 and 3 due to cloudiness, is overwhelmed by the increase in albedo.

The results for the three Indian Ocean regions are shown in Figs. 3.76-3.78. There are no significant changes between periods 1 and 3 for either of these three regions other than in the shapes of the diurnal longwave emission cycles. There are, however, differences from region to region for any given period. Note, for example, the higher albedos in the Northern Indian Ocean sector and the corresponding decreased longwave emission.

3.8.2 Diurnal Gradients in Time and Space

The most succint form to examine the nature of the diurnal budgets is by calculating time and space gradients. These clearly illustrate important differential processes that feedback into atmospheric and surface heating. Figure 3.79 presents the two diurnal tendency cycles of Q* over the Indian sub-continent between the pre-monsoon onset - monsoon onset, and monsoon -onset-post-monsoon onset periods. The key feature of this diagram is the decrease of radiative energy into the India sub-continent during the course of June (this radiative blocking process was illustrated at the larger scale in sub-section 3.5.3). Here, however, we see that on a diurnal time scale, as the monsoon undergoes initiation, although there is total radiative blocking from one period to the next, the deficit arises from solar-daytime processes; at night the tendency is for the continent to gain radiative energy.

If we examine an oceanic region next to India, in this case the Arabian Sea, and plot the same two tendency cycles (Figure 3.80), it shows the same phenomena as above between periods 1 and 2 (June 1-10 to

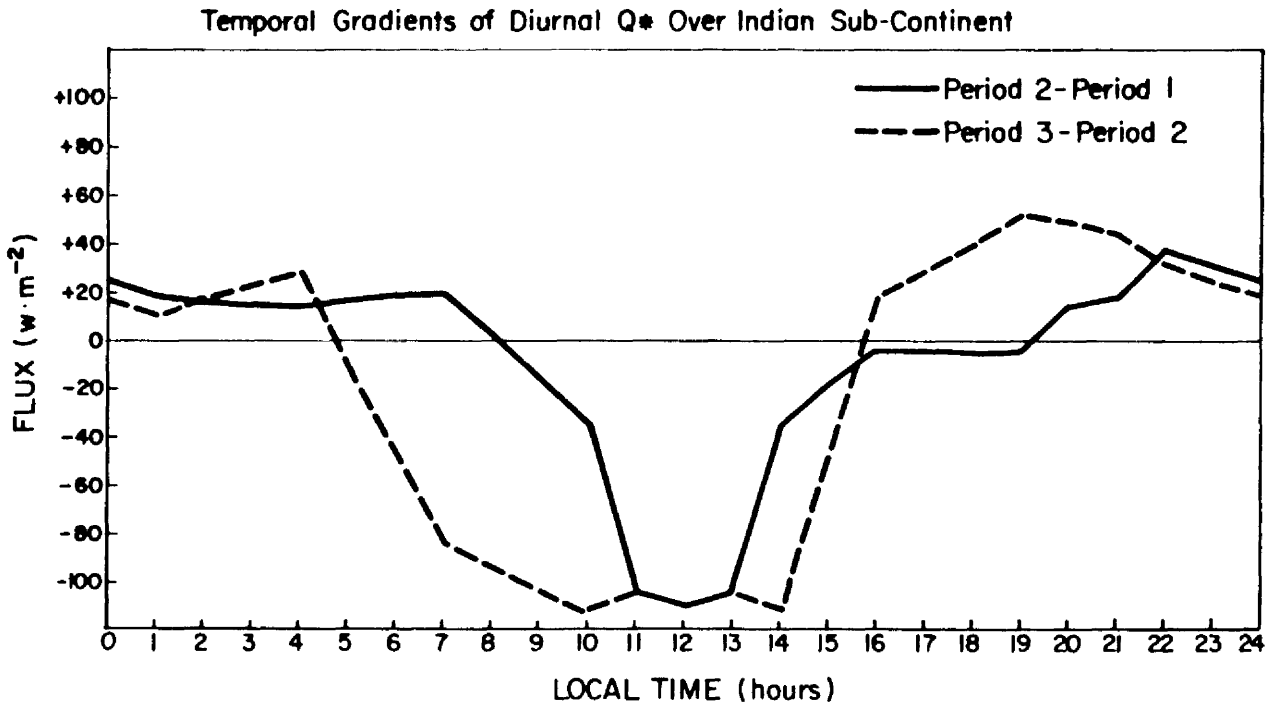

Fig. 3.79. emporal gradient of diurnal Q* over Indian Sub-continent.

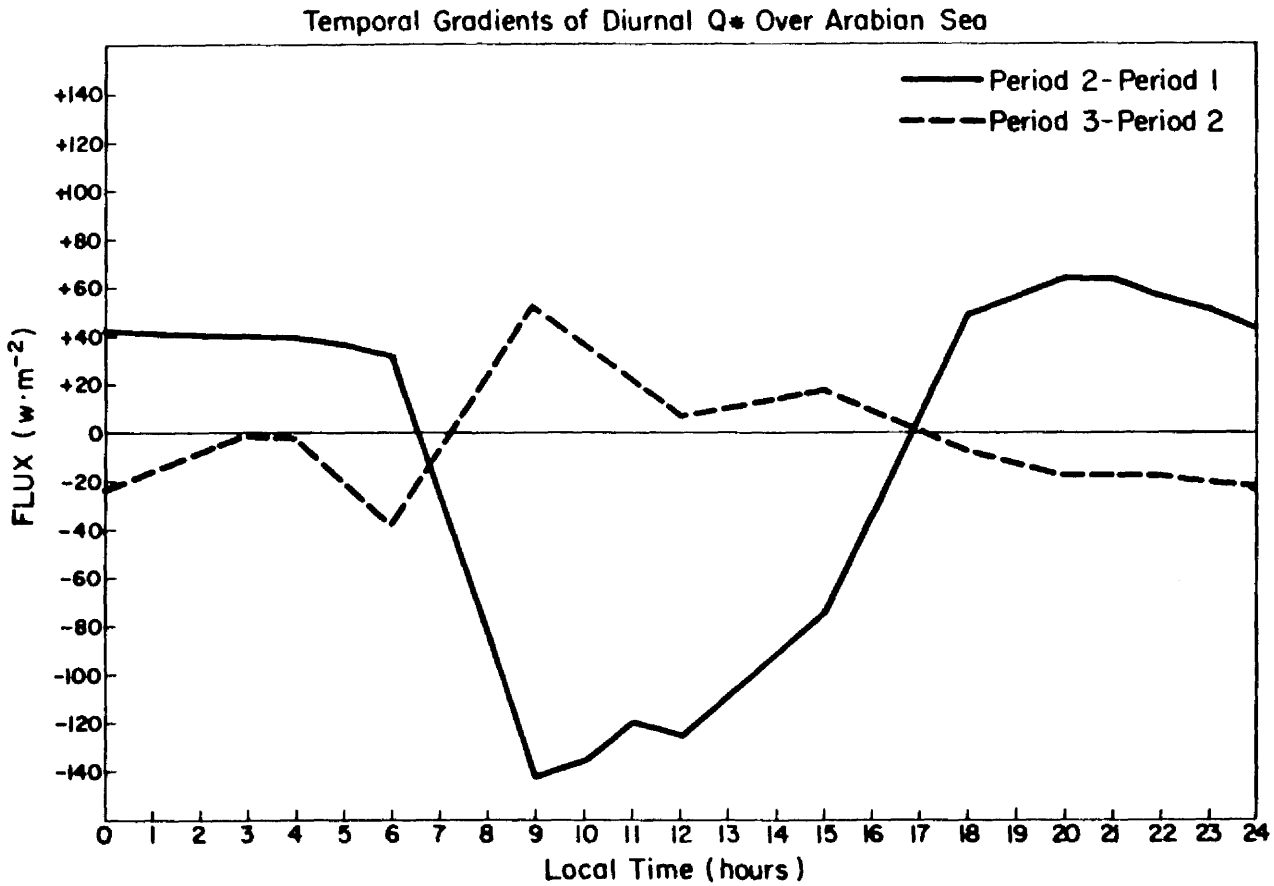

Fig. 3.80. Same as Fig. 3.79 for Arabian Sea

June 11-20), but between periods 2 and 3 (June 11-20 to June 21-30) the Arabian Sea undergoes slight daytime convergence and slight nighttime divergence.

Finally, in Fig. 3.81, the spatial gradients between the Indian sub-continent region and the Arabian Sea region are plotted. Because the diurnal cycles are not perfectly resolved with the 3-hour sampling interval, and because there are unequal populations in the diurnal statistical averages, this calculation is not considered highly quantiative (thus the oscillations in the plots). However, in a qualitative sense, during periods 1 and 2, we see that the Indian sub-continent tends to receive more net radiative input than the Arabian Sea. After monsoon onset, however, the sub-continent undergoes a transition to extensive cloudiness and the reverse situation occurs as the spatial differential becomes generally negative.

3.9 On Radiative Decoupling

A recent article by Stephens and Webster (1984) has pointed out a characteristic of clouds that has prevented the use of radiation budget data for estimates of atmospheric heating. The phenomonon they refer to is radiative decoupling, which is the process in which cloud fields detach the downward solar and longwave source term from the surface in substantially different manners. The basic physical principals behind this effect are that the downward longwave flux is highly dependent on the level of cloud base and the integrated moisture column up to cloud base, whereas solar insolation at the surface is conditioned mostly by the integrated liquid water content within the cloud and is thus insensitive to cloud height. A cloud which grows vertically tends to reduce K↓ (surface) without impacting L↓ (surface); raising a given

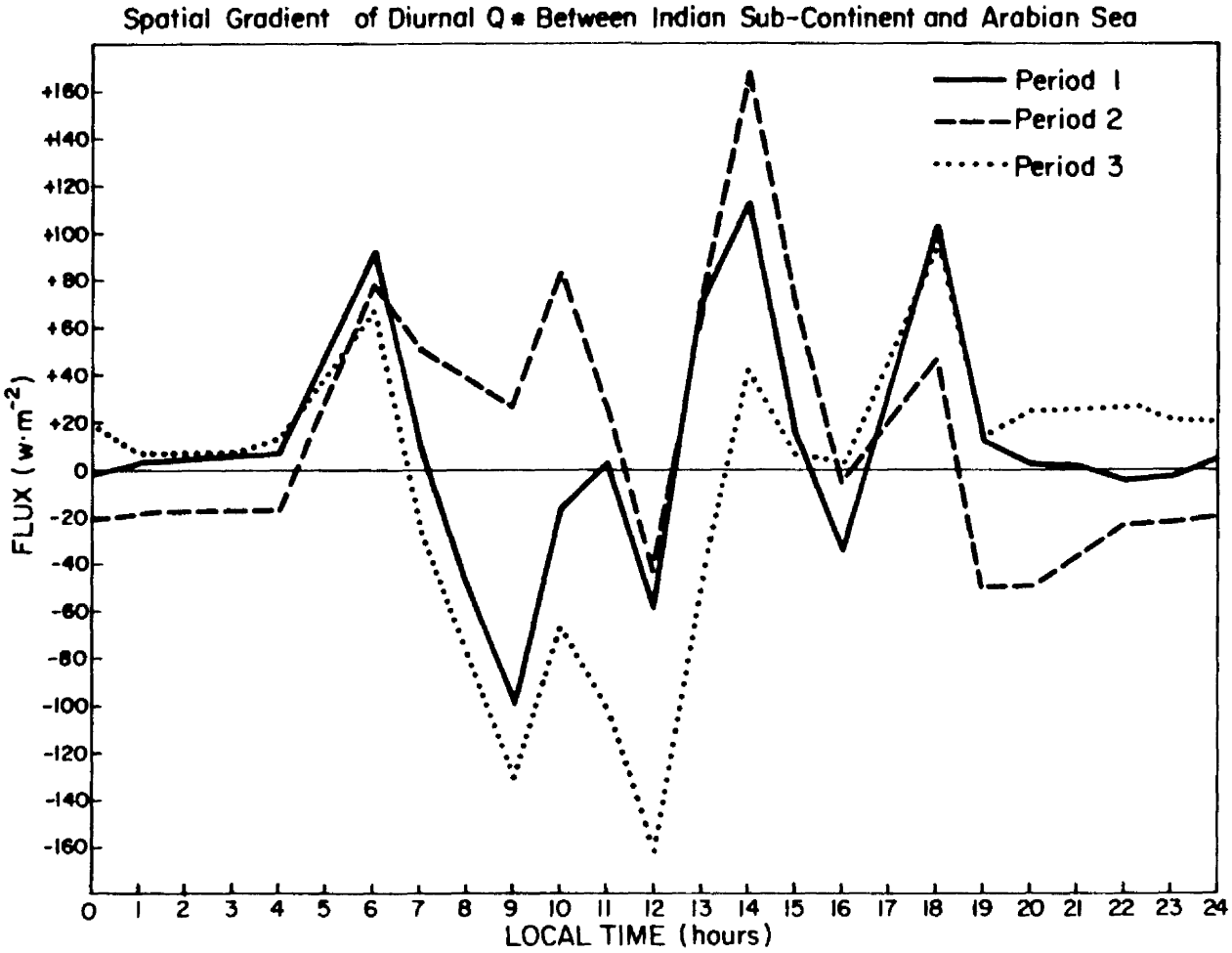

Fig. 3.81. Spatial gradient of diurnal Q* between Indian Sub-continent and Arabian Sea.

cloud's base height, with no change in cloud thickness, tends to reduce L↓ (surface) without impacting K↓ (surface). This is the process of cloud decoupling that has raised the spector of TOA radiation budget parameters being poor choices for parameterizing the effects of surface temperature and albedo in Energy Balance Climate Models (EBCM's).

An analogous problem concerns the role of clouds and surface backgrounds on decoupling or 'decorrelating' the TOA radiation budget parameters from each other. The following analysis is not presented as a conclusive test of cloud decorrelation but as evidence that no single RADBUD parameter can be used exclusively to monitor the radiation climate. The experiment here is straightforward. A correlation table for the 5^{o} zonal and meridional averages of A, K↑, and Q* over the 4-month AVHRR data period is calculated. The degree of variability of the correlation coefficient is then used as a measure of how much cloud fields decouple TOA RADBUD parameters. Table 3.14 provides the correlation coefficient tabulations. This table also includes the average value of A, L↑ (day), and Q* for the 5^{o} zonal and meridional time series.

The results are rather interesting. The correlations between A and L↑ are relatively high (in a negative sense) and consistent for the zonal averaged time series, with the exception of the 5^{o}-10^{o}N zone, where the coefficient dips to -0.52. This zone, of course, undergoes extensive cloudiness throughout the course of the monsoon. On the other hand, the A-L↑ correlations for the meridionally averaged time series are very low throughout the almost purely desert and semi-arid regime of East Africa and the Arabian Peninsula, but quickly jump up to high negative values in the oceanic domain. The impact of the meridional

TABLE 3.14

Three Way Correlation Tabulation Between the AVHRR Retrievals of the Time Series of 5° Zonal and Meridional Averages

	Latitude Zone	AVE(A)	AVE(L↑)	AVE(Q*)	r(A-L↑)	r(A-Q*)	r(L↑-Q*)
1	0- 5	30.9	277	616	- .73	- .87	.38
2	5-10	30.0	282	637	- .52	- .96	.31
3	10-15	29.9	273	656	- .89	- .99	.84
4	15-20	28.9	255	689	- .94	-1.00	.91
5	20-25	25.0	243	746	- .96	- .99	.94
6	25-30	24.4	240	743	- .86	- .97	.80
7	30-35	25.6	235	711	- .82	- .92	.72
	Longitude Zone	**AVE(A)**	**AVE(L↑)**	**AVE(Q*)**	**r(A-L↑)**	**r(A-Q*)**	**r(L↑-Q*)**
1	30- 35	26.6	282	677	- .63	- .95	.37
2	35- 40	25.4	285	691	- .34	- .94	.00
3	40- 45	26.3	291	672	- .06	- .82	- .50
4	45- 50	26.2	293	671	- .26	- .77	- .39
5	50- 55	21.3	284	743	- .64	- .87	- .22
6	55- 60	19.6	275	776	- .78	- .96	.58
7	60- 65	20.3	267	776	- .84	- .99	.80
8	65- 70	23.4	255	746	- .94	-1.00	.92
9	70- 75	27.4	248	701	- .96	-1.00	.93
10	75- 80	31.6	245	649	- .93	- .99	.88
11	80- 85	28.9	240	688	- .94	-1.00	.92
12	85- 90	31.3	226	671	- .95	-1.00	.93
13	90- 95	38.5	215	589	- .94	-1.00	.93
14	95-100	41.0	217	553	- .82	-1.00	.78

strip containing Southern Indian (75^{o}-80^{o}E), a strip which contains very little ocean, imparts a slight relative minimum on the absolute value of the A-L↑ correlation sequence.

The A-Q* correlations are always high and negative, but since Q* is the instantaneous noontime value, this is not surprising. The L↑-Q* correlations, on the other hand, are highly variable. They are low in the zonal averaged equatorial belts, and sporadically low in the desert portion of the meridional averages.

One is easily led to the conclusion that cloudy regions over a uniform ocean surface, or relatively cloud free regions over a continental surface, decouple the longwave and shortwave processes at the top-of-atmosphere in a similar manner. This is, of course, an intuitively obvious result in much the same way as the Stephens-Webster (1984) findings. Cloud fields or continental surfaces can remain relatively invariant in the albedo field while the emitted infrared field fluctuates due to variations in cloud top height -- in the case of cloud fields; or due to variations in surface temperature from a variety of sources (solar insolation, surface moisture, boundary layer humidity) -- in the case of continental regions. Conversely, for the cloud case, variations in the thickness of layer cloud can lead to large changes in A without significantly altering L↑. And over large scale cloud free continental regions the emission temperature can remain invariant, whereas the albedo is varying due only to directional reflectance effects.

An important point to note is that not only are there a variety of processes that can lead to radiative decoupling, but that cloud fields and continental regions can manifest themselves in similar ways to the

decorrelate radiation budget terms. This being the case, the criticisms leveled at EBCM's, which attempt to link surface temperature with a single radiation budget parameter, as a means to calculate energy balance, are valid. It remains to be seen how much improvement can be made with this methodology.

3.10 Conclusions and Further Research Problems

The principal findings of this study have been based on analyzing radiation budget parameters over a variety of space and time scales for the 1979 southwest monsoon. First the evolution of the monsoon was presented by the use of high resolution (1/2 by 1/2 degree) 5-day averages of contoured radiation exchange fields. These maps provide a first hand view of many of the elements that make up a complete monsoon season. The pre-monsoon conditions, the early tropical storms, the northward propagation of the monsoon MCZ, the advance of the S.E. Asian monsoon, the explosive southwest monsoon onset, the surges, fluctuations, and breaks of the monsoon, and the seasonal changes over the Tibetan Plateau, are all well depicted through use of the contoured pentad averages.

To provide an evolutionary view at a much larger scale, Nimbus-7 NFOV net radiation maps (6 day averages) are presented. These maps illustrate very clearly the cellular pattern in net radiation across the eastern hemispheric tropics. A very interesting research problem involves the search for clues that would relate the cellular pattern to monsoon onset and intensity; i.e., the use of the net radiation parameter in the detection of monsoon teleconnections.

When the monsoon is presented on the zonal average scale over the complete monsoon domain, a very clear portrayal of the oscillatory

nature of the monsoon is seen. The northward propagating MCZ, of period 40-50 days, is the dominant feature although the quasi-biweekly and short period oscillations are clearly in evidence. The meridionally averaged monsoon, in particular the time-longitude section of net radiation, exhibits the signature of a monsoon break. The breaks are most evident in the radiation fields at western Indian longitudes. The meridionally averaged monsoon also exhibits an albedo merging effect between the Bay of Bengal and the Tibetan Plateau, once monsoon onset takes place. An important remaining problem, concerning the use of time-latitude and time-longitude sections is the degree of interannual variability of the zonally and meridionally averaged monsoon.

One of the more striking features, in terms of radiative forcing, is the systematic reduction of radiative input into the complete monsoon domain during the initiation phase. The analyses of the net radiation maps derived from the AVHRR data suggest that the depletion of energy during June, with resect to local noon, is on the order of 5 peta-watts. An important research topic concerns the year to year variation of the magnitude and regularity of the blocking effect.

An examination of localized area time series of radiation budget parameters has been presented. It was noted that although localized time series quite clearly indicate the major monsoon episodes, they tend to obscure the oscillatory nature of the monsoon, particularly the long period and quasi-biweekly oscillations.

The local area time series, constructed from Nimbus-7 narrow-field-of-view measurements, and those estimated from the AVHRR data are generally in good correspondence. One exception is the net radiative term over desert. The AVHRR Q* estimates correlate very poorly with the

Nimbus-7 NFOV measurements over a region on the Arabian Peninsula.

The periodogram analysis shows that both the zonal average time series and the local area time series generate power at the three dominant modes of monsoon oscillation (short period, quasi-biweekly period, long period), although at the zonal average scale the quasi-biweekly mode tends to proliferate over a range of frequencies.

The diurnally averaged monsoon is obtained by dividing the monsoon domain up into 12 sub-regions. Within each sub-region the evolution of the monsoon is presented through three 10-day periods corresponding to pre-monsoon onset (June 1-10), monsoon onset (June 11-20), and post-monsoon onset (June 21-30). By calculating time and space gradients of the diurnal cycles, the magnitudes of differential radiative convergence is obtained. This process is highlighted by calculating temporal gradients of Q* over the Indian sub-continent. Although there is systematic radiative divergence over the three 10-day periods (the radiative blocking effect), the nighttime period of the diurnal cycle tends to show radiative convergence.

Finally, the concept of cloud induced radiative decoupling of the shortwave and longwave surface radiative fluxes is reviewed. It is pointed out that there is an analogous decoupling effect taking place at the top-of-atmosphere. Correlative analysis is used to show how variation in the zonal and meridional cloud and surface backgrounds tends to decorrelate the principal radiative budget terms of albedo, infrared emission, and net radiation.

4.0 INVESTIGATION OF THE SURFACE ENERGY BUDGETS IN REMOTE DESERT AND MOUNTAIN ENVIRONMENTS

The characterization and quantification of the global surface energy budget is a growing concern for a variety of disciplines in the atmospheric sciences. Historically, surface energy exchange was of principal interest to microclimatologists, particularly those concerned with agricultural disciplines and crop forecasting. However, since the advent of operational numerical weather prediction models (NWP models), their closely related cousin - the general circulation model (GCM), and the more infant mesoscale and cloud models, there is a new community of user scientists keenly interested in the atmospheric lower boundary condition on both global and smaller scales; see e.g. Benoit (1976), Carlson and Boland (1978), Deardorff (1978), McCumber and Pielke (1981), Wetzel (1978), and Zhang and Anthes (1982).

Our science does not have a globally consistent climatology of the key surface energy budget parameters as a function of time of day or year or even more importantly from year to year. Nor do we expect to have such a climatology in the near future. This is the concern of an international body of geoscientists operating under the auspices of a proposed new program called the 'International Satellite Land Surface Climatology Project' (ISLSCP); see Rasool and Bolle (1984). As the title indicates, the principal platform for compiling a global climatology will be the satellite, presumably the international network of operational polar orbiting and geostationary weather satellites, the land resources satellite systems such as LANDSAT, and possibly future

systems similar to NASA's experimental Heat Capacity Mapping Mission (HCMM) satellite which carries the Heat Capacity Mapping Radiometer (HCMR); see NASA (1978).

4.1 Background

The justification for moving forward with such a program is, in part, based on various recent numerical simulations which point out the sensitivity of the short term climate to surface processes, particularly the surface hydrological cycle [see Kurbatkin et al. (1979), Rind (1982), Rowntree and Bolton (1983), Shukla and Mintz (1982), Walker and Rowntree (1977), Yeh et al. (1983, 1984)]. A central issue, however, is the reliability of remote sensing techniques applied to the problem of estimating surface parameters related to thermal, moisture, and radiation processes. There has been notable progress in this area, although mostly in the way of feasibility studies.

There have been a number of very basic studies directed at monitoring surface temperature processes with weather satellite imagery and the relationship of temperature and temperature changes to such phenomena as severe weather [Zandlo et al. (1982)], cold air drainage [Chen et al. (1979), Fritschen et al. (1982)], geological composition [Watson (1975) and Kahle (1977)], and land use [Shih and Chen (1984)]. A potential problem in studies along these lines is how to interpret temperature changes because of varying surface emissivity [see Kornfield and Susskind (1977), Sutherland and Bartholic (1977), Sutherland et al. (1979)]. In terms of the shortwave spectrum, Tarpley et al. (1984) have discussed NOAA's ongoing program to monitor a vegetation index based on differencing the visible and near-infrared measurements obtained from the polar orbiting weather satellites.

A relatively new method of investigation addresses the problem of how to estimate the actual surface flux exchange terms from satellite temperature and brightness (or albedo) information. Carlson et al. (1981) have developed an algorithm for using HCMM satellite derived surface temperatures in conjunction with a one dimensional boundary layer model to estimate the surface sensible and latent heat fluxes and the associated thermal inertia and moisture availability parameters, over urban areas. Thermal inertia, which is a measure of heat transfer at a ground-air interface, is related to the diurnal heat capacity through the earth rotation rate. Diurnal heat capacity is a direct measure of the heat flux required to raise a given material a unit of temperature, and thus, is a direct measure of temperature change for a given ground surface according to the rate of heat exchange. Moisture availability is related to the efficiency a given surface will evaporate its water content. The Carlson et al. (1981) study followed a long term concern with monitoring urban heat islands with satellites [Rao (1972), Carlson et al. (1977), Matson et al. (1978)].

Price (1977, 1980, 1982) has developed formulae for estimating these same parameters, based on satellite derived surface temperature and albedo, for application to the larger scales. His technique has been tested on HCMM data. Gurney and Hall (1983) have also used HCMM data to estimate evapotranspiration rates in the sub-artic. Recently Wetzel et al (1984) employed a one dimensional boundary layer model [Wetzel (1978)] to test the feasibility of using geosynchronous satellite IR data to estimate soil moisture content. They identified the mid-morning surface temperature rate of change (normalized by the surface net shortwave radiation term) as the parameter most sensitive to

soil moisture. This relationship was tested, using GOES data, over a region of the midwest United States with moderate success.

Chou and Atlas (1982) have taken a somewhat different approach in estimating sensible and latent heat exchange over coastal waters during cold air outbreaks. Their approach is based on detecting an indirect parameter controlled by surface energy change, in this case the length of the cloud free path from coastline to offshore cloud edge.

The estimation of radiative fluxes at the surface using top-of-atmosphere (TOA) satellite measurements has been under investigation for a number of years. Vonder Haar and Ellis (1976), Tarpley (1979), Gautier et al. (1980), Hay (1981), and Raphael (1983) have all reported on methods designed to estimate surface insolation from visible satellite measurements. Möser and Raschke (1984) have extended this approach by including the IR data in the retrieval of the surface insolation. Darnell et al. (1983) have considered the same problem in the longwave spectrum (i.e. estimating downward longwave flux at the surface), and Pinker and Corio (1984) have studied the correlation between the TOA IR term and the surface net radiation term.

The above studies all tend to suggest that a great deal of information concerning surface processes can be deduced from the satellite, albeit with a good deal of scatter for instantaneous type retrievals. Nevertheless, these algorithms can be applied in conjunction with ground truth programs in order to tune up empirical coefficients intrinsic to the retrieval algorithms themselves. There is already a diverse body of literature concerning observations of the surface energy budget. For a sampling of studies describing various components of the surface energy budget for natural earth surfaces such

as arctic tundra, bare soil, desert, forest, grasslands, hilly terrain, snow cover, and urban heat islands see Dabbert and Davis (1978), Federer (1968), Hicks et al. (1975), Idso et al. (1969), McKay and Thurtell (1978), Monteith and Szeicz (1961), Moore (1976), Weller and Holmgren (1974), Wendler (1971), Yap and Oke (1974).

Studies along these lines are augmented by parameterization techniques designed to estimate radiation exchange, sensible heat exchange, and latent heat exchange as well as the critically important subsurface storage term [see Debruin and Holtslag (1982) and Moore (1976)].

The future challenge will be one of combining the surface ground truth experiments with the satellite algorithms in a categorical fashion. This has been partially facilitated by recent emphasis on the compilation of global terrain type maps needed in the categorization process [see Matthews (1983a, 1983b)].

This report does not intend to propose a solution to the global land surface climatology problem. Instead, a methodology for combining surface measurements with satellite measurements that has specific applications for a global climatology is offered. In the course of this research, surface-based instrumentation systems have been developed which are utilized to examine surface energy budgets in remote desert environments and have been recently upgraded for use in remote mountainous terrain. The underlying philosophy here is that before a satellite climatology of surface processes can commence, it will be essential to directly and quantitatively describe the energy budgets of

a large set of global coordinates that can then be used as 'tie-down' points for the interpolative approach implicit in any global satellite study.

Although there is nothing particularly sophisticated about the individual components of the monitoring stations, the principal advantages of the integrated systems are that 1) they are designed for use in remote and somewhat hostile environments which characterize much of the global land surface; 2) they are virtually automatic systems once deployed; 3) they make use of modern microprocessor technology for on-line processing of high frequency data streams into convenient statistical parameters formatted in conventional physical units; 4) they record the results onto conventional tape cassette packs for additional processing on simple computer systems; 5) they require no auxillary power systems to operate in the field; conventional 1.5 volt batteries are sufficient; and most importantly 6) they incorporate a set of sensors that yield a virtually complete description of surface variables that control and modulate the surface energy budget.

In the remainder of this chapter descriptions are given of: 1) the sensor components and electronics of the surface monitoring stations along with the deployment approach; 2) the applications of the stations in a first generation mode in the deserts of Saudi Arabia; 3) a preliminary experiment in mountainous terrain utilizing an upgraded monitoring system; and 4) a proposed experiment in the remote reaches of the Tibetan Plateau. This chapter concludes with some comments on how the measurements from these systems can be combined with satellite measurements to close the external boundaries of atmospheric energy budget studies.

4.2 Monitoring Surface Energy Budget Processes from Remote Platforms

The motivation for developing a surface energy budget system has its roots in various ongoing CSU research projects concerned with the radiative characteristics of the Southwest Summer Monsoon. The initial data sets used in the scientific analyses were based on a variety of data compilations and measurements taken from different types of platforms and sensor systems developed during the 1979 Summer Monsoon Experiment (SMONEX) and the 1963-1964 International Indian Ocean Expedition (IIOE). These have included digital VIS-IR imagery from the GOES-1 geosynchronous and TIROS-N polar orbiting operational NOAA weather satellites (see Smith and Vonder Haar, 1983; and Smith and Graffy, 1982); wide-field-of-view (WFOV) and narrow-field-of-view (NFOV) Earth Radiation Budget (ERB) data and Scanning Multichannel Microwave Radiometer (SMMR) data from the Nimbus-7 experimental NASA satellite (see Jacobowitz, et al., 1978 and Gloerson and Hardis, 1978); flux radiometer, bugeye photometer and dropsonde data from the NASA Convair 990 experimental jet aircraft (see Ackerman and Cox, 1980; Smith et al., 1980; Davis et al., 1980; Davis and Cox, 1982; Bolhofer, et al., 1981; and International MONEX Management Centre - Summer, 1981).

Additional sources have included the gridded-assimilated upper air dynamic and thermodynamic parameters from the FGGE level III-b archive [see Bengtsson et al. (1982)]; special atlases of meteorological and satellite data [see Krishnamurti, et al. (1979, 1980a, 1980b, 1983), Martin and Howland (1983), Virji, et al. (1982) and Young, et al. (1980)]; climatological oceanic, surface and upper air data from the compilations of the 1963-1964 IIOE and other sources [see Hastenrath and Lamb (1979a, 1979b), Ramage et al. (1972), Ramage and Raman (1972), and

Wyrtki (1971)]; the seven volume meteorological monograph series of the IIOE published from 1969-1978 [Badgley et al. (1972), Bunker and Chaffee (1969), Gordon and Taylor (1975), Miller and Keshavamurthy (1978), Nicholson (1969), Portman and Ryznar (1971), and Sadler (1969)]; the climatological survey of Takahashi and Arakawa (1981); and finally the reference book guides to monsoons by Ramage (1971) and Lighthill and Pearce (1981).

In the course of these studies attention has been focused on one of the lesser documented, radiatively driven components of the Southwest Monsoon System, i.e. the Arabian Peninsula heat low [see Ackerman and Cox (1982), Ackerman, et al. (1983), Blake, et al. (1983), and Smith, et al. (1982a, 1982b)]. A critical deficiency in studies of the growth and structure of the various heat exchange terms relevant to Arabian heat low studies is a detailed description of the lower surface boundary. There are historical reasons for this data gap in Saudi Arabia, foremost the remoteness of the terrain, and until very recently, the lack of a modern weather service. Therefore, when an opportunity presented itself to our department in 1981 to conduct experiments within the Kingdom of Saudi Arabia, I seized upon the opportunity to advance the investigation of the Arabian heat low first initiated during the Saudi Arabian phase of the 1979 Summer Monsoon Experiment.

The research opportunity came about as a result of a widely focused, joint economic agreement between the governments of Saudi Arabia and the United States of America. In this agreement, sanctioned by the U.S. Departments of State and Treasury and the Saudi Arabian Ministries of Foreign Affairs and Finance and National Economy, a project called ARMETED was established to develop and support an

Institute of Meteorology and Arid Land Studies (IMALS) within King Abdul-Aziz University (KAAU) in the Red Sea coastal city of Jeddah. The principal parties who initially spearheaded this project were Dr. Abdubar Al-gain, now the Director of the Saudi Arabian Meteorology and Environmental Protection Agency (MEPA), and Professor Martin Fogel of the University of Arizona's School of Renewable Natural Resources. The project itself was administered by the Consortium for International Development (CID), an organization made up by a 12-member western U.S. university group basically concerned with economic aid and development of third world countries. Members of the School of Renewable Natural Resources at the University of Arizona, who acted in the role of project leaders, subcontracted with the Department of Atmospheric Science, Colorado State University, to provide educational and research support to the IMALS (now the Faculty of Meteorology and Environmental Science - FMES). The eventual result of these arrangements was a CID supported research project designed to conduct surface energy budget experiments at four sites within the Kingdom of Saudi Arabia. These experiments were then facilitated by KAAU-IMALS, MEPA, and the Saudi Arabian Ministry of Defense and Aviation.

In order to carry out the measurement program it was essential that a surface energy budget monitoring system be developed that would be tailored to the remoteness of desert environments, would be able to withstand the hostilities of heat and windblown sand, could operate and record data with simple battery-driven electronics, would be relatively portable and easy to operate with minimal technical support, and would be obtainable at reasonable cost. These constraints were dictated mostly by environmental, technical, logistical and budgetary conditions

that were somewhat out of my control; they were not necessarily the preferred constraints.

In the course of the initial research project a first generation system was developed by Professor Steve Cox and his engineering staff which had the capacity to monitor the upward and downward shortwave and longwave radiative exchange, the atmospheric state parameters at one level, the winds at one level, and the subsurface heat storage at several levels. By applying various averaging strategies and incorporating the residual method, i.e.:

$$[\text{Sensible} + \text{Latent Heat}] = [\text{Net Radiation}] - [\text{Storage}] \qquad (4.1)$$

to retrieve a combined sensible-latent heat flux term, it was possible to describe in quantitative detail, for the first time, some of the basic properties of the Arabian Desert surface energy budget. Examples of this research will be discussed in subsequent sections.

Due to the success of the initial Arabian experiments, I entered a cooperative arrangement with Professor Elmar Reiter to conduct similar studies in remote mountainous terrain. The eventual goal of this second project is the deployment of advanced (second generation) systems in the Rocky Mountain region and on the Tibetan Plateau. Serendipity played a role because this objective happened to suit both Professor Reiter's mountain meteorology interests in North American and Asia, along with the SMONEX goal of investigating another of the important heat source regions embedded with the overall Southwest East Asian Monsoon System (the Tibetan elevated heat source). These concerns with the dynamical barrier and thermal memory effects of elevated land masses, and their feedbacks with the planetary circulation, are discussed in a series of

recent publications [Reiter (1982), Reiter and Ding (1980, 1981), Reiter and Gao (1982), Reiter and Tang (1984), and Tang and Reiter (1984)].

4.3 Description of the Present System Configuration

Before going into a description of the system, it is pointed out that insofar as sensor technology and system deployment is concerned, there is nothing here that is claimed to be particularly innovative or that could not have been accomplished in the last 20 years. In this regard it is noted that virtually all of the system components are off-the-shelf, fairly conventional items. Instead the efforts have been more concerned with applications; i.e. the retrieval of complete surface energy budget descriptions and the combination of these data with satellite measurements to fully describe external atmospheric boundary conditions. It is believed that this methodology has numerous applications in the area of climate studies and problems in climate change. The major focus in terms of the hardware has been with system reliability and electronics. In that regard a very dependable and fully automatic system design that requires a minimum of maintenance and provides the maximum allowable field pre-processing capability has been developed.

The present system is configured in two parts - a radiation, rainfall, wind, state parameters, and subsurface heat and moisture monitoring station (referred to hereafter as the Radiaton Station), and a 4-level tower eddy flux monitoring station (hereafter referred to as the Tower Station). Schematic illustrations of the Radiation Station and the Tower Station are provided in Figs. 4.1 and 4.2. All sensors on the two systems are interfaced with programmable, microprocessor driven data loggers which periodically record their memory contents onto

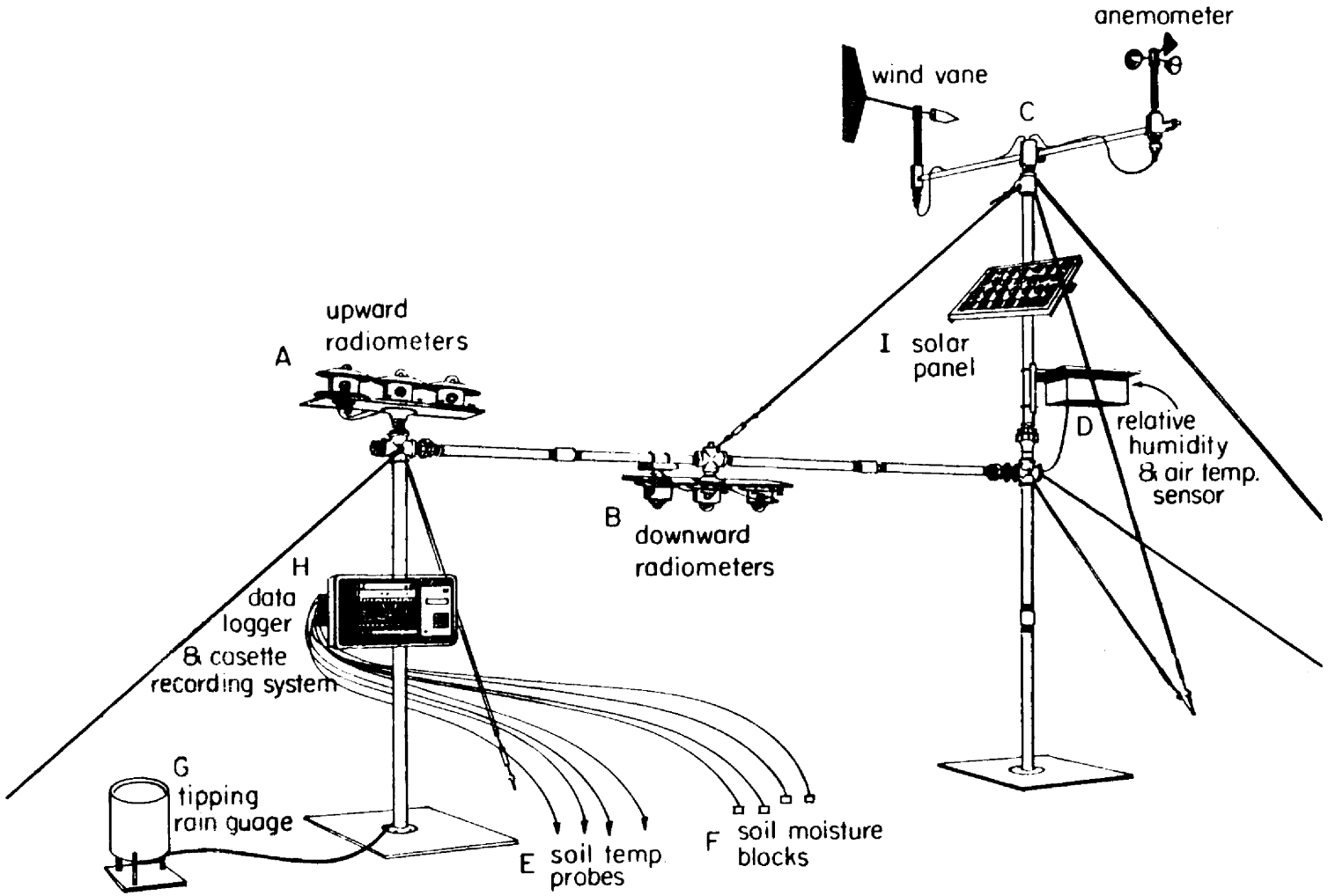

Fig. 4.1. Schematic illustration of the Radiation Station.

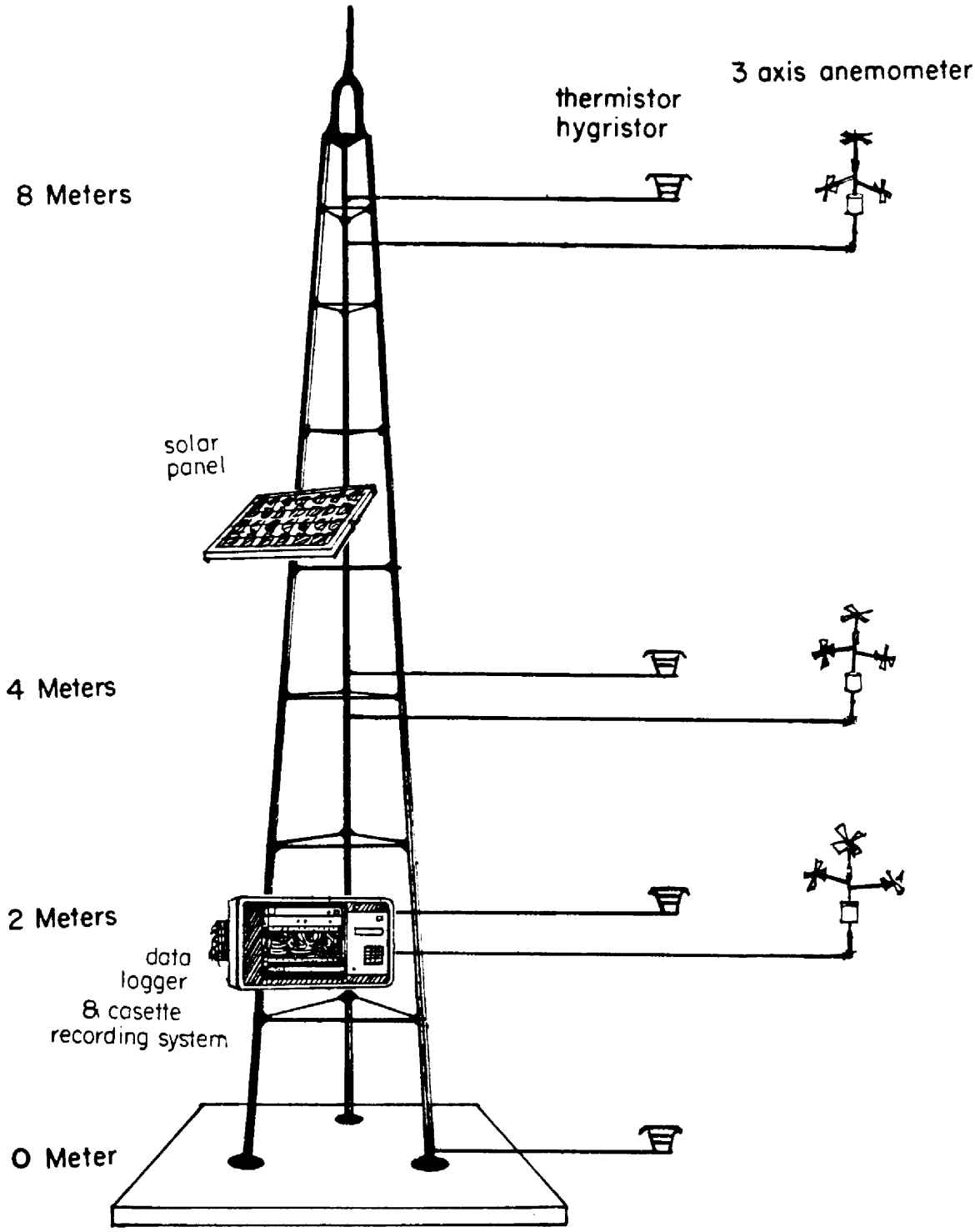

Fig. 4.2. Schematic illustration of the Tower Station.

conventional cassette tape recorders. The data logger and recording electronics are powered by rechargeable battery packs which are continually repowered (during sunny conditions) by single-panel solar energy collector-converter system.

4.3.1 The Radiation Station

The sensor package on a Radiation System consists of the following (photographic illustrations of a deployed Radiation Station are shown in Fig. 4.3):

1. Two (upward and downward looking) Eppley Precision Spectral Pyranometers (PSP) with WG-295 quartz outer and inner hemispheres for broadband (0.2-4.0 μm) solar radiation monitoring,
2. Two (upward and downward looking) Eppley Precision Spectral pyranometers (PSP) with R68 Schott colored glass outer hemispheres and WG-295 quartz inner hemispheres for near-infrared (0.7-4.0 μm) solar radiation monitoring,
3. Two (upward and downward looking) Eppley Precision Infrared Radiometers (PIR) with silicon domes and dome-sink calibrating thermistors for broadband (2.0-50.0 μm) terrestrial radiation monitoring,
4. A temperature-relative humidity probe (thermistor/ hygristor element) enclosed in a wooden solar shelter for ambient state parameter monitoring,
5. A cup anemometer and wind vane pair for ambient wind monitoring,
6. A set of 4 soil temperature probes (thermistors) for subsurface heat storage monitoring,

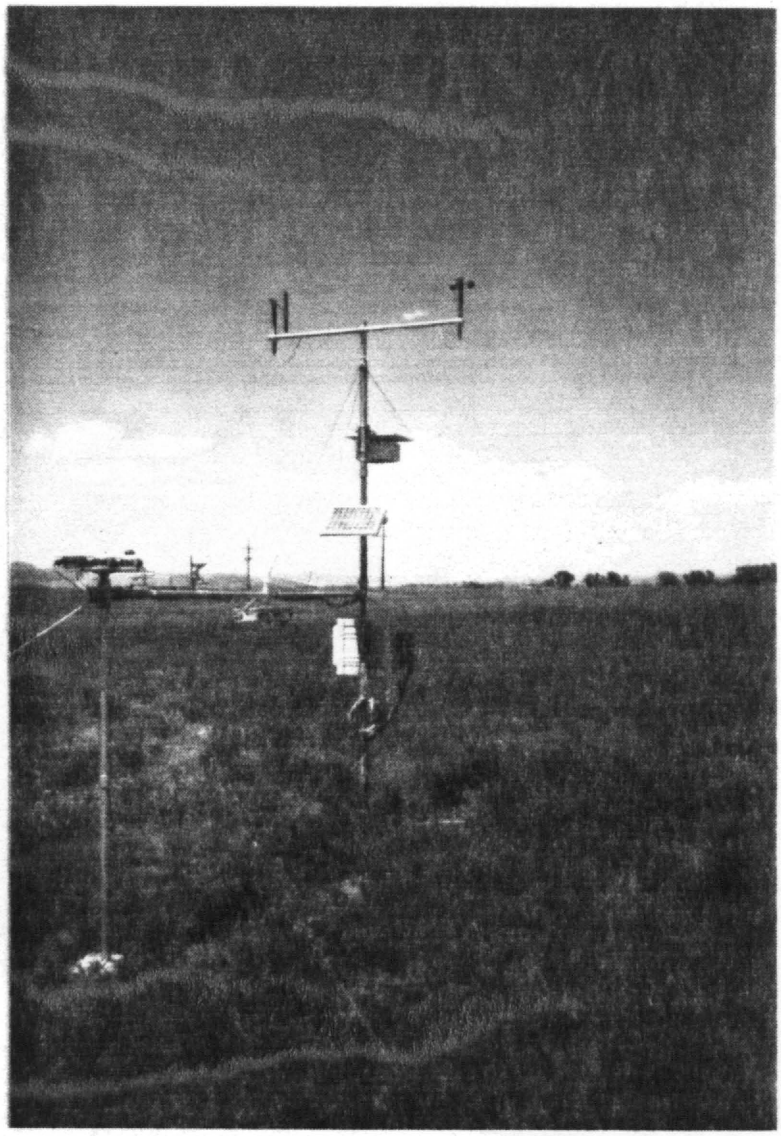

Fig. 4.3a. A Radiation Station deployed near the CSU Flight Facility.

Fig. 4.3b. Hand held soil probes (thermistors and soil blocks) and a rainguage situated some meters away from the main frame of the Radiation Station.

7. A set of 4 soil moisture blocks for subsurface soil moisture storage monitoring, and
8. A tipping rain guage for precipitation monitoring.

All of the above sensors operate in a transducive mode in conjunction with a Campbell Scientific Inc. (CSI) CR-7 data logger control module. The sensors are individually wired through detachable cable couplers to the CR-7 analog input interface. The CR-7 control module, in conjunction with an excitation card, then provide the necessary impulses along the transducer circuits at a sampling interval selected by the station operator. The control module incorporates arithmetic registers and a digital memory to which statistical compilations of the raw data samples are sent at every integration time step. The integration time steps for each individual sensor are programmable and selectable by the station operator just as the impulse sampling time is programmable and selectable.

The CR-7 programming panel (a photographic illustration is provided in Fig. 4.4) is easily accessed, simple to operate (16 keys), and includes a powerful software capability which enables the insertion of calibration factors, statistical transforms, and a variety of interrogation and display-readout procedures such that the final data products are processed and recorded in the preferred physical units and in reduced statistical form (e.g. means, variances, standard deviations, minimum-maximum values). These features are important because they; first, eliminate the time consuming and unpleasant chore of returning to the laboratory with mounds of engineering tapes which require reformatting, calibration, and reduction processing; second, allow real

Fig. 4.4. A close up photograph of a CSI CR-7. The programming panel is on the right; the analog interface, A-D converter and I/O modules are exposed to illustrate the wiring configuration. A cassette tape recorder (not shown) is mounted on a plate on the left front side. The cable mounts are seen at the left on the outside of a fiberglass enclosure which includes a front panel that completely seals the electronics.

time interrogation of the direct sensor outputs and derived parameters (e.g. maximum 24 temperature or net radiation values) in the conventional physical units to which we are accustomed (this allows for instantaneous quality control checks of the sensors); and third, provide a means to initiate scientific analysis in the field immediately, only requiring of the field scientist to bring along pencil, graph paper, and a six-pound cassette tape playback printer.

To those who have worked in the field, the third point is especially important if the experimental design is still in a state of flux. Since the sampling times, integration times, calibration constants and derived parameters are all under operator control through the programming panel, a few minutes spent plotting up actual data may motivate making corrections or improvements to the data processing or sensor deployment configurations. Of course, if the field scientist is so inclined, there is nothing to prevent carrying along more powerful data analysis systems such as the now popular inexpensive microcomputer systems incorporating disk packs, CRT displays, and hard copy printers and plotters.

The Radiation Station is easy to assemble and disassemble and can be deployed by two people in approximately one and one-half hours with a minimum of tools. The total system which includes sensors, data logging and recording electronics, cabling, frame members, mounting brackets, wires, ground supports, setup tools, expendables, the solar panel, and a fiberglass enclosure for environmentally sealing the data logger can all be placed in three standard size military footlockers (the frame members break down into 3-foot sections) for easy transport by car, bus, plane, mule cart or camel. The transport issue should not be dispensed with

lightly if one is considering making measurements in truly formidable environments.

Maintenance of the system is trivial. The upward radiometer domes require periodic cleaning if "sticky" air pollutants are in evidence. Cassette tapes require replacement after a length of time which is mostly dictated by the selected integration-output interval and total number of derived parameters. Integration times of on the order of 30 minutes allow for up to two months of data recording on a single 60 minute cassette tape. Finally, the battery packs need to be rigorously recharged from wall power every 2 or 3 months (more frequently if cloudiness is excessive). The only nuisance factor in maintaining the system is the fact that the soil moisture blocks have limited lifetimes, particularly in silty soils and must be replaced periodically (1-6 months). The system is not designed for extreme wintertime conditions, particularly if glaze or rime ice is at hand. However, system degradation is not total under iceing conditions; only the hygristor elements and the rainguage are incapacitated. The hygristor elements are effectively destroyed by undergoing a freeze-thaw cycle. The radiometers, of course, become ineffective if ice would adhere to any portion of the domes.

It should be noted that the sensors that have been selected for use on the system are simple, relatively inexpensive, and not necessarily state of the art (the hygristors and soil moisture blocks for example). There is nothing to prevent exchanging the simple, inexpensive, and somewhat slow response detectors with more exotic sensors, (e.g. Barnes Infrared Directional Radiometers, Sonic Anemometers, Lyman-Alpha Humidiometers, Neutron Counters), however, there is a price to be paid

for trying to incorporate state-of-the-art technology. That is, the advantages of low cost, portability, no external power requirements, and ease of operation and maintenance are quickly lost. It is believed that the averaging of a steady uninterrupted stream of data from conventional, off-the-shelf imperfect sensors, from a nearly automated system, has distinct advantages over coping with ad-hoc power sources, exotic calibration devices, precision mounting frames, and the like, which often result in an unsteady, intermittent stream of perfect measurements. There is no exaggeration intended here; in the end, simplicity will yield results whether it be satellites or surface energy budget systems. From the author's point of view, this is an axiomatic principal.

The Radiation Station is designed to retrieve:

I) The full complement of the radiative exchange terms, i.e.

1) Upward and downward UV-VIS, near-IR, and broadband ($K\uparrow$, $K\downarrow$) solar fluxes,

2) Surface reflectance in the UV-VIS, near-IR, and broadband spectrums,

3) Upward and downward broadband ($L\uparrow$, $L\downarrow$) fluxes and equivalent flux temperatures,

4) UV-VIS, near-IR, broadband solar, and broadband IR net fluxes, and

5) Total radiative net flux (Q) at the surface which is a principal term in the surface heat exchange equation:

$$Q = K\downarrow - K\uparrow + L\downarrow - L\uparrow \qquad (4.2)$$

II) The subsurface heat storage term (S), which is obtained from a subsurface integration process:

$$S = C_s \cdot \bar{\rho} \cdot \int_{d_o}^{o} \frac{dT(z,t)}{dt}\, dz \qquad (4.3)$$

in which C_s is the heat capacity of the soil, $\bar{\rho}$ is the mean soil density, and a temperature function, [T(z,t)] is developed by fitting the subsurface thermistor data with a wave-like function. The lower limit of integration (d_o) is defined to be that level at which there ae no discernable temperature waves or trends with respect to the time scale of investigation.

III) The subsurface moisture storage term (SM), which is used to diagnose the surface evaporation (E) and thus the latent heat (LH) exchange:

$$E = -\frac{dSM}{dt}$$

$$LH = \bar{\rho} \cdot L \cdot E \qquad (4.4)$$

in which L is the latent heat of evaporation.

IV) The sensible heat term (SH), which is diagnosed from I, II, and III above:

$$SH = Q - S - LH \qquad (4.5)$$

V) A measure of the total rainfall (R), which is a useful parameter in land surface studies for its own sake, and in addition, provides an independent but qualitative check on the soil moisture monitors. There is not a direct relationship between SM and R, i.e.:

$$R \neq \frac{dSM}{dt} \tag{4.6}$$

because of horizontal surface transport (runoff) and subsurface transport (percolation) processes.

VI) Finally, measures of the ambient air temperature (T), relative humidity (RH), and wind ($\bar{V}$) conditions, which are used in conjunction with the radiation and rainfall parameters to interpret the changes and discontinuities taking place in the energy budget process and needed in parameterization formulations.

4.3.2 The Tower Station

The second part of the surface energy budget system is the Tower Station. This component of the system is designed to monitor temperature, moisture, and winds at four levels as indicated in Fig. 4.2 (winds are measured at three levels, but not directly at the surface). The electronics module on the station (the CR-7) has a specially prepared firmwave card, a programmable read only memory (PROM), which is designed to operate as an eddy flux processor. That is, it compiles sums, sums of squares, and sums of cross products used in the calculation of variance-covariance and correlation matrices at each of the three upper levels. These matrices are the essential ingredient in the computation of the eddy heat, moisture, and momentum fluxes. In addition, mean values are collected at all four levels.

As with the Radiation Station, the sampling times and integration times are operator selectable. The integration time can be thought of as the bar operator in, for example, the expression for vertical heat flux $\rho C_p \langle \overline{w'T'} \rangle$. The eddy flux module for the CR-7 was specifically prepared by Campbell Scientific Inc., based on CSU design

specifications. In the present configuration, the software overhead required during a sampling interval limits the maximum sampling rate to once per second. It is shown in Section 4.5, that this does not appear to present any problems in resolving the turbulent heat exchange process.

The sensor package on a Tower Station consists of the following (photographic illustrations of a deployed Tower Station are shown in Fig. 4.5):

I) Three sets of R. M. Young Inc. u-v-w low threshold propeller anemometers mounted at 2, 4, and 8 meters.

II) A set of 4 temperature-specific humidity probes (thermistor/hygristor elements) enclosed in metallic ventilation shelters shelters coated with a glossy white paint. These units are mounted at 0, 2, 4, and 8 meters. The tower has been designed such that the T-q probes can be aligned at 60°, 120°, or 180° angles with respect to the anemometers.

With this sensor configuration and the capabilities of the eddy flux software module, the following parameters are then calculated at the upper three levels:

1) Means, variances, and standard deviations of T, q, u, v, and w,

2) A five-way variance-covariance matrix including the heat and moisture variances ($\overline{T'^2}$, $\overline{q'^2}$), the eddy heat and moisture flux terms ($\overline{w'T'}$,$\overline{w'q'}$), and the components of a Reynolds matrix ($\overline{u'^2}$,$\overline{v'^2}$,$\overline{w'^2}$,$\overline{u'v'}$,$\overline{u'w'}$,$\overline{v'w'}$). The associated correlation matrix is also calculated. The

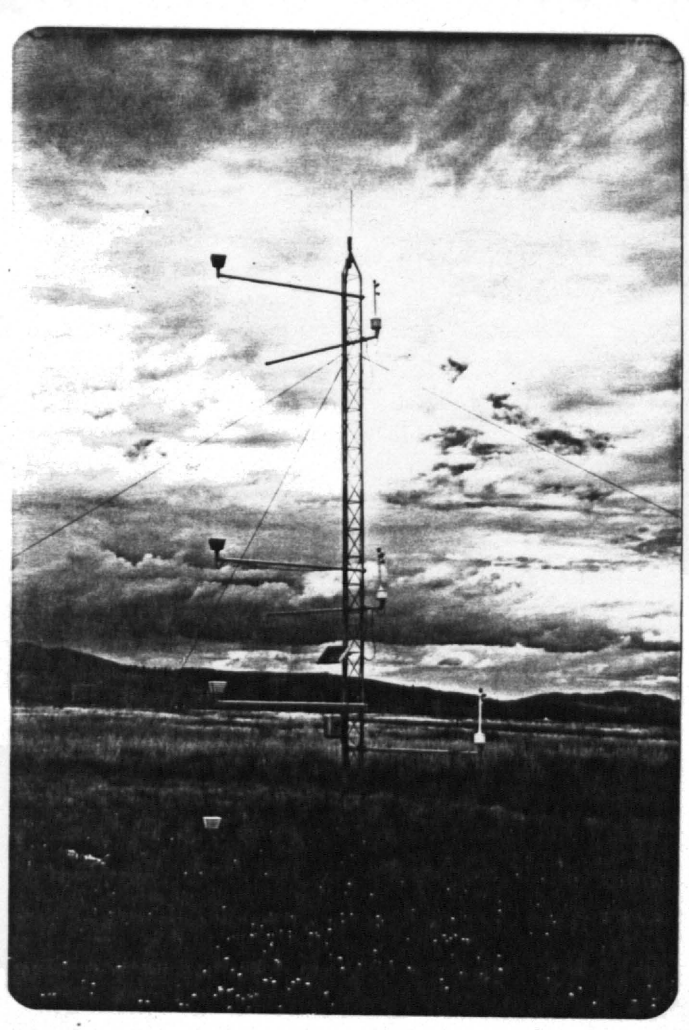

Fig. 4.5a. A Tower Station deployed near the CSU Flight Facility. The foothills to the northwest of Fort Collins are seen in the background.

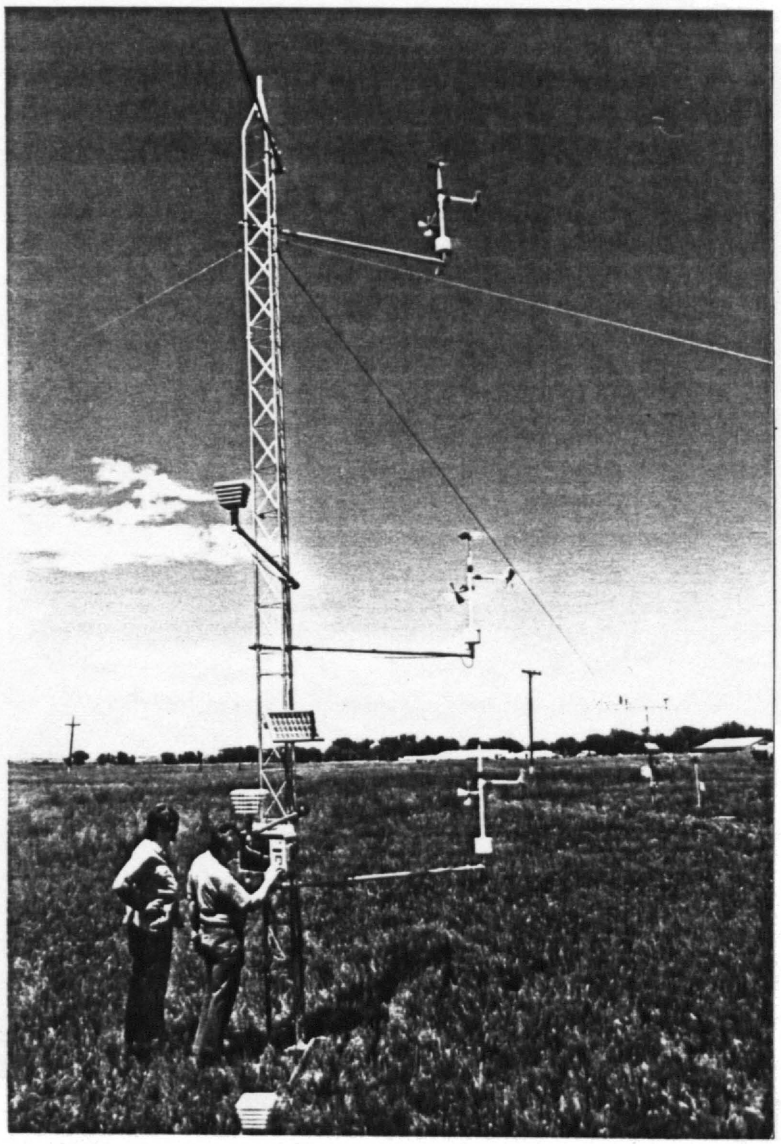

Fig. 4.5b. The author and Professor Reiter are shown reprogramming the eddy flux data logger on the Tower Station.

horizontal heat and moisture flux terms are not calculated by the processor.

In addition the means, variances, and standard deviations of T and q are calculated at the surface level.

As with the Radiation Station, the deployment of this system is relatively simple and straightforward (setup time is approximately three hours for two people). All of the equipment can be placed in three footlockers with the exception of the tower itself which breaks down into three 10-foot sections. A solar panel is used to recharge the data logger and recording electronics battery pack. The only maintenance requirements are the removal of the styrofoam anemometer propellers in excessively high winds, and the periodic rigorous recharging of the electronics battery pack. As in the case of the Radiation Station, the Tower Station has not been designed for icy and snowy conditions which render the anemometers and hygristors useless.

As before, the sensors are simple, inexpensive, and as a result are not expected to achieve maximum precision. In particular the hygristor elements used on the tower have relatively slow response times in comparison with state-of-the-art technology. Therefore, it is not expected that the direct measures of vertical moisture flux will be extremely accurate. This is a misleading detraction, however, if one considers the system design as a whole. The philosophy on this topic follows.

4.3.3 Simultaneous Use of the Two Stations

The two stations used in tandom have been designed to have the capability to monitor the sensible and latent heat fluxes in three independent modes. The Radiation Station, because it does an excellent

job of monitoring the radiation budget, is able to produce, by the residual method, the sensible and latent heat terms whose accuracy is dictated by uncertainties in calculating subsurface heat and moisture. There are uncertainties due both to vertical resolution and others due to sensor inaccuracies [e.g. soil moisture blocks, even when used under optimum conditions, are known to yield uncertainties on the order of 25 percent (Hendrie, 1983)]. On the other hand, the Tower Station provides direct measures of $\langle\overline{w'T'}\rangle$ and $\langle\overline{w'q'}\rangle$. There are uncertainties in these measures also. First, the anemometers, thermistors, and hygristors are not instantaneous response detectors; their response times are on the order of the maximum allowable sampling time (1 second). Second, the thermistor-hygristor elements are not placed directly within the air space of the anemometer propellers (to avoid dynamic interference), and thus there is potential for very high frequency destructive interference (again this is minimal at the maximum allowable sampling time). However, the Tower Station provides excellent measures of $\overline{T}$ and $\overline{q}$ at four levels and direct measurements of $\overline{w'^2}$ at three levels (there are, of course, uncertainties in the vertical velocity variance terms). These measures thus provide a means to apply similarity theory which avoids any direct measure of $\langle\overline{w'T'}\rangle$ and $\langle\overline{w'q'}\rangle$. For instance in the case of the eddy heat flux:

$$\overline{w'T'} = U^*T^* \tag{4.7}$$

where:

$$U^* = (\overline{u'w'})^{1/2} \doteq (\overline{w'^2}/1.35)^{1/2} \tag{4.8}$$

and T^* is diagnosed iteratively from:

$$T^* = (\bar{T} - \bar{T}_o)/F_t(\xi, z_o, z) \tag{4.9}$$

where for the stable case ($\xi > 0$):

$$F_t = (0.74/K)\ \ell n(z/z_o) + 4.7\xi \tag{4.10}$$

and for the unstable case ($\xi < 0$):

$$\begin{aligned} F_t &= (0.74/K) \cdot \ell n[z/z_o - \psi_2] \\ \psi_2 &= \ell n[(1+Y)/2] \\ Y &= (1-9\xi)^{1/2} = 0.74/\phi_H \end{aligned} \tag{4.11}$$

and the Monin-Obukhov stability parameter (ξ) is given by:

$$\xi = z/H = g \cdot K \cdot (z+z_o)\ \overline{w'T'}/(\bar{T} \cdot U^{*3}) \tag{4.12}$$

In the above expressions, z is height, U* and T* are the friction velocity and scaling temperature; z_o is the roughness length, where:

$$z_o \doteq z/\exp[(K/U^*) \cdot \bar{U}(z)] \tag{4.13}$$

and T_o and $\bar{T}$ are the mean temperatures at z_o and z, respectively; K is von Kármáns constant (≈ 0.35); and F_t, ϕ_H, and H are Paulson's expression, the dimensionless temperature gradient, and the Obukhov height respectively [see Businger (1983) for a discussion of the above formulations].

This three-way approach to estimate the critically important vertical transports of sensible and latent heat allow a variety of permutations in cross-checking and intercomparison to arrive at the best possible estimates of surface storage and heat-moisture conduction. Additionally, there is a fourth option of using (and independently

assessing) either parameterization techniques such as the bulk aerodynamic method (i.e. drag coefficient theory), or simpler techniques such as the Priestley and Taylor (1972) model. In drag theory, surface sensible and latent heat terms are approximated by:

$$SH = C_D \cdot \rho \cdot C_p \cdot \bar{U} (T - T_s) \tag{4.14}$$

$$LH = C_D' \cdot \rho \cdot L \cdot \bar{U}(q - q_s)$$

where C_D and C_D' are empirical heat and moisture drag coefficients, $\bar{U}$ is the mean surface wind, and the terms in parentheses are the surface-air gradients of temperature and moisture directly at the surface. It is noted that over land surfaces, a moisture drag coefficient is best formulated in terms of a soil moisture efficiency factor (M) and a surface resistance term R_q such that $C_D' \cdot \bar{U} = M/R_q$. In the less physical approaches such as the method of Priestley and Taylor (1972), only the terms of net radiation, air temperature, and surface moisture are used to estimate SH and LH; see DeBruin and Holtslag (1982).

4.4 A Measurement Program in the Deserts of Saudi Arabia

The first instance of actually deploying a Radiation Station in the field took place during May and June, 1981 outside the Saudi Arabian cities of Jeddah, Taif, and near the village of Sharouwrah (within the Arabian Empty Quarter). It was during this period that equipment shakedown tests and experimental design tests were first carried out; see Smith, et al. (1982a). The first generation system was configured somewhat differently than the present second generation system. First of all the data loggers were of a less sophisticated design (CSI CR-21's), however, they had demonstrated excellent field reliability.

Secondly, soil moisture blocks and rainguages were not used and soil temperatures were generally monitored at only three levels. The moisture parameters were not considered essential for the desert interior, since precipitation at a given site in the Empty Quarter is generally a rare event.

The initial tests in Jeddah and Taif rendered positive results which then led to a preliminary expedition to a site in the desert Empty Quarter; i.e., near the village of Sharouwrah which is northeast of the notch forming the common border of North Yeman and South (Democratic) Yeman. The principal scientific objectives of the Sharouwrah expedition were to:

1) Characterize the surface energy budget of the Arabian Desert Empty Quarter,
2) Contribute to the data base needed to investigate the development and structure of the Arabian Peninsula thermal low,
3) Investigate the overall role of the Arabian Peninsula heat exchange process on the Southwest Summer Monsoon System.

There was an additional technical objective of putting the radiation system to the test in a relatively hostile environment to determine if it was capable of returning a scientifically useful data record while operating in an automatic mode.

The essence of the Empty Quarter geography is sand, sand dunes, and more sand dunes. There is no vegetation and rain is as scarce as hen's teeth. The station was erected during a minor sand storm, during late afternoon and into dusk on June 1 by three of us (myself,a Syrian colleague Dr. Sakkal, and an Egyptian Technician - Mr. Salah). It was

an arduous task requiring over twice the amount of time needed for assembly under normal circumstances. Four Saudi Arabian army 4-wheel drive vehicles, which escorted us to the site, were immobilized in the sand (buried to their axels) in the course of the exercise. Although we were wrapped in the local Arab headgear, our ears, eyes, noses, and throats were innundated with sand by the time we returned to our quarters. On the following day, the weather relented somewhat and we were able to tidy up the site and obtain some photographs of the assembled system. We were relectant to wait for optimum conditions to assemble the station because at that time we had no assurance from the local military command that we would be allowed to stay in the area for any extended period.

The measurements extracted from these preliminary tests firmly demonstrated the capability of the system and the reliability of the sensors. Various examples of these early tests are provided in Figs. 4.6 through 4.8. Photographs of the Sharouwrah area are provided in Fig. 4.9. These measurements represent some of the very first detailed high resolution energetic depictions of the western escarpment and the desert interior of Saudi Arabia.

Based on a follow-up agreement with the Arabian Ministry of Defense and Aviation, permission was granted to continue a measurement program outside of the village of Sharouwrah throughout the month of June, 1981. The following year three additional sites were established outside the cities of Jeddah and Taif, and near the village of Najran. These sites form a somewhat crooked monitoring vector from the Red Sea Coast into the Empty Quarter Desert interior. The VIS-channel METEOSAT photograph in Fig. 4.10 indicates all four sites: 1) Jeddah (coastal); 2) Taif

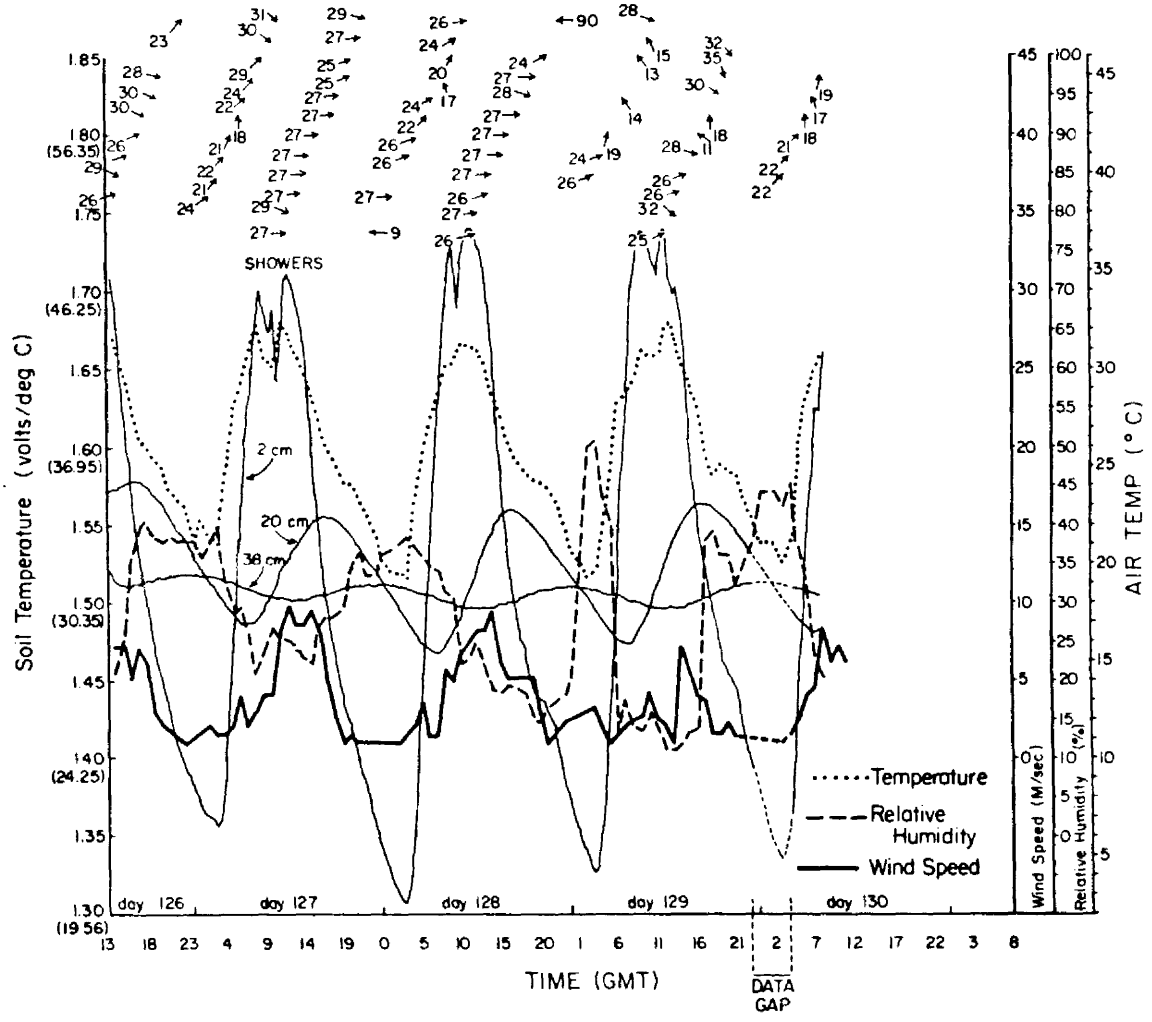

Fig. 4.6. Wind, temperature, humidity, and soil parameters taken from May 6 to May 10, 1981 in the mountain city of Taif, located southeast of Mecca, on the western escarpment of the Arabian Peninsula.

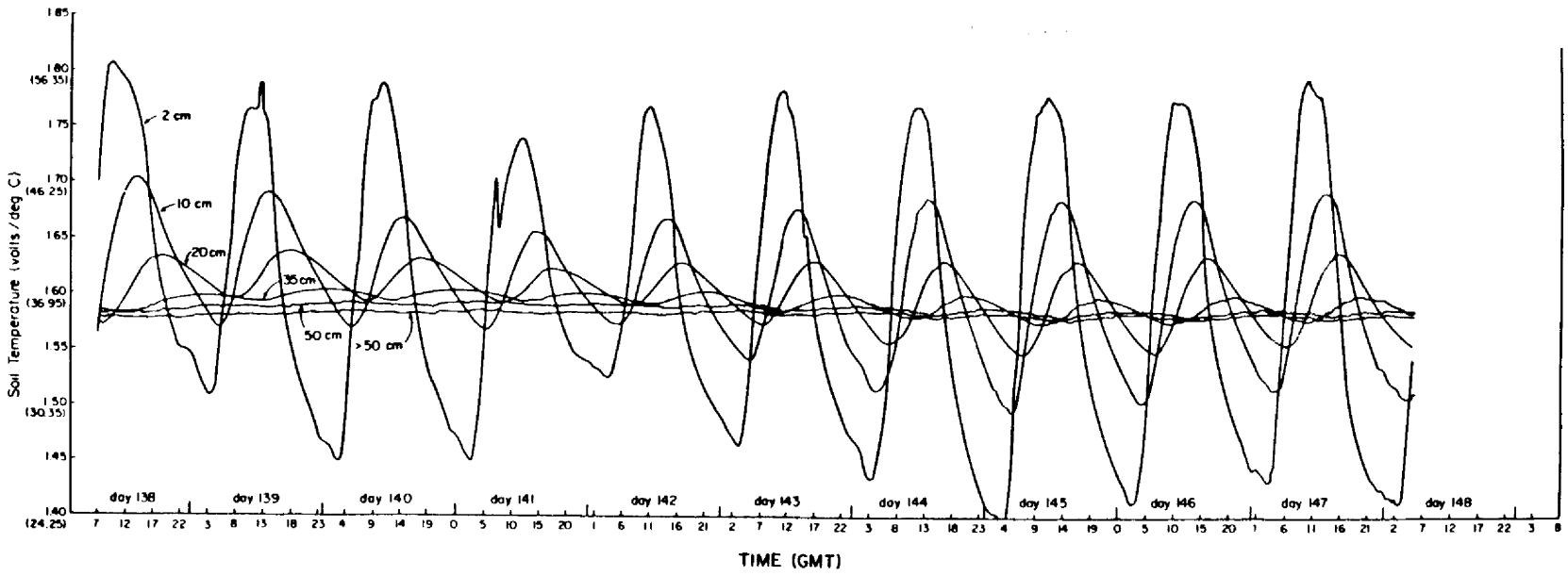

Fig. 4.7. Subsurface soil temperatures at six depths taken from May 18 to May 28, 1981 on top of a Barchane sand dune immediately to the west of Jeddah.

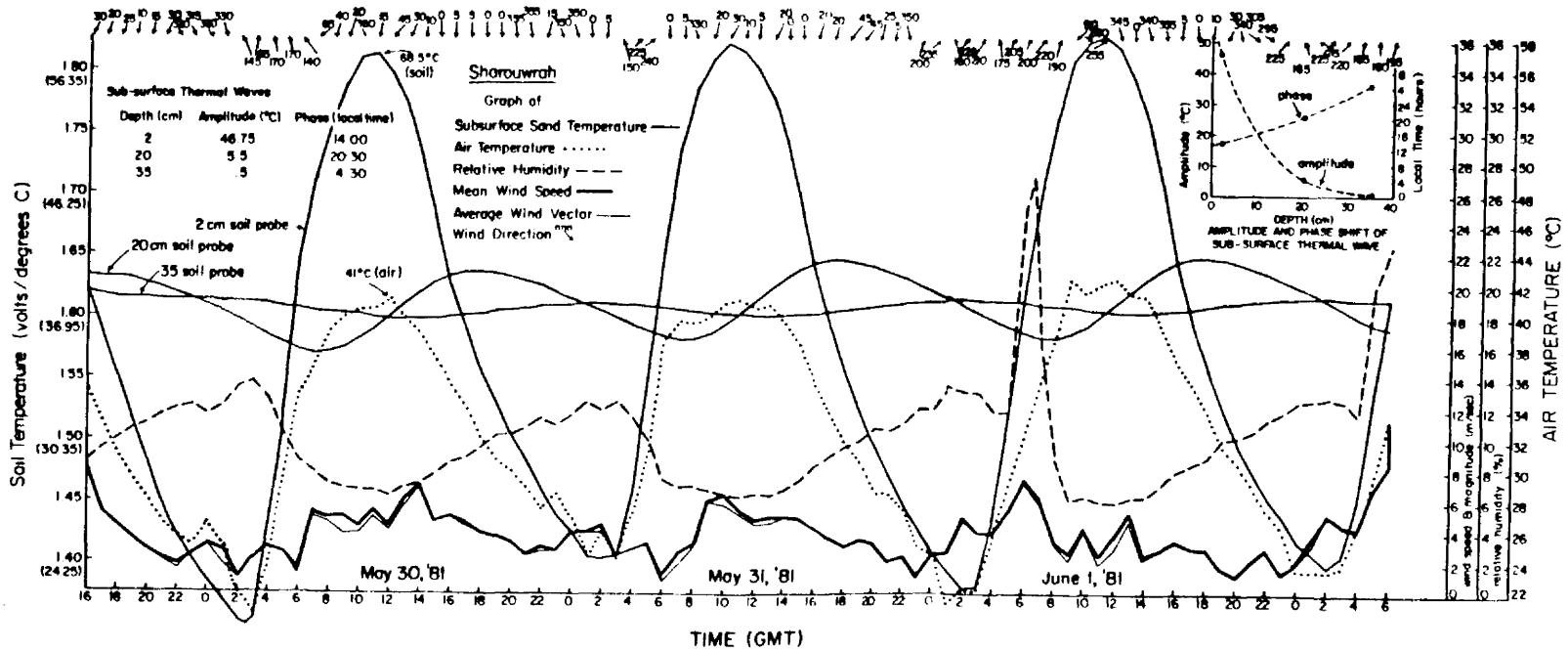

Fig. 4.8a. Preliminary measurements taken near the village of Sharouwrah, within the Arabian Empty Quarter, from June 1 to 5, 1981. The wind, temperature, humidity, and soil temperature measurements are plotted. At the top right of this figure is a phase-amplitude inset of the subsurface temperature waves.

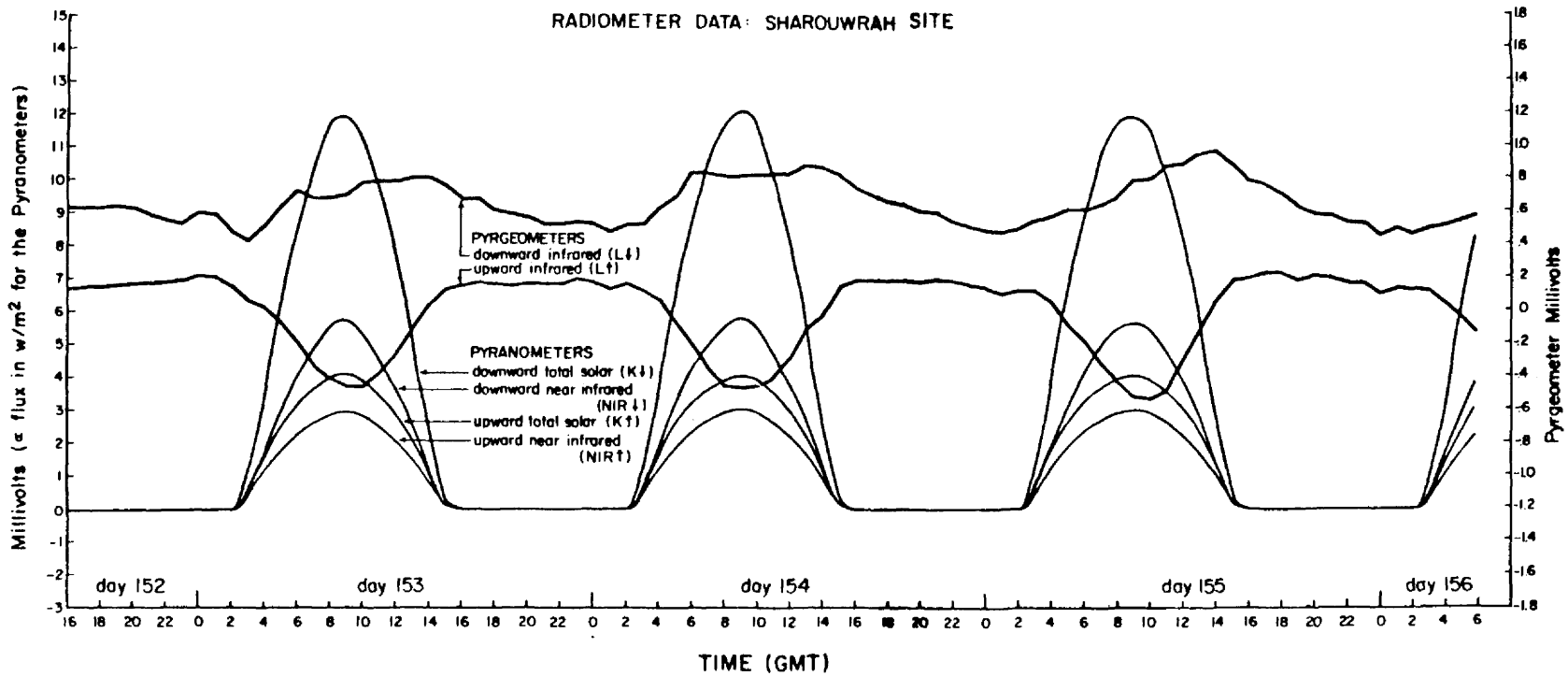

Fig. 4.8b. The radiometer outputs in uncalibrated units (millivolts). The pyrgeometer signals are not yet adjusted for thermal drifts in the instrument and are thus not proportional to irradiance.

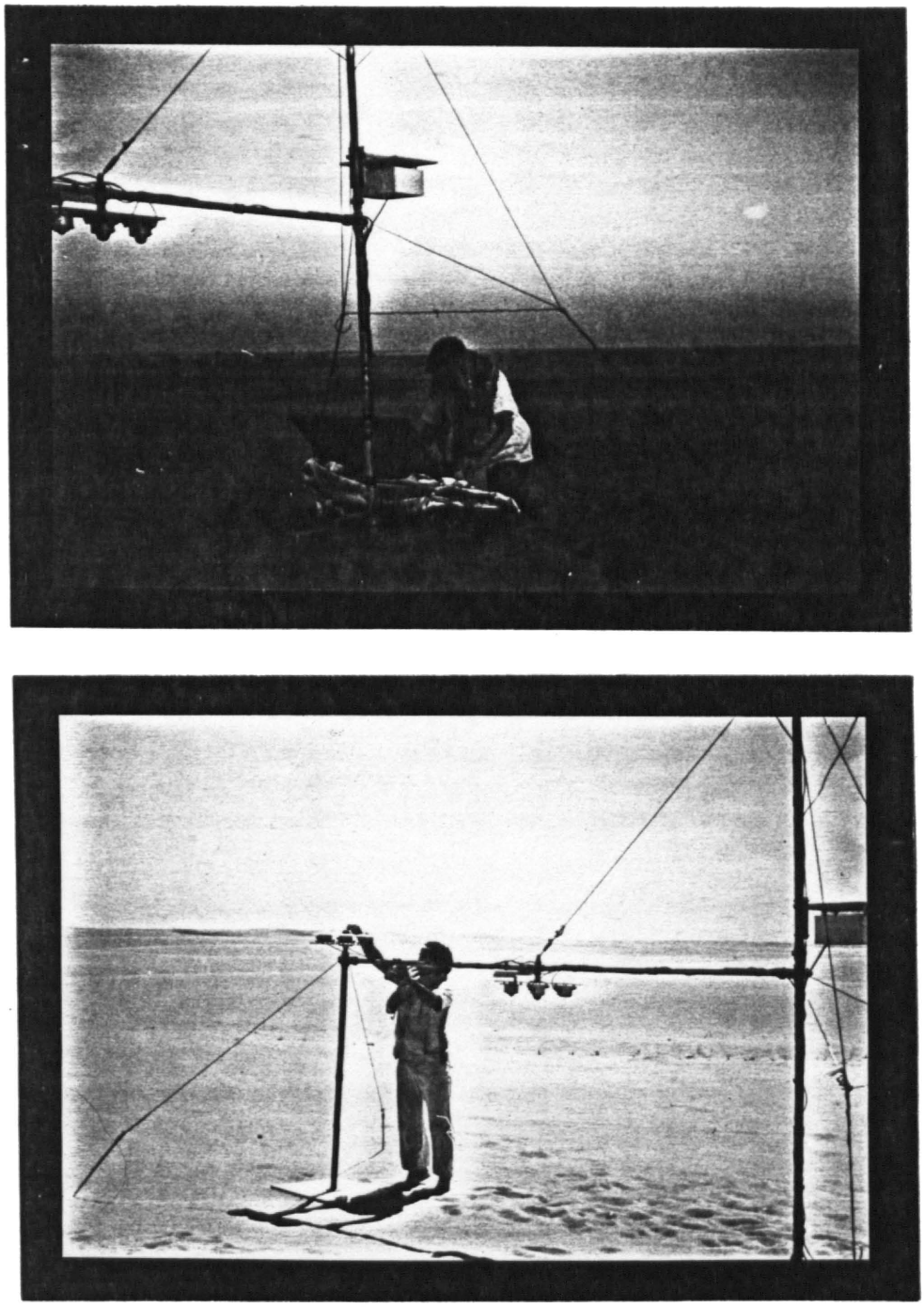

Fig. 4.9a. The top photograph shows the author activating the data loggers on the eve of the first Sharouwrah test (June 1, 1981), following a sand storm. The electronics were placed in a footlocker which was then partially buried in the sand and covered with a solar blanket to minimize solar heating damage to the electronics. The bottom photograph shows Professor Sakkal cleaning the upward radiometer domes the following morning.

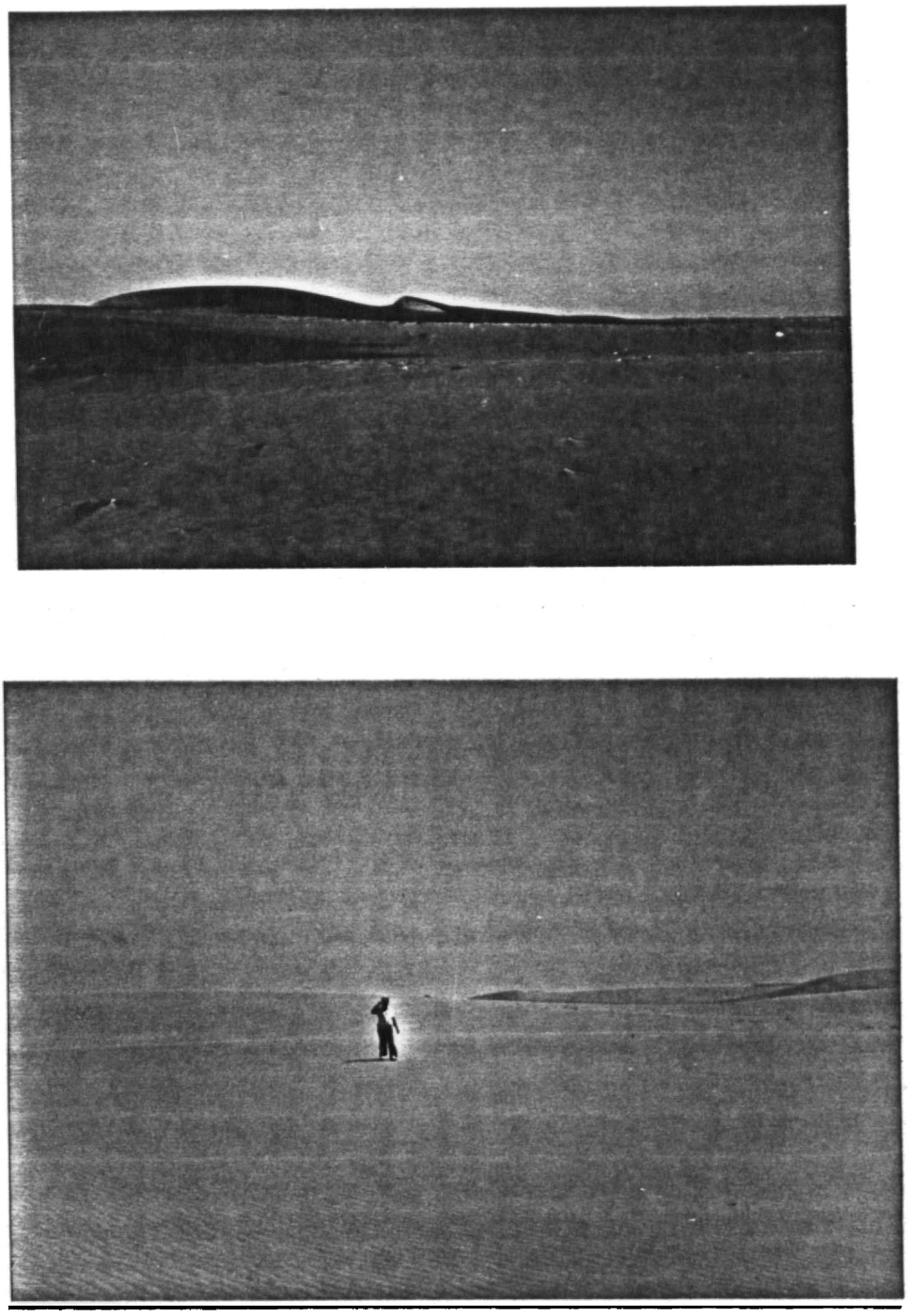

Fig. 4.9b. Dune scenes from the Empty Quarter (north of Sharouwrah). In the bottom photograph, the project technician (Mr. Salah) is seen walking toward the measurement station.

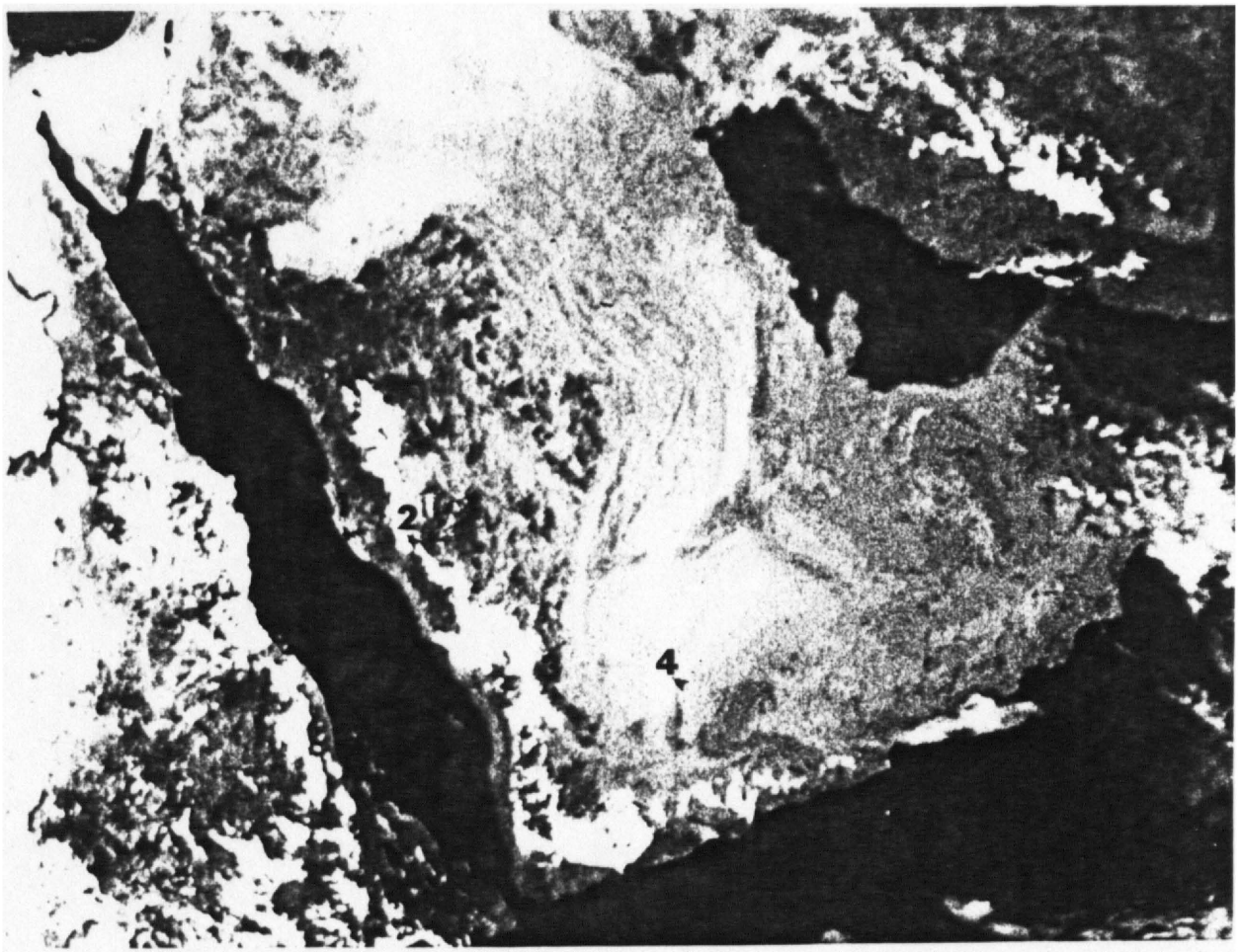

Fig. 4.10. METEOSAT image (VIS channel) of Arabian Peninsula indicating the four Saudi Arabian monitoring sites: 1) Jeddah, 2) Taif, 3) Najran, 4) Sharouwrah. The satellite image was kindly provided by Prof. G. E. Hunt.

(western escarpment); 3) Najran (oasis village at west edge of Empty Quarter); and finally 4) Sharouwrah (deep in the Empty Quarter interior). Data has been collected intermittently from these sites starting in early 1982 and into the spring of 1983 at which time the project was terminated.

In the following figures various results of the Saudi Arabian measurement program are presented. Figure 4.11 presents the half-hourly temperature-humidity record from Sharouwrah during June, 1981. There are two salient features seen in these plots. The first is the virtually uniform diurnal periodicity in both temperature and moisture variables. The second is seen in the relative humidity trace which on June 5-6 starts to spike, on days June 7-8 spikes from a mean monthly daytime maximum of approximately 15 percent up to over 50 percent, then back to about 25 percent on June 9, and finally back to its typical value for the month of 15 percent. The explanation appears to be the result of a super intensification of the desert heat low during a period when the sun is at its zenith at that latitude, which apparently leads to a strong and lasting enough daytime pressure gradient to bring moisture from outlying regions. Although it is a short burst of moisture (4-5 days), it has an interesting feedback effect in putting a ripple in the desert surface radiation budget due to nonreciprocal effects in shortwave absorption and longwave cooling.

In Figs. 4.12-4.13 the June radiative flux and solar reflectance traces from Sharouwrah are illustrated. The diurnal periodicity of all the terms in the radiative budget are very distinct in Fig. 4.12. The solar reflectances shown in Fig. 4.13 include three components; the two principal spectral regions (UV-VIS, Near-IR), and the total spectrum.

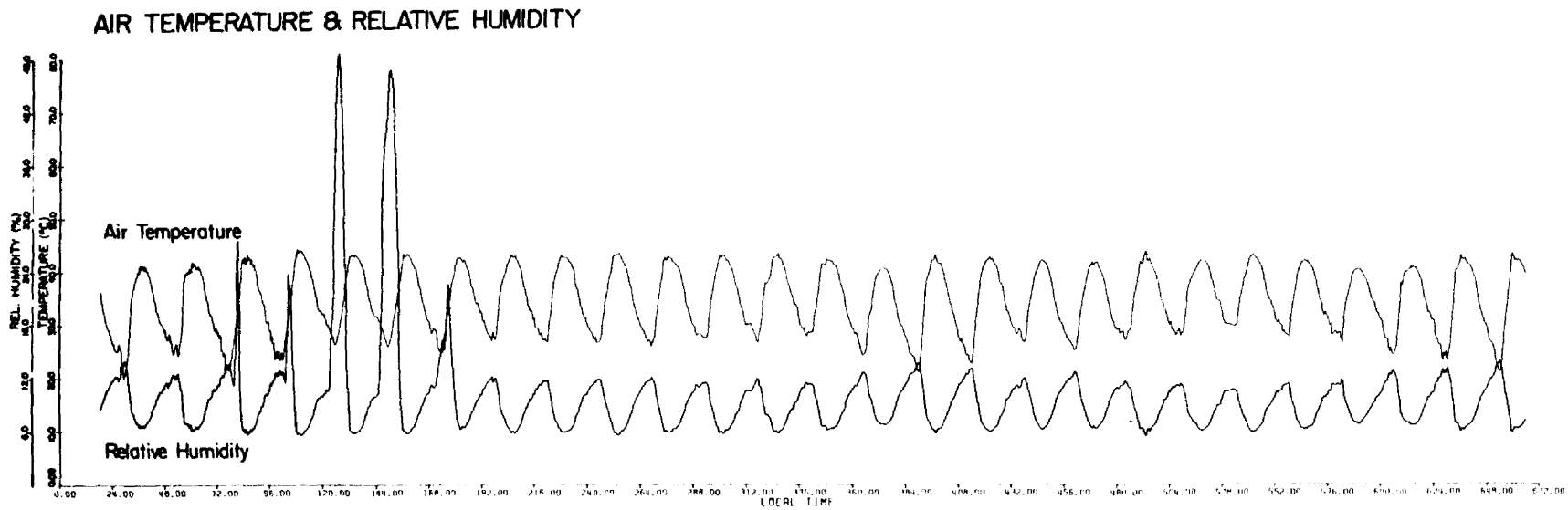

Fig. 4.11. Half hourly data traces of air temperature and relative humidity during June, 1981 at the Sharouwrah site.

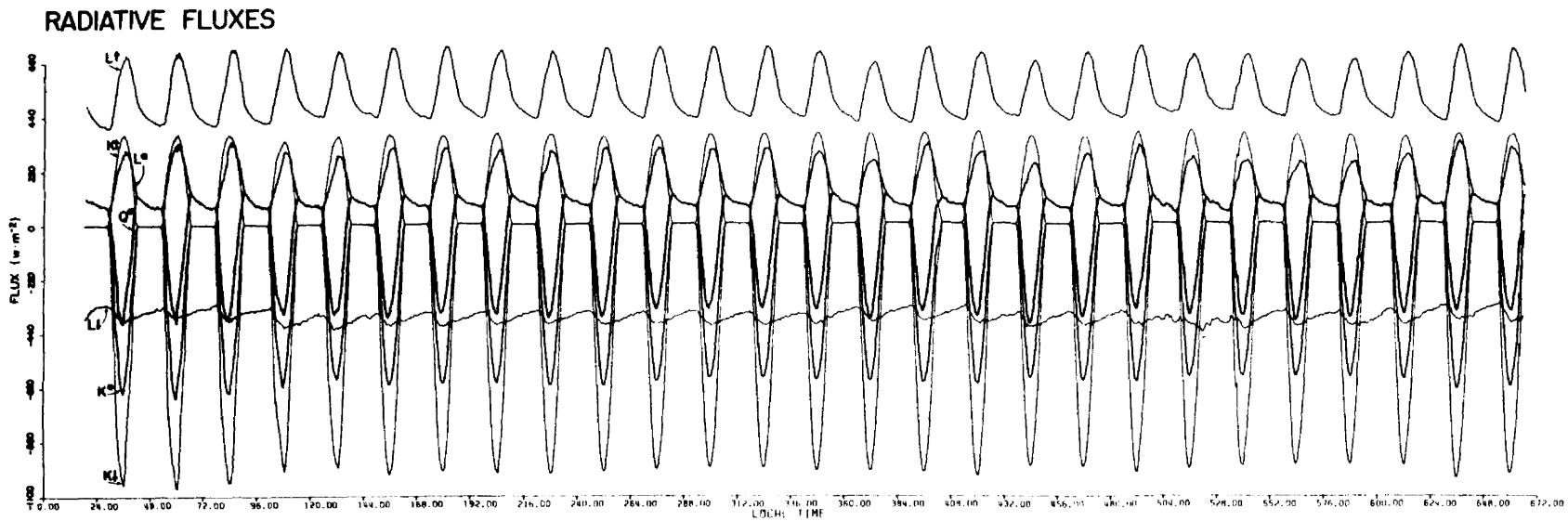

Fig. 4.12. Half hourly radiative flux signals during June, 1981 at the Sharouwrah site. The definition of symbols is as follows: K↓, K↑, K* are the downward, upward, and net solar fluxes; L↓, L↑, L* are the associated infrared terms; finally Q* is the total net radiative flux.

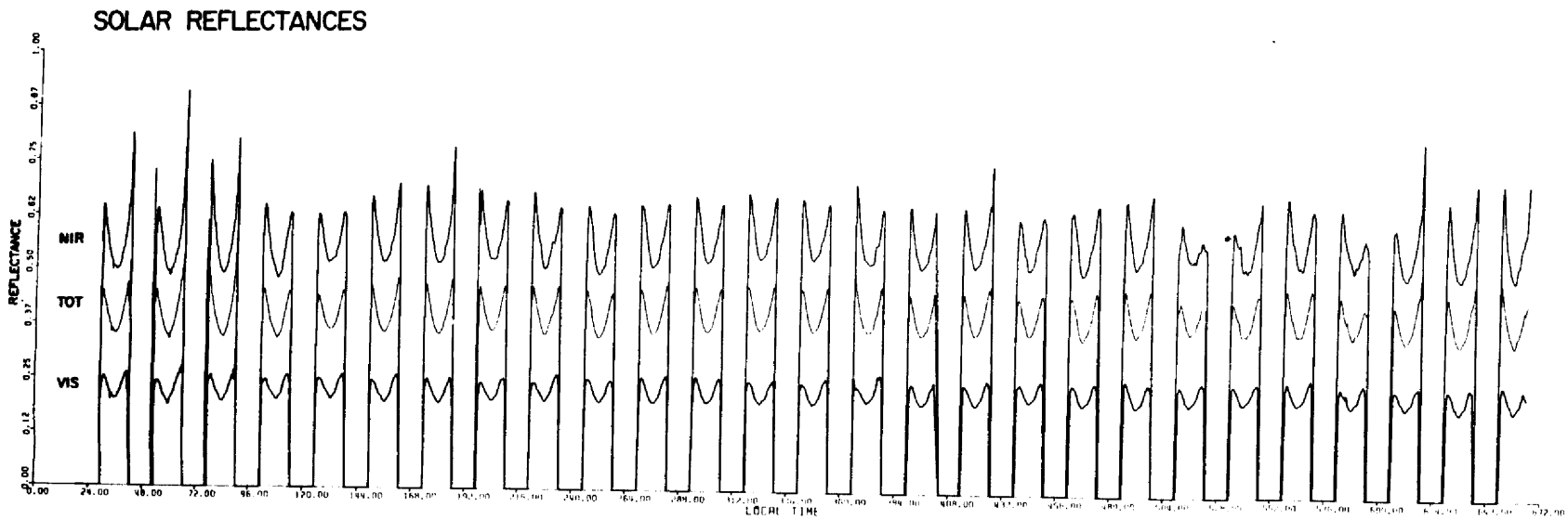

Fig. 4.13. The visible (VIS), near-infrared (NIR), and total solar (TOT) directional reflectance signals for June, 1981 at the Sharouwrah site.

Two important features are in evidence here. The first is the very obvious directional reflectance variation as a function of solar zenith angle. The second is the dramatic differences between Near IR and UV-VIS albedo; the Near-IR term, which is on the order of 50 percent at noon, is over twice that of the UV-VIS term.

In Fig. 4.14 the radiative terms, first seen in the form of hourly traces in Figs. 4.12 and 4.13, are presented in the form of one-month diurnal averages. Of particular interest in Fig. 4.14 is the not quite symmetric nature of the longwave net term (L*), which then leads to asymmetry in the total surface net radiation (Q*). The impact of these diurnal asymmetries on heat low circulations is not fully understood; it is pointed out that formulating diurnal variations with sinusoidal functions often flys in the face of reality.

The diurnal surface directional reflectance terms, also shown in Fig. 4.14, demonstrate clearly the large magnitude difference between near-infrared and visible desert albedo. These values are obtained by simply taking the ratios of upward fluxes to downward fluxes. The magnitude of these spectral differences is somewhat abnormal for most natural earth surfaces, with respect to top of atmosphere exchange. Given the general dryness of the interior Arabian Desert atmosphere, it can be assumed that the integrated daily near-infrared albedo, measured at the surface, is very close to that which would be determined at the top-of-atmosphere. This excess loss can help explain why deserts often appear to be such dramatic energy sinks when viewed from space. The anomalously large near-infrared term (the near-infrared spectrum contains nearly half the solar energy) gives an added boost to the total reflectance loss term. This effect has been difficult to assess with

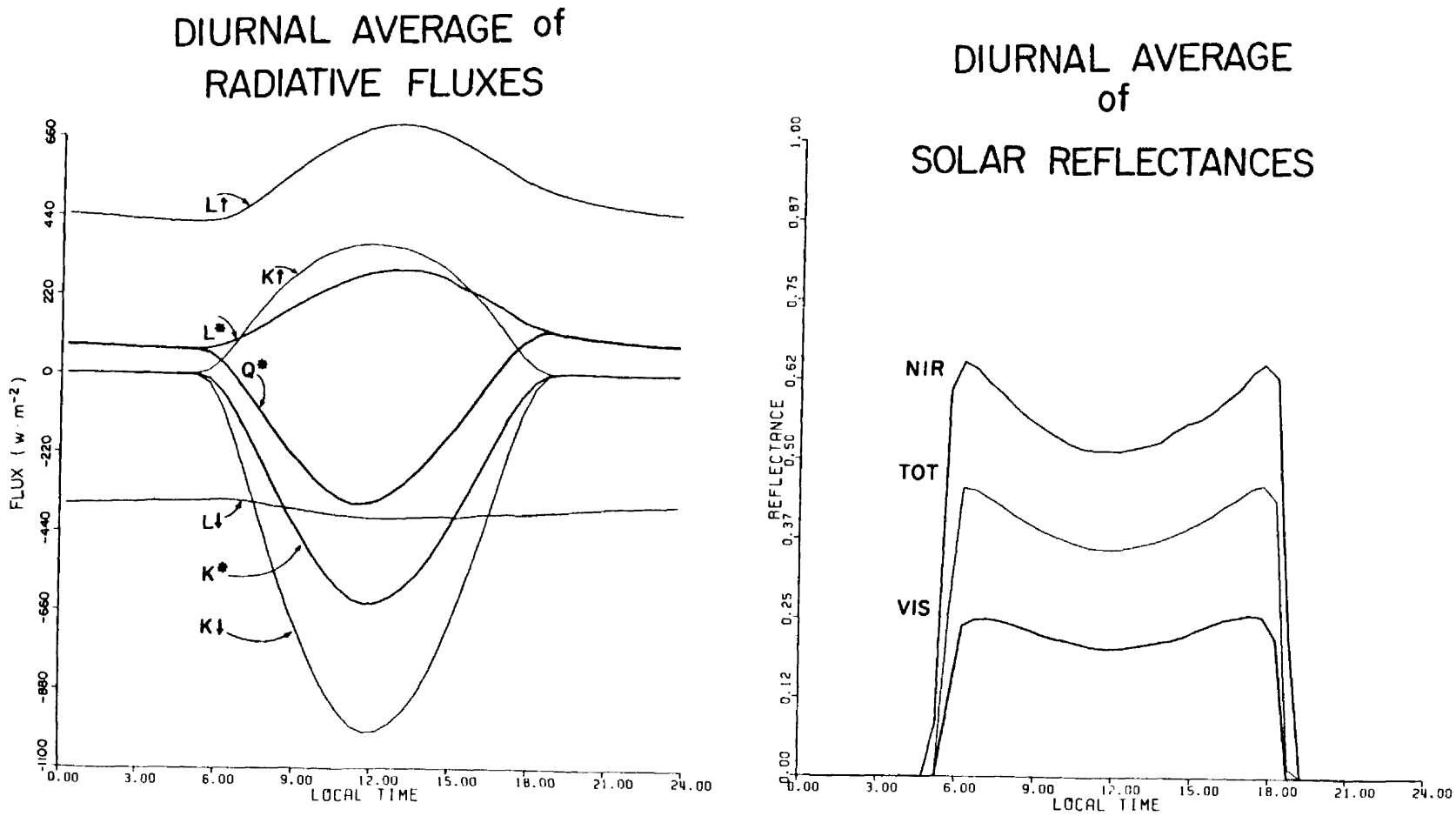

Fig. 4.14. Diurnal averages of the seven terms of the surface radiation budget (left) and the three-dimensional reflectance terms (right).

low resolution broadband satellite radiation budget sensors and impossible to assess with high resolution weather satellite sensors which incorporate only visible bandpass detectors. Oddly enough, however, during the summer months the Arabian Peninsula tends to be radiatively neutral (this is discussed in Section 4.7 and in detail in Chapter 5).

The dune sands in the Arabian Empty Quarter are fascinating. Quite often in the course of my stay, the daytime superadiabatic surface transition layer, in conjunction with the often moderate and steady winds, would raise a veil of sand off the desert floor, which would then meander in streaks and wisps across the dunes. At other times when the winds were quiescent, there was nothing but stillness and the etched out sand patterns to contend with. It is important to keep in mind that the Empty Quarter, or the Rub Al Khali, is an extensive desert (the local bedouin refer to it as the sands), on the order of one million square kilometers, and the Sharouwrah site is only one coordinate point. However, a quick glance at the METEOSAT photo in Fig. 4.10 demonstrates there is some degree of homogeneity to this region and that the Sharouwrah site is clearly not anomalous.

During the 1981 Sharouwrah measurement period, sub-surface sand temperatures were monitored at three depths (2, 20 35 cm). The diurnal temperatures tended to zero at approximately 40 cm. By fitting the soil temperature data with a mathematical expression that has characteristics of a modified gamma function (the individual hourly data did not suggest a simple sinusoidal character), a vertically integrated subsurface storage term is obtained (see Eq. 4.3). By coupling the storage term (S) with the net radiative terms (Q*), an estimate of the bulk surface

sensible heating term (SH) is then found. The diurnal cycles of these parameters are shown in Fig. 4.15. Note again the lack of daily symmetry which is driven in large part by the nonsinusoidal character of the subsurface storage term.

The other Saudi Arabian sites under investigation show some similar properties to the deep interior although with changes in magnitude. In Fig. 4.16 a summer-winter comparison between the diurnal radiative and total surface energy budgets is presented for the mountainous Taif site on the western escarpment. Part a of the figure gives the directional radiative fluxes, part b the net radiative fluxes, and part c the principal surface energy budget components. In parts a and b the unit standard deviation lines are drawn in conjunction with the diurnal means. Note that an obvious difference at this location between winter and summer is that the variance of downward solar radiation is larger in winter due to intermittant cloudiness. The differences in mean magnitude are, of course, driven by change in the mean solar zenith angle. This same phenomenon is also seen in the net radiative fluxes. The graphs in part c illustrate a simple compression of the surface energy budget parameters as the season moves from summer to winter.

Finally in Fig. 4.17 the midwinter, late winter, and summer cases for the radiation (part a) and surface energy budget (part b) terms at Najran, which is located at the western edge of the Empty Quarter, are illustrated. Note again the higher variance of $K\downarrow$ in winter but the much higher variance of the solar terms at Najran in summer than in Taif during summer. This is undoubtly due to intermittant intensifications of dust outbreaks in the Empty Quarter region which occur during the summer months and lead to an aerosol shortwave absorption perturbation;

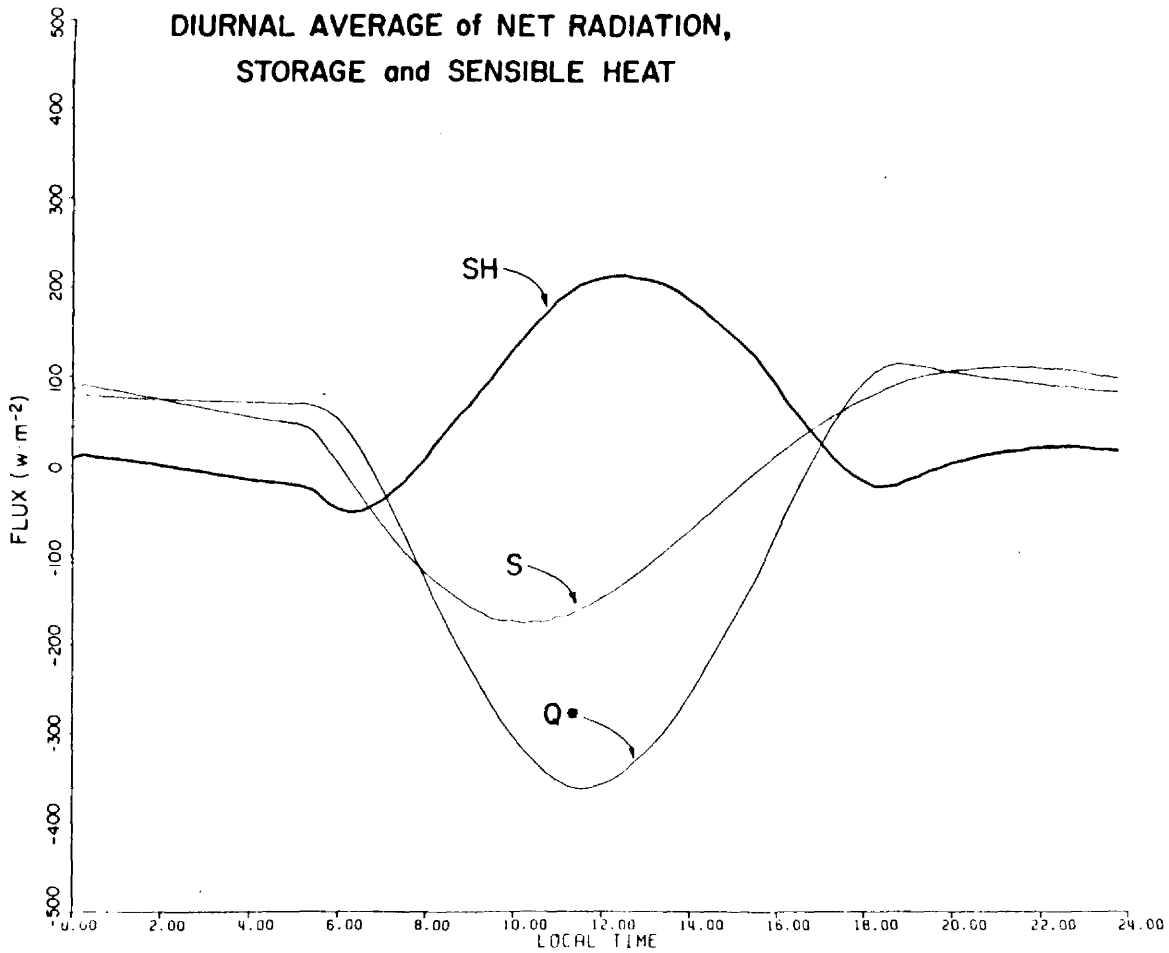

Fig. 4.15. Diurnal averages of the three principal components of the surface energy budget during June, 1981 at Sharouwrah. The definition of symbols is as follows: Q* is the net radiative flux, S is the subsurface storage term, and SH is the bulk sensible heat term.

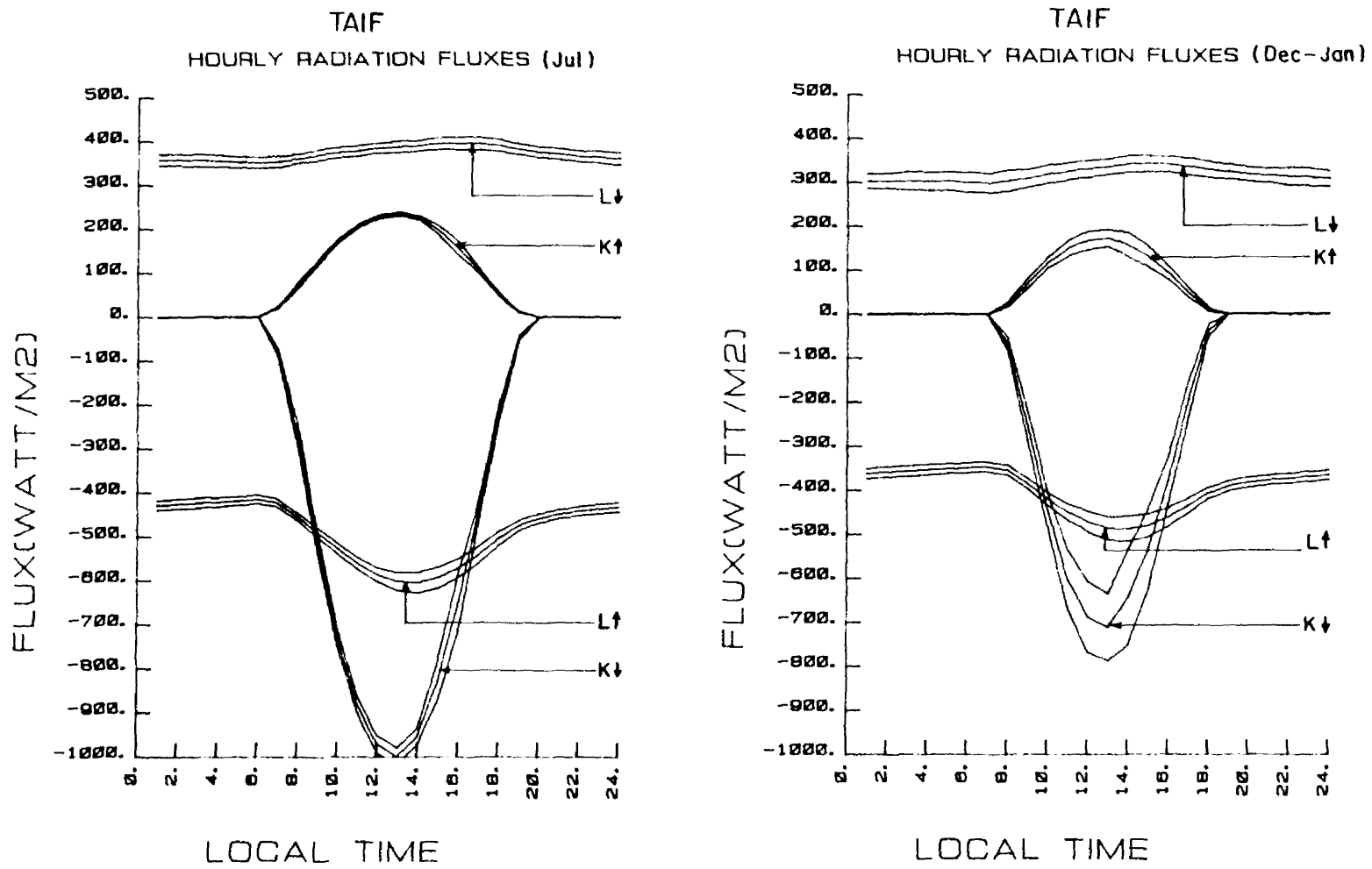

Fig. 4.16a. Summer (left part) and winter (right part) diurnal averages of directional radiative fluxes at Taif, Saudi Arabia. The one standard-deviation lines are plotted along with the means.

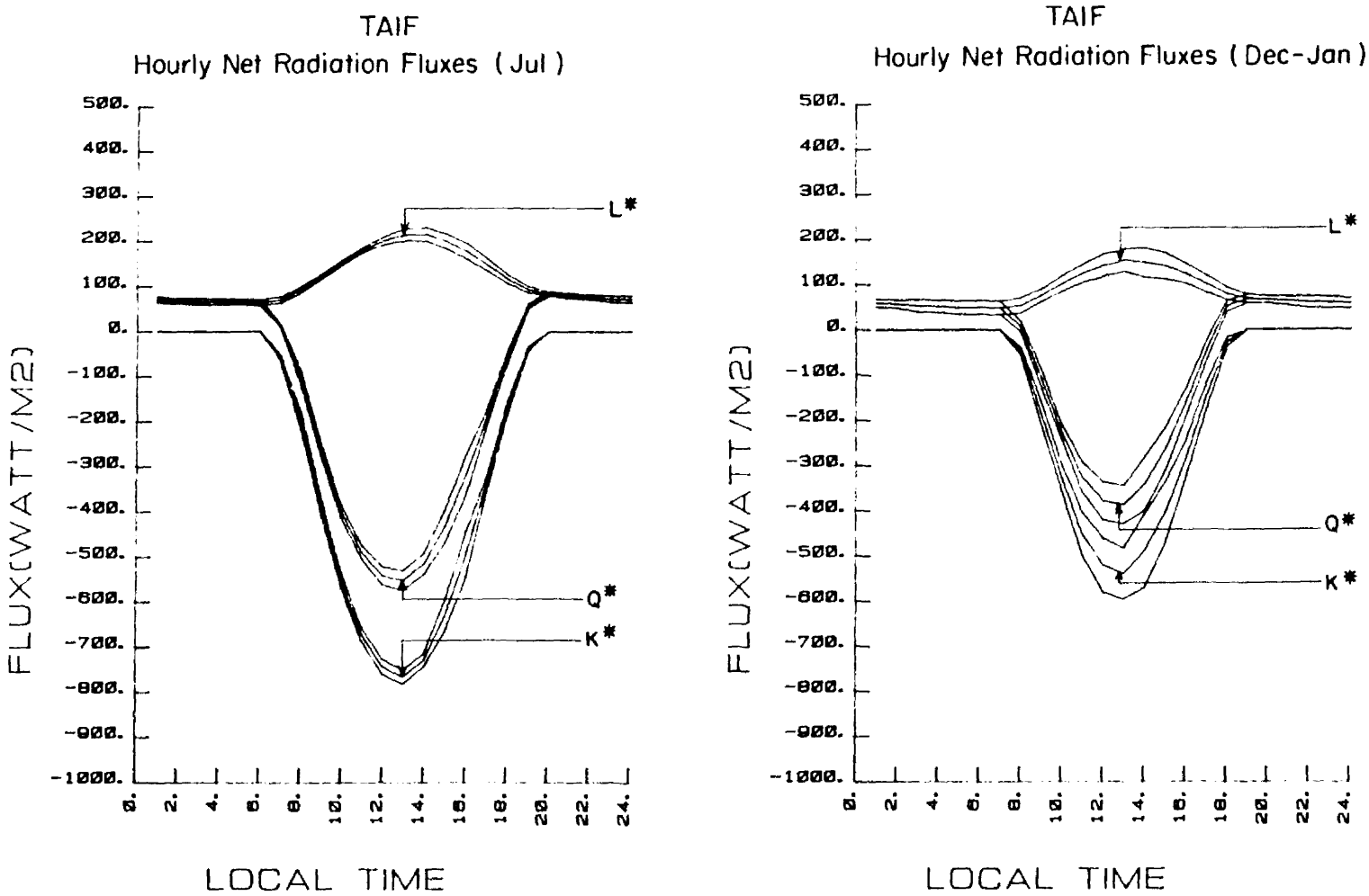

Fig. 4.16b. Same as Fig. 4.16a for the net radiative fluxes.

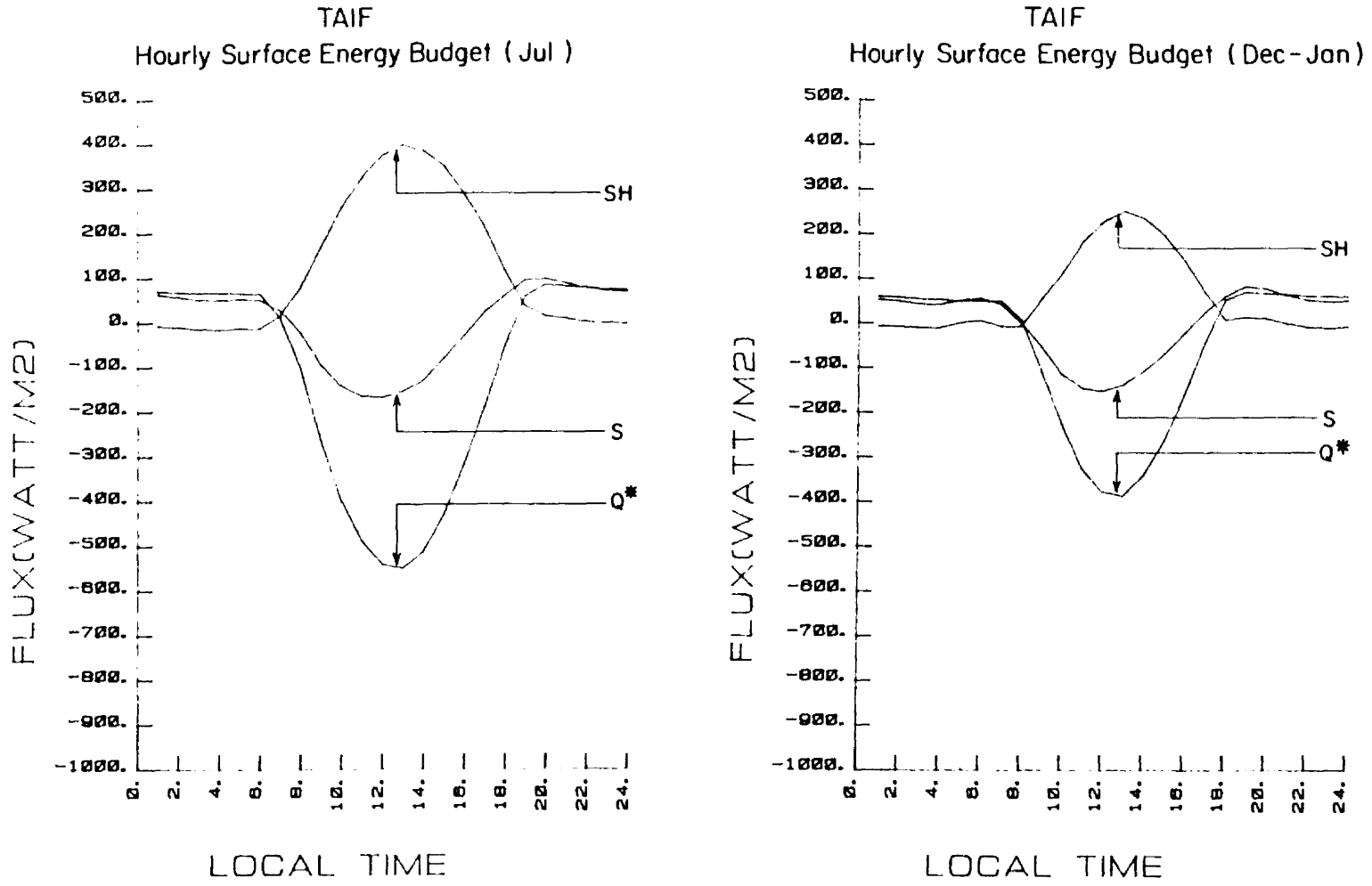

Fig. 4.16c. Same as Fig. 4.16a for the surface energy budget terms. The standard deviation lines are not plotted.

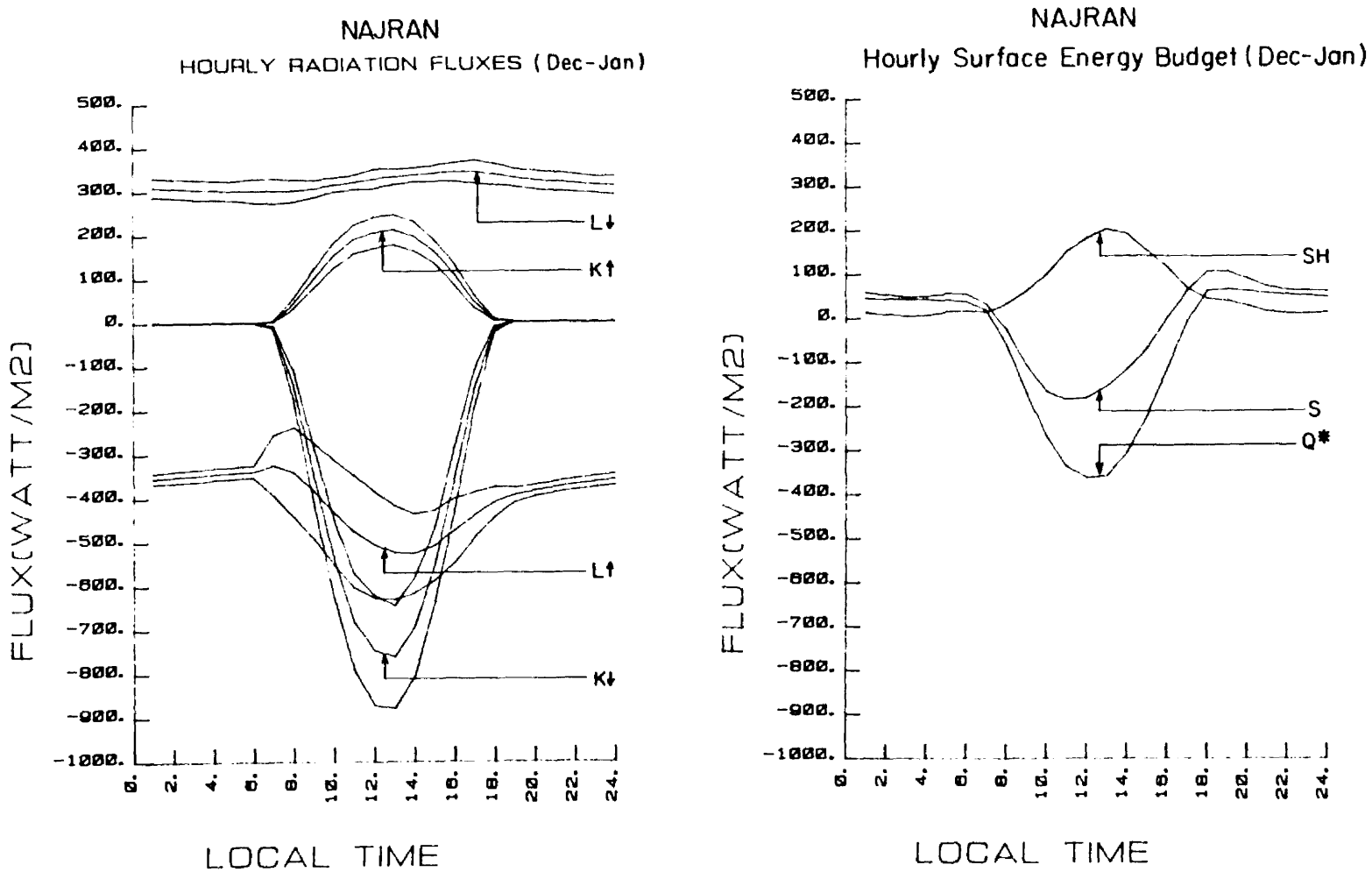

Fig. 4.17a. Midwinter (December-January) diurnal averages of directional radiative fluxes (left part) and suface energy budget components (right part) at Najran, Saudi Arabia. The one standard deviation lines are given for the directional radiative fluxes.

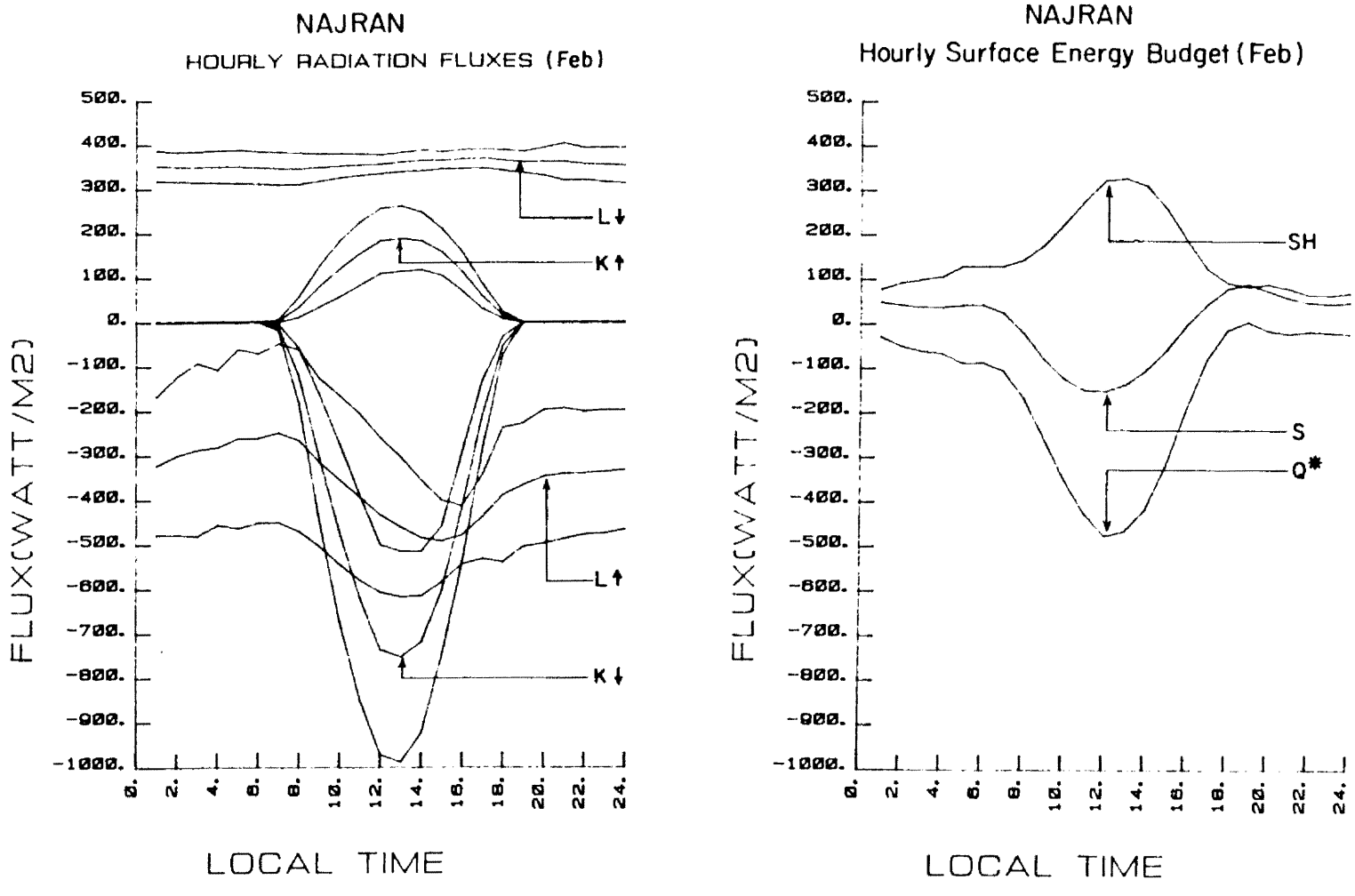

Fig. 4.17b. Same as Fig. 4.17a for late winter (February).

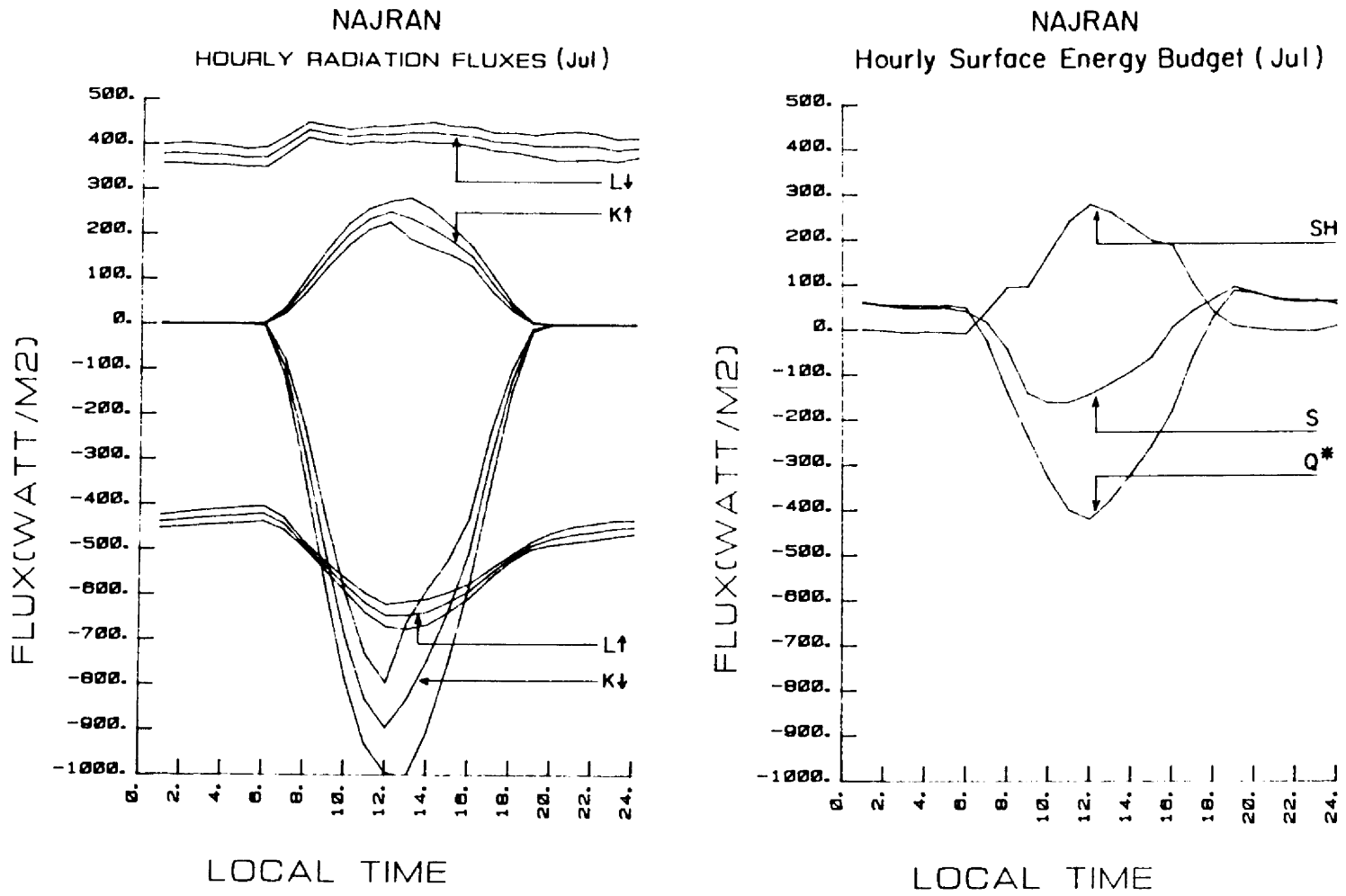

Fig. 4.17c. Same as Fig. 4.17a for summer (July).

see Ackerman and Cox (1982). The surface energy budgets indicate that sensible heating of the atmosphere moves from a midwinter noon maximum of approximately 220 $W \cdot m^{-2}$ to 300 $W \cdot m^{-2}$ in February. This larger magnitude of heating is also found in July.

The significance of these findings in regards to previous studies must eventually be assessed. Before any well-formulated theory of the development, structure and maintenance of desert heat lows is put forth, a well-defined description of the surface energy budget components is required; see Leslie (1980). Also these data are needed to evaluate the performance of planetary boundary layer (PBL) parameterizations such as that of Berkofsky (1976) which relates the top of PBL vertical velocity to surface albedo. In addition, it remains to be seen whether the desertification albedo theory [positive feedback effect - Charney (1975)], can withstand more realistic descriptions of the energy exchange process often lacking in numerical prediction models; see the updated Charney et al. (1977) experiment, Idso and Deardorff (1978), and Leslie (1980). Given the critical importance of this topic to the problem of subtropical land management and its implications for global climate, it is crucial that the deserts be continued to be given the most careful scrutiny [see Bryson (1973), Jakson and Idso (1975), Nicholson (1978, 1980), Otterman (1974), and Wade (1974)].

4.5 Tests at High Elevation at a Rocky Mountain Site

A full dual-station configuration, as described in Section 4.3, has recently been deployed (September, 1983) at a mountainous site, west of Fort Collins, Colorado. The objectives of this preliminary mountain measurement program involved carrying out trial preparations, shakedown tests, and sensor sampling and integration tests essential for an

expedition to the Gobi desert in The Peoples Republic of China (PRC) which took place during March-April, 1984. This experiment was coordinated with the International Symposium on the Qinghai-Xizang Plateau and Mountain Meteorology held in Beijing, March 20-24. The eventual target site for a 1985 operational plateau experiment will be near the old Tibetan city of Lhasa, at approximately 30°N, 91°E (Fig. 4.18 provides a TIROS-N satellite image with the proposed site indicated with black arrows). Two additional sites in the northern plateau region (Lake Kuku Nor), and west of Lhasa (Xigaze) are also being proposed. This project is being coordinated with the Academia Sinica and the State Meteorological Administration of the PRC.

The Rocky Mountain site presently in use is directly north of the Mummy Range in Rocky Mountain National Park, at a Colorado State University Forestry campus called Pingree Park ($40^{\circ}35'$N, $105^{\circ}40'$W). The elevation at this site is approximately 9,500 feet (2900 meters). The site itself is located in a mountain valley just east of the Continental Divide. The Radiation and Tower Stations were erected in a forest clear-cut, adjacent to a meadow area which lies in a major part of the headwaters of the Poudre River drainage basin. A photograph of the site, including the two stations, is shown in Fig. 4.19. Upon the completion of the tests to be discussed, the Pingree site will be used along with a site on Storm Peak near Steamboat Springs, Colorado, to carry out cooperative measurement programs in conjunction with the experimental Plateau program in the PRC. A significant aspect of the research is to understand the analogous energetics roles of both plateaus; see Tang and Reiter (1984).

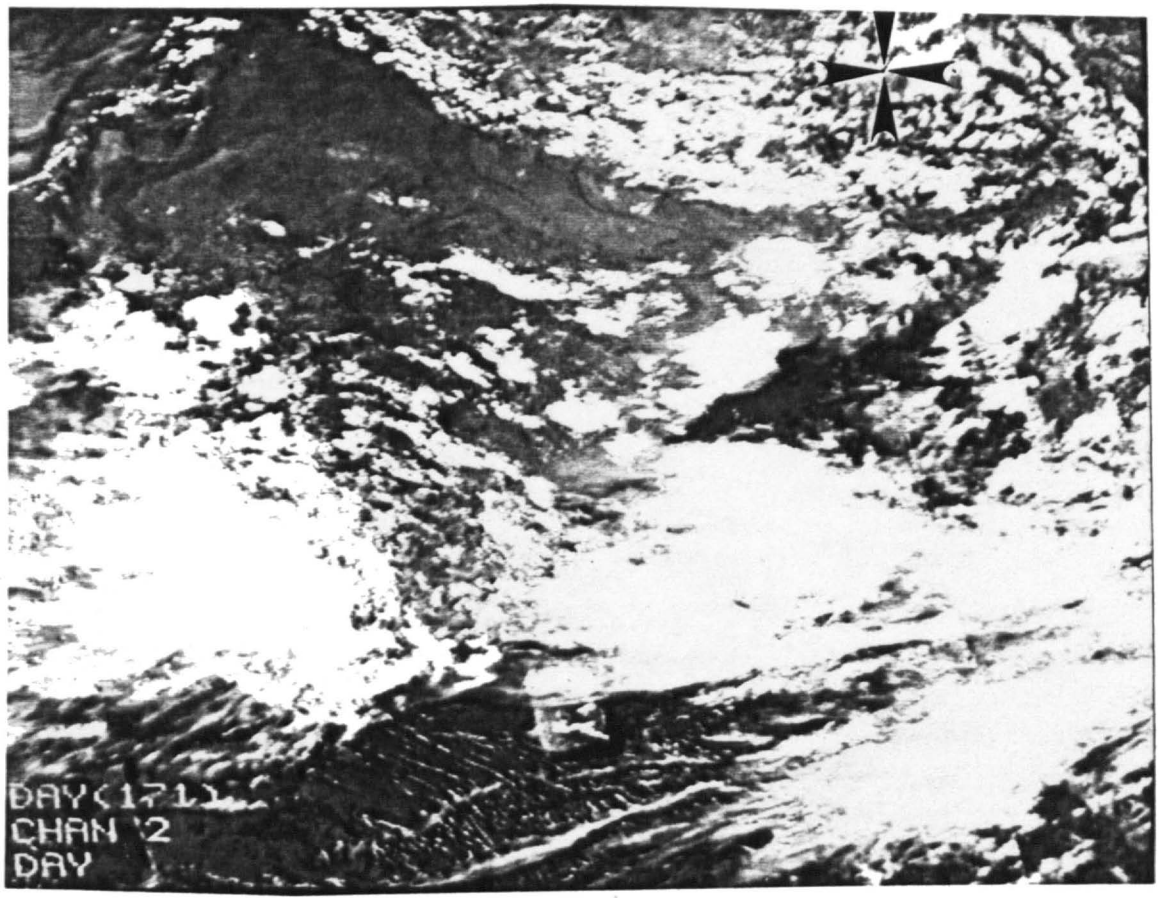

Fig. 4.18. A TIROS-N image (channel 1:0.55-0.90 μm) of the Indian Sub-continent and the Tibetan Plateau. The proposed monitoring site near Lhasa is indicated with black arrows.

Fig. 4.19. Photographic illustration of the Pingree Park mountain site. The view is to the south; the Mummy Range is seen in the background. The Radiation Station is seen at the right; the Tower Station at the left.

The following presents results from two brief Tower Station experiments which were essential before launching a measurement program in the PRC. The first experiment, called the 'Sampling Interval Test', was designed to determine the effect of the CR-7 sampling time on the derived mean quantities and eddy flux terms. The second experiment, called the 'Integration Time Test', was designed to determine the effect of the averaging time period (bar operator) on the derived parameters. The first test was required to determine if a sampling time of one second is sufficient to monitor vertical flux structure. One second sampling is the upper allowable limit with the eddy flux firmware unit in the Tower Station's data logger and also close to the order of the response time of the tower's sensors. The second test was needed to define a maximum integration time for characterizing the turbulent fluctuations. From an operations point of view, the longer the specified integration time, the longer the station can remain unattended because of tape recording space. It is emphasized that these are relatively qualitative tests and yet they reveal much about the impact of sampling and integration times on monitoring the turbulent boundary layer parameters.

Before discussing the Tower Station test results, Fig. 4.20 is presented as a means to characterize the data from a mountain Radiation Station and to set the tone for the typical background meteorological conditions during mid-autumn at the Pingree site. In this figure, the state parameters, wind parameters, soil temperature and moisture parameters, and total solar radiation parameters are presented for the period September 24 to October 6, 1983. Data samples were taken every 15 minutes. It is clear from this illustration that there are obvious

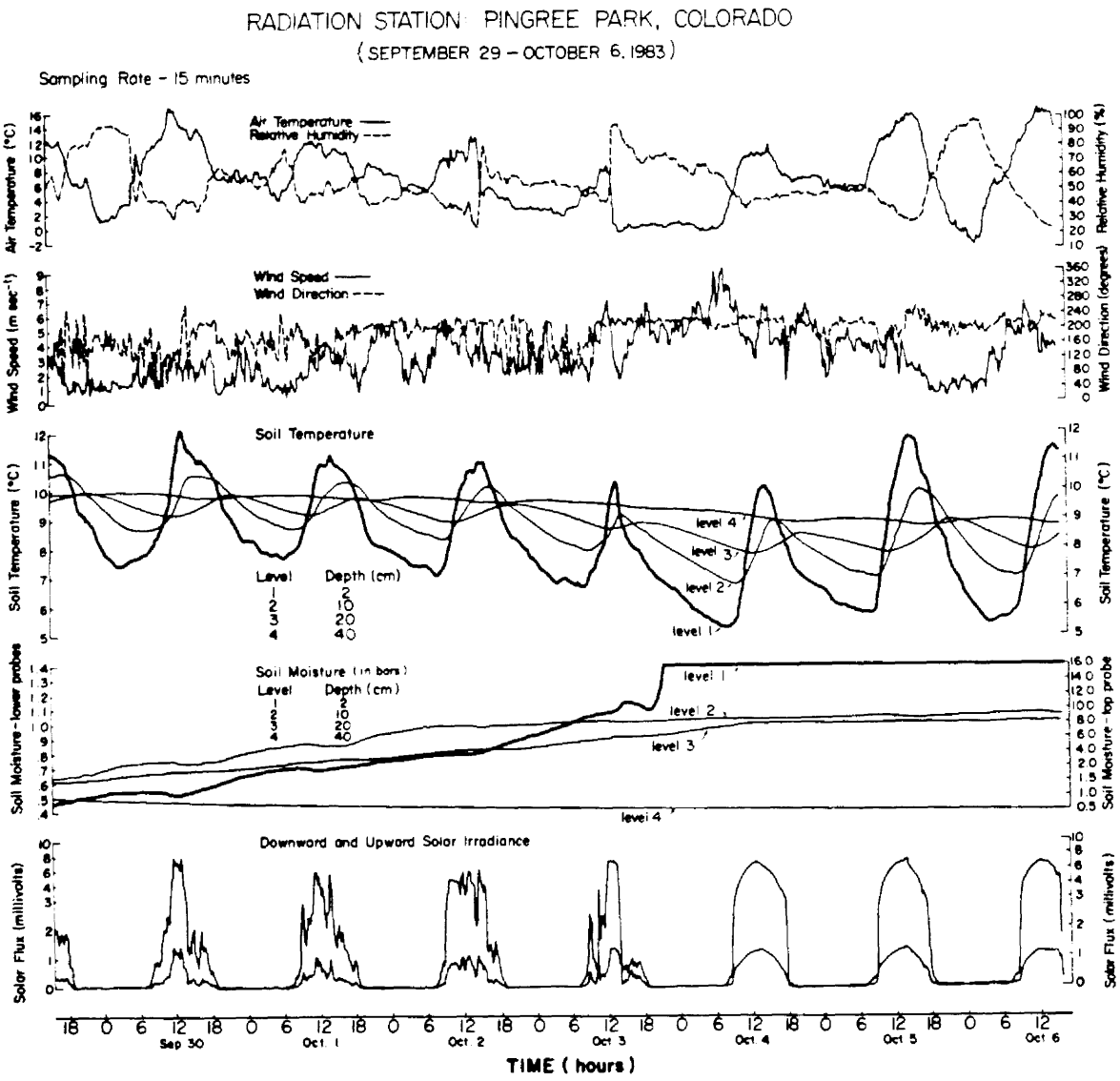

Fig. 4.20. Time series of Radiation Station parameters from September 30 to October 6, 1983 at Pingree Park, CO.

diurnal periodicities in the thermal parameters (both above and below the surface), that the subsurface is undergoing a cooling trend, and that the winds tend to show very little diurnal preference in either magnitude or direction. The soil is drying out during this period (there was no rain throughout), except at the deepest level (40 cm) where the moisture remained relatively constant (the surface probe dried completely on October 3 and went off scale). It is apparent from the solar fluxes (these have been plotted in engineering units because the calibration constants were unavailable at the time) that the first five days underwent intermittent cloudiness, whereas the last three days were relatively cloud free. The cloudiness has a dramatic effect on destroying the uniformity of the diurnal waves in the air temperature and moisture parameters, as well as deamplifying the subsurface soil temperature waves.

The results from the 'Sampling Interval Test' are shown in Figs. 4.21 to 4.24. This experiment was conducted during midday on October 4, 1983, a relatively cold autumn day, with nearly neutral PBL conditions, and undergoing intermittent, light snow showers. Six different sampling intervals were incorporated in the runs; 1, 2, 3, 4, 5, and 10 second. Each run lasted 20 minutes. The integration remained at 1 minute throughout the two-hour test. In Figs. 4.21 and 4.22 the temperature and relative humidity means at all four levels are plotted. It is fairly evident that the mean properties at any tower level are relatively unaffected by the sampling time. The temperature dip and corresponding relative humidity spike seen around 14:30 are associated with a 20-25 minute snow shower that was associated with almost complete

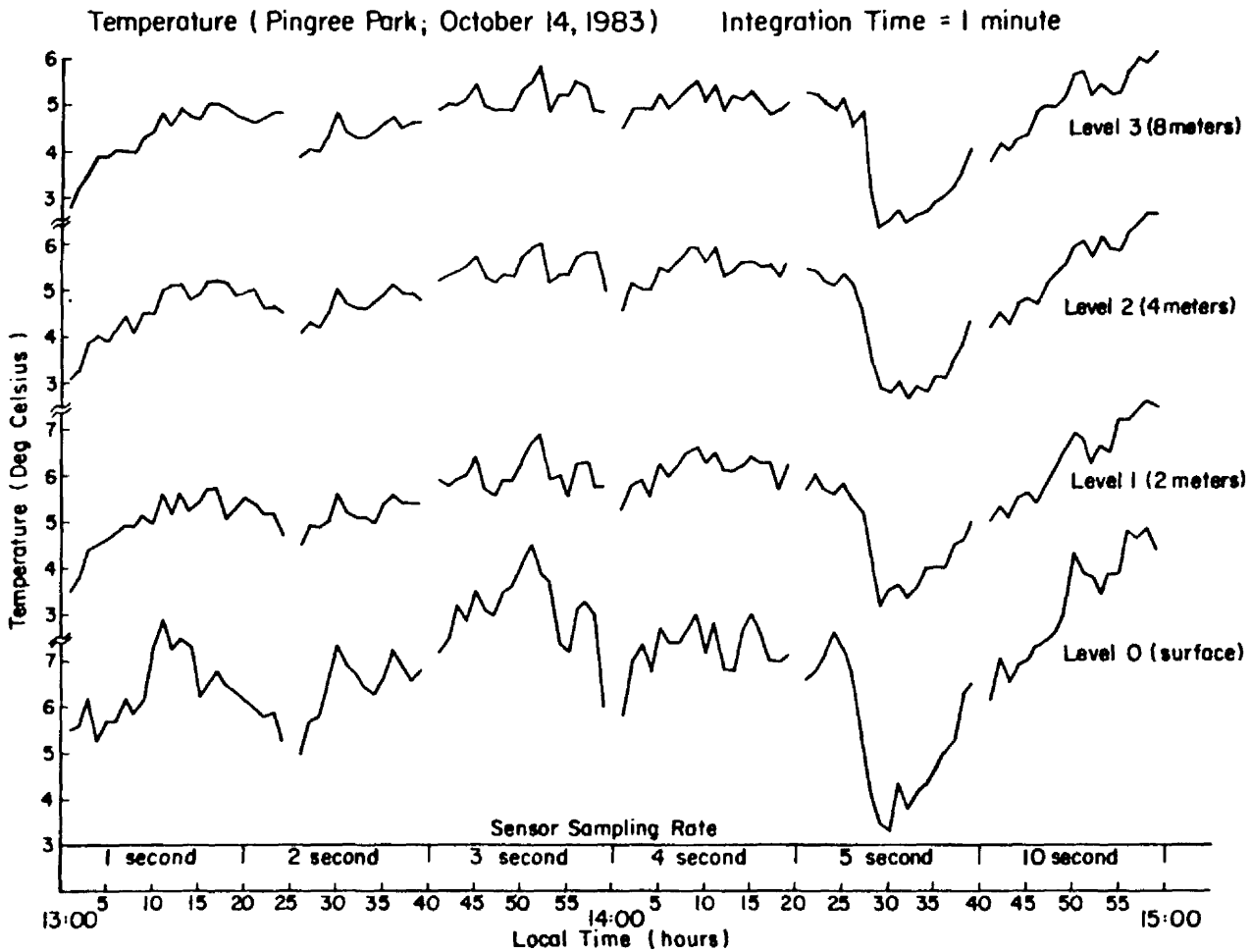

Fig. 4.21. Mean temperature runs from the 'Sampling Interval Test' held at Pingree Park on October 14, 1983.

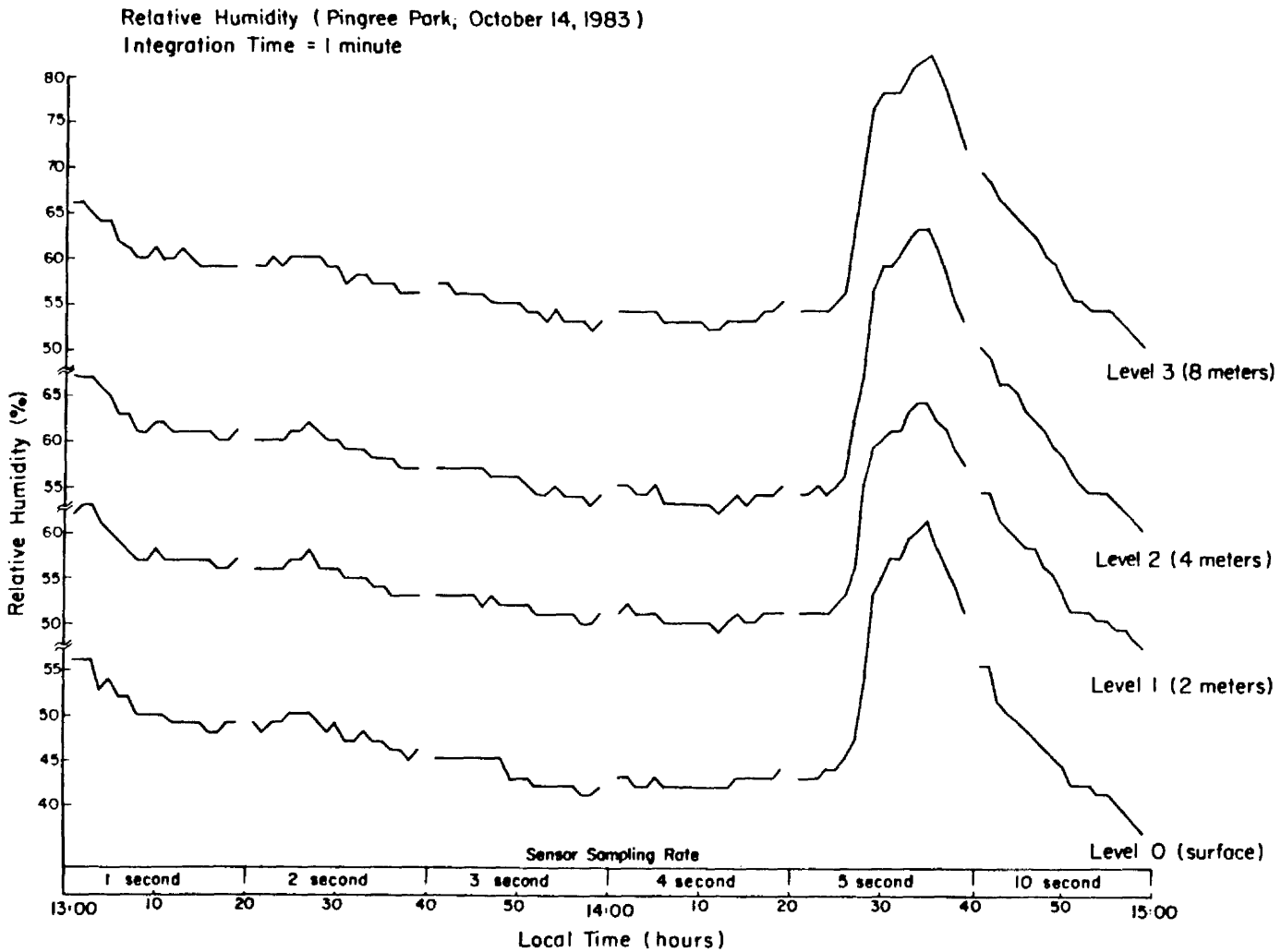

Fig. 4.22. The same as Fig. 4.21 for mean relative humidity.

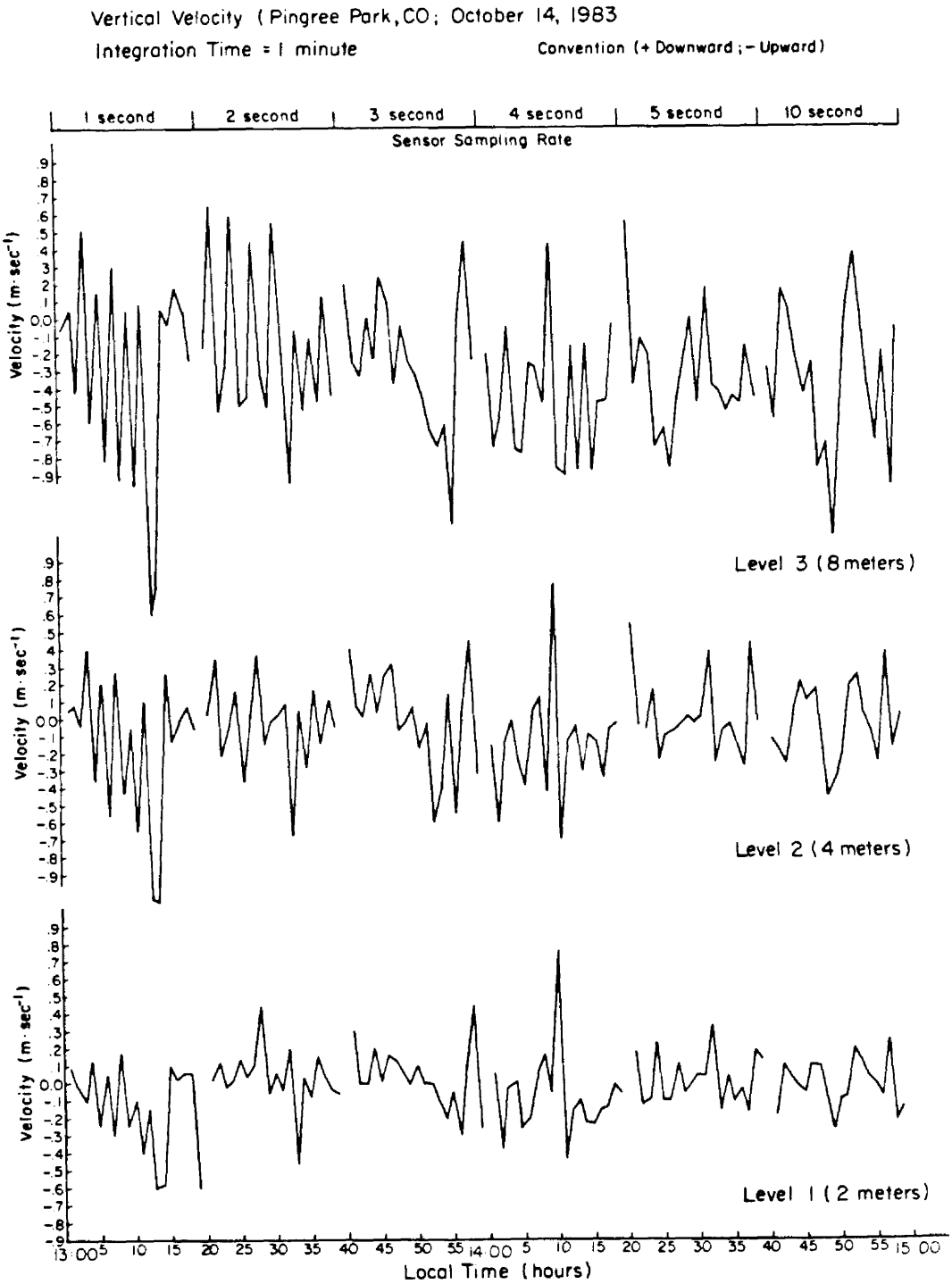

Fig. 4.23. The same as Fig. 4.21 for mean vertical velocity.

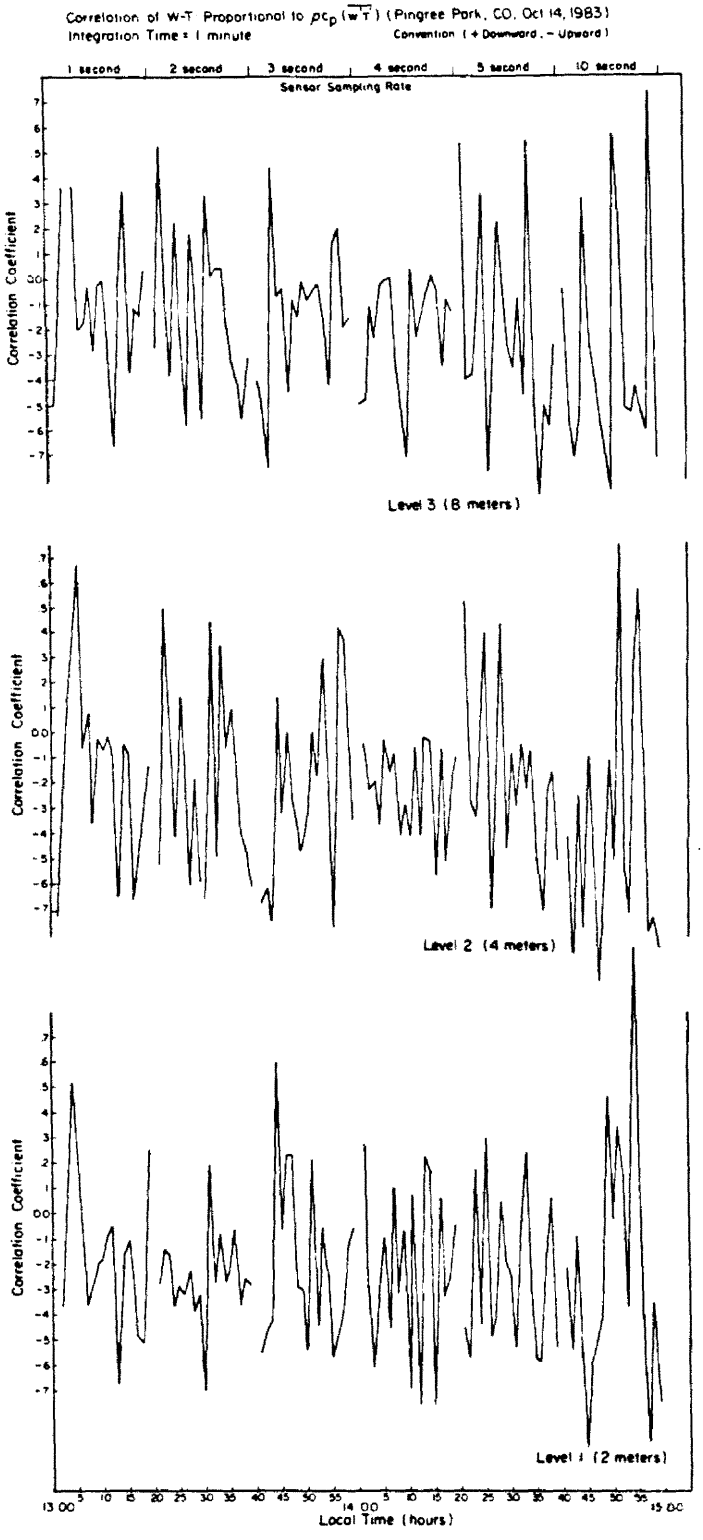

Fig. 4.24. The same as Fig. 4.21 for the correlation between vertical velocity and temperature.

cloud cover. This event was followed by sunny skies and a rapid increase in temperature.

An examination of Fig. 4.23 indicates that mean vertical velocity ($\bar{w}$) may be affected by the longer sampling times. The oscillations are on the order of 2 to 3 minutes and when the number of samples included in an average is reduced by an order of magnitude (from 1 to 10 seconds), the high frequency oscillations do not appear to be resolved as well. Qualitatively it appears that there is little difference between 1- or 2-second sampling. The significance of this result is that by adopting a 2-second sampling strategy, three more levels to the tower could be added without overextending the CR-7 processing requirements. It is noted here that the sign convention used for w is opposite the normal convention. That was due to a communication error between the author and lead engineer and has been recently corrected.

The vertical velocity-temperature correlations shown in Fig. 4.24 are rather interesting in light of the results seen in Fig. 4.23. The correlations, of course, are proportional to eddy heat flux. These results indicate that neither the time-scale of the turbulent plumes nor the resolution of their magnitude are highly impacted by degrading the sampling interval. This indicates that the 1-second sampling time interval will be sufficient.

The results from the 'Integration Time Tests' are shown in Figs. 4.25- 4.29. These tests were carried out on October 27 over a 5 hour, 30 minute period on a relatively warm and slightly unstable autumn day. The integration time was initially set to 1 minute at 11:00 a.m., then degraded to 2 minutes at 11:40, to 4 minutes at 12:20, to 8 minutes at 13:00, and finally to 16 minutes at 15:00. The temperature and vertical

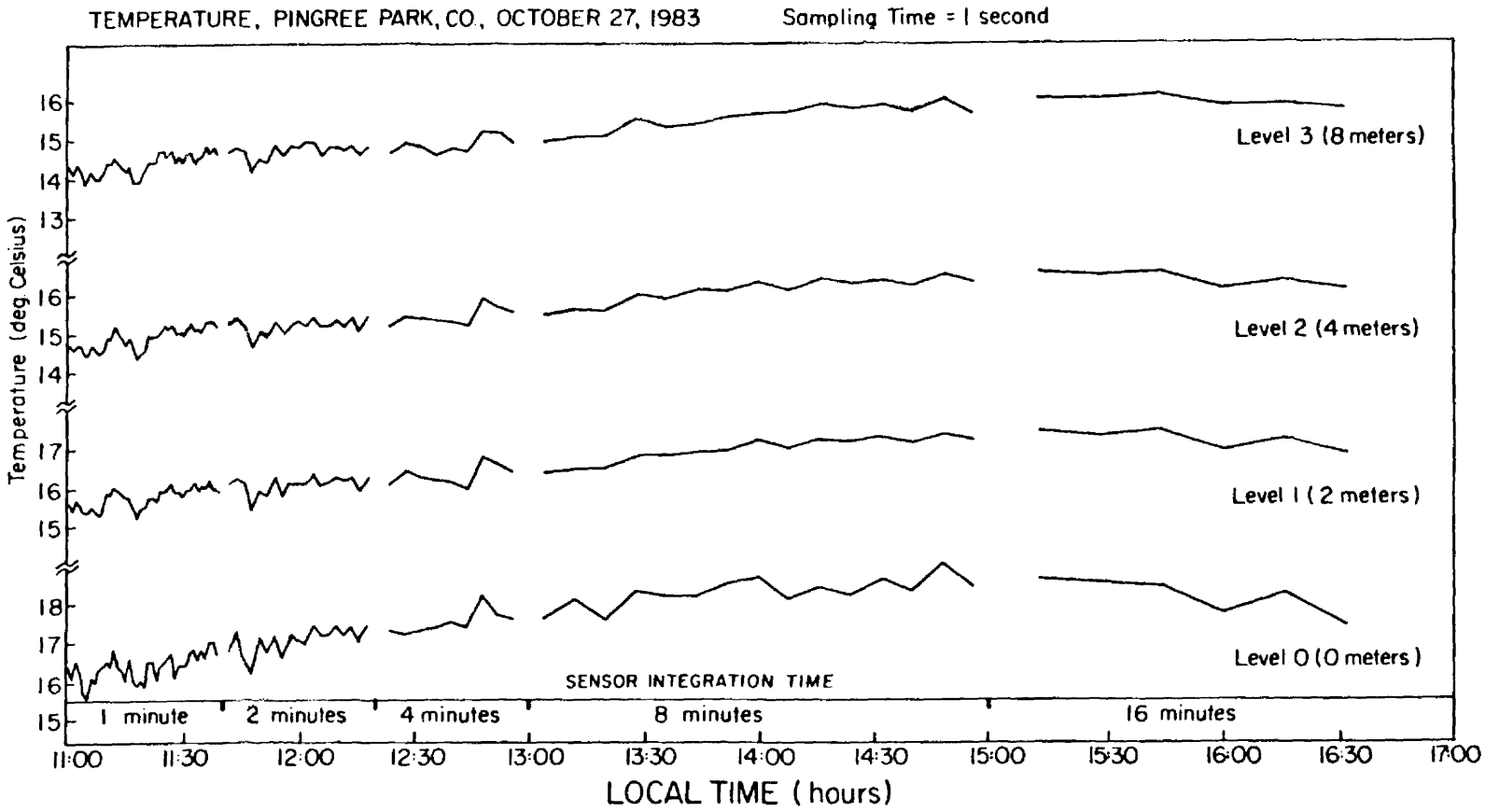

Fig. 4.25. Mean temperature runs from the 'Integration Time Test' held at Pingree Park on October 27, 1983.

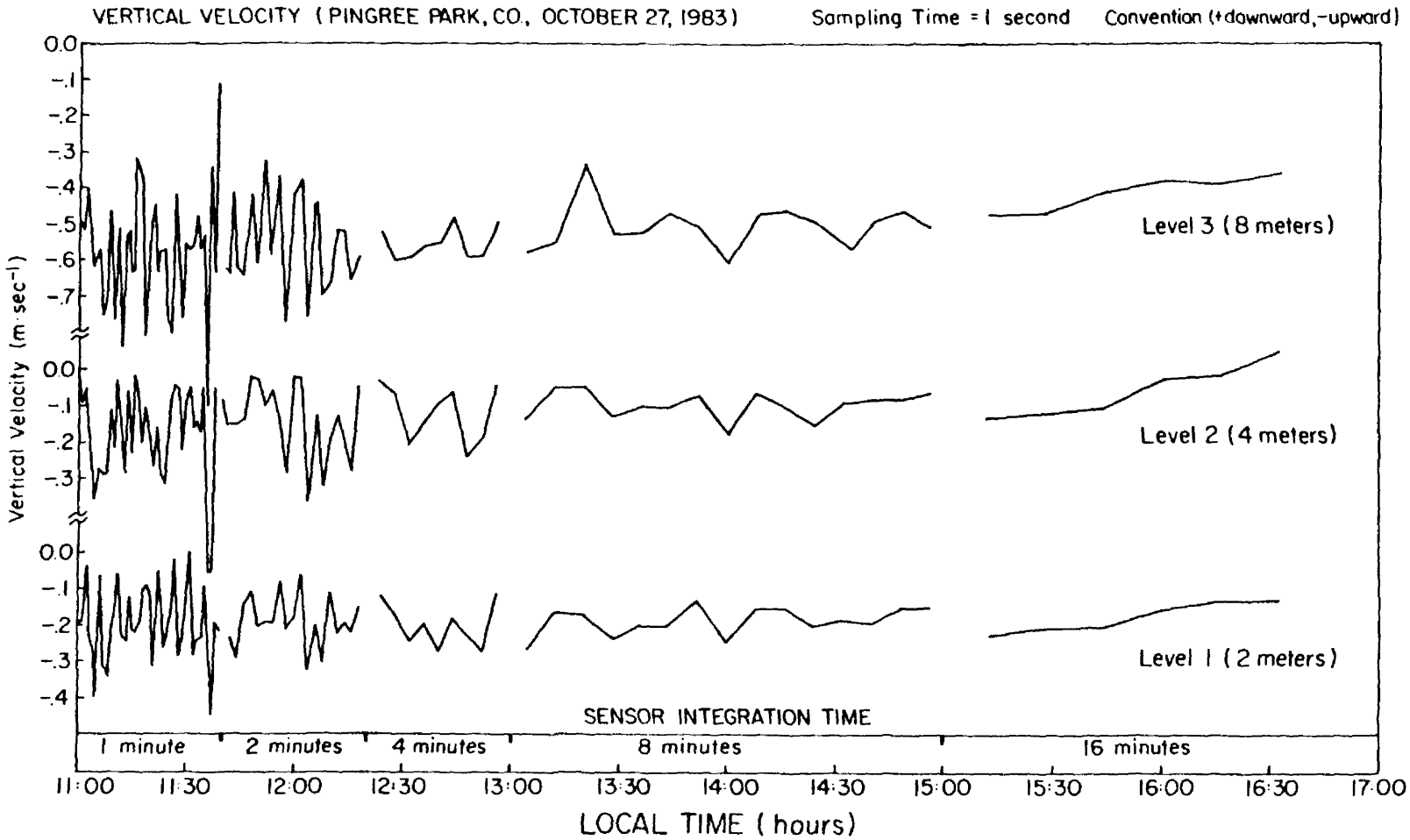

Fig. 4.26. The same as Fig. 4.25 for mean vertical velocity.

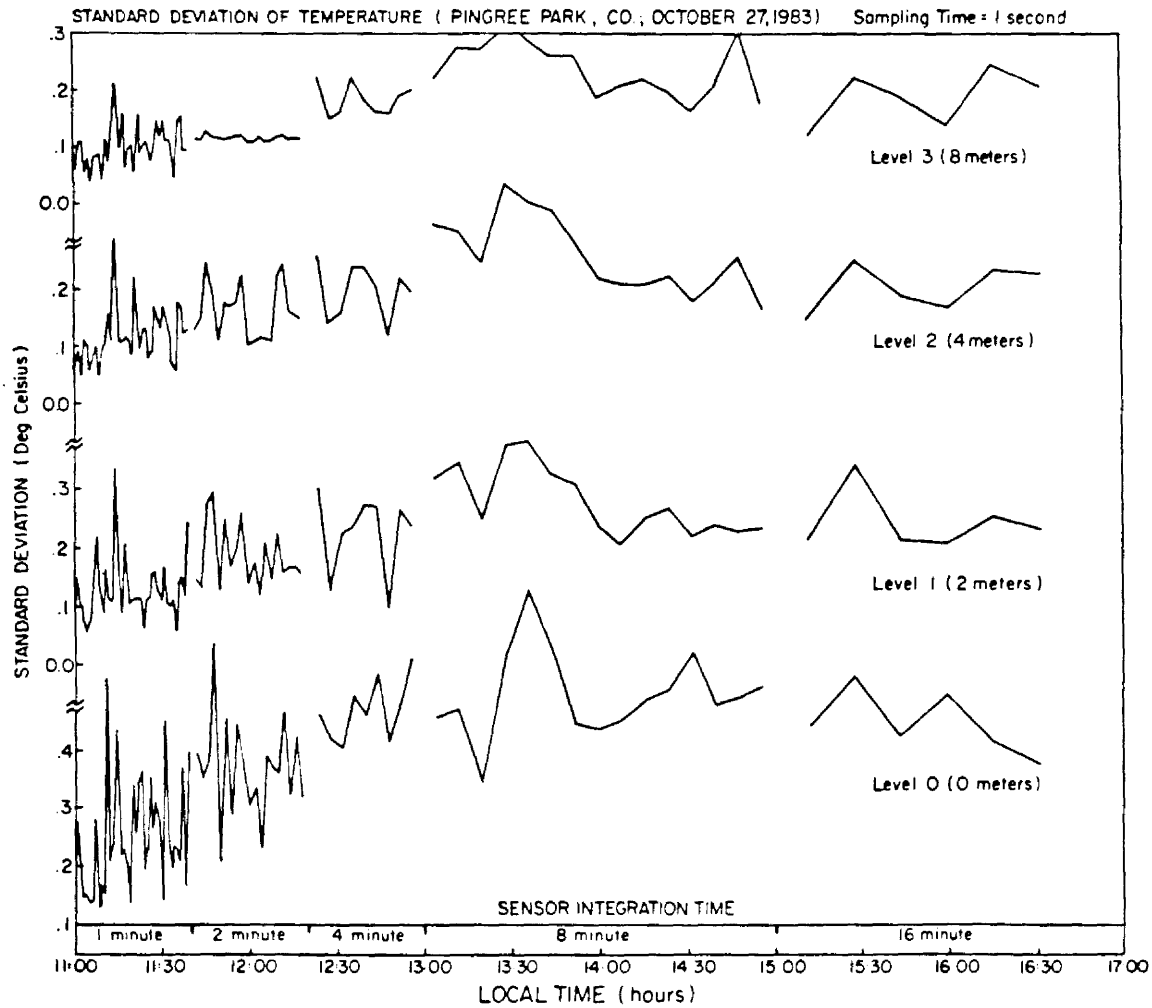

Fig. 4.27. The same as Fig. 4.25 for standard deviation of temperature.

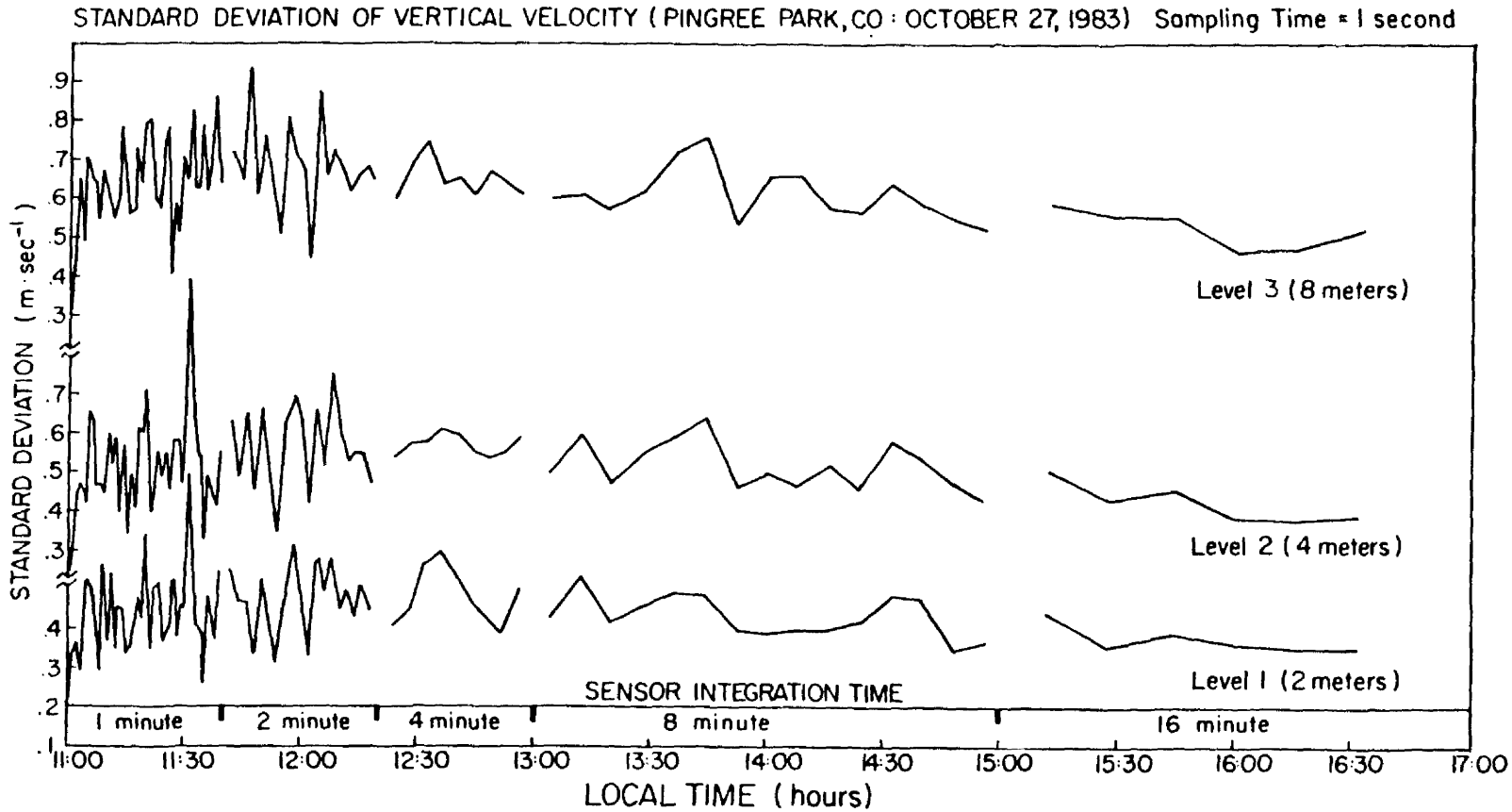

Fig. 4.28. The same as Fig. 4.25 for standard deviation of vertical velocity.

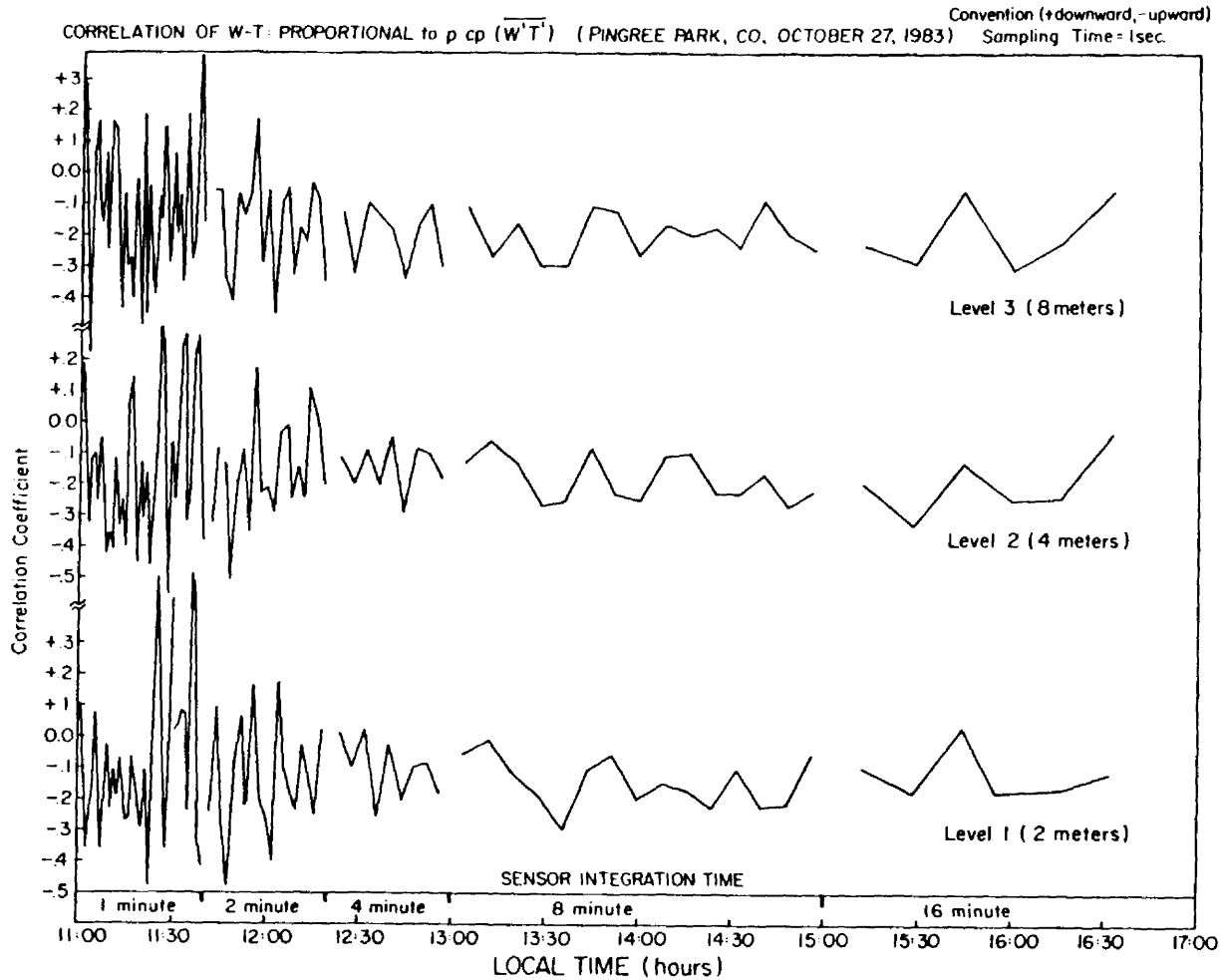

Fig. 4.29. The same as Fig. 4.25 for the correlation between vertical velocity and temperature.

velocity means at all levels are shown in Figs. 4.25 and 4.26. It is clear from these plots that in order to retrieve the structure of the fluctuations a 1- to 2-minute bar operator must be retained. The mean values at the longer integration times are still correct, however, there is no remaining evidence how they achieved their mean value. This is strong justification for operating with high frequency integration resolution during periods when the PBL is undergoing transitions from stable to neutral, and neutral to unstable conditions or vice-versa. The standard deviation terms of temperature and vertical velocity are shown in Figs. 4.27 and 4.28. It is evident from these plots that the time scale of variability of the thermal term (T) and the dynamic term (w) are virtually equivalent (3 to 5 minutes). Since the integration time scale should be selected on the basis of the fastest varying component in a given flux term, redundant statistics are not necessarily recorded by operating at the 1 to 2 minute integration time scales.

Finally in Fig. 4.29, the correlations proportional to eddy heat flux are shown. Whereas the high frequency plume structure can only be resolved from the 1- to 2-minute integration times, it is evident that the main features of the overall sensible heat transport process are reasonably well depicted at an integration time scale on the order of 10 minutes. Thus, for situations when the 'Tower Station' would go unattended for extended periods (30 days), a 10-minute integration time would be appropriate. For instances when an operator is hovering over the site, the 1-minute integration time would be preferable.

The results of the two tests, albeit qualitative, indicate that the data retrieval design built into the data logger firmwave will not inhibit the measurement program. All of the sensors showed remarkable

durability even during subzero, dry snow shower conditions. No individual sensor component failed over a 3-month period. The anemometer propellors were removed twice in that time due to extremely high wind conditions. The overall performance of the system, the quality of the data, and the ease of operation thus provide the basic initiative needed to extend the measurement program to the PRC and the Qinghai-Xizang Plateau.

4.6 A New Experiment on the Qinghai-Xizang Plateau

The proposed measurement program on the Qinghai-Xizang Plateau is directed at two separate mountain meteorology topics. The first concerns the impact of the plateau on the Southwest and East Asian Summer Monsoon and the larger scale planetary wave structure; the second concerns improving the knowledge of the surface energy budget of the plateau and its impact on the overall tropospheric heat budget profile [see Lau and Li (1984), Luo and Yanai (1984), and Nitta (1983)].

One dual station, as outlined in Section 4.3, was delivered to the PRC in March, 1984. This system was deployed in the Gobi desert (immediately north of the Plateau) during the first two weeks of April, 1984 and then again during June and July, 1984. Very preliminary results of the Gobi field program are presented in Figs. 4.30-4.31 without discussion.

The objective, in 1985, is to deploy various stations at different sites over the vast plateau region, in recognition of the fact that there are large meridional and zonal gradients of heat sources and moisture sinks, as well as multiple vertical circulation cells, over the vast Tibetan highland region; see Yeh (1981). An insight into the intricate geologic-geographic fabric of the Tibetan Plateau can be found

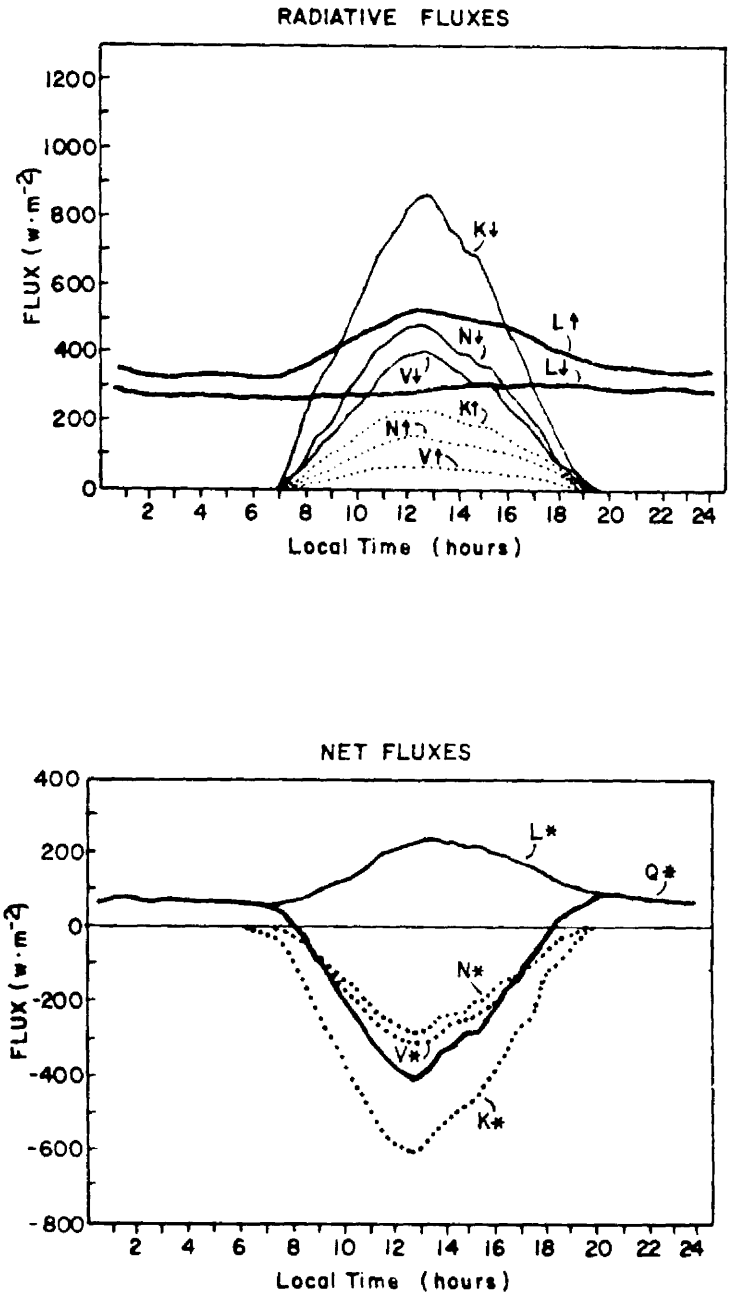

Fig. 4.30. Diurnal averages of surface directional radiative fluxes (top) and surface net radiative fluxes (bottom) in the Gobi desert, April 8–14, 1984.

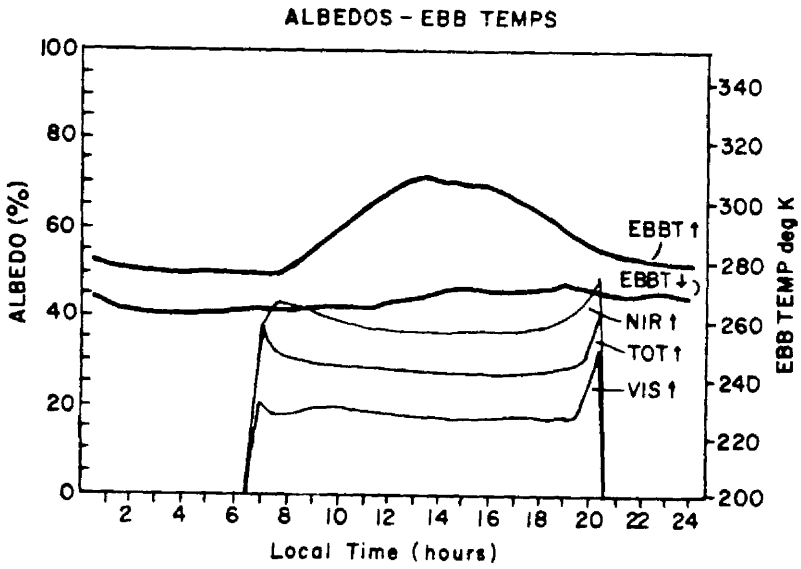

Fig. 4.31. Same as Fig. 4.30 for surface directional reflectance and upward/downward equivalent black body temperatures.

in Reiter and Reiter (1981). By means of example, Fig. 4.32 provides a photo of the Himalayan Range near the Indian border city of Srinagar taken from the Convair-990 during the Bombay phase of the 1979 Summer Monsoon Experiment.

The role of the Tibetan Plateau as both an orographic barrier and an elevated heat source on the large-scale circulation has been well established through the examination of synoptic data [see Flohn (1950, 1953, 1957, 1968), Gao et al. (1981), Reiter and Gao (1982), Riehl (1959), Yeh et al. (1957)], annulus experiments [see Chang et al. (1977), Yeh and Chang (1974), and Yeh (1981)], and numerical model experiments [see Godbole (1973) and Hahn and Manabe (1975)]. Its downstream impact on weather systems in Northern and Eastern China [see Tao and Ding (1981)], and its important role in setting the timetable for the evolution, positioning, and maintenance of the Southwest Monsoon and interacting with the monsoon surges and breaks [see Chang (1981) and Hahn and Manabe (1975)], and its controlling influence on replacing the southern branch of the split jet (subtropical jet) with the tropical easterly jet in conjunction with the upper tropospheric plateau anticyclone and anti-Hadley cell (Yeh's Tsingha-Tibetan high) during the monsoon season [see Flohn (1968), Koteswaram (1958), Krishnamurti (1971), Krishnamurti et al. (1973), Krishnamurti and Bhalme (1976), T. Murakami (1958), Yin (1949)] are now well accepted ideas.

Although modeling results are not always realistic--see the classic observationalist versus modeller debate between Sadler and Ramage (1976) and Hahn and Manabe (1976)--it has required numerical model experiments and model frameworks to provide some of the essential detail in the vertical and horizontal structure of the dynamic and thermodynamic

Fig. 4.32. Photograph of the Himalayan Range near Srinagar, India taken from the NASA Convair-990 on June 11, 1979.

fields over the adjacent to the plateau, their seasonal variability, and their diurnal characteristics; see Kuo and Qian (1981). These studies, in conjunction with in-depth observational studies, such as that of Flohn (1968), Luo and Yanai (1983), and T. Murakami (1981a, 1981b), provide an excellent description of plateau meteorology.

In recent years, based on the FGGE data sets and long-term Chinese data archives, some of the first detailed accounts of the atmospheric and surface energy budget processes over the plateau have been published; see Luo and Yanai (1984), Nitta (1983), and Yeh and Gao (1979). Nevertheless, there remain large gaps in the data, particularly concerning radiative properties, the structure of the divided-cell heat low, radiative heating rates, precise estimates of sensible and latent heat exchange (particularly over the mountain peaks) and subsurface heat storage (Yanai, 1983). These data gaps provide the motivation for our proposed experiments.

There is still much to be learned about plateau meteorology; the similarities and differences between the roles of the Qinghai-Xizang Plateau and the North American Rocky Mountains [see Reiter and Tang (1984) and Tang and Reiter (1984)]; the structure and role of the summer plateau heat low and its comparisons and contrasts to desert heat lows; the manner in which the surface radiation budget controlls the sensible heat exchange process; and finally the nature of the diurnal and seasonal cycles of deep soil temperatures; their interannual variation and the impact of the processes on the planetary circulation and the teleconnective feedback cycle [see Reiter and Ding (1980, 1981), and Reiter (1982)]. These are some of the scientific problems that will be addressed in 1985.

4.7 Combining Surface Measurements with Satellite Data

One of the mainstream strategies now employed in investigating surface and atmospheric processes, is the combining of measurement platforms providing different detection perspectives. A chief ingredient in the multiple platform experiment has been the array of operational and experimental satellites whose unique large-scale observation capabilities have advanced scientific field work far beyond what had been possible in the pre-satellite days. The results of the GARP Atlantic Tropical Experiment (GATE); the First GARP Global Experiment (FGGE) and its embedded summer and winter monsoon experiments (SMONEX and WMONEX); the Alpine Experiment (ALPEX); the ongoing International Satellite loud Climatology Project (ISCCP) and its associated scientific component the First ISCCP Regional Experiment (FIRE); and the proposed International Satellite Land Surface Climatology Project (ISLSCP) represent a sequence of scientific investigations in which the satellite platform has played, and is continuing to play, a first order role, if not the lead role.

By the same token, it is the intent to utilize satellite data in conjunction with aircraft and surface data to assist in the process of examining radiative and energetic processes over the Arabian Desert heat low, the Rocky Mountain region, and the remote Tibetan Plateau. A conceptual illustration of the measurement strategy for studies of the Arabian heat low has been shown in Fig. 2.22. This figure illustrated how polar orbiting and geosynchronous operational weather satellites, along with the Nimbus 7 experimental spacecraft, have been used in conjunction with Convair-990 data and surface data to probe the atmospheric volume containing the Arabian heat low feature. The weather

satellite imagery (see Fig. 4.33) is used to make estimates of radiative exchange and to describe the cloud fields over the terrestrial surfaces. By utilizing the satellite to provide top-of-atmosphere boundary conditions, the surface data to provide the lower boundary conditions, and the aircraft radiation and dropsonde data to provide vertical profiles and atmospheric conditions [see Ackerman et al. (1983)], the bulk atmospheric radiative exchange process can be described. The Arabian heat low will be discussed in detail in Chapter 5.

Figures 2.24 and 2.25 presented results obtained from the multiple-platform approach. In these diagrams of the diurnal solar and infrared cycles over the Arabian Empty Quarter, the satellite derived albedos and longwave emittances are plotted along with top-of-atmosphere albedos and emittances obtained from surface measurements, aircraft measurements, and theoretical radiative transfer model calculations. In addition, the atmospheric shortwave transmittance and absorptance terms, the surface albedo and longwave exchange terms, and the theoretical clear sky shortwave transmittance are all plotted.

These types of analyses are crucial to the understanding of deserts and the desertification process. It is noted that although the now accepted view of deserts is that they generally act as radiative energy sinks (due to their high albedo), the Arabian heat low over the course of a monsoon season departs radically from this picture. By plotting a time series of the radiation budget components over the desert Empty Quarter, obtained from the Earth Radiation Budget (ERB) instrument flown on the NASA Nimbus-7 spacecraft, it can be seen that much of the time the Empty Quarter is either a slight radiative source region or radiatively neutral. Figure 4.34 illustrates a net radiation map

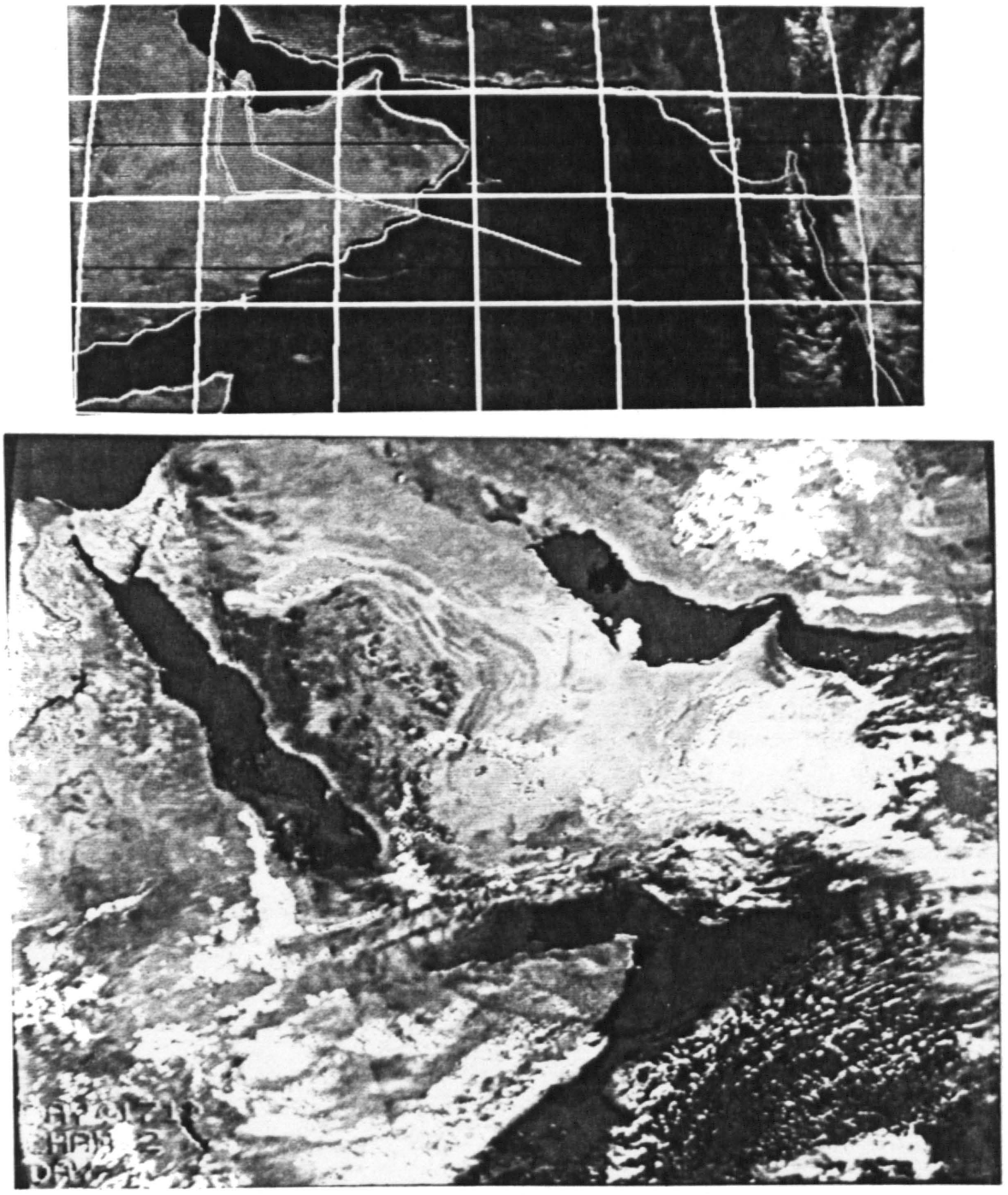

Fig. 4.33. Examples of GOES-1 (top) and TIROS-N (bottom) weather satellite imagery. The GOES-1 image is a VIS channel sector, taken at 11:00 LT on June 10, 1979. The flight track of a CV-990 differential heating mission (flown that day out of Dhahran, Saudi Arabia) is seen super-imposed over the image. The TIROS-N image is a near-IR sector (channel 2:0.7-1.02 μm) taken at 15:00 LT on June 20, 1979.

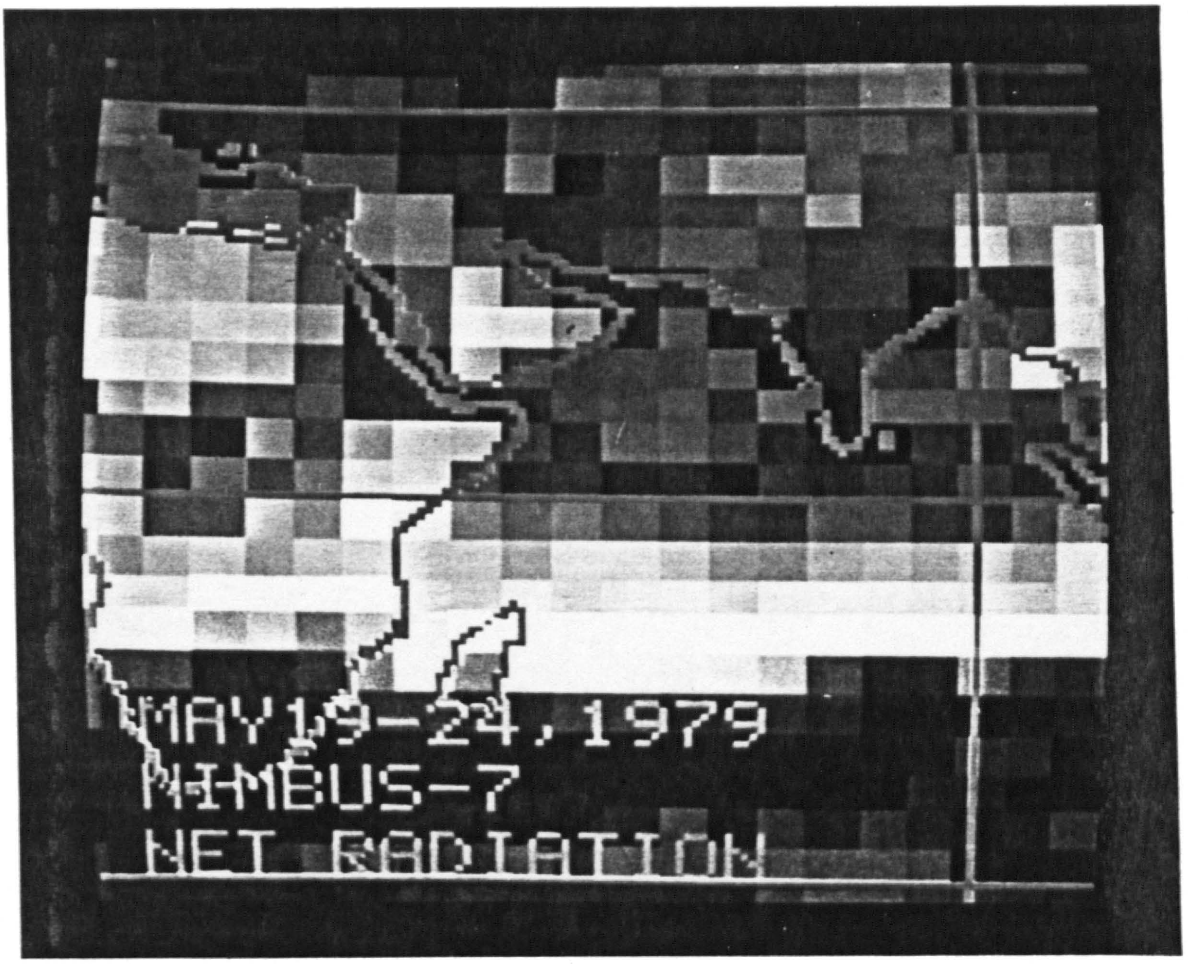

Fig. 4.34. Net radiation map of the monsoon region for the period May 19-24, 1979 derived from the Nimbus-7 ERB-NFOV data. The color scheme is given below the figure.

compiled from ERB Narrow-Field-of-View (NFOV) measurements. In Fig. 4.35 the radiation components from the ERB target centered over the Arabian Peninsula are plotted from the beginning of May to the end of August, 1979. Note how the net term hovers around the zero line. Note also, that there is a reasonable indication of an approximately five to seven day periodicity in the radiation budget components, particularly after the onset of the Southwest Indian Monsoon (June 10-20). This is rather interesting considering that the Empty Quarter remains virtually cloud free throughout. The explanation most likely lies in periodic outbreaks of dust and/or high level moisture and cirrus cloud due to oscillations in the dynamical fields noted by others [see Khrishnamurti and Bhalme (1976), M. Murakami (1977), Sikka and Gadgil (1980), Webster et al. (1977), Webster and Chou (1980), and Webster (1983)].

If the above process is contrasted with that taking place over the Tibetan Plateau during the same period, major differences are noted. Figure 4.36 illustrates the radiative components from the ERB-NFOV target centered near the Tibetan city of Lhasa (29^{o}'15'N; 87^{o}30'E). For this area it is shown that the oscillations are of a much higher amplitude, that the region maintains a radiative surplus throughout the course of the monsoon, and the oscillations begin prior to the onset of the Southwest Monsoon depression.

By combining satellite data with the Tibetan measurements, it will be possible to improve our understanding of Tibetan Plateau energetics. The weather satellites, in particular, are powerful tools for high resolution examination of the ongoing meteorological and energetic processes; see Fig. 4.37 for examples. In recent years a powerful satellite data base has been developed for carrying out some of these

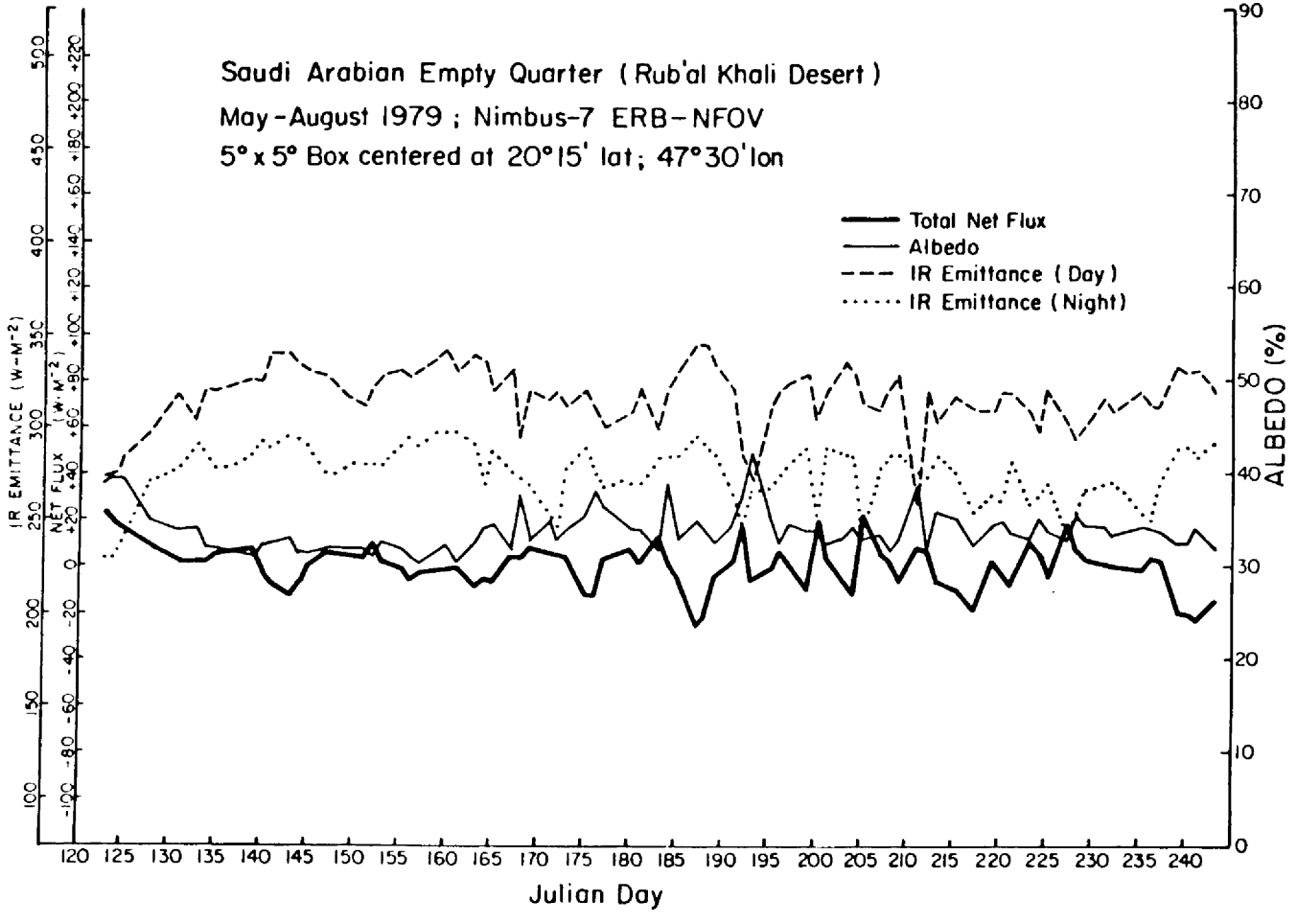

Fig. 4.35. Time series of radiation budget terms (albedo, daytime and nighttime infrared emittance, net flux) over the Saudi Arabian Empty Quarter from May through August, 1979.

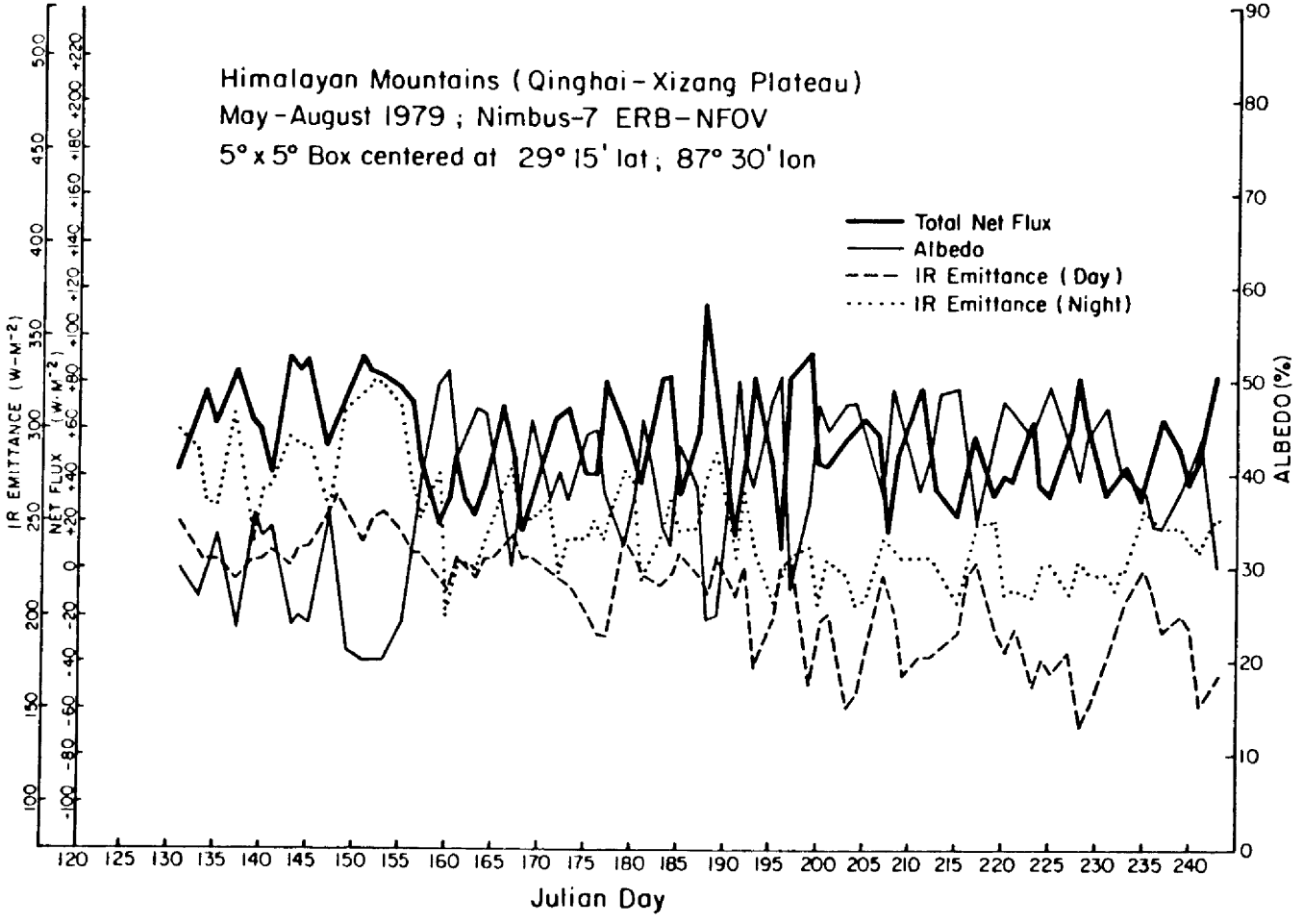

Fig. 4.36. Same as Fig. 4.35 for a region centered near the Tibetan city of Lhasa.

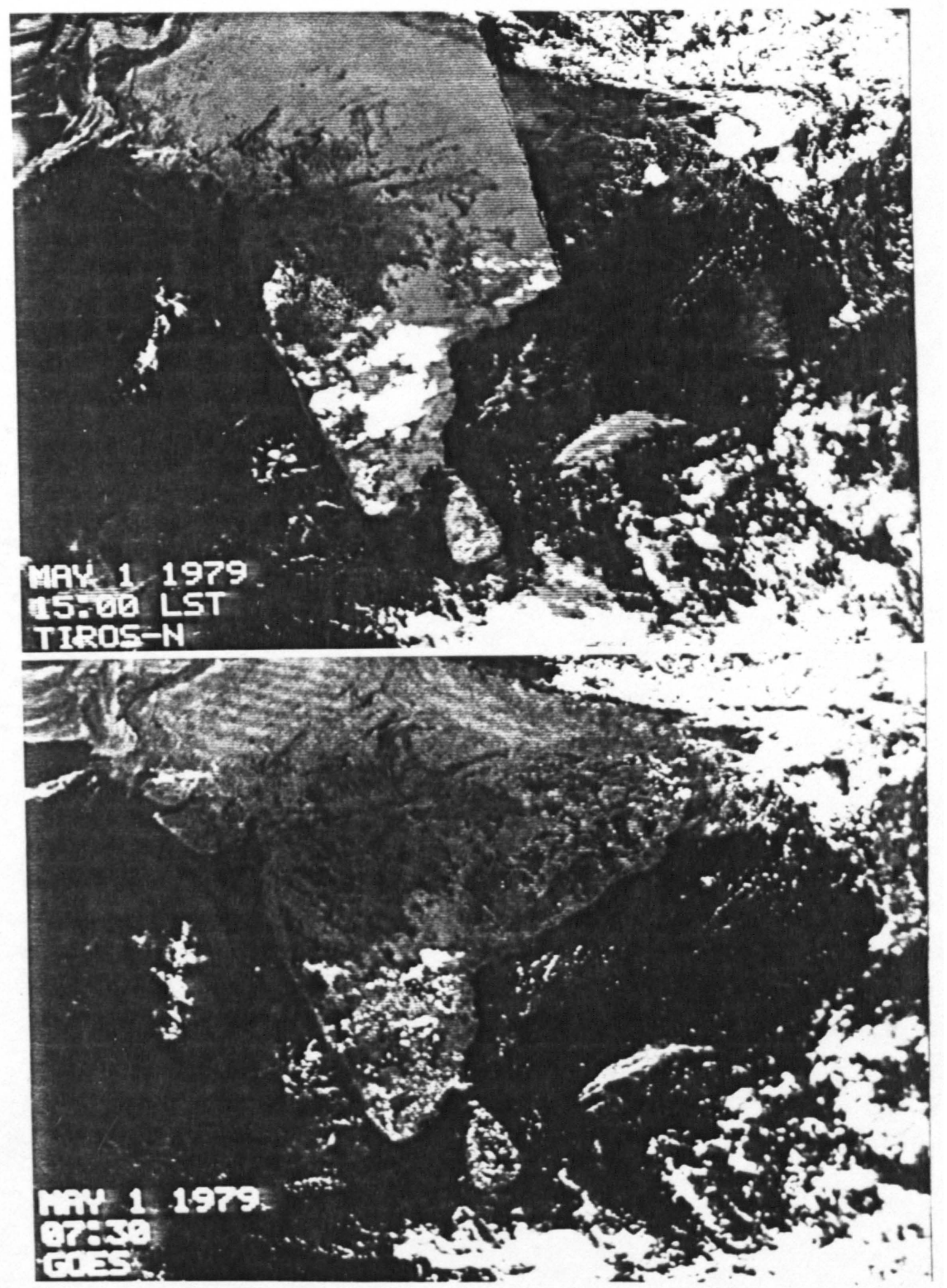

Fig. 4.37. Examples of TIROS-N channel 1 and GOES-1 VIS imagery taken on the same day (May 1, 1979) at different times. The TIROS-N image is at approximately 15:00 LT, whereas the GOES-1 image is at approximately 12:30 LT.

investigations [see Smith and Vonder Haar (1983)]. These data will eventually be used in conjunction with the Tibetan Plateau surface measurement program.

4.8 Summary

A surface energy budget monitoring program carried out in remote desert and mountain environments has been described. This program has been designed to characterize the surface heat exchange process in lowland and highland deserts known to interact with large-scale monsoon systems. In order to implement the surface measurement program various surface energy budget systems have been developed and tested. The results of these tests demonstrate that the systems are capable of returning quantitative and detailed measurements of the surface energy exchange process. These systems have proved dependable, relatively maintenance free, and their automated microprocessing capability have eliminated much of the lag time between observation and analysis due to carrying out most of the calibration and data reduction procedures (statistical processing) in the field. These systems thus have a definite role in future attempts to develop a global land surface climatology. They are relatively inexpensive, easy to operate, and will provide excellent ground truth needed for the development of satellite algorithms and parameterizations.

The systems have been deployed in the deserts of Saudi Arabia and the Colorado Rocky Mountains. A dual-system configuration was recently deployed in the Gobi Desert. In 1985 various of these dual stations will be deployed on the Tibetan Plateau. The results of the Arabian measurement program illustrate not only the daily and diurnal processes that characterize the desert interior, they also illustrate some unique

radiative features characteristic of excessively dry desert regions and have provided critical surface boundary information needed in the description and understanding of the Arabian Desert heat low.

The tests at Pingree Park have demonstrated the feasibility of using less expensive, but maintenance free sensors for monitoring components of the PBL turbulent heat exchange process. Discussion has been provided of a four-way approach for calculating the sensible and latent heat exchange terms and how the 'Radiation' and 'Tower' Stations used in tandem offer a multimode solution to estimating the critically important surface energy exchange terms. Plans to deploy various dual-station configurations on the Tibetan Plateau in 1985 have been provided. Some very preliminary results of the 1984 Gobi Desert experiment have been presented. Explanations of how the surface energy budget stations can be used in conjunction with satellite data to complete the specification of the external boundary conditions, essential in any thorough treatment of atmospheric energetics, have been given. In this context various examples and approaches of how to implement this methodology for both the Arabian Desert and the Tibetan Plateau have been provided.

5.0 THE STRUCTURE AND ROLE OF THE ARABIAN HEAT LOW

The Arabian heat low is the dominant summertime feature of the southern Arabian Peninsula and yet it has remained an allusive feature in the overall make up of the Southwest Monsoon system which controls the summertime weather patterns over the South Asian and Arabian sub-continent. This is not without its reasons. The southern Rub-Al-Khali Desert of the Arabian Peninsula (the British referred to this region as the Empty Quarter) is one of the foremost data void regions of the world and as a result, little has been documented concerning the specific nature and role of the heat low itself; see Holm (1960) for a geomorphological survey. In addition, there has been a historical tendency to overlook the individuality of heat lows; climatologists are prone to bunch them together with the implication that the properties of one would characterize the properties of others. Thus, there has not been a thorough attempt to distinguish the characteristics of heat lows from one another. As a result, the southwest U.S. heat low, the belt of heat lows throughout North Africa, Arabia, Iraq and Pakistan, and the Australian heat low are often viewed as a coherent chain of sub-tropical desert hot spots. It appears, however, that nothing could be further from the truth. The Arabian Peninsula supports a well defined sub-tropical heat low that reveals its own unique features and most likely plays a role within the general circulation unlike any other heat low system.

5.1 Background

In Charney's now classic 1975 paper on Sahelian desertification and drought, the underlying dynamical forcing of desert maintenance was ultimately due to the pre-supposed radiative deficit characteristics of the Sahara and Arabian deserts. In his study, Nimbus-3 satellite observations were presented in support of this theory. By assuming radiative deficit conditions over a desert region, first order equilibrium theory would require a transport of heat into the region. This can be accomplished by vertical subsidence arising from large scale meridional overturning (e.g. a Hadley cell circulation), or by a variety of divergent north-south or east-west monsoonal circulations. In the course of Charney's investigation, the heat flow required to balance the radiative deficit was increased synthetically by enhancing the surface albedo -- this increase was presumably related to overgrazing and destruction of the vegatative ground cover in the Sahel itself; see Wade (1974). Since the increased subsidence would lead to increased drying (i.e. reduction in rainfall), the response to an increase in albedo would serve to accelerate the destruction of vegetation, thus leading to a metastable or possibly unstable desertification mechanism (positive feedback). The essence of this theory, which was first proposed by Otterman (1974), has been supported by the model experiments of Berkofsky (1976) although a critical assumption in his model physics tied vertical velocity directly to the net radiation term, via the albedo modulation, thus imposing a self-supporting mechanism for testing the role of albedo on the subsidence field itself.

The findings of the present investigation are somewhat at odds with the Charney (1975) results. This would not be the first time that these

results have been questioned. In a follow-up study by Charney, et al. (1977), it was shown how a surface evapo-transpiration mechanism could compete or even dominate the albedo effect in terms of controlling rainfall. This result has been expanded upon by Leslie (1980) in an investigation of the Australian heat low. In the later study it was shown that a desert circulation is poorly simulated without a fairly careful treatment of the surface energy budget (i.e. radiative versus sensible heat exchange). This investigation considers the importance of resolving surface energy budget processes.

The results presented here in regards to the Arabian heat low demonstrate that one of the classic underpinnings in describing desert systems may be fallacious, i.e. they are not necessarily radiatively deficit. Secondly, although deserts may be maintained as relative energy sinks they can maintain themselves as absolute energy sources, thus challenging the concept that the mean Hadley cell alone serves as an equilibrium mechanism for the whole belt of sub-tropical desert heat lows. The results of the present analysis indicate that the Arabian heat low is basicaly radiatively neutral or even slightly positive at the upper boundary and that the lower tropospheric layers are energetically surplus due to a combination of sensible heating, dry convection, and enhanced shortwave absorption into a remarkably deep aerosol laden mixed layer.

If these findings are correct, the role of the Arabian desert as well as the roles of the eastern Sahara, the Somali-Chalbi, the Pakistan Rajputann-Great Indian (Thar or West Rajastan), and Iranian deserts may have to be re-evaluated insofar as their influence on the large scale Southwest-East Asian Monsoon System. If deserts can, in fact, be

maintained as absolute energy source regions, their boundary effects on monsoon circulations would be in stark contrast to their once supposed effects as energy sink regions. Since these great deserts serve as a circumscribing arc to the Southwest Monsoon system, it stands to reason that energy exchange between the oceanic-Indian sub-continent regions and the northwest desert regions is a critical factor in determining monsoon onset, maintenance and intensity.

In the following sections the energetics of the Arabian heat low are discussed with principal focus on radiative processes. Section 5.2 describes the basic experimental design and the relevant data sets. Section 5.3 discusses specific features of the heat low and its vertical structure. Section 5.4 provides discussion on the possible role of the heat low as an embedded feature of the Southwest Monsoon.

5.2 Design of the Experiment

The first in-depth investigation of the Arabian heat low was provided by the Saudi Arabian Phase of the 1979 Summer Monsoon Experiment (SMONEX). Prior to that time the Arabian heat low had been characterized as a conventional desert heat low embedded in the belt of sub-tropical heat lows extending from the west African Sahara through Libya, Egypt, the Arabian peninsula and on into the deserts of Iran, Pakistan and India; see Ramage (1966, 1971). The Arabian heat low had never been particularly noted for any special characteristics and due to its being situated in one of the more notable data void regions of the world, it had never been given the careful scrutiny it would otherwise deserve; see Pedgley (1974). One obtains an appreciation for the lack of information available on the great Arabian desert by a simple glance at one of the more recent compilations of climatic data concerning the

Arabian peninsula, such as that of Takahashi and Arakawa (1981). This collection of climate statistics does not include any reports on the entire Empty Quarter - most of the peninsula data is coastal with large gaps along the coasts and within the northern and central interiors. Thus the 1979 experiments represented a unique first step in direct examination of the atmosphere over the Rub-al-Khali desert.

5.2.1 Data Sources

The principal data sets used in this investigation have been derived from three sources: 1) the experimental and operational weather satellite network deployed in time for the 1979 First GARP Global Experiment (FGGE); 2) the NASA Convair-990 aircraft missions flown to support the pre-monsoon Saudi Arabian Phase of the 1979 SMONEX; and 3) a specialized surface energy budget station I deployed in the Saudi Arabian Empty Quarter during the month of June, 1981. This observational approach employs platforms above the atmosphere (satellite), within the atmosphere (aircraft), and below the atmosphere (surface station) thus enabling a specification of both atmospheric boundary conditions and a measure of the vertical structure. The measurement strategy is illustrated schematically in Fig. 5.1.

The satellite data sets have been derived from both the polar-orbiting and geosynchronous weather satellites which provided coverage over the Southwest Monsoon region during 1979 (TIROS-N and GOES-1) as well as the Nimbus-7 experimental satellite. This later platform played an important supporting role in the FGGE based on the variety of specialized remote sensing instruments which it carried, designed to retrieve estimates of the radiation budget, cloudiness and water vapor fields, oceangraphic parameters, stratospheric structure and aerosol

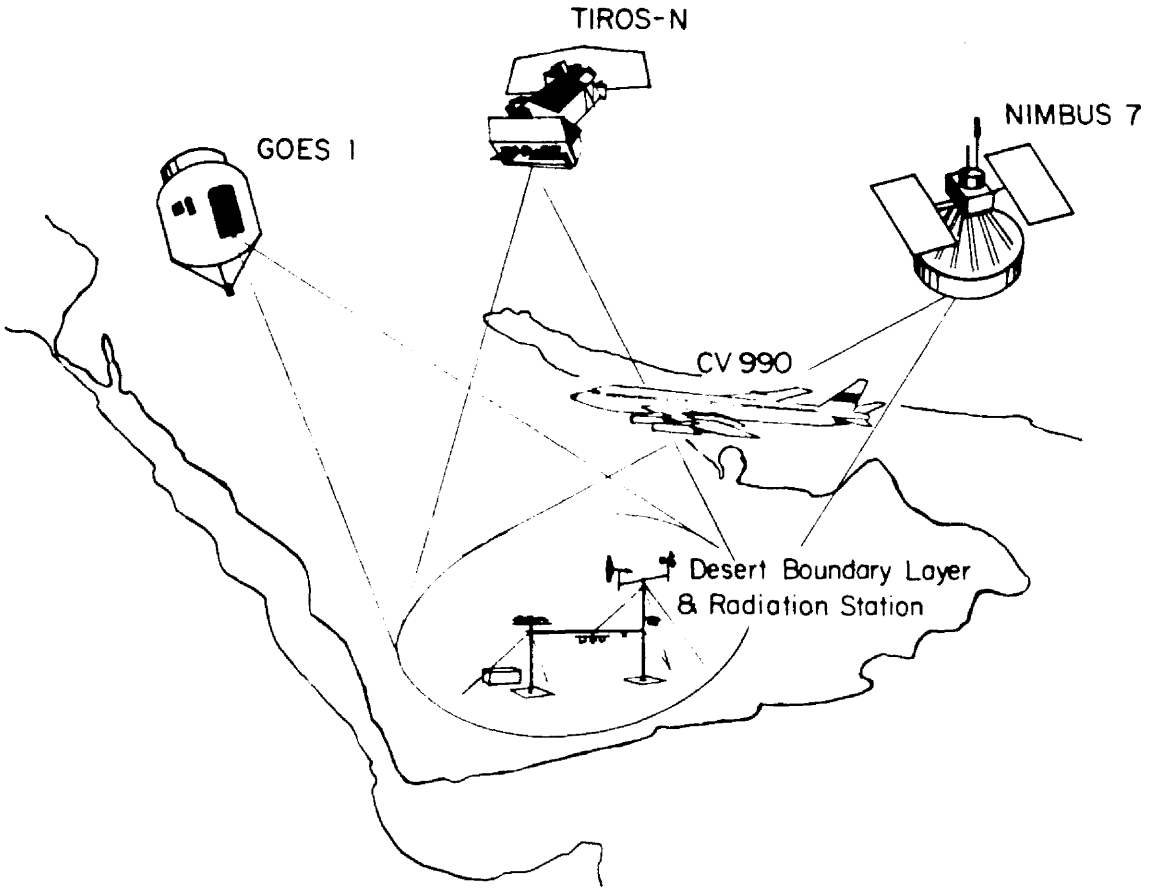

Fig. 5.1. Schematic illustration of the observational platform network.

concentrations, ozone distributions and variations in the cryosphere; see NASA (1978). For this investigation, measurements from the Narrow-Field-of-View (NFOV) radiometers on the Earth Radiation Budget (ERB) instrument have been employed to examine the time history of the top of atmosphere radiation budget over the heat low region. The weather satellite data sets have been described by Smith and Graffy (1982), Smith and Vonder Haar (1983) and reviewed in Chapter 3. A description of the methodology used to transform the digital VIS-IR imagery obtained from the weather satellite imaging radiometers into radiation budget quantities was discussed in Chapter 2.

The aircraft data relevant to this study were derived from a sequence of five radiation survey and dropsonde missions flown out of the Arabian coastal city of Dhahran, located on the west side of the Arabian Gulf. These flights have been described by Bolhofer, et al. (1981) and Smith, et al. (1980). All of the excursions were designed to collect measurements on the radiative, thermodynamic, and dynamic structure of the heat low, based on upward and downward mounted flux radiometers (Epply pyranometers and pyrgeometers) and a dropsonde release system. The five flights took place on May 6, 9, 10, 12 and 14, 1979. The first and last of these flights included legs over the Arabian Sea leaving and returning to the peninsula on the southern Oman coast. These two flights were designed to recover additional information on the differential heating differences over desert and ocean. The middle three flights were strictly confined to the middle and northeastern portions of the Arabian empty quarter. All of these three flights, as well as the last flight, included stepwise descents close to the desert surface enabling a first order measure of the lower

atmosphere vertical profile of radiative flux exchange. The mission maps provided in Fig. 5.2 illustrate the flight tracks for the missions flown on May 6, 9 and 14.

5.2.2 Description of the Surface Station

As described, the Saudi Arabian Phase of the 1979 SMONEX provided direct aircraft observations within the Empty Quarter and provided the impetus for the compilation of a much more extensive satellite data base. However, the 1979 observational program did not include a surface measurement component. To that end I conducted a small surface observation program within the interior of the Empty Quarter during June, 1981, the month which can be associated with the three critical phases of the 1979 Southwest Monsoon, the pre-monsoon phase, monsoon onset phase and post-monsoon onset phase; see Smith, et al. (1982).

The basic objective of the surface program was to obtain a measure of energy exchange directly at the surface boundary within the heat low region. This was accomplished by deploying a specially designed surface energy budget station near the village of Sharouwrah ($17^{o}45'N$; $47^{o}12'E$), a site located in the southwest quadrant of the Empty Quarter region, aproximately 250 km from the coordinate which can be associated with the center of the heat low. This initial observational phase was then augmented in 1982-1983 by the placement of additional stations at the cities of Najran ($17^{o}37'N$; $44^{o}27'E$), Taif ($21^{o}29'N$; $40^{o}32'E$), and Jeddah ($21^{o}30'N$; $39^{o}12'E$). These four sites thus formed a somewhat meandering vector from the excessively dry Empty Quarter interior out to the very moist Red Sea port city of Jeddah. A visible METEOSAT image of the Arabian Peninsula region (kindly provided by G. E. Hunt), seen in Fig. 5.3, contains annotation indicating these four sites. In the following

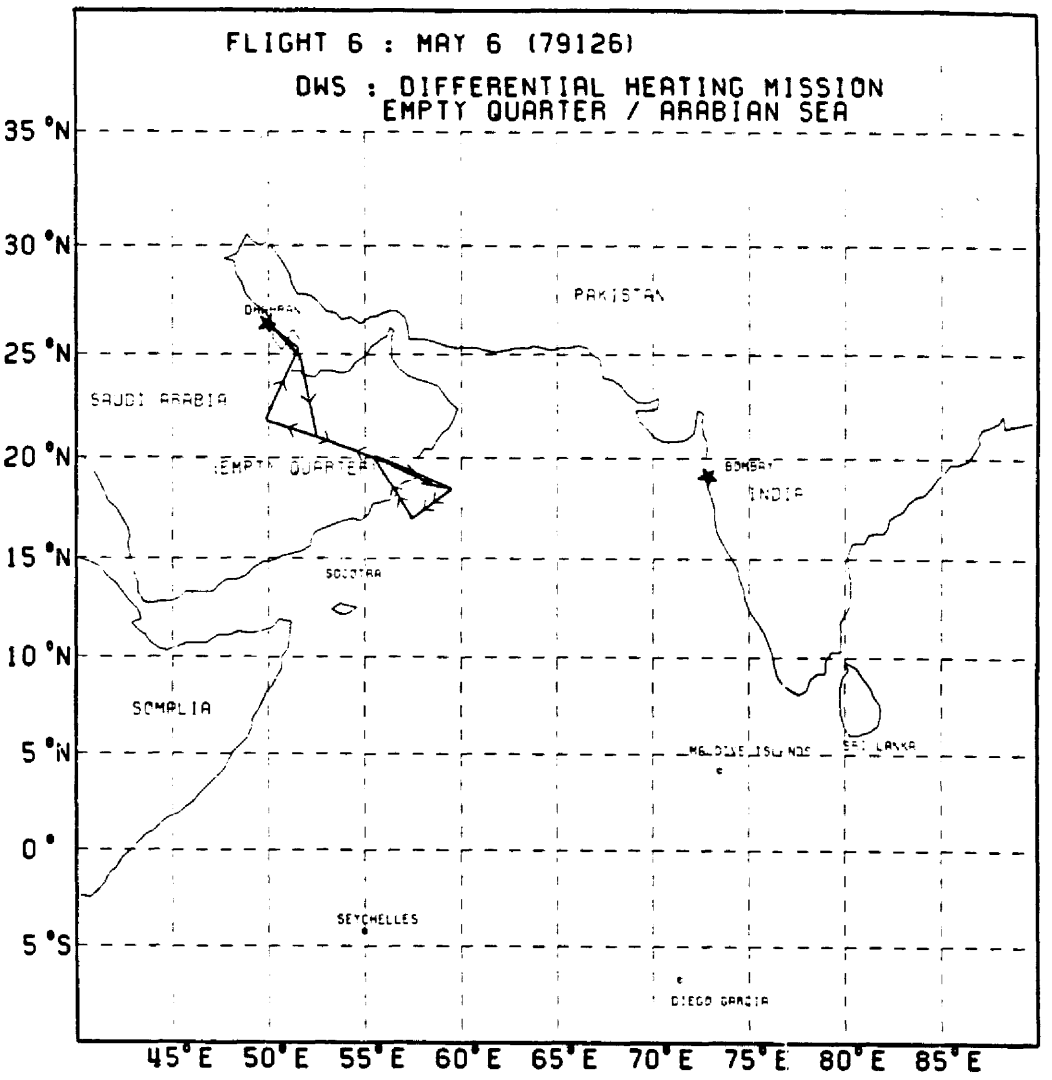

Fig. 5.2a. Mission map of the May 6, 1979 differential heating mission.

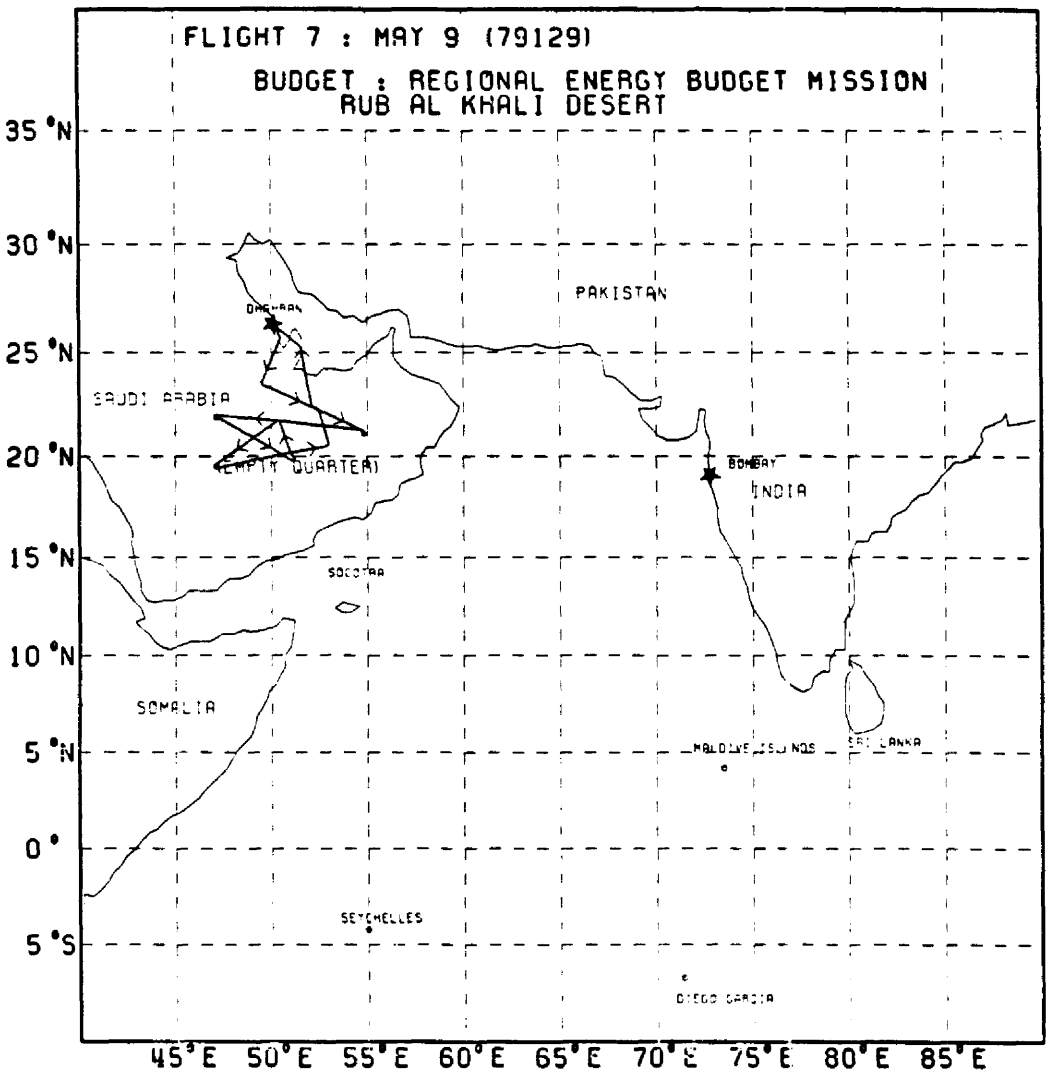

Fig. 5.2b. Same as Fig. 5.2a for the May 9, 1979 regional energy budget mission.

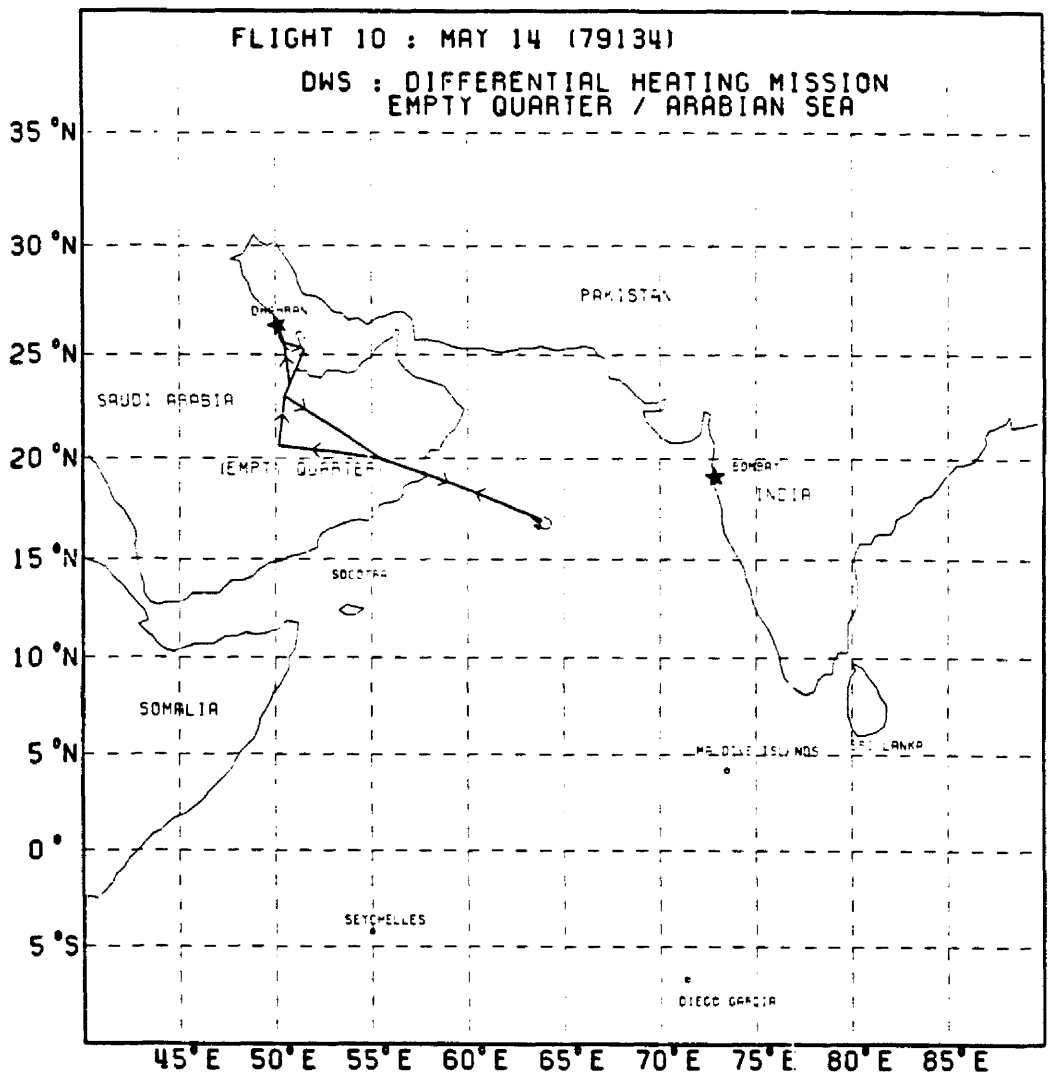

Fig. 5.2c. Same as Fig. 5.2a for the May 14, 1979 differential heating mission.

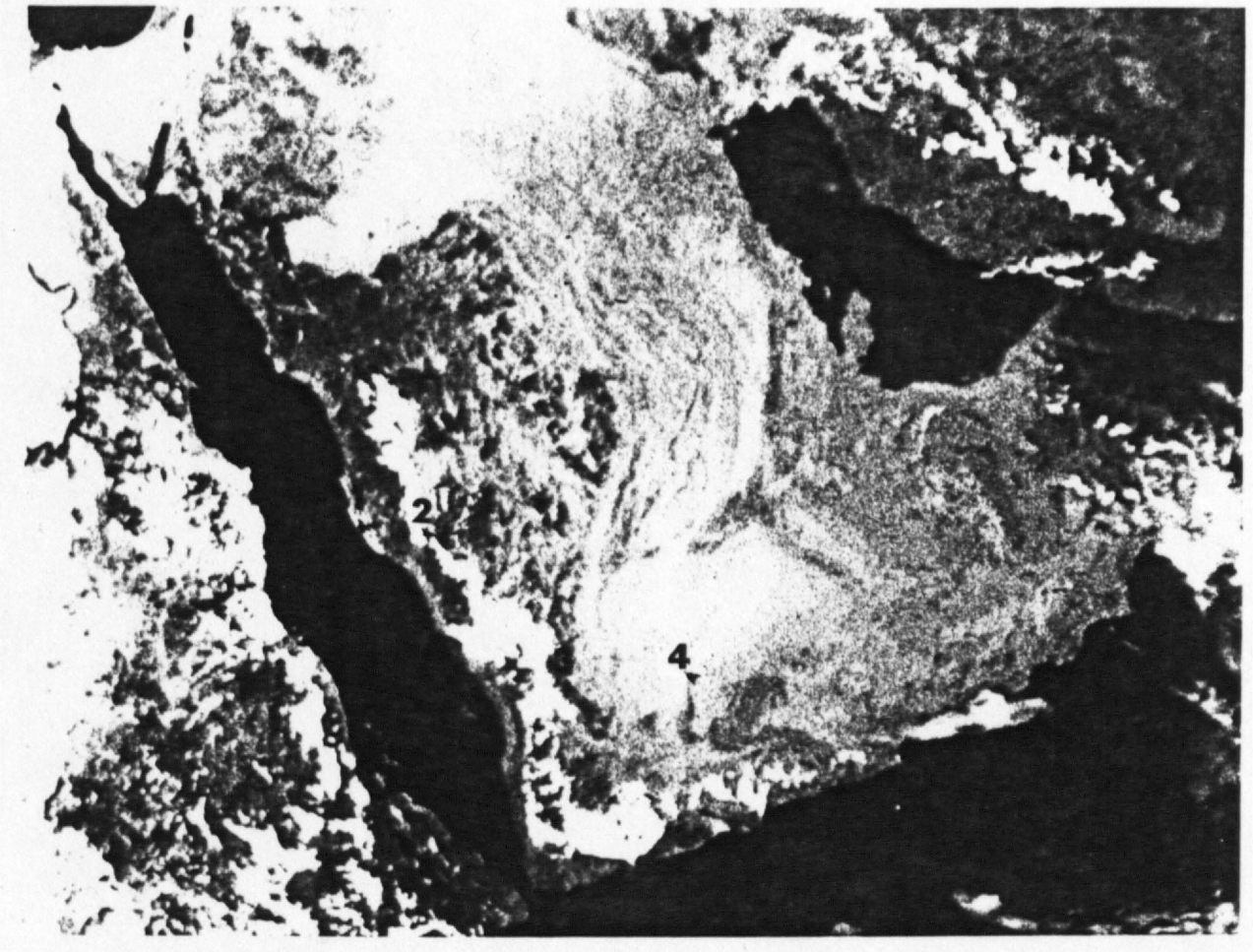

Fig. 5.3. A visible METEOSAT image of the Arabian Peninsula with the four surface measurement sites indicated (1-Jeddah; 2-Taif; 3-Najran; 4-Sharouwrah).

analysis only data from the June, 1981 Sharouwrah site have been incorporated.

The surface station included an assembly of sensors which were used to describe the exchange of shortwave and longwave radiation, the sub-surface thermal storage and the near surface state and wind parameters. Because surface moisture exchange processes are virtually non-existent in this region, precipitation monitoring and soil moisture sensors were not included as part of the system design. The sensor transducers were wired to specialized micro-processor driven data loggers designed by Campbell Scientific Incorporated (CR-21's). A detailed description of the design and deployment of the surface stations was discussed in Chapter 4. A schematic illustration of the surface station deployed at the Sharouwrah site is shown in Fig. 5.4.

Since the surface data incorporated in this investigation were obtained in 1981, in contrast to the satellite and aircraft data which were obtained in 1979, there is a two year difference involved in combining the data sets. This difference, however, is not presumed to obscure the essential energy exchange processes taking place within the heat low. The desert is virtually cloudless during this time of year, the surface is almost totally free of vegetation, and the basic Hadley cell driven subsidence field is fairly rythmic on an annual basis. This suggests that interannual variations at the surface are relatively small. Thus the measured surface properties of 1981 are assumed to be representative of those that would have been found in 1979. Although data set consistency would have been preferred, the nature of observational research in the atmosphere is one of siezing upon targets

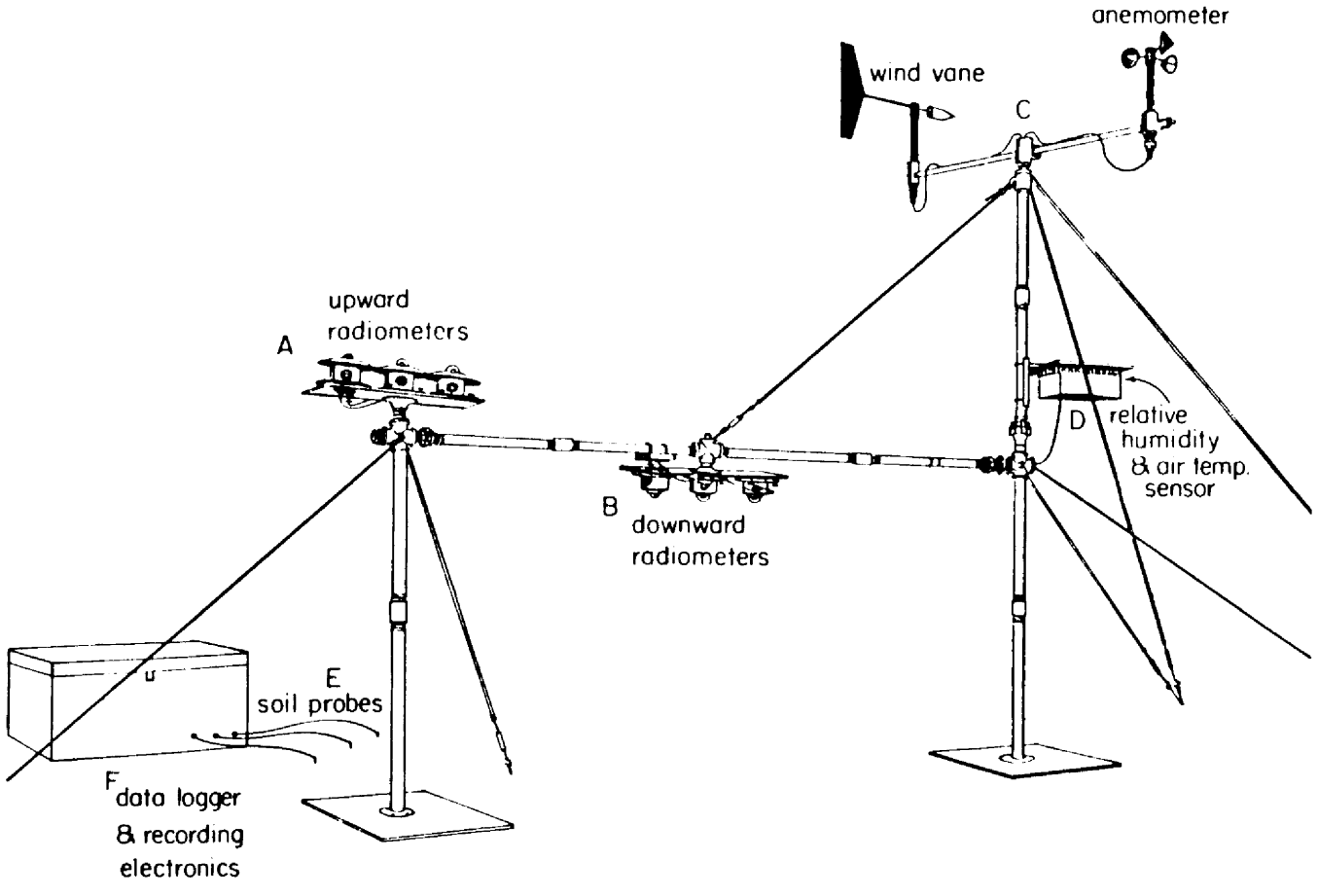

Fig. 5.4. Schematic illustration of the Sharouwrah surface energy budget station.

of opportunity at different times and places and attempting a reasonable synthesis of the various analyses.

5.2.3 Data Applications

The experimental approach employed in this investigation has been based on combining observations from the three platforms (satellite, aircraft, surface) in conjunction with various radiative transfer calculations. These results along with the findings of Ackerman and Cox (1982), hereafter AC-82, and Blake, et al. (1983), hereafter B-83, describe the principal energetics of the heat low. The two later studies have described important features of the heat low; AC-82 examined the role of the desert aerosol on the vertical structure of shortwave heating and its implications; B-83 has provided an in-depth analysis of the heat low thermodynamic structure based on the dropsonde profiles obtained from the Saudi Arabian Phase CV-990 missions.

In this study the surface and aircraft measurements are used both to describe direct radiative properties of the heat low, as well as to describe the initial conditions needed in the modeling of atmospheric transmission and in converting narrow band satellite radiance measurements to broad band flux estimates. Thus the surface and aircraft measurements have had both a direct and an indirect role in describing the heat low. As a result, there is implicit consistency enforced on the top-of-atmosphere radiation budget boundary condition as described by the weather satellite data. As an independent check on the weather satellite estimates, a time series of NFOV Earth Radiation Budget observations, taken from the Nimbus-7 experiment is used to independently assess the upper boundary.

5.3 Energetics of the Arabian Heat Low

The following sub-sections highlight the basic energetics of the Arabian heat low based on the multi-platform measurement system and the investigations of AC-82 and B-83.

5.3.1 Large Scale Fields

A starting point for examining the radiative characteristics of the Arabian heat low comes from an examination of the albedo and temperature isopleths in the context of the larger scale monsoon region. In Fig. 5.5, four 5-day averaged albedo maps are presented. These time intervals correspond to immediately prior to the monsoon onset period of 1979 (June 5-10), during the onset period (June 11-15, June 16-20), and immediately after the monsoon onset period (June 21-25). These maps illustrate instantaneous (noontime) broad band reflectance estimates based on channel 1 from the 4-channel TIROS-N Advanced Very High Resolution Radiometer (AVHRR). Although the original AVHRR satellite (TIROS-N) was placed in a 3:00-15:00 LT sun-synchronous orbit, the reflectances have been adjusted to noontime levels according to a directional reflectance normalization scheme which utilized both Narrow-Field-Of-View (NFOV) and Wide-Field-Of-View (WFOV) broad band reflectance values measured by the Nimbus-7 Earth Radiation Budget (ERB) instrument.

The interesting highlight that can be noted in these isopleth time series is the dominance of three features: first, the Arabian deserts (Rub-al-Khali and Nafud); second, the Tibetan Plateau and its southern flank of the Himalayan range; and third, the monsoon cloud systems first appearing within the Burma monsoon and over the Indian Ocean and Arabian Sea, then the Bay of Bengal, and finally over the Indian sub-continent.

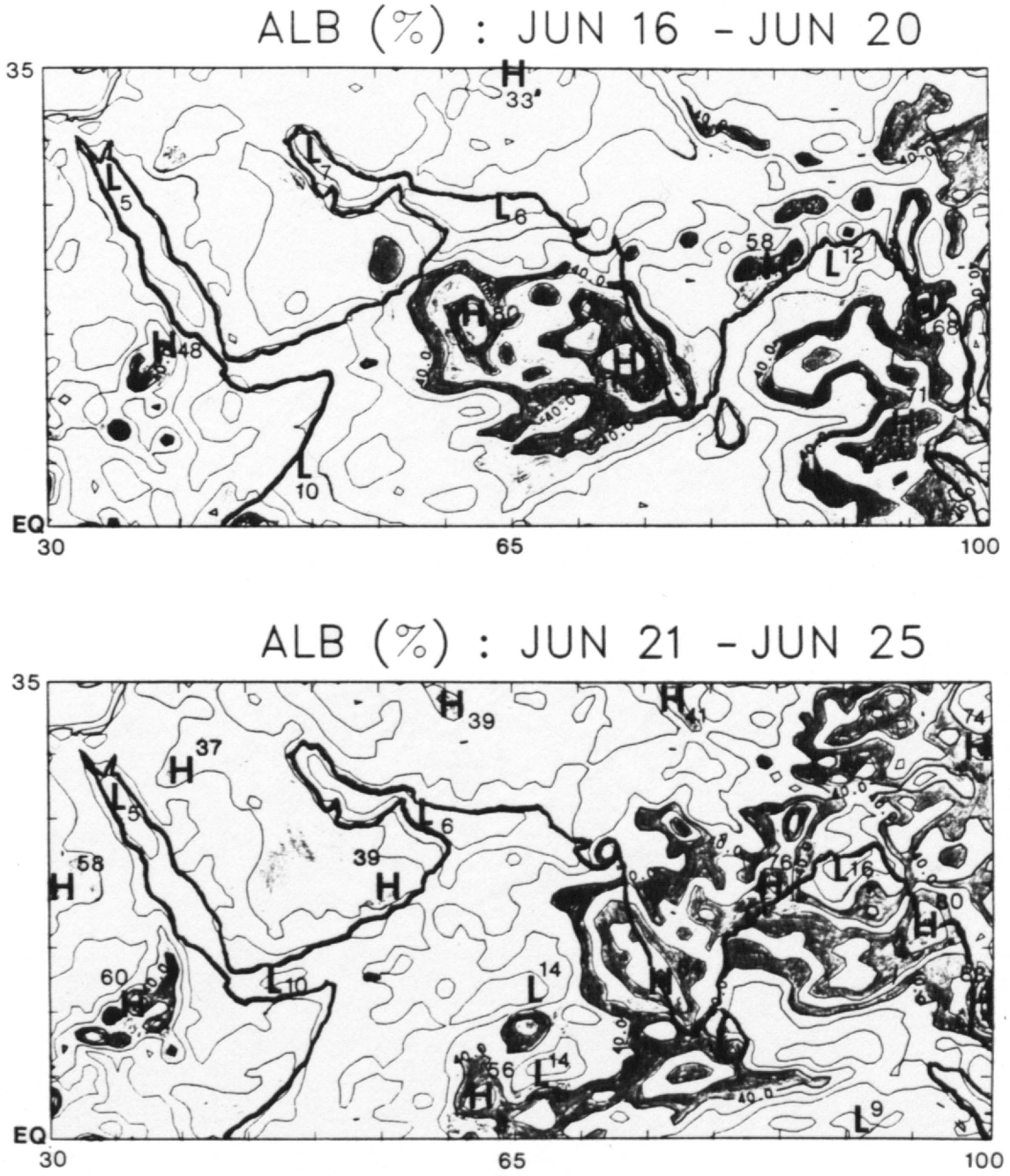

Fig. 5.5a. Five day averaged instantaneous albedo fields (referenced to local noon) over the Southwest Monsoon region during 1979. Top of figure covers the June 6-10 period; bottom of figure covers the June 11-15 period.

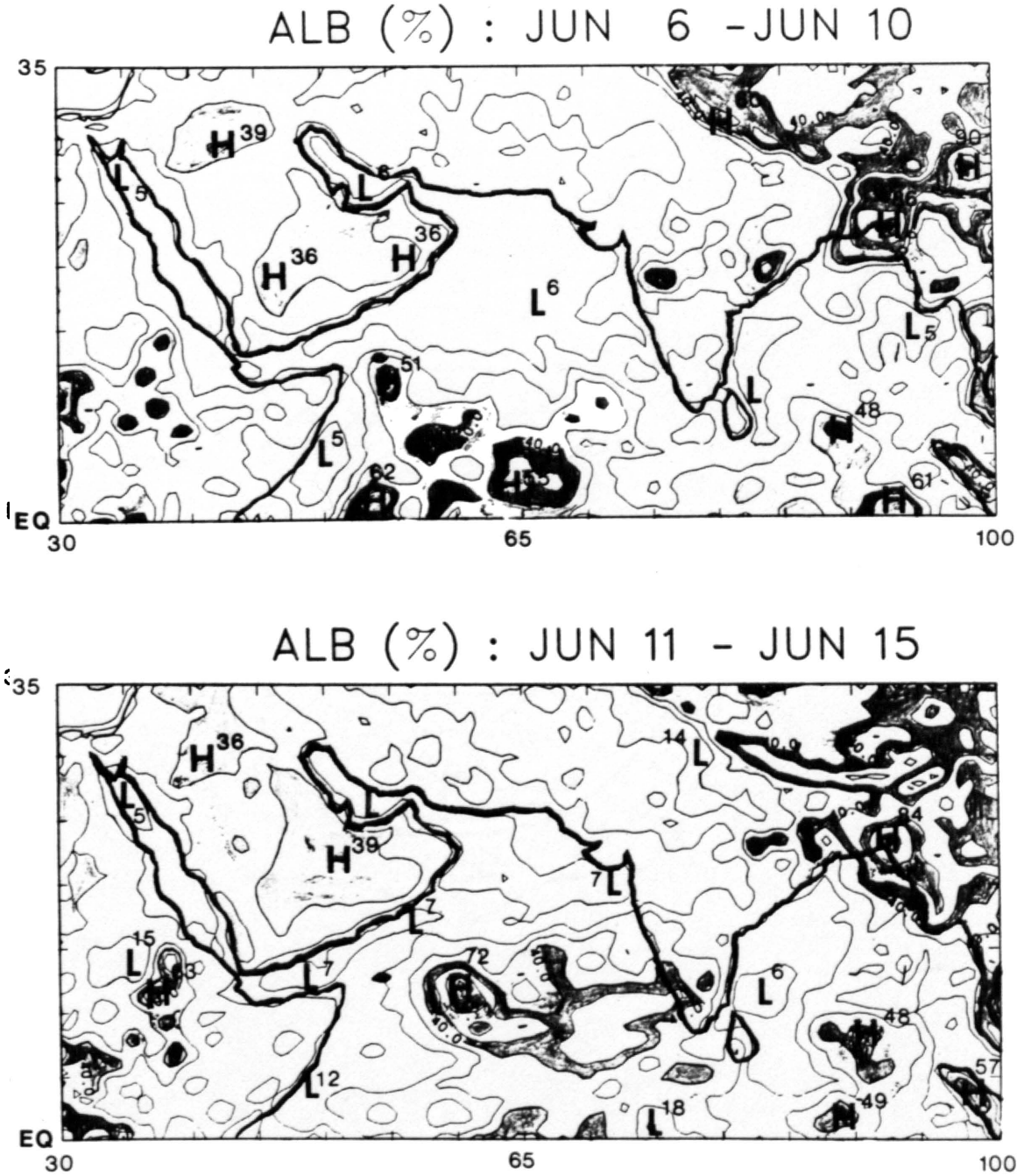

Fig. 5.5b. Same as Fig. 5.5a for the June 16-20 period (top) and June 21-25 period (bottom).

This is one of the peculiar aspects of terrestrial albedo, in that it is a parameter which is highly independent of latitude and elevation. The key difference between the high albedo field over the Arabian Peninsula and those over the Tibetan Plateau region and in conjunction with the monsoon clouds, is that the former is a stationary and relatively consistent feature throughout the course of the monsoon season. On the other hand, the albedo field over the Tibetan Plateau undergoes dramatic changes during the course of the monsoon season, due to partially compensatory processes. During late spring and summer, snow melt particularly on the peaks, tends to reduce albedo whereas cloudiness associated with the monsoon tends to increase albedo (mostly in the eastern plateau region as the western plateau is substantially drier). Finally, the albedo field associated with monsoon cloudiness is mostly non-stationary and tends to be modulated by periodic bursts in the intensity of the monsoon, at various time scales.

The more salient features of the heat low region are better described by the thermal fields. In Fig. 5.6, longwave flux maps derived from TIROS-N AVHRR channel 4 measurements are presented for the same four periods. These maps demonstrate the intense surface heating associated with the heat low; note the dramatic contrast between peninsula fluxes and those throughout the rest of the monsoon region. It is this intense surface heating centered within the Arabian Empty Quarter that leads to surface pressure low required to force the weak thermal surface cyclone associated with the heat low. The surface pressure field illustrated in Fig. 5.7 [(from van de Boogaard (1977)] is used to illustrate the mass response to this heating. Fig. 5.8, from Ramage and Raman (1972), illustrates the idealized low level daytime

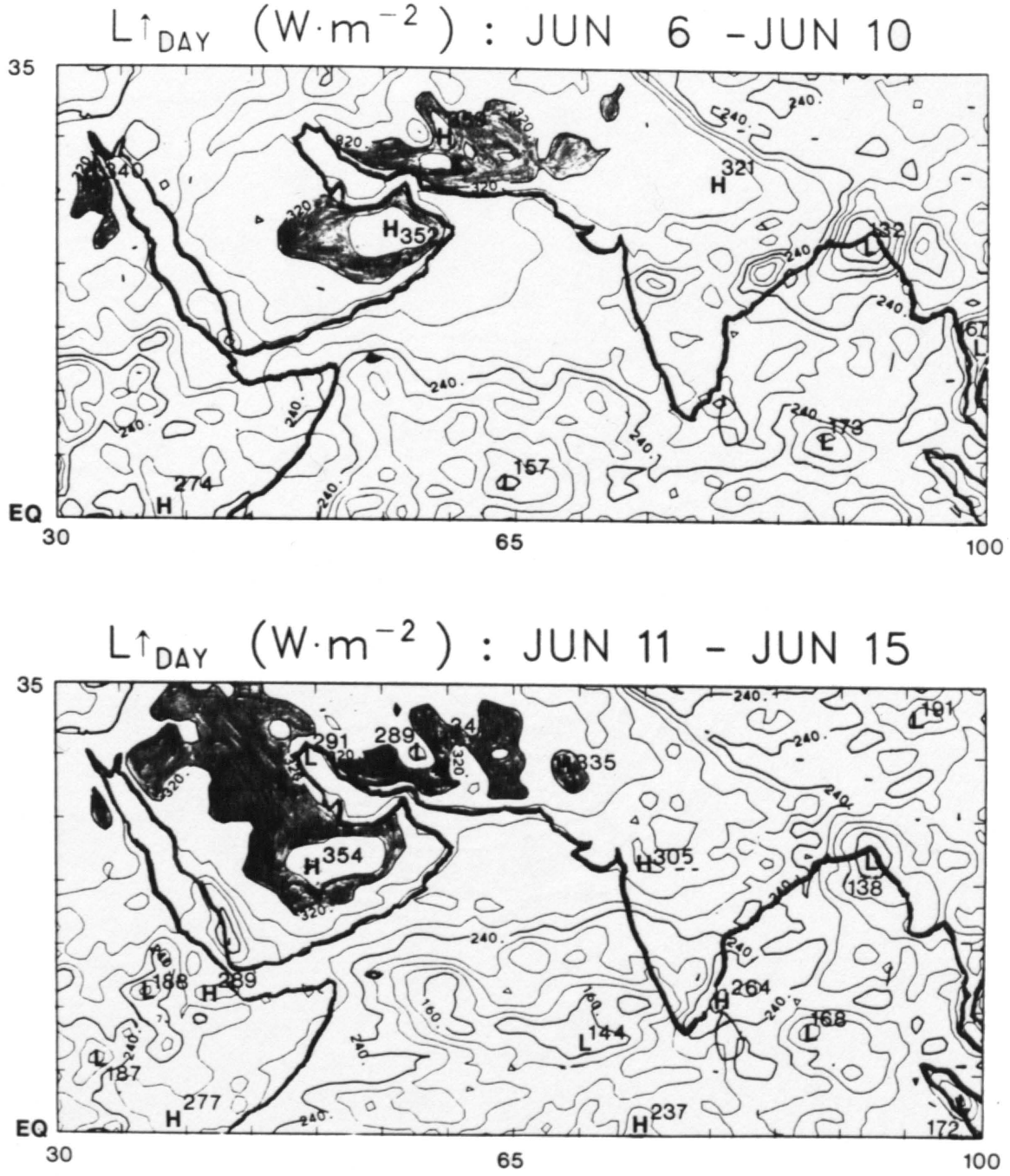

Fig. 5.6a. Five day averaged emitted longwave flux fields (referenced to local noon) over the Southwest Monsoon region during 1979. Top of figure covers the June 6-10 period; bottom of figure covers the June 11-15 period.

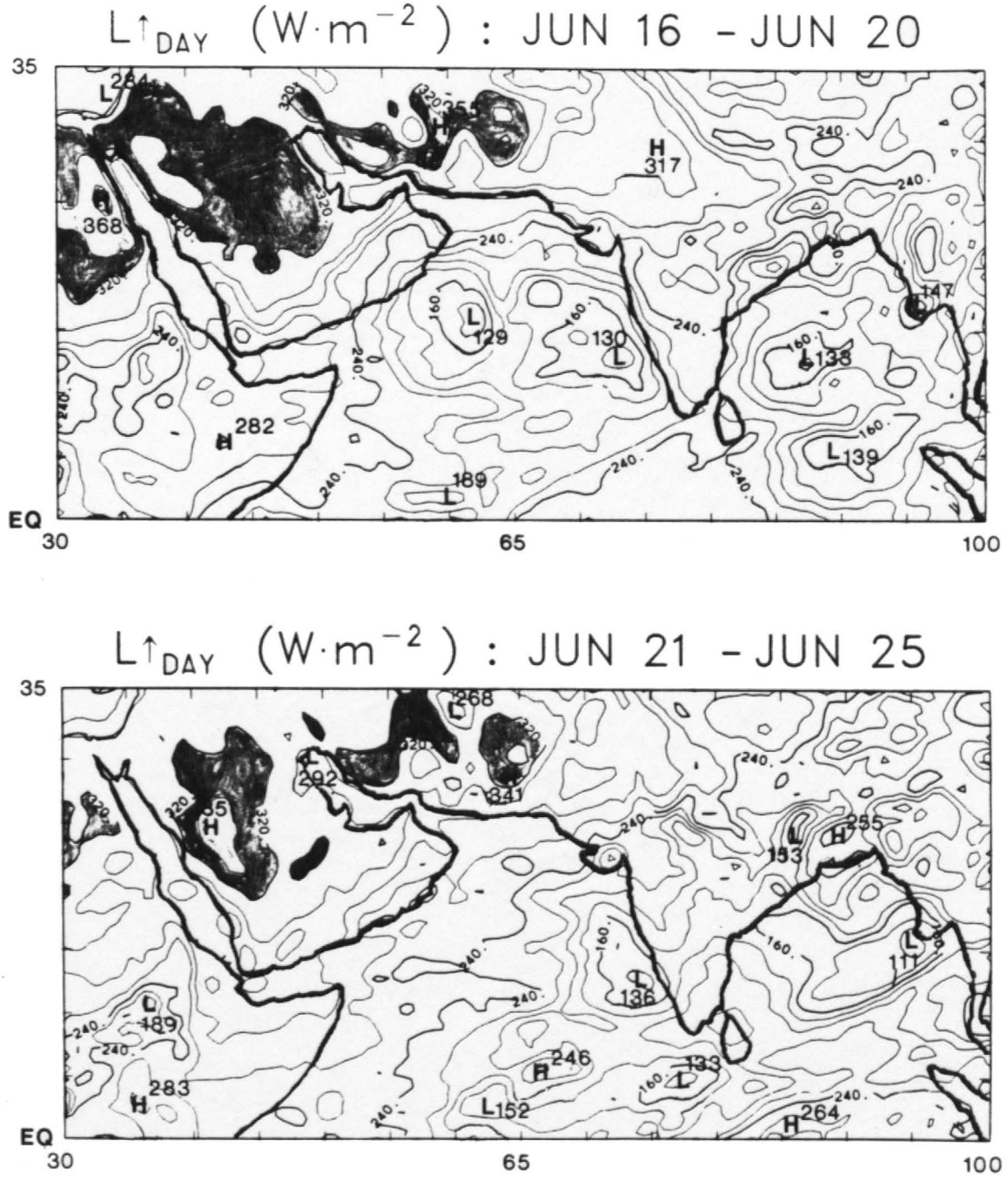

Fig. 5.6b. Same as Fig. 5.6a for the June 16-20 period (top) and June 21-25 period (bottom).

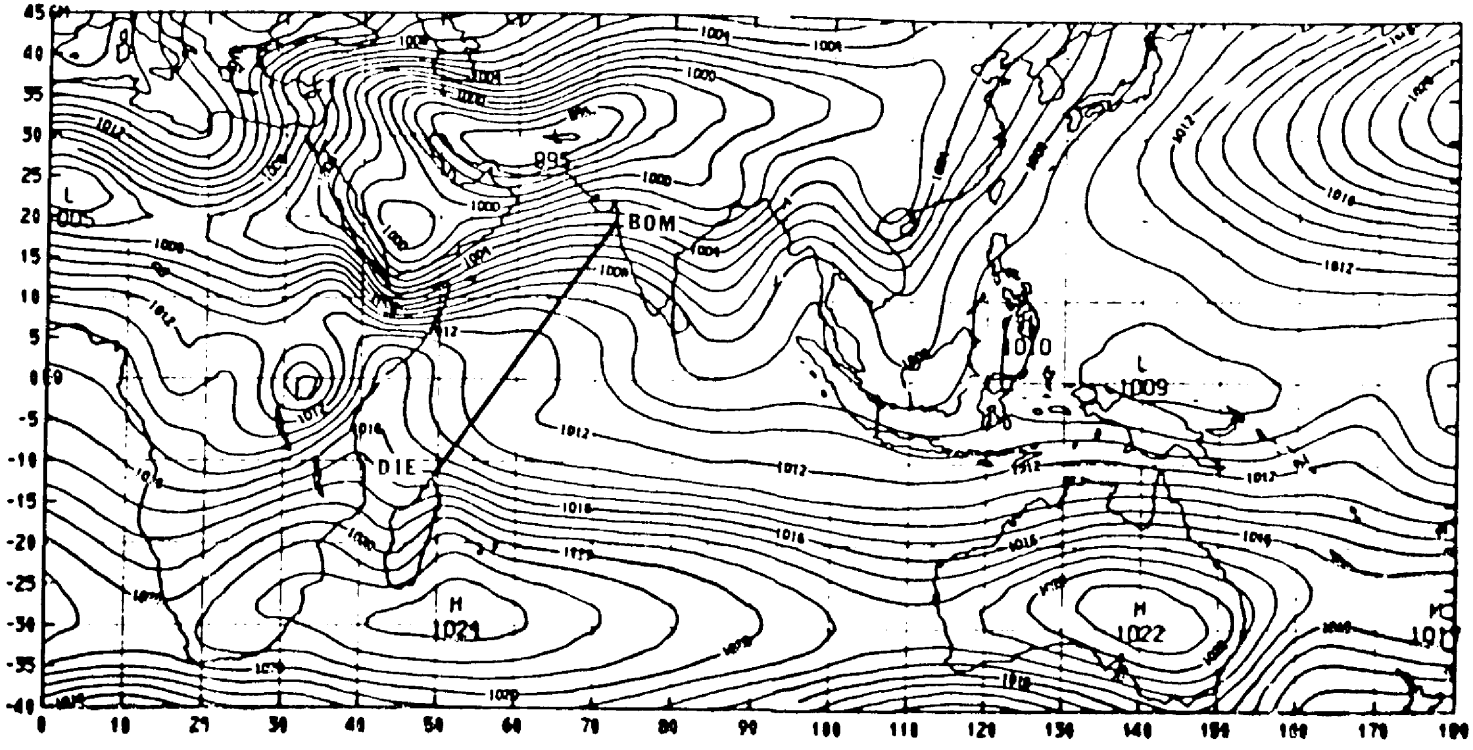

Fig. 5.7. Surface pressure field representative of mean July conditions over Southwest Monsoon region [from van de Boogaard (1977)].

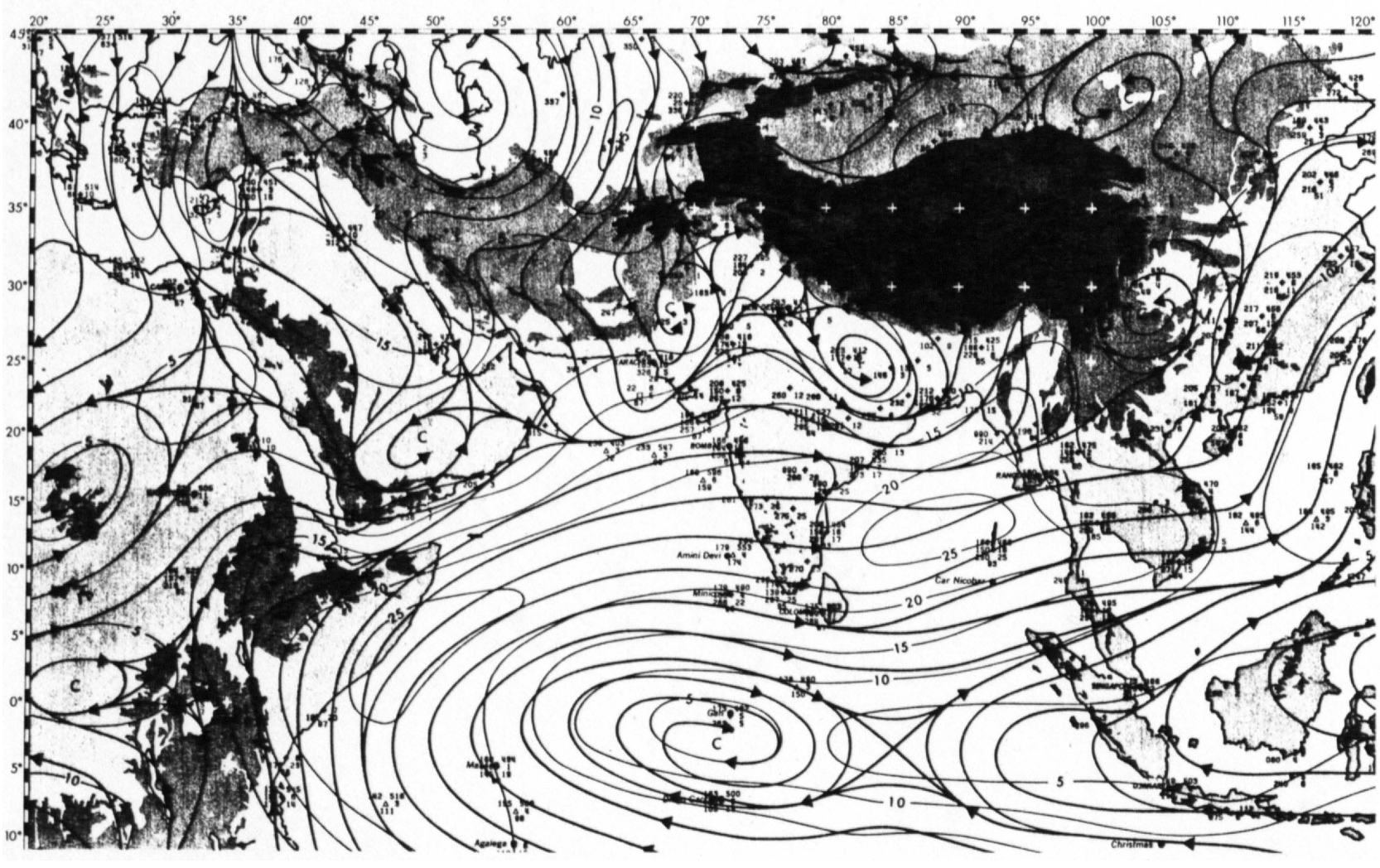

Fig. 5.8. Streamline field at 850 mb representative of mean July conditions over Southwest Monsoon region [from Ramage and Raman (1972)].

circulation pattern associated with the heat low. Although this analysis was based more on continuity estimates rather than actual observations (Raman, personnel communication), it nevertheless shows the characteristic mean low level circulation associated with a shallow heat low. A further discussion of the daytime surface cyclone can be found in B-83.

Finally, Fig. 5.9 illustrates the sequence of four top-of-atmosphere net radiation maps corresponding to local noontime exchange. In these figures the low level contours of total radiative exchange are highlighted. We see again the three dominant radiative features of the monsoon system, the Arabian Peninsula, the Tibetan Plateau and the monsoon cloud systems. In addition, the semi-arid east African sector and the extensive Maximum Cloud Zone (MCZ) associated with the ITCZ illustrate reduced values of net flux. Note that an absolute deficit region is found over the Tibetan Plateau - the reader is reminded that these are isopleths of instantaneous noontime net flux exchange at the atmosphere's upper boundary, not daily averaged values. The rather interesting aspect of these maps is that they illustrate how in the early stages of monsoon onset, the Indian sub-continent region is virtually surrounded by relative minimums in terms of net radiation, suggesting in a very simple sense that the latent heating of monsoon rainfall is in high demand from all quarters.

5.3.2 Vertical Structure of the Heat Low

The vertical structure of the Arabian heat low has yet to be completely documented throughout the course of its development and lifetime. However, dropsonde measurements from the SMONEX Empty Quarter missions describe quite well the mid-May situation. The dominant

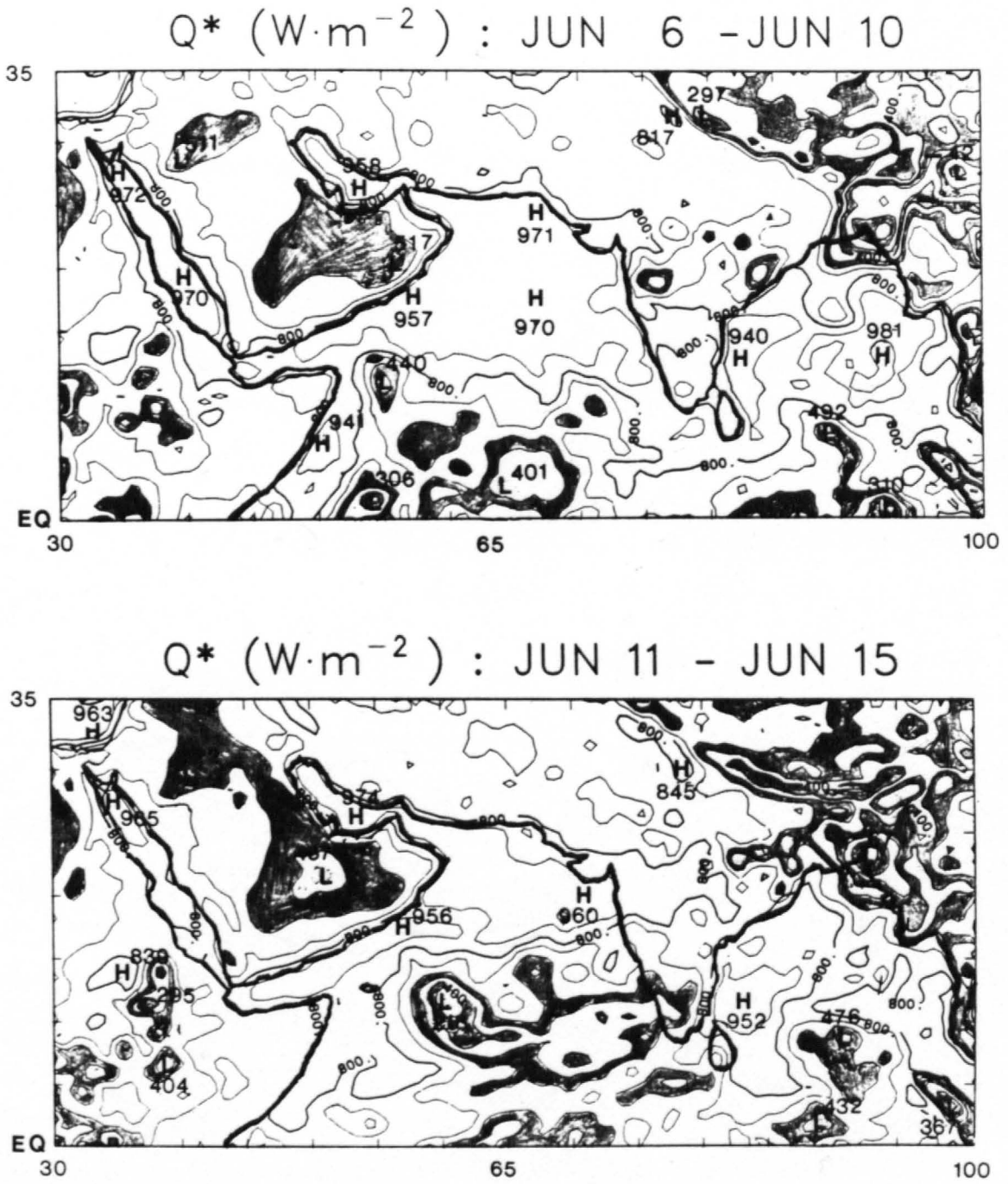

Fig. 5.9a. Five day averaged top-of-atmosphere instantaneous net net radiation fields (referenced to local noon) over the Southwest Monsoon region during 1979. Top of figure covers the June 6-10 period; bottom of figure covers the June 11-15 period.

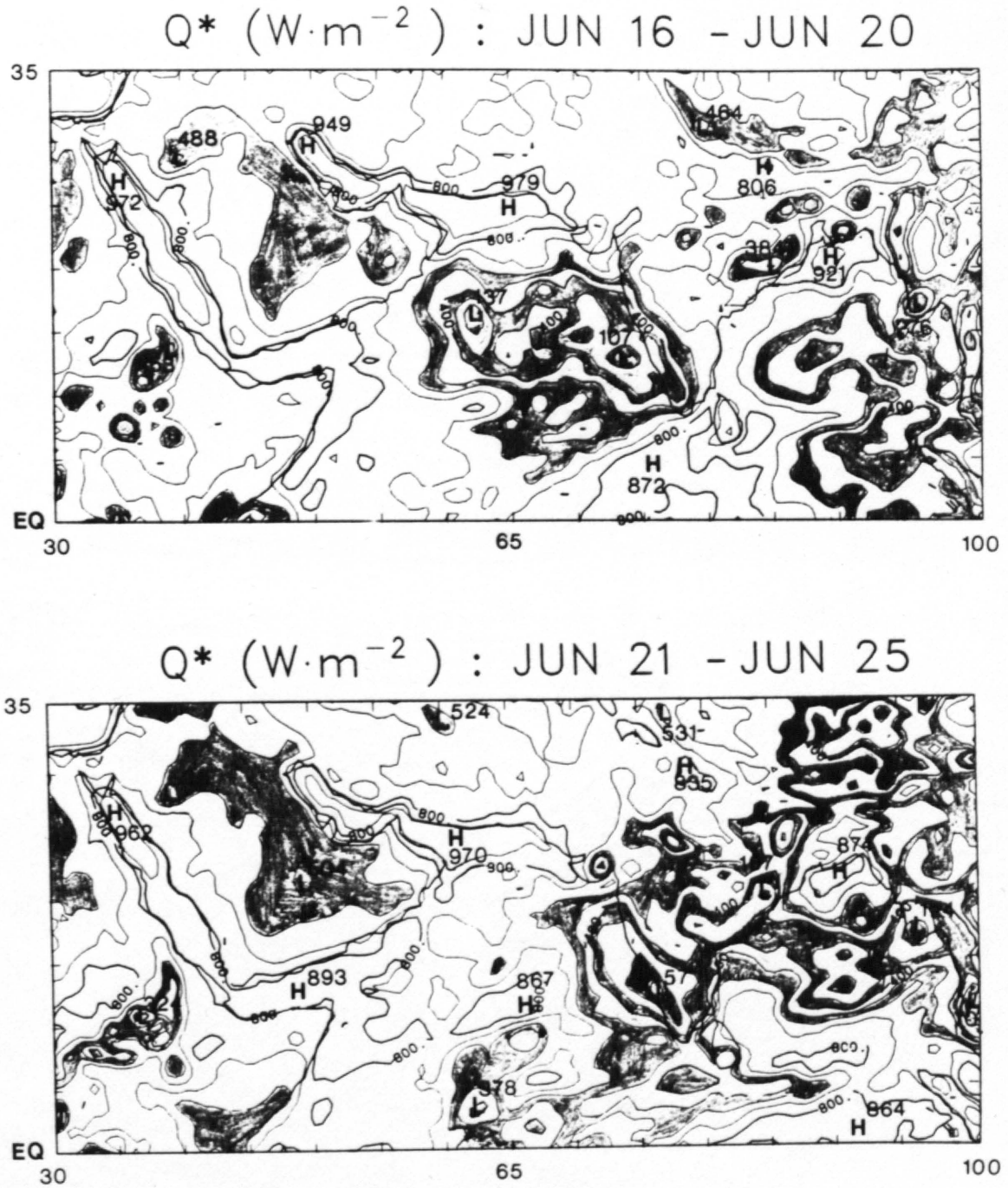

Fig. 5.9b: Same as Fig. 5.9a for the June 16-20 period (top) and the June 21-25 period (bottom).

feature is the remarkably deep boundary layer associated with the heat low region. Fig. 5.10 illustrates average potential temperature and moisture profiles for the three energy budget missions on May 9, 10 and 12, 1979 (the profile data were kindly provided by S. A. Ackerman). Note the top of the well mixed layer is not reached until 550 mb. Above 550 mb, θ increases rapidly until 475 mb at which point the rate of increase drops off to approximately $0.07^{o}C \cdot mb^{-1}$.

The vertical circulation field associated with the heat low was first reported by B-83 based on kinematic analyses of the May 9, 10 and 12 missions. In Fig. 5.11 the omega profiles according to the B-83 investigation are plotted corresponding to daytime conditions and nighttime conditions. The daytime profile is based on an average of May 9 and 10 data; the nighttime profile is based on the very early morning flight of May 12. Note the daytime profile indicates a shallow upward motion field capped by a subsidence field peaking at approximately 775 mb. This represents the surface cyclone feature which Ramage and Raman (1972) earlier postulated from the synoptic scale data. At night, surface heating is so weakened by the very efficient longwave radiative cooling that the surface cyclone is dissipated. The subsidence field which is at its maximum value at 550 mb, then extends to the surface.

5.3.3 Radiative Properties of the Desert Surface

The surface pyranometer and pyrgeometer measurements of the June, 1981 period illustrate one of the almost unique characteristics of deserts, that is their almost perfectly rythmic diurnal modulation. The upward and downward visible (VIS: 0.2-0.7 μm), near-infrared (NIR: 0.7-4.0 μm), and total solar fluxes (K:0.2-4.0 μm) for June 2-28 are seen in Fig. 5.12. Figure 5.13 provides the upward and downward surface

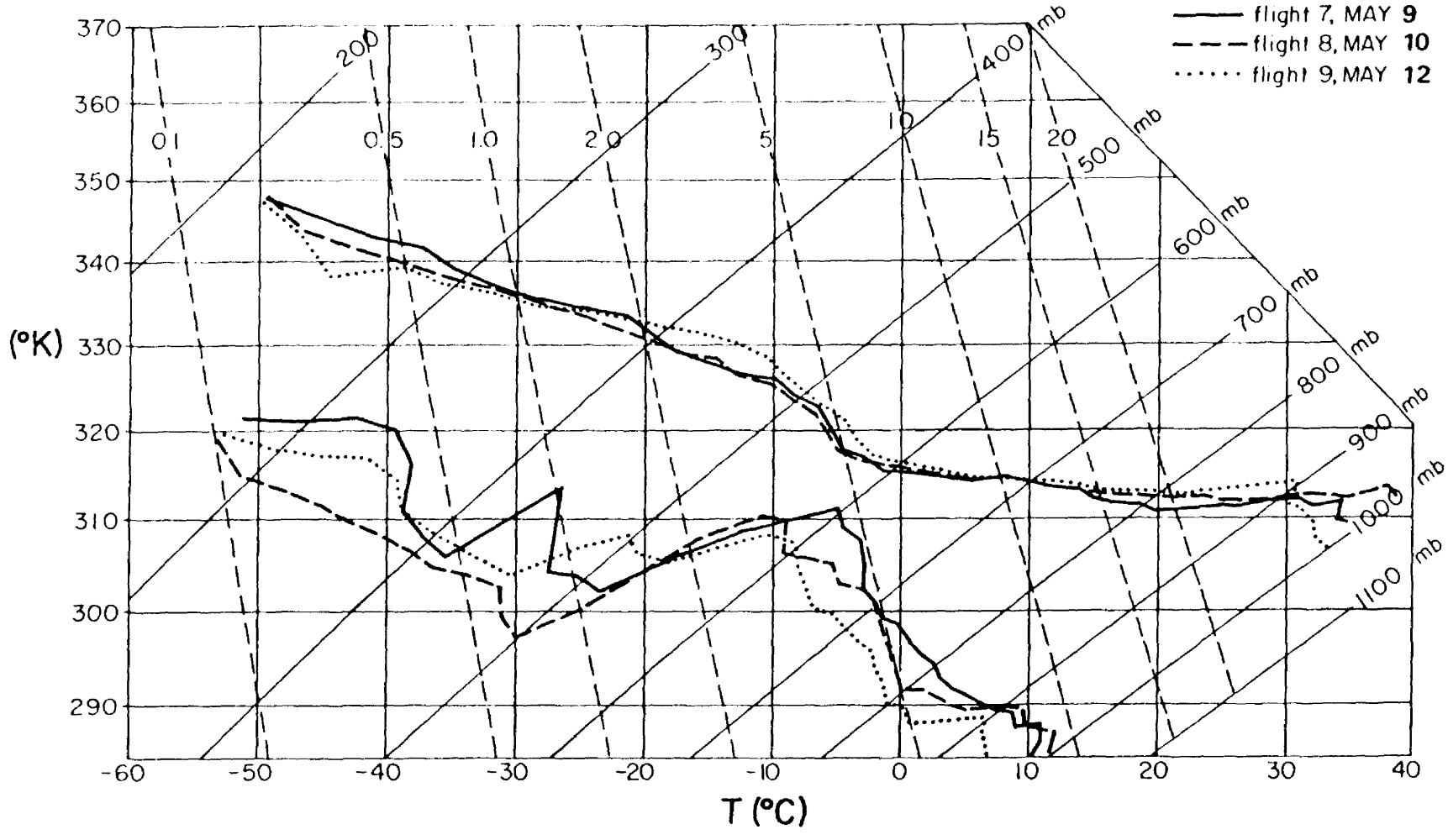

Fig. 5.10. Thermodynamic structure of the Arabian heat low based on the May 9, 10 and 12 Empty Quarter missions.

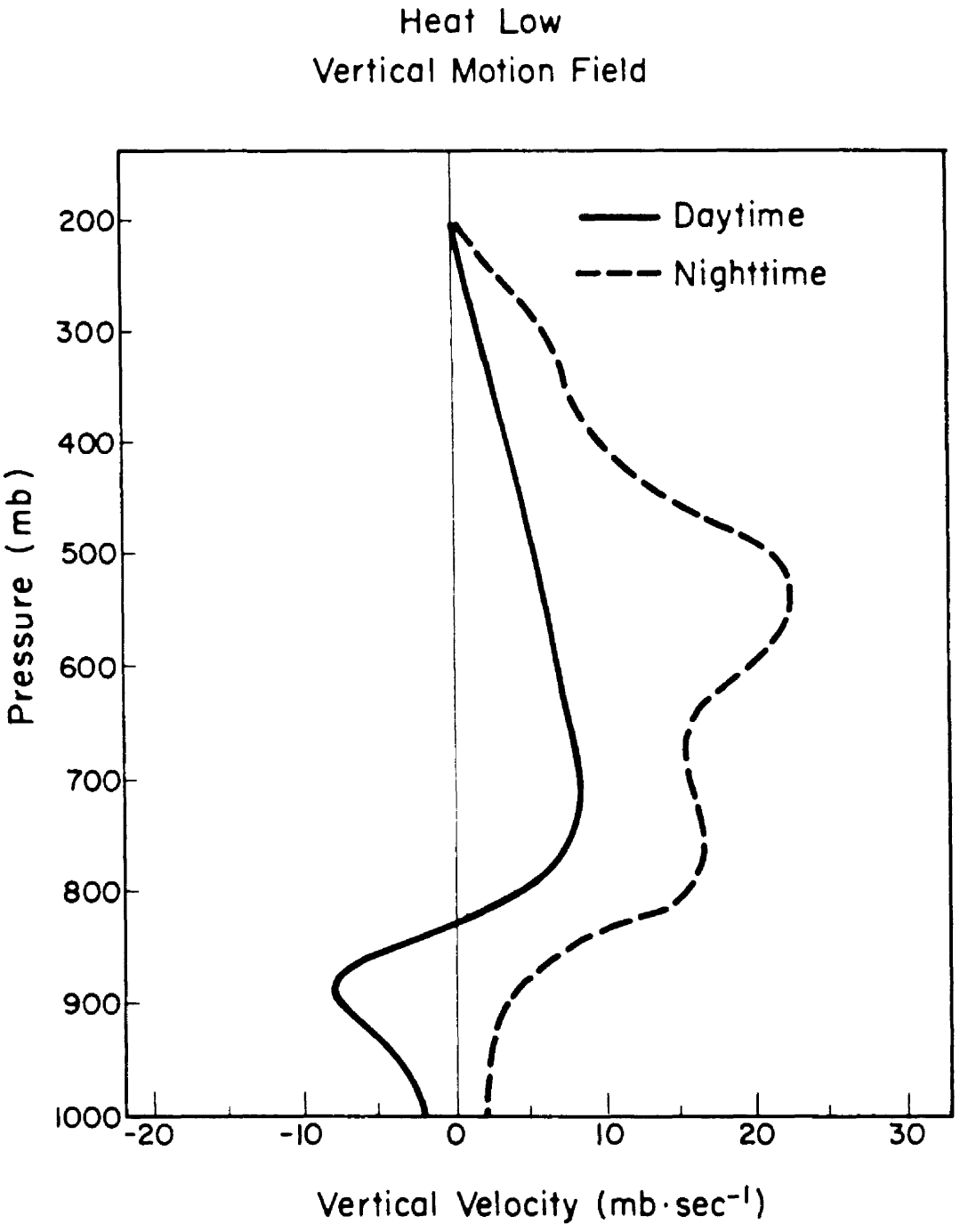

Fig. 5.11. Daytime and nighttime vertical motion profiles over the Arabian heat low region based on the kinematic analyses of Blake, et al (1983).

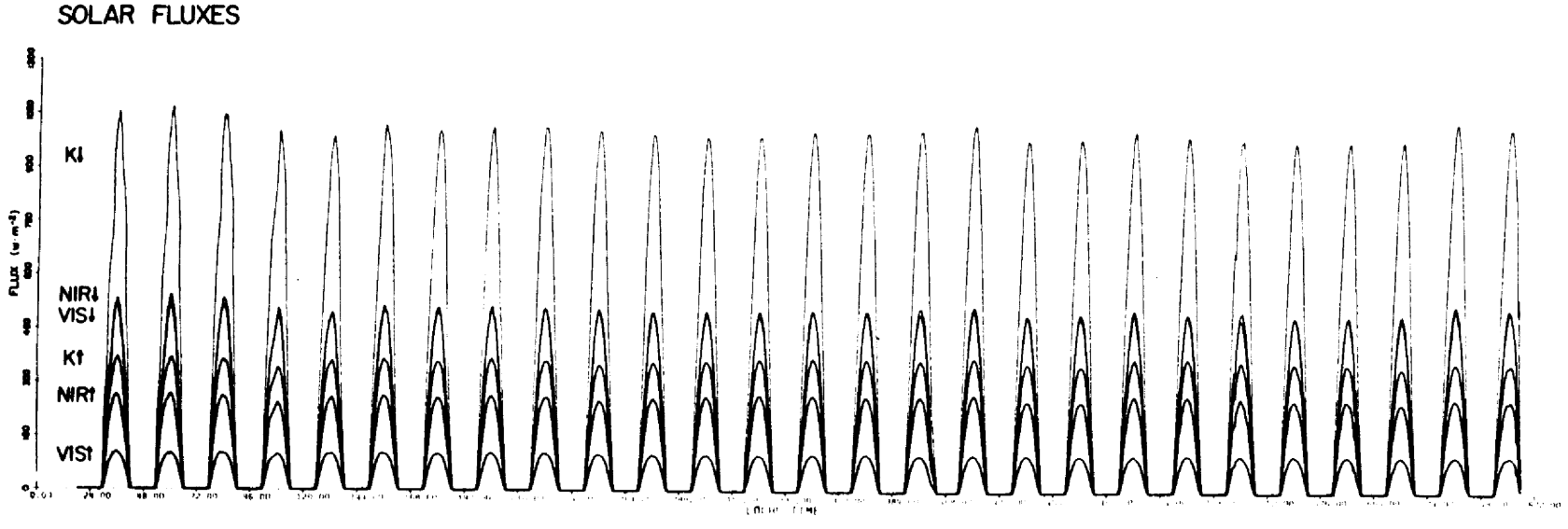

Fig. 5.12. Time series (15 minute sampling) of upward and downward solar fluxes (VIS, NIR, total) for the June, 1981 period at Sharouwrah, Saudi Arabia.

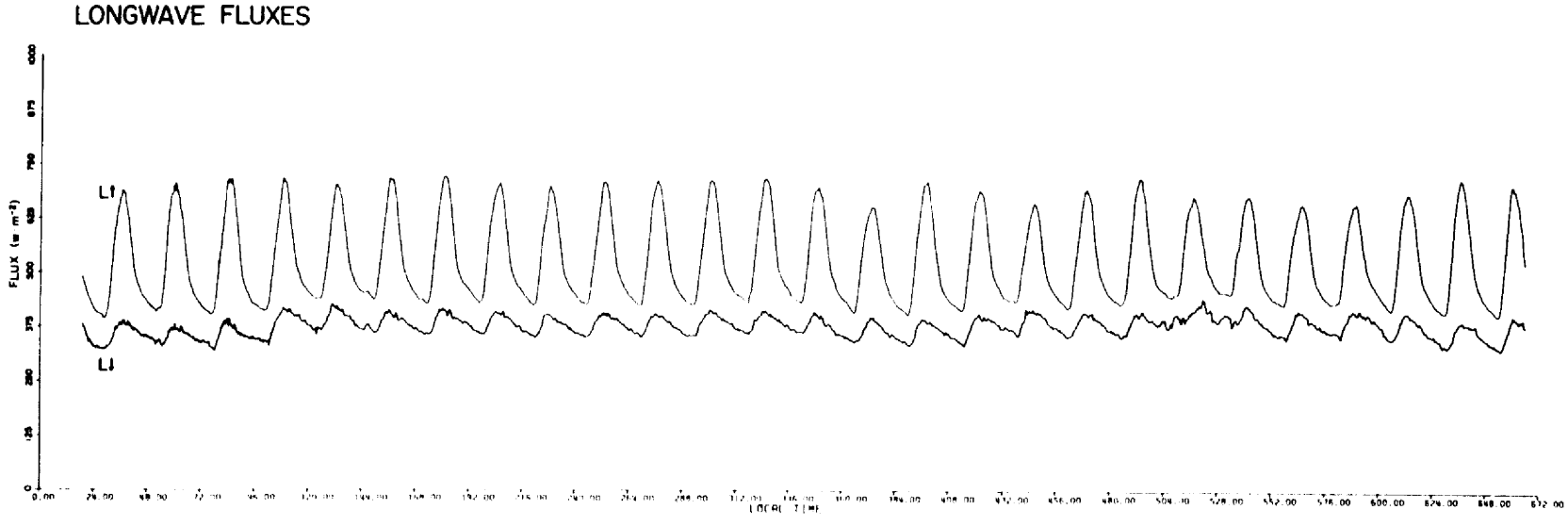

Fig. 5.13. Same as Fig. 5.12 for longwave fluxes (total infrared spectrum).

longwave fluxes (L:3.0-50.0 μm) for the same period. Note the almost monotonous periodicity in these processes and the virtually invariant amplitude of the daytime peaks. Note also the sinusoidal appearance of the solar fluxes as opposed to the somewhat skewed appearance of the longwave fluxes. This skewness should impart a slight skew effect in the net flux term. It also suggests that surface heating and thus, sensible heat release, are also skewed away from local noon symetry.

In the calibration of the pyrgeometers (Eppley PIR's with silicon domes) the instrument source effect was removed with an empirical formulation of S. K. Cox and colleagues (personnel communication). The heat diffusion process within the radiometers is approximated by a quadratic expansion of the internal-external temperature gradient obtained from the dome and thermopile sink thermistors implanted into the radiometers by Eppley Labs. A pyrgeometer calibration in flux units (L) takes the form:

$$L = K_1 \cdot V + \sigma \cdot \varepsilon \cdot T_s^4 + K_2 \cdot \sigma \cdot (T_d^4 - T_s^4) \qquad (5.1)$$

where T_d and T_s are the dome and sink temperatures, V is the radiometer output voltage, K_1 is the radiometer sensitivity factor, ε is a bulk radiometer emissivity (≈ 1.0), σ is Stefan-Boltzmann's constant, and K_2 is the empirical thermal gradient coefficient.

The pyranometer calibrations were based on the sensitivity factors provided by Eppley Labs. Two types of pyranometers were used; a total solar configuration (Eppley PSP with WG-295 quartz outer and inner hemispheres), and a near-infrared configuration (PSP with an R68 Schott glass filter outer hemisphere and a WG-295 quartz inner hemisphere).

The ultraviolet-visible region (VIS) term is obtained by differencing the total and near-infrared terms.

By diurnally averaging the radiometer data and presenting all terms of the surface radiation budget, Fig. 5.14 is obtained. In this illustration radiative contributions to the atmosphere are considered positive; radiative losses are considered negative. The key features of this diagram are the intense symetric solar insolution at the surface ($\approx$1000 W $\cdot$ m^{-2} at noon), the intense but asymetric surface longwave flux associated with the heating of the surface ($\approx$ 700 W $\cdot$ m^{-2} at noon), the relatively flat downward longwave term, ($\approx$ 400 W $\cdot$ m^{-2}), and finally the skew symetric net term (Q*) which peaks at local noon at approximately -365 W $\cdot$ m^{-2}.

Another interesting feature of the Empty Quarter surface is the difference in magnitude of the VIS and NIR albedos. The directional reflectance functions of the two spectral components and the total component (TOT) are shown in Fig. 5.15. Note that the NIR albedo is in excess of a 2:1 ratio with respect to the VIS albedo. This is a general feature of bare soils, i.e. NIR > VIS albedo, however in the case of the Empty Quarter dune sand which have a reddish appearance, the relationship is somewhat exaggerated. This figure also demonstrates that the magnitude of the directional reflectance effect (i.e. as the solar zenith angle increases, albedo increases) is greater for the near-infrared spectrum than it is for the visible spectrum. These results also illustrate there is virtually symmetry about local noon (no differences in the morning and afternoon diffusing and scattering processes).

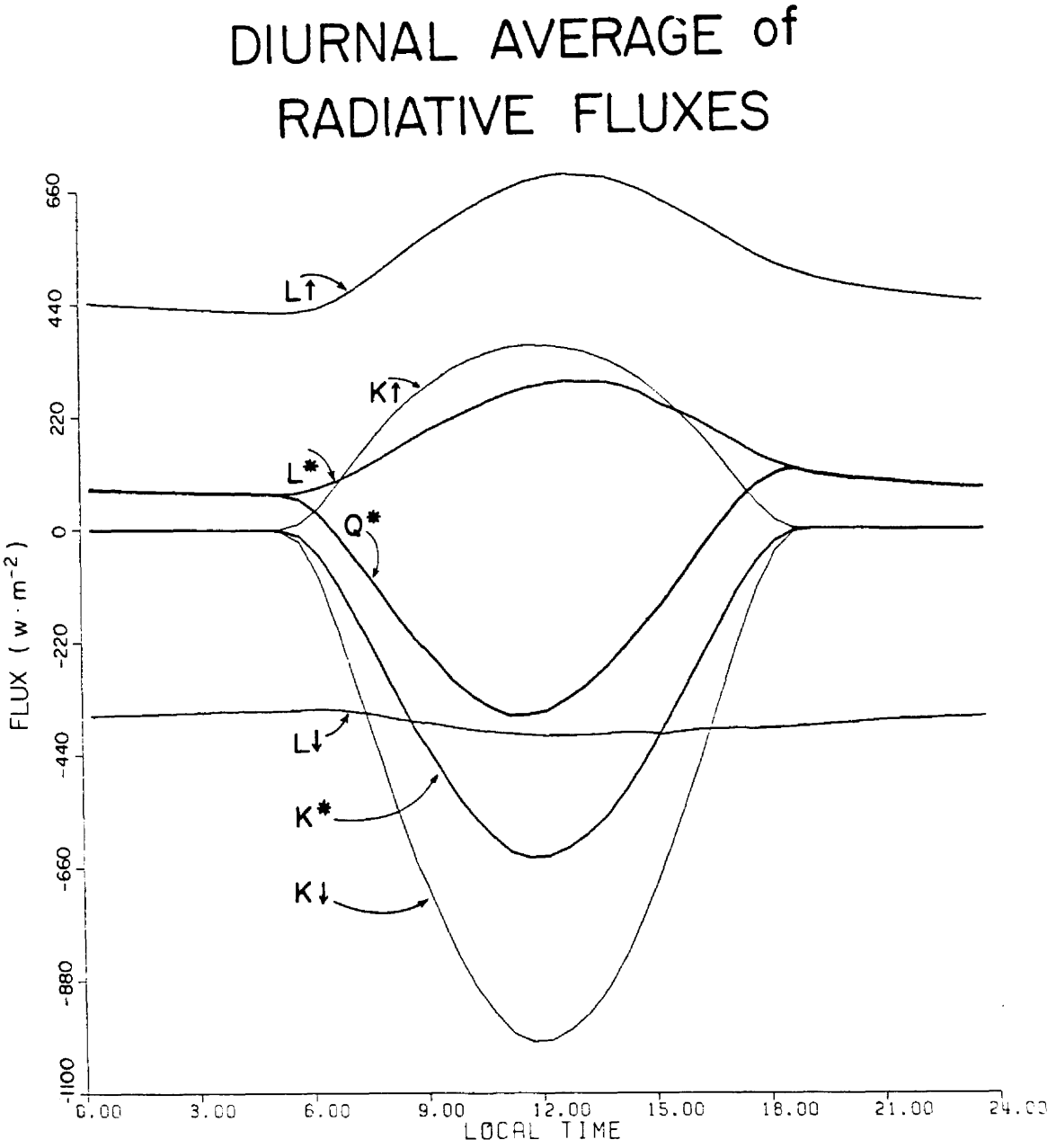

Fig. 5.14. Diurnal surface radiation budget for June, 1981 at Sharouwrah, Saudi Arabia. The shortwave upward, downward and net terms are indicated by K↑ , K↓ , K*; the longwave upward, downward and net terms are indicated by L↑ , L↓ , L*; total net is indicated by Q*.

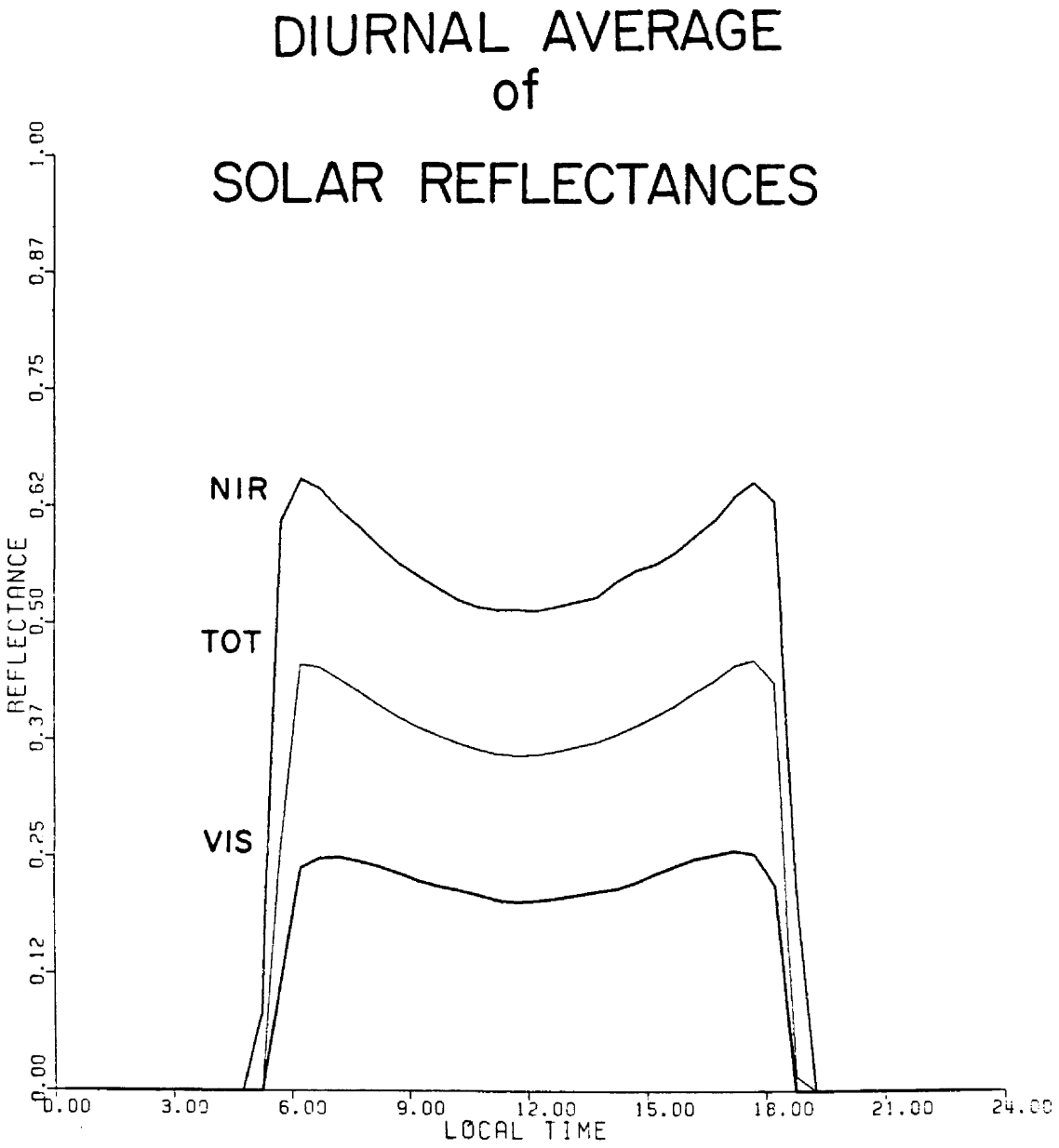

Fig. 5.15. Surface directional reflectance in the visible (VIS), near-infrared (NIR) and total solar (TOT) spectrums for June, 1981 at the Sharouwrah site.

The daily averaged reflectances for the two main solar spectrums along with the total are shown in Fig. 5.16. Note that the VIS spectrum exhibits much less variation than the NIR spectrum as might be expected (variations in atmospheric moisture will serve to modulate near-infrared spectrum absorption far more than the visible spectrum absorption).

5.3.4 Dynamical and Thermodynamical Surface Conditions

The surface conditions measured at the Sharouwrah site during June, 1981 exhibit fairly uniform diurnal cycles. Figure 5.17 illustrates both the air temperature (AT) and relative humidity (RH) cycles. After sunup the air temperature increases rapidly, peaking to about 43^{o}C at approximately one hour after local noon, and then decreasing rather gradually until the following sunrise. The average June minimum temperature is approximately 27^{o}C. The mixing ratio remains relatively uniform throughout the month (with one major exception to be discussed) - therefore, the relative humidity trace is simply a reflection of the temperature trace. Daytime humidities are on the order of 10 to 12 percent which explans why so little summertime cloudiness is observed over the southern Arabian Peninsula.

The winds are generally northerly from late morning until late evening, rapidly turning to southwesterly as the nighttime period progresses and the heat low momentarily dissipates. The diurnal cycle of wind direction for the June period is shown in Fig. 5.18. The thick dashed line is a smoothed representation of the averages. It can be noted here that the impact of the heat low on the dynamical field begins to take place at approximately 9:00 LT and retains its impact until midnight.

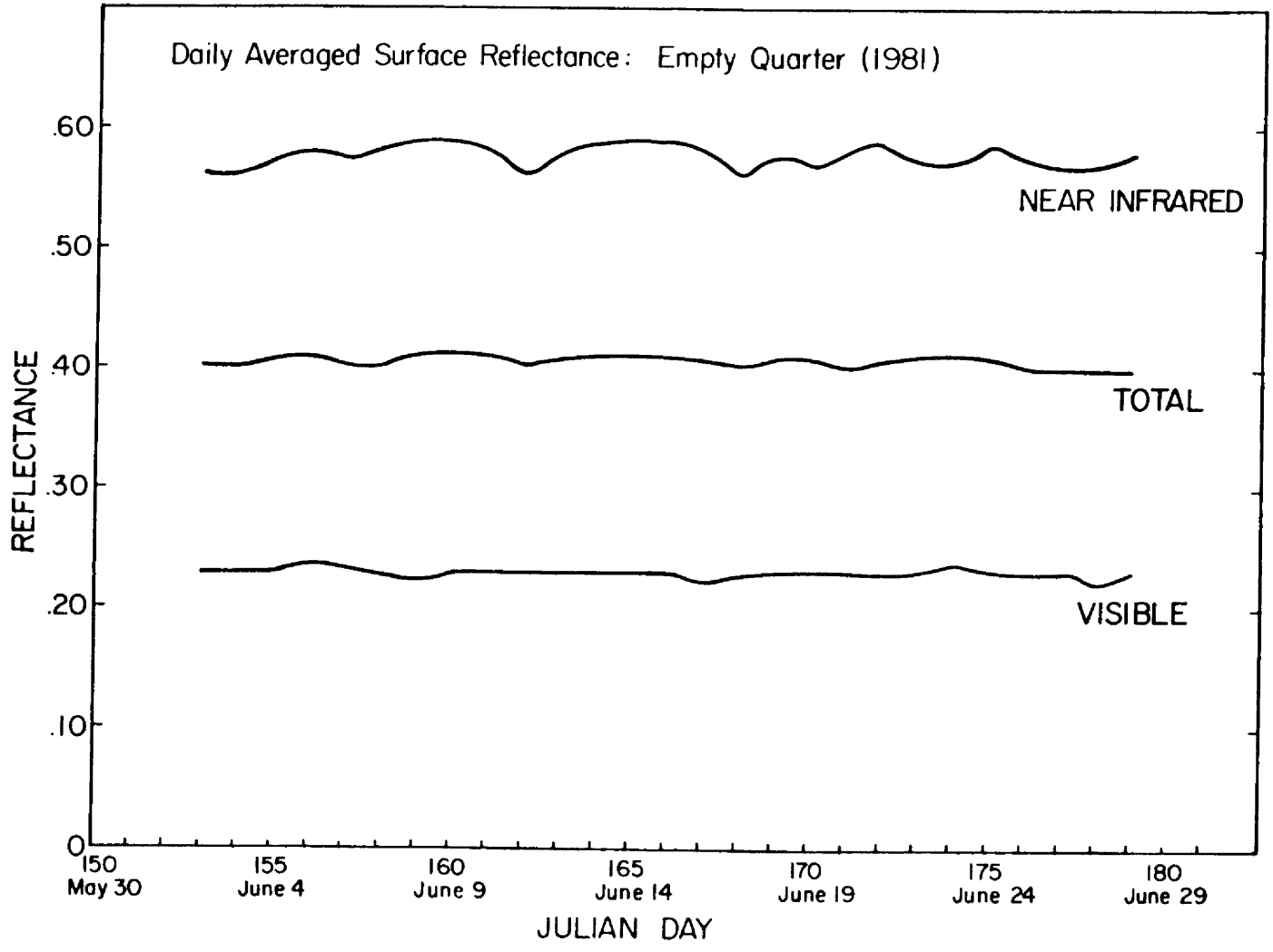

Fig. 5.16. Daily averaged surface reflectance in the visible, near-infrared and total solar spectrums for the June, 1981 period at the Sharouwrah site.

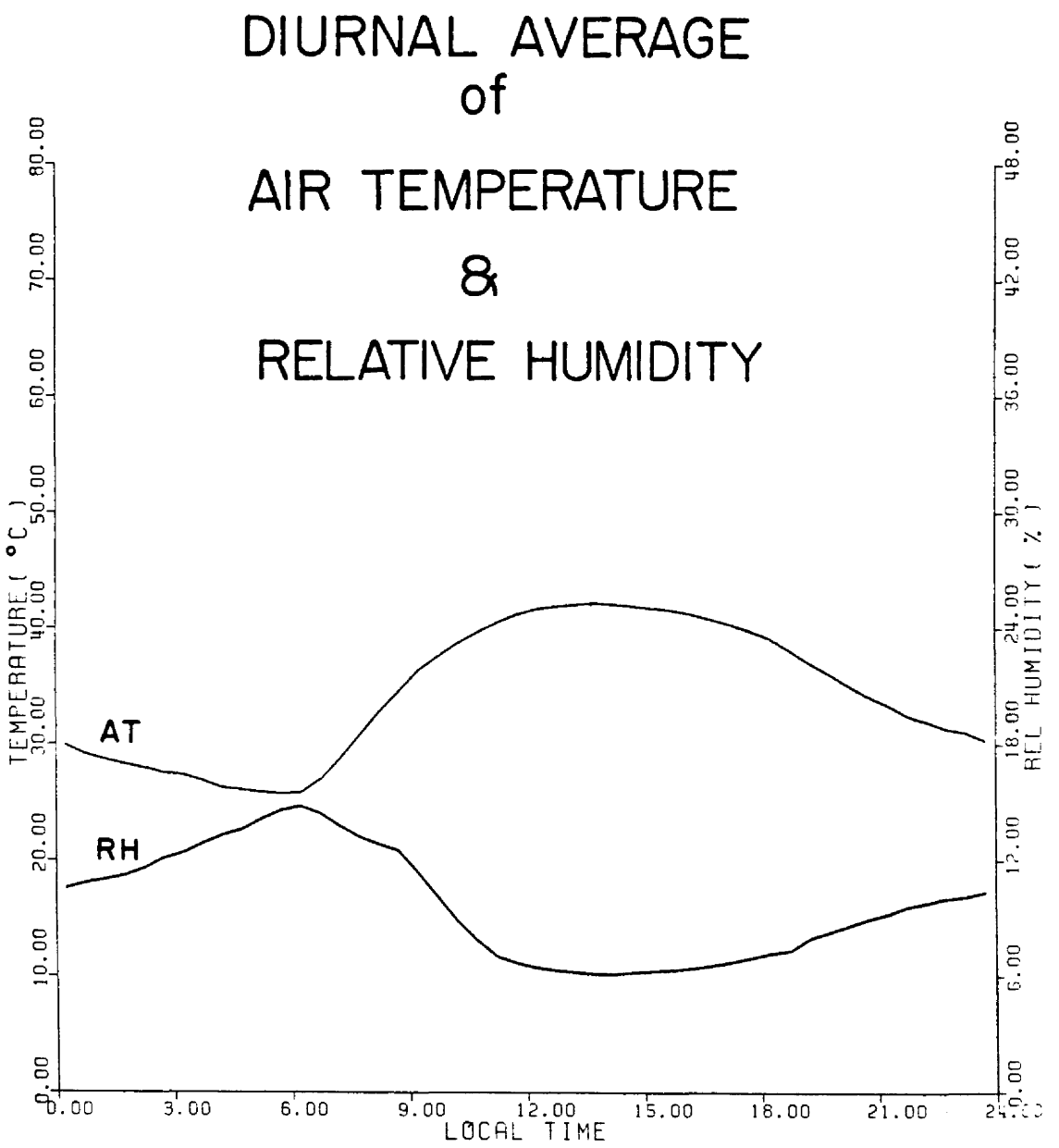

Fig. 5.17. Diurnal averages of temperature and relative humidity during June, 1981 at Sharouwrah, Saudi Arabia.

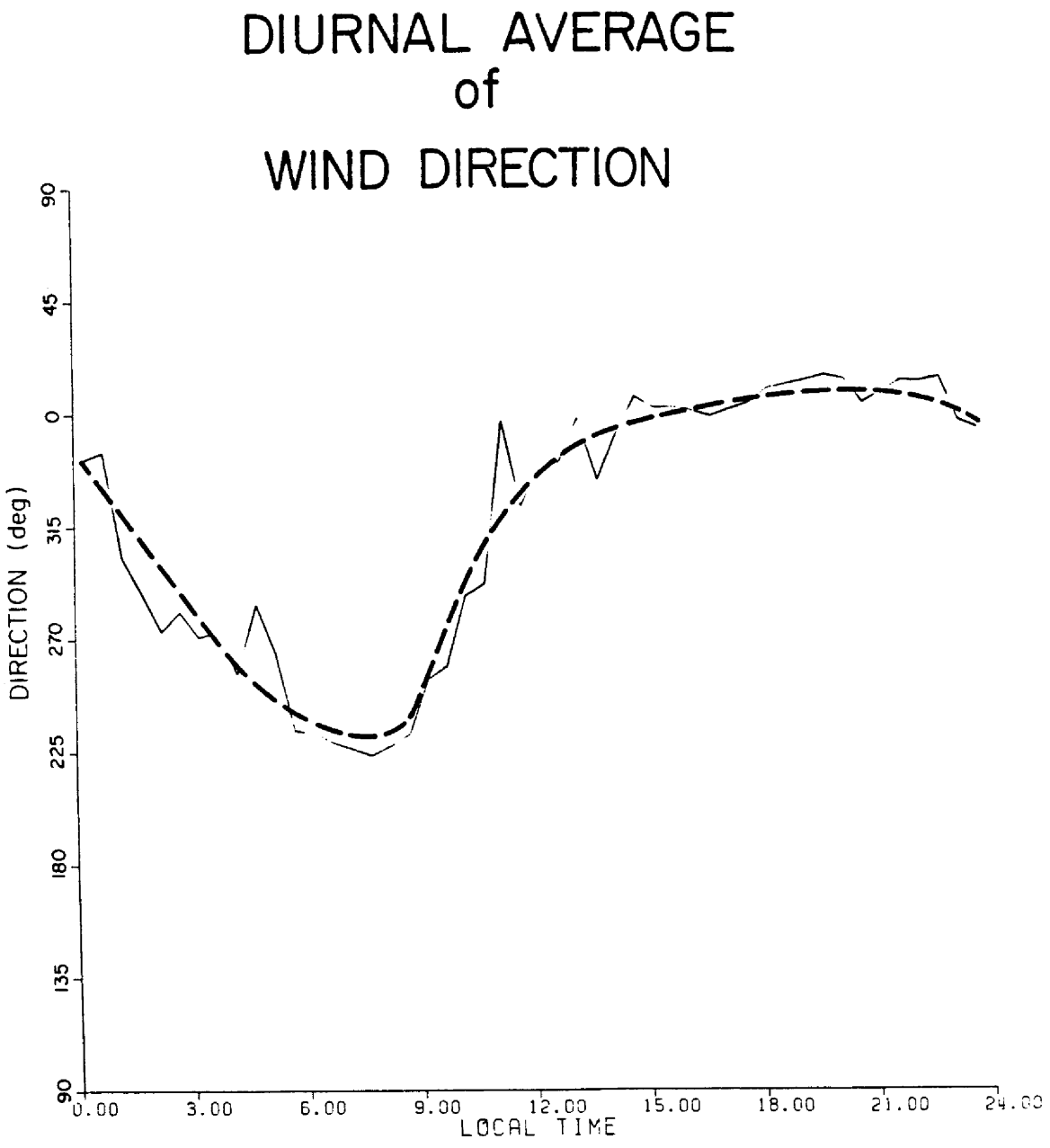

Fig. 5.18. Same as Fig. 5.17 for wind direction. The thick dashed line is a smoothed representation.

The wind speeds are most intense from approximately 9:00 to 18:00 LT. A rather interesting, but yet to be explained feature, is a relative noontime lull in the magnitude of the winds. This is shown in a plot of the diurnal cycle in Fig. 5.19. It is also noted that the relative lull is associated with a peak in the variability of the wind speed (indicated by the standard deviation cycle). The 15 minute sampled wind speed trace shown in Fig. 5.20 demonstrates that the daily cycle is fairly regular. The winds rarely exceed 8 $m \cdot sec^{-1}$ or fall below 1 $m \cdot sec^{-1}$.

5.3.5 Surface Temperatures and Thermal Storage

Surface skin temperatures in the Arabian Empty Quarter are extreme. The diurnal daytime-nighttime differences were observed to go as high as 48-50°C (as shown in Fig. 5.21). The heating can become so intense that a superadiabatic layer of a few inches deep forms which is unstable enough to raise a veil of sand off the desert floor. Streaks of sand are then swept over the desert by the surface winds creating an astonishing visual effect on the unwary observer. Prior to this superheating effect in the early morning, almost total quiescence prevails such that all the shifting and sweeping of the prior afternoon and evening are now etched out in new patterns. It is no wonder that all the great prophets have risen from a desert environment. The combination of heat, barrenness, remoteness and meandering sand is enough to create a zealot out of anyone.

In order to estimate the surface energy budget, sub-surface sand temperatures were monitored as a means of estimating the ground storage term. By combining ground storage (S) with the net radiative term (Q*)

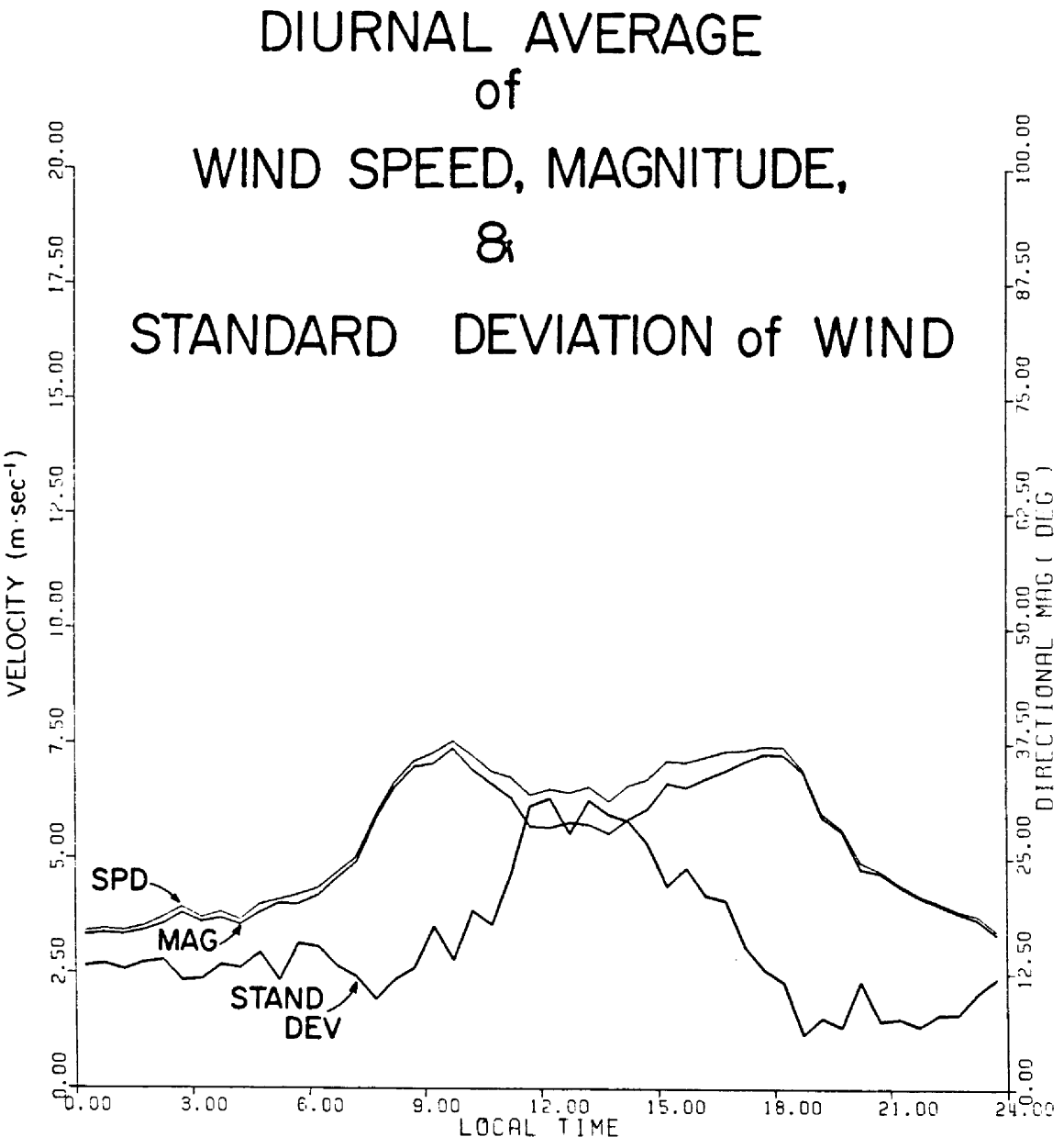

Fig. 5.19. Same as Fig. 5.17 for wind speed [AVE (V)], wind magnitude [AVE $((u^2 + v^2)^{1/2})$] and standard deviation of wind speed.

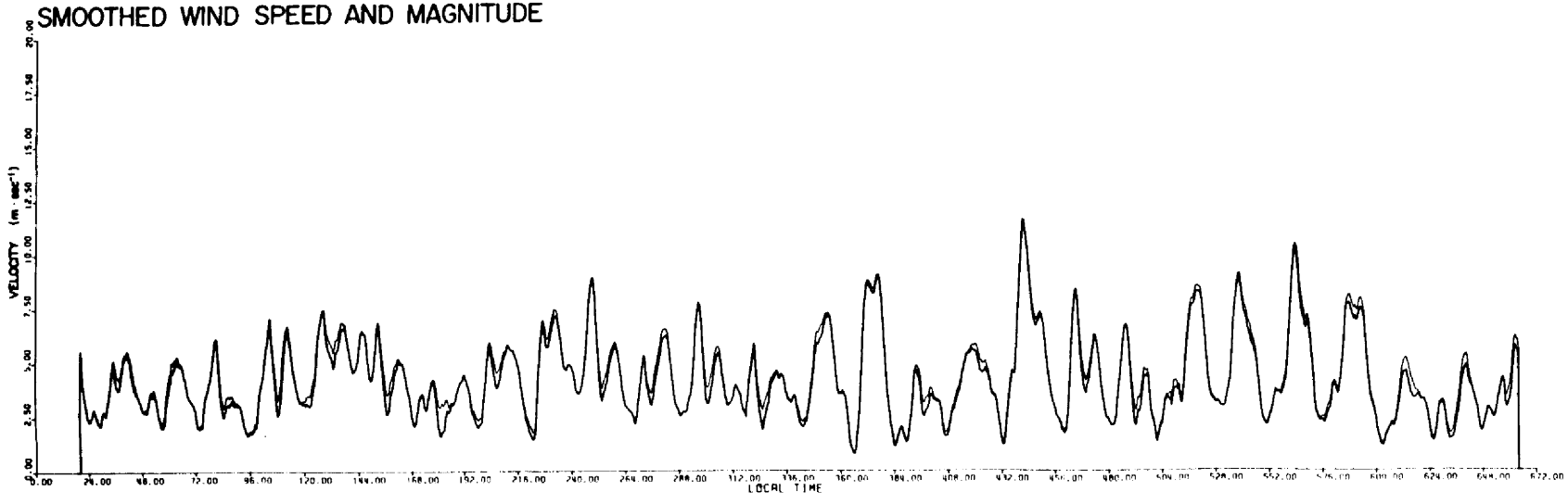

Fig. 5.20. Time series (15 minute sampling) of wind speed and magnitude during June, 1981 at Sharouwrah.

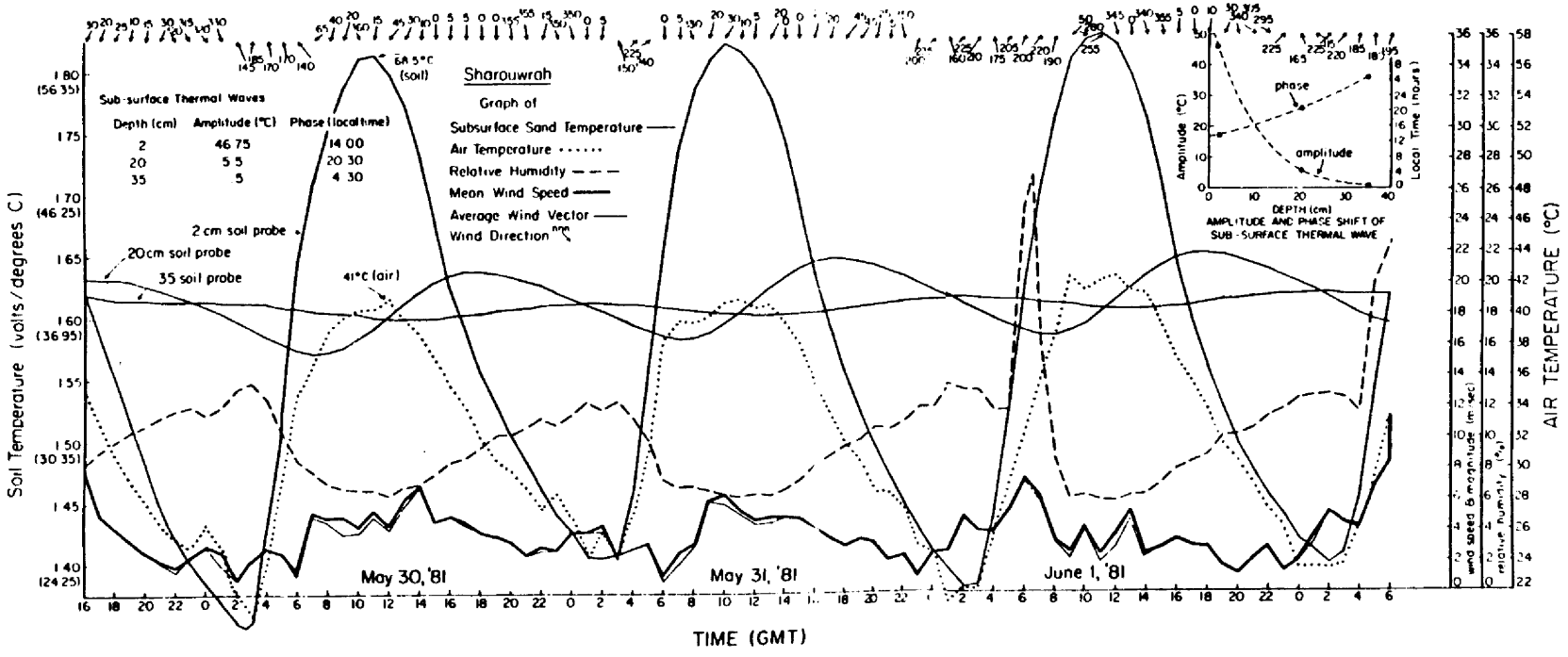

Fig. 5.21. Time series (15 minute sampling) of sub-surface temperatures (2, 20, 35 cm), air temperature, relative humidity, wind speed and magnitude, and wind direction from May 30 to June 1, 1981 at Sharouwrah, Saudi Arabia. The diagram in the upper right hand corner provides the amplitude (°C) and phase (local time) as a function of depth of the sub-surface thermal waves. The small table in the upper left hand corner gives the peak amplitudes at each measuring depth (June, 1981).

a first order estimate of the sensible heat (SH) transport is possible through the so-called residual method, i.e.:

$$SH = -Q^* - S \tag{5.2}$$

Here we have ignored the role of latent heat (according to the local Bedouin rain falls briefly and lightly once every 10 years in Sharouwrah). This formulation also assures there is no significant lateral transport of heat, which under homogeneous conditions holds true. Given the fact that the Empty Quarter is more or less a continuous maze of sand and sand dunes, the homogenity assumption is presumed to be valid.

In order to monitor sub-surface storage, soil thermistors were placed at three depths (2, 20 and 30 cm). The diurnal averages of the June data at these three depths are presented in Fig. 5.22. Note the easily observed phase-shifted amplitude decrease with depth. To illustrate the day to day variability, the daily averaged data are plotted in Fig. 5.23. Note the upper two depths (2 and 10 cm) have a range of only about $4.5^{o}C$ for the complete month. It is also interesting to note that during a ground cooling phase, the daily averaged near surface value (2 cm) can go below the values at the lower depths.

The sub-surface heat storage term is obtaned from an integration process:

$$S = C_s \cdot \bar{\rho} \int_{do}^{o} \frac{dT(z,t)}{dt}\, dz \tag{5.3}$$

where C_s and $\bar{\rho}$ are the specific heat and mean density of the sand, respectively [taken to be $0.8 \cdot 10^3$ $J \cdot kg^{-1} \cdot deg^{-1}$ and 1.6 $kg \cdot m^{-3}$ from Oke (1978)], and T(z,t) is the sub-surface temperature as a

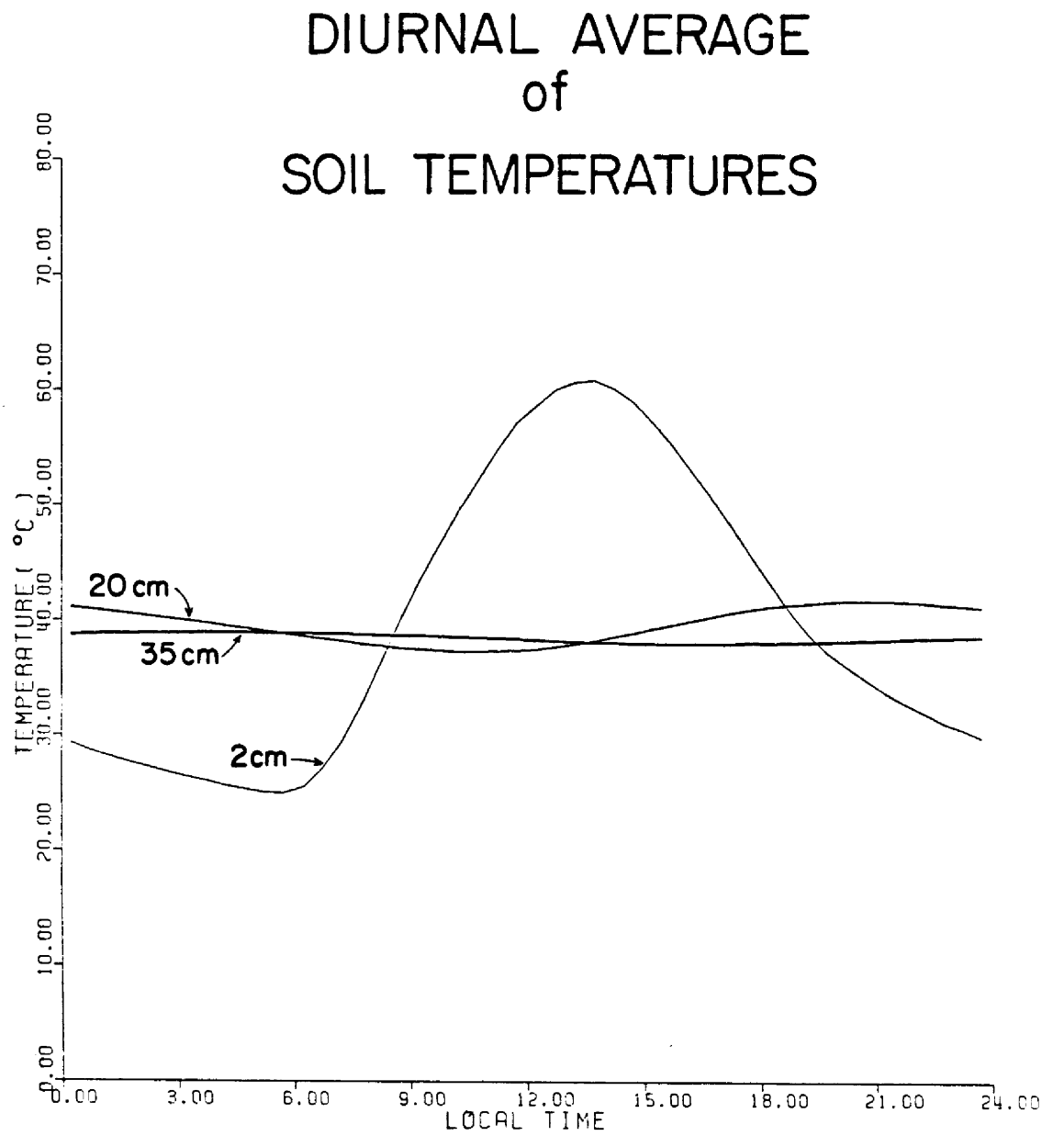

Fig. 5.22. Diurnal averages of sub-surface sand temperatures at three depths (2, 20, 35 cm) at the Sharouwrah site (June, 1981).

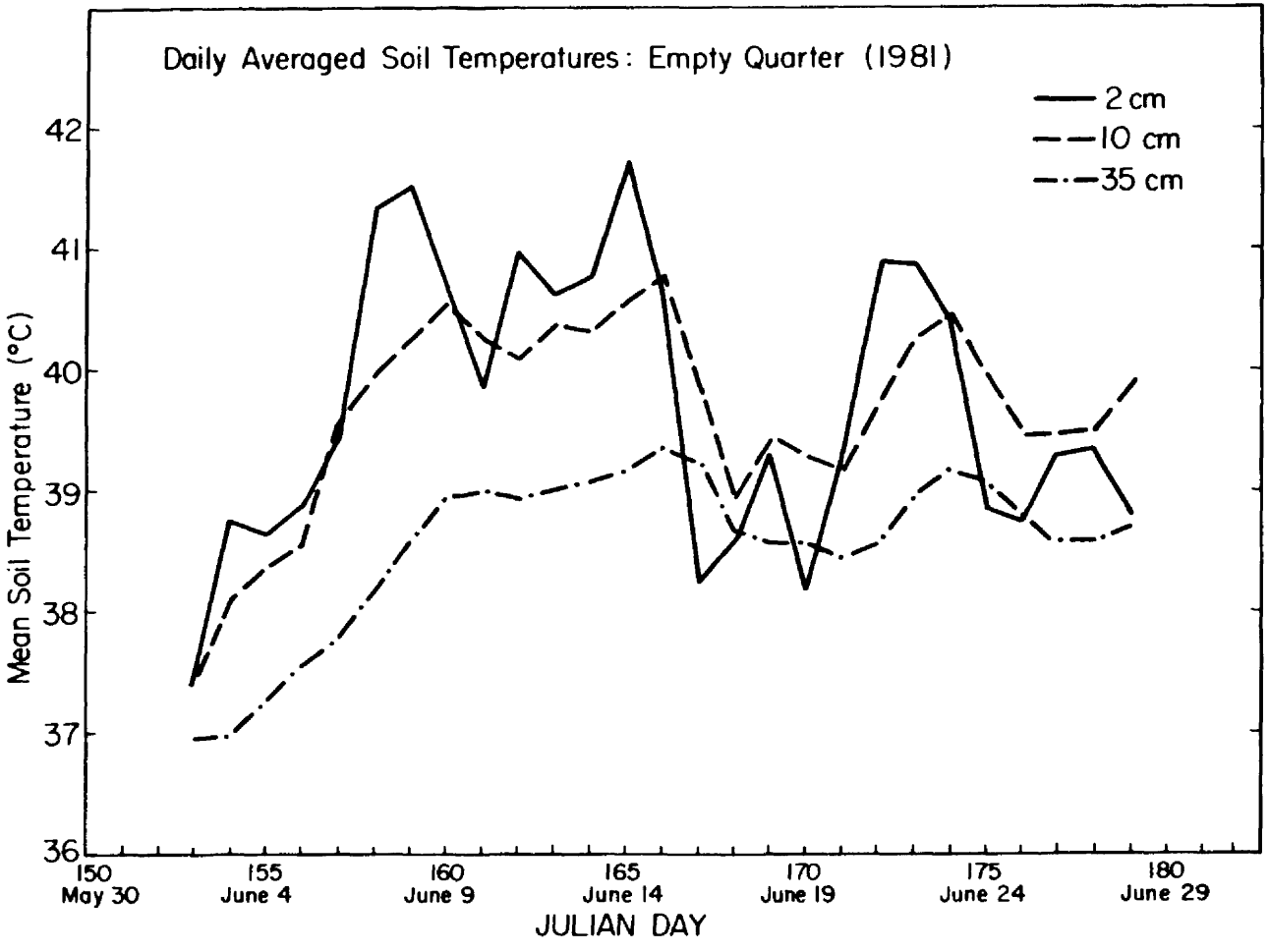

Fig. 5.23. Daily averaged soil temperatures at the three measurement depths at Sharouwrah (June, 1981).

function of depth and time. The integration takes place over a depth d_o, which represents the level at which the diurnal thermal perturbations nearly become zero (approximately 50 cm).

In general, sub-surface thermal oscillations are well behaved such that analytic representations can be used, thus simplifying and improving the accuracy of the integration. To enable an accurate calculation of the storage term, it is thus desireable to obtain a mathematical expression for the sub-surface temperature as a function of depth and time. This approach provides a means to integrate an analytic function of a relatively smooth and continuous process rather than attempting to use a finite difference procedure which would most likely lead to significant errors with only three levels being monitored. A classical formulation thus has been applied to express sub-surface thermal waves incorporates a straightforward sinusoidal oscillator function in conjunction with an exponentially decaying amplitude term. The oscillator function generates the desired shape and phase characteristics of the sub-surface thermal waves; the amplitude term expresses the peak diurnal variation as a function of soil depth. In the classic notation a thermal wave at any given depth is said to vary with respect to a uniform mean value ($\bar{T}$) characteristic of the total layer induced by thermal perturbations and invariant with depth. Mathematically, the temperature at any given depth (z) or time (t) can then be expressed as follows [see e.g. Oke (1978) or Sellers (1975)]:

$$T(z,t) = \bar{T} + \Delta\bar{T})_z \cdot \sin [\omega \cdot t-(\omega/2K_s)^{1/2} \cdot z] \qquad (5.4)$$

where ω is the wave frequency ($2\pi/P$; P = 24 hours), K_s is the soil

thermal diffusivity factor [a property of any soil given in $m^2 \cdot sec^{-1}$ and expressing the time constant required for temperature changes to travel within the soil], and $\bar{\Delta T})_z$ is the diurnal amplitude of the wave at any given depth:

$$\bar{\Delta T})_z = \bar{\Delta T})_o \exp\ [-z \cdot (\pi/K_s \cdot P)^{1/2}] \qquad (5.5)$$

where $\bar{\Delta T})_o$ is the surface amplitude boundary condition.

It would be possible to express the Sharouwrah measurements within this framework, however, it is apparent from a cursory examination of the actual measurements (see Fig. 5.24) that the above sinusoidal representation would entail two basic flaws. The first involves the wave form itself. The waves are not sinusoidal in character, instead they appear to be skewed toward the evening side, suggestive of a modified gamma function. Secondly, the daytime and nighttime excursions are not symetric, a condition which would lead to the simple exponential amplitude expression underestimating the daytime highs and overestimating the nighttime lows.

In order to improve the accuracy in mathematically expressing the sub-surface thermal process, a more realistic model was developed for the June Sharouwrah data. The basic form of Eq. 5.4 was retained, i.e. a reference temperature used in conjunction with an amplitude and oscillatory function pair, however, the amplitude and oscillatory functions were altered. The adopted formulation is as follows:

$$T(z,t) = T_{ref} \pm AMP(j) \cdot A(z) \cdot J[t_m(t,z)] \qquad (5.6)$$

where T_{ref} is the June reference temperature ($T_{ref} = 39.56^{o}C$); AMP(j) is an amplitude scaling factor as a function of the day number (j = 153,

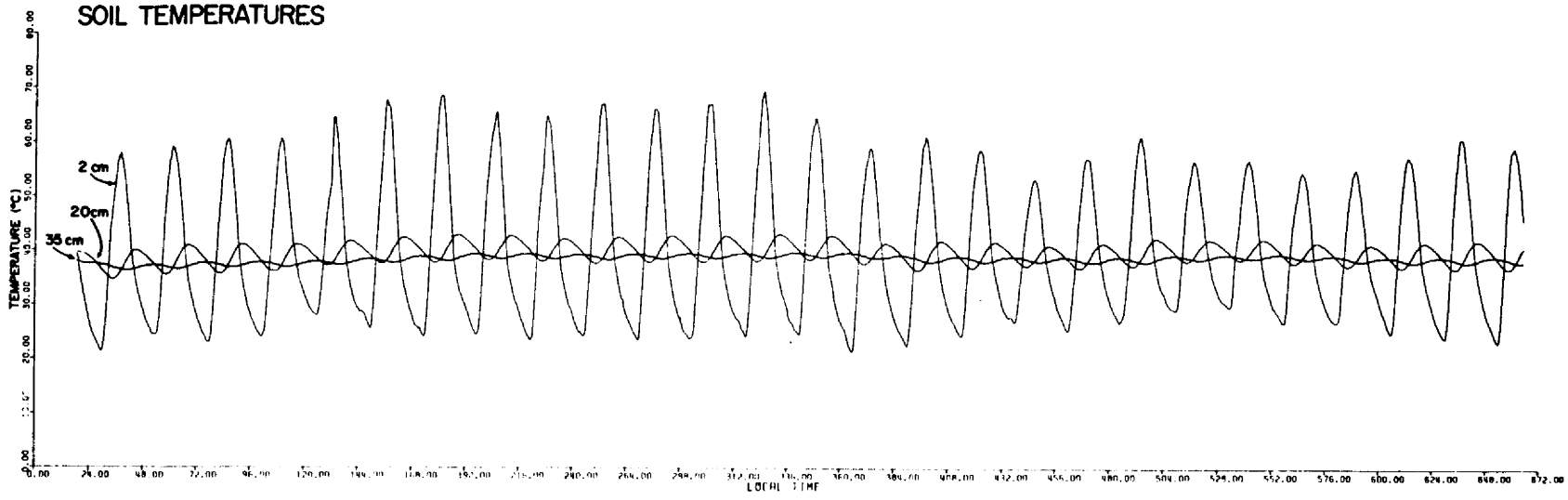

Fig. 5.24. Time series (15 minute sampling) of soil temperatures at the three measurement depths at Sharouwrah (June, 1981).

178); +AMP is used when the oscillatory function is positive, -AMP is used when the oscillatory function is negative [for the June period AMP ranges from 15.2 to 26.4°C]; A(z) is a normalized amplitude function or shape factors as a function of depth; and $J[t_m(t,z)]$ is the oscillatory function given in terms of a modified time variable which is explained below.

The normalized amplitude function is expressed as:

$$A(z) = [\exp [b \cdot (50-z)] - 1.0] / [\exp (b \cdot 50) - 1.0] \quad (5.7)$$

where b is an empirical coefficient (b = 0.10139) and 50 cm designates the maximum depth to which the diurnal thermal wave is assumed to extend. Note that this function is normalized between 0 (at z=50 cm) and 1.0 (at z=0 cm). The normalized amplitude is then scaled by AMP(j).

The oscillatory function is expressed as:

$$J(t_m) = \exp [\alpha_1 (\ln (t_m) - (t_m^{\alpha_2} - 1)/\alpha_2] + \ln(z)] - 1.0 \quad (5.8)$$

where α_1 and α_2 are empirical coefficients (α_1 = 1.44548, α_2 = 1.98104). Note that J is a function of a modified time variable (t_m) which itself is a function of local time (t = 0, 24) and depth (z =0,50). The modified time variable is designed with the nodal points of a thermal wave in mind (i.e. the maximum and minimum peaks and the ascending and descending reference temperature crossings) and is referenced to the daily minimum. The following expression provides the definition for modified time:

$$t_m = \text{mod} (t_r + 24, 24) / (8 + a_3 \cdot z) \quad (5.9)$$

where t_r is the relative time or the time difference in hours between t and the time of minimum temperature for a given depth on a given day, expressed as:

$$t_r = t + a_1 \cdot z + a_2 \cdot z^2 - 5 \qquad (5.10)$$

Note that in Eqs. 9 and 10, a_1, a_2 and a_3 are found empirically (a_1 = -0.2350764, a_2 = -0.0028606, a_3 = +0.8268045), and the constant 5 in Eq. 5.10 designates the local time in hours at which the surface is assumed to reach its minimum value (i.e. $t_r = 0$). If (10) is evaluated at z = 50 cm for $t_r = 0$, t is found to be 23:54 LT. In Eq. 5.9, the numerator can be thought of as an elapsed time from the most recent minimum temperature; the denominator normalizes the times of occurrence of the wave nodes with depth.

In the modified time coordinate system, the values t_{n1}, t_{n2}, t_{n3}, and t_{n4} designate the nodal time occurrence of the wave nodes:

t_{n1} = modified time of the minimum temperature (0.0)

t_{n2} = modified time at which $J(t_m)$ intersects T_{ref} in an ascending fashion (0.46079686) (5.11)

t_{n3} = modified time of the maximum temperature (1.0)

t_{n4} = modified time at which $J(t_m)$ intersects T_{ref} in a descending fashion (1.70116212)

In terms of modified time AMP is positive when $t_{n2} \leq t_m < t_{n4}$; AMP is negative when $t_m < t_{n2}$ or $t_m \geq t_{n4}$. The day index (j) is decreasd by 1 unit with respect to local time if $t_r < 0$ or increased by 1 unit if $t_m > t_{n4}$. This keeps the day index in association with modified time as opposed to actual local time. To summarize:

$$
\begin{array}{r|l}
+\text{AMP} & t_{n2} \leq t_m < t_{n4} \\
-\text{AMP} & t_m < t_{n2} \text{ or } t_m \geq t_{n4} \\
\\
j & t_r \geq 0 \text{ or } t_m \leq t_{n4} \\
j-1 & t_r < 0 \\
j+1 & t_m > t_{n4}
\end{array}
\qquad (5.12)
$$

The above formulation and the optimal fit coefficients provide a reasonably good rendition of the June data. Fig. 5.25 illustrates a comparison between the actual measurements (solid line) and the analytic formulation (dotted line). It is noted that between June 5-15, the analytic expression underestimates the daytime peak value of the 2 cm probe, on the order of $6^{\circ}C$. There are two possibilities as to why this may be the case. The first is the fitting procedure may be inadequate; the second is that the data values during this period may be biased. Since the fitting procedure was designed to minimize a normalized mean square error at all three levels, and the 20 and 35 cm fit is fairly good during those periods, it appears possible that the 2 cm measurements are not truly representative of the 2 cm depth. What could be the cause of this? There is a very simple explanation. The depth of the probe in the sand may have, in fact, been perturbed by the surface wind. Since the lead to the probe acts as a slight obstruction, a wake effect around the probe can, in fact, remove a small pocket of sand adjacent to the probe coordinate, particularly when the surface layer of sand is as loose as that of the Sharouwrah region. It is impossible to verify what caused the discrepancy since daily checks of the surface probe depth were not taken. For purposes of this investigation the

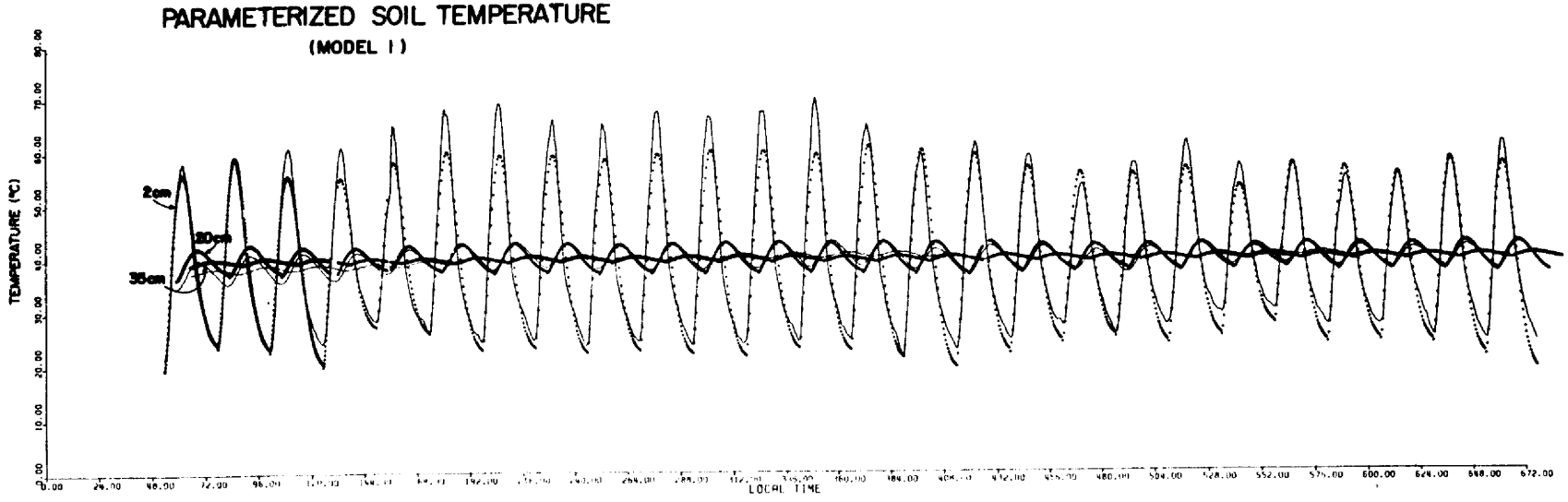

Fig. 5.25. Comparison between the measured sub-surface sand temperatures (solid line) and the calulations from the analytic formulation (dotted line).

analytic formulation has been used for purposes of calculating sub surface storage.

To test the predictability of the diurnal amplitude of surface temperature in terms of an easily observed dynamic variable, one simple experiment has been performed. The measured diurnal surface temperature amplitudes from June 3 to June 28 were plotted in conjunction with a bulk Richardson Number, defined as:

$$Ri_B = g \cdot (T_s - T_{a)} \; / \; [(T_s + T_a)/2 \cdot (V^2/3)] \tag{5.13}$$

where T_s and T_a are the surface temperature and air temperature, respectively, V is the magnitude of the surface wind and the value 3 represents the height in meters of the wind and air temperature sensors. The results from this experiment are given in Fig. 5.26. The points fall in three distinct groups (the numbers correspond to the June day). The correlation is very low. There is some tendency for the data to cluster in three groups although there does not appear to be any underlying evidence that dynamically forced heat diffusion plays a dominant role. It can be seen, however, that the three very stable days (9, 15, 22) where $Ri^B > 0.25$, are those days for which the observed daily peak temperature appears as a local maximum with respect to the adjacent days. This is reasonable since sporadic localized stability will tend to reduce heat flow from the surface and tend to drive up the relative surface temperature level.

5.3.6 The Surface Energy Budget

As illustrated in the previous figures, the dominant feature of the heat low is its diurnal modulation. Combining the net radiative flux (Q*) with the estimate of sub-surface thermal storage (S) allows the

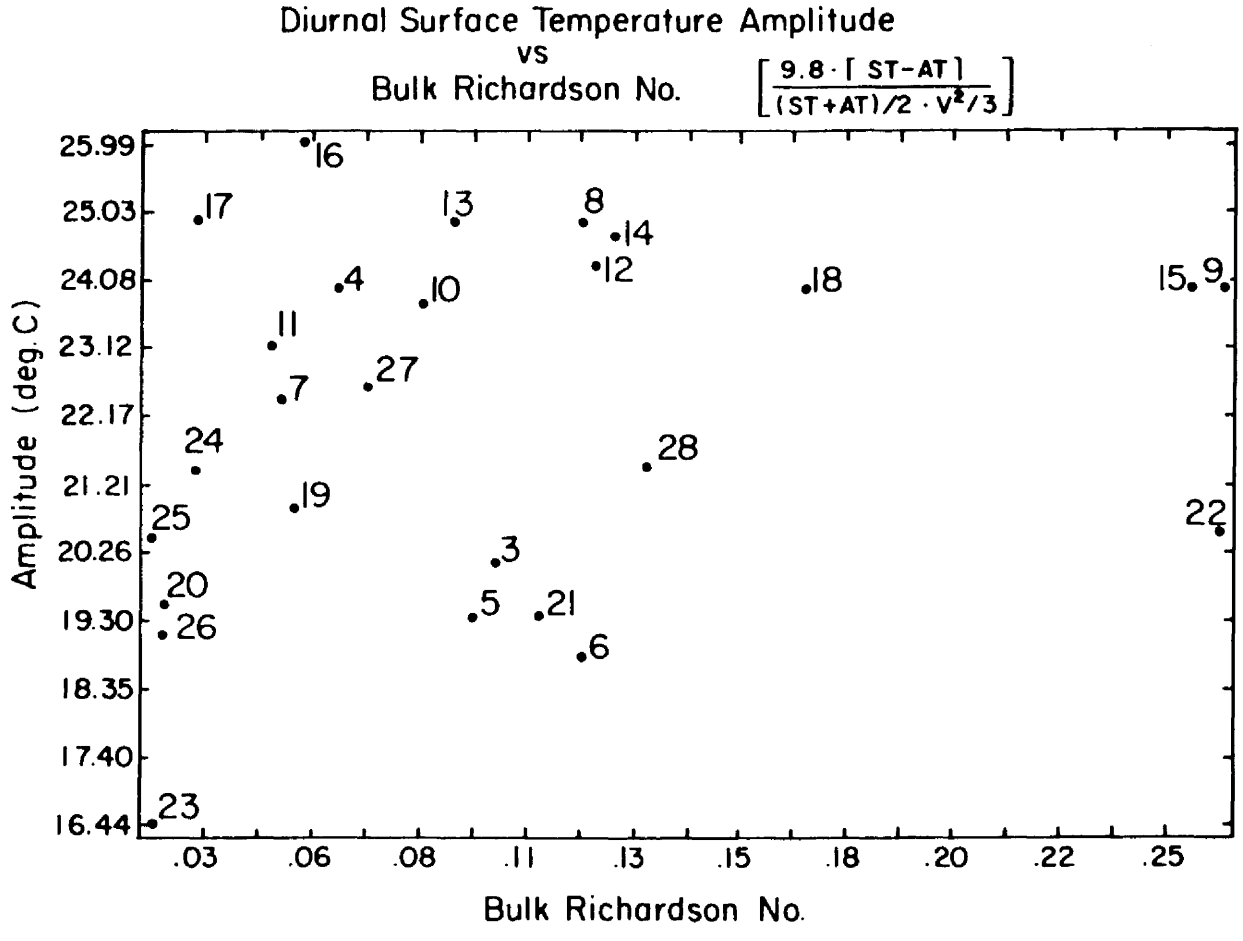

Fig. 5.26. Scattergram of the diurnal amplitude of surface temperature versus bulk Richardson number for the June, 1981 Sharouwrah data.

estimation of sensible heat transport (SH) as a residual. These processes are illustrated in Fig. 5.27 at a 15 minute time scale for the month of June. One notes that the variation in amplitude of SH is driven almost exclusively by the variations in Q*. The diurnal averages for the month of June 1981 are shown in Fig. 5.28. It is easily apparent that a desert surface acts as a very efficient heat source. Radiative energy is momentarily gained by the sand but is quickly released through conductive processes. Although there is virtually no long-term storage, the pattern of the sensible heat cycle is in effect driven by a short-term (daily) asymmetric storage cycle, which in turn leads to an asymmetry in the sensible heating cycle. These asymmetries arise from the non-linear heat diffusion process within the first 50 centimeters of the sand. Since the radiation cycle is not in phase with the storage process (the former is nearly in phase with local noon), the sensible heat cycle is phase shifted away from local noon. The skew and degree of phase shift in the sensible heat transfer cycle can be considered as a desert's signature. These parameters will be altered as the heat capacity of the sand changes due to either geologic conditions or the addition of soil moisture.

If the surface energy budget is illustrated in its daily averaged representation as shown in Fig. 5.29, an entirely different view of the desert surface is obtained. These plots suggest that in a daily sense:

$$SH = -Q^* \tag{5.14}$$

since:

$$\frac{1}{24}\int_0^{24} S(t)dt \doteq 0 \tag{5.15}$$

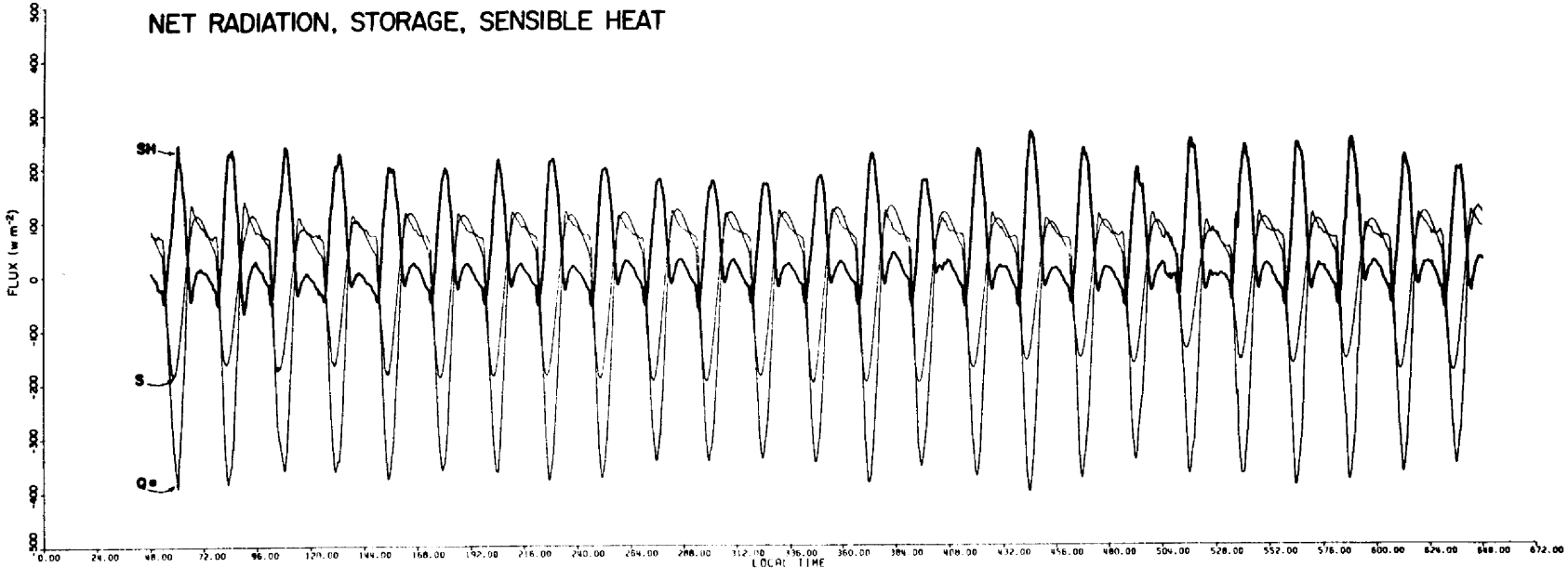

Fig. 5.27. Time series (15 minute sampling) of the principal surface energy budget terms [sensible heat (SH); storage (S); net radiation (Q*)] at Sharouwrah (June, 1981).

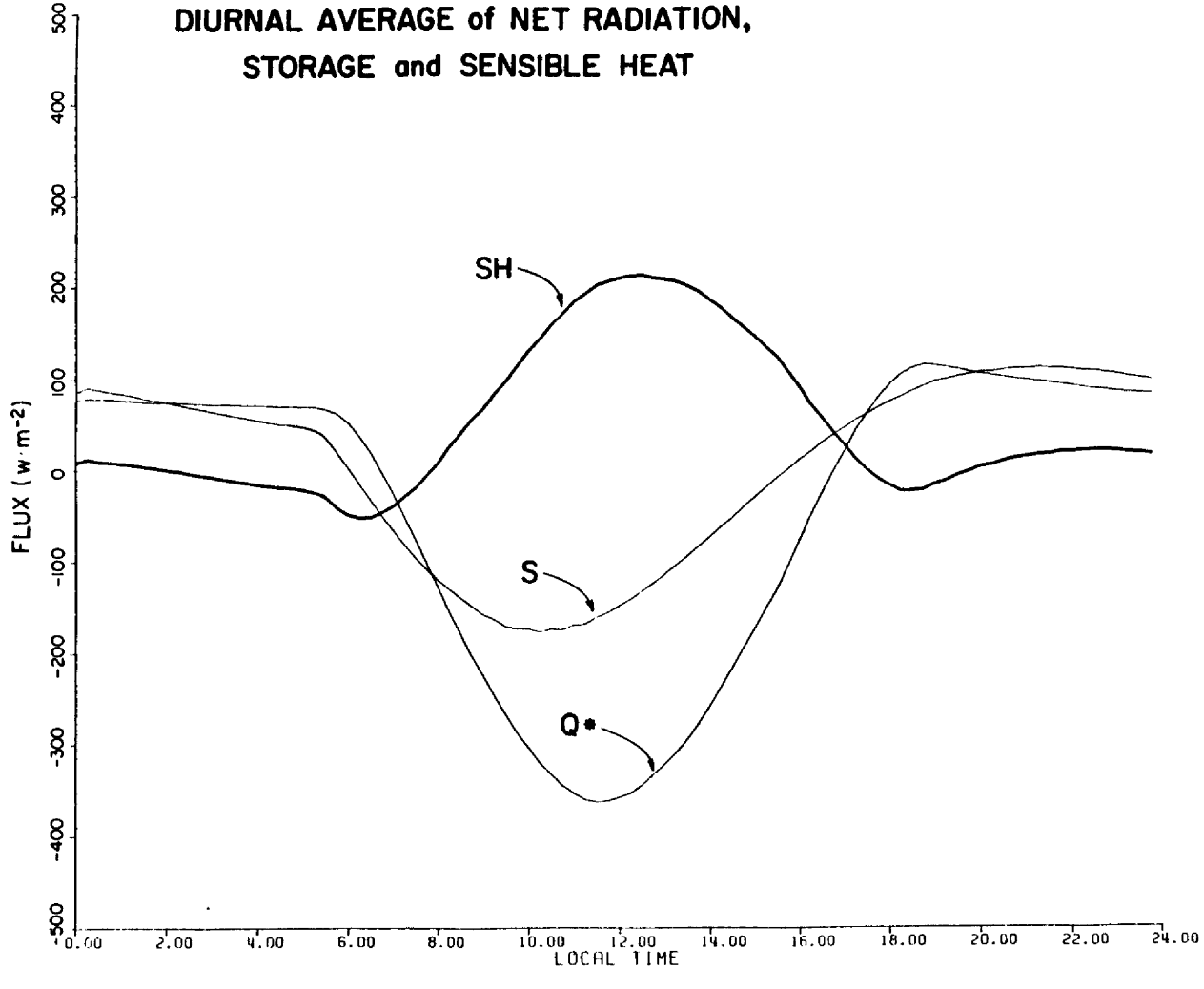

Fig. 5.28. Diurnal averages of the three principal terms in the surface energy budget at Sharouwrah (June, 1981).

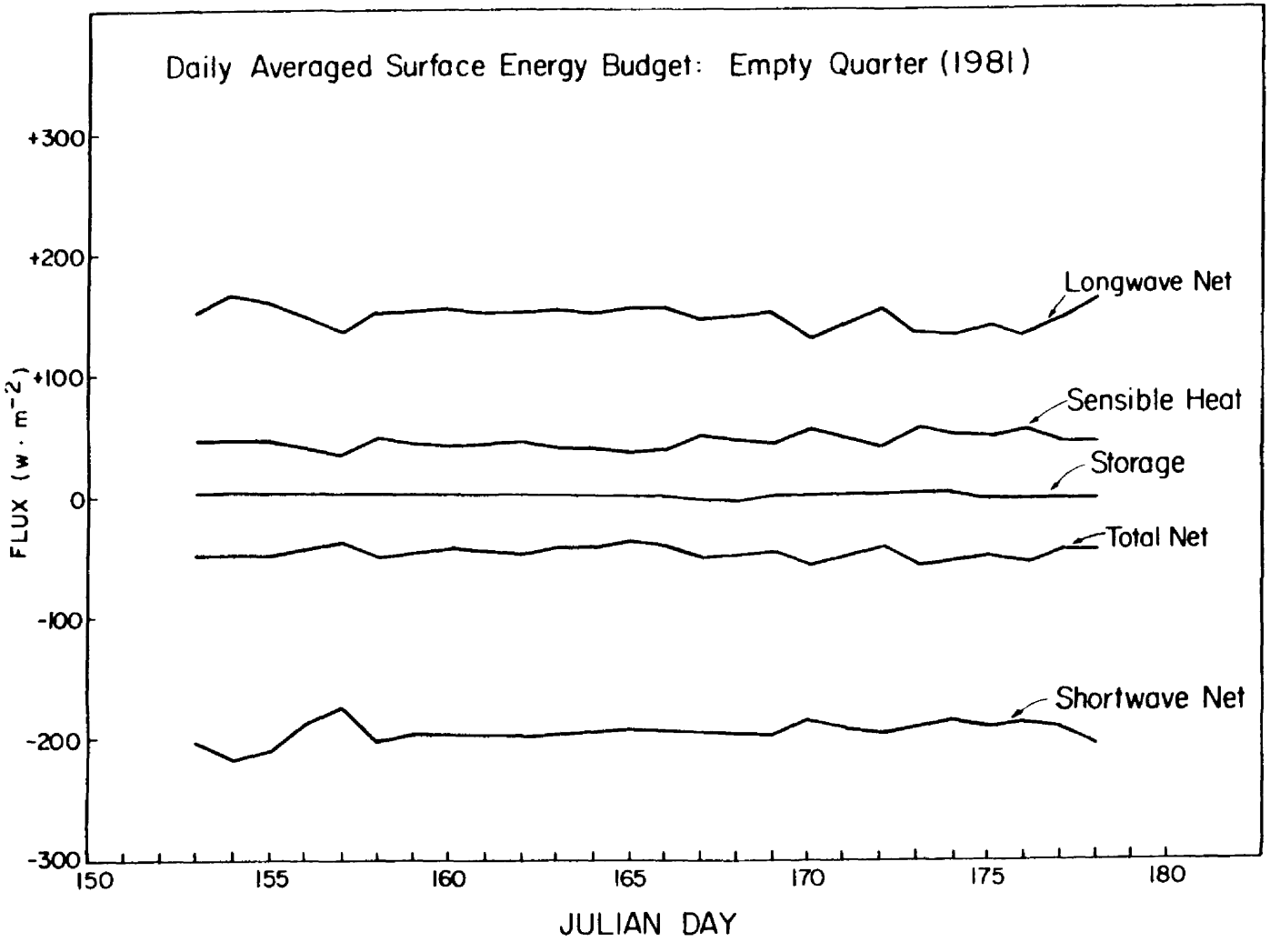

Fig. 5.29. Daily averaged surface energy budget process at Sharouwrah, Saudi Arabia during June, 1981.

It is seen that the daily surface energy budget is relatively constant over this period; however, there are perturbations in the trace. The perturbation during the day 155 - 158 period has a rather interesting source. If we examine the time series of state parameters for this period, as shown in Fig. 5.30, it can be noted that beginning on day 155 and ending on day 159 the relative humidity of the Sharouwrah site spikes rather dramatically during the daytime hours, particularly on days 157 - 158. The explanation for this event is due to a momentary increase in the intensity of the heat low. There are two possibilities as to the cause. A direct explanation would be that during this period the sun is at zenith at local noon, thus maximizing the strength of the daytime heating. The intensification of the heating, in turn, is just enough to sustain a daytime pressure gradient which is sufficient to transport moisture from the Red Sea coast and possibly out of the Hadramawt in Democratic Yeman (South Yeman). A second possibility is the indirect mechanism proposed by Ramage (1961). An inrease in the intensity of latent heat release to the south or east serves to increase subsidence over the heat low and thus the possibility of a moisture source through an indirect circulation. This moisture, in turn, interrupts the radiative exchange such that more solar convergence into the atmosphere takes place, thus increasing the shortwave net term. This effect is partially compensated by a decrease in the longwave net (the downward longwave flux is increased) due to increased emission from the pure rotational and rotational-vibration water vapor bands. The overall result is that the total net radiation is increased (thus moving it closer to zero) and therefore the sensible heating term is decreased.

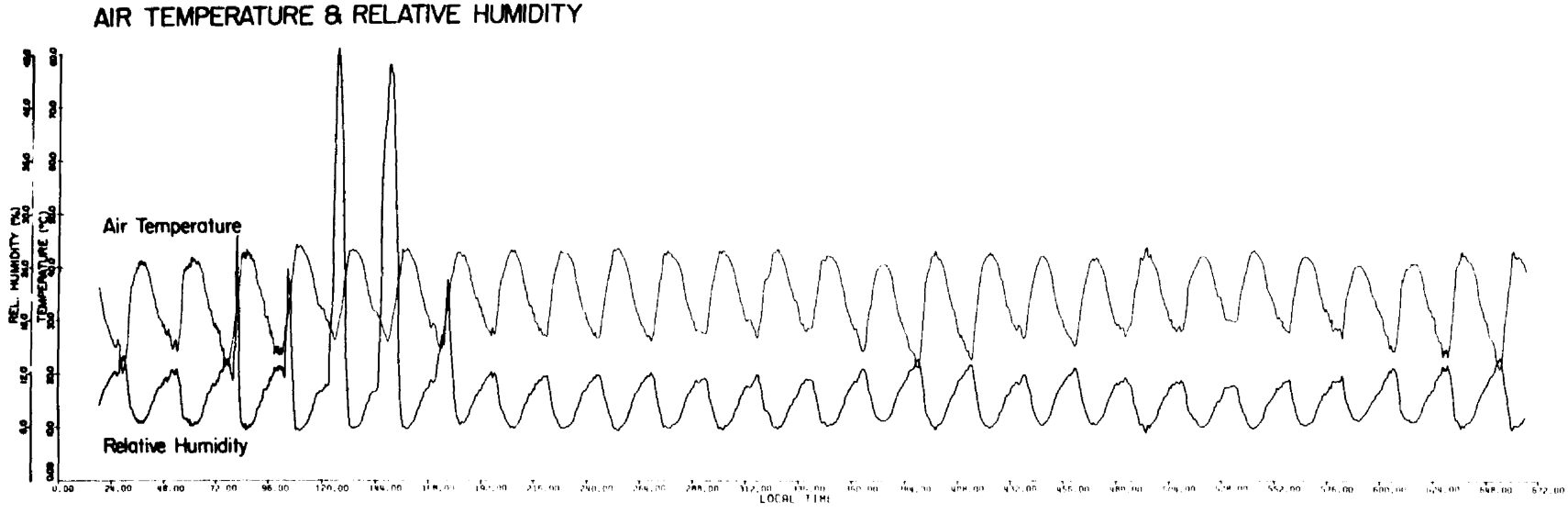

Fig. 5.30. Time series (15 minute sampling) of the air temperature and relative humidity at Sharouwrah during June, 1981.

Therefore there is a negative feedback effect taking place within the heat low. By increasing the heat low intensity, the surface cyclone draws moisture into the region which serves to decrease heat transport at the lower boundary. This negative feedback process may be somewhat unique to the Arabian heat low based on the land-water configuration which provides a readily available moisture source to the thermal 'heat pump'.

5.3.7 The Radiation Budget

A principal feature of the Arabian heat low that cannot be discounted in understanding its structure is the aerosol (dust) layer associated with the deep boundary layer. This aerosol layer and its radiative impact have been investigated in detail by AC-82 who found that shortwave convergence into the aerosol layer was approximately double that of a cloud and aerosol free atmosphere; see also Ellingson and Serafino (1984) and Kondratyev, et al. (1976). Longwave radiative exchange is not significantly altered by the dust component. Therefore, the dust layer provides a direct mechanism for inhibiting the radiative sink. The diurnal structure of the enhanced shortwave absorption is shown in Fig. 5.31. The dotted line (top curve) illustrates the clear sky transmittance representation of the heat low region based on an average temperature-mixing ratio profile derived from the CV-990 Empty Quarter flights. This result has been derived from a broad band radiative transfer model designed to incorporate the parameterized effects of aerosol and cloud. The albedo condition at the lower boundary of the model was based on measurements from the Sharouwrah surface station. The surface albedo curve is plotted as a dashed line in Fig. 5.31. The dash-dot curve illustrates the actual atmospheric

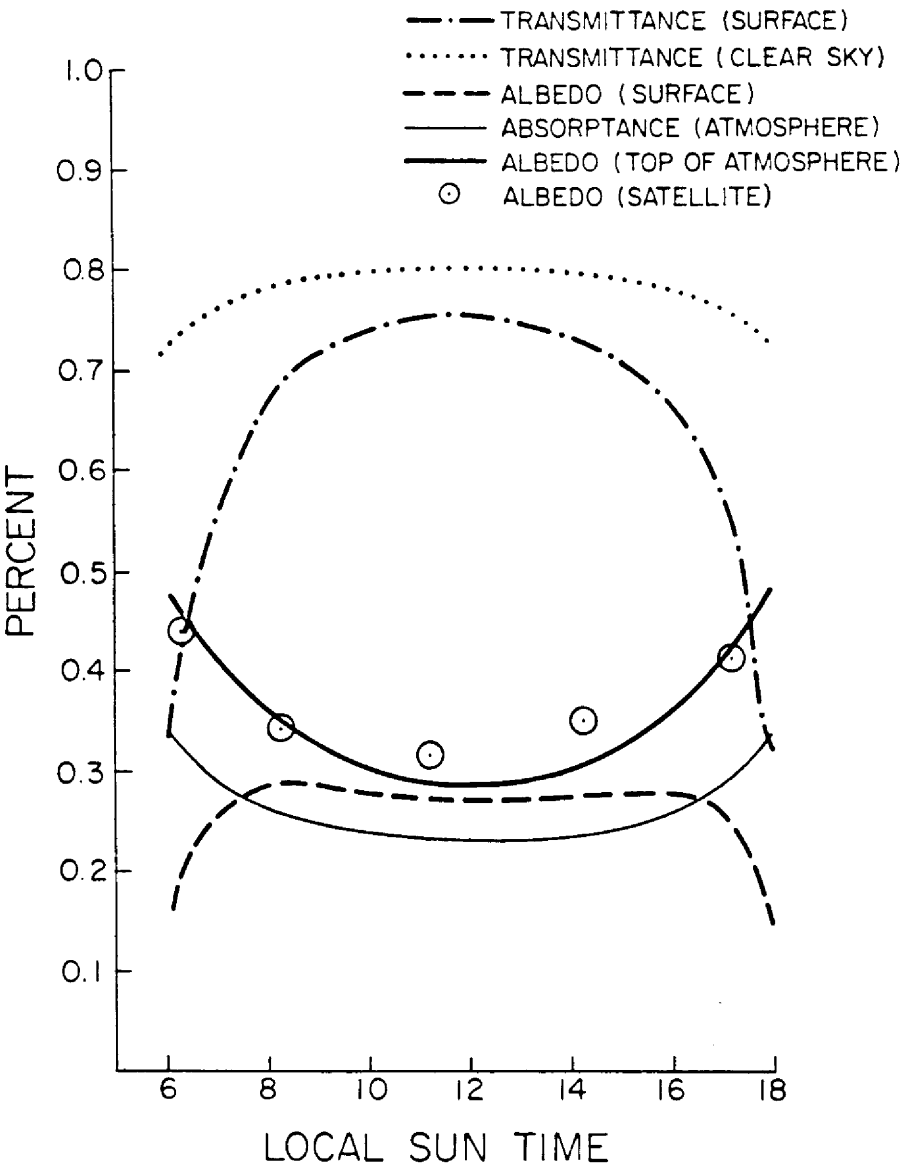

Fig. 5.31. Diurnal processes of shortwave radiation exchange within the Arabian heat low representative of June conditions.

transmittance; this calculation includes the effect of the aerosol loading. A broad band parameterization of dust fractional absorptance developed in the AC-82 investigation has been used to obtain the diurnal atmospheric absorptance curve (thin solid line). The model generated top-of-atmosphere albedo (thick solid line) has been validated with a satellite derived estimate of the desert albedo diurnal cycle (circles with dots). The satellite estimates were based on the parameterization techniques discussed in Chapter 2.

The important feature to note in this group is the dominant role of the aerosol. By differencing the clear sky and actual transmittance integrals, one obtains the absorptance due to the dust alone. This enhanced daytime shortwave absorptance is large enough to overcome the daily longwave cooling to the extent that the daily radiative divergence becomes negative from 500 to 800 mb as demonstrated in AC-82.

The satellite derived top-of-atmosphere radiation budget indicates that the Arabian heat low region is not radiatively deficit, but in fact slightly radiatively surplus. Daily time series for May - August, 1979 of the principal radiation budget terms for a 5 x 5^{o} box centered over the heat low region are shown in Fig. 5.32. These data have been obtained from the Nimbus 7 ERB Narrow-Field-of-View radiometer. The mean of the net radiation term over the four month period is +1.5 $W \cdot m^{-2}$ (the standard deviation is 9 $W \cdot m^{-2}$). In essence, the heat low region is effectively radiatively neutral at the upper boundary; it is assuredly not a radiative sink region. These results dispute the classic notion that all desert heat lows act in the role of radiative sinks. If, in fact, the Arabian heat low is a total energy source

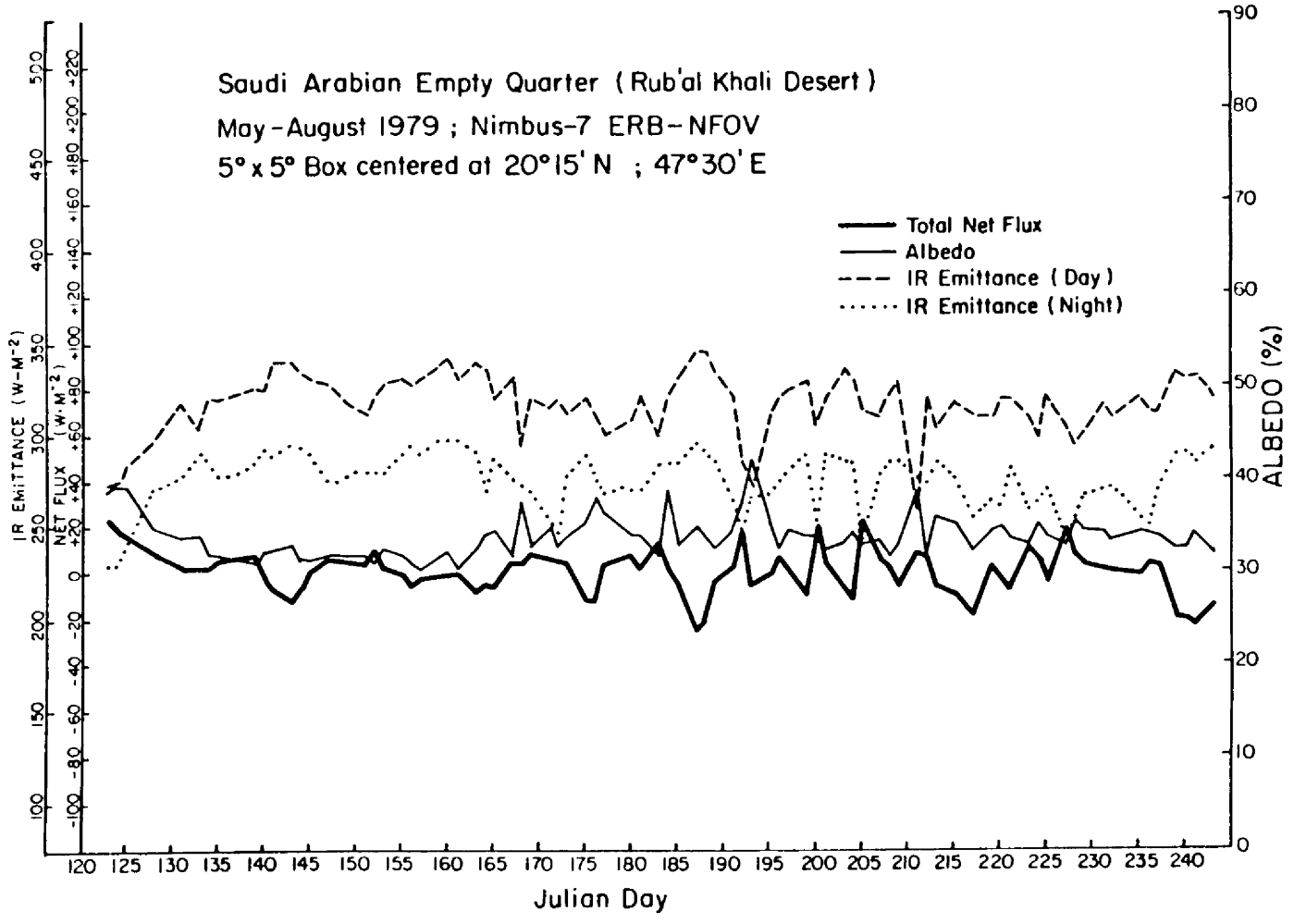

Fig. 5.32. Daily time series of the radiation budget parameters over the Arabian heat low from May through August, 1981. These data were obtained from the Nimbus 7 ERB Narrow-Field-Of-View radiometers.

region, i.e. contributing energy to surrounding monsoon processes, the essential question is one of how the energy excess is realized by the monsoon system.

5.4 Possible Role of the Heat Low

We have seen in the previous section, based on Nimbus 7 NFOV observations, that the net radiative convergence in the middle layers of the heat low is not dominated by longwave cooling in the remainder of the column. In fact, if we accept the mean value of the Nimbus 7 time series as the baseline, the heat low region is in slight radiative surplus. It is clearly not an absolute radiative sink, although as seen in the Nimbus 7 NFOV net radiation image illustrated in Fig. 5.33, it is a relative radiative sink.

If we compare the radiative divergence profile of AC-82 to the sensible heating rate at the surface and the required adiabatic warming rates due to the large scale subsidence field capping the heat low region, a composite picture of the vertical profile of energy exchange is obtained. A schematic illustration is shown in Fig. 5.34. The heat low can be characterized as a three layer system. The lower two layers form the deep mixed layer from the surface to 550 mb. The upper layer is a region in which the radiative cooling rate ($\approx 0.9^{\circ}C \cdot day^{-1}$) is approximately balanced by adiabatic heating ($\approx 0.8^{\circ}C \cdot day^{-1}$ subsidence warming). The middle layer from 800 to 550 mb is undergoing both radiative and subsidence heating ($\approx 1.0^{\circ}C \cdot day^{-1}$ and $0.5^{\circ}C \cdot day^{-1}$ respectively). The radiative convergence results from enhanced daytime shortwave absorption due to a substantial aerosol component (dust). The middle tropospheric dust is most likely maintained by dry convection and transport of dust stirred up at the surface by the daytime surface

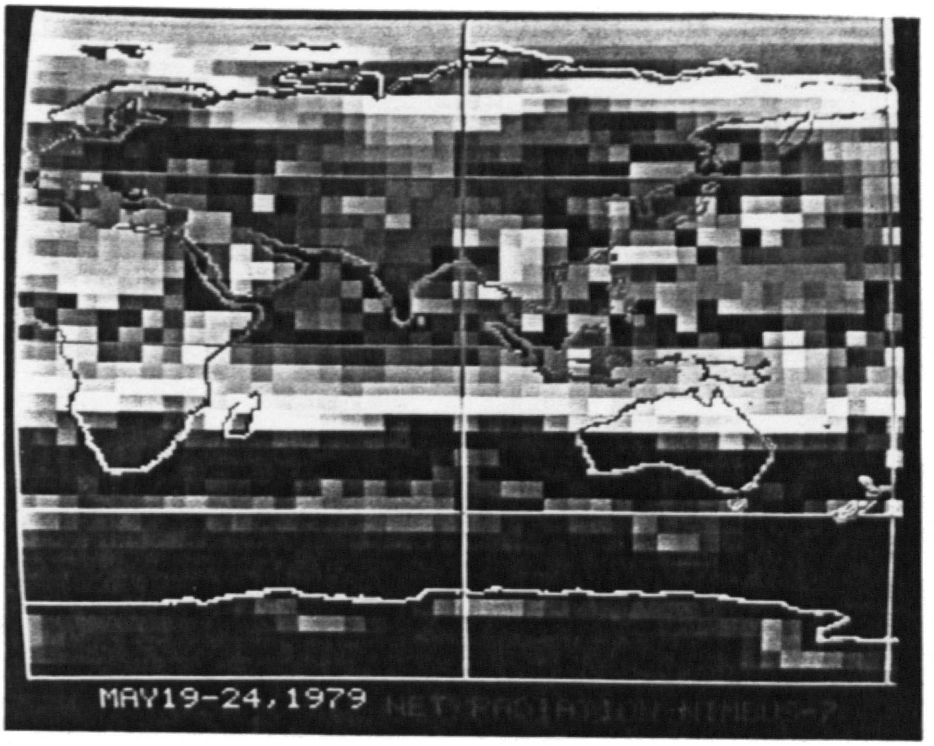

Fig. 5.33. Net radiation field derived from the Nimbus 7 ERB-NFOV radiometers over the Eastern Hemisphere from May 19-24, 1979 [KEY ($W \cdot m^{-2}$): dark red to light red ranges from +140 to +80; dark brown to light yellow ranges from +80 to -10; white to grey ranges from -10 to -20; light green to dark green ranges from -20 to -140; light blue to dark blue ranges from -140 to -200].

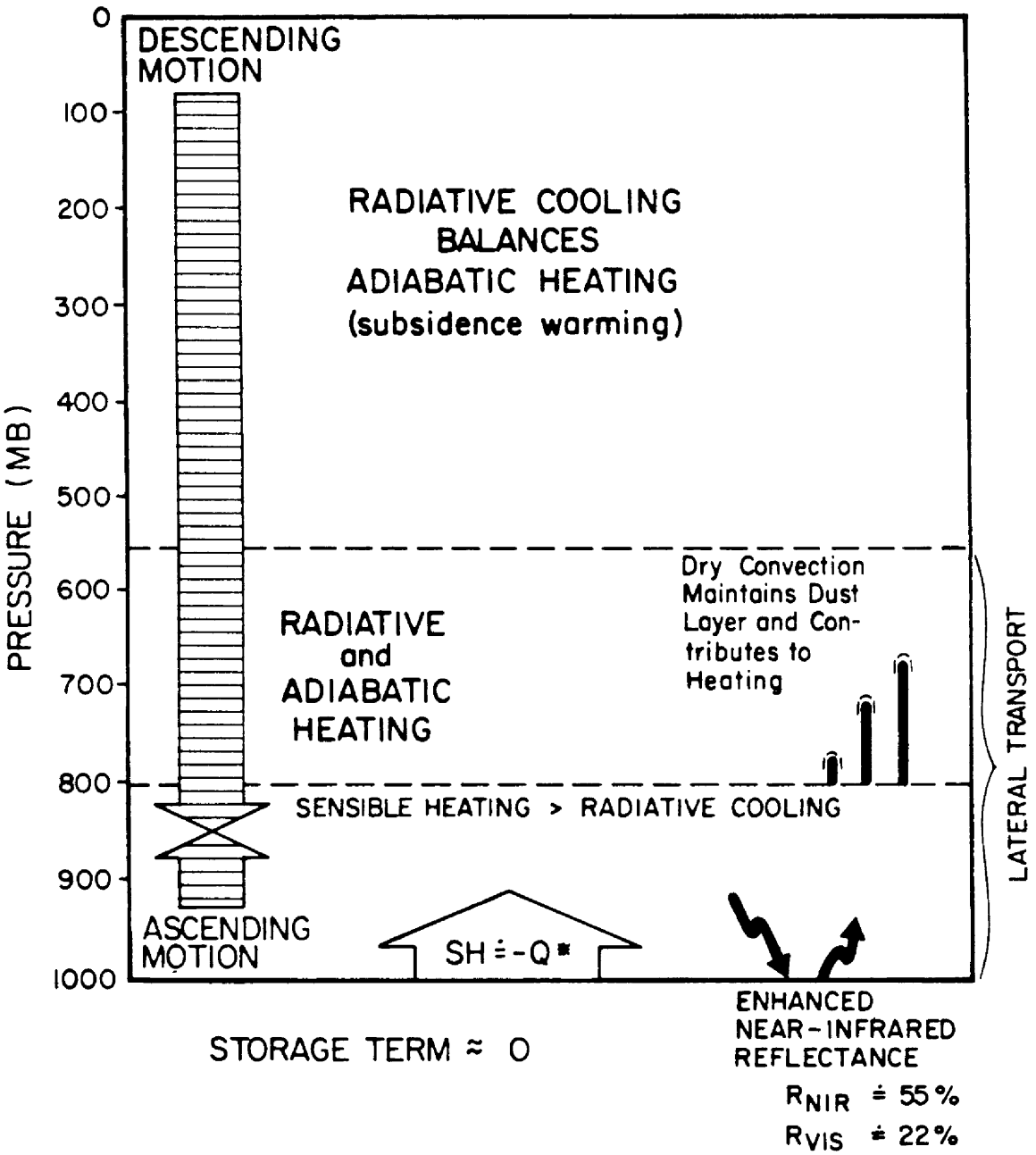

Fig. 5.34. Conceptual three layer structure of the Arabian heat low.

cyclone. Although it has yet to be demonstrated that the aerosol layer is maintained locally or by external transport, a reasonable conclusion is that much of the dust component originates from the superadiabatic layer within the heat low region itself. No direct observations are offered which suggest that dry convection is acting to maintain the middle tropospheric dust load; this is an inferred property based on the bumpiness and consistent chop that characterized our flights in and out of the Sharouwrah airstrip.

Finally in the lower layer (surface to 800 mb) the sensible heating ($\approx 2.2^{o}C \cdot day^{-1}$) dominates radiative divergence ($\approx 1.0^{o}C \cdot day^{-1}$ radiative cooling) resulting in a net lower tropospheric warming. The important radiation budget feature of the surface itself is the large difference in visible and near-infrared albedo. The results of the surface energy budget analysis suggests that a first order parameterization that is applicable at the surface, is $SH = -Q^{*}$ (for time scales longer than a day), since in the daily mean the storage term is approximately zero.

These results suggest that the middle and lower troposphere undergo net energy gain due to the diabatic processes overcoming the sustained adiabatic processes. The only possible equilibrium mechanism that can be posed to maintain this warming process is that the lower and middle layers must laterally transport heat out of the heat low region. Based on the vertical wind structure analysis of B-83 it appears that heat would be exhausted to the southeast in the general direction of the northwestern Arabian Sea. Ramage (1966) has pointed out how the great heat low belt from Somalia to Pakistan is a net exporter of cyclonic vorticity over the Northern Arabian Sea.

An important feature of the northwestern Arabian Sea during the summer period is that the thermodynamic structure exhibits a low level inversion. Ramage (1971) has described this feature as a pure subsidence inversion. Although a detailed description has yet to be obtained (see Reverdin and Sommeria, 1983), preliminary studies of Sen and Das (1980) and Rao, et al.(1980) suggest that the strength of the Arabian Sea inversion weakens towards the east and to the south. The peak inversion strength ($\approx 10^{o}C$) is found in the general vicinity of the point where the East African Jet (EAJ) splits into its northern branch and southern branch; see Findlater (1971). An additional third stream indicating features of a low level jet core has been documented by Gupta, et al.(1980). The northern two branches of this jet system [i.e. the double jet structure documented by the studies of Findlater (1969, 1971, 1972)] are critical features of the monsoon system in that they serve to generate and transport moisture to the west coast of India that is realized as monsoon precipitation; see also Rao et al. (1981).

Sen and Das (1980) have pointed out that the air properties capping the thermal inversion in the western Arabian Sea appear to be of continental origin rather than driven by an air-sea interface process. Thus an immediate conclusion is that the excess strength of the western Arabian Sea inversion is partly maintained by air mass dynamics rather than simply a subsidence inversion. As schematically illustrated in Fig. 5.35, the lateral exhaust mechanism out of the heat low region could serve to maintain a strong thermal inversion over the western Arabian sea jet cores. This jet system is most efficient in feeding moisture to the monsoon if moisture can be confined to the boundary layer and not be lost to explosive convective systems as it travels

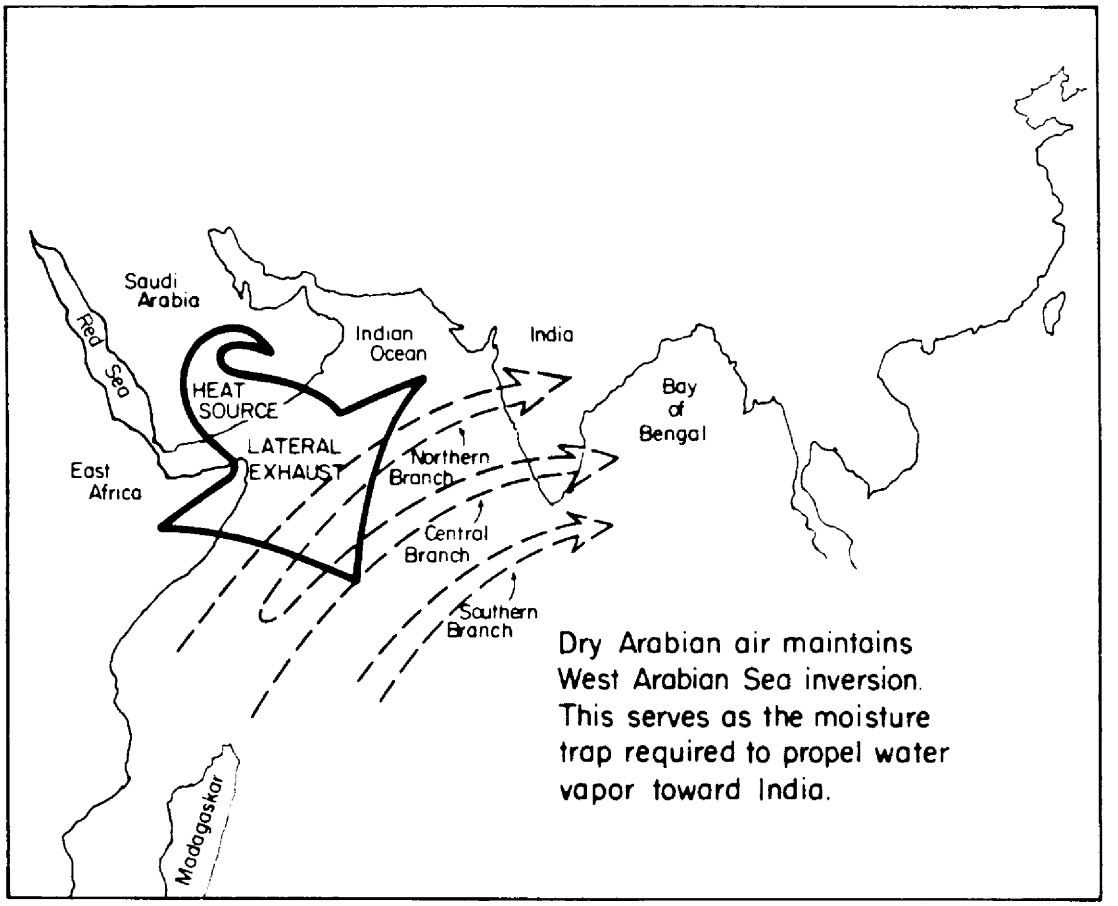

Fig. 5.35. Schematic illustration of the possible role of Arabian heat low in supporting the maintenance of Southwest Monsoon rainfall.

toward the west Indian coast. The importance of cross-Arabian Sea water vapor transport in supporting monsoon rainfall has been discuseed by Cadet and Reverdin (1981).

There is no reason to believe that a western Arabian Sea air mass inversion must be solely driven by an Arabian heat source. The semi-arid and desert regions of East Africa, Iran and Pakistan may also contribute to the process; see Grossman and Duran (1984). A further remaining question in monsoon dynamics is the degree to which the deserts surrounding the Arabian Sea tend to prevent the lower troposphere from adhering to a baratropic basic state. The degree of baroclinicity needed to describe the structure, maintenance and oscillations of the EAJ is a theoretical problem that remains under study; see Anderson (1976), Bannon (1979a, 1979b, 1982), Hart (1977), Krishnamurti and Wong (1979), Krishnamurti, et al.(1976, 1983), and Rubenstein (1981). It is recognized, however, that more thorough experiments in this region of the world are needed in order to fully understand the role of the African and Middle Eastern deserts on the Southwest Monsoon system.

5.5 Summary

The preceding analysis has examined various aspects of the Arabian heat low with the intent of describing its structure and assessing its significance within the context of the Southwest Monsoon. The structure of the heat low is summarized as follows. In terms of the large scale radiative fields, the Arabian Empty Quarter exhibits the high albedo properties characteristic of another principal heat souce region within the Southwest Monsoon domain (the Tibetan Plateau), as well as the extensive monsoon cloud systems. The factor which differentiates the

high albedo desert from the other two features is that the desert albedo is a stationary and relative constant signal whereas the Tibetan Plateau's albedo signal, albeit stationary, is seasonally modulated. The monsoon cloud system's signal is non-stationary and modulated by dynamic monsoon oscillations. In the longwave spectrum the Arabian Empty Quarter is the dominant monsoon feature in terms of emitted infrared radiation over the monsoon domain. The strength of the IR signal denotes the intense surface heating associated with the heat low and is thus indicative of why the pressure field adjusts to form the surface depression associated with the thermal low. The net radiation fields indicate the relative radiative sink properties of the desert heat low but also show that this desert feature is not unlike a vast circumscribing ring of additional relative radiative sink features that surround the principal source of latent heat release within the southwest monsoon, i.e., the monsoon trough. Presumably this pattern of net radiation is a necessary condition for energy balance within the monsoon domain.

The vertical thermodynamic structure of the heat low is highlighted by deep mixed layer properties extending to approximately 550 mb. During the daytime, a shallow surface cyclone forms in adjustment to the surface pressure gradient; this feature is capped by the subsidence field extending to nearly 850 mb. During the late nighttime-early morning period, after infrared radiative cooling dissipates the thermal anomaly, the subsidence field extends to the surface.

The radiative properties of the desert surface are remarkable in terms of their regular diurnal periodicity. The almost pure rythmic nature of the surface radiation budget distinguishes the extremely dry

Empty Quarter region from the surrounding regions in which moisture processes interrupt the uniformity of surface radiation exchange. An important property of the desert surface is the more than 2 to 1 difference between near-infrared and visible directional reflectance. The high albedo properties of a desert surface are effectively driven by this spectral discontinuity, a feature of deserts not detectable with VIS channel weather satellite instruments. There is an important implication concerning this property of the desert surface. Since the strong lines responsible for significant water vapour absorption of solar radiation are all located in the near-infrared spectrum, it is the combination of boundary layer moisture and the shape of the near-infrared spectral directional reflectance function which control the shortwave surface radiation budget. This effect has avoided detection by weather satellites and is not easily quantified with the classical large field-of-view radiation budget type instruments. This property of deserts is best illustrated by noting the variation in the daily averaged near-infrared directional reflectance time series in contrast to the near flatness of the visible directional reflectance time series.

The wind and state parameters at the surface also exhibit a very steady and well organized diurnal structure. One feature of the wind field which has not been explained is the relative lull in wind speed at local noon when surface heating would be most intense. The diurnal cycle of wind direction would indicate that the surface cyclone, associated with the thermal low, would be sustained until after local midnight.

Day-night surface skin temperatures exhibit extreme differences up to 48-50^{o}C. This is a unique signature of the moisture deficit sub-

tropical deserts. It is the lack of moisture which allows both the unblocked shortwave convergence (which leads to the intense daytime heating) and the excessive longwave divergence (which leads to the efficient nighttime cooling). It was noted that the diurnal amplitude of surface skin temperature was not well correlated with boundary layer stability (in this case a bulk Richardson Number). This suggests, indirectly, that it is the total optical path of boundary layer moisture which radiatively controls the magnitude of day-night skin temperature differences, whereas wind driven heat diffusion plays a somewhat minor role.

It was also noted how the diurnal heat storage term deviates from local noon symmetry; this results from the systematic phase-shifting with depth of the subsurface thermal waves (characteristic of almost all natural earth surfaces). This asymmetry is manifested in an assymetry in the surface sensible heat cycle. The magnitude of the asymmetry, along with the more obscure non-sinusoidal nature of the subsurface thermal waves, can be considered as quantitative signatures of a desert. It is pointed out that as surface vegetation and subsurface moisture enter the picture, the ground capacitance and conductivity will be altered so as to modify the shapes of the ground heat storage cycle and the subsurface thermal waves.

The diurnal amplitudes of the surface energy budget terms are high, indicating that the desert surface is an efficient absorber-emitter (approaching black body). Since the asymmetry in the diurnal ground heat storage cycle(S) leads to a reversed asymmetry in the diurnal sensible heat exchange cycle (SH), the latter is thus phase shifted past local noon and out of phase with the diurnal surface net radiation cycle

(Q*). On the other hand, it is emphasized that the desert is a poor heat capacitor so that it does not exhibit any significant daily trends in the surface energy budget terms (no thermal memory). Because of the low heat capacity of sand, the desert tends to withstand seasonal drifts in the surface energy budget and thus a first order approximation for surface sensible heat exchange, on a daily averaged time scale, is SH = -Q*. Nevertheless, there are perturbations in the daily averaged surface energy budget, one of which arises from a surge of moisture during an intensification of the heat low. The impact of this event is to eventually reduce the sensible heat exchange, a type of negative feedback process.

The top-of-atmosphere radiation budget measurements from Nimbus-7 indicate that the Arabian heat low is not radiatively deficit, but instead, radiatively neutral or even slightly radiatively surplus. This condition arises from the convergence of shortwave radiation into the aerosol laden deep mixed layer, an energy gain effect which serves to overcome infrared cooling and the high desert albedo. The combined diabatic processes (radiative and sensible heating), in conjunction with the adiabatic subsidence heating over the heat low, leads to the heat low region acting as an absolute energy source. It's vertical structure can be summarized as a three layer atmosphere in which the lower and middle layers undergo steady state total heating.

In order to balance this total heating effect it is hypothesized that the excess heat is laterally transported off the Arabian peninsula out over the western Arabian Sea. Thermal advection would serve to maintain the strong low level temperature inversion associated with region (an air mass inversion effect superimposed on the large scale

subsidence inversion). This inversion is assumed to be a important control in retaining low level moisture within the confines of the monsoon low level jet such that it can be effectively transported into the monsoon trough.

Aside from the basic structure of the heat low, and its possible role in influencing one portion of the monsoon system (i.e. the northwestern Arabian Sea), a far more reaching question is posed concerning the role of the broader scale subtropical desert system encompassing the Southwest Monsoon to the west and north. Clearly, latent heat release within the tropical maximum cloud zone (MCZ) and the monsoon rains is a dominant mode of energy exchange within the monsoon system. Consequently, the deserts are required to absorb a certain portion of this heating through the indirect process of zonal and meridional overturning (secondary circulations). These secondary circulations lead to the quasi-steady state subsidence fields required for desert maintenance. Subsidence and the associated precipitation suppression are critical in desert maintenance for the middle eastern and south Asian deserts since they are adjacent to the Mediterranean and Indian Ocean moisture sources. It is the potential availability of moisture which distinguishes these deserts from the mid-latitude and polar deserts which are totally devoid of moisture sources either from the lack of transport mechanisms to the continental interiors or because they are situated in rain shadows. Sub-tropical deserts are thus characterized as relative energy sinks which help organize the large scale circulation to redistribute the excess energy associated with the tropics.

However, this view of deserts is only operative at the very large scales. There would appear to be scales of influence embedded within the larger domain (synoptic and sub-synoptic scales) in which the deserts manifest themselves as local energy sources to processes which feed back to the larger scale, in particular, feed back to processes which influence the distribution of moisture which the deserts themselves lack. Considering deserts in that light leads one to speculate whether one region's desert gives rise to another region's Savannah. The possibility certainly then exists that desertification (or the more contemporary term of desertization) is not a process of overall desert expansion, but rather one of desert redistribution. Arabia, after all, was a fertile region approximately 5,000 years ago, albeit the climate was presumably warmer; see Glantz (1977).

An important numerical experiment of Hahn and Manabe (1975), concerning the role of orography on the Southwest Monsoon, demonstrated that the Tibetan Plateau was essential for a monsoon climate in Southern Asia. This result was obtained by rerunning a July simulation after removing the mountain topography. It would be interesting to test the role of the great Middle Eastern-South Asian desert crescent in much the same fashion as this would provide insight on whether seasonal and interannual changes in desert climate are important in influencing monsoon climate.

Clearly, more study is needed to understand the role of the Arabian heat low and the much larger surrounding desert system on the mean monson circulation and in invoking perturbations to the system. Nevertheless, it now seems reasonable to conclude that individual deserts and their associated heat lows provide a mixture of conditions

for the atmosphere to assimilate; the Arabian heat low being just one part of a whole fabric of desert environments.

6.0 CONCLUSIONS

The following provides a final summary of the four part dissertation. It has been shown in Chapter 2, concerning the parameterization study, that weather satellite filtered radiance measurements are readily adaptable for radiation budget analyses, but only within certain limits of accuracy. It is very important to understand that the time and space scales chosen for an analysis scheme dictate the resulting biases and RMS uncertainties. It is pointed out that the problem of transforming narrow band satellite radiances to broad band flux estimates is best treated as a problem in atmospheric physics, not statistical regression. By choosing the former course, there is not only considerable room for improvement, but also the solutions will exhibit more solid foundations for diagnosing the causes and effects of the uncertainties.

It has been shown that the NB-NFOV to BB-WFOV relationships are highly non-linear and strongly forced by natural variations in atmospheric and surface properties. The impacts of these non-linearities on the more localized space and time scales, are considered in Chapter 3 in conjunction with ERB narrow-field-of-view (NFOV) scanner data. It has been shown that the selected radiation budget averaging strategy may preclude the requirement of applying portions of the parmeterized transformation model. The foremost example is the cancellation of bi-directional reflectance normalization effects when taking daily averages of shortwave fluxes over an ocean-cloud domain.

There are obvious cases in the existing literature in which weather satellite RADBUD estimates have been used in such a fashion to obscure scientific understanding, not to clarify. One must always guard against this possibility when using indirect measures of a physical process. In-so-far as the ultimate objectives of developing the parameterization scheme, the primary concern is with the generation of high resolution daily and diurnal time series of the radiation exchange terms over the SMONEX region. The weather satellite analyses are used to understand the role of radiative forcing associated with the Southwest Monsoon system and to characterize the dramatic and discontinuous gradients associated with the radiation budget parameters going from pre-monsoon to monsoon-onset phases, and during the monsoon-surge and monsoon-break oscillations that characterize a complete Southwest Monsoon season.

In Chapter 3, radiation budget parameters deriverd from three satellite systems have been analyzed over a variety of space and time scales for the 1979 Southwest Monsoon. First the evolution of the monsoon is presented by the use of high resolution (1/2 by 1/2 degree) 5-day averages of contoured radiation exchange fields. These maps provide a first hand view of many of the elements that make up a complete monsoon season. The pre-monsoon conditions, the early tropical storms, the northward propagation of the monsoon MCZ, the advance of the S.E. Asian monsoon, the explosive southwest monsoon onset, the surges, fluctuations, and breaks of the monsoon, and the seasonal changes over the Tibetan Plateau, are all well depicted through use of the contoured pentad averages.

To provide an evolutionary view, at a much larger scale, Nimbus-7 NFOV net radiation maps (6 day averages) are presented. These maps illustrate very clearly the cellular pattern in net radiation across the eastern hemispheric tropics. An interesting research problem involves the search for clues that would relate the cellular pattern to monsoon onset and intensity; i.e., the use of the net radiation parameter in the detection of monsoon teleconnections.

When the monsoon is presented on the zonal average scale over the complete monsoon domain, a very concise portrayal of the oscillatory nature of the monsoon is seen. The northward propagating MCZ, of period 40-50 days, is the dominant feature although the quasi-biweekly and short period oscillations are clearly in evidence. The meridionally averaged monsoon, in particular the time-longitude section of net radiation, exhibits the signature of a monsoon break. The breaks are most evident in the radiation fields at western Indian longitudes. The meridionally averaged monsoon also exhibits an albedo merging effect between the Bay of Bengal and the Tibetan Plateau, once monsoon onset takes place. An important remaining problem concerns the degree of interannual variability of the zonally and meridionally averaged monsoon.

One of the more striking features, in terms of radiative forcing, is the systematic reduction of radiative input into the complete monsoon domain during the initiation phase (radiative blocking). An analysis of the net radiation maps derived from the AVHRR data suggest that the depletion of energy, during June, with resect to local noon, is on the order of 5 peta-watts. It is not known at this time what the year to

year variation of the magnitude and regularity of the blocking effect would be.

An examination of localized area time series of radiation budget parameters has been presented. It was noted that although localized time series quite clearly indicate the major monsoon episodes, they tend to obscure the exact oscillatory nature of the monsoon, particularly the long period and quasi-biweekly oscillations.

The local area radiation budget time series, constructed from Nimbus-7 narrow-field-of-view measurements, and the corresponding time series estimated from the AVHRR data, are generally in good correspondence. One exception is the net radiative term over desert. The AVHRR $\overline{Q^*}$ estimates correlate very poorly with the Nimbus-7 NFOV Q* measurements over a region on the Arabian Peninsula because of the near constancy of desert radiation properties.

The periodogram analysis shows that both the zonal average time series and the local area time series generate power at the three dominant modes of monsoon oscillation (short period, quasi-biweekly period, long period), although at the zonal average scale the quasi-biweekly mode tends to proliferate over a range of frequencies.

The diurnally averaged monsoon is obtained by dividing the monsoon domain up into 12 sub-regions. Within each sub-region the evolution of the monsoon is presented through three 10-day periods corresponding to pre-monsoon onset (June 1-10), monsoon onset (June 11-20), and post-monsoon onset (June 21-30). By calculating time and space gradients of the diurnal cycles, the magnitudes of differential radiative convergence is obtained. This process is highlighted by calculating temporal gradients of Q* over the Indian sub-continent. Although there is

systematic radiative divergence over the three 10-day periods (the radiative blocking effect), the nighttime tendency during the diurnal cycle tends to show radiative gain. In other words, the radiative blocking effect is a shortwave (daytime) process partially offset by longwave convergence.

Finally, the concept of cloud induced radiative decoupling of the shortwave and longwave surface radiative fluxes is reviewed. It is pointed out that there is an analogous decoupling effect taking place at the top-of-atmosphere. Correlative analysis is used to show how variation in the zonal and meridional cloud and surface backgrounds tends to decorrelate the principal radiative budget terms of albedo, infrared emission, and net radiation.

Chapter 4 describes a surface energy budget monitoring program that has been carried out in remote desert and mountain environments. This program has been designed to characterize the surface heat and moisture exchange terms in lowland and highland deserts known to interact with large-scale monsoon systems. In order to implement the surface measurement program, various surface energy budget systems have been designed and tested. They have returned quantitative and detailed measurements of the surface energy exchange process. These systems have proved dependable, relatively maintenance free, and their automated microprocessing capabilities have eliminated much of the lag time between observation and analysis because most of the calibration and data reduction procedures (statistical processing) are carried out in the field.

These systems have a definite role in future attempts to develop a global land surface climatology such as outlined in a new WMO program

called the International Satellite Land Surface Climatology Project. The systems are relatively inexpensive, easy to operate, and will provide excellent ground truth needed for the development of satellite algorithms and parameterizations.

The systems have been deployed in the deserts of Saudi Arabia and the Colorado Rocky Mountains; a dual-system configuration was recently deployed in the Gobi desert. In 1985 various of these dual stations will be deployed on the Tibetan Plateau within the Peoples Republic of China.

The results of the Arabian measurement program illustrate not only the daily and diurnal processes that characterize the desert interior, they also illustrate some unique radiative features characteristic of excessively dry desert regions and provide critical surface boundary information needed in the description and understanding of the Arabian desert heat low. Some preliminary results concerning the radiative characteristics of the Gobi desert have also been shown.

The tests at Pingree Park, Colorado have demonstrated the feasibility of using less expensive, but maintenance free sensors for monitoring components of the PBL turbulent heat exchange process. A four-way approach for calculating the sensible and latent heat exchange terms has been described in conjunction with a discussion of how the 'Radiation' and 'Tower' Stations, used in tandem, offer a multi-mode solution to estimating the surface energy exchange terms.

Finally, a description of how the surface energy budget stations can be used in conjunction with satellite and aircraft data to complete the specification of the external boundary conditions, essential in any thorough treatment of atmospheric energetics. In this context, various

examples of how to implement the multi-platform monitoring approach for both the Arabian desert and the Tibetan Plateau have been provided.

Based on the multi-platform monitoring strategy outlined in Chapter 4, Chapter 5 goes on to examine the Arabian heat low with the objective of describing its structure and assessing its significance within the context of the Southwest Monsoon. The structure of the heat low is summarized as follows. In terms of the large scale radiative fields, the Arabian Empty Quarter exhibits the high albedo properties characteristic of another principal heat souce region within the Southwest Monsoon domain (the Tibetan Plateau), as well as the extensive monsoon cloud systems. The factor which differentiates the high albedo desert from the other two features is that the desert albedo is a stationary and relative constant signal whereas the Tibetan Plateau's albedo signal, albeit stationary, is seasonally modulated. The monsoon cloud system's signal is non-stationary and modulated by dynamic monsoon oscillations. In the longwave spectrum the Arabian Empty Quarter is the dominant monsoon feature in terms of emitted infrared radiation over the monsoon domain.

The strength of the IR signal denotes the intense surface heating associated with the heat low and is thus indicative of why the pressure field adjusts to form the surface depression associated with any thermal low. The net radiation fields indicate the relative radiative sink properties of the desert heat low but also show that this desert feature is not unlike a vast circumscribing ring of additional relative radiative sink features that surround the principal source of latent heat release within the southwest monsoon, i.e., the monsoon trough.

Presumably this pattern of net radiation is a necessary condition for energy balance within the monsoon domain.

The vertical thermodynamic structure of the heat low is highlighted by deep mixed layer properties extending to approximately 550 mb. During the daytime, a shallow surface cyclone forms in adjustment to the surface pressure gradient; this feature is capped by the subsidence field extending to nearly 850 mb. During the late nighttime-early morning period, after infrared radiative cooling dissipates the thermal anomaly, the subsidence field extends to the surface.

The radiative properties of the desert surface are remarkable in terms of their regular diurnal periodicity. The almost pure rythmic nature of the surface radiation budget distinguishes the extremely dry Empty Quarter region from most surrounding regions in which moisture processes interrupt the uniformity of surface radiation exchange.

An important property of the desert surface is the more than 2 to 1 difference between near-infrared and visible directional reflectance. The high albedo properties of a desert surface are effectively driven by this spectral discontinuity, a feature of deserts not detectable with VIS channel weather satellite instruments. There is an important implication concerning this property of the desert surface. Since the strong lines responsible for significant water vapour absorption of solar radiation are all located in the near-infrared spectrum, it is the combination of boundary layer moisture and the shape of the near-infrared spectral directional reflectance function which control the shortwave surface radiation budget. This effect has avoided detection by weather satellites and is not easily quantified with the classical large field-of-view radiation budget type instruments. This property of

deserts is best illustrated by noting the variation in the daily averaged near-infrared directional reflectance time series in contrast to the near flatness of the visible directional reflectance time series.

The wind and state parameters at the surface also exhibit a very steady and well organized diurnal structure. One feature of the wind field which has not been explained is the relative lull in wind speed at local noon when surface heating would be most intense. The diurnal cycle of wind diretion would indicate that the surface cyclone, associated with the thermal low, would be sustained until after local midnight.

Day-night surface skin temperatures exhibit extreme differences up to 48-50^{o}C. This is a unique signature of the moisture deficit sub-tropical deserts. It is the lack of moisture which allows both the unblocked shortwave convergence (which leads to the intense daytime heating) and the excessive longwave divergence (which leads to the efficient nighttime cooling). It was noted that the diurnal amplitude of surface skin temperature was not well correlated with boundary layer stability (in this case a bulk Richardson Number). This suggests, indirectly, that it is the total optical path of boundary layer moisture which radiatively controls the magnitude of day-night skin temperature differences, whereas wind driven heat diffusion plays a somewhat minor role.

It was also noted how the diurnal heat storage term deviates from local noon symmetry; this results from the systematic phase-shifting with depth of the subsurface thermal waves (characteristic of almost all natural earth surfaces). This asymmetry is manifested in an assymetry in the surface sensible heat cycle. The magnitude of the asymmetry,

along with the more obscure non-sinusoidal nature of the subsurface thermal waves, can be considered as quantitative signatures of a desert. It is pointed out that as surface vegetation and subsurface moisture enter the picture, the ground capacitance and conductivity will be altered so as to modify the shapes of the ground heat storage cycle and the subsurface thermal waves.

The diurnal amplitudes of the surface energy budget terms are high, indicating that the desert surface is an efficient absorber-emitter (approaching black body). Since the asymmetry in the diurnal ground heat storage cycle(S) leads to a reversed asymmetry in the diurnal sensible heat exchange cycle (SH), the latter is thus phase shifted past local noon and out of phase with the diurnal surface net radiation cycle (Q^*). On the other hand, it is emphasized that the desert is a poor heat capacitor so that it does not exhibit any significant daily trends in the surface energy budget terms (no thermal memory). Because of the low heat capacity of sand, the desert tends to withstand seasonal drifts in the surface energy budget and thus a first order approximation for surface sensible heat exchange, on a daily averaged time scale, is $SH = -Q^*$. Nevertheless, there are perturbations in the daily averaged surface energy budget, one of which arises from a surge of moisture during an intensification of the heat low. The impact of this event is to eventually reduce the sensible heat exchange, a type of negative feedback process.

The top-of-atmosphere radiation budget measurements from Nimbus-7 indicate that the Arabian heat low is not radiatively deficit, but instead, radiatively neutral or even slightly radiatively surplus. This condition arises from the convergence of shortwave radiation into the

aerosol laden deep mixed layer, an energy gain effect which serves to overcome infrared cooling and the high desert albedo. The combined diabatic processes (radiative and sensible heating), in conjunction with the adiabatic subsidence heating over the heat low, leads to the heat low region acting as an absolute energy source. It's vertical structure can be summarized as a three layer atmosphere in which the lower and middle layers undergo steady state total heating.

In order to balance this total heating effect it is hypothesized that the excess heat is laterally transported off the Arabian peninsula out over the western Arabian Sea. Thermal advection would serve to maintain the strong low level temperature inversion associated with region (an air mass inversion effect superimposed on the large scale subsidence inversion). This inversion is assumed to be a important control in retaining low level moisture within the confines of the monsoon low level jet such that it can be effectively transported into the monsoon trough.

Aside from the basic structure of the heat low, and its possible role in influencing one portion of the monsoon system (i.e. the northwestern Arabian Sea), a far more reaching question is posed concerning the role of the broader scale subtropical desert system encompassing the Southwest Monsoon to the west and north. Clearly, latent heat release within the tropical maximum cloud zone (MCZ) and the monsoon rains is a dominant mode of energy exchange within the monsoon system. Consequently, the deserts are required to absorb a certain portion of this heating through the indirect process of zonal and meridional overturning (secondary circulations). These secondary circulations lead to the quasi-steady state subsidence fields required

for desert maintenance. Subsidence and the associated precipitation suppression are critical in desert maintenance for the middle eastern and south Asian deserts since they are adjacent to the Mediterranean and Indian Ocean moisture sources. It is the potential availability of moisture which distinguishes these deserts from the mid-latitude and polar deserts which are totally devoid of moisture sources either from the lack of transport mechanisms to the continental interiors or because they are situated in rain shadows. Sub-tropical deserts are thus characterized as relative energy sinks which help organize the large scale circulation to redistribute the excess energy associated with the tropics.

However, this view of deserts is only operative at the very large scales. There would appear to be scales of influence embedded within the larger domain (synoptic and sub-synoptic scales) in which the deserts manifest themselves as local energy sources to processes which feed back to the larger scale, in particular, feed back to processes which influence the distribution of moisture which the deserts themselves lack. Considering deserts in that light leads one to speculate whether one region's desert gives rise to another region's Savannah. The possibility certainly then exists that desertification (or the more contemporary term of desertization) is not a process of overall desert expansion, but rather one of desert redistribution. Arabia, after all, was a fertile region approximately 5,000 years ago, albeit the climate was presumably warmer.

Previous numerical experiments, concerning the role of orography on the Southwest Monsoon, have demonstrated that the Tibetan Plateau is essential for the mean monsoon climate in Southern Asia. These results

are obtained by removing mountain topography during a simulation and comparing results to a reference experiment. It would be interesting to test the role of the great Middle Eastern-South Asian desert crescent in much the same fashion as this would provide insight on whether seasonal and interannual changes in desert climate are important in influencing monsoon climate.

Clearly, more study is needed to understand the role of the Arabian heat low and the much larger surrounding desert system on the mean monson circulation and in invoking perturbations to the system. Nevertheless, it now seems reasonable to conclude that individual deserts and their associated heat lows provide a mixture of conditions for the atmosphere to assimilate; the Arabian heat low being just one part of a whole fabric of desert environments.

7.0 REFERENCES

Abel, P. G., and A. Gruber, 1979: An improved model for the calculation of longwave flux at 11 μm. NOAA Tech. Report NESS 106, NOAA-NESS, Washington, DC, 24 pp.

Ackerman, S. A., and S. K. Cox, 1980: Colorado State University radiation instrumentation and data reduction procedures from the Convair-990 during Summer MONEX. Dept. Atmos. Sci. Paper No. 325, Colo. State Univ., Fort Collins, CO, 72 pp.

Ackerman, S. A., and S. K. Cox, 1982: The Saudi Arabian heat low: Aerosol distributions and thermodynamic structure. J. Geophys. Res., 87, 8991-9002.

Ackerman, S. A., E. A. Smith and S. K. Cox, 1983: Surface and atmospheric radiative exchange over the Arabian peninsula. Preprint Vol. of the Fifth AMS Conf. on Atmospheric Radiation, Amer. Meteor. Soc., Boston, MA, 481-483.

Ananthakrishnan, R., 1977: Some aspects of the monsoon circulation and monsoon rainfall. Pure Appl. Geophys., 115, 1209-1249.

Ananthakrishnan, R., and R. N. Keshavamurty, 1970: On some aspects of the fluctuations in the pressure and wind fields over India during the summer and winter monsoon seasons. Proc. Symp. Tropical Meteorology, Honolulu, HI.

Anderson, D. L. T., 1976: The low-level jet as a western boundary current. Mon. Wea. Rev., 104, 907-921.

Anderson, J. R., and R. D. Rosen, 1983: The latitude-height structure of 40-50 day variations in atmospheric angular momentum. J. Atmos. Sci., 40, 1584-1591.

Arking, A., and S. Vemury, 1983: The Nimbus 7 ERB data set: A critical analysis. Submitted to the J. Geophys. Res.

Badgley, F. I., C. A. Paulson, and M. Miyake, 1972: Profiles of wind, temperature and humidity over the Arabian Sea. IIOE Meteorological Monographs, No. 6, East-West Center Press, Honolulu, Hawaii, 62 pp.

Bannon, P. R., 1979a: On the dynamics of the east African jet. I: Simulations of mean conditions for July. J. Atmos. Sci., 36, 2139-2152.

Bannon, P. R., 1979b: On the dynamics of the east African jet. II: Jet transients. J. Atmos. Sci., 36, 2153-2168.

Bannon, P. R., 1982: On the dynamics of the east African jet. III: Arabian Sea branch. J. Atmos. Sci., 39, 2267-2278.

Barnes, J. C., and M. D. Smallwood, 1982: TIROS-N series direct readout services users' guide. Technical Report, National Environmental Satellite Service (prepared by ERT, Inc.), NOAA, Dept. of Commerce, Washington, D.C.

Bartman, F. L., 1967: The reflectance and scattering of solar radiation by the earth. Technical Report 05863-11-T, Dept. of Aerospace Eng., Univ. of Michigan, Ann Arbor, MI, 257 pp.

Bengtsson, L., M. Kanamitsu, P. Kallberg, and S. Uppala, 1982: FGGE 4-dimensional data assimilation at ECMWF. Bull. Amer. Meteor. Soc., 63, 29-43.

Bennett, J. R., and J. Young, 1971: The influence of latitudinal wind shear upon large-scale wave propogation into the tropics. Mon. Wea. Rev., 99, 202-214.

Benoit, R., 1976: A comprehensive parameterization of the atmospheric boundary layer for general circulation models. NCAR cooperative thesis No. 39, McGill Univ. and the National Center for Atmospheric Research, 278 pp.

Berkofsky, L., 1976: The effect of variable surface albedo on the atmospheric circulation in desert regions. J. Appl. Meteor., 15, 1139-1144.

Bess, T. D., R. N. Green, and G. L. Smith, 1980: Deconvolution and analysis of wide-angle longwave radiation data from Nimbus 6 Earth Radiation Budget Experiment for the first year. NASA Technical Paper 1746, Langley Research Center, Hampton, VA, 59 pp.

Bess, T. D., R. N. Green, and G. L. Smith, 1981: Deconvolution of wide field-of-view radiometer measurements of earth-emitted radiation. Part II: Analysis of first year of Nimbus-6 ERB data. J. Atmos. Sci., 38, 474-488.

Bhalme, H. N., and S. S. Parasnis, 1975: 5-6 days oscillations in the pressure gradients over India during southwest monsoon. Indian J. Meteor. Hydrol. Geophys., 26, 77-80.

Bignell, K. J., 1970: The water vapour infrared continuum. Quart. J. Roy. Meteor. Soc., 96, 390-403.

Blake, D. W., T. N. Krishnamurti, S. V. Low-Nam, and J. S. Fein, 1983: Heat low over the Saudi Arabian desert during May 1797 (Summer MONEX). Mon. Wea. Rev., 111, 1759-1775.

Bolhofer, W., M. Chambers, D. Frey, J. Kuettner and S. Unninayar, 1981: Summer MONEX U.S. research flight missions, May-July 1979. NCAR Technical Note TN-168-STR, National Center for Atmospheric Research, Boulder, CO, 220 pp.

Briegleb, B., and V. Ramanathan, 1982: Spectral and diurnal variations in clear sky planetary albedo. J. Appl. Meteor., 21, 1160-1171.

Brode, R. W., and M. Mak, 1978: On the mechanism of the monsoonal mid-tropospheric cyclone formation. J. Atmos. Sci., 35, 1473-1484.

Brooks, D. R., and P. Minnis, 1984a: Comparison of longwave diurnal models applied to simulations of the earth's radiation budget experiment. J. Clim. Appl. Meteor., 23, 155-160.

Brooks, D. R., and P. Minnis, 1984b: Simulation of the earth's monthly average regional radiation balance derived from satellite measurements. J. Clim. Appl. Meteor., 23, 392-403.

Bryson, R. A., 1973: Drought in Sahelia; who or what is to blame. Ecologist, 3, 366-371.

Budyko, M. I., 1974: Climate and life. Academic Press, 508 pp.

Bunker, A. F., and M. Chaffee, 1969: Tropical Indian Ocean clouds. IIOE Meteorological Monographs, No. 4, East-West Center Press, Honolulu, Hawaii, 193 pp.

Businger, J. A., 1973: Turbulent transfer in the atmospheric surface layer. Workshop on Micrometeorology (D. Haugen, Editor), Published by Amer. Meteor. Soc., Boston, MA, 67-100.

Cadet, D., and P. Olorgy-Togbe, 1977: The propogation of tropical disturbances over the Indian Ocean during the summer monsoon. Mon. Wea. Rev., 105, 700-708.

Cadet, D., and G. Reverdin, 1981: Water vapour transport over the Indian Ocean during summer 1975: Tellus, 33, 476-487.

Campbell, G. G., 1980: Energy transport within the earth's atmosphere ocean system from a climate point of view. Ph.D. Dissertation, Dept. of Atmos. Sci., Colo. State Univ., Ft. Collins, CO.

Campbell, G. G., and T. H. Vonder Haar, 1978: Optimum satellite orbits for accurate measurement of the earth's radiation budget, summary. Dept. Atmos. Sci. Paper No. 289, Colo. State Univ., Fort Collins, CO, 61 pp.

Campbell, G. G., and T. H. Vonder Haar, 1980a: Climatology of radiation budget measurements from satellites. Dept. Atmos. Sci. Paper No. 323, Colo. State Univ., Ft. Collins, CO, 74 pp.

Campbell, G. G., and T. H. Vonder Haar, 1980b: An analysis of two years of Nimbus 6 earth radiation budget observations: July 1975 to June 1977. Dept. Atmos. Sci. Paper No. 320, Colo. State Univ., Ft. Collins, CO, 83 pp.

Carlson, T. N., J. A. Augustine, and F. E. Boland, 1977: Potential application of satellite temperature measurements in the analyses of land use over urban areas. Bull. Amer. Meteor. Soc., 96, 91-114.

Carlson, T. N., and F. E. Boland, 1978: Analysis of urban rural canopy using a surface heat flux/temperature model. J. Appl. Meteor., 17, 998-1013.

Carlson, T. N., J. K. Dodd, S. G. Benjamin, and J. N. Cooper, 1981: Satellite estimation of the surface energy balance, moisture availability and thermal inertia. J. Appl. Meteor., 20, 67-87.

Carr, F. H., 1977: Mid-tropospheric cyclones of the summer monsoon. Pure Appl. Geophys., 115, 1383-1412.

Cess, R. D., 1976: Climate change: An appraisal of atmospheric feedback mechanisms employing zonal climatology. J. Atmos. Sci., 33, 1831-1843.

Cess, R. D., B. P. Briegleb, and M. S. Lian, 1982: Low-latitude cloudiness and climate feedback: Comparative estimates from satellite data. J. Atmos. Sci., 39, 53-59.

Cess, R. D., and V. Ramanathan, 1978: Averaging of infrared cloud opacities for climate modeling. J. Atmos. Sci., 35, 919-922.

Chang, C. C., 1981: A contrasting study of the rainfall anomalies between central Tibet and central India during the summer monsoon season of 1979. Bull. Amer. Meteor. Soc., 62, 20-22.

Chang, C. P., 1977: Some theoretical problems of the planetary scale monsoons. Pure Appl. Geophys., 115, 1089-1109.

Chang, K. S., C. C. Chen, M. Y. Chou, K. C. Lee, C. S. Sung, K. F. Wang, K. C. Yang, T. C. Yeh, and C. C. Chang, 1977: The annulus simulation of the movement of Tsinghai-Tibetan high and its application to the forecast of summer flow pattern of high troposphere. Sci. Sinica, 20, 631-644, 5 plates.

Charney, J. G., 1969: A further note on large-scale motions in the tropics. J. Atmos. Sci., 26, 182-185.

Charney, J. G., 1975: Dynamics of deserts and drought in the Sahel. Quart. J. Roy. Meteor. Soc., 101, 193-202.

Charney, J., W. J. Quirk, S. H. Chow, and J. Kornfield, 1977: A comparative study of the effects of albedo change on drought in semi-arid regions. J. Atmos. Sci., 34, 1366-1385.

Charney, J. G., and J. Shukla, 1981: Predictability of monsoons. Monsoon dynamics (edited by J. Lighthill and R. P. Pearce), Cambridge Univ. Press, London, 99-109.

Chen, E., L. H. Allen, J. F. Bartholic, R. G. Bill, and R. A. Sutherland, 1979: Satellite sensed winter nocturnal temperature patterns of the everglades agricultural area. J. Appl. Meteor., 18, 992-1002.

Chou, S. H., and D. Atlas, 1982: Satellite estimates of ocean-air heat fluxes during cold air outbreaks. Mon. Wea. Rev., 110, 1434-1450.

Coakley, J. A., 1975: The two stream approximation in radiative transfer including the angle of the incident radiation. J. Atmos. Sci., 32, 409-418.

Corbell, R. P., C. J. Callahan, and W. J. Kotsch, 1976: The GOES/SMS user's Guide. Joint Publication of NOAA-NESS and NASA-GSFC, Washington, D.C., 118 pp.

Cox, S. K., 1973: Infrared heating calculations with a water vapour pressure broadened continuum. Quart. J. Roy. Meteor. Soc., 99, 669-679.

Cox, S. K., M. C. Polifka, K. Griffith, A. Rockwood, and D. Starr, 1976: Radiative transfer computational routines for atmospheric science application. Tech. Report, Dept. of Atmos. Sci., Colo. State Univ., Ft. Collins, CO, 75 pp.

Dabbert, W. F., and P. A. Davis, 1978: Determination of energetic characteristics of urban-rural surfaces in the greater St. Louis area. Boundary Layer Meteor., 14, 105-121.

Darnell, W. L., S. K. Gupta, and W. F. Staylor, 1983: Downward longwave radiation at the surface from satellite measurements. J. Clim. Appl. Meteor., 22, 1956-1960.

Davis, J. M., and S. K. Cox, 1981: Regional properties of angular reflectance models. Dept. Atmos. Sci. Paper No. 338, Colo. State Univ., Ft. Collins, CO, 126 pp.

Davis, J. M., and S. K. Cox, 1982: Reflected solar radiances from regional scale scenes. J. Appl. Meteor., 21, 1698-1712.

Davis, J. M., C. Vogel, and S. K. Cox, 1980: A multidirectional photodiode array for the measurement of solar radiances. Dept. Atmos. Sci. Paper No. 322, Colo. State Univ., Fort Collins, CO, 42 pp.

Deardorff, J. W., 1978: Efficient prediction of ground surface temperature and moisture, with inclusion of a layer of vegetation. J. Geophys. Res., 83, 1889-1903.

DeBruin, H. A. R., and A. A. M. Holtslag, 1982: A simple parameterization of surface fluxes of sensible and latent heat during daytime compared with the Penman-Monteith concept. J. Appl. Meteor., 21, 1610-1621.

Deirmendjian, D., and Z. Sekera, 1954: Global radiation resulting from multiple scattering in a Rayleigh atmosphere. Tellus, 6, 382-398.

Dirmhirn, I., and F. D. Eaton, 1975: Some characteristics of the albedo of snow. J. Appl. Meteor., 14, 375-399.

Dittberner, G. J., and T. H. Vonder Haar, 1973: Large-scale precipitation estimates using satellite data: Application to the Indian monsoon. Pure Appl. Geophys., 21, 317-334.

Edlin, H. L., and A. Huxley, 1973: Atlas of plant life. John Day Co., New York, 128 pp.

Eliot, T., 1895: India Met. Memoirs, 6, 3, p. 89.

Ellingson, R. G., and R. P. Ferraro, 1983: An examination of a technique for estimating the longwave radiation budget from satellite radiance observations. J. Clim. Appl. Meteor., 22, 1416-1423.

Ellingson, R. G., and J. C. Gille, 1978: An infrared radiative transfer model. Part 1: Model description and comparison of observations with calculations. J. Atmos. Sci., 35, 523-545.

Ellingson, R. G., and G. N. Serafino, 1984: Observations and calculations of aeresol heating over the Arabian Sea during MONEX. J. Atmos. Sci., 41, 575-589.

Ellis, J. S., 1978: Cloudiness, the planetary radiation budget, and climate. Ph.D. Dissertation, Dept. of Atmos. Sci., Colo. State Univ., Ft. Collins, CO, 129 pp.

Ellis, J. S., and T. H. Vonder Haar, 1976: Zonal average earth radiation budget measurements from satellites for climate studies. Dept. Atmos. Sci. Paper No. 240, Colo. State Univ., Ft. Collins, CO, 50 pp.

Ellis, J. S., T. H. Vonder Haar, S. Levitus, and A. H. Oort, 1978: The annual variation in the global heat balance of the earth. J. Geophys. Res., 83, 1958-1962.

Elterman, L, 1964: Atmospheric attenuation model, 1964, in the ultraviolet, visible, and infrared regions for altitudes to 50 km. Tech. Report, AFCRL-64-740, Air Force Cambridge Research Laboratories, Bedford, MA, 40 pp.

Ensor, G. J, 1978: The NOAA geostationary satellite system. National Environmental Satellite Service, NOAA, Dept. of Commerce, Washington, D.C., 101 pp.

ERB Science Team, 1981: Earth radiation budget tape documentation. Requirement documents No. 10-Revision F, System and Applied Science Corp., Riverdale, MD.

Federer, C. A., 1968: Spatial variation of net radiation, albedo, and surface temperature of a forecast. J. Appl. Meteor., 7, 789-795.

Findlater, J., 1969: A major low-level air current near the Indian Ocean during the northern summer. Quart. J. Roy. Meteor. Soc., 95, 362-380.

Findlater, J., 1971: Mean monthly airflow at low levels over the western Indian Ocean. Geophys. Memoirs, vol. 16, no. 115, 53 pp.

Findlater, J., 1972: Aerial explorations of the low-level cross-equatorial current over eastern Africa. Quart. J. Roy. Meteor. Soc., 98, 274-289.

Flohn, H., 1950: Studien zur allgemeinen zirkulation der atmosphare III. Ber. Deut. Wettard., 18, 34-50.

Flohn, H., 1953: Wilhelm meinardus und die revision unserer vorstellung von der atmospharischen zirkulation. Z. Meteor., 7, 97-108.

Flohn, H., 1957: Large scale aspects of the 'Summer Monsoon' in South and East Asia. J. Meteor. Soc. Japan, 75th Anniversary Vol., 180-186.

Flohn, H., 1968: Contributions to a meteorology of the Tibetan highlands. Dept. Atmos. Sci. Paper No. 130, Colo. State Univ., Fort Collins, CO, 120 pp.

Fortuna, J. J., and L. N. Hambrick, 1979: The operation of the NOAA polar satellite system. NOAA Tech. Memo. NESS 60, NOAA-NESS, Washington, DC, 127 pp.

Fritschen, L. J., L. K. Balick, and J. A. Smith, 1982: Interpretation of infrared nighttime imagery of a forested canopy. J. Appl. Meteor., 21, 730-734.

Gao, Y. X., M. C. Tang, S. W. Luo, Z. B. Shen, and C. Li, 1981: Some aspects of recent research on the Qinghai-Xizang Plateau meteorology. Bull. Amer. Meteor. Soc., 62, 31-35.

Gautier, C., G. Diak, and G. Masse, 1980: A simple physical model to estimate incident solar radiation at the surface from GOES satellite data. J. Appl. Meteor., 19, 1005-1012.

Geleyn, J. F., A. Hense, and H. J. Preuss, 1982: A comparison of model generated radiation fields with satellite measurements. Beitr. Phys. Atmos., 55, 253-286.

Glantz, M. H. (editor), 1977: Desertification. Westview Press, Boulder, CO, 346 pp.

Gloerson, P. and L. Hardis, 1978: The Scanning Multichannel Microwave Radiometer (SMMR) Experiment. The Nimbus 7 User's Guide, NASA-Goddard Space Flight Center, Greenbelt, MD, 213-245.

Godbole, R. V., 1973: Numerical simulation of the Indian Summer Monsoon. J. Meteor. Geophys., 24, 1-14.

Godbole, R. V., and R. R. Kelkar, 1971: Influence of various physical factors upon the radiative equilibrium of the atmosphere. Indian J. Meteor. Geophys., 22, 161-168.

Goody, R., 1952: A statistical model for water vapour absorption. Quart. J. Roy. Meteor. Soc., 78, 165-169.

Goody, R., 1964: The transmission of radiation through an inhomogeneous atmosphere. J. Atmos. Sci., 21, 575-581.

Gordon, A. H., and R. C. Taylor, 1975: Computations of surface layer air parcel trajectories, and weather in the oceanic tropics. IIOE Meteorological Monographs, No. 7, East-West Center Press, Honolulu, Hawaii, 112 pp.

Green, R. N., 1981: The effect of data analysis techniques on the interpretation of wide angle longwave radiation measurements. J. Atmos. Sci., 38, 2045-2055.

Green, R. N., 1983: Accuracy and resolution of earth radiation budget estimates. J. Atmos. Sci., 40, 977-985.

Griffith, K. T., S. K. Cox, and R. G. Knollenberg, 1980: Infrared radiative properties of tropical cirrus clouds inferred from aircraft measurements. J. Atmos. Sci., 37, 1077-1087.

Griggs, M., and W. A. Marggraf, 1967: Measurement of cloud reflectance properties and the atmospheric attenuation of solar and infrared energy. Technical Report AFCRL-68-0003, Air Force Cambridge Research Laboratories, Bedford, MA, 156 pp.

Grossman, R. L., and D. R. Durran, 1984: Interaction of low-level flow with the western Ghat mountains and offshore convection in the summer monsoon. Mon. Wea. Rev., 112, 652-672.

Gruber, A., 1978: Determination of the earth-atmosphere radiation budget from NOAA satellite data. NOAA Tech. Report NESS 76, NOAA-NESS, Washington, DC, 28 pp.

Gruber, A., I. Ruff, and C. Earnest, 1983: Determination of the planetary radiation budget from TIROS-N satellites. NOAA Tech. Report NESDIS 3, NOAA-NESDIS, Washington, DC, 12 pp.

Gruber, A., and J. S. Winston, 1978: Earth-atmosphere radiative heating based on NOAA scanning radiometer measurements. Bull. Amer. Meteor. Soc., 59, 1570-1573.

Gube, M., 1980: Outgoing longwave flux computations from METEOSAT data. ESA J., 4, 381-396.

Gube, M., 1982a: Radiation budget parameters at the top of the earth's atmosphere derived from METEOSAT data. J. Appl. Meteor., 21, 1907-1921.

Gube, M., 1982b: Planetary albedo estimates inferred from METEOSAT data. ESA J., 6, 53-69.

Gupta, M. G., M. C. Pant, M. S. Rawat, and I. C. Goel, 1980: Low level results of Summer MONEX field phase research (Part 6). FGGE Operations Report Vol. 9, WMO-ICSU, Geneva, 275-290.

Gurney, R. J., and D. K. Hall, 1983: Satellite derived surface energy balance estimates in the Alaskan sub-Arctic. J. Clim. Appl. Meteor., 22, 115-125.

Hahn, D. G., and S. Manabe, 1975: The role of mountains in the South Asian monsoon circulation. J. Atmos. Sci., 32, 1515-1540.

Hahn, D. G., and S. Manabe, 1976: Reply. J. Atmos. Sci., 33, 2258-2262.

Hall, J. B., and B. R. Barkstrom, 1981: Earth radiation budget experiment (ERBE) science implementation plan (Revision 1). NASA-Langley Research Center, Report ERBE 2-2-3-1-81-10-00, Hampton, VA, 142 pp.

Hambrick, L. N., and D. R. Phillips, 1980: Earth locating image data of spin-stabilized geosynchronous satellites. NOAA Technical Memo. NESS 111, NOAA, Dept. of Commerce, Washington, D.C., 49 pp.

Hanel, R. A., 1969: Infrared Interferometer Spectrometer (IRIS) Experiment. The Nimbus 3 Users' Guide, NASA-Goddard Space Flight Center, Greenbelt, MD, 39-72.

Hart, J. E., 1977: On the theory of the East African low level jet stream. Pure Appl. Geophys., 115, 1263-1282.

Hartman, D. L., and D. A. Short, 1980: On the use of earth radiation budget statistics for studies of clouds and climate. J. Atmos. Sci., 37, 1233-1250.

Hastenrath, S., and P. J. Lamb, 1979a: Climatic atlas of the Indian Ocean. Part I: Surface climate and atmospheric circulation. Univ. of Wis. Press, Madison, WI.

Hastenrath, S., and P. J. Lamb, 1979b: Climatic atlas of the Indian Ocean. Part II: The oceanic heat budget. Univ. of Wis. Press, Madison, WI, 93 pp.

Hay, J. E., 1981: The mesosale distribution of solar radiation at the earth's surface and the ability of satellites to resolve it. Reprint from Satellite and Forecasting of Solar Radiation, Proceedings of First Workshop on Terrestrial Solar Resource Forecasting and on Use of Satellites for Terrestrial Solar Resource Assessment, American Section of the Int. Solar Energy Soc., Inc., Univ. of Delaware, Newark, DE, 76-85.

Heddinghaus, T. R., and A. F. Krueger, 1981: Annual and interannual variations in outgoing longwave radiation over the tropics. Mon. Wea. Rev., 109, 1208-1218.

Hendrie, K., 1983: Personal communication. Illinois State Water Survey, Champaign, IL.

Hicks, B. B., P. Hyson, and C. J. Moore, 1975: A study of eddy fluxes over a forest. J. Appl. Meteor., 14, 58-66.

Holm, D. A., 1960: Desert geomorphology in the Arabian Peninsula. Science, 132, 1369-1379.

Hughes, 1980: Geostationary operational environmental satellite (GOES). Technical Report, Prepared by Hughes Aircraft Co. Space and Communications Group for NOAA and NASA, NASA Goddard Space Flight Center, Greenbelt, MD.

Hussey, W. J., 1979: The TIROS-N/NOAA operational satellite system. Technical Report, National Environmental Satellite Service, NOAA, Dept. of Commerce, Washington, D. C., 35 pp.

Idso, S. B., D. G. Baker, and B. L. Blud, 1969: Relations of radiative fluxes over natural surfaces. Quart. J. Roy. Meteor. Soc., 95, 244-257.

Idso, S. B., and J. W. Deardorff, 1977: Comments on 'The effect of variable surface albedo on the atmospheric circulation in desert regions'. J. Appl. Meteor., 17, 560.

International MONEX Management Centre (Summer) 1981: Summer MONEX Field Phase Report, FGGE Operations Report, Vol. 8, Global Atmospheric Research Programme, ICSU-WMO, Geneva, Switzerland.

Jackson, R. D., and S. B. Idso, 1975: Surface albedo and desertification. Science, 189, 1012-1013.

Jacobowitz, H., T. S. Chen, and I. Ruff, 1976: Preliminary model of the angular reflectance and emittance of the ocean surface derived from the Nimbus 6 ERB experiment. Proc. Symp. Radiation in the Atmosphere, IAMAP, Garmisch-Partenkirchen, FRG, 286-288.

Jacobowitz, H., W. L. Smith, H. B. Howell, and F. W. Nagle, 1979: The first 18 months of planetary radiation budget measurements from the Nimbus 6 ERB Experiment. J. Atmos. Sci., 36, 501-507.

Jacobowitz, H., L. L. Stowe, and J. R. Hickey, 1978: The Earth Radiation Budget (ERB) Experiment. The Nimbus 7 Users' Guide, NASA-Goddard Space Flight Center, Greenbelt, MD, 33-70.

Jenne, R. L., H. L. Crutcher, H. V. Loon, and J. J. Taljaard, 1974: A selected climatology of the southern hemisphere -- computer methods and data availability. NCAR Technical Note NCAR-TN/STR-92, National Center for Atmospheric Reseach, Boulder, CO, 91 pp.

Jensenius, J. S., J. J. Cahir, and H. A. Panofsky, 1978: Estimation of outgoing longwave radiation from meteorological variables accessible from numerical models. Quart. J. Roy. Meteor. Soc., 104, 119-130.

Johnson, R. H., and R. A. Houze, Jr. 1984: Monsoon convection. Monsoon meteorology, to be published by Oxford Press, in progress.

Julian, P. R., and R. A. Madden, 1981: Comments on a paper by T. Yasunari: A quasi-stationary appearance of 30 to 40-day period in the cloudiness fluctuations during the summer monsoon over India. J. Meteor. Soc. Japan, 59, 435-437.

Kahle, A., 1977: A simple thermal model of the earth's surface for geologic mapping by remote sensing. J. Geophys. Res., 82, 1673-1680.

Kelkar, R. R., and R. V. Godbole, 1970: The dependence of longwave radiation on cloudiness, water vapour content and temperature. Indian J. Meteor. Geophys., 21, 613-622.

Keshavamurty, R. N., 1973: Power spectra of large-scale disturbances of the Indian southwest monsoon. Indian J. Meteor. Geophys., 24, 117-124.

Keshavamurty, R. N., and S. T. Awade, 1970: On the maintenance of the mean monsoon trough over north India. Mon. Wea. Rev., 98, 315-320.

Kidwell, K. B., 1979: NOAA polar orbiter data (TIROS-N and NOAA-6) Users' Guide - Preliminary version. Technical Report, National Climatic Center, NOAA, Dept. of Commerce, Washington, D.C.

King, M. D., and R. J. Curran, 1980: The effect of a nonuniform planetary albedo on the interpretation of earth radiation budget observations. J. Atmos. Sci., 37, 1262-1278.

Kneizys, F. X., E. P. Shettle, W. O. Gallery, J. H. Chetwynd, Jr., L. W. Abreu, J. E. A. Selby, R. W. Fenn, and R. A. McClatchey, 1980: Atmospheric transmittance/radiance: Computer code LOWTRAN 5. Environmental Research Paper No. 697, Air Force Geophysics Laboratory, Hanscom AFB, MA, 233 pp.

Kondratyev, K. Y., R. M. Welch, O. B. Vasiliev, V. F. Zhvaler, L. S. Ivlev, and V. F. Rodionov, 1976: Comparison between the measured and calculated spectral characteristics of shortwave radiation in the free atmosphere over the desert (from the data of the CAENEX-70 Expeditions). Dept. Atmos. Sci. Paper No. 261, Colo. State Univ., Fort Collins, CO, 79 pp.

Kondratyev, K. Ya., 1969: Radiation in the atmosphere. Academic Press, New York, 912 pp.

Korff, H. C., J. J. Gailiun, and T. H. Vonder Haar, 1974: Radiation measurements over a snowfield at an elevated site. Dept. Atmos. Sci. Paper No. 221, Colo. State Univ., Fort Collins, CO, 33 pp.

Kornfield, J., and J. Susskind, 1977: On the effect of surface emissivity on temperature retrievals. Mon. Wea. Rev., 105, 1605-1608.

Koteswaram, P., 1950: Upper air 'lows' in low latitudes in the Indian area during SW monsoon season and 'breaks' in the monsoon. Indian J. Meteor. Geophys., 1, 162-164.

Koteswaram, P., 1958: The easterly jet stream in the tropics. Tellus, 10, 43-87.

Krishnamurti, T. N., 1971: Observational study of the tropical upper tropospheric motion field during the northern hemisphere summer. J. Appl. Meteor., 10, 1066-1096.

Krishnamurti, T. N., and P. Ardanuy, 1980: The 10 to 20-day westward propagating mode and 'breaks in the monsoon'. Tellus, 33, 15-26.

Krishnamurti, T. N., P. Ardanuy, Y. Ramanathan, and R. Pasch, 1979: Quick look 'Summer MONEX atlas', Part II: The onset phase. FSU Report No. 79-5, NSF Grant ATM 78-19363, Dept. of Meteor., Florida State Univ., Tallahassee, FL, 205 pp.

Krishnamurti, T. N., P. Ardanuy, Y. Ramanathan, and R. Pasch, 1981: On the onset vortex of the summer monsoon. Mon. Wea. Rev., 109, 344-363.

Krishnamurti, T. N., and H. N. Bhalme, 1976: Oscillations of a monsoon system. Part I: Observational aspects. J. Atmos. Sci., 33, 1937-1954.

Krishnamurti, T. N., S. Cocke, R. Pasch, and S. Low-Nam, 1983: Precipitation estimates from rainguage and satellite observations - Summer MONEX. FSU Report No. 83-7, NSF Grant 78-19363, Dept. of Meteor., Florida State Univ., Tallahassee, FL, 373 pp.

Krishnamurti, T. N., S. M. Daggupaty, J. Fein, M. Kanamitsu, and J. D. Lee, 1973: Tibetan high and upper tropospheric tropical circulations during northern summer. Bull. Amer. Meteor. Soc., 54, 1234-1249.

Krishnamurti, T. N., P. Greiman, Y. Ramanathan, R. Pasch, and P. Ardanuy, 1980a: Quick look 'Summer MONEX atlas', Part I: Saudi Arabian phase. FSU Report No. 80-4, NSF Grant ATM 78-19363, Dept. of Meteor., Florida State Univ., Tallahassee, FL, 71 pp.

Krishnamurti, T. N., and R. S. Hawkins, 1970: Mid-tropospheric cyclones of the southwest monsoon. J. Appl. Meteor., 9, 442-458.

Krishnamurti, T. N., M. Kanimitsu, R. Godbole, C. B. Chang, F. Carr, and J. H. Chow, 1975: Study of a monsoon depression (I): Synoptic structure. J. Meteor. Soc. Japan, 53, 227-240.

Krishnamurti, T. N., M. Kanimitsu, R. Godbole, C. B. Chang, F. Carr, and J. H. Chow, 1976: Study of a monsoon depression (II): Dynamical structure. J. Meteor. Soc. Japan, 54, 208-225.

Krishnamurti, T. N., J. Molinari, and H. L. Pan, 1976: Numerical simulation of the Somali jet. J. Atmos. Sci., 33, 2350-2362.

Krishnamurti, T. N., J. Molinari, H. L. Pan, and V. Wong, 1977: Downstream amplification and formation of monsoon disturbances. Mon. Wea. Rev., 105, 1281-1297.

Krishnamurti, T. N., Y. Ramanathan, P. Ardanuy, R. Pasch, and P. Greiman, 1980b: Quick look 'Summer MONEX atlas', Part III: The depression phase, FSU Report No. 80-8, NSF Grant ATM 78-19363, Dept. of Meteor., Florida State Univ., Tallahassee, FL, 71 pp.

Krishnamurti, T. N., and D. Subrahmanyam, 1982: The 30-50 day mode at 850 mb during MONEX. J. Atmos. Sci., 39, 2088-2095.

Krishnamurti, T. N., and V. Wong, 1979: A planetary boundary layer model for the Somali jet. J. Atmos. Sci., 36, 1895-1907.

Krishnamurti, T. N., V. Wong, H. L. Pan, R. Pasch, J. Molinari, and P. Ardanuy, 1983: A three-dimensional planetary boundary layer model for the Somali jet. J. Atmos. Sci., 40, 894-908.

Kuo, H. L., and Y. F. Qian, 1981: Influence of the Tibetan Plateau on cumulative and diurnal changes of weather and climate in summer. Mon. Wea. Rev., 109, 2337-2356.

Kurbatkin, G. P., S. Manabe, and D. G. Hahn, 1979: The moisture content of the continents and the intensity of summer monsoon circulation. Meteor. Gidrol., 11, 5-11.

Lacis, A. A., and J. E. Hansen, 1974: A parameterization for the absorption of solar radiation in the earth's atmosphere. J. Atmos. Sci., 31, 118-133.

Lau, K. M., and P. H. Chan, 1984a: Short term climate variability and atmospheric teleconnections from satellite-observed outgoing longwave radiation. Part I: Simultaneous relationships. J. Atmos. Sci., 40, 2735-2750.

Lau, K. M., and P. H. Chan, 1984b: Short term climate variability and atmospheric teleconnections from satellite-observed outgoing longwave radiation. Part II: Lagged correlations. J. Atmos. Sci., 40, 2751-2767.

Lau, K. M., and M. T. Li, 1984: The monsoon of East Asia and its global associations - a survey. Bull. Amer. Meteor. Soc., 65, 114-125.

Lauritson, L., G. J. Nelson, and F. W. Porto, 1979: Data extraction and calibration of TIROS-N/NOAA radiometers. NOAA Tech. Memo. NESS 107, NOAA-NESS, Washington, DC, 58 pp., 2 Appendicies.

Leslie, L. M., 1980: Numerical modeling of the summer heat low over Australia. J. Appl. Meteor., 19, 381-387.

Liebmann, B., and D. L. Hartmann, 1982: Interannual variations of outgoing IR associated with tropical circulation changes during 1974-78. J. Atmos. Sci., 39, 1153-1162.

Lighthill, J., and R. P. Pearce, 1981: Monsoon dynamics. Cambridge Univ. Press, London, 735 pp.

Liou, K. N., 1980: An introduction to atmospheric radiation. Academic Press, New York, 392 pp.

London, J., and T. Sasamori, 1971: Radiative energy budget of the atmosphere. Space Reseach XI, Akademie-Verlag, 639-649.

Luo, H. L., and M. Yanai, 1983: The large-scale circulation and heat sources over the Tibetan Plateau and surrounding areas during the early summer of 1979. Part I: Precipitation and kinematic analyses. Mon. Wea. Rev., 111, 922-944.

Luo, H. L., and M. Yanai, 1984: The large-scale circulation and heat soures over the Tibetan Plateau and surounding areas during the early summer of 1979, Part II: Heat and moisture budgets. Accepted for Publication by the Mon. Wea. Rev.

Lyons, S. W., 1981: Planetary-scale aspects of outgoing longwave radiation and vorticity over the global tropics during winter. Mon. Wea. Rev., 109, 1773-1787.

Madden, R. A., and P. R. Julian, 1971: Detection of a 40-50 day oscillation in the zonal wind in the tropical Pacific. J. Atmos. Sci., 28, 702-708.

Madden, R. A., and P. R. Julian, 1972a: Description of global-scale circulation cells in the tropics with a 40-50 day period. J. Atmos. Sci., 29, 1109-1123.

Madden, R. A., and P. R. Julian, 1972b: Further evidence of global-scale 5-day pressure waves. J. Atmos. Sci., 29, 1464-1469.

Mak, M., 1975: The monsoonal mid-tropospheric cyclogenesis. J. Atmos. Sci., 32, 2246-2253.

Mak, M., 1983: A moist baroclinic model for monsoonal mid-tropospheric cyclogensis. J. Atmos. Sci., 40, 1154-1162.

Malkmus, W., 1967: Random Lorentz band model with exponential tailed S-1 line-intensity distribution function. J. Opt. Soc. Amer., 57, 323-329.

Martin, D. W., and M. R. Howland, 1983: Daily Arabian Sea rainfall during the onset of the 1979 monsoon. Space Science and Engineering Center, Univ. of Wis., Madison, WI, Submitted to Papers in Meteorological Research for publication.

Matson, M., E. P. McClain, D. McGinnis, and J. Pritchard, 1978: Satellite detection of urban heat islands. Mon. Wea. Rev., 106, 1725-1734.

Matthews, E., 1983a: Global vegetation and land use: New high-resolution data bases for climate studies. J. Clim. and Appl. Meteor., 22, 474-486.

Matthews, E., 1983b: Global vegetation and land use data bases for climate studies. Bull. Amer. Meteor. Soc., 64, 793.

McClatchey, R. A., R. W. Fenn, J. E. A. Selby, F. E. Volz, and J. S. Garing, 1972: Optical properties of the atmosphere (Third Edition). Environmental Research Papers, No. 411, Air Force Cambridge Research Laboratories, Bedford, MA, 108 pp.

McCulloch, A. W., 1969: The Medium Resolution Infrared Radiometer (MRIR) Experiment. The Nimbus 3 Users' Guide, NASA-Goddard Space Flight Center, Greenbelt, MD, 67-107.

McCumber, M. C., and R. A. Pielke, 1981: Simulation of the effects of surface fluxes of heat and moisture in a mesoscale numerical model, 1. Soil layer. J. Geophys. Res., 86, 9929-9938.

McKay, D. C., and G. W. Thurtell, 1978: Measurements of the energy fluxes involved in the energy budget of a snow cover. J. Appl. Meteor., 17, 339-349.

Meleshko, V. P., and R. T. Wetherald, 1981: The effect of a geographical cloud distribution on climate: A numerical experiment with an atmospheric general circulation model. J. Geophys. Res., 86, 11995-12014.

Mertz, G. J., and L. A. Mysak, 1984: Evidence for a 40-60 day oscillation over the western Indian Ocean during 1976 and 1979. Mon. Wea. Rev., 112, 383-386.

Miller, F. R., and R. N. Keshavamurthy, 1978: Structure of an Arabian Sea summer monsoon system. IIOE Meteorological Monographs, No. 1, East-West Center Press, Honolulu, 94 pp.

Minnis, P., and E. F. Harrison, 1984: Diurnal variability of regional cloud and surface radiative parameters derived from GOES data, Part III: November 1978 radiative parameters. Submitted to J. Clim. Appl. Meteor.

Misra, B. M., 1972: Planetary pressure waves of 4 to 5-day period in the tropics. Mon. Wea. Rev., 100, 313-316.

Monteith, J. L., and G. Szeicz, 1961: The radiation balance of bare soil and vegetation. Quart. J. Roy. Meteor. Soc., 87, 159-170.

Moore, C. J., 1976: A comparative study of radiation balance above forest and grassland. Quart. J. Roy. Meteor. Soc., 102, 889-899.

Moser, W., and E. Raschke, 1984: Incident solar radiation over Europe estimated from METEOSAT data. J. Clim. Appl. Meteor., 23, 166-170.

Murakami, M., 1971: On the disturbances appearing in precipitation near the ITC zone in the tropical Pacific. J. Meteor. Soc. Japan, 49, 184-189.

Murakami, M., 1976: Analysis of summer monsoon fluctuations over India. J. Meteor. Soc. Japan, 54, 15-31.

Murakami, M., 1977: Spectrum analysis relevant to the Indian monsoon. Pure Appl. Geophys., 115, 1149-1166.

Murakami, M., 1978: Investigation of monsoon lows by the method of spectrum analysis. Indian J. Met. Hydrol. Geophys., 29, 26-35.

Murakami, T., 1958: The sudden change of upper westerlies near the Tibetan Plateau at the beginning of summer season. J. Meteor. Soc. Japan, 36, 239-247 (in Japanese).

Murakami, T., 1972: Equatorial stratospheric waves induced by diabatic heat sources. J. Atmos. Sci., 29, 1129-1137.

Murakami, T., 1973: On the interaction between the zonal mean flow and equatorial waves excited by diabatic heat sources at 20° latitude. J. Atmos. Sci., 30, 984-995.

Murakami, T., 1974: Steady and transient waves excited by diabatic heat sources during the summer monsoon. J. Atmos. Sci., 31, 340-357.

Murakami, T., 1976: Cloudiness fluctuations during the summer monsoon. J. Meteor. Soc. Japan, 54, 175-181.

Murakami, T., 1980a: Temporal variations of satellite-observed outgoing longwave radiation over the winter monsoon region. Part I: Long period (15-30 day) oscillations. Mon. Wea. Rev., 108, 408-426.

Murakami, T., 1980b: Temporal variations of satellite-observed outgoing longwave radiation over the winter monsoon region. Part III: Short period (4-6 day) oscillations. Mon. Wea. Rev., 108, 427-444.

Murakami, T., 1980c: Empirical orthogonal function analysis of satellite-observed outgoing longwave radiation during summer. Mon. Wea. Rev., 108, 205-222.

Murakami, T., 1981a: Orographic influence of the Tibetan Plateau on the Asiatic winter monsoon circulation. Part I: Large scale aspects. J. Meteor. Soc. Japan., 59, 40-65.

Murakami, T., 1981b: Orographic influence of the Tibetan Plateau on the Asiatic winter monsoon circulation, Part II: Diurnal variations. J. Meteor. Soc. Japan, 59, 66-84.

NASA, 1978a: Heat capacity mapping mission. User's Guide, Goddard Space Flight Center, Greenbelt, MD, 120 pp.

NASA, 1978b: The Nimbus 7 User's Guide. Goddard Space Flight Center, Greenbelt, MD, 263 pp.

Nicholson, J. R., 1969: Meteorological data catalogue. IIOE Meteorological Monographs, No. 3, East-West Center Press, Honolulu, Hawaii, 59 pp.

Nicholson, S. E., 1978: Climatic variations in the Sahel and other African regions during the past five centuries. J. Arid Environ., 1, 3-34.

Nicholson, S. E., 1980: The nature of rainfall fluctuations in subtropical West Africa. Mon. Wea. Rev., 108, 473-487.

Nimbus Project, 1975: Medium Resolution Infrared Radiometer (MRIR). The NIMBUS 2 Users' Guide, NASA-Goddard Space Flight Center, Greenbelt, MD, 39-72.

Nitta, T., 1983: Observational study of heat sources over the eastern Tibetan Plateau during the summer monsoon. J. Meteor. Soc. Japan, 61, 590-605.

Ohring, G., and S. Adler, 1978: Some experiments with a zonally averaged climate model. J. Atmos. Sci., 35, 186-205.

Ohring, G., and P. F. Clapp, 1980: The effect of changes in cloud amount on the net radiation at the top of the atmosphere. J. Atmos. Sci., 37, 447-454.

Ohring, G., P. F. Clapp, T. R. Heddinghaus, and A. F. Krueger, 1981: The quasi-global distribution of the sensitivity of the earth-atmosphere radiation budget to clouds. J. Atmos. Sci., 38, 2539-2541.

Ohring, G., and A. Gruber, 1983: Satellite radiation observations and climate theory. Advances in Geophys., 25, 237-304.

Ohring, G., A. Gruber, and R. Ellingson, 1984: Satellite determinations of the relationship between total longwave radiation flux and infrared window radiance. J. Clim. Appl. Meteor., 23, 416-425.

Oke, T. R., 1978: Boundary layer climates. Halsted Press, London, 372 pp.

Oort, A. H., and E. M. Rasmusson, 1971: Atmospheric circulation statistics. NOAA Professional Paper No. 5, National Oceanic and Atmospheric Administration, U.S. Department of Commerce, Washington, DC, 323 pp.

Oort, A. H., and T. H. Vonder Haar, 1976: On the observed annual cycle in the ocean-atmosphere heat balance over the northern hemisphere. J. Phys. Ocean., 6, 781-800.

Otterman, J., 1974: Baring high-albedo soils by overgrazing: A hypothesized desertification mechanism. Science, 186, 531-533.

Paltridge, G. W., and C. M. R. Platt, 1976: Radiative processes in meteorology and climatology. Elsevier Scientific Pub. Co., Amsterdam, 318 pp.

Paltridge, G. W., and C. M. R. Platt, 1981: Aircraft measurements of solar and infrared radiation and the microphysics of cirrus clouds. Quart. J. Roy. Meteor. Soc., 107, 367-380.

Payne, R. E., 1972: Albedo of the sea surface. J. Atmos. Sci., 29, 959-970.

Pedgley, D. E., 1974: Winter and spring weather at Riyadh, Saudi Arabia. Meteor. Magazine, 103, 225-236.

Pinker, R. T., and L. A. Corio, 1984: Surface radiation budget from satellites. Mon. Wea. Rev., 112, 209-215.

Portman, D. J., and E. Ryznar, 1971: An investigation of heat exchange. IIOE Meteorological Monographs, No. 5, East-West Center Press, Honolulu, Hawaii, 78 pp.

Potter, G. L., H. W. Ellsaesser, M. C. MacCracken, and C. S. Mitchell, 1981: Climate change and cloud feedback: The possible radiative effects of latitudinal redistribution. J. Atmos. Sci., 38, 489-493.

Price, J. C., 1977: Thermal inertia mapping: A new view of the earth. J. Geophys. Res., 82, 2582-2590.

Price, J. C., 1980: The potential of remotely sensed thermal infrared data to infer surface soil moisture and evaporation. Water Resources Res., 16, 787-795.

Price, J. C., 1982: On the use of satellite data to infer surface fluxes at meteorological scales. J. Appl. Meteor., 21, 1111-1122.

Priestley, C. H. B., and R. J. Taylor, 1972: On the assessment of surface heat flux and evaporation using large-scale parameters. Mon. Wea. Rev., 100, 81-92.

Raghavan, K., 1973: Break-monsoon over India. Mon. Wea. Rev., 101, 33-43.

Ramage, C. S., 1966: The summer atmospheric circulation over the Arabian Sea. J. Atmos. Sci., 23, 144-150.

Ramage, C. S., 1971: Monsoon meteorology. Academic Press, New York, NY, 296 pp.

Ramage, C. S., F. R. Miller, and C. Jefferies, 1972: Meteorological atlas of the International Indian Ocean Expedition: Volume 1 - The surface climate of 1963 and 1964. National Science Foundation, U.S. Government Printing Office 1972 0-474-383, Washington, DC, 12 pp. - 144 charts.

Ramage, C. S., and C. V. R. Raman, 1972: Meteorological atlas of the International Indian Ocean Expedition. Vol. 2: Upper Air. National Science Foundation, U.S. Government Printing Office, 1972, 0-474-383, Washington, DC, 13 pp, 121 charts.

Ramamurthy, K., 1969: Some aspects of the break in the Indian southwest monsoon during July and August. Forecasting Manual No. IV-18.3, India Meteor. Dept., Poona, 1-57.

Ramaswamy, C., 1962: Breaks in the Indian summer monsoon as a phenomenon of interaction between the easterly and the sub-tropical westerly jet streams. Tellus, 14, 337-349.

Randel, D. L., 1983: Space-time variations in the earth radiation budget. Masters Thesis, Dept. Atmos. Sci., Colo. State Univ., Ft. Collins, CO, 96 pp.

Rao, G. V., N. La Seur, and D. N. Sikdar, 1980: Vertical structure of the low level flow in the vicinity of Socotra based on the aerial observation of June 24, 1979. Results of Summer MONEX Field Phase Research (Part A), FGGE Operations Report Vol. 9, WMO-ICSU, Geneva, 275-290.

Rao, G. V., W. R. Schaub Jr., and J. puetz, 1981: Evaporation and precipitation over the Arabian Sea during several monsoon seasons. Mon. Wea. Rev., 109, 364-370.

Rao, P. K., 1966: A study of the onset of the monsoon over India during 1962 Using TIROS-IV radiation data. Indian J. Meteor. Geophys., 17, 347-356.

Rao, P. K., 1972: Remote sensing of urban heat islands from an environmental satellite. Bull. Amer. Meteor. Soc., 53, 647-648.

Raphael, C., 1983: Models for estimating solar irradiance at the earth's surface from satellite data: An initial assessment. Report No. 83-1, Canadian Climate Centre, Downsview, Ontario, 332 pp.

Raschke, E., 1969: Angular characteristics of the reflectance of the earth-atmosphere system as obtained from a synchronous satellite. Space Research, 9, 580-585.

Raschke, E., and W. R. Bandeen, 1970: The radiation balance of the planet earth from radiation measurements of the satellite Nimbus II. J. Appl. Meteor., 9, 215-238.

Raschke, E., T. H. Vonder Haar, W. R. Bandeen, and M. Pasternak, 1971: The radiation balance of the earth-atmosphere system during June and July 1969 from Nimbus 3 radiation measurements - some preliminary results. Space Research XI - Akademie Verlag, 661-667.

Raschke, E., T. H. Vonder Haar, W. R. Bandeen, and M. Pasternak, 1973a: The annual radiation balance of the earth - atmospheric system during 1969-70 from Nimbus 3 measurements. J. Atmos. Sci., 30, 341-364.

Raschke, E., T. H. Vonder Haar, M. Pasternak, and W. R. Bandeen, 1973b: The radiation balance of the earth-atmosphere system from Nimbus 3 radiation measurements. NASA Tech. Note TN D-7249, Goddard Space Flight Center, Greenbelt, MD, 72 pp.

Rasool, S. I., and H. J. Bolle, 1984: ISLSCP: International satellite land-surface climatology project. Bull. Amer. Meteor. Soc., 65, 143-144.

Reed, R. J., D. C. Norquist, and E. E. Recker, 1977: The structure and properties of African wave disturbances as observed during Phase III of GATE. Mon. Wea. Rev., 105, 317-333.

Reiter, E. R., 1982: Where we are and where we are going in mountain meteorology. Bull. Amer. Meteor. Soc., 63, 1114-1122.

Reiter, E. R., and Y. H. Ding, 1980: The role of Qinghai-Xizang Plateau in feedback mechanisms affecting the planetary circulation. Sci. Atmos. Sinica, 4, 300-309.

Reiter, E. R., and Y. H. Ding, 1981: The role of Qinghai-Xizang Plateau in feedback mechanisms affecting the planetary circulation. Sci. Atmos. Sinica., 5, 9-22.

Reiter, E. R., and D. Y. Gao, 1982: Heating of the Tibet Plateau and movements of the South Asian high during spring. Mon. Wea. Rev., 110, 1694-1711.

Reiter, E. R., and G. J. Reiter, 1981: Tibet - The last frontier. Bull. Amer. Meteor. Soc., 62, 4-13.

Reiter, E. R., and M. C. Tang, 1984: Plateau effects on diurnal circulation patterns. Mon. Wea. Rev., 112, 638-651.

Reverdin, G., and G. Sommeria, 1983: The dynamical structure of the planetary boundary layer over the Arabian Sea, as deduced from constant level balloon trajectories. J. Atmos. Sci., 40, 1435-1452.

Riehl, H., 1959: On production of kinetic energy from condensation heating. In The Atmosphere and the Sea in Motion, The Rossby Memorial Volume, New York, NY, The Rockefeller Institute Press, 381-399.

Rind, D., 1982: The influence of ground moisture conditions in North America on summer climate as modeled in the GISS GCM. Mon. Wea. Rev., 110, 1487-1494.

Roberts, R. E., J. E. A. Selby, and L. M. Biberman, 1976: Infrared continuum absorption by atmospheric water vapor in the 8-12 μm window. Appl. Optics., 15, 2085-2090.

Robinson, G. D., 1958: Some observations from aircraft of surface albedo and the albedo and absorption of cloud. Arch. Meteor. Geophys. and Bioklimatol., 9, 28-41.

Rodgers, C. D., 1968: Some extensions and applications of the new random model for molecular band transmission. Quart. J. Roy. Meteor. Soc., 94, 99-102.

Rodgers, C. D., and C. D. Walshaw, 1966: The computation of infrared cooling rate in planetary atmospheres. Quart. J. Roy. Meteor. Soc., 92, 67-92.

Rowntree, P. R., and J. A. Bolton, 1983: Simulations of the atmospheric response to soil moisture anomalies over Europe. Quart J. Roy. Meteor. Soc., 109, 501-526.

Rubenstein, D. M., 1981: The daytime evolution of the East African jet. J. Atmos. Sci., 38, 114-128.

Ruff, I., R. Koffler, S. Fritz, J. S. Winston, and P. K. Rao, 1968: Angular distribution of solar radiation reflected from clouds as determined from TIROS-IV radiometer measurements. J. Atmos. Sci., 25, 323-332.

Sadler, J. C., 1969: Average cloudiness in the tropics from satellite observations. IIOE Meteorological Monographs, No. 2, East-West Center Press, Honolulu, Hawaii, 22 pp. - 12 plates.

Sadler, J. C., and C. S. Ramage, 1976: Comments on 'The role of mountains in the South Asian monsoon circulation'. J. Atmos. Sci., 33, 2255-2258.

Saha, K., 1971a: Mean cloud distributions over tropical oceans. Tellus, 23, 183-195.

Saha, K., 1971b: Cloud distributions over equatorial Indian Ocean as revealed by satellites. Indian J. Meteor. Geophys., 22, 389-396.

Salmonson, V. V., 1968: Anisotropy in reflected solar radiation. Dept. Atmos. Sci. Paper No. 128, Colo. State Univ., Fort Collins, CO, 143 pp.

Salmonson, V. V., and W. E. Marlatt, 1968: Anistropic solar reflectances over white sand, snow, and stratus clouds. Dept. Atmos. Sci. Paper No. 120, Colo. State Univ., Fort Collins, CO, 41 pp.

Sanders, F., 1984: Quasi-geostrophic diagnosis of the monsoon depression of 5-8 July 1979. J. Atmos. Sci., 41, 538-552.

Sasamori, T., J. London, and D. V. Hoyt, 1972: Radiation budget of the southern hemisphere. Meteor. Mon., 13, 9-23.

Saunders, R. W., and G. E. Hunt, 1983: Some radiation budget and cloud measurements derived from Meteosat 1 data. Tellus, Accepted for publiation.

Saunders, R. W., L. S. Stowe, G. E. Hunt, and C. F. England, 1983: An intercomparison between radiation budget estimates from METEOSAT 1, Nimbus 7 and TIROS-N satellites. J. Clim. Appl. Meteor., 22, 546-559.

Schneider, S. H., 1972: Cloudiness as a global climatic feedback mechanism: The effects on the radiation balance and surface temperature of variations in cloudiness. J. Atmos. Sci., 29, 1413-1422.

Schneider, S. H., W. M. Washington, and R. M. Chervin, 1978: Cloudiness as a climatic feedback mechanism: Effects on cloud amounts of prescribed global and regional surface temperature changes in the NCAR GCM. J. Atmos. Sci., 35, 2207-2221.

Schwalb, A., 1978: The TIROS-N/NOAA A-G Satellite Series. NOAA Tech. Memo, NESS 95, NOAA-NESS, Washington, DC, 75 pp.

Science News, 1983a: Widespread concern over satellite sale. Science News, 123, 181.

Science News, 1983b: Weather satellites won't be sold. Science News, 124, 375.

Sellers, W. D., 1965: Physical climatology. The Univ. of Chicago Press, Chicago, 272 pp.

Sen, P. N., and H. P. Das, 1980: Low level inversion over Arabian Sea and Indian summer monsoon. Results of Summer MONEX Field Phase Research (Part A), FGGE Operations Repot Vol. 9, WMO-ICSU, Geneva, 225-233.

Shih, S. F., and E. Chen, 1984: On the use of GOES thermal data to study effects of land use on diurnal temperature fluctuation. J. Clim. Appl. Meteor., 23, 426-433.

Short, D. A., and R. F. Cahalan, 1983: Interannual variability and climatic noise in satellite observed outgoing longwave radiation. Mon. Wea. Rev., 111, 572-577.

Short, D. A., and J. M. Wallace, 1980: Satellite-inferred morning-to-evening cloudiness changes. Mon. Wea. Rev., 108, 1160-1169.

Shukla, J., and Y. Mintz, 1982: Influence of land-surface evapotranspiration on the the earth's climate. Science, 215, 1498-1500.

Shukla, J., and Y. Sud 1981: Effect of cloud-radiation feedback on the climate of a general circulation model. J. Atmos. Sci., 38, 2337-2353.

Sikka, D. R., 1977: Some aspects of the life history, structure and movement of monsoon depressions. Pure Appl. Geophys., 115, 1501-1529.

Sikka, D. R., and S. Gadgil, 1980: On the maximum cloud zone and the ITCZ over Indian longitudes during the Southwest Monsoon. Mon. Wea. Rev., 108, 1840-1853.

Sikka, D. R., and B. Grossman, 1980: Summer MONEX chronological weather summary (1st edition). International MONEX Management Centre, New Delhi, India, 49 pp.

Simmonds, I., and C. Chidzey, 1982: The parameterization of longwave flux in energy balance climate models. J. Atmos. Sci., 39, 2144-2151.

Smith, E. A., 1980a: Orbital mechanics and analytic modeling of meteorological satellite orbits. Dept. Atmos. Sci. Paper No. 321, Colo. State Univ., Ft. Collins, CO, 161 pp.

Smith, E. A., 1980b: The modulation by tropical cloud systems of the bulk radiative heat budget. Vol. Extended Abstracts, 1980 International Radiation Symposium, Colo. State Univ., Ft. Collins, CO, 352-354.

Smith, E. A., S. A. Ackerman, S. K. Cox, and T. H. Vonder Haar, 1980: Summer MONEX high altitude aircraft radiation measurements. Atlas of MONEX Aircraft Measurements, Dept. Atmos. Sci., Colo. State Univ., Fort Collins, CO, 84 pp.

Smith, E. A., S. K. Cox, and T. H. Vonder Haar, 1982b: Preliminary results from an Arabian heat low boundary layer experiment. Extended Abstract Vol. of the International Conf. on the Scientific Results of the Monsoon Experiment, Bali, Global Atm. Res. Prog., ICSU-WMO, Geneva, 1-7 to 1-12.

Smith, E. A., and J. Graffy, 1982: A TIROS-N AVHRR digital data set for analysis of the 1979 southwest summer monsoon. Special Report under NSF Grant ATM-7820375, Dept. Atmos. Sci., Colo. State Univ., Fort Collins, CO, 15 pp., 617 plates, 41 tables.

Smith, E. A., and D. R. Phillips, 1972: Automated cloud tracking using precisely aligned digital ATS pictures. IEEE Trans. on Computers, C-21, 715-729.

Smith, E. A., M. M. Sakkal, S. A. Ackerman, S. K. Cox, and T. H. Vonder Haar, 1982a: An investigation of the radiative boundary conditions during the development of the southwest monsoon Saudi Arabian heat low. Working paper series #1, KAU Faculty of Meteorology and Environmental Studies and University of Arizona, Tucson, AZ, 52 pp.

Smith, E. A., and T. H. Vonder Haar, 1980a: A first look at the summer MONEX GOES satellite data. Preprint of the AIAA 15th Thermophysics Conference, American Inst. of Aeronautics and Astronautics, New York, NY, 16 pp.

Smith, E. A., and T. H. Vonder Haar, 1980b: Satellite measurements and analysis of the radiation budget over MONEX. Annual Report, NSF Grant ATM-7820375, Dept. Atmos. Sci., Colo. State Univ., Ft. Collins, CO, 69 pp.

Smith, E. A., and T. H. Vonder Haar, 1980c: The development of a multispectral radiative signature technique for estimation of rainfall from satellites -- atmospheric environments and complex indicies of refraction for water and ice. Tech. Report, Cooperative Institute for Research in the Atmosphere, Colo. State Univ., Fort Collins, CO, 49 pp.

Smith, E. A., and T. H. Vonder Haar, 1983: Satellite measurements and analysis of the radiation budget, cloudiness, and precipitation over MONEX. Final Report NSF-ATM-8200808, Dept. Atmos. Sci., Colo. State Univ., Fort Collins, CO, 2 volumes - 276 pp., 13 appendicies.

Smith, E. A., T. H. Vonder Haar, J. R. Hickey, and R. Maschhoff, 1983: The nature of the short period fluctuations in solar irradiance received by the earth. Climatic Change, 5, 211-235.

Smith, E. A., T. H. Vonder Haar, and M. Whitcombe, 1979: GATE satellite-surface radiation archives. Final Data Compilation Report, NSF Grant ATM-76-82697, Dept. Atmos. Sci., Colo. State Univ., Fort Collins, CO, 210 pp.

Smith, G. L., and T. D. Bess, 1983: Annual cycle and spatial spectra of earth emitted radiation at large scales. J. Atmos. Sci., 40, 998-1015.

Smith, G. L., and R. N. Green, 1981: Deconvolution of wide field-of-view radiometer measurements of earth-emitted radiation. Part I: Theory. J. Atmos. Sci., 38, 461-473.

Smith, W. L., L. D. Herman, T. Schreiner, H. B. Howell, and P. Menzel, 1981: Radiation budget characteristics of the onset of the summer monsoon. Proceedings of the International Conference on Early Results of FGGE and Large-Scale Aspects of its Monsoon Experiments, Tallahasse, FL, pp. 6.16-6.26.

Smith, W. L., J. Hickey, H. B. Howell, H. Jacobowitz, D. T. Hilleary, and A. S. Drummond, 1977: Nimbus-6 Earth Radiation Budget Experiment. Appl. Optics, 16, 306-318.

Smith, W. L., D. T. Hilleary, H. Jacobowitz, H. B. Howell, J. R. Hickey, and A. J. Drummond, 1975: The Earth Radiation Budget (ERB) Experiment. The Nimbus 6 Users' Guide, NSAS-Goddard Space Flight Center, Greenbelt, MD, 109-139.

Soule, H. V., 1983: Nimbus-6 and 7 Earth Radiation Budget (ERB) sensor details and component tests. NASA Tech. Memo. 83906, NASA-Goddard Space Flight Center, Greenbelt, MD, 32 pp., 5 Appendicies.

Stephens, G. L., 1976: An improved estimate of the IR cooling in the atmospheric window region. J. Atmos. Sci., 33, 5, 806-809.

Stephens, G. L., 1977: Transfer of radiation in cloudy atmospheres. Ph.D. Dissertation, Dept. of Meteorology, University of Melbourne, 396 pp.

Stephens, G. L., 1978: Radiation profiles in extended water clouds, II: Parameterization schemes. J. Atmos. Sci., 35, 2123-2132.

Stephens, G. L., S. Ackerman, and E. A. Smith, 1984: A shortwave parameterization revised to improve cloud absorption. J. Atmos. Sci., 41, 687-690.

Stephens, G. L., G. G. Campbell, and T. H. Vonder Haar, 1981: Earth radiation budgets. J. Geophys. Res., 86, 9739-9760.

Stephens, G. L., and P. J. Webster, 1979: Sensitivity of radiative forcing to variable cloud and moisture. J. Atmos. Sci., 36, 1542-1556.

Stephens, G. L., and P. J. Webster, 1984: Cloud decoupling of the surface and planetary radiative budgets. J. Atmos. Sci., 41, 681-686.

Stowe, L. L., 1983: The Nimbus-7 ERB sub-target radiance tape (STRT) data base for radiation budget studies. Bull. Amer. Meteor. Soc., 64, 1366.

Stowe, L. L., and M. D. Fromm, 1983: Nimbus-7 ERB sub-target radiance tape (STRT) data base. NOAA Techn. Memo. NESDIS 3, National Environmental Satellite and Data Information Service, NOAA, Dept. of Commerce, Washington, D.C., 54 pp.

Sutherland, R. A., and J. F. Bartholic, 1977: Significance of vegetation in interpreting thermal radiation from a terrestrial surface. J. Appl. Meteor., 16, 759-763.

Sutherland, R. A., J. F. Bartholic, and J. F. Gerber, 1979: Emissivity correction for interpreting thermal radiation from a terrestrial surface. J. Appl. Meteor., 18, 1165-1171.

Takahashi, K., and H. Arakawa, 1981: Climates of southern and western Asia. World Survey of Climatology Vol. 9, Elsevier Scientific Pub. Co., Amsterdam, 333 pp.

Tang, M. C., and E. R. Reiter, 1984: Plateau monsoons of the northern hemisphere: A comparison between North America and Tibet. Mon. Wea. Rev., 112, 617-637.

Tao, S. Y., and Y. H. Ding, 1981: Observational evidence of the influence of the Qinghai-Xizang (Tibet) Plateau on the occurrence of heavy rain and severe convective storms in China. Bull. Amer. Meteor. Soc., 62, 23-30.

Tarpley, J. D., 1979: Extimating incident solar radiation of the surface from geostationary satellite data. J. Appl. Meteor., 18, 1172-1181.

Tarpley, J. D., S. R. Schneider, and R. L. Money, 1984: Global vegetation indices from the NOAA-7 meteorological satellite. J. Clim. Appl. Meteor., 23, 491-494.

van de Boogaard, H. M., 1977: The mean Circulation of the tropical and sub-tropical atmosphere--July. NCAR Technical Note 118, National Center of Atmospheric Research, Boulder, CO.

Virji, H., W. L. Smith, A. J. Schreiner, and L. D. Herman, 1982: Earth-atmosphere radiation balance from geostationary satellite data for the summer monsoon onset region (Summer MONEX onset period: 11-20 June 1979). Tech. Report under NSF Grant ATM-8205386, Space Science and Engineering Center - NOAA/NESS Development Lab., Univ. of Wisconsin, Madison, WI, 252 pp.

Vonder Haar, T. H., 1968: Variations of the earth's radiation budget. Ph.D. Dissertation, Dept. of Meteorology, Univ. of Wisconsin, Madison, WI, 118 pp.

Vonder Haar, T. H., and J. S. Ellis, 1974: Atlas of radiation budget measurements from satellites (1962-1970). Dept. Atmos. Sci. Paper No. 231, Colo. State Univ., Fort Collins, CO, 180 pp.

Vonder Haar, T. H., and J. S. Ellis, 1976: Solar energy microclimate as determined from satellite observations. In Solar energy utilization, SPIE 68, 18-22.

Vonder Haar, T. H., E. Raschke, M. Pasternak, and W. Bandeen, 1972: The radiation budget of the earth-atmosphere system as measured from the Nimbus 3 satellite (1969-1970). Space Research XII - Akademie Verlag, 491-498.

Vonder Haar, T. H., and V. E. Suomi, 1969: Satellite observations of the Earth's Radiation budget. Science, 163, 667-669.

Vonder Haar, T. H., and V. E. Suomi, 1971: Measurements of the earth's radiation budget from satellites during a 5-year period. Part I: Extended time and space means. J. Atmos. Sci., 23, 305, 314.

Wade, N., 1974: Sahelian Drought: No victory for western aid. Science, 185, 234, 237.

Walker, J., and P. R. Rowntree, 1977: The effect of soil moisture on circulation and rainfall in a tropical model. Quart. J. Roy. Meteor. Soc., 103, 29-46.

Wallace, J. M., and C. P. Chang, 1969: Spectrum analysis of large-scale wave disturbances in the tropical lower troposphere. J. Atmos. Sci., 26, 1010-1025.

Wallace, J. M., and L. A. Chang, 1972: On the application of satellite data on cloud brightness to the study of tropical wave disturbances. J. Atmos. Sci., 29, 1400-1403.

Walshaw, C. D., 1957: Integrated absorption by the 9.6 micron band of ozone. Quart. J. Roy. Meteor. Soc., 83, 315-321.

Wark, D. Q., G. Yamamoto, and J. H. Lienesch, 1962: Methods of estimating infrared flux and surface temperature from meteorological satellites. J. Atmos. Sci., 19, 369-384.

Watson, K., 1975: Geologic applications of thermal infrared imagery. Proc. IEEE, G3, 128-137.

Webster, P. J., 1978: Lateral effects on monsoon systems. Indian J. Meteor. Hydrol. Geophys., 29, 235-244.

Webster, P. J., 1983: Mechanisms of monsoon low-frequency variability: Surface hydrological effects. J. Atmos. Sci., 40, 2110-2124.

Webster, P. J., and L. C. Chou, 1980: Low-frequency transitions of a simple monsoon system. J. Atmos. Sci., 37, 368-382.

Webster, P. J., L. C. Chou, and K. M. Lau, 1977: Mechanisms affecting the state, transition and evolution of the monsoons. Pure Appl. Geophys., 115, 1463-1491.

Webster, P. J., and K. M. Lau, 1977: A simple Ocean-atmosphere climate model: Basic model and a simple experiment. J. Atmos. Sci., 34, 1063-1084.

Weickmann, K. M., 1983: Intraseasonal circulation and outgoing longwave radiation modes during northern hemisphere winter. Mon. Wea. Rev., 111, 1838-1858.

Welch, R. M., S. K. Cox, and J. M. Davis, 1980: Solar radiation and clouds. Meteorological Monographs, 17, Amer. Meteor. Soc., Boston, MA, 96 pp.

Weller, G., and B. Holmgren, 1974: The microclimates of the Arctic tundra. J. Appl. Meteor., 13, 854-862.

Wendler, G., 1971: An estimate of the heat balance of a valley and hill station in Central Alaska. J. Appl. Meteor., 10, 684-693.

Wetherald, R. T., and S. Manabe, 1980: Cloud cover and climate sensitivity. J. Atmos. Sci., 37, 1485-1510.

Wetzel, P. J., 1978: A detailed parameterization of the atmospheric boundary layer. Ph.D. Dissertation, Dept. Atmos. Sci. Paper No. 302, Colo. State Univ., Fort Collins, CO, 195 pp.

Wetzel, P. J., D. Atlas, and R. H. Woodward, 1984: Determining soil moisture from geosynchronous satellite infrared data: A feasibility study. J. Clim. Appl. Meteor., 23, 375-391.

Winston, J. S., A. Gruber, T. I. Gray, M. S. Varnadore, C. L. Earnest, and L. P. Mannello, 1979: Earth-atmosphere radiation budget analyses derived from NOAA satellite data. June 1974 - February 1974 (Volumes 1 and 2). Atlas of Results, NOAA-NESS, Washington, D.C.

Winston, J. S., and A. F. Krueger, 1977: Diagnosis of the satellite-observed radiative heating in relation to the summer monsoon. Pure and Appl. Geophys., 115, 1131-1144.

Wiscombe, W., 1982: The ATRAD Model. Tech. Report, Dept. of Appl. Science, New York Univ., New York, NY, 26 pp.

Wydick, J. E., 1983: Broadband albedo estimates from narrowband multispectral satellite measurements. Preprint Vol. of Fifth AMS Conf. on Atmospheric Radiation, Amer. Meteor. Soc., Boston, MA, 403-406.

Wyrtki, K., 1971: Oceanographic atlas of the International Indian Ocean Expedition. Prepared by the University of Hawaii under Grants GP-5463, GA-1279 and GA-10277, National Science Foundation, Washington, D.C., 531 pp.

Yanai, M., 1983: Personnel communication.

Yanai, M., T. Murayama, T. Nitta, and Y. Hayashi, 1968: Power spectra of large scale disturbances over the tropical Pacific. J. Meteor. Soc. Japan, 46, 308-323.

Yap, D., and T. R. Oke, 1974: Eddy-correlation measurements of sensible heat fluxes over a grass suface. Boundary Layer Meteor., 7, 151-163.

Yasunari, T., 1976: Spectral analysis of monsoonal precipitation in the Nepal Himalaya. Seppyo, 38, 59-65.

Yasunari, T., 1979: Cloudiness fluctuations associated with the northern hemisphere summer monsoon. J. Meteor. Soc. Japan, 57, 227-242.

Yasunari, T., 1980: A quasi-stationary appearance of 30 to 40 day period in the cloudiness fluctuations during the summer monsoon over India. J. Meteor. Soc. Japan, 58, 225-229.

Yasunari, T., 1981: Structure of an Indian summer monsoon system with around 40-day period. J. Meteor. Soc. Japan, 59, 336-354.

Yeh, T. C., 1981: Some characteristics of the summer circulation over the Qinghai-Xizang (Tibet) Plateau and is neighborhood. Bull. Amer. Meteor. Soc., 62, 14-19.

Yeh, T. C., and C. C. Chang, 1974: A preliminary experimental simulation on the heating effect of the Tibetan Plateau on the general circulation over Eastern Asia in summer. Sci. Sin., 17, 397-420.

Yeh, T. C., and Y. X. Gao, 1979: The meteorology of the Qinghai-Xizang (Tibet) Plateau. Science Press, Beijing, 278 pp. (in Chinese).

Yeh, T. C., S. W. Lo, and P. C. Chu, 1957: The wind structure and heat balance in the lower troposphere over Tibetan Plateau and its surrounding. Acta. Meteorologia, 28, 108-121.

Yeh, T. C., R. T. Wetherald, and S. Manabe, 1983: A model study of the short-term climatic and hydrologic effects of sudden snow-cover removal. Mon. Wea. Rev., 111, 1013-1024.

Yeh, T. C., R. T. Wetherald, and S. Manabe, 1984: The effect of soil moisture on the short-term climate and hydrology change - a numerical experiment. Mon. Wea. Rev., 112, 474-490.

Yin, M. T., 1949: A synoptic-aerologic study on the onset of the summer monsoon over India and Burma. J. Meteor., 6, 393-400.

Young, J. A., H. Virji, D. P. Wylie, and C. Lo, 1980: Summer Monsoon wind sets from geostationary satellite data: Summer MONEX - 1 May to 31 July, 1979. Space Science and Engineering Center, Dept. of Meteor., NSF Grant ATM 78-21873, Univ. of Wis., Madison, WI, 127 pp.

Zandlo, J. A., W. L. Smith, W. P. Menzel, and C. M. Hayden, 1982: Surface temperature determination from an amalgamation of GOES and TIROS-N radiance measurements. J. Appl. Meteor., 21, 44-50.

Zangvil, A., 1975: Temporal and spacial behavior of large-scale disturbances in tropical cloudiness deduced from satellite brightness data. Mon. Wea. Rev., 103, 904-920.

Zhang, D., and R. A. Anthes, 1982: A high resolution model of the planetary boundary layer-sensitivity tests and comparisons with SESAME-79 data. J. Appl. Meteor., 21, 1594-1609.